© Copyright 2022

Austin Ryan Anderson

Further Investigation of a New RC Slab-Column Connection for Improved Seismic Performance of Multi-Story Buildings

Austin Anderson

A dissertation

submitted in partial fulfillment of the

requirements for the degree of

Master of Science in Civil Engineering

University of Washington

2022

Reading Committee:

Dawn E. Lehman, Chair

Charles W. Roeder

Marc O. Eberhard

Program Authorized to Offer Degree:

Civil and Environmental Engineering

University of Washington

Abstract

Further Investigation of a RC Slab to CFT Column Connection for Improved Seismic Behavior of Multi-Story Buildings

Austin Ryan Anderson

Chair of the Supervisory Committee:
Dawn E. Lehman
Civil and Environmental Engineering

Concrete Filled Steel Tube (CFST) columns have several advantages over reinforced concrete columns in that: (1) the steel tube provides confinement of the concrete and reduces damage to the concrete core, (2) they possess very high shear capacities, (3) the steel tube is placed at the optimum location for flexural resistance, and (4) they sustain large drift demands without damage. CFSTs also accelerate construction since: (1) the steel tube acts as permanent formwork, (2) in a slab-column system, the columns and slabs may be cast simultaneously, (3) most of the internal reinforcement can be eliminated.

Previously an experimental program was undertaken to investigate a proposed connection for use in flat-plate construction. The connection consists of steel rings on either side of the column with post-tensioned bolts to connect the rings and provide active confinement to the slab. The forces

are transferred from the upper column to the lower column through reinforcement welded to the inside of the tube of the lower column. The ring also increases the critical perimeter for shear. A four-specimen program investigated the impact of the following design variables: (1) ring size, (2) number of bolts within the ring flange, and (3) bolts outside of the ring. A reference specimen using conventional stud-rail detailing was built. This experimental program aimed to further that research by investigating the effect of slab depth on the connection. In addition, two full-scale push-through tests were conducted to better understand the two-way shear behavior of the proposed connection.

The conventional stud-rail connection sustained damage at low drift levels, which resulted in loss of strength. This behavior compromises the integrity and resilience of flat-plate buildings. The new connection provides drift capacities of 4% or greater before strength loss and mitigates damage, meeting the structural objective of integrity and resilience after a large seismic event. The research suggests that the ring dimension depends on both the column size and thickness of the slab. Test results showed better behavior with two rows of bolts on the ring flange. Although bolts outside the ring are beneficial, this detail was deemed impractical for new construction but may be viable for increasing shear capacity in retrofit design. Two-way shear strength resulted in a higher capacity for the connection with the larger ring flange and that ACI predictions of capacity were conservative.

TABLE OF CONTENTS

LIST OF FIGURES

LIST OF TABLES

ACKNOWLEDGEMENTS

I would like to acknowledge first and foremost my advisors Dawn Lehman and Charles Roeder for their guidance during my research. The contributed significantly to my understanding of the subject and have helped me tremendously in getting my thesis to where it is today. I would also like to thank Marc Eberhard for serving on my committee.

I would also like to thank the National Science Foundation for funding my research without their support this research does not happen. In addition, I would like to thank Farwest Steel for donating the slab reinforcement for my thin slab specimens.

There are many people that helped during my construction and testing phases. The most prominent is Vince Chaijaroen. His countless hours coordinating with me and helping with planning and inspecting helped to keep all of the students safe and testing running smoothly. The students I would also like to acknowledge include: Alec Yeutter, Joe Kaldestad, Spencer Lindsey, Kira Twitchell, Will Bergendahl, Will Krause, Clayton Black, Carolyn Donohoe, John Paul Gaston, among others that helped.

Finally I would like to acknowledge my family and friends. Their words of encouragement and support helped tremendously and I can't thank them enough for all they have done for me to help me accomplish this task.

Chapter 1. INTRODUCTION

1.1 RESEARCH IMPETUS

Concrete filled steel tubes (CFSTs) have shown promise for use as columns. They are stronger in shear, axial, and flexure loading than similarly sized reinforced concrete (RC) columns (Stephens 2016). CFSTs have been shown to sustain loads surpassing yielding of the column without loss of strength or deformability. These qualities make them well suited for construction of columns in high seismic regions.

These qualities also are beneficial for Vertical Evacuation Structures (VES). VESs are found in locations along the coast with high seismicity. After a coastal earthquake is triggered a tsunami wave follows. As a result VESs have to adopt a different design philosophy in which the superstructure is able to withstand minimal damage under near fault earthquake loading and remain functional after the sequential loading of the tsunami often at much larger demands than the earthquake. This makes CFSTs, especially circular, uniquely beneficial in this regard. They have higher stiffness limiting damage to other components of the superstructure. The higher capacity strengths make them more efficient for design of higher demands required of VESs. The concrete fill restrains local buckling and assures increased ductility of the steel tube. The tube confines and reinforces the concrete to assure greater shear resistance and composite behavior.

The limitation to the use of CFSTs has been the connection of the column to other structural components. Previous research has investigated CFSTs in use for bridge construction, but few studies have investigated CFST connections in RC buildings. CFSTs are efficient for construction. The tubes act as permanent formwork and eliminates the need for internal reinforcement to resist shear and flexure. This is particularly helpful in high seismic regions that require stricter transverse detailing of RC columns. The column and slab can be cast simultaneously reducing typical construction sequencing.

1.2 PROPOSED CONNECTION

Current design practices have shown the popularity of the use of slab-column gravity systems. A new CFST to RC slab connection for slab-column systems shown in Figure 1.1 will be studied in this research. The connection consists of a CFST column that is discontinuous through the slab. The CFSTs have rings welded to both ends of the tube and are detailed as shown in Figure 1.2. The rings allow for the tubes to be fastened to the slab with bolts that are then post-tensioned to confine the slab region beneath the ring. In addition to securing the columns to the slab, the ring flange also extends the critical perimeter of the connection providing increased punching strength to the connection. To allow for transfer of loading between the top and bottom column, the column has longitudinal reinforcement passing through the discontinuous region of the column. The reinforcement is welded to the lower tube and extends the development length into the upper tube. The reinforcement is also bent below the top surface of the slab to allow for easier placement of the upper tube after the slab has been cast.

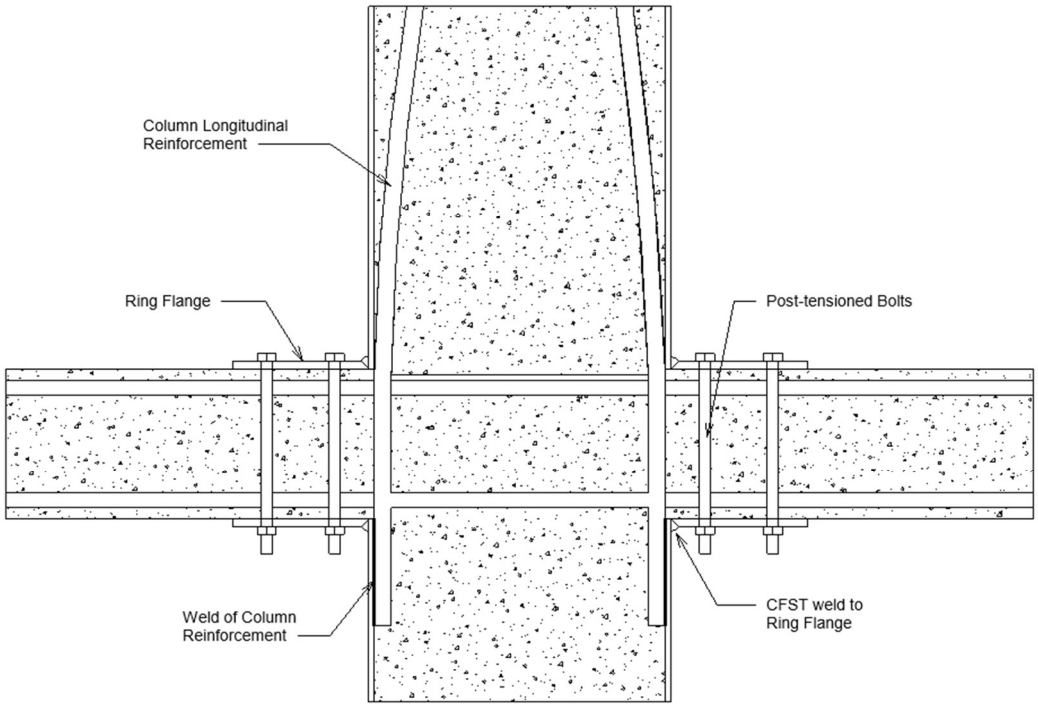

Figure 1.1. New Connection Details

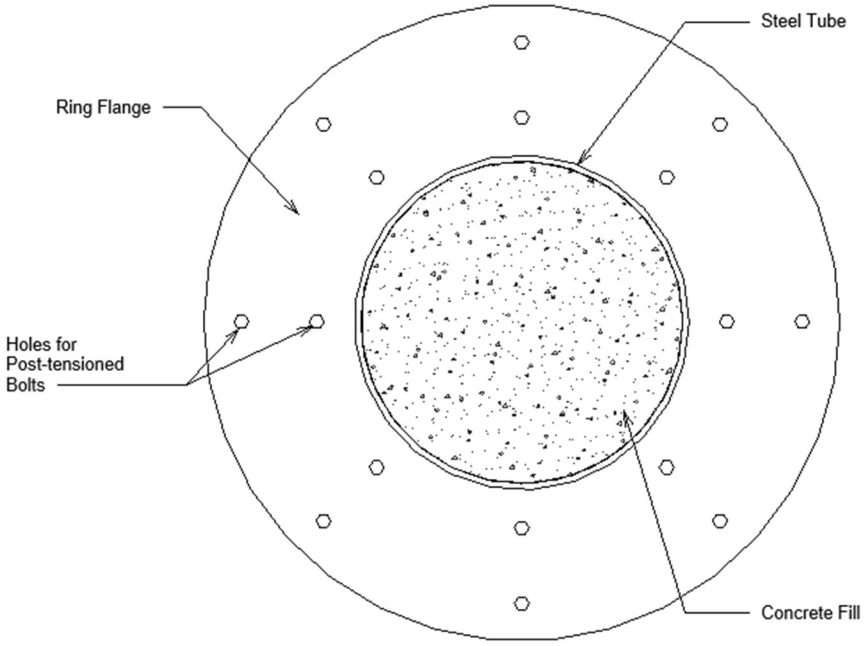

Figure 1.2. Ring Details

1.3 RESEARCH OBJECTIVES

The research builds upon a previous study of the new connection by Yeutter (2020). He compared different configurations of the ring to a reference specimen designed using stud rails. The specimens were subjected to combined-loading where an axial load was applied to the column to simulate gravity load, and a cyclic lateral deformation of the specimen was applied to investigate the behavior of the connection at increasing drift levels due to seismic loading. This experimental study extends that research by investigating the relationship between the width of the ring flange and the slab depth. This is done to evaluate the depth of the slab as a viable design parameter for sizing the ring flange. These specimens combined with the results presented by Yeutter, were observed to initiate strength loss due to flexural mechanisms. For that purpose two additional specimens were tested to investigate how the connection behaves when subjected to punching shear loading.

1.4 ORGANIZATION OF THESIS

In the investigation of the research objectives the thesis consists of an additional seven chapters that cover the following topics:

- **Chapter 2: Literature Review**, provides a summary of previous experimental work that relates to the testing of flat plate structures in both combined-loading and punching shear resistance.
- **Chapter 3: Experimental Test Program**, provides the specimen geometry as well as the setups and procedures of experimental testing.
- **Chapter 4: Experimental Observations Combined-Loading Specimens**, provides the observations made during testing of the thin slab specimens subjected to combined-loading.
- **Chapter 5: Data Analysis of Combined-Loading Specimens**, analysis of the results from the combined loading tests and comparison of the results to the previous study by Yeutter.
- **Chapter 6: Experimental Observations and Data Analysis of Punching Specimens**, provides the observations made during testing of the punching specimens as well as analysis of their results.
- **Chapter 7: Evaluations of Results Using Design Expressions**, compares the results of testing to existing design expressions.
- **Chapter 8: Summary, Conclusions, and Future Work**, presents the main findings of the experimental test program and provides recommendations for future research.

Chapter 2. LITERATURE REVIEW

This chapter summarizes previous testing programs that are relevant to the research of this thesis. In addition this chapter also presented the results from Phase 1 of the research program that preluded the research of this thesis.

The testing programs are separated into two different groups: (a) cyclic tests of specimens subjected to axial loading in the column and, horizontal drift history and (b) monotonically loaded punching specimen

The objectives of the chapter are to:

- Review previous research investigating conventional slab-column connections. Both cyclic tests and monotonic punching tests were reviewed.
- Identify the primary design parameters that control slab-column connection behaviors.
- Investigate previous test setups to determine which would be best suited for the tests of this paper.
- Use the prior data to investigate the accuracy of current design equations in the US and international concrete codes.

The test program summaries consisted of:

- Research objectives
- Testing parameters
- Specimen geometry
- Test setup
- Test procedure
- Results
- Research Conclusions

The testing programs are separated into two separate sections. The first section discusses test programs under combined loading. The latter section discusses test programs subjected to monotonic axial loading of the column to identify punching strength.

Table 2.1 provides information about the test specimens subjected to combined loading. The slab dimensions and column dimensions are given. Specimen scale varied from half-scale to full scale which is easiest to see by the variation in slab depth. The longitudinal reinforcement ratios are given for both the top and bottom slab as well with majority of the top reinforcement ratio being between 0.5 and 1.5 percent. Throughout the literature shear reinforcement has evolved. Earlier tests relied upon stirrups to provide additional shear strength to the specimens while later tests introduced stud rails and shear capitals as ways to investigate the viability of other forms or shear reinforcement.

Table 2.1. Unbalanced Moment Specimen Details

Year	Authors	No. of Tests	Slab Dimensions (in.)			Column Dim. (in.)	Longitudinal Reinforcement Ratio (%)		Transverse (Shear) Reinforcement
			Length	Width	Height		Top	Bot.	
1974	Hawkins, Mitchell, & Sheu	6	156	84	6	12x12	0.57 to 1.29	0.26 to 0.56	None, Stirrups
1975	Hawkins, Mitchell, & Hanna	5	156	84	6	12x12	0.90 to 2.01	0.49 to 0.87	Stirrups
1976	Symonds	6	156	84	6	12x12	0.57 to 1.10	0.40 to 0.56	None, Stirrups
1976	Ghali, Elmasri, & Dilger	6	72	72	6	12x12	0.50 to 1.50	0.17 to 0.50	None
1987	Elgabry & Dilger	5	71	71	5.9	12x12	0.50 to 1.50	0.17 to 0.50	Stud Rails
1992	Pan & Moehle	4	144	144	4.8	10.8x10.8	0.73	0.29	None
1992	Wey & Durrani	4	114	78	4.5	10x10	0.96	1.23	Shear Capitals
2002	Robertson, Kawai, Lee, & Enomoto	4	118	108	4.5	9.8x9.8	0.74	0.74	None, Closed Hoop, Single Leg Stirrups, Headed Studs
2020	Yeutter	4	156	72	10	20 Dia.	1.00	1.00	Headed Studs, Post-Tensioned Bolts with Ring Flange

Additional information about the combined loading test programs is found in Table 2.2. This table provides information for two other important variables that affect these test programs, including, the additional gravity shear on each specimen. For slab-column connections subjected

to combined-loading one of the possible failure modes is two-way punching. The applied shear stress had two components: (1) stress due to gravity loading and (2) shear stress developed to resist the unbalanced moment. It is important to include the additional additional gravity shear applied to test specimens because it can reduce the ductility. This additional gravity load is typically accounting for the superimposed dead load (10-20 psf) and the live load (20-100 psf). However, in an earthquake, seismic evaluation methods only use one-quarter of this live load, or 5-25 psf and in many cases, there is little to no live load at the time of the earthquake. Given that typical slab thicknesses are between 6 and 12 in. the self-weight contribution to the dead load is 75-150 psf. The addition of gravity load is approximately between 15 and 45 psf. In some cases, including the research reported herein, this additional load was not applied to the test specimens.

In addition, Table 2.2 provides type of loading. This refers to how the lateral loading is applied to the slab-column connection. All of the test programs included used uniaxial loading of the specimens. The majority of test programs used pseudo-static loading with the exception of Ghali, Elmasri, and Dilger (1976) who compared the effects of pseudo-static and dynamic loading of their specimens.

Table 2.2. Unbalanced Moment Test Details

Year	Author	Gravity Load (kip)	Gravity Shear (psi)	Loading Type
1974	Hawkins, Mitchell, & Sheu	28.2 to 33.7	94.9 to 107.7	Pseudo
1975	Hawkins, Mitchell, & Hanna	28.3 to 29.9	95.3 to 100.7	Pseudo
1976	Symonds	53.0 to 61.0	178.5 to 205.4	Pseudo
1976	Ghali, Elmasri, & Dilger	29.0	91.1	Pseudo and Dynamic
1987	Elgabry & Ghali	33.7 to 101.2	128.3 to 385.3	Pseudo
1992	Pan & Moehle	14.0 to 22.8	61.1 to 97.2	Pseudo
1992	Wey & Durrani	9.0	13.5 to 42.8	Pseudo
2002	Robertson, Kawai, Lee, & Enomoto	11.5 to 11.7	53.6 to 54.7	Pseudo
2020	Yeutter	9.8	6.5 to 10.4	Pseudo

Table 2.3 compares the test programs investigated for the punching tests. These tests consisted of a rectangular (most commonly square) slab supported on all edges with a column in the center of the slab; the column is loaded axially. The slab depth was similar throughout the testing programs; however, the slab area varied significantly. The variation in column size is also

important to note due to how the column size affects the two-way shear critical perimeter and therefore the overall two-way shear strength of the specimens.

The longitudinal reinforcement is also provided. The top reinforcement refers to the side that would be experiencing the maximum tension stress, although test specimens may have been tested upside down due to limitations of testing equipment. Due to the top side of the specimen experiencing tension while the bottom side experiences compression, the bottom flexural reinforcement ratio is typically significantly lower than the top. Typically testing programs included one specimen without shear reinforcement to act as a control specimen, while the other test were comprised of variations of a particular shear reinforcement to examine the effectiveness in improving the two-way shear capacity of the specimens.

Table 2.3. Punching Shear Specimen Details

Year	Author	No. of Tests	Slab Dimensions (in.)			Column Dim. (in.)	Longitudinal Reinforcement Ratio (%)		Transverse (Shear) Reinforcement
			Length	Width	Height		Top	Bot.	
2016	Dam & Wight	3	120	120	10	12x12	0.84	0.34	None, Stud Rails
2019	Jang & Kang	6	72.8	72.8	8.3	17.7x17.7	0.77 to 1.53	0.31 to 0.77	None, Single Leg Stirrups
2019	Saleh, Kalfat, Abdouka,& Al-Mahaidi	4	90.6	90.6	7.9	7.9x7.9	1.50	0.26	None, L-Shaped CFRP Laminate

2.1 UNBALANCED MOMENT TEST PROGRAMS

2.1.1 *Hawkins, Mitchell, and Sheu (1974)*

In the mid 1970's, researchers at the University of Washington intiated an experimental testing program that would span three papers and fourteen flat plate slab-column connection specimens. Hawkins, Mitchell, and Sheu conducted the first set of tests. The purpose of the overall test program was to develop design criteria for a ductile slab-column connection as well as an analytical procedure to predict energy absorption capabilities of the connection given an arbitrary lateral loading.

Hawkins, Mitchell, and Sheu's work focused on establishing a relationship between the test parameters of flexural reinforcement ratio, presence of shear reinforcement, and load history with the strength, ductility, energy absorption, and energy dissipation. The testing program consisted of six full scale interior slab column connections. Four of which had no shear reinforcement while the other two used integral beam stirrups for shear reinforcement. The dimensions were the same for all six specimens: the slab was 156 x 84 x 6 in. (length, width, and depth) and the columns were square measuring 12 x 12 in. in plan and extended 42 in. above and below the slab. Figure 2.1 shows that the pivot point was at 48 in. above and below the slab. The reinforcement variations were tabulated by Hawkins, Mitchell, and Sheu and the table has been replicated below in Table 2.4. Specimens S1 and S4 were identical and only differed in load history. It should be noted that when describing the shear reinforcement, spacing refers to the distance between individual stirrups while the reinforced length refers to the distance from the face of the column to the stirrup furthest from the face.

Table 2.4. Hawkins, Mitchell, and Sheu (1974) Specimen Details

Specimen	Top Bars			Bottom Bars			Shear Reinforcement		
	Bar Size (No.)	Bar Spacing (in.)	Reinf. Ratio (%)	Bar Size (No.)	Bar Spacing (in.)	Reinf. Ratio (%)	Bar Size (No.)	Spacing (in.)	Reinforced Length (in.)
S1	6	7.5	1.29	4	7.5	0.56	None		
S2	5	7.5	0.90	4	9.0	0.49	None		
S3	4	7.5	0.57	3	9.0	0.26	None		
S4	6	7.5	1.29	4	7.5	0.56	None		
SS1	6	7.5	1.29	4	7.5	0.56	3	1.5	14.25
SS2	5	7.5	0.90	4	0.90	0.49	2	1.5	9.75

Each specimen was subjected to combined loading that comprised of three different loading systems. A prestressed rod running through the columns applied an axial load to the column to simulate gravity loading of upper stories. The gravity load jacking system simulated gravity loading on the slab and consisted of four jacks positioned at four points along a circle with a 3 ft. radius centered at the column. Back pressure in the gravity jacks ensured that the jacks would apply a constant gravity load once they reached the target load for each test. The lateral jacking system consisted of four pairs of push-pull type jacks located in a line along the edges of the slab 6 ft. from the column center. The pairs worked in opposite directions on opposite ends of the slab to impose the bending moments at the connection.

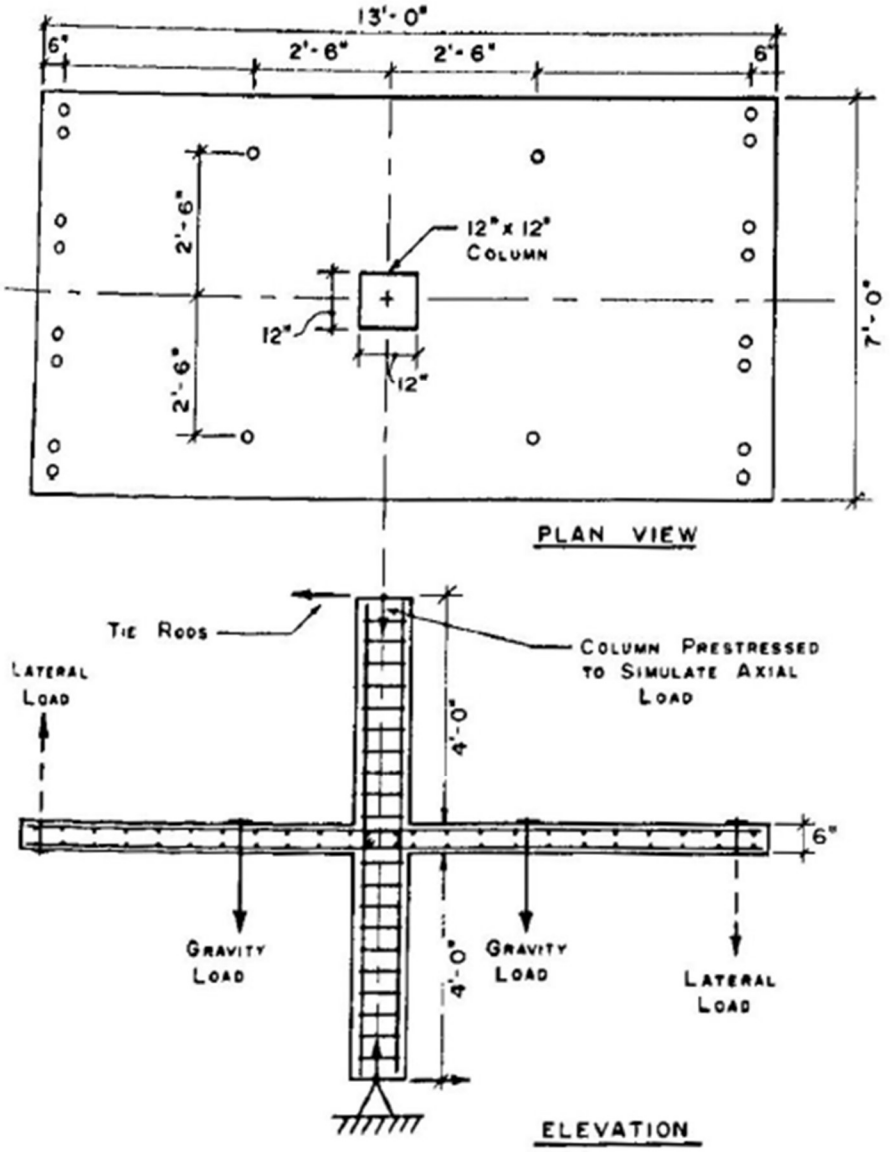

Figure 2.1. Hawkins, Mitchell, and Sheu (1974) Test Setup

The testing procedure began with prestressing rod extending through the column to 50 kips. The gravity shear force was applied in three equal increments to reach the target load. The lateral load was then applied in one direction in increments of approximately 1.1 kips up to the target load, then decreased in similar increments back to zero before being loaded in the opposite direction. This process made up a single cycle of loading.

The lateral loading of Specimens S1 and S2 were loaded so that each cycle increased the lateral load applied before being pushed to failure. Specimens S1 and S2 were cycled twice and once respectively before being pushed to failure. Specimens S3 and S4 started at a lower initial

lateral load than Specimens S1 and S2 and were loaded in sequences that consisted of 5 cycles per sequence with each subsequent sequence targeting a 1.1 kip increase in lateral force. This load history was referred to as high intensity reversed cyclic loading. Specimen S3 failed during its first sequence. Specimen S4 failed during its fifth sequence at a lower load than Specimen S1. The sequences of Specimens SS1 and SS2 targeted a specific displacement in contrast to the previous force controlled tests. After completion of cyclic loading of Specimens S3, S4, and SS2, the residual shear capacity of the specimens was examined by loading the specimens with only the gravity load jacking system to simulate pure shear loading of the connection.

Instrumentation was used to record applied loads, deflections, rotations, and strains at half cycle peaks for single cycles. For sequences that repeated the target load or displacement for multiple cycles, measurements were recorded at the half cycle peaks for the last cycle of the sequence. Crack maps were also record at each loading increment to understand the behavior of the connection leading up to failure.

Specimen S1 was loaded beginning at 80 percent of the moment-transfer capacity predicted by ACI 318-71. The specimen did not fail until reaching 60 percent greater than the predicted moment transfer capacity. Specimen S1's failure was characterized as a punching failure with the damage focused near the face of the column on the side where the shear stress due to unbalanced moment was additive to the shear stress due to gravity loading of the slab. Moment transfer capacity and ductility after failure were negligible. All bars in the column region are suspected of yielding before failure, suggesting flexural degradation also influenced the failure mode of Specimen S1.

The dead load applied to Specimen S2 was 20 percent higher than the design dead load. S2 failed at a load roughly 30 percent greater than the ACI 318-71 predicted moment transfer capacity. The failure mode was determined to be by punching failure. The inclined crack was seen originating near the face of the column on the compression side and propagating out to about one slab thickness away from the column face on the tension side. Moment transfer capacity and ductility after failure were negligible. While some yielding occurred in the top flexural reinforcement, bottom reinforcement never exceed 50 percent of the yield strain. This behavior led researchers to believe that shear controlled the failure of Specimen S2.

Specimen S3 was cycled at the same load four times, before failing on the fifth cycle at a lower load and deflection than the previous cycles. The four initial cycles were at 80 percent of

the ACI predicted capacity, while load reached during the fifth cycle was only 65 percent of the ACI predicted capacity. Specimen S3 suffered punching failure with damage extending further around the column than noticed in Specimens S1 and S2. Crack development for Specimen S3 was noticeably less than for specimens with higher flexural reinforcement. The moment-transfer capacity and ductility were negligible after failure. Bars through the column and immediately adjacent to the column yielded during the first half cycle. The bottom reinforcement never exceeded 60 percent of the expected yield stress indicating that shear controlled the failure mode of this specimen.

Specimen S4 was nominally identical to Specimen S1 subjected to a different lateral loading sequence. Specimen S4 failed at a lateral load about 53 percent greater than the ACI predicted moment transfer capacity which was like the failure of Specimen S1. The failure was determined by punching at the column face, the extent of damage was similar to Specimen S1. After failure the moment transfer capacity and ductility were negligible. Yielding of top reinforcement began during the final target drift sequence. By the cycle at which Specimen S4 failed top bars going through the column as well as the first bar on either side of the column had yielded. The bottom bars did not seem to yield; however, there was some doubt about the validity of one of the bottom gages that seemed to yield far before any of the other bars. Due to the outlier behavior of the one bottom bar, the yielding is believed to have been confined to the top reinforcement similar to Specimens S2 and S3 and indicating that shear controlled the failure of Specimen S4.

Specimen SS1 underwent many more cycles than the other unreinforced specimens. At discontinuation of the test, due to increasing strength degradation between cycles, all of the top flexural reinforcement had yielded, while the bottom reinforcement had yield for bars through the column as well as the next two bars on either side of the column. The connection showed there was still considerable reserve for energy dissipation at the end of testing. Stirrups parallel to the direction of loading had small strains until crushing of the concrete. After that yielding was recorded. Stirrups on the reinforcement transverse to the direction of loading reached strains near yield at the end of testing. No punching failure was evident at the end of testing. There was crushing located at the column face. The visual concrete damage as well as the strain gage measurements indicate flexure controlled the failure of Specimen SS1. Specimen SS1 failed at a load 130 percent greater than ACI predicted capacity for a non-shear reinforced slab, and 25

percent greater than the ACI predicted capacity for a shear reinforced slab. Comparison of the load-deflection envelops show that Specimens SS1 and S4 behaved similarly up to yielding of the top steel. Specimen SS1 was able to sustain a higher loading than the ultimate loading reached by S4 at a deflection twice the ultimate deflection of Specimen S4. The presence of shear reinforcement had little impact on the shape of the hysteretic curve for SS1.

Specimen SS2 sustained a punching failure after a malfunction with the lateral loading system caused a sharp peak load to be applied to the specimen. The specimen was then cycled at deflection limits approximately equal to the maximum deflection from the spike loading. The strength steadily degraded during this cycling. Punching failure is believed to have occurred because the diagonal lines in the critical perimeter connecting the ends of the shear reinforcement were too close to the column corners, triggering a premature punching failure. Top reinforcement passing through the column and immediately outside of the column yielded. Post punching failure, the bottom reinforcing bars passing through the column yielded; however, this was only on the side where the punching failure had occurred. Due to the sharp peak load, stirrup yielding adjacent to the side column faces was observed. The stirrups adjacent to the front and back faces of the column did not yield until later cyclic loading near the end of testing. It is believed that the specimen sustained a flexure-shear failure. After the punching failure Specimen SS2 still had considerable ductility, reaching twice the deflection of Specimen S2 while supporting the same ultimate load of Specimen S2. Hysteretic loops where wide until crushing of concrete caused them to become more thin like the hysteretic loops of Specimen SS1.

Specimens S3, S4, and SS2 were all tested to investigate the post-peak residual shear capacity. Specimens S3 and S4 showed that they could reach a residual capacity of approximately 35 percent greater than the applied dead load. Any loading past the target dead load value resulted in large rotations of the specimens with eccentricities. Specimen SS2 reached a residual capacity 70 percent greater than the target dead load. Specimen SS2 did not show any sensitivity to eccentricities.

Hawkins, Mitchell, and Sheu stated that there was not adequate information to draw definitive conclusions from this set of 6 tests; however, there were some trends that were notable.

- High intensity reversed cyclic loadings can result in connections having maximum capacities as much as 20 percent less than those of similar connections loaded monotonically to failure.

- The magnitude of the lateral load for yield of the top bars of the slab passing through the column is probably the critical factor dictating the strength of connections subjected to high intensity reversed cyclic loading.
- The critical factors determining the response of connections with shear reinforcement are the amount, extent and spacing of the shear reinforcement, the force corresponding to initial yielding of the top bars of the slab passing through the column and the force corresponding to crushing of the concrete on the compression face of the slab at the slab-column interface.
- After punching or concrete crushing, the lateral load capacity of a connection with shear reinforcement decreases with increased cycling. The rate of decrease is faster when a punching failure has occurred.
- The shear reinforcement should extend sufficiently far out from the column that a potential failure surface joining the ends of the reinforced length approaches no closer than one and one half times the slab thickness to the column perimeter.

2.1.2 *Hawkins, Mitchell, and Hanna (1975)*

Hawkins, Mitchell, and Hanna conducted five tests on interior slab column connections. The primary objectives of their research were to determine the following.

- How to adequately detail transverse slab reinforcement for the connections.
- The residual gravity capacity of slabs that have undergone reversed cyclic loading.
- The effects of concentrating flexural slab reinforcement within the column region, defined as $1.5h$ on either side of the column, with h being the thickness of the slab.

Therefore the testing parameters were the amount and distribution of flexural reinforcement in the slab, the size, type, and length of the stirrups, and the load history for the tests.

The specimens were designed to replicate a full scale prototype structure. The dimensions remained the same for all five specimens with a slab that was 156 x 84 x 6 in. and a square column of 12 x 12 in. extending 48 in. above and below the slab. The specimens varied in reinforcement. Specimens SS1, SS2, and SS5 all had evenly distributed flexural reinforcement, while Specimens

SS3 and SS4 had matching flexural reinforcement that was concentrated in the column region. All of the specimens had shear reinforcement in the form of stirrups with 135° bends; however, in Specimens SS1 and SS2 half of the transverse reinforcement was single horizontal leg stirrups while the other half were double horizontal leg stirrups. The spacing of the stirrups was a constant 1.5 in. for all specimens, but the size and length varied from No. 2 bars to No. 3 bars and 11.25 in. to 15.75 in., respectively. The exact detailing of the specimens is tabulated below in Table 2.5. Specimens SS3 and SS4 are have identical detailing, but their loading history was varied.

Table 2.5. Hawkins, Mitchell, and Hanna (1975) Specimen Details

Specimen	Top Bars			Bottom Bars			Shear Reinforcement		
	Bar Size (No.)	Bar Spacing (in.)	Reinf. Ratio (%)	Bar Size (No.)	Bar Spacing (in.)	Reinf. Ratio (%)	Bar Size (No.)	Spacing (in.)	Reinforced Length (in.)
SS1	6	7.5	1.29	4	7.5	0.59	3	1.5	15.75
SS2	5	7.5	0.9	4	9	0.49	2	1.5	11.25
SS3	6, 4	5, 8	1.1	4, 3	5, 8	0.56	3	1.5	14.25
SS4	6, 4	5, 8	1.1	4, 3	5, 8	0.56	3	1.5	14.25
SS5	5	7.5	0.9	4	9	0.49	2	1.5	12.75

The setup of these tests followed the same setup as Hawkins, Mitchell, and Sheu which is shown in Figure 2.1 and is described in Section 2.2.1.

The test results from Hawkins, Mitchell, and Sheu were compared with the results from Hawkins, Mitchell, and Hanna and showed that specimens with adequate shear reinforcement and similar flexural reinforcement had improved ductility, energy absorption, and strength than specimens without shear reinforcement. The amount of improvement between the specimens appeared to increase with decreasing flexural reinforcement ratios. Specimens with shear reinforcement also showed improved residual strength than specimens without shear reinforcement. For comparing the types of stirrups used in the shear reinforcement there was no appreciable difference in either half of the shear reinforcement types of Specimens SS1 and SS2 so the remaining three specimens used single horizontal leg stirrups. Comparison of Specimens SS2 and SS5 helped to investigate the effect of varying the length of the shear reinforcement. Specimen SS2 failed in punching at a considerably lower lateral load than Specimen SS5. This was attributed to the formation of a shear crack developing at the corner of the column. Due to the difference in the ultimate strengths of Specimens SS2 and SS5 it was determined that the distance

of the critical perimeter to the corner of the column should also be considered in determining the required length of shear reinforcement.

Specimens SS3 and SS4 had concentrated flexural reinforcement in their column region that resulted in a higher flexural reinforcement ratio than Specimen SS1 within that column region. The reasoning behind this concentration was to have more flexural reinforcement in the slab region that was thought to be effected by lateral loading rather than more flexural reinforcement across the entire slab especially if areas outside the column region may not need it. There was no marked improvement in the strength or ductility of Specimen SS4 relative to the other specimens. However, Specimen SS3 which had a less severe loading pattern than Specimen SS4 showed some improvement over Specimen SS1. Comparing the results of Specimens SS3 and SS4 with the results of Specimens SS2 and SS5 which had lower reinforcement ratios showed that there was a definite limit to the amount of flexural reinforcement that was effective in the column region.

The test results led Hawkins, Mitchell, and Hanna to draw the following conclusions:

- A flat plate slab to column connection will behave in a ductile manner and have adequate residual shear strength if properly designed and detailed integral beam stirrup reinforcement is provided in the slab.
- The beneficial effects of providing properly designed and detailed integral beam stirrup reinforcement in the slab are: (a) an increase in the ductility of the connection at ultimate load, (b) an increase in the energy absorption of the connection along with a decrease in stiffness with cycling, (c) a change in the hysteretic behavior of connections with low reinforcement ratios from a shear to a moment type of energy dissipation mechanism, (d) an increase in the strength particularly for low reinforcement ratios, and (e) an increase in the residual shear capacity.
- In order for the stirrups to be fully effective they must be detailed so that: (a) they are closed hoops with a longitudinal reinforcing bar in each corner, (b) they are anchored by $135°$ standard bends around one or more longitudinal bars, and (c) they extend far enough out from the column face into each column strip that the wide beam shear force V_u on the periphery… does not result in a shear stress V_u/bd exceeding $2\sqrt{f'_c}$… and that the perimeter does not approach closer than $1.5h$ to the column perimeter.

- The behavior of the connection, especially for low reinforcement ratios, is likely to be improved if the flexural reinforcement is concentrated around the immediate column region.

2.1.3 *Symonds (1976)*

Symonds continued the University of Washington's testing program. The research tested five interior slab column connections with the test parameters being the amount and distribution of flexural reinforcement as well as the presence of shear reinforcement in the slab.

The specimens had the same geometric dimensions, with the slab being 156 x 84 x 6 in. and the column being 12 x 12 in. extending 48 in. above and below the slab. The flexural reinforcement varied between Specimens S6, S7, and S8, with S6 having a high concentration of flexural reinforcement in the column region. Specimens SS6 and SS7 had the same flexural reinforcement of Specimens S7 and S6, respectively, with the addition of shear reinforcement. The flexural and shear reinforcement in Specimen SS6 match the reinforcement in Specimen SS4 from Hawkins, Mitchell, and Hanna. The reinforcement variations have been tabulated below in Table 2.6.

Table 2.6. Symonds (1976) Specimen Details

Specimen	Top Bars			Bottom Bars			Shear Reinforcement		
	Bar Size (No.)	Bar Spacing (in.)	Reinf. Ratio (%)	Bar Size (No.)	Bar Spacing (in.)	Reinf. Ratio (%)	Bar Size (No.)	Spacing (in.)	Reinforced Length (in.)
S6	6, 4	5, 8	1.10	4, 3	5, 8	0.56	None		
S7	5	7.5	0.90	4	9	0.49	None		
S8	4	7.5	0.57	3	9	0.40	None		
SS6	5	7.5	0.90	4	9	0.49	2	1.5	12.75
SS7	6, 4	5, 8	1.10	4, 3	5, 8	0.56	3	1.5	20.25

The testing setup for Symonds' testing mimicked the previous University of Washington testing programs and is shown in Figure 2.1 and is described in Section 2.2.1. The research used the procedure by Hawkins, Mitchell, and Sheu. The column was first prestressed to 50 kips. The gravity load was applied in seven increments to reach the target value for testing. The lateral load was increased in three increments to reach a desired steel strain or displacement of the slab and was then decreased in three increments to zero. After a half cycle the loading direction was

reversed. The sequences of cycling that made up the test procedure consisted of three full cycles at a target displacement before increasing the target displacement for the next test sequence. The sequence deflections were selected based upon target strains in the top flexural reinforcement through the column. Cycling continued until the slabs failed. In addition, for some specimens, the loading was continued to determine the residual capacity.

The testing of the specimens without shear reinforcement focused on the effects of the amount and distribution of flexural reinforcement. All of the specimens showed higher levels of strain in the flexural reinforcement in the column region than outside of it. This was true for all of the specimens without shear reinforcement regardless of how the flexural reinforcement was distributed. The amount of flexural reinforcement seemed to effect the propagation of yielding of the top slab flexural reinforcement across the slab. As the flexural reinforcement ratio decreased going from Specimens S6 to S8, the number of bars that yielded across the slab increased. In addition the load and deflection at failure were also higher for specimens with higher flexural reinforcement. Specimen S7 had wider hysteretic loops than Specimen S6. This relationship of hysteretic width to flexural reinforcement ratio was difficult to determine in Specimen S8, which had yielded all of the flexural reinforcement across the top slab from the gravity loading alone. The gravity loading also yielded the top flexural reinforcement through the column as well as immediately outside the column for Specimen S7. This initial yielding could have decreased the stiffness of the specimens leading to wider hysteretic loops.

Specimens SS6 and SS7 both exhibited a punching response at the peak load, with the failure surfaces being outside the shear-reinforced region. The strains in the stirrups were relatively small throughout testing. Specimens SS6 and SS7 had more extensive yielding across the top slab flexural reinforcement in comparison to their respective specimens without shear reinforcement. Specimens SS6 and SS7 were more ductile than their counterparts suggesting that the presence of shear reinforcement can improve ductility in the connection.

The residual shear tests showed that the slab moved down almost as a rigid body. During the testing of Specimen S6, the top bars had undergone larger amounts of debonding so that they contributed little to the residual strength. However, the bottom bars acted similarly to dowels and were believed to contribute significantly to the residual strength. For Specimens SS6 and SS7 a large crack formed on the sides of the slab and is attributed to the extent of stirrups and bond splitting forces created by the bars transverse to the longitudinal direction of the slab. The test

results led Symonds to make the following conclusions about slab column connections with low moment to shear ratios:

- Considerable ductility can be achieved with properly detailed stirrup reinforcement even for connections in which the flexural steel is stressed inelastically by the gravity loading prior to the application of the lateral loading. … With properly detailed stirrups, there is little loss in capacity subsequent to crushing of the concrete at the column face.
- The provision of properly detailed integral beam stirrups results in larger and wider hysteresis loops than for companion specimens without stirrups. The concentration of the flexural reinforcement in the column region results in a higher capacity, little increase in ductility and a decrease in the damping ratio.
- Including shear reinforcement increases the residual shear capacity for a connection. The residual capacity of connections without shear reinforcement is less than one half that with stirrups.
- The critical factors determining the response of the connection are the amount, extent and spacing of the shear reinforcement, the concentration of flexural reinforcement in the column regions, and the extent of yielding before the application of the lateral loading.
- The width of the slab considered effective for an equivalent frame analysis for lateral loadings should be not greater than the column width plus d within a distance equal to the slab thickness from the column face. Outside of that region, the effective width can be taken as the panel width.

2.1.4 *Ghali, Elmasri, and Dilger (1976)*

Ghali, Elmasri, and Dilger tested six full scale specimens. The objectives of the research was to investigate the effects of dynamic loading on flat plate connections. Half of the specimens were loaded statically to act as a control group. The connection strength, energy dissipation, and ductility were all used as measurements to assess the connection's viability.

The test parameters were the loading type and the flexural slab reinforcement, varying from 0.5 percent up to 1.5 percent. The specimens were designed to represent a full scale interior flat plate slab-column connection with the slab edges representing approximately where the lines of contraflexure would be. The slab was 72 x 72 x 6 in. and the column was 12 x 12 in. with a distance of 46 in. between the points of applied loading for the lateral force. The flexural reinforcement was evenly distributed for both the top and the bottom of the slab and was comprised of #4 bars. The bottom flexural reinforcement was approximately one-third of amount of the top reinforcement. None of the specimens had shear reinforcement. The column had a reinforcement ratio of 4.25 percent to resist cracking. The table below describes the variation in the specimens.

Table 2.7. Ghali, Elmasri, and Dilger (1976) Specimen Details

Specimen	Top Bars			Bottom Bars			Shear Reinforcement		
	Bar Size (No.)	Bar Spacing (in.)	Reinf. Ratio (%)	Bar Size (No.)	Bar Spacing (in.)	Reinf. Ratio (%)	Bar Size (No.)	Spacing (in.)	Reinforced Length (in.)
SM 0.5	4	8	0.5	4	24	0.17	None		
DM 0.5	4	8	0.5	4	24	0.17	None		
SM 1.0	4	4	1.0	4	12	0.33	None		
DM 1.0	4	4	1.0	4	12	0.33	None		
SM 1.5	4	2.67	1.5	4	8	0.5	None		
DM 1.5	4	2.67	1.5	4	8	0.5	None		

For convenience of the testing laboratory the specimen was tested at an 90° angle to what it would be in an actual structure. To account for the gravity loading, a constant axial force was applied to the column. The lateral forces were applied by jacks at the columns and acted in opposite directions. The four sides of the slab were simply supported with possibility of the corners lifting due to the axial loading of the column.

During testing the gravity load was slowly applied to a force of 29 kips and was intended to remain constant. For the specimens loaded statically, the lateral forces were applied slowly by a closed-loop hydraulic circuit so that the column displacements could be controlled. The displacement was incremented in steps that were approximately 6 minutes long out to a target displacement of 2.5 in. at each end of the column. For the specimens loaded dynamically the same target displacement of 2.5 in. was introduced rapidly. While the original programming was supposed to reach the displacement in 0.1 seconds, due to the dynamic response the rate was slowed down to approximately 0.3 seconds for each specimen.

The specimens with a reinforcement ratio of 0.5% failed at a lower ultimate moment than specimens with higher flexural reinforcement ratios. This specimen did however yield many of the bars in the specimen before punching failure, showing a more ductile behavior than the specimens with a higher reinforcement ratio. The crack pattern was also influenced by the amount of flexural reinforcement. Specimens with higher reinforcement ratios sustained fewer less cracks before forming a crack that would become excessively large and ultimately result in a punching failure. The lower the reinforcement ratio the greater the angle of the shear failure plane.

There was no conclusive correlation between crack pattern and loading type. The loading type did influence the strength and ductility of the response. When loaded dynamically the specimens showed an increase in strength with the increase being greater for specimens with higher flexural reinforcement ratios. The tests also showed that dynamic loading improved the connection's energy absorption capacity as well as rotation at failure.

These results led the researchers to making the following conclusions:

- Increase in the flexural reinforcement ratio increases the ultimate moment transferred M_u up to a limit (1 %). With higher flexural steel ratios, failure occurs due to shear before mobilization of the full flexural strength. The available methods to predict the ultimate strength need improvement to correctly incorporate the effect of reinforcement. The increase in flexural reinforcement has unfavorable effect on the energy absorption capacity. This should warn against using highly reinforced slabs when resistance to earthquakes or blasts are considered.
- Failure occurs at higher M_u compared to static loading when applied at a high rate, and the increase corresponds to the expected strength of the materials concrete and steel due to rapid straining. Compared to static loading, the energy absorption capacity and the rotation are higher with dynamic loading.

2.1.5 *Elgabry and Ghali (1987)*

Elgabry and Ghali investigated the accuracy of designs for shear stud reinforcement in flat plate slabs. The research consisted of five test specimens that varied in the detailing of shear reinforcement.

The testing parameters were the diameter of the stud stems, the stud rail width, the thickness of the stud heads and rails, the length of the stud rails as well as the type of steel used in the stud rails. The specimens represented full scale interior slab column connections with the geometric dimensions being consistent for all five specimens. The slab dimensions were 74.8 x 74.8 x 5.9 in. and were simply supported approximately 2 in. in from the edges of the specimen. The column dimensions were 9.8 x 9.8 in. extending 27.6 in. above and below the slab. The flexural reinforcement for the slab was also consistent for all of the specimens. The top reinforcement consisted of No. 5 bars that were increased in concentration within the column strip area, $c + 3h$. The bottom reinforcement consisted of No. 3 bars at a slightly larger spacing than the top flexural reinforcement.

Table 2.8. Elgabry and Ghali (1987) Specimen Details

Specimen	Top Bars			Bottom Bars		
	Bar Size (No.)	Bar Spacing (in.)	Reinf. Ratio (%)	Bar Size (No.)	Bar Spacing (in.)	Reinf. Ratio (%)
1	5	5.3, 6.7	1.0	3	7.9	0.42
2	5	5.3, 6.7	1.0	3	7.9	0.42
3	5	5.3, 6.7	1.0	3	7.9	0.42
4	5	5.3, 6.7	1.1	3	7.9	0.42
5	5	5.3, 6.7	1.1	3	7.9	0.42

The stud stem diameters were the same for both Specimens 2 and 3 and Specimens 4 and 5. Specimens 2 and 3 varied in the horizontal length the stud rails extended from the column perimeter. Specimens 4 and 5 varied the length of the stud rails and the spacing. The steel used to manufacture the shear stud reinforcement in Specimens 2 and 3 were hot-rolled steel flats with a yield strength of 40 ksi, while the steel used in Specimens 4 and 5 were cold-finished steel flats with a yield strength of 54 ksi. In addition to the differences in between the specimens, the studs along line AB, which was in the direction of loading, varied in comparison to the other lines of shear stud reinforcement. In Specimens 2 and 3 the stud rail width was varied while Specimens 4 and 5 had thicker anchor plates for the studs along line AB than the other lines.

Table 2.9. Elgabry and Ghali (1987) Shear Reinforcement Details

Specimen	Stud Diameter	Distance from Column face to		Spacing Between rows of studs	Number of rows of studs	Total number of studs
		First row of studs	Last row of studs			
1	-	-	-	-	-	-
2	0.5	0.5d	2.75d	0.75d	4	32
3	0.5	0.5d	4.25d	0.75d	6	48
4	0.375	0.35d	2.75d	0.5d up to a distance of 0.85d then spacing is increased to 0.95d	4	32
5	0.375	0.35d	4.25d	0.5d up to a distance of 1.35d then spacing is increased to 0.95d	6	48

Table 2.10. Elgabry and Ghali (1987) Anchor Heads and Bottom Strips

Specimen	Stud Diameter	Anchor head dimensions, thickness x width x length divided by stud Diameter D		Bottom anchor strip dimensions, thickness x width x length, divided by stud Diameter D		Steel type and yield strength
		Line AB	Other Lines	Line AB	Other Lines	
1	-	-	-	-	-	-
2	0.5	0.5 x 3 x 3	0.5 x 3 x 3	0.5 x 2 x 29.7	0.5 x 2 x 29.7	Hot-rolled Flats (40 ksi)
3	0.5	0.5 x 3 x 3	0.5 x 3 x 3	0.5 x 2 x 43.4	0.5 x 2 x 43.4	Hot-rolled Flats (40 ksi)
4	0.375	0.66 x 2.66 x 2.93	0.5 x 2.66 x 2.93	0.66 x 2.66 x 39.6	0.5 x 2.66 x 39.6	Cold-finished Flats (54 ksi)
5	0.375	0.66 x 2.66 x 2.93	0.5 x 2.66 x 2.93	0.66 x 2.66 x 57.9	0.5 x 2.66 x 57.9	Cold-finished Flats (54 ksi)

The test setup required the specimen to be tested with the slab vertical. The edges of the slab were pinned approximately 2 in. from the edges. The column was axially loaded to act as the shear force for the specimen. The column was loaded at approximately 4 in. from the ends of the columns in equal and opposite directions to simulate lateral loading.

During the testing there was first a service load level followed by a test to failure. During the service load level, the axial force, V, was kept constant while the lateral load, H, was cycled

10 times. The shear force was then increased to the testing load, V_{test}, and was kept constant as the lateral loading was increased from zero to failure.

Specimens 2 through 5 failed due to punching shear within the shear reinforced zone. In comparison with calculations for the allowable stresses for the specimens, the actual stresses at failure within the shear reinforced zone exceed the allowable stresses. This indicates that the equations for used for the allowable stress limit are safe. In Specimens 4 and 5 the actual stresses at $d/2$, outside the shear reinforced area were greater than the allowable stresses, but the specimens did not fail in that region indicating that the limit for stresses outside the shear reinforcement zone are also safe.

Specimens 4 and 5 come close to yielding the inner most stud line near failure of the specimen. Specimens 2 and 3 were over-reinforced and therefore were not close to yielding. Comparison of Specimen 1 to the other specimens with shear reinforcement showed an increase in the specimen's strength as well as an increase in specimen ductility.

These tests results led to the following conclusions:

- … prove the effectiveness of well-anchored stud-shear reinforcement in increasing the shear strength and ductility of slab-column connections subjected to shear force and unbalanced moment.
- … the validity of the design code provisions suggested by Dilger and Ghali (reference 4 in paper) when shear-moment transfer takes place between the slab and columns.

2.1.6 *Pan and Moehle (1992)*

Pan and Moehle conducted four tests that investigated the effects of biaxial loading and different levels of gravity loading on flat plate slab-column connections. In addition one of the specimens was repaired study changes in behavior for repaired connections compared to their original behavior. Specimens were tested after punching failure to verify the adequacy of continuous slab flexural reinforcement at preventing progressive collapse.

The testing parameters for this study were the lateral loading directions as well as the applied gravity shear load. Since both of these parameters are external the four specimens created were nominally identical. The slab geometry was 144 x 144 x 4.8 in. with a column geometry of 10.8 x 10.8 in. with a height of 72 in.. The flexural reinforcement layout was the same for all

specimens as well. The reinforcement in the top side of the slab consisted of No. 3 bars spaced at 3 in. within the middle 18 in. of the slab, the spacing then changed to 4.5 in. and 9 in. as the bars move away from the column. The reinforcement in the bottom side of the slab also consisted of #3 bars that were uniformly spaced at 9 in. with some bars within the column strip being discontinuous if they were perpendicular to the direction of loading as shown in Figure 2.2 below. The overall specimen details are in Table 2.11.

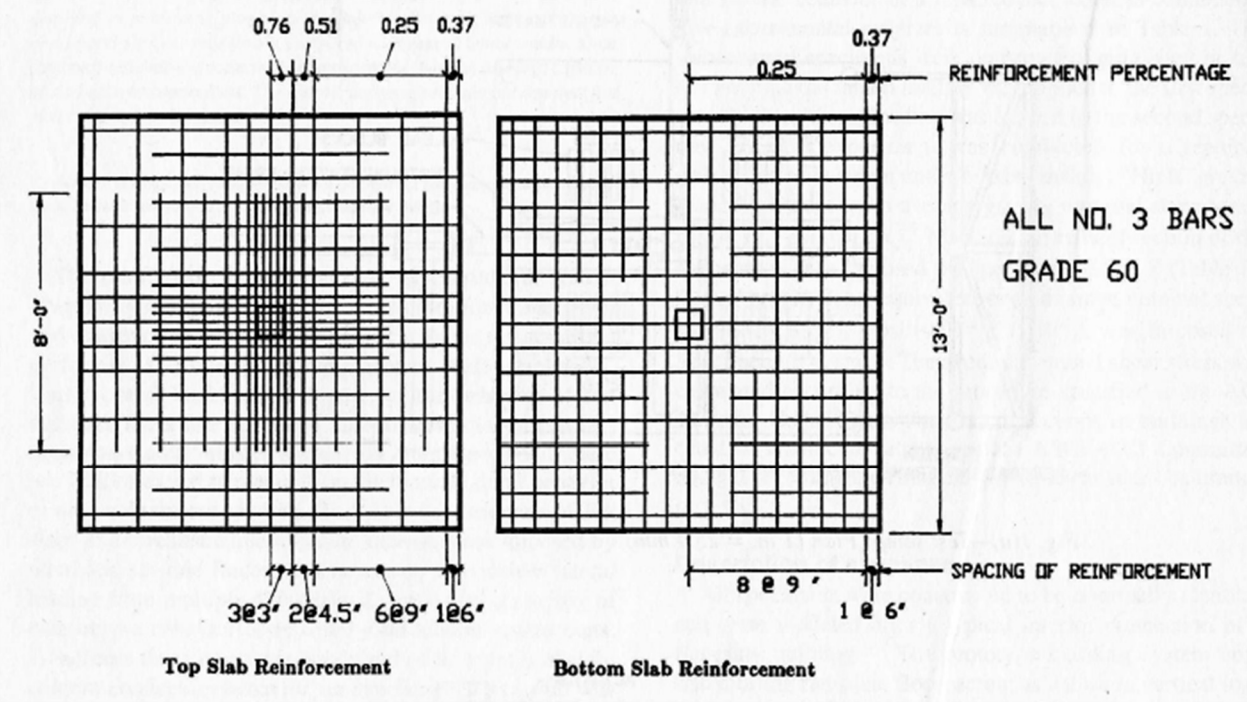

Figure 2.2. Pan and Moehle (1992) Slab Reinforcement

Table 2.11. Pan and Moehle Specimen Details

Specimen	Top Bars			Bottom Bars			Shear Reinforcement		
	Bar Size (No.)	Bar Spacing (in.)	Reinf. Ratio (%)	Bar Size (No.)	Bar Spacing (in.)	Reinf. Ratio (%)	Bar Size (No.)	Spacing (in.)	Reinforced Length (in.)
1	3	9, 4.5, 3	0.39	3	9	0.19	None		
2	3	9, 4.5, 3	0.39	3	9	0.19	None		
3	3	9, 4.5, 3	0.39	3	9	0.19	None		
4	3	9, 4.5, 3	0.39	3	9	0.19	None		

Variation of the testing was found in the test procedures. The first four specimens were tested in two sets. Each set had one specimen that would be tested with uniaxial lateral loading

while the other was tested with biaxial lateral loading. The first set, consisting of Specimen 1 and Specimen 2, had a higher average gravity nominal shear stress at $1.4\sqrt{f'_c}$ compared to the second set, consisting of Specimen 3 and Specimen 4, which had an average nominal shear stress of $0.88\sqrt{f'_c}$. The final specimen, Specimen 5, was constructed by repairing Specimen 4 after its testing. The damaged concrete was removed and replaced by a layer of epoxy and nonshrink grout.

The test setup had universal bearings at the column ends as well as on the eight transducer struts that supported the edges of the slabs as roller supports. With the given support conditions a significant amount of in-plane rigid-body twisting was expected, so a frame was constructed and attached to the west edge of the slab to restrain the torsion.

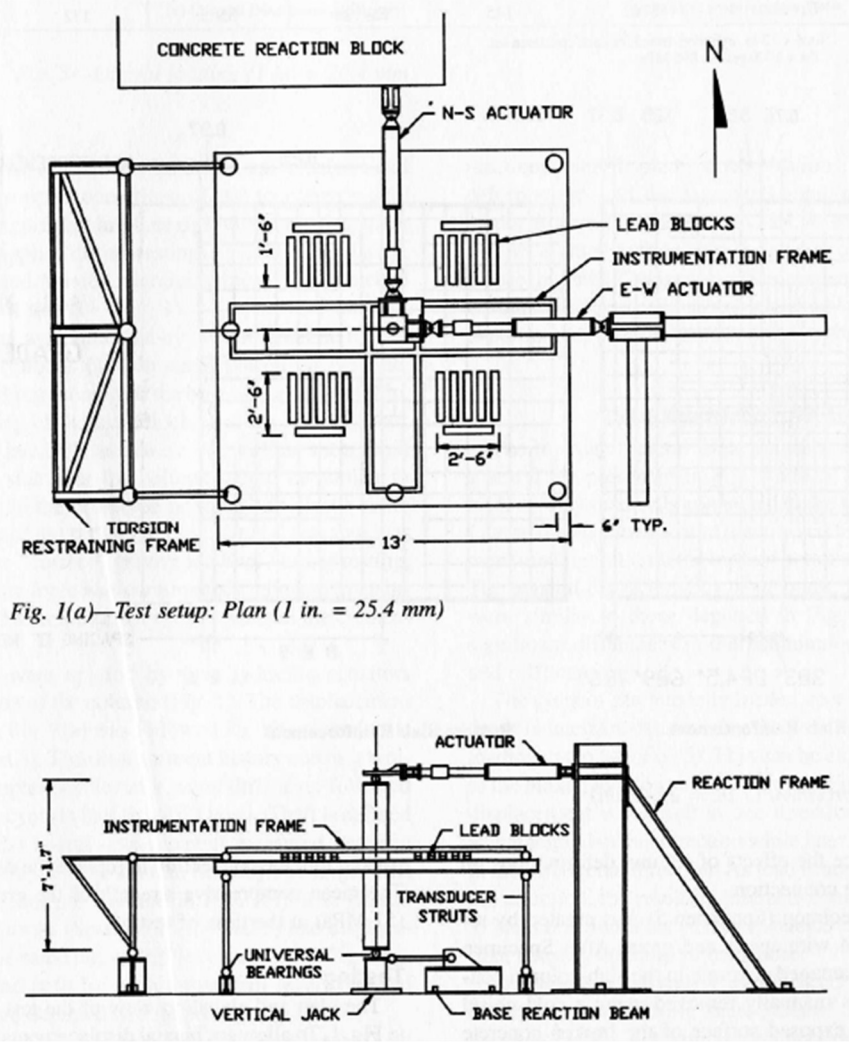

Fig. 1(a)—Test setup: Plan (1 in. = 25.4 mm)

Figure 2.3. Pan and Moehle (1992) Test Setup

Gravity loads were applied through a combination of the slab self-weight, lead blocks placed on the slab, and a vertical jacking force applied at the bottom of the column. The vertical jacking force on the column was continuously adjusted to maintain the specified average gravity shear stress at the connections. The lateral load was applied by two separate actuators attached at the top of the column acting in different directions. For uniaxial loading the actuator in the East-West pushed the specimen through displacement controlled cycles. The typical cyclic pattern involved two cycles at one target displacement followed by a third cycle at half of the target displacement before moving on to the next target drift level. For biaxial loading the same target drifts were followed; however, the load path followed a pattern shown in Figure 2.4. Cycles were continued after the initial rupture of the specimens until the connection had completely punctured. Afterwards the vertical jacking force was increased to evaluate the effectiveness of the continuous bottom flexural reinforcement at the total simulated dead and live loads.

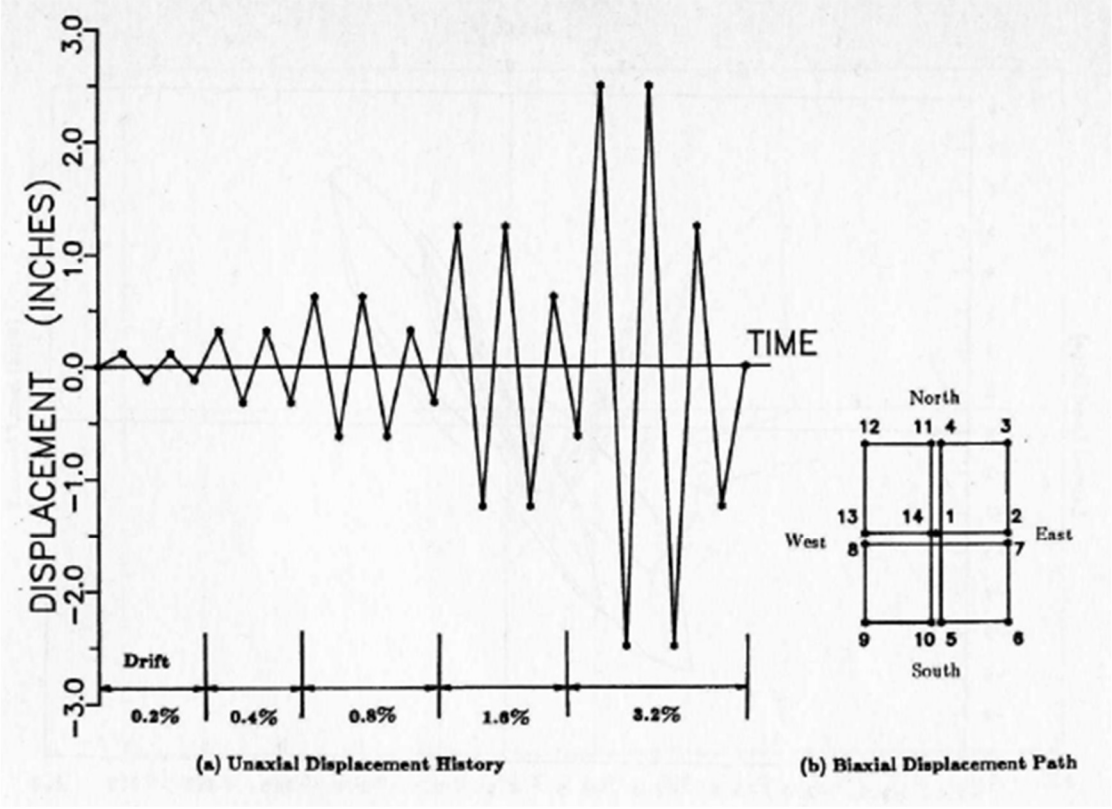

Figure 2.4. Pan and Moehle (1992) Displacement History

Specimens 1-4 lost strength due to punching damage. The specimens exhibited an inclined crack at an angle of 30° and damage at the surface of the top slab that exposed the top flexural reinforcement. Specimen 5 lost strength due to punching damage with the crack initiating at the interface of the original concrete and grout.

Comparing the uniaxial test results to the biaxial test results showed a significant reduction in strength, drift capacity, ductility and stiffness. Comparing the strength in the East-West direction, Specimen 2 failed at a 21% lower strength than Specimen 1. This strength disparity was more significant in the North-South direction with a drop of 36% in strength. The drift in the East-West direction was similar; however, the maximum drift of Specimen 2 in the North-South direction was much lower than the maximum drift of Specimen 1 in the East-West direction. For the specimens with the lower shear gravity ratios, Specimen 4 failed at a strength 4% lower than Specimen 3. Specimen 4 showed a significant decrease in strength in the North-South direction of 21%. Specimen 3 reached a higher maximum drift of 4.76%, while Specimen 4 failed at a maximum drift of 3.21% in the East-West direction and 1.54% in the North-South direction.

Increasing the gravity shear ratio reduced the strength, drift, ductility, and stiffness of the connection. Specimen 3 had a 50% greater lateral strength than the other uniaxial specimen, Specimen 1. The maximum drift of Specimen 3 was over 200% greater than Specimen 1. Similar differences in lateral strength and maximum drift were found for the biaxial tests; however, it should be mentioned that the maximum drift reduction was closer to 150% from Specimen 4 to Specimen 2.

Specimen 5 showed a reduction in strength and stiffness as expected, but Specimen 5 was able to sustain the gravity load while also withstanding equal maximum drifts as Specimen 4. There was significant difference of lateral strength in the directions of loading. This is attributed to uneven damage and yielding of the previous test or the quality of workmanship in the repair.

The continuous bottom flexural reinforcement through the column was approximately a third of the ACI-ASCE Committee 352 model. This proved to be more than enough for the post failure loading of the slab. Loading of Specimen 1 reached 45 kips before termination of the test, which was more than the 15 kips indicated by ACI-ASCE Committee 352.

The results of the of the test program led to the following conclusions:

- Biaxial lateral loading reduces the lateral stiffness, strength, and available drift capacity of reinforced concrete slab-column connections.

- The magnitude of the gravity load shear carried by the slab is a primary variable affecting the lateral behavior of reinforced concrete flat plates.
- Continuous bottom slab reinforcement should be placed directly over the columns of flat plates to prevent progressive collapse in the event of a connection shear failure. Bottom bars effectively suspend the slab after punching failure and enable the slab-column connection to sustain gravity loads under continued cycles of lateral loading.
- The results of a single repaired slab-column test indicated that the repaired connection retained its original drift capacity. However, the strength was not regained by the repair procedure.

2.1.7 *Wey and Durrani (1992)*

Wey and Durrani conducted an experimental program that covered three interior slab column connections. A cyclic lateral force was applied statically to each of the specimens to examine the behavior of slab column connections with shear capitals. Shear capitals are a method to increase a slab column connection's two-way shear capacity by increasing the slab thickness near the column. The test specimens were compared to a control specimen from a previous test.

The parameter of interest for the experimental program was the size of the shear capital. The specimens mentioned in the experimental study had the same specimen geometry. The slab was 114 x 78 x 4.5 in. while the column was 10 x 10 in.. The flexural reinforcement was consistent between the specimens as well and is shown in Table 2.12. The shear caps of the different specimens varied the size, length and width, while maintaining a consistent depth of 3.5 in.. The largest shear cap size was determined using ACI 318-89.The smallest shear cap was determined to be a half scale size convenient for construction. The third size was decided to be exactly in the middle of the other two sizes as shown in Table 2.13. The shear capitals were reinforced with a standard hook to anchor vertical bars to the slab and flexural reinforcement to resist positive moment during reverse cyclic loading.

Table 2.12. Wey and Durrani (1992) Specimen Details

Specimens	Top Bars			Bottom Bars			Shear Reinforcement		
	Bar Size (No.)	Bar Spacing (in.)	Reinf. Ratio (%)	Bar Size (No.)	Bar Spacing (in.)	Reinf. Ratio (%)	Bar Size (No.)	Spacing (in.)	Reinforced Length (in.)
SC0	3	3.5, 9	0.96, 0.32	3	3.5, 9	1.23, 0.32	None		
SC6	3	3.5, 9	0.96, 0.32	3	3.5, 9	1.23, 0.32	None		
SC4	3	3.5, 9	0.96, 0.32	3	3.5, 9	1.23, 0.32	None		
SC2	3	3.5, 9	0.96, 0.32	3	3.5, 9	1.23, 0.32	None		

Table 2.13. Wey and Durrani (1992) Shear Capital Details

Specimens	Shear Capital Dimensions (in.)			Flexural Reinforcement in SC		
	Length	Width	Depth	Bar Size (No.)	Bar Spacing (in.)	Reinf. Ratio (%)
SC0	None			None		
SC6	24	24	3.5	3	7.0, 7.5	0.52
SC4	32	32	3.5	3	7.0, 7.5	0.59
SC2	40	40	3.5	3	7.0, 7.5	0.63

The base of the column was pin connected to the testing frame while the top was pin connected to a beam that the actuator applied the lateral drift history to. After the initial gravity load was applied to the slab, the free ends were attached to reaction links that acted as roller supports. Channels were bolted to the free ends to spread the reaction across the width of the slab. The specimens were subjected to the same gravity loads during the test. The load was determined to be the full dead load along with 30% of the live load of the prototype structure. This resulted in the use of 20 0.45 kip weights hanging from cables that were anchored to the slab. There was no axial load applied to the column. The lateral load was applied at the top of the column and the test setup is shown in Figure 2.5.

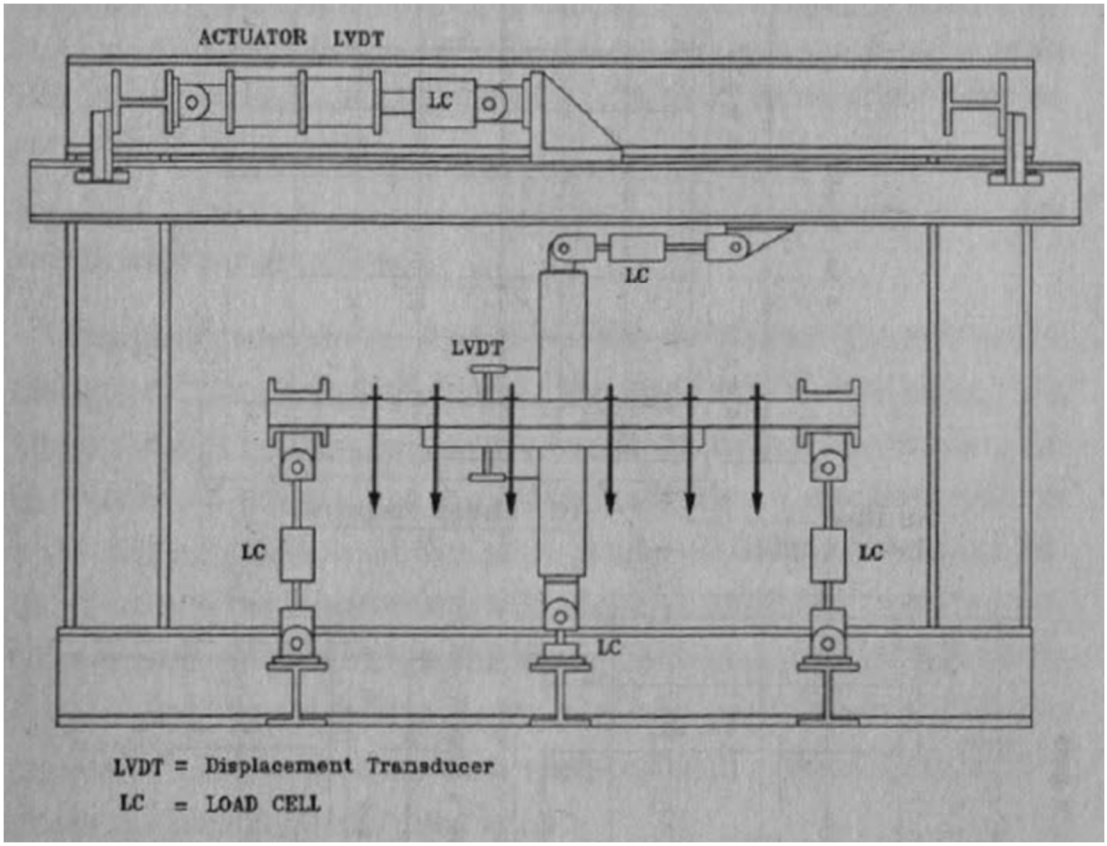

Figure 2.5. Wey and Durrani (1992) Test Setup

The test used linear variable displacement transducers (LVDTs) at the top of the column and at 8 in. from the column face on the top and bottom of the slab. The LVDT at the top of the column was used to measure the drift of the specimen during testing. The LVDTs spaced 8 in. away from the column face were used to determine the rotation of the connection with respect to the column. The test also used strain gages in the slab as well as the shear capital to monitor the extent of yielding in both. Load cells located at the top of the column as well as under the column and free ends measured the lateral force and reactions of the specimen during the test.

Behavior of the specimens were similar up to 1% drift. Flexural cracks formed on the top surface of the slab at edges of the shear cap or near the face of the column and would spread across the entirety of the slab by around 1% drift. Similar flexural cracks would begin to form on the bottom side of the slab around 0.75% drift. Specimen SC0 exhibited a punching damage mode at 5% drift and sustained a punching cone failure surface. Specimen SC6 failed in punching shear at 6% drift; however, the shear crack formed at the bottom of the slab on the edge of shear capital and propagated upwards towards the column creating an inverted punching cone. Specimens SC4

and SC2 failed due to flexural hinging at the shear capital edges at a drift of 6%. The peak strengths of the specimens showed that specimens with shear capitals had a 90-130% increase in strength compared to the control specimen. The size of the shear capital did not impact the strength of the connection until 3% drift. Beyond that drift level, the larger shear capitals showed higher peak strengths. The initial stiffness of the shear capital specimens was about 50% greater than Specimen SC0, this is expected since the moment of inertia of the specimens were increased by the presence of the shear capital. Up to 1.5% drift there was no connection between the presence of a shear capital and the stiffness degradation of the specimens. From drifts between 2-6%, the results showed that as shear capital size increased the stiffness degradation reduction increased.

Strain gages showed yielding in the shear capitals of Specimen SC6 for both vertical and horizontal bars at around 2% drift. The horizontal strain gages in Specimens SC4 and SC2 stayed below yield throughout the test. The vertical strain gages in Specimens SC4 and SC2 were near yield but still showed to be effective in forcing a flexural hinging failure outside of the shear capital region.

Test results were compared to ACI 318-89 and showed that ACI underestimated the capacity of the slab outside the shear capital region to transfer unbalance moment to the slab. In addition, ACI did not account for the failure method in Specimen SC6 in the possible locations of punching shear failures. The results of the experimental program led to the following conclusions:

- When lateral loads are expected to produce net positive moment at the connection, the length of the shear capital should not be less than four times the height of the slab plus the largest column dimension. For example a 10 in. square column supporting a 5 in. thick slab would require a column capital of 30 in.
- The presence of a properly detailed shear capital in a slab-column connection subject to lateral as well as gravity loads will increase the strength, stiffness, and energy dissipation of that connection. Improvement of the response of the connection by an increase in size of the shear capital is more evident at drifts larger than 2 percent.
- When investigating the critical section near the face of the shear capital, the width of the slab effective in transferring a portion of the unbalanced moment to the column by flexure should be increased from $c_2 + 3h$ to $L_{sc} + 3h$, where L_{sc} is the length of the shear capital transverse to the direction of lateral loading.

- For shear capitals to be effective, they should be properly reinforced. Vertical reinforcement near the shear capital edge should be anchored into the slab, and horizontal reinforcement should be provided for flexural resistance against load reversals.

2.1.8 *Robertson, Kawai, Lee, Enomoto (2002)*

The testing program studied three different types of shear reinforcement and compared the results to a control specimen without shear reinforcement. The purpose behind the study was to determine the viability of newer shear reinforcement that was easier to install than what was considered traditional slab shear reinforcement at the time, such as closed hoop stirrups and shear heads.

The specimens were nominally the same other than the shear reinforcement. The slab geometry was 118 x 108 x 4.5 in. with the longer span being in the direction of applied moment. The column was 9.8 x 9.8 in. and extended 27.8 in. above and below the slab. The top flexural reinforcement was more concentrated within the effective width of the slab, while the bottom flexural reinforcement only had a tighter spacing in within the column region. Outside of these concentrations of rebar, the top and bottom reinforcement layout were the same. And are more detailed in Table 2.14.

The specimen name conventions used the shear reinforcement they had. Specimen 1C was the control specimen without shear reinforcement. Specimen 2CS had closed hoop stirrups spaced at 2.5 in. which was greater than the ACI maximum spacing. Specimen 3SL had single leg stirrups of the same spacing. Specimen 4HS had headed stud shear reinforcement.

During testing the specimen's base was pin connected to the strong floor, while the top was pin connected to a hydraulic actuator. The free edges of the slab perpendicular to the direction of loading were supported by three calibrated rods that allowed rotation translation in the horizontal directions.

Table 2.14. Robertson, Kawai, Lee, and Enomoto (2002) Specimen Details

Specimen	Top Bars			Bottom Bars			Shear Reinforcement		
	Bar Size (No.)	Bar Spacing (in.)	Reinf. Ratio (%)	Bar Size (No.)	Bar Spacing (in.)	Reinf. Ratio (%)	Bar Size (No.)	Spacing (in.)	Reinforcement Type
1C	3	3.9, 8.9	0.74, 0.37	3	3.9, 8.9	0.74, 0.37	None		
2CS	3	3.9, 8.9	0.74, 0.37	3	3.9, 8.9	0.74, 0.37	2	2.6	Closed hoop stirrups
3SL	3	3.9, 8.9	0.74, 0.37	3	3.9, 8.9	0.74, 0.37	2	2.6	Single leg stirrups
4HS	3	3.9, 8.9	0.74, 0.37	3	3.9, 8.9	0.74, 0.37	2	2.6	Headed-studs

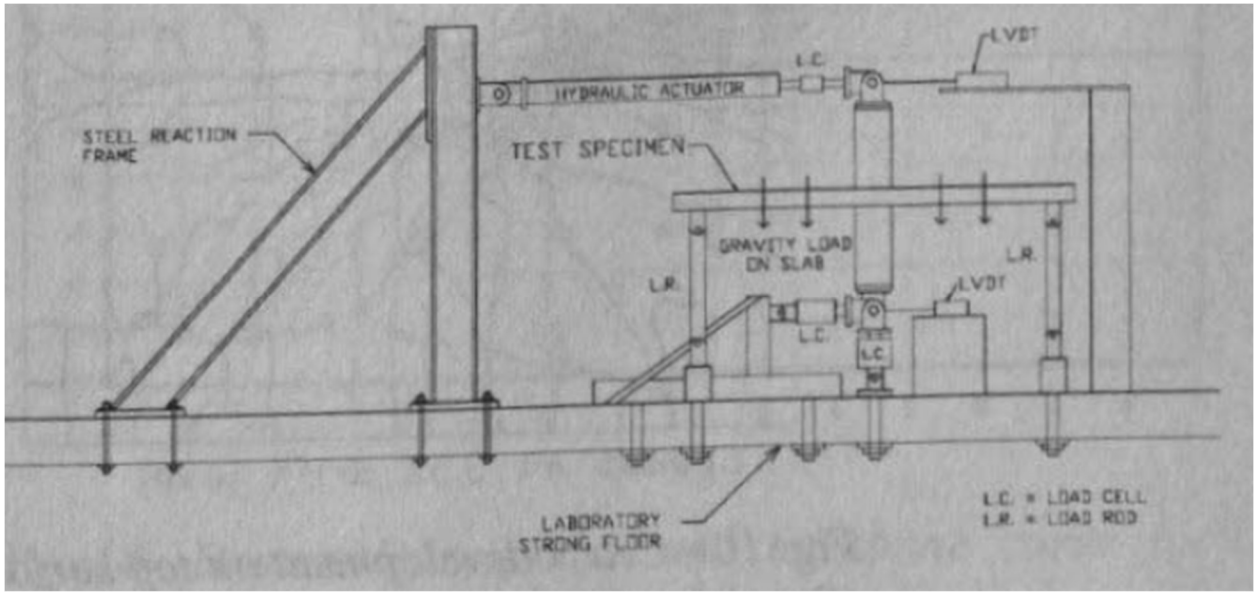

Figure 2.6. Robertson, Kawai, Lee, and Enomoto (2002) Test Setup

To achieve the target gravity load equivalent to the full dead load plus 30% of the live load, concrete weights were hung from cables attached to the slab. These weights were attached before the calibrated rods were placed to confine the gravity load the slab; however, due to cracking during the testing some of the gravity load would be redistributed to the calibrated rods.

The lateral loading was defined by two different phases of testing. Due to equipment restraints the hydraulic actuator stroke could not reach the full 8% target drift. Phase I would incrementally increase the displacement in both directions until the drift reached 5%. Then the actuator would be repositioned for Phase II so that it only applied displacement in one direction allowing the specimens to reach 8% drift.

Load cells in the hydraulic actuator and calibrated rods recorded the column and slab bending moments and shears. The horizontal displacement at the top and bottom of the column was tracked. Strain gages were placed on horizontal and vertical legs of the shear reinforcement to determine their effectiveness.

The initial gravity loading caused flexural cracks to form near the column face. The lateral loading caused these flexural cracks to extend the entire width of the slab and initiated diagonal torsional cracks to form adjacent to the column faces. At 3.5% drift 1C suddenly failed in punching shear with little warning. None of the specimens with shear reinforcement experienced punching failure even at drifts of 8%. From the backbone curves of the hysteretic responses, the specimens with shear reinforcement had no more than 15% reduction in peak strength at 8% drift.

Strain gages indicated yielding near the column face in the top reinforcement at 2% drift. The yielding occurred at similar drift levels for all specimens. The strain gages on the shear reinforcement showed no signs of yielding with vertical bars reaching approximately 75% of the yield stain at the maximum drift.

The test results were compared to ACI 318-99 to create a shear ratio of the experimental shear demand to the ACI predicted capacity. 1C failed at a lower shear demand than predicted by ACI. The specimens with shear reinforcement had a shear ratios ranging from 0.92 to 1.00 indicating that collapse was imminent, although experimental data showed no signs of this. Based on the results of the tests the following conclusions were made:

- The load-drift envelopes … indicate that the specimens with slab shear reinforcement experienced peak lateral loads up to 22% greater than that of the control specimen while displaying superior ductility. These connections failed in flexure without reaching the full capacity of the shear reinforcement.
- Based on the limited number of tests in this program, the ACI Code procedure for predicting punching shear failure under combined gravity and lateral loading was unconservative for the connection without shear reinforcement when subjected to

cyclic lateral loading, but conservative for the connections with shear reinforcement.

- All three types of slab shear reinforcement – namely, open-hoop stirrups with clip closure, single-leg stirrups, and welded-head studs – proved equally effective in resisting punching shear failure of the slab-column connections under relatively low levels of gravity shear. In all cases, the shear reinforcement spacing of $s = \frac{2}{3}d$ exceeded the ACI 318-99 Code maximum spacing requirement of $s = \frac{d}{2}$. Consideration should be given to relaxing the $\frac{d}{2}$ maximum spacing requirement for shear reinforcement in slabs. This is particularly appropriate for headed shear studs where the stud spacing is more precisely maintained during construction than for shear stirrups.

2.1.9 *Yeutter (2020)*

Yeutter investigated the proposed connection. This was the first phase of the study presented here.

The new connection uses CFST columns to reduce the reinforcement and remove formwork. The ring acts similar to a column capital. The post-tensioned bolts act as shear reinforcement. The CFST columns extended from the top and bottom faces of the slab out to mid floor height. The ring flanges were welded to the ends of the tube that were in contact with the top and bottom faces of the slab. Prestressed bolts created a clamping effect of the two ring flanges confining the slab column joint region. The bolts made a circular peripheral line of eight bolts around the column spaced at 2.25 in. for the first peripheral line and 4.5 in. for each peripheral line after. Longitudinal column reinforcement was welded to the bottom tube and passed through the slab into the upper tube.

The tests studied the effects of the ring flange size and the number of bolts beyond the ring flange used as shear reinforcement. The specimens were nominally the same. The slab dimensions were 156 x 72 x 10 in. with a 20 x 0.375 in. circular steel tube extending 63.875 in. below the slab and above the slab to the point of lateral loading. The slab was reinforced with No. 8 bars at 9 in. in both directions. The specimen details are given in the table below.

Table 2.15. Yeutter (2020) Specimen Details

Specimen	Top Bars			Bottom Bars			Shear Reinforcement		
	Bar Size (No.)	Bar Spacing (in.)	Reinf. Ratio (%)	Bar Size (No.)	Bar Spacing (in.)	Reinf. Ratio (%)	Bar Size (in.)	Spacing (in.)	Reinforcement Type
SR_4_10_5	8	9	1.00	8	9	1.00	0.5	5	Stud Rails
PTB_4.5_1_0	8	9	1.00	8	9	1.00	0.75	-	Post-tensioned Bolts with Ring Flange
PTB_4.5_1_4	8	9	1.00	8	9	1.00	0.75	4.5	Post-tensioned Bolts with Ring Flange
PTB_9_2_0	8	9	1.00	8	9	1.00	0.75	4.5	Post-tensioned Bolts with Ring Flange

The new connection would be compared to a reference Specimen, SR_4_10_5, which used shear stud-rails common in flat plate construction. Three specimens investigated the test parameters. To investigate the ring size needed, Specimen PTB_4.5_1_0 had a ring size approximately equal to $\frac{d}{2} = 4.5\ in.$ while Specimen PTB_9_2_0 had a ring size approximately equal to $d = 9\ in.$. To compare the effect of the number of post-tensioned bolts beyond the ring flange, specimen PTB_4.5_1_4 was identical to specimen PTB_4.5_1_0 in ring flange size, but had four peripheral lines of post-tensioned bolts through the slab beyond the perimeter of the ring flange.

The base of the column was pin connected to a strong floor of the self-loading test frame. The top of the column was permitted to freely rotate and move horizontally in the direction of loading. To simulate inflection points at the ends of the slab perpendicular to the direction of loading, slab end roller supports were created. The roller supports consisted of two clevises connected by a truss member. This allowed the free rotation and horizontal translation in the direction of loading at the ends of the slab.

An axial load was applied to the column to simulate upper story gravity loading. As the column was displaced the $P - \Delta$ effects of the column axial load contributed to the slab moment. No external gravity loads were applied to the slab.

The lateral load was provided by a MTS actuator connected to the contraflexure point of the upper column. The column was cyclic displaced to increasing drift targets. The specimens were cycled twice per target drift level before increasing the drift to the next target drift level.

Load cells integral to the actuators for axial and lateral loading as well as load cells in the truss members of the slab end roller supports measured the reactions, shears, and moments during testing. A LVDT was attached at the point of lateral loading to measure the force drift response. Additional LVDTs were placed along the edge of the slab in the direction of loading to measure the deformed shape of the slab. The deformed shape would be used to help determine the failure mechanism of the connection. Strain gages were placed on slab flexural reinforcement in the direction of loading, on shear reinforcement of the reference specimen, and on the longitudinal (vertical) column reinforcing bars. The strain gages on the column reinforcement was to indicate if there was a weak column relative to the slab.

Cracking and yielding in the slab occurred at similar drift levels for all specimens, although it should be noted that for SR_4_10_5 the outermost bars did not yield. SR_4_10_5 spalled at a higher drift level than PTB_4.5_1_0 and PTB_4.5_1_4. This is thought to be due to the prestress force on the flange. Crushing was at similar drift levels for SR_4_10_5 and PTB_4.5_1_0. These specimen reached crushing at approximately 0.7% lower drift that the other two specimens. This was attributed to the lack of confinement provided by the stud rails in SR_4_10_5 and the lack of shear reinforcement in PTB_4.5_1_0 beyond the ring flange.

The backbone curves of the tests showed a higher peak lateral strength for the prestressed bolt connections than the reference specimen. Both SR_4_10_5 and PTB_4.5_1_0 showed lateral strength degradation after reaching their peak lateral forces. PTB_4.5_1_4 and PTB_9_2_0 plateaued after reaching their peak lateral forces around 3.5% drift until 6% drift. Specimens PTB_4.5_1_4 and PTB_9_2_0 showed increased energy dissipation in the connection. PTB_4.5_1_0 showed similar energy dissipation to SR_4_10_5 until PTB_4.5_1_0 failed at 4.9% drift. The deformed shapes of the slabs indicated that plastic hinging formed in all the specimens around 4.1% drift. These results led to the following conclusions:

- The proposed connection provides a viable alternative to traditional connections for slab-column gravity systems in reinforced concrete construction as shown by high drift capacity and lack of degradation of lateral force resistance to high drifts.
- The proposed connection has the potential when appropriately detailed to provide a greater drift capacity than a slab-column connection using traditional stud rail shear reinforcement as shown by the drift capacities and lateral force resistance of Specimens PTB_4.5_1_4 and PTB_9_2_0.
- Either a sufficiently large ring flange or a small ring with additional prestressed shear bolts is needed for a ductile, high drift capacity slab-column connection.
- A flexural response was predicted by most of the design codes examined and was observed as the primary response during testing.

2.2 PURE SHEAR TEST PROGRAMS

2.2.1 *Dam and Wight (2016)*

The research project conducted by Dam and Wight examined the viability of stud rails in an orthogonal layout with long stud rail lengths. Because of the way ACI defines the critical perimeter in the case of slabs with shear reinforcement, the diagonal region between the orthogonal shear reinforced regions extending from each face of the column is just as effective as the regions confined by the shear reinforcement. There is no limit imposed on the size of this diagonal region even when the confinement of the shear reinforcement is less effective due to increased distance between the orthogonal shear reinforcement.

The study looked to examine the behavior of three full scale test specimens. One specimen would be a control specimen, S08C. One specimen had an orthogonal stud rail layout, S08O, with three stud rails per column face. The last specimen had a radial stud rail layout, S08R, with two stud rails per column face and a stud rail at each corner of the column. The specimens had slab dimensions of 120 x 120 x 10 in.. While a column located at the center of the slab extended 11 in. above the slab and 15 in. below the slab. The flexural reinforcement was designed using yield line theory that resulted in #5 bars at 4 1/8 in. spacing for the bottom bars and #4 bars at 6 ½ in. spacing for the top bars. The shear reinforcement consisted of 12 identical stud rails in each specimen with a stud diameter of 3/8 in. spaced at 4 1/8 in. The full details of the specimen are given in the table below.

Table 2.16. Dam and Wight (2016) Specimen Details

Specimen	Top Bars			Bottom Bars			Shear Reinforcement		
	Bar Size (No.)	Bar Spacing (in.)	Reinf. Ratio (%)	Bar Size (No.)	Bar Spacing (in.)	Reinf. Ratio (%)	Bar Size (No.)	Spacing (in.)	Reinforcement Type
S08C	5	4.1	0.84	4	6.5	0.34	None		
S08O	5	4.1	0.84	4	6.5	0.34	3	4.13	Orthogonal Stud Rails
S08R	5	4.1	0.84	4	6.5	0.34	3	4.13	Radial Stud Rails

The test setup had eight reinforced concrete blocks with neoprene bearing pads to simply support the specimen near the edges. The spacing of the blocks were symmetric and formed a circle with a diameter of 120 in. equal to the length and width of the specimens. The vertical downward force was applied at the top of the column by a hydraulic jack. Due to the downward force the primary tension reinforcement was in the bottoms of the slabs. This is upside-down for how the connection would behave in the field.

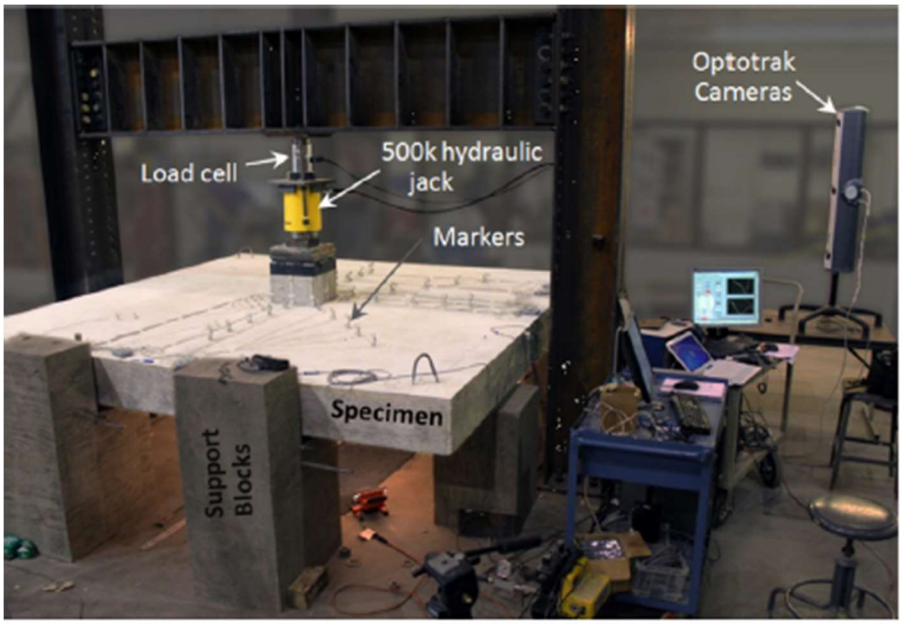

Figure 2.7. Dam and Wight (2016) Test Setup

The specimen was loaded in increments of 20 kips until it neared the predicted capacity. Smaller increments were used to capture the failure behavior more accurately. Once the peak was recorded the specimen was loaded to failure which was defined as 60% of the peak force. 40 total strain gages were placed on the flexural and the shear reinforcement. An LVDT was placed on the bottom of the slab to measure the displacement of the column. The column displacements and slab displacement as well as slab expansion were measured by an Optotrak Certus System.

All of the specimens failed in punching shear after some of the tensile reinforcement reached yield. The behavior between the specimens were similar to a displacement of 0.5 in. Between 0.5 in. and 1.0 in. Specimen S08C failed. The specimens with shear reinforcement showed similar behavior to a displacement of 1.0 in. at this displacement Specimen S08O reached the peak loading and began to lose strength gradually. Specimen S08O eventually failed due to

punching shear failure with a failure surface extending outside of the shear reinforced region. The strength of Specimen S08R began to plateau until reaching peak loading between 1.75 and 2.0 in. displacement. Specimen S08R lost strength quickly and had a failure plane within the shear reinforced zone.

The maximum strain in the shear studs of Specimen S08O showed that the studs did not yield in that specimen. This is consistent with the failure surface in Specimen S08O. Specimen S08R had strains in the first two peripheral lines of studs that had yielded, and two studs that had fractured as well. The final punching shear failure occurred shortly after the fracture of those studs so the failure is attributed to their failure reducing the shear stiffness and allowing the wider inclined cracks.

The failure surface of the control specimen showed the inclined cracks at an average angle of 30 degrees from the horizontal. The inclined cracks extended until reaching the flexural reinforcement on the compression side of the slab and then propagated toward the edge of the slab indicating a dowel action failure. The failure plane of Specimen S08O showed some cracks in the shear reinforced region, however, none of the cracks became failure planes. Instead the failure surface propagated along the tension reinforcement until reaching the ends of the stud rails then formed inclined cracks between 35 and 45 degrees. Additionally the failure surface did not follow the critical perimeter as defined by ACI. Instead the failure surface resembled a cruciform shape hugging more tightly to the edges of the stud rail regions. Specimen S08R had multiple inclined cracks within the shear reinforced region. The failure surface had inclined cracks starting from the face of the column extending past 3d/2 away from the column. An acoustic investigation indicated the cracks in the shear region formed a roughly circular region of damage. Specimen S08R is suspected of behaving in a flexure controlled manner until the fracture of the two studs caused it to fail in punching shear.

In comparison with ACI, Specimen S08C was in agreement with the ACI predicted shear capacity. Specimens S08C and S08R sustained demands that were approximately 10% lower than the ACI predicted capacities. This is believed to be due to the significant yielding of the flexural reinforcement limiting the shear strength.

The test series led to the following conclusions:

- Shear studs are effective for increasing shear strength of slab column connections.

- Radial and orthogonal layouts of shear studs both increase the shear strength of slab-column connections, but the radial layout is better than the orthogonal layout in terms of providing ductile post-flexural yielding behavior in slab-column connections.
- In the calculation of shear strength, the perimeter of the critical section outside the shear reinforced region, b_0, should be reduced if the distance between any two adjacent studs exceeds $2d$.
- The ACI Building Code does not give conservative predictions for the shear strength of slab-column connections for slabs that contain shear reinforcement, but also have a low flexural reinforcement ratio.
- The load required to develop a flexural mechanism in the slab region around a column should be included when evaluating the effective shear strength of the slab-column connections.

2.2.2 *Jang and Kang (2019)*

The test program investigated the effects of flexural reinforcement and shear reinforcement on slab-column connection responding in two-way shear. Six specimens were tested with varying flexural reinforcement ratios and varying shear reinforcement. The results were compared to ACI 318-14 and KCI 2012 to evaluate if these code equations sufficiently characterized two-shear behavior in slab column connections and what improvements could be made to the codes increase their accuracy.

The test parameters were the amount of flexural reinforcement and the amount of shear reinforcement. To properly investigate these parameters the six test specimens were separated into two groups of three. The first group had a low flexural reinforcement ratio, while the second had twice the flexural reinforcement. Within each group there was one control specimen without any shear reinforcement, a specimen with low shear reinforcement, and a specimen with twice the shear reinforcement of the lightly shear reinforced specimen.

The slab geometry of 72.8 x 72.8 x 8.3 in. was consistent for all six test specimens. The column of dimensions 17.7 x 17.7 in. extended 7.9 in. below the slab. The reinforcement details are provided in Table 2.17.

Table 2.17. Jang and Kang (2019) Specimen Details

Specimen	Top Bars			Bottom Bars			Shear Reinforcement		
	Bar Size (No.)	Bar Spacing (in.)	Reinf. Ratio (%)	Bar Size (No.)	Bar Spacing (in.)	Reinf. Ratio (%)	Bar Size (No.)	Bar Spacing (in.)	Reinforcement Type
SP-1	5	5.9	0.77	3	5.1	0.31	None		
SP-2	5	5.9	0.77	3	5.1	0.31	3	3.34	2 rows single-leg stirrups
SP-3	5	5.9	0.77	3	5.1	0.31	3	3.34	4 rows single-leg stirrups
SP-4	5	3.0	1.53	3	5.9	0.77	None		
SP-5	5	3.0	1.53	3	5.9	0.77	3	3.34	2 rows single-leg stirrups
SP-6	5	3.0	1.53	3	5.9	0.77	3	3.34	4 rows single-leg stirrups

The specimens were tested upside down for convenience with the punching load applied at the end of the bottom column. The slab was supported at each edge by a 39.3 in. that was 7.9 in. from the slab edge. The specimen's vertical displacements were measured by LVDTs located at the center of the column, the column faces and between the column face and support on all four sides. Strain gages were placed on the flexural reinforcement as well as the single leg stirrups to capture their contributions to the connection strength throughout the test. A load gage at the point of loading recorded the punching force applied to the specimens.

All of the low flexural reinforcement specimens, SP-1 through SP-3, reached ultimate load at a similar displacement. Specimen SP-1 had the lowest ultimate load as expected; however, Specimens SP-2 and SP-3 failed at a similar load indicating that directly adding the shear capacity of the shear reinforcement to the overall shear strength of the connection may not be a suitable assumption. Specimen SP-3 showed a more ductile failure than Specimen SP-2 which may be attributed to the increased shear reinforcement. For the high flexural reinforcement specimens the

ultimate strength of the specimens increased as the shear reinforcement increased. The stiffness of the high flexural reinforcement ratio specimens was greater than that of the low flexural reinforcement specimens. Additionally, Specimen SP-4 failed at a higher peak force than either Specimen SP-2 or Specimen SP-3 indicating that the amount of flexural reinforcement can be an important factor in increasing connection two-way shear strength.

Examination of the concrete cracking after testing revealed more small distributed cracks in the high flexural reinforcement ratio specimens than the low flexural reinforcement ratio specimens. Specimens SP-2 and SP-3 showed more distinct failure surfaces than Specimens SP-5 and SP-6. In the specimens with low amount of shear reinforcement, the single leg stirrup hooks had unbent due to the applied punching load and allowed to concrete cover to burst out. Specimens SP-3 and SP-6 showed no signs of this behavior as their reinforcement maintained their shape.

The strain gages on the flexural reinforcement showed no yielding at the onset of initial diagonal cracking with the strains at initial diagonal cracking ranging from $0.33 - 0.58\varepsilon_y$. From this it is believed that the amount of flexural or shear reinforcement do not affect the onset of initial diagonal cracking. Specimen SP-1 showed no signs of flexural reinforcement yielding before failure. SP-2 had no flexural yielding of reinforcement, but did show an increase in strain in flexural reinforcement compared to Specimen SP-1. Specimen SP-2 had a stirrup yield at the critical section. Specimen SP-3 did not yield in either flexural or shear reinforcement. Specimen SP-4 had similar strains in the flexural reinforcement at ultimate load as Specimen SP-1 did, however the flexural reinforcement went on to yield as the slab was displaced past the displacement at ultimate load. Specimen SP-5 did not yield in flexural reinforcement at ultimate load; however, two bars showed that they yielded after continuation of displacement of the slab. Specimen SP-5 had a stirrup yield at the critical section similarly to Specimen SP-2. Specimen SP-6 showed no signs of yielding at its initial peak, but upon regaining strength it had multiple bars as well as stirrups yield.

The test results were compared to ACI 318-14 and KCI 2012. ACI was accurate in predicting the results of specimens with low flexural reinforcement and low shear reinforcement. KCI and ACI both grossly overestimated the strength of Specimen SP-3 which had low flexural reinforcement and high shear reinforcement. This is due to the codes directly adding shear strength of the reinforcement to the overall shear strength of the specimen without considering what factors may limit the full strength of the shear reinforcement from contributing to the connection shear

strength. A modification to the KCI code was proposed that multiplies the shear reinforcement contribution by a strength reduction factor that is dependent on the flexural reinforcement ratio of the slab. The strength reduction factor was calibrated based off these six specimens, but was used to analyze 73 other existing test results with noticeable improvement of predictability of failure load. The test program and results led to the following conclusions:

- Due to the punching shear test on the slab-column connection, the amounts of shear reinforcement and flexural reinforcement interactively affect the punching shear strength of the slab-column connection. Specifically, the amount of flexural reinforcement has a significant influence on the behavior of the slab-column connection.
- Experimental results indicated that the increase of shear reinforcement for a low flexural reinforcement ratio had limitations in increasing the punching shear strength of the connection. When the flexural reinforcement ratio was low, the damage caused by flexure reduces the shear resistance of the shear reinforced slab-column connection.
- Conversely, it was confirmed that the shear strength increases with shear reinforcement, when the flexural reinforcement ratio is more than a certain amount. Therefore, the shear strength capacity equations should include the flexural reinforcement.
- In a previous study by Eom et al. (2018), if the amount of shear reinforcement was increased regardless of the amount of flexural reinforcement, the ultimate punching strength increased after the initial diagonal crack. However, in this study, the slab-column connection, which had a small amount of flexural reinforcement, behaved differently. Therefore, in itself, the amount of shear reinforcement does not determine this strength increase after initial diagonal cracking, but the flexural reinforcement should be more than a certain amount for this strength increase after initial diagonal cracking.
- Experimental results compared to KCI 2012 (KCI 2012) design expressions and the ACI 318 (ACI 2014) design expressions indicate that the punching shear strength evaluation formula of KCI 2012 (KCI 2012), which considers the effect of the flexural reinforcement ratio on the shear strength, is more accurate than that of ACI

318 (ACI 2014). However, in both design formula, shear strength evaluation for the shear reinforcement tends to overestimate the shear strength when the flexural reinforcement ratio is low and the amount of shear reinforcement is large, as the effect of the flexural reinforcement on the shear strength, by the amount of shear reinforcement, is not considered.

- Thus, the strength reduction factor for the shear reinforcement considering the effect of flexural reinforcement was proposed. Using the proposed method, the punching shear strength of the shear reinforced slab-column connection could be estimated more stably. And the validity of the proposed strength reduction factor was verified by comparing its prediction results with existing test data.

2.2.3 *Saleh, Kalfat, Abdouka, Al-Mahaidi (2019)*

The test program looked into ways to retrofit existing slab-column connections by using Sika CarboShear laminate composite fiber reinforced polymers (L-CFRPs). Typical retrofits consist of steel bolts installed in predrilled holes. Replacing the steel bolts with L-CFRPs bonded to the concrete by an epoxy was the objective of the research.

Four full-scale test specimens were constructed and tested. The slab dimensions of 90.6 x 90.6 x 7.9 in. were consistent for all four specimens. A column was not cast as part of the slab, instead a loading plate of 7.9 x 7.9 x 1.2 in. was placed in the center of the slab and the load was applied to simulate loading from a column. The flexural reinforcement was consistent for all the tests and is provided in Table 2.18.

Table 2.18. Saleh, Kalfat, Abdouka, and Al-Mahaidi (2019) Specimen Details

Specimen	Top Bars			Bottom Bars			Shear Reinforcement
	Bar Size (No.)	Bar Spacing (in.)	Reinf. Ratio (%)	Bar Size (No.)	Bar Spacing (in.)	Reinf. Ratio (%)	
CS	6	5.9	1.50	4	11.8	0.26	None
SS1	6	5.9	1.50	4	11.8	0.26	L-Shaped CFRP Laminate
SS2	6	5.9	1.50	4	11.8	0.26	L-Shaped CFRP Laminate
SS3	6	5.9	1.50	4	11.8	0.26	L-Shaped CFRP Laminate

The arrangement of the L-CFRP was varied between tests. The laminate used in the retrofit was L-shaped with one leg being 7.9 in. and the other being 3.9 in.. The long leg was inserted into the predrilled hole, while the shorter leg was used to anchor the laminate to the slab. The variation in arrangement was to determine what the most efficient way of anchoring the laminate would be for practice. Specimen CS was a control specimen and therefore had no shear reinforcement. Specimen SS1 had two laminates per predrilled hole, one laminate anchored at the top of the slab, the other anchored at the bottom of the slab. Specimen SS2 had one laminate per predrilled hole, with the laminates in the first two perimeters of holes anchored at the bottom of the slab and the laminates at the third perimeter anchored at the top of the slab. In this way the anchored side would always be near the assumed inclined shear crack. After Specimen SS2 it was realized how difficult for construction anchoring from the bottom side of the slab could be, so Specimen SS3 had all laminates anchored on the top side of the slab.

A concentric load was applied to the bottom of the slab while spreader beams, at each slab edge, resisted the slab from moving upward. The spreader beams were tied to the strong floor by four high tensile strength threaded bars, one per spreader beam. The slab was simply supported with two steel plates located near the ends of the spreader plate to act as the supports. All the supports were equal distance from the center of the slab. The punching load was applied by a 3000 kN hydraulic jack at a rate of 0.5mm/min.

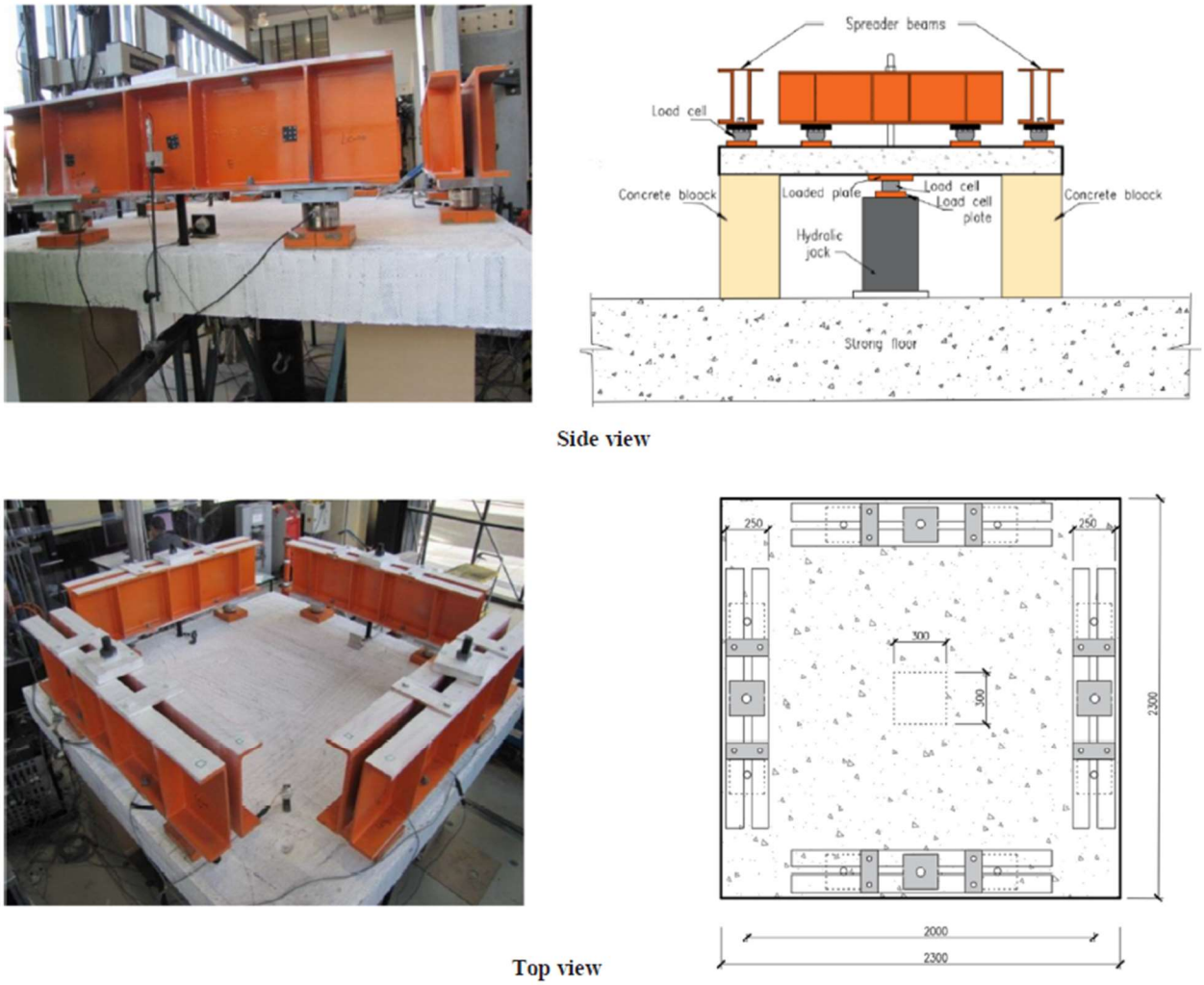

Figure 2.8. Saleh, Kalfat, Abdouka, and Al-Mahaidi (2019) Test Setup

The specimens each had six strain gages attached to measure yielding of flexural reinforcement across the slab. The gages were placed where the maximum moment was expected to occur moving out across the slab to determine the extent of bar yielding in each direction. In addition, strain gages were also placed on the laminate to determine the shear reinforcement's contribution to the shear strength and possible aid in understanding the propagation of the inclined shear cracks. Load cells attached to actuator as well as the support plates recorded the applied load and subsequent reactions of the specimens. A photogrammetry measurement technique was used to determine the vertical displacements of the slab and inclinometers measured the rotation of the slab due to bending.

The load-displacement curves show changes at 200 kN for all specimens and between 900-1000 kN for the strengthened specimens. This behavior is attributed to flexural cracks forming around 200 kN and shear cracking starting around 900-1000 kN. The control specimen, CS, had a linear response after its initial flexural cracking up until the point of failure. The failure of Specimen CS was abrupt and showed no ductile past the ultimate load. The strengthened specimens showed significant ductility between start of shear cracks and ultimate load. After reaching ultimate loading the strengthened specimens experienced a sudden drop in strength. All strengthened specimens failed outside of the shear reinforced region. Strengthened specimens showed an increase of 91-104% in two-way shear strength and a 225-400% increase in deflection at failure compared to Specimen CS.

The failure load of the strengthened specimens was compared to the predicted flexural strength capacity determined by yield line theory. Specimen SS3 was to closest to reaching flexural capacity, failing at a load 6% lower than the predicted capacity. This lead researchers to believe that there is no more efficient arrangement of the L-CFRPs that would have increased the shear capacity without causing the slab to fail in flexure. The deflections and rotations of the slab recorded by other instrumentation supported the increase in ductility of strengthened specimens.

Specimen CS failed in a brittle manner. The failure was categorized as a punching failure due to sudden loss of strength and formation of a circumferential crack pattern due to the inclined cracking. The strengthened slabs first formed flexural cracks near the edges of the loading plate. The punching shear cracks formed on the bottom side of the slab and outside of the reinforced zone. The shear cracks propagated outward toward the edges of the slab. Specimens SS1 and SS2 had similar inclination of cracks, and a similar punching cone shape. Punching cracks did not propagate to the top, tension, side face of Specimen SS3.

Strain measurements in the flexural reinforcement before 200 kN of applied force were negligible indicating that the flexural reinforcement contributed very little to the initial behavior of the specimens. Specimens CS and SS1 did not yield in flexure. Specimens SS2 and SS3 had all bars yield prior to ultimate load. Strain gages placed on the L-CFRPs showed that before formation of inclined cracks the strain in L-CFRPs were generally low. After formation of inclined cracks, L-CFRPs transferred most of the load across cracks, therefore increasing the shear capacity of the specimens. The laminates closest to the loading plates showed the highest strain.

The results of the study led to the following conclusions:

- The control specimen failed at 569 kN and the strengthened specimens SS1-SS3 failed at peak loads corresponding to 1121 kN, 1087 kN and 1163 kN which corresponded to a strength increase of 97%, 91% and 1014% respectively. A significant improvement was observed in the deflection of all the strengthened slabs at the ultimate respect to the control slab. The Specimen SS3 showed a maximum deflection increase of 400% compared to the control Specimen CS, while the Specimen SS2 shows a minimum increase of about 225%.
- All the strengthened specimens (SS1, SS2 and SS3) exhibited a punching damage mode outside the shear reinforced zone. This response was attributed to the presence of the L-CFRP which provided adequate resistance to shift the crack outside the strengthened area.
- The maximum FRP strains recorded for Specimens SS1, SS2 and SS3 at location of P1 (80 mm from the loading plate) were 5404, 5200, 5300 microstrain, respectively.
- Based on an evaluation of punching shear strength prediction models available in the EC2 (2004) and ACI318 (2014), it was concluded that provided the FRP stress levels at failure were obtained based on a design strain of 4000 microstrain, the existing models could be used to predict the capacity of the strengthened specimens to a good level of accuracy.
- In this research, the best estimation of the shear capacity and failure location of the tested specimens was obtained using the Fib Model mode MC 2010.

Chapter 3. EXPERIMENTAL TEST PROGRAM

The experimental program was a continuation of a previous study conducted by Yeutter (2020). The tests consisted of two different testing configurations, one investigation combined-loading, while the other focused on punching of the connection. The following sections will present the combined-loading specimens first, followed by the punching specimens. The chapter will cover the following topics:

- Test Specimens and Matrix
- Specimen Construction
- Specimen Materials
- Experimental Test Setup
- Instrumentation
- Testing Procedures

3.1 TEST SPECIMENS AND MATRIX

The proposed connection offers a way to connect a CFST column to a RC slab. This is shown in Figure 3.1. The CFST column is discontinuous through the slab to allow for the slab flexural reinforcement to pass through the column. To connect the column to the slab, a circular steel ring referred to as the ring flange was welded to the top and bottom of the tubes. The ring flange is detailed in Figure 3.2. The holes allowed for bolts to be placed through the upper ring flange to the lower ring flange. The bolts are then post-tensioned to secure the tubes to the slab. In order to provide a load path between the columns and from diaphragm to column, column longitudinal reinforcement is placed in the column discontinuous region. For ease of construction the column reinforcement is welded to the lower CFST tube and continued into the upper tube. In addition the column longitudinal reinforcement should be slightly bent to allow for easier

placement of the upper CFST tube over the reinforcement during construction. The benefits of using the CFST column to RC slab connection are as follows:

- CFST columns have larger shear, axial and flexural capacities than traditional RC columns
- Tube acts as permanent formwork, so additional column forms are not needed
- Tube acts similar to the reinforcement of a RC column so no internal reinforcement is needed outside of the discontinuous region
- Eliminate the need for column splicing
- Ring flange increases punching capacity by increasing critical perimeter so no slab shear reinforcement is needed

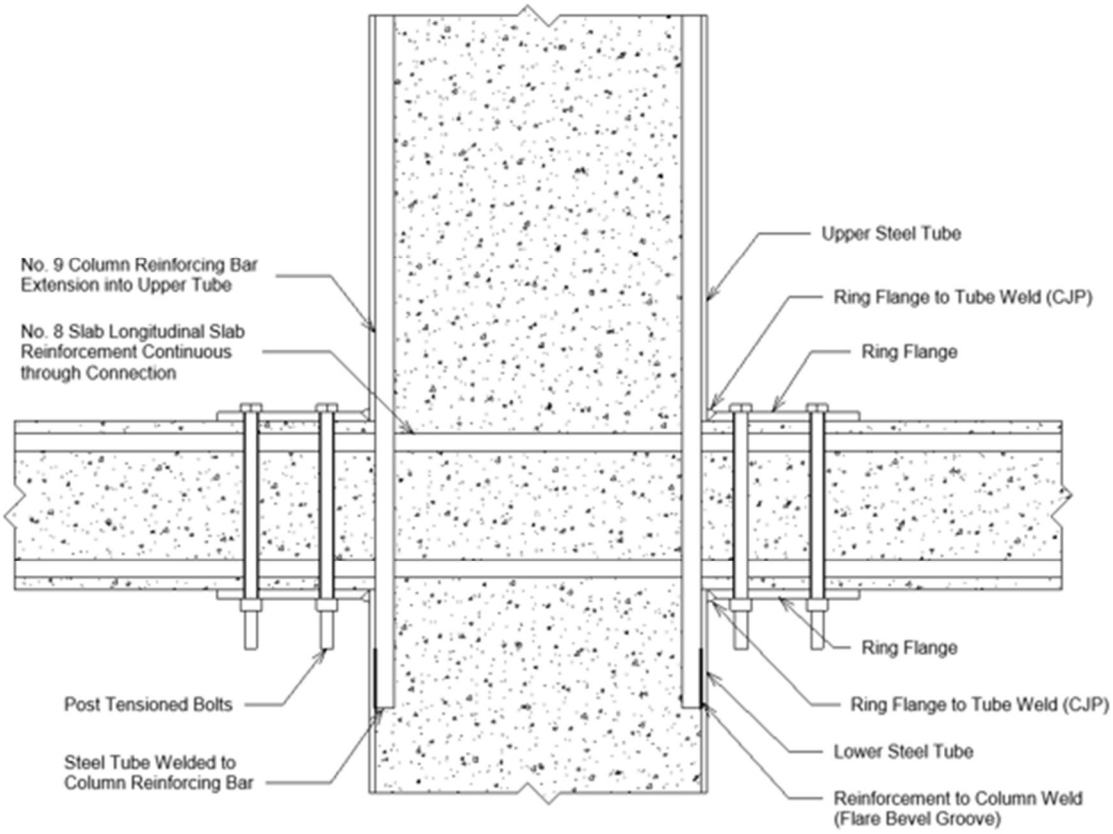

Figure 3.1. CFST Column with Ring Flange to RC Slab Connection

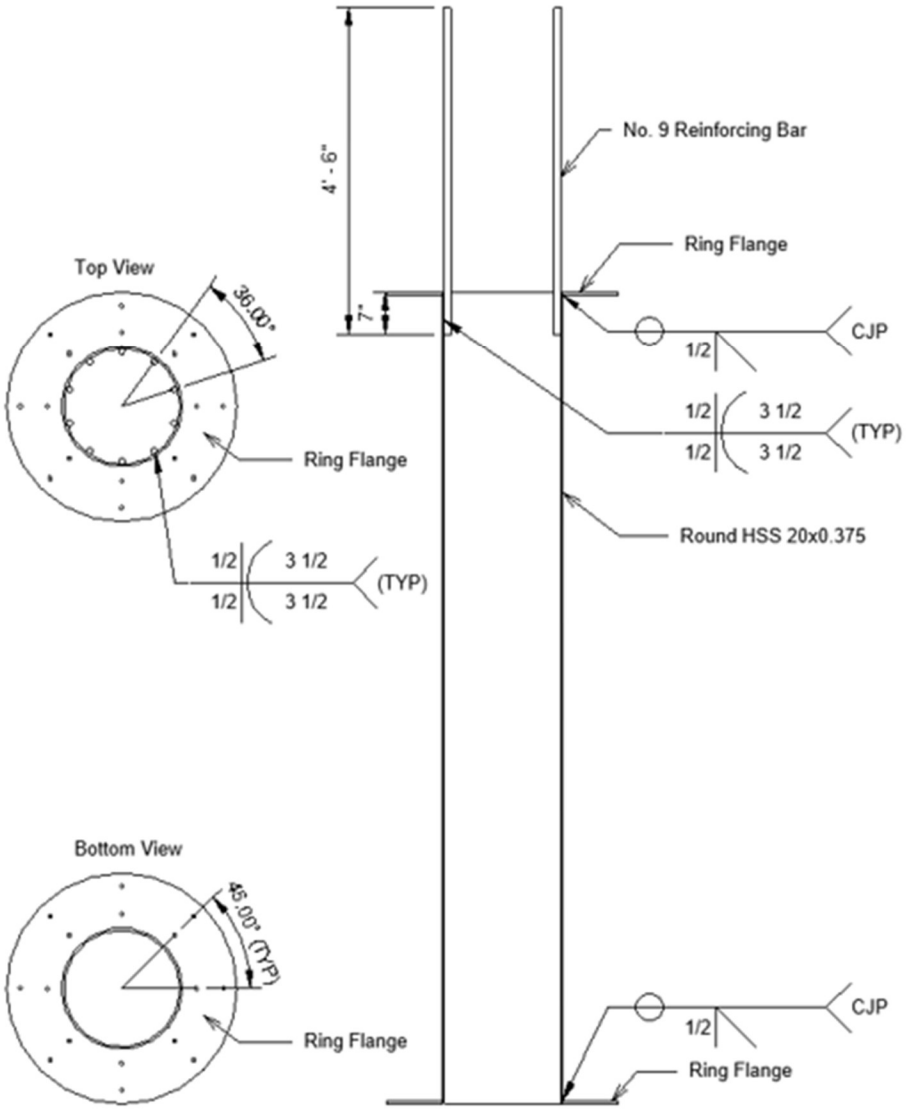

Figure 3.2. Example CFST Shop Drawing

Figure 3.3 provides the test matrix for the combined-loading specimens and includes Yeutter's specimens to provide comparison. Yeutter's tests included a reference specimen that had no ring flange and utilized stud rails for the shear reinforcement. The stud rail details are provided by the specimen naming convention given in Table 3.1. The three other specimens varied (1) the size of the ring flange, (2) number of perimeters of bolts on the ring, (3) number of perimeters of bolts off the ring. This is shown in the proposed connection's naming convention provided in Table 3.2. The combined-loading tests conducted during this experimental work varied the slab depth

and ring size to investigate if the slab depth could be used to determine the size of the ring flange. They are named PTB_4.5_1_0_6 and PTB_9_2_0_6.

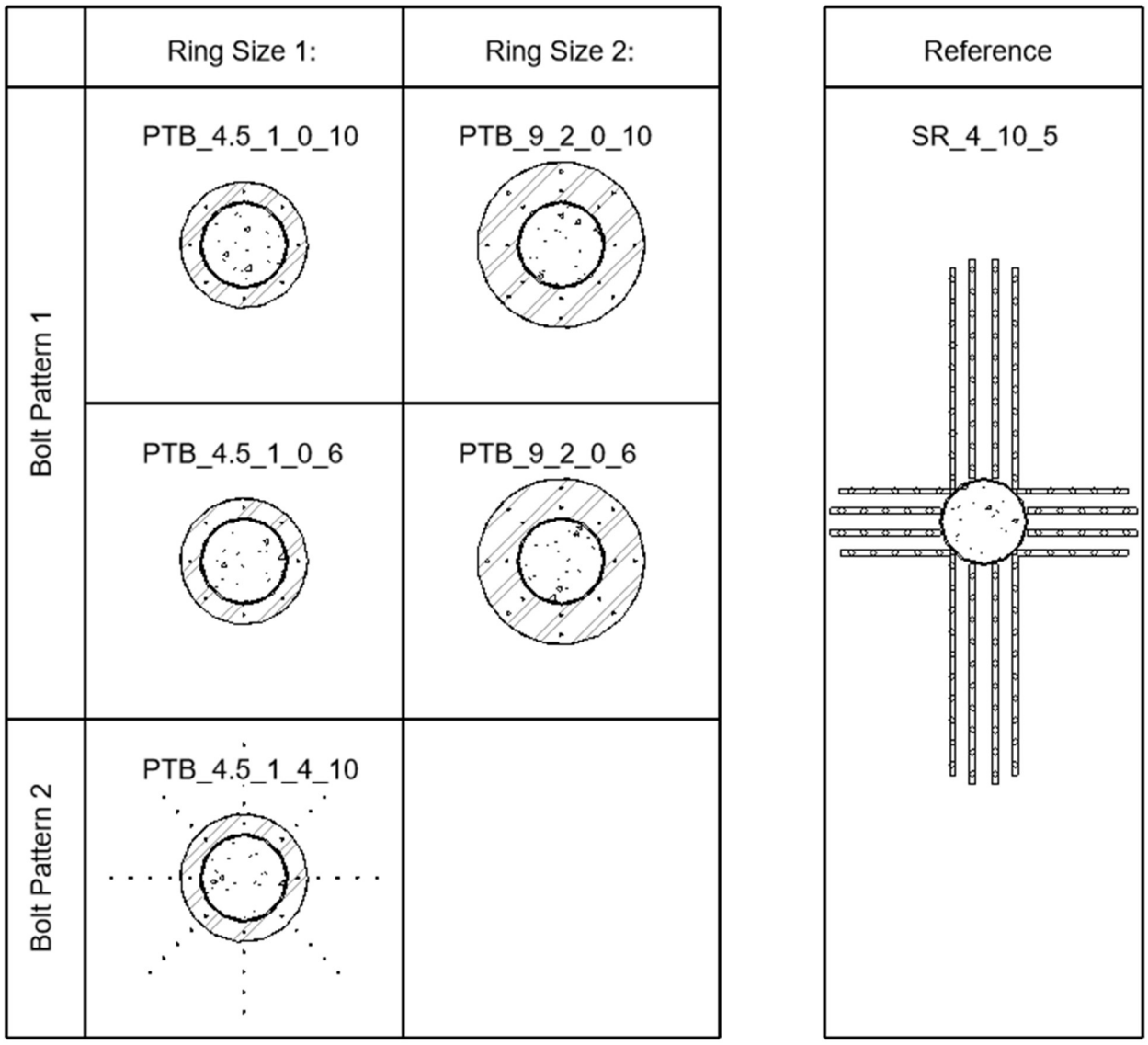

Figure 3.3. Combined-Loading Test Matrix

Table 3.1. Naming Convention for Reference Specimen

Specimen ID	Type of Shear Reinforcement	No. of Rails per Column Face	No. of Studs per Rail	Stud Spacing (in)	Slab Depth (in)
SR_4_10_5_10	Stud Rails	4	10	5	10

Table 3.2. Naming Convention for Combined-Loading Specimens

Specimen ID	Type of Shear Reinforcement	Ring Size (in)	No. of Bolts on Ring	No. of Bolts off Ring	Slab Depth (in)
PTB_4.5_1_0_10	Post Tensioned Bolts	4.5	1	0	10
PTB_4.5_1_4_10	Post Tensioned Bolts	4.5	1	4	10
PTB_9_2_0_10	Post Tensioned Bolts	9	2	0	6
PTB_4.5_1_0_6	Post Tensioned Bolts	4.5	1	0	6
PTB_9_2_0_6	Post Tensioned Bolts	9	2	0	6

Yeutter's specimens were designed based off a prototype vertical evacuation structure (VES). The VES required higher live loads and wider column spacing which led to a slab design with the following detailing:

- Specified concrete strength, $f'c = 4000\ psi$
- Slab depth of 10 in. with concrete cover of ¾ in.
- ASTM A615 Grade 60 No. 8 bars spaced at 9 in. OC in both directions.

This resulted in a flexural reinforcement ratio of 1%. Due to the cyclic nature of the loading equal flexural reinforcement was placed on the top and bottom of the slab. The column size was determined using the plastic stress distribution method (PSDM) in accordance with Part 16 Chapter I Section 2a of the 14th edition of the AISC Steel Construction Manual. Which resulted in columns with the following detailing:

- 20 in. OD pipe with 3/8 in. wall thickness
- Specified concrete strength, $f'c = 4000\ psi$

The slab dimensions were chosen based on the limitations of the test setup. The columns were chosen to be half a story height above and below the slab at the assumed points of contraflexure. To accommodate the MTS actuator connected near the top of the upper column as well as to provide clearance for the loading plate of the Baldwin testing machine the length of the

upper column was increased. However, the point of loading of the upper column is the same distance away from the center of the slab as the pinned support at the base of the lower column. This resulted in a lower column of 65 7/8 in. and an upper column of 84 7/8 in. for the 6 in. slab specimens. Figure 3.4 shows the slab geometry and reinforcement layout for the specimens from phase 2 of testing. The differences between their geometry and the specimens from phase 1 are the slab depth and the size of the reinforcement used.

The slab longitudinal reinforcement was consistent with the flexural reinforcement ratio of from phase 1 testing. (1%). This resulted in using No. 6 bars at 9 in. OC in both directions. ASTM A615 Grade 80 bars were used to improve the flexural strength and possibly force a two-way shear failure under combined-loading. Due to the cyclic nature of the testing the slab longitudinal reinforcement is consistent in both the top and bottom of the slab. With the direction of loading being in the North-South direction, it was decided that the East-West slab reinforcement would be placed inside the envelope created by the North-South bars. This requirement of fitting within the envelope made it difficult to use bars with 180 degree bends due to the minimum bend diameter. Accordingly, slab reinforcement in the East-West direction have 90 degree bends since they were expected to experience negligible stress from the cyclic loading.

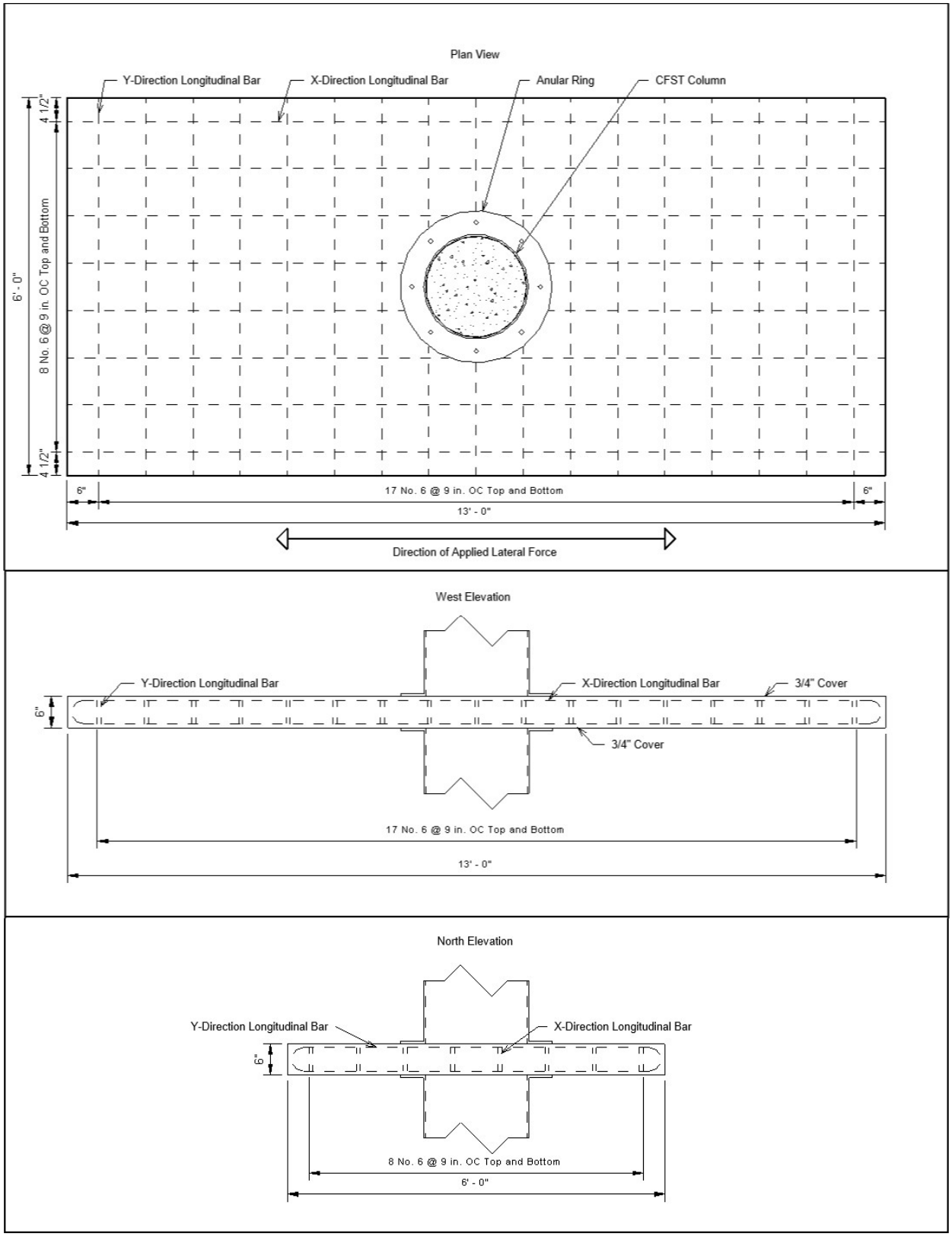

Figure 3.4. Longitudinal Reinforcement Layout

The results from phase 1 and 2 of testing indicated that all of the specimens had failed in flexure. As a result, two specimens were constructed to be tested in punching shear. The test parameters are given in Figure 3.5. The ring width was varied to see its effects on the punching strength of the connection.

Most prior punching shear tests had square slab dimensions to provide symmetric loading to all sides of the specimen. The punching specimens had a slab of 6ft. x 6ft. which was limited by the space available beneath the Universal Baldwin Testing Machine. A slab depth of 10 in. was used to increase the probability of a punching failure while keeping dimensions consistent with specimens from phase 1.

The tubes used for the CFST columns had the same outer diameter and wall thickness as the tubes used for the combined-loading specimens. The column heights were reduced to limit potential $P - \Delta$ effects on the punching behavior. The top column was 12 in. in height while the bottom column was 9 in. The upper column transferred the punching force to the slab while the lower column satisfied the boundary condition for the bottom side of the slab. Column longitudinal reinforcement was not needed for the punching shear test specimens.

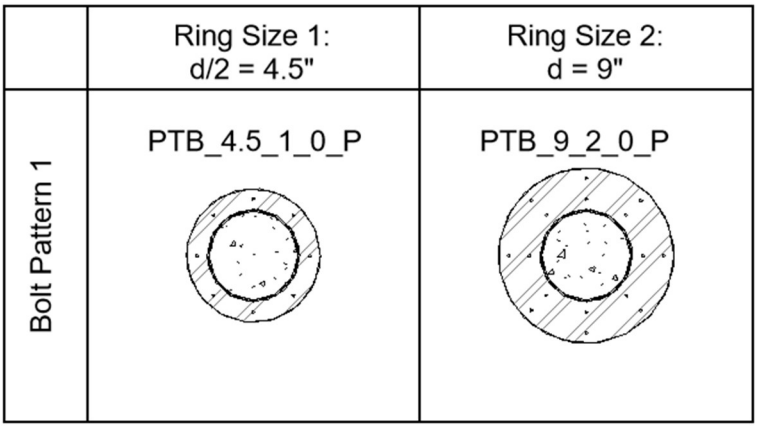

Figure 3.5. Punching Test Matrix

The flexural reinforcement for the specimen was designed to ensure a punching failure. The slab capacity was predicted using ACI 318-19, KCI 2012, and a shear friction model from Birkle (2003). The strength was calculated under the assumption that the ring flange would confine the concrete beneath it and force the punching failure away from the column, thereby increasing the critical perimeter and the punching strength. It was found from a constructed database of

punching tests in Chapter 2 that the KCI 2012 had the most accurate prediction. The KCI punching capacity and the flexural strength of the slab are both dependent upon the flexural reinforcement ratio. The slabs predicted flexural capacity was determined using a yield line model. The flexural reinforcement ratio was then modified until the predicted KCI punching capacity was greater than the predicted flexural capacity indicating a punching failure. This resulted in flexural reinforcement ratio of 1.79%. Figure 3.6 provides the layout of the flexural reinforcement.

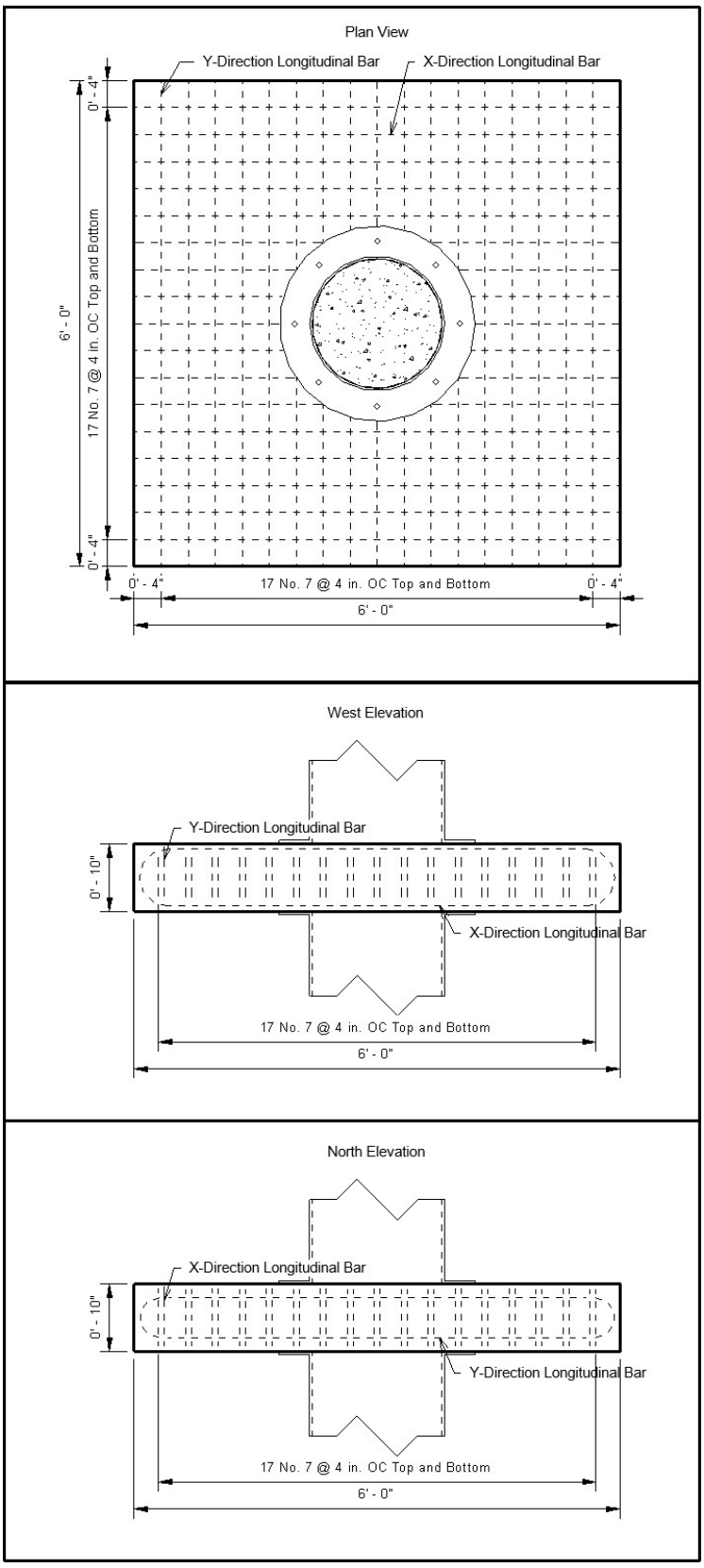

Figure 3.6. Slab Longitudinal Reinforcement Layout for Punching Specimens

3.2 SPECIMEN CONSTRUCTION

The test specimens were constructed in two stages. The combined-loading specimens were constructed for phase 2 of testing followed by the punching specimens for phase 3.

3.2.1 *Formwork*

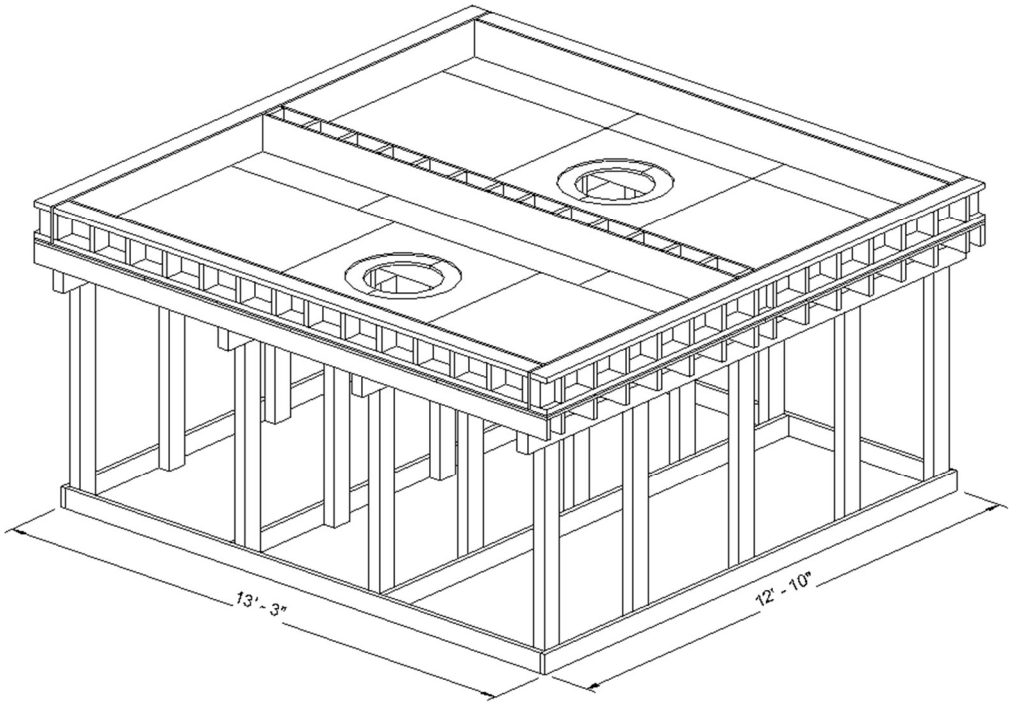

Figure 3.7. Formwork for Combined-Loading Specimens

The formwork for the combined-loading specimens developed in the University of Washington Structural Engineering Laboratory by Yeutter (2020) was used for this test program. The formwork, shown in Figure 3.7, was able to support two specimens cast simultaneously. 20 in. holes were cut in the center to accommodate the lower tube. The circular inlay around the hole was for the ring flange to sit in so that it would be flush to the bottom face of the slab. Side walls were fastened to the plywood by steel bolts to resist hydrostatic pressure from the concrete during casting. The slab thickness was changed for phase 2 of testing which required some small

modifications to the side walls to see when the concrete reached 6 in. in height. For the punching specimens in phase 3 of testing the dimensions of the slab changed resulting modification of side walls to accommodate the slab geometry. The support structure remained unchanged for construction of all of the test specimens.

3.2.2 *Column Fabrication*

The CFST tubes for the columns were cut to length by an oxy-acetylene torch specialized for tube cutting. Once cut to length the tubes were set aside until the ring flange was ready to be welded. In order to ensure precision of the ring flange dimensions, the ring flanges were professionally manufactured. The rings were cut to size with the correct number and placement of bolt holes added. The rings were then prepped for a complete joint penetration (CJP) weld between the steel tube and the inner diameter edge of the ring flange. The preparation included a ¼" root gap as well as a 45° bevel of the inner edge of the ring. Welding of the ring flange to the slab end of the tubes was done by a certified welder. For the combined-loading specimens the steel tubes were laid down horizontally and the longitudinal column reinforcement was welded to the inside of the lower tubes at a depth of 7 in. This left the rest of the column longitudinal reinforcement protruding out of the tube. After casting of the slab it was difficult to place the upper tube over the column longitudinal reinforcement. The reinforcement was bent in order to accommodate the placement of the upper column.

3.2.3 *Slab Fabrication*

The lower column tube was placed into the formwork with the column longitudinal bars protruding vertically. The slab rebar cage was built to the dimensions specified in Figure3.4. Threaded slab inserts were placed in order to attach lifting loops after casting of the slab. Polyvinyl Chloride (PVC) tubes were used to provide holes in the slab through which the post-tensioned bolts could be placed to secure the tubes to the slab. The ring flange bolt holes were caulked to prevent concrete from entering. Where the slab reinforcement interfered with the vertical PVC tubes, the slab reinforcement was moved minimally to allow for a vertical bolt hole through the slab. In order to ensure the PVC tubes remained vertical during casting a plywood ring with bolt

holes matching the ring flange was placed to secure the tops of the PVC tubes. The plywood ring was supported on 2x4s that spanned the transverse direction of the slab. Strain gauges had been applied to the slab reinforcement before assembly of the rebar cage. Both slab and column strain gauge wires were carefully guided out of the slab with the wires shielded in between slab reinforcement to protect them during casting. The wires were also supported at mid height of the slab to reduce the stress acting on them during testing. The formwork was caulked to prevent any leakage of the concrete. The forms were then greased to ease in their removal after casting.

The only differences between slab fabrication for the combined-loading specimens and the punching shear specimens were the spacing of the slab reinforcement and type of lifting loops used. The punching shear specimens' slab reinforcement is shown in Figure 3.6. The lifting loops were constructed by bending ASTM A615 No. 3 bars into a shape that the lifting chains would be able to fit through. The location of the lifting loops were closer to the slab edge to avoid effecting the behavior of the test.

3.2.4 *Casting*

A concrete mix for structural applications was used for the bottom column and slab. The mix is identical to the mix used in the specimens from the research conducted by Yeutter (2020). Specimens cast in two phases. A first cast for the lower column and slab after which the second cast would fill the upper column. For the first phase of casting a line pump truck was used to pump concrete from the concrete truck up onto the elevated forms. While the slabs were being finished, 36 concrete cylinders were constructed for material testing. After finishing the slabs, wet burlap was placed on the surface to allow the concrete to cure. The wet burlap stayed in place for a minimum of three days. The upper columns were then moved into place. Four of the PVC tubes that created holes in the slab were removed. Bolts were placed in the holes and tightened to anchor the upper tube to the slab. Due to an uneven surface of the slab, a grout pad was poured to fill any gaps between the ring flange and the slab surface. The upper columns were then cast using a crane carrying a bucket of concrete. Specimens cured for a minimum of 28 days before testing.

The punching shear specimens followed a similar casting process. The concrete mix for the upper column differed from the mix for the lower column and slab due to the small amount of

concrete needed. The concrete for the upper column was mixed in the University of Washington Materials Lab. The upper columns were cast by using shovels to place the concrete in the tubes.

3.3 SPECIMEN MATERIALS

3.3.1 *Concrete*

Table 3.3 shows the use of the concrete cylinders collected during casting.

Table 3.3. Cylinders for Concrete Material Testing

Components Cast	Cylinder Use	Number Made
Slab and Lower Column	7 Day Strength	3
	14 Day Strength	3
	21 Day Strength	3
	28 Day Strength	3
	Test Day Compressive Test	6
	Extra Cylinders in case of poor consolidation	6
Upper Column	Test Day Compressive Test	6

Cylinders were stored in a lime bath until testing. Compressive tests used covers on the ends of the cylinder to create a level surface for the load to be applied to. The results of the test day strengths are given in Table 3.4. The upper column strength for the punching specimens was higher as a result of the mix design strength being approximately 10,000 psi.

Table 3.4. Test Day Concrete Properties

Specimen ID	Compressive Test: (psi)			
	Slab and Lower Column		Upper Column	
	Mean	St. Dev.	Mean	St. Dev
PTB_4.5_1_0_6	7430.0	258.7	7368.2	202.4
PTB_9_2_0_6	7617.6	75.2	7426.4	124.6
PTB_4.5_1_0_P	6424.2	288.9	9222.8	266.0
PTB_9_2_0_P	6685.4	140.6	9162.4	536.5

3.3.2 *Reinforcing Bars*

Bars for the specimens were ordered from two different suppliers. This was due to the desired strength of the slab reinforcement for the combined-loading specimens. The slab reinforcement for the combined-loading specimens was donated by Farwest Steel Corporation. The column reinforcement for the combined-loading specimens as well as the slab reinforcement for the punching shear specimens were supplied by Addison Construction Supply. Slab reinforcement for the combined-loading specimen consisted of A615 Gr. 80 steel. Column longitudinal reinforcement for the combined-loading specimens were A706 Gr. 60 steel so that they could be welded to the inside of the tube. The slab reinforcement for the punching shear specimens were A615 Gr. 60 steel.

The stress-strain relationship was measured by testing three bars of each size and grade. The results for the combined-loading specimens are given in Table 3.5. The stress-strain results for the punching specimens are provided by Table 3.6. The stress-strain curves are provided in Figures 3.8-3.10

Table 3.5. Combined-Loading Specimen Reinforcing Bar Properties

	Reinforcing Bar			
	Slab		Column	
	Average	St. Dev.	Average	St. Dev.
Steel Grade	A615 Gr. 80	-	A706 Gr. 60	-
Specified Yield Stress (ksi)	80	-	60	-
Measured f_y (ksi)	93.9	0.56	71.7	7.60
Measured ε_y	0.0035	$5.7 * 10^{-4}$	0.0028	$1.7 * 10^{-4}$
Measured f_u (ksi)	126.1	0.39	110.7	6.68
Measured ε_u	0.1145	0.004	0.1049	0.008
Measured f_r (ksi)	91.3	0.465	85.1	6.37
Measured ε_r	0.3665	0.123	0.1254	0.024

Table 3.6. Punching Shear Loaded Specimen Reinforcing Bar Properties

	Reinforcing Bar			
	Slab		Column	
	Average	St. Dev.	Average	St. Dev.
Steel Grade	A615 Gr. 60	-	-	-
Specified Yield Stress (ksi)	60	-	-	-
Measured f_y (ksi)	69.7	0.15	-	-
Measured ε_y	0.0023	$9.1 * 10^{-4}$	-	-
Measured f_u (ksi)	107.2	0.16	-	-
Measured ε_u	0.1064	0.008	-	-
Measured f_r (ksi)	80.0	1.00	-	-
Measured ε_r	0.472	0.041	-	-

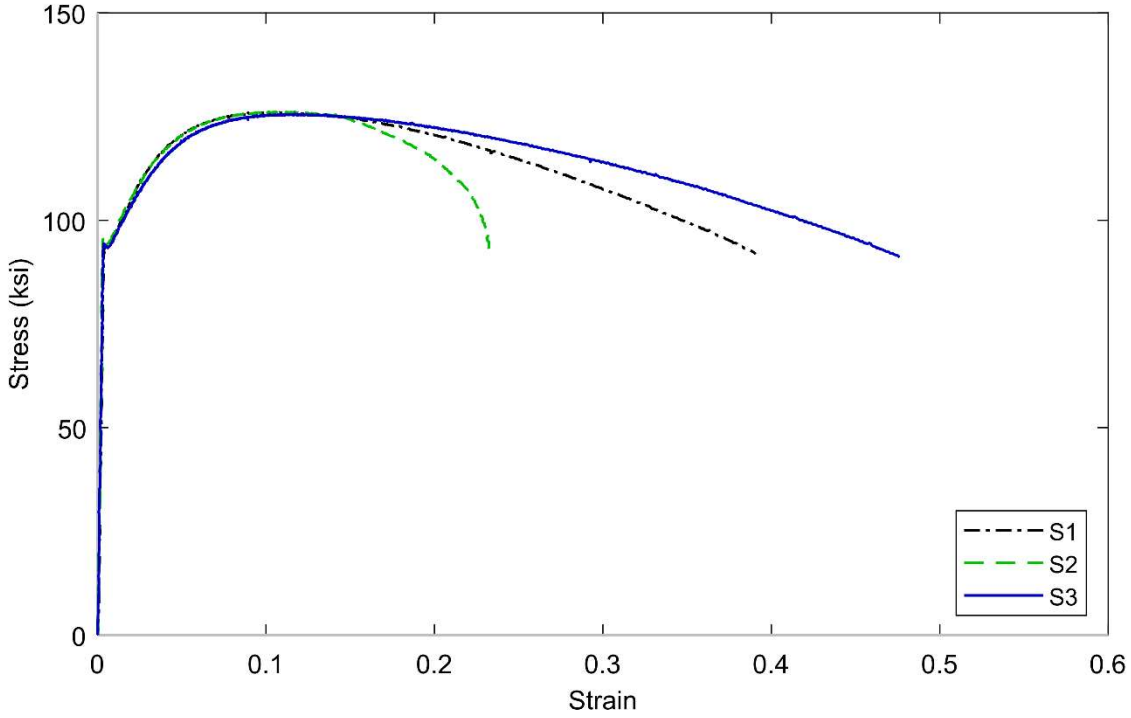

Figure 3.8. Stress vs. Strain A615 No. 6 Gr. 80 Reinforcing Bars

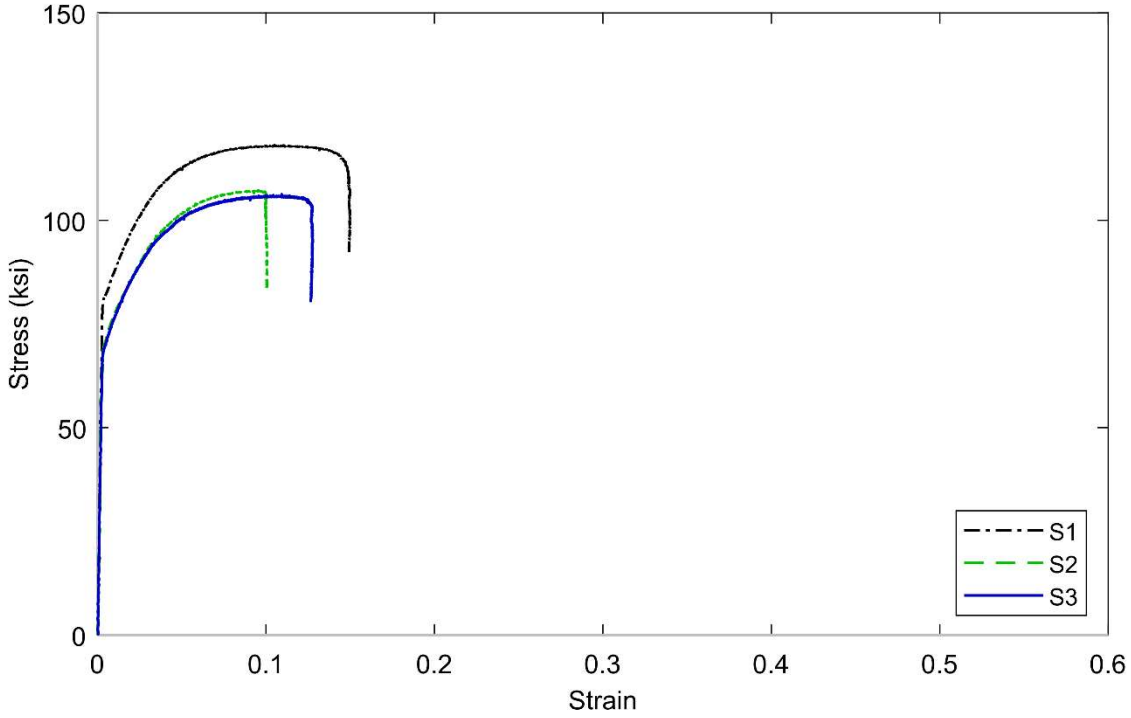

Figure 3.9. Stress vs. Strain A706 No. 9 Gr. 60 Reinforcing Bars

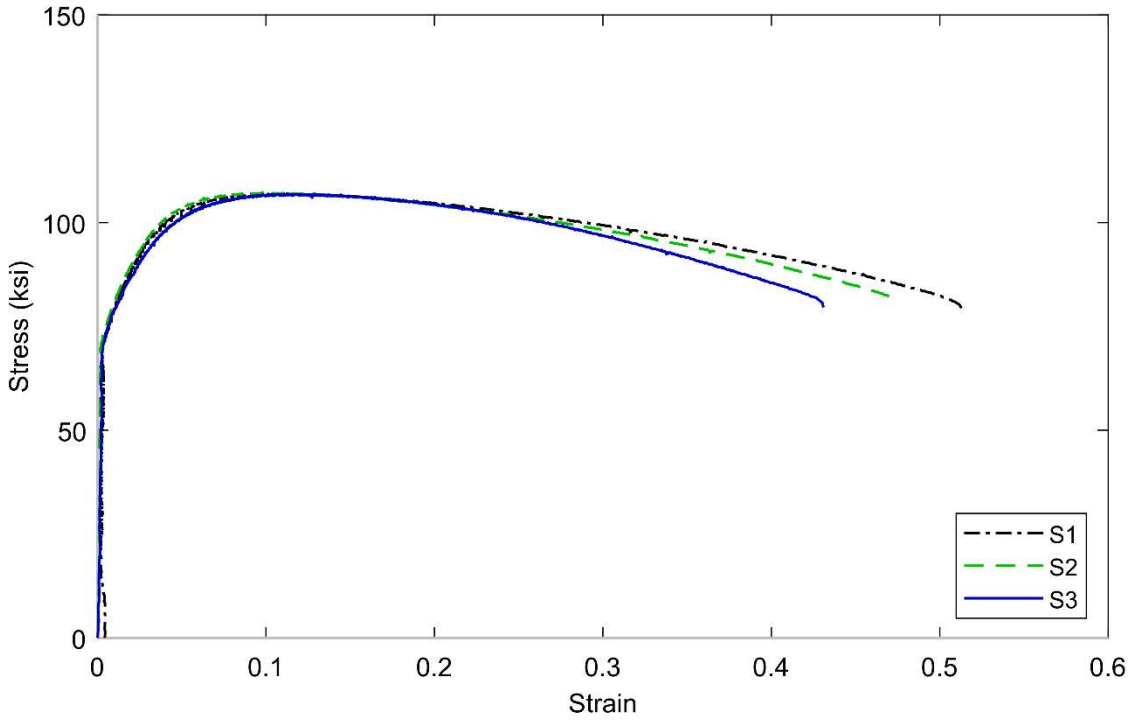

Figure 3.10. Stress vs. Strain A615 No. 7 Gr. 60 Reinforcing Bars

3.3.3 *Steel Tubes and Ring Flanges*

Steel tubes were donated by Skyline Steel. They are ASTM A252 Gr. 3 spiral welded tubes with a 60 ksi minimum yield strength. The tubes were 3/8 in. thick. Material properties were reported by the manufacturer.

The ring flanges were manufactured off-site by a local steel distributor. The rings were cut from an ASTM A572 steel plate. The thickness of the plate was ½ in. Ring flanges were welded to the tubes using Coreshield 8 E70 5/64 in. diameter wire. Material properties are summarized in Table 3.7.

Table 3.7. Column and Ring Material Properties

	Tube	Ring
Steel Grade	A252 Gr. 3	A572 Gr. 50
Specified Yield Stress (ksi)	60	50
Reported Yield Stress (ksi)	62.0	-
Reported Ultimate Stress (ksi)	68.9	-

3.4 EXPERIMENTAL TEST SETUP AND PROCEDURE

This section provides information about the testing setup and procedures for the phase 2 and phase 3 of testing. The information for the specimens subjected to combined-loading will be presented first. This will cover the following aspects of their testing:

- Lateral Load Application
- Vertical/Axial Load Application
- Experimental Test Setup
- Experimental Test Procedure

The specimens subjected to punching shear will present similar information. The punching shear specimens were only subject to a vertical load application so there is no section on lateral load application.

3.4.1 *Lateral Load Application for Combined-Loading Specimens*

Figure 3.10 shows the test setup for the combined-loading specimens. Lateral displacements were applied by the MTS Actuator to simulate a seismic event. The displacements increased during testing to investigate the deformation and lateral resistance of the connection. The MTS actuator had a capacity of 220 kips and a stroke range of ±10 in.. The MTS actuator was

secured to the upper column by four 1 in. high strength rods, spreader plates, and rubber pads. The rods were prestressed to secure the actuator to the column. Spreader plates and rubber pads allowed distribution of the actuator force over a larger area to avoid local damage to the specimen. Additional plates were placed between the actuator and the South face of the column to assure that the column was vertical at mid-stroke of the actuator.

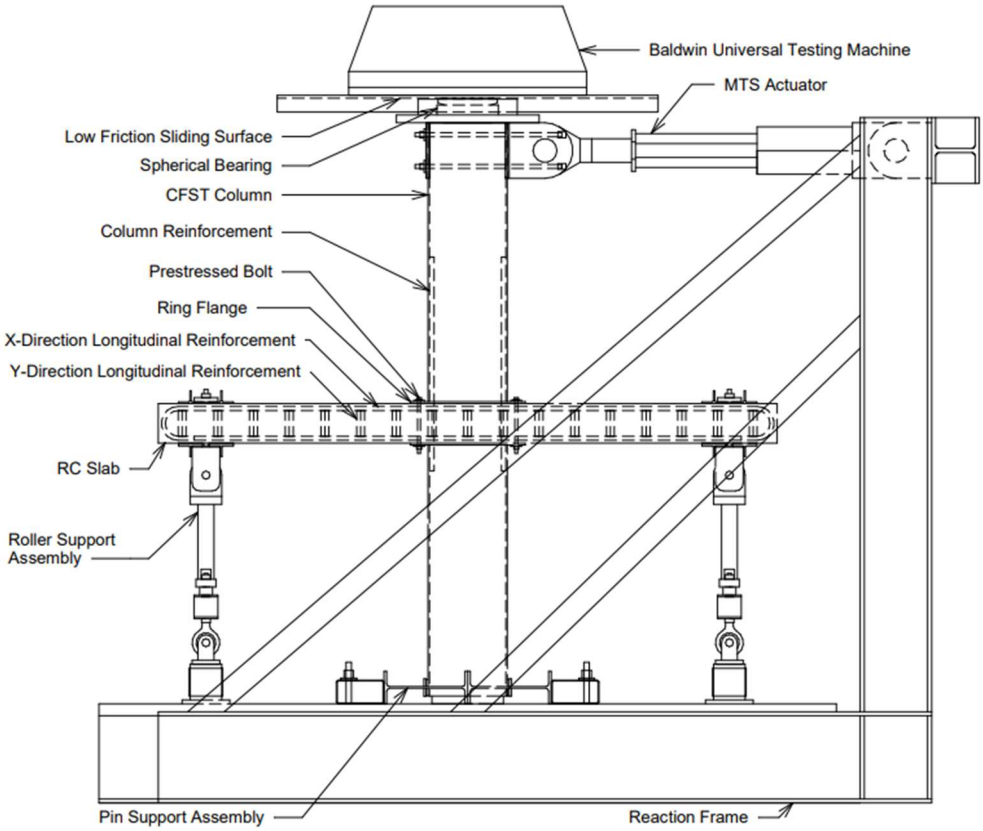

Figure 3.11. Combined-Loading Tests Setup

3.4.2 *Vertical/Axial Load Application for Combined-Loading Specimens*

Vertical loading was applied by the 2400 kip Baldwin press as shown in Figure 3.11. At the point of load application a steel bearing was placed that allowed the Baldwin cross head to

remain horizontal while applying the axial load in a direction perpendicular to the top of the column. In addition to the friction force, a layer of hydrostone helped keep the bearing in place.

3.4.3 *Experimental Test Setup for Combined-Loading Specimens*

In order to replicate the boundary conditions expected in a building, supports were added to the base of the column and ends of the slab. The base of the column simulated a pin by using a steel collar to restrict horizontal movement of the bottom of the column as seen in Figure 3.11. The collar was fit around the north and south face of the lower column and then bolted together and prestressed to the reaction frame. A ½ in. layer of cotton duck was placed between the collar and the lower column face. The flexibility of the cotton duck pads allows for small deformations that would accommodate the small rotations expected at the base of the column.

Each end of the slab was supported by two struts. The struts, shown in Figure 3.12, allow for free horizontal movement of the slab as a result of the two clevises. The struts were attached to the slab by the threaded rod. The threaded rod passed through a hole in the slab and a nut fastened spreader plates to the top and bottom face of the slab as seen in Figure 3.11. The threaded rods were then prestressed to make the attachment more secure. The struts were fixed to the self-reacting frame by the threaded rode on the bottom.

At the top of the column the roller support condition was simulated by a bearing and channel configuration. The flat side of a channel was bolted to the Baldwin crosshead. The inside face of the channel web and flanges were lined with stainless steel. The stainless steel was then greased with PST-540. This reduced the amount of friction on the bearing along the channel tract. The steel spherical bearing was placed between the column and channel tract, thus allowing for free movement of the top column in the direction of loading. The shape of the bearing allowed for the load from the Baldwin to be applied parallel to the longitudinal axis of the column regardless of rotation due to column displacement.

Figure 3.13 shows a free body diagram of the applied loads and support reactions due to cyclic testing.

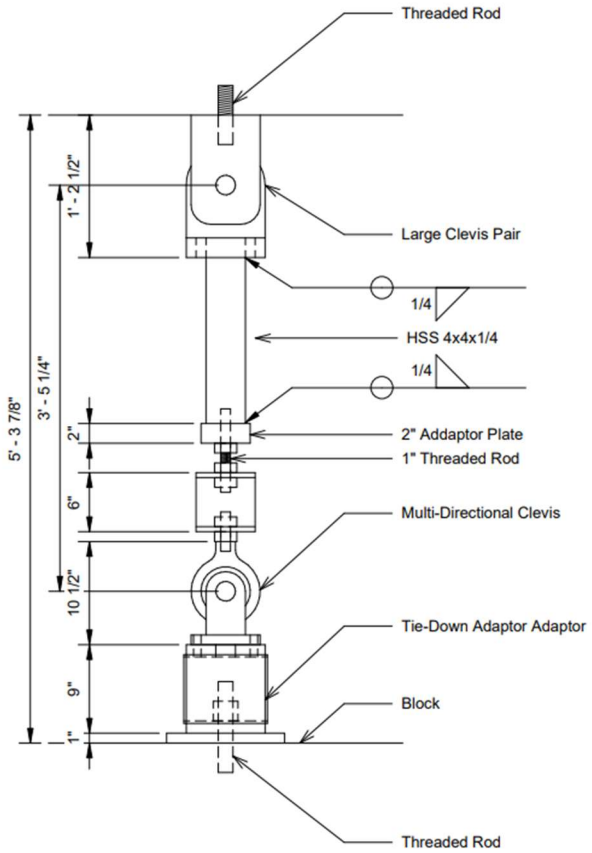

Figure 3.12. Slab End Roller Support

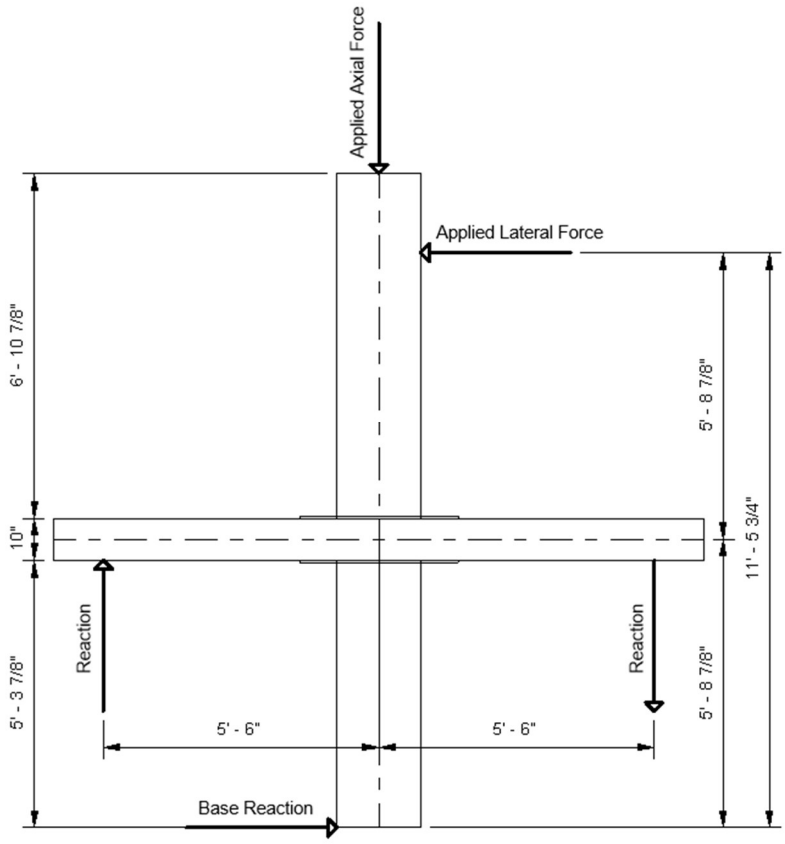

Figure 3.13. Combined-Loading Tests Free Body Diagram

3.4.4 *Experimental Test Procedure for Combine- Loading Specimens*

A checklist was completed to make sure the actuators and instrumentation were running properly. Once the checklist was verified testing began. The testing procedures were as follows:

Initializing:

1. Data acquisition systems were initialized
2. Axial load was applied by the Baldwin Universal Testing Machine
3. Hex nuts integral to the Slab End Roller Supports were tightened to restrict vertical movement of the slab ends

For Each Target Displacement:

4. Begin with one full cycle at target displacement
5. Initiate a second cycle at the same target displacement, holding at the negative peak

6. Cracks were marked in black, crack sizes were recorded, crack maps were updated to record cracking, spalling, and crushing, and pictures were taken to record cracks, spalling, crushing, and bar buckling
7. The cycle is continued and halted when the actuator force reads zero force
8. The residual displacement was recorded and the crack sizes were measured
9. Cycle was continued and held at the positive peak
10. Cracks were marked in red, crack sizes were recorded, crack maps were updated to record cracking, spalling, and crushing, and pictures were taken to record cracks, spalling, crushing, and bar buckling
11. The cycle was continued and halted when the MTS actuator read zero force
12. The residual displacement was recorded and the crack sizes were measured
13. The cycle is continued until the MTS displacement is back to zero ending the second cycle
14. Steps 4-13 were repeated at increasing target displacements until specimen failure was reached

Test Conclusion:

15. Data acquisition systems were halted and the data was saved
16. Slab End Roller Supports were loosened
17. Axial load was removed from the column
18. Spalling was removed and more photos were taken of the specimen after testing

3.4.5 *Vertical/Axial Load Application for Punching Specimens*

Figure 3.14 shows the punching specimens being subjected to axial loading of the column which resulted in a punching load applied to the slab. The Baldwin was used to apply the axial load. A steel bearing was used to accommodate any issues with the leveling of the top column. The base of the spherical bearing had a smaller footprint than the CFST tube so that the load would be directly applied to the concrete. Due to the short column heights the development length could not be achieved so a steel spreader plate that was wider than the CFST column was placed between the column and the bearing.

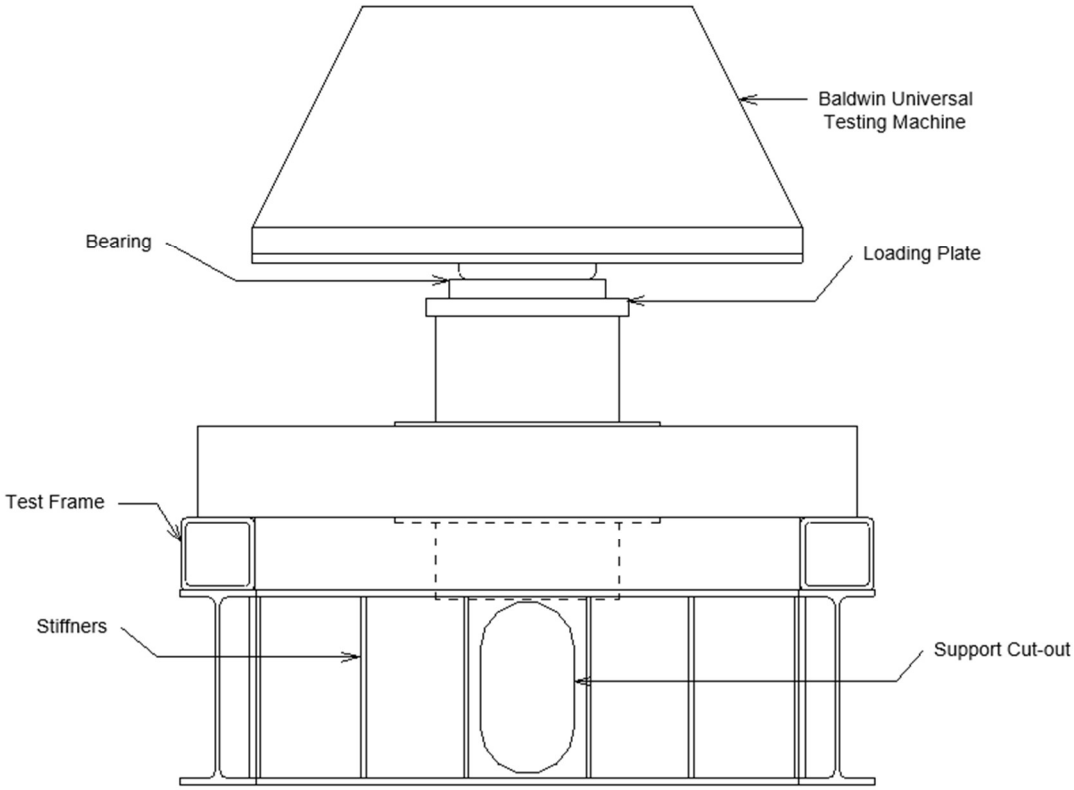

Figure 3.14. Punching Shear Test Setup

3.4.6 *Experimental Test Setup for Punching Shear Specimens*

Figure 3.15 shows the test specimen was placed on a rectangular test frame that supported the edges of the slab. To protect the edges from damage, cotton duck pads were placed between the slab and the surface of the support. As the load was applied to the column in the center of the slab the supports apply a reaction force to the edges in the opposite direction simulating punching loading applied to the bottom face of the slab. This is inverted in comparison to punching in a building where tension would instead be on the top face of the slab. This meant that the face of interest is on the underside of the test specimen. To be able to view the underside a W21x68 was used for the supports with an 8x8x1/2 HSS bolted to the top flange. The height of the W21x68 allows for photos to be taken through the cut-outs shown in Figure 3.14. But due to the slenderness of the W21x68, stiffeners were added to ensure the specimens

would reach punching failure before damaging the edge supports. To keep the test frame from moving during testing the bottom flanges of the supports were anchored to the laboratory floor.

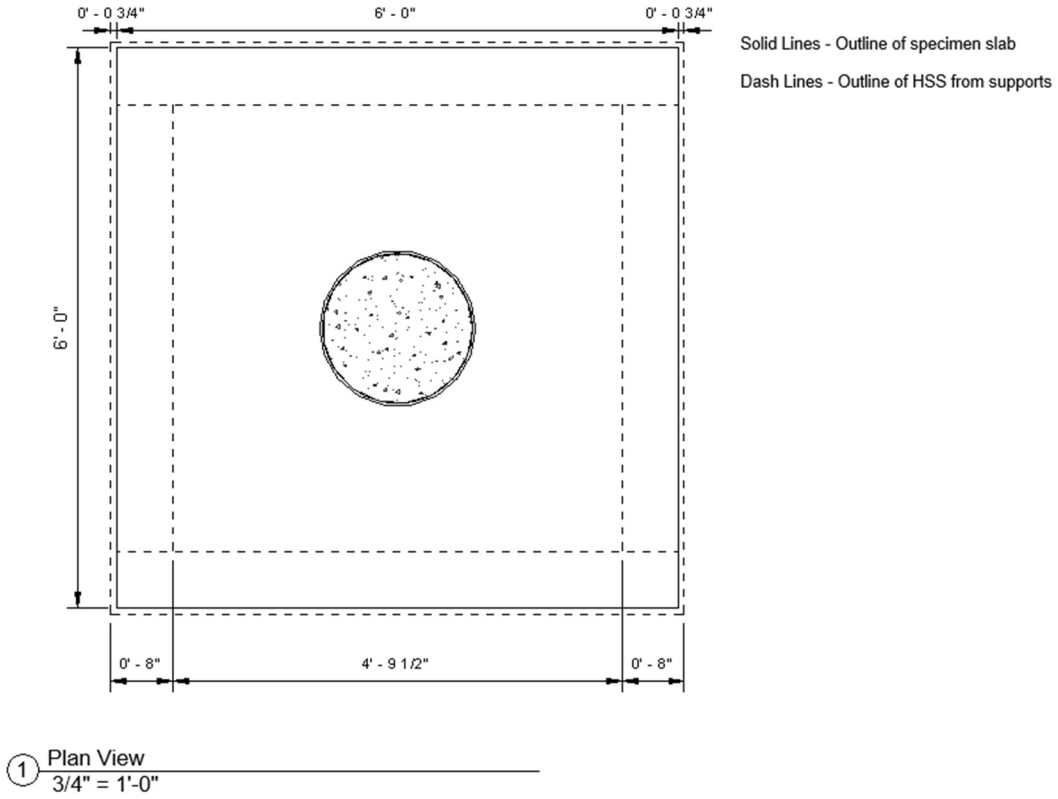

Figure 3.15. Punching Shear Tests Plan View

3.4.7 *Experimental Test Procedure for Punching Shear Specimens*

Punching shear tests followed similar testing procedures between the two tests. The day of test a checklist was used to inspect the setup, instrumentation, and testing equipment were working properly. After the checklist was approved by the lab manager testing began, following the steps shown below:

Initializing:

1. Begin Data acquisition systems
2. Move Baldwin crosshead so that it is nearly in contact with the column loading plate

Application of Force:

3. Data acquisition systems begin recording
4. Baldwin Universal Testing Machine applies an axial force to the column at a rate of 20 kips/min
5. Photos of underside of slab begin
6. Hold test at 250 kips to switch from load rate testing to a displacement rate of 0.005 in./sec.
7. Continue loading through peak force, record peak force and determine failure load
8. Once specimen has load ~30% of its peak strength end test

Test Conclusion:

9. Data acquisition systems were stopped and the data was saved
10. Load left in place to take photos of the specimen under loading
11. Remove the applied loading
12. Additional photos of the specimen were taken after testing was completed to inspect damage in a safer setting.

For the specimen with the 4.5 in. ring the load rate was changed after the specimen reached peak strength to 0.01 in./sec. in order to end the test more quickly. The 9 in. ring specimen was held at 150 kips to switch from load controlled to displacement controlled testing at a rate of 0.01 in./sec..

3.5 Instrumentation for Combined-Loading Specimens

In order to understand how the connection behaves under combined-loading an instrumentation plan was constructed to measure the following:

- Loading of Specimen
- Imposed Displacement
- Local Displacements
- Strains

The following sections will discuss which instruments were used to record these measurements and the relevance to the behavior of the connection.

3.5.1 *Lateral Load Response of Combined-Loading Specimens*

The MTS actuator that imposes the target displacements during the testing has a load cell that measures the lateral force applied to the top of the column. The actuator has a built in LVDT that can measure the displacement of the column, but due to deformations of the cross beam that the actuator is attached to, the displacements were inaccurate. A string potentiometer was attached to a reference column measured the displacement of the North face of the column at the MTS load application height. This measured displacement was used for the lateral response of the specimen.

The axial force applied to the column is measured by a load cell built into the Baldwin. As the column displaces the gravity load is no longer in line with the column at zero displacement. This offset introduces significant $P - \Delta$ effects to the connection. The moment due to the $P - \Delta$ effects is removed by determining the displacement the column at the location of the applied axial load and multiplying by the magnitude of the load applied.

3.5.2 *Support Reactions of Combined-Loading Specimens*

Figure 3.13 shows the slab end roller support reactions which indicate the amount of shear and moment transferred from the column to the slab. The reactions are measured by load cells integrated at each of the four support struts. By summing the measured force at each strut the shear in the slab can be determined. Multiplying the determined shear by a lever arm gives the moment in the slab.

3.5.3 *Local Displacements of Combined-Loading Specimens*

To understand the slab displacements vertical string potentiometers where attached to the bottom side of the slab in the locations given in Figure 3.17. As the slab vertically displaces during testing the array of string potentiometers plots the displacement. The majority of the slab damage and deformations were expected to occur around the joint which is why there is a higher density of string pots at that location. The string potentiometers were connected by piano wire to threaded rods that were screwed into slab inserts.

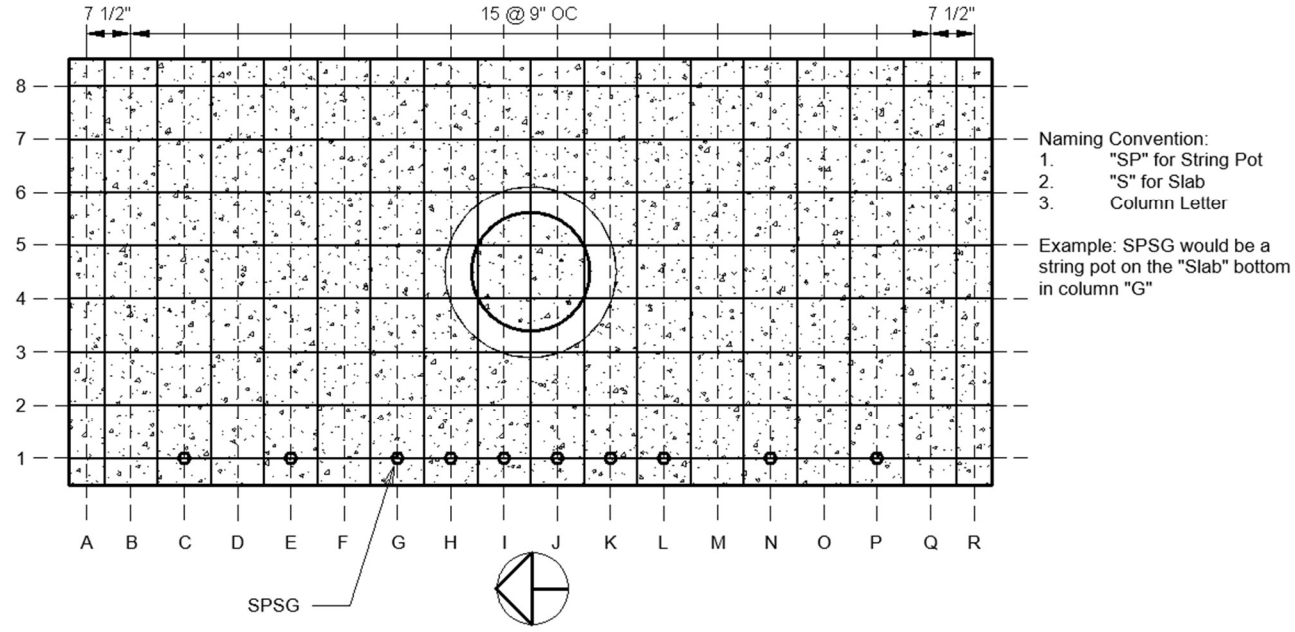

Figure 3.16. Combined-Loading String Pot Layout

3.5.4 *Strain Gauges of Combined-Loading Specimens*

Strain gauges were applied to the slab flexural reinforcement as shown in Figure 3.17. The gauges inform the research on which reinforcing bars have yielded and where to better understand the behavior of the connection. Due to the cyclic nature of the lateral loading strain gauges were attached to the top and bottom reinforcement. High concentrations of strains are helpful in identifying the location of flexural hinges or high deformation requirements. The extent of reinforcement engaged by the lateral loading can be seen as the strain gauges are applied to one half of the specimen. The other half is assumed to be symmetric. Additional strain gauges were attached to the longitudinal column reinforcement shown in Figure 3.18.

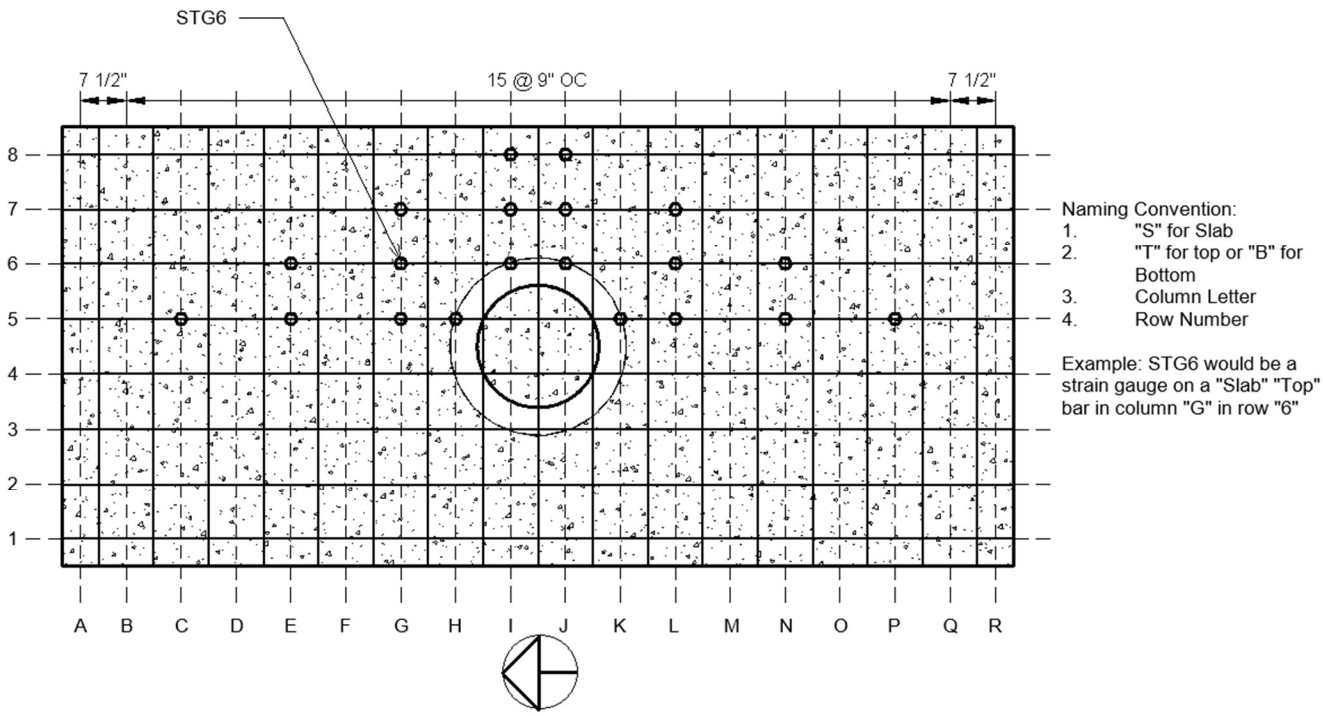

Figure 3.17. Combined-Loading Strain Gauge Layout

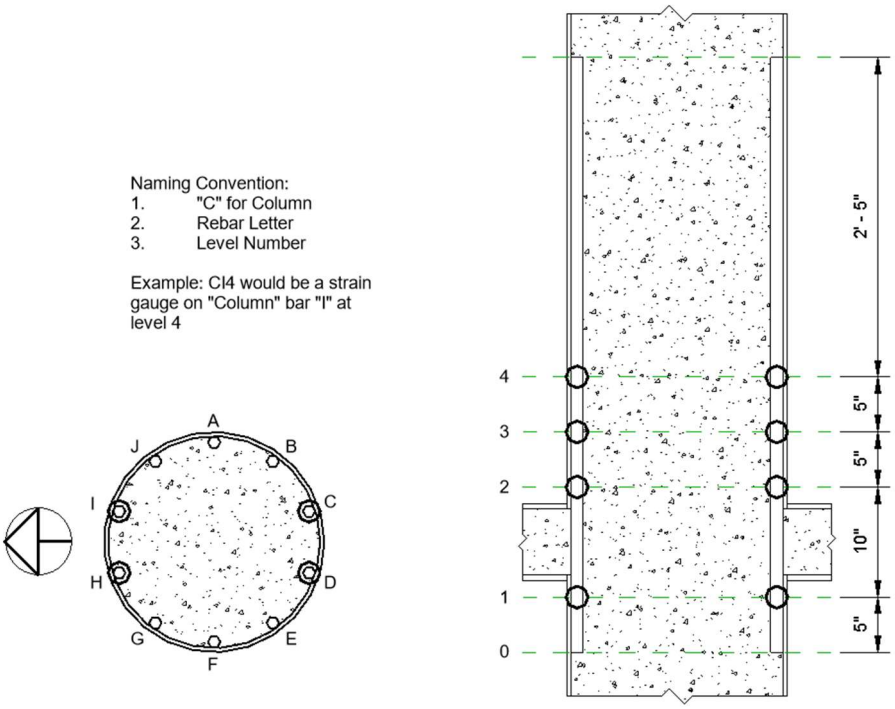

Figure 3.18. Combined-Loading Column Strain Gauge Layout

3.6 INSTRUMENTATION FOR PUNCHING SPECIMENS

The instrumentation plan for the punching specimens was developed to measure the following behaviors:

- Loading of the Specimen
- Imposed Displacement
- Local Displacement
- Strains

The following sections will discuss how the similar instruments were used to measure the differing behavior of the punching shear tests.

3.6.1 *Global Behavior*

The Baldwin Universal Testing Machine was used to apply a force to the column of the punching shear specimens. It is equipped with an internal load cell to measure the force that was applied. The Baldwin is capable of measuring the displacement of its crosshead. However, it is difficult to control the crosshead to be in contact with the loading plate on top of the specimen's column without generating a force. The vertical displacement of the specimen was measured using string potentiometers connected to the lower column at the four cardinal directions. The string potentiometers were fastened to the laboratory floor and connected to lower column by screws held in place by a magnet. The overall column displacement was taken as the average of the four displacements.

3.6.2 *Local Displacement of the Punching Shear Specimens*

The total string potentiometers attached to the underside of the specimen are shown in figure 3.19. In addition to the four attached to the edge of the column, the string pots extend in the North and West directions to measure the displaced shape of the slab during testing.

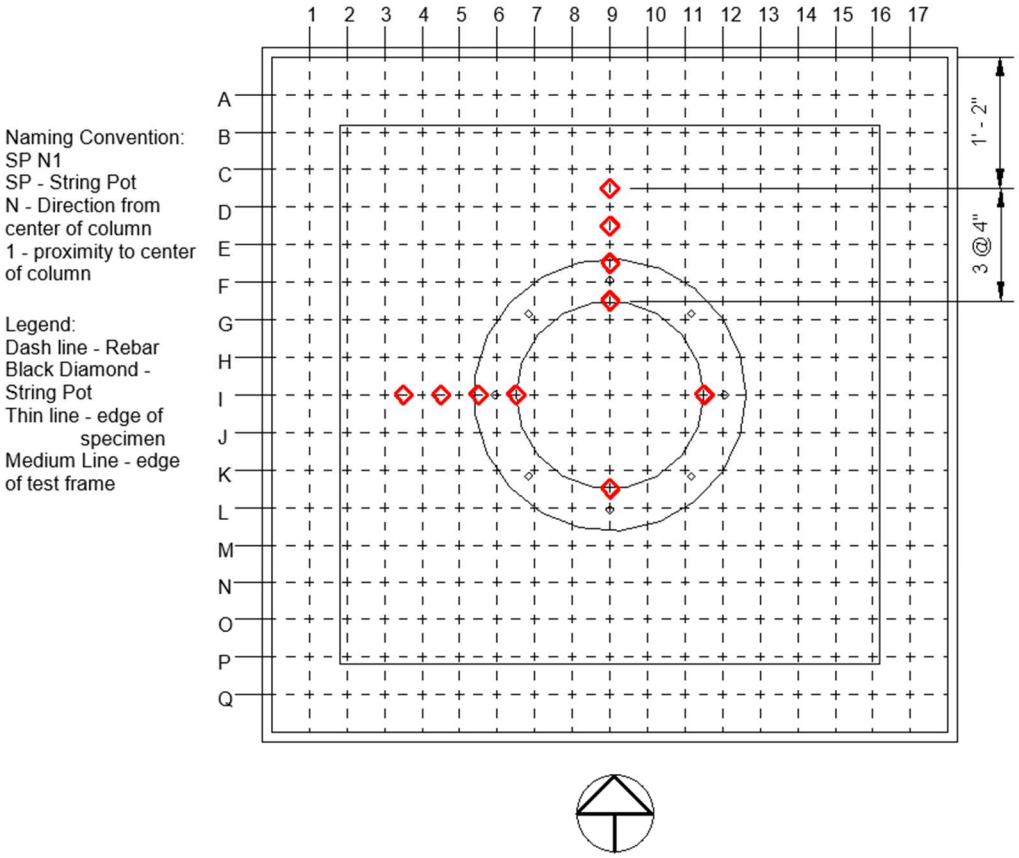

Figure 3.19. String Pot Layout for PTB_4.5_1_0_P

3.6.3 *Strains of the Punching Shear Specimens*

Strain gauges were attached the bottom flexural reinforcement at the locations shown in Figure 3.20. The strain gauges are positioned around the ring where strains are expected to be the highest for the flexural reinforcement. In addition the strain gauges extend in the North and West direction to capture how yielding extends across the slab. Only two directions were chosen since symmetry is assumed. The purpose of the strain gauges is to monitor the flexural response of the specimen up to peak loading. If the flexural response in elastic or most nearly elastic, punching failure is likely.

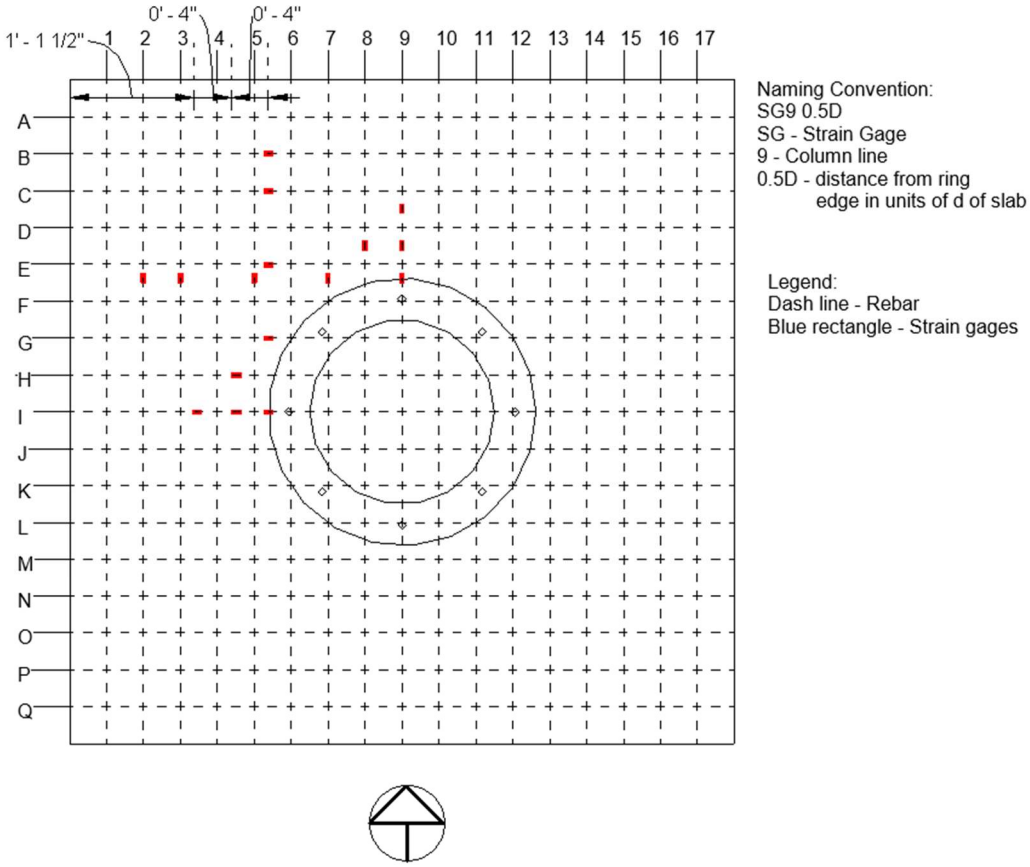

Figure 3.20. Strain Gauge Layout of PTB_4.5_1_0_P

Chapter 4. EXPERIMENTAL OBSERVATIONS FOR COMBINED-LOADING SPECIMENS

This chapter provides the observed response of the cyclic combined-loading tests. For each test, the following information is provided, (1) damage observations – crack patterns, and (2) the measured global force-drift response. To maintain consistency with Phase 1 tests conducted by Yeutter (2020) the damage observations will use the same nomenclature.

Each specimen was cycled under displacement-controlled loading with the target and measured drifts provided in Table 4.1. The deformation of the test setup was included in the target drift and therefore, the measured displacement is less than the target because it only includes specimen deformation.

Table 4.1. Displacements/Target Drifts and Measured Drifts

Series	Target Disp. (in.)	Target Drift (%)	Measured Drift (%)			
			PTB_4.5_1_0_6		PTB_9_2_0_6	
			North	South	North	South
1	0.5	0.36	-0.36	0.34	-0.30	0.40
2	1.0	0.73	-0.70	0.67	-0.66	0.75
3	1.5	1.09	-1.04	1.02	-0.99	1.09
4	2.0	1.45	-1.39	1.38	-1.36	1.44
5	3.0	2.18	-2.10	2.09	-2.07	2.16
6	4.0	2.90	-2.80	2.78	-2.74	2.84
7	5.0	3.63	-3.47	3.48	-3.43	3.54
8	6.0	4.36	-4.18	4.18	-4.16	4.28
9	7.0	5.08	-4.91	4.91	-4.89	5.00
10	8.0	5.81	-5.62	5.63	-5.58	5.61
11	9.0	6.53	-6.31	6.36	-	-

4.1 Overview of Damage States

The progression of damage during the testing helps to inform how the connection would behave when subjected to different drift levels under an extreme loading event. It also aids in risk assessment during the design phase of a project. Knowing how the connection will behave at a certain drift can then be related to probabilities of certain events to allow for more informed decision making. Table 4.2 provides descriptions of the damage states. The subsections that follow provide descriptions of each damage state.

Table 4.2. High Drift Cycle Typical Crack Opening at Peaks

Damage State	Description
Cracking	Cracking initiates (Stage 1) and Crack pattern completes (Stage 2)
Yielding	Longitudinal reinforcement yields
Spalling	Concrete cover separates from core concrete
Crushing/Exposure of Reinforcement	Cover concrete has completely spalled and longitudinal reinforcement is exposed
Bar Buckling	Exposed longitudinal reinforcement buckles (observed out of plane movement)

4.1.1 *Cracking*

To explain the displacement and the location of damage of the specimen the cardinal coordinate system will be used. North corresponds to the horizontal actuator in compression; South corresponds to the horizontal actuator in tension. The crack maps are marked with different colors corresponding to the different directions for which they were first observed. Crack lengths marked with blue indicate actuator in compression, red to indicate actuator in tension.

The first cycle at each target drift level is completed without any pauses so observation at the different directional peaks is not possible. Therefore, inference about how the slab should crack was used in determining which colors to mark the crack lengths. The gridlines on the crack maps are at 1 ft. x 1 ft. spacing. This grid was drawn onto the specimen to aid in the accuracy of the crack maps.

An example crack map from testing of Specimen PTB_4.5_1_0_6 is shown in Figure 4.1. Crack maps will be shown for the drift levels where cracking across the width of the specimen is first noticed (Stage 1 cracking), where the last significant increase in crack length is recorded (Stage 2 cracking), and at an intermediary target drift. These drift levels were selected provide progression of cracking during loading. All crack maps are in Appendix B.

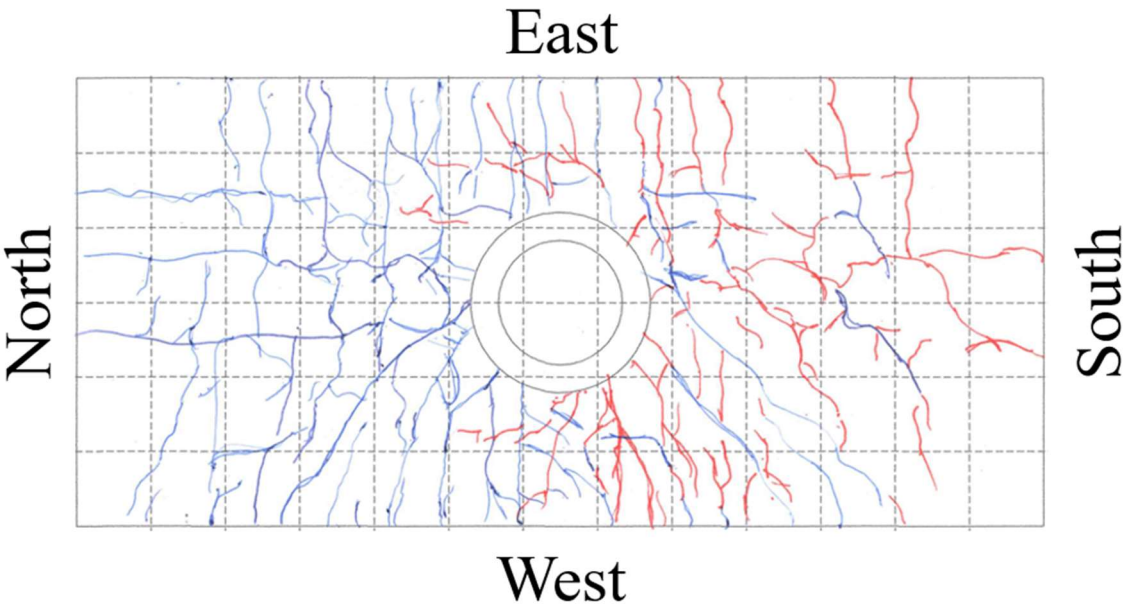

Figure 4.1. Example of Crack Map of Bottom of Slab

4.1.2 *Yielding*

Yielding was the only damage state that was measured using instrumentation, specifically by the strain gauges that were applied to the longitudinal reinforcement. The solid lines represent

the slab perimeter, the outer diameter of the steel tube, and the outer diameter of the ring flange. Dashed lines represent the flexural reinforcement of the slab.

Figure 4.2 shows a typical plot used to indicate the range of strain measured by the strain gauges. The origin, (0, 0), is at the Northwest corner of the slab. The symbols signify the following:

- Black Circle: Strain is in the elastic range
- Red Circle: Strain exceeds yield
- Red Diamond: Strain exceeds ultimate strain (corresponding with the ultimate strength)
- Red X: Strain meets or exceeds the measured fracture strain
- Black X: Strain gauge was broken before start of testing

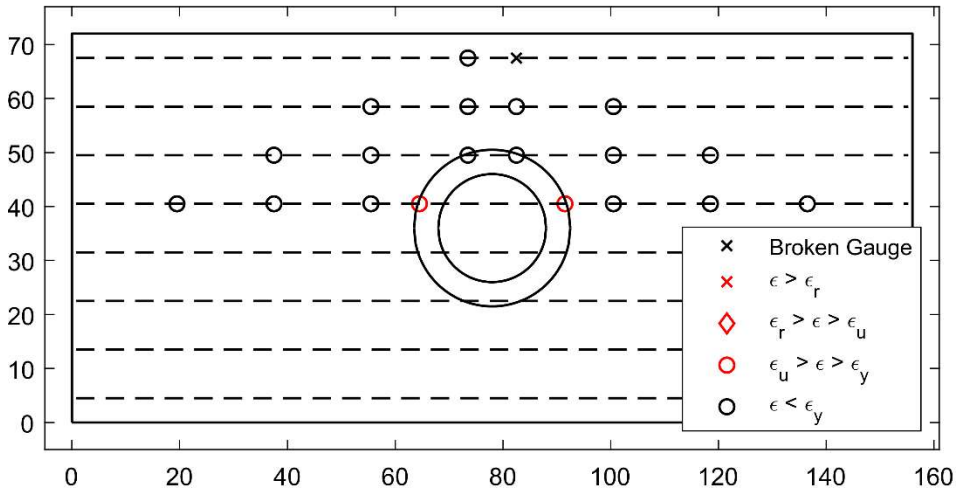

Figure 4.2. Example Reinforcement Strain Summary

Yielding was broken up into two limit states. (1) Onset of yielding is defined by the drift level at which the first strain gauge signifies yielding of a bar. (2) Full yielding is defined by at least one strain gauge on each reinforcing bar indicates yielding of the bar. This signifies that there is yielding across the full width of the slab.

Strain gauge measurements used in the figure are taken as the maximum strain at the peak drifts of a given drift level. The plots summarizing the strain gauge behavior throughout the test are provided in Appendix C. Extent of yielding is quantified by one of two states: (1) Onset of

yielding, defined by the drift level at which the first strain gauge signifies yielding of as bar. (2) Full yielding is defined by at least one strain gauge on each reinforcing bar signifies yielding. Indicating yielding across the full width of the slab.

4.1.3 *Spalling*

Spalling results from large monotonic compression strains (typically compressive strains between -0.005 and -0.008) or cyclic loading from tension to compression where cracking due to tension loading can reduce the compressive strain corresponding to spalling. The longitudinal reinforcement in one direction is placed at the same depth and therefore after cracking, which can result in cracking at this plane and results in the cover delaminating from the concrete below the reinforcement. Spalling initiate in the slab-column joint region, as refined by ACI critical section.

Figure 4.3 shows an example of initial spalling within the critical section from PTB_4.5_1_0_6. The figure includes a graphic to the right of the photo that indicates photo location.

Figure 4.3. Example of Spalling

4.1.4 *Crushing*

Crushing is defined as the complete loss of concrete cover revealing concrete core damage (beyond the cover). An example of concrete crushing is shown in Figure 4.4.

Figure 4.4. Example of Core Concrete Crushing

4.1.5 *Bar Buckling*

Bar buckling typically follows crushing of the concrete and depends on the length of the spalled region along the bar length. Bar buckling depends on the unsupported length and tangent stiffness of the bar, which reduces locally with yielding. Crushing of the concrete reduces the compressive strength of the core concrete, and transfers the force to the flexural reinforcement. With the reduced modulus and increased unsupported length and compressive force, buckling of the bar is expected. Figure 4.5 provides an example of bar buckling. Since the reinforcement is not always visible during testing, the observation of bar buckling will only refer to damage that is visible during testing.

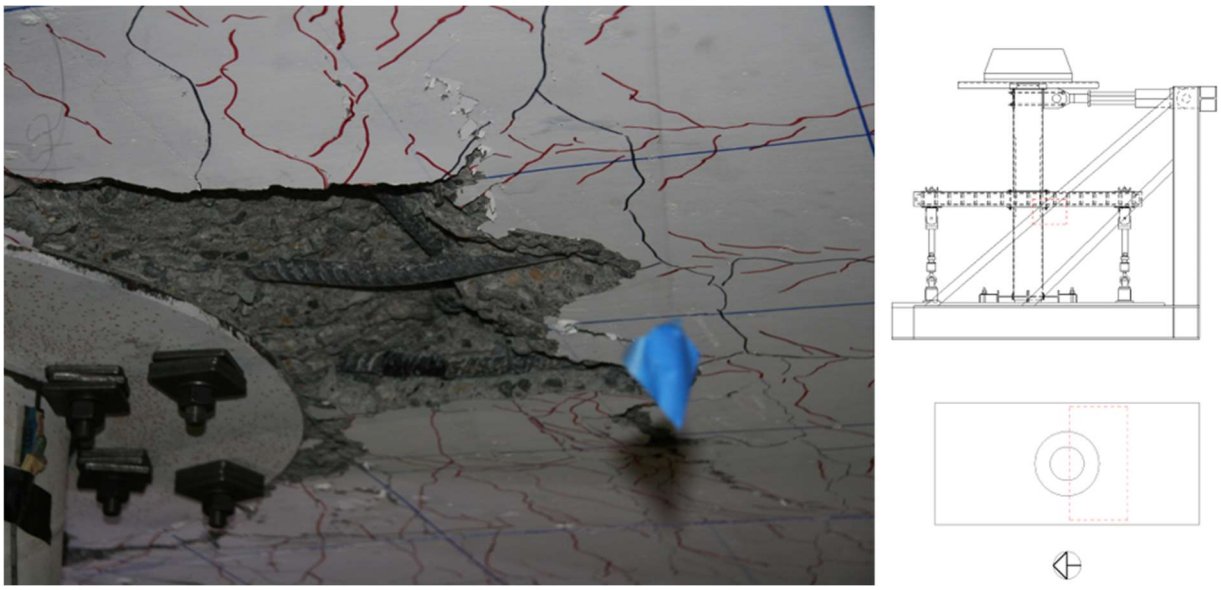

Figure 4.5. Example of Bar Buckling

4.2 SPECIMEN PTB_4.5_1_0_6

Testing of PTB_4.5_1_0_6 was performed on May 26, 2021 in the University of Washington Structural Engineering Laboratory. The following sections provide the specimen's global measured response and the damage observations at increasing drift level ranges: low, moderate, and high.

4.2.1 *Global Response and Specimen Geometry*

Specimen PTB_4.5_1_0_6 had a 4.5 in. wide ring flange and a 6 in. slab. A more detailed description of the specimen is provided in Chapter 3. There were no unexpected stoppages during testing. The induced drift and resulting lateral loading can be seen in Figure 4.6 and Figure 4.7 respectively. The figures are quantified in Table 4.3.

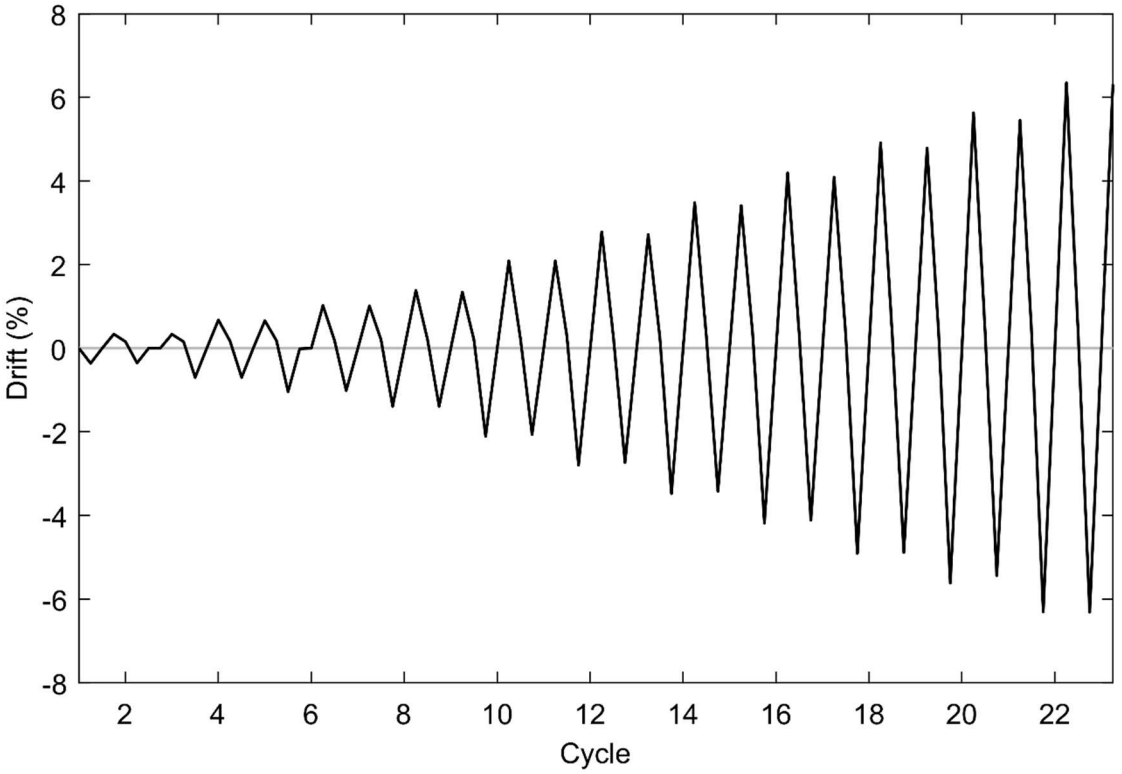

Figure 4.6. Induced Drift History (PTB_4.5_1_0_6)

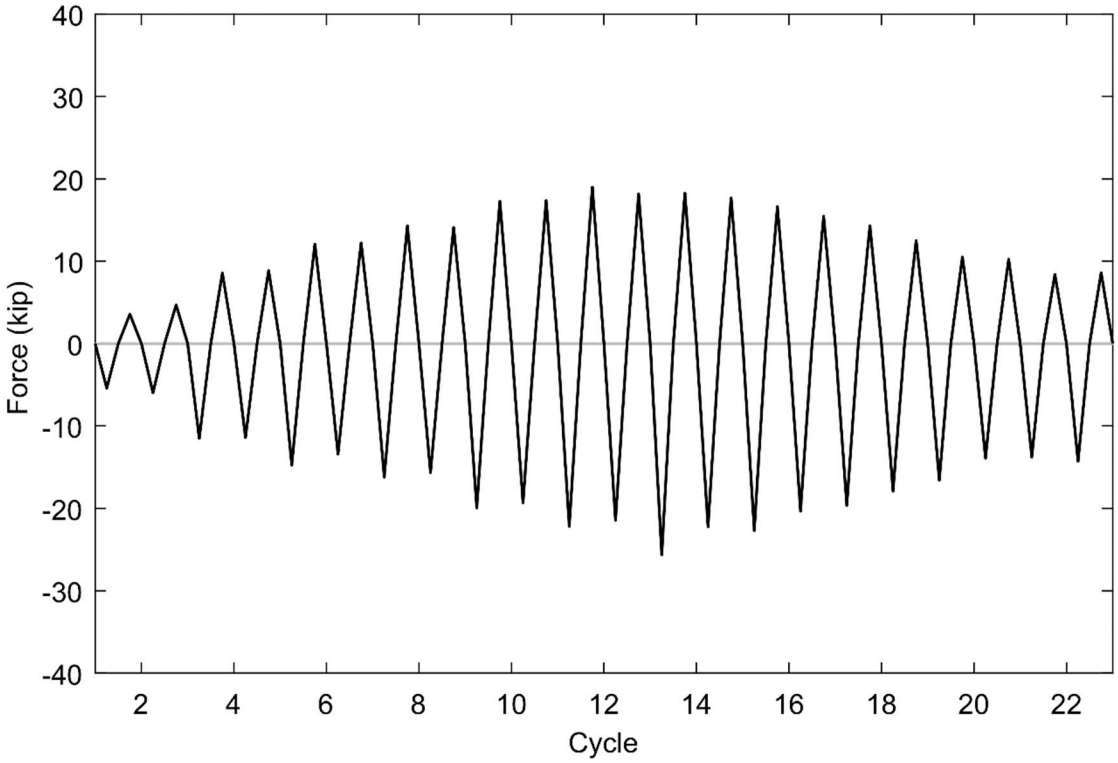

Figure 4.7. Applied Lateral Load History (PTB_4.5_1_0_6)

The maximum measured lateral force of 25.6 kips occurred on the negative peak of the first cycle at 3.6% drift. The specimen completed 22 cycles before the test was ended due to a loss of strength satisfying the testing criteria for failure. The lateral resistance increased until around the 13th cycle, when the resistance plateaued for a few cycles. Testing was stopped at a loss of approximately 50% of the ultimate strength.

Table 4.3. Maximum Resistances and Drifts in Each Cycle (PTB_4.5_1_0_6)

Cycle	Maximum Measured Resistance (kips)		Maximum Drift (%)	
	Tension	Compression	Tension	Compression
1	3.6	-5.4	0.34	-0.36
2	4.7	-6.0	0.33	-0.35
3	8.6	-11.5	0.67	-0.70
4	8.8	-11.4	0.66	-0.70
5	12.1	-14.7	1.02	-1.04
6	12.2	-13.4	1.01	-1.01
7	14.3	-16.2	1.38	-1.39
8	14.1	-15.7	1.34	-1.39
9	17.3	-19.9	2.09	-2.11
10	17.4	-19.3	2.09	-2.06
11	19.0	-22.2	2.78	-2.80
12	18.2	-21.5	2.71	-2.74
13	18.3	-25.6	3.48	-3.48
14	17.7	-22.2	3.41	-3.42
15	16.6	-22.7	4.19	-4.18
16	15.5	-20.3	4.09	-4.11
17	14.3	-19.6	4.91	-4.91
18	12.5	-17.9	4.79	-4.89
19	10.5	-16.6	5.63	-5.62
20	10.2	-13.9	5.45	-5.44
21	8.4	-13.8	6.35	-6.31
22	8.6	-14.3	6.31	-6.31

Figure 4.8 shows the measured hysteretic response of PTB_4.5_1_0_6 which has been normalized using the predicted flexural strength across the width of the slab. Figure 4.9 shows the same normalized drift response with the $P - \Delta$ effects removed.

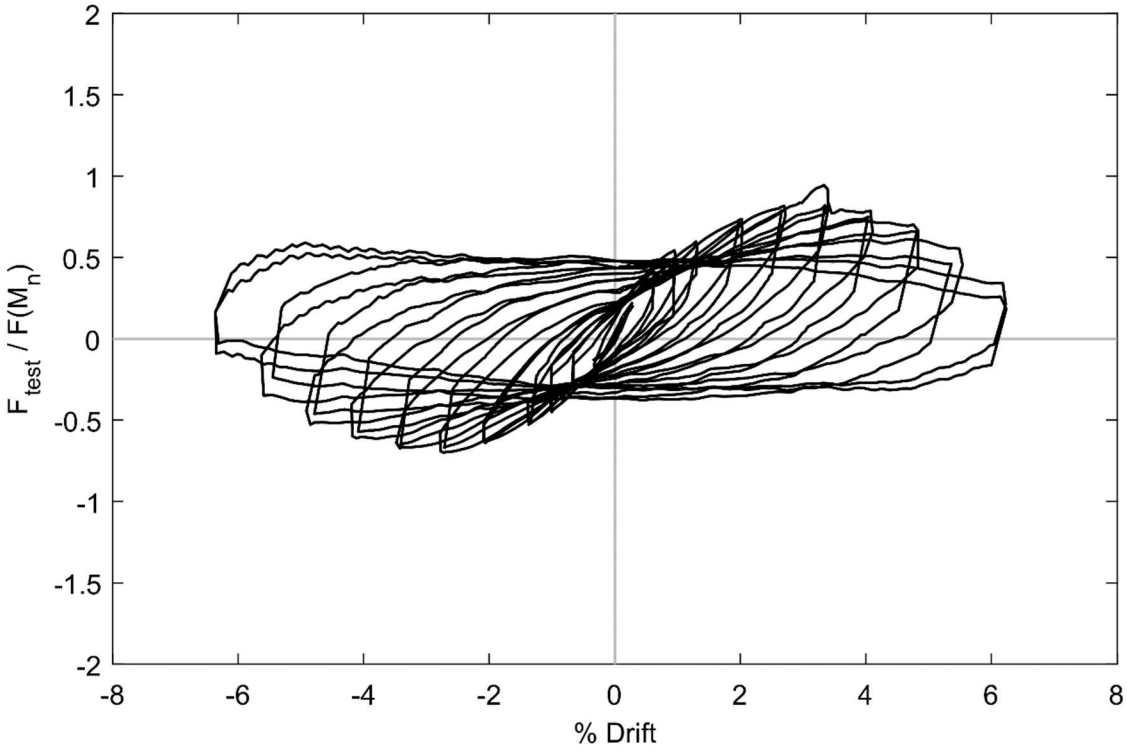

Figure 4.8. Normalized Drift Response (PTB_4.5_1_0_6)

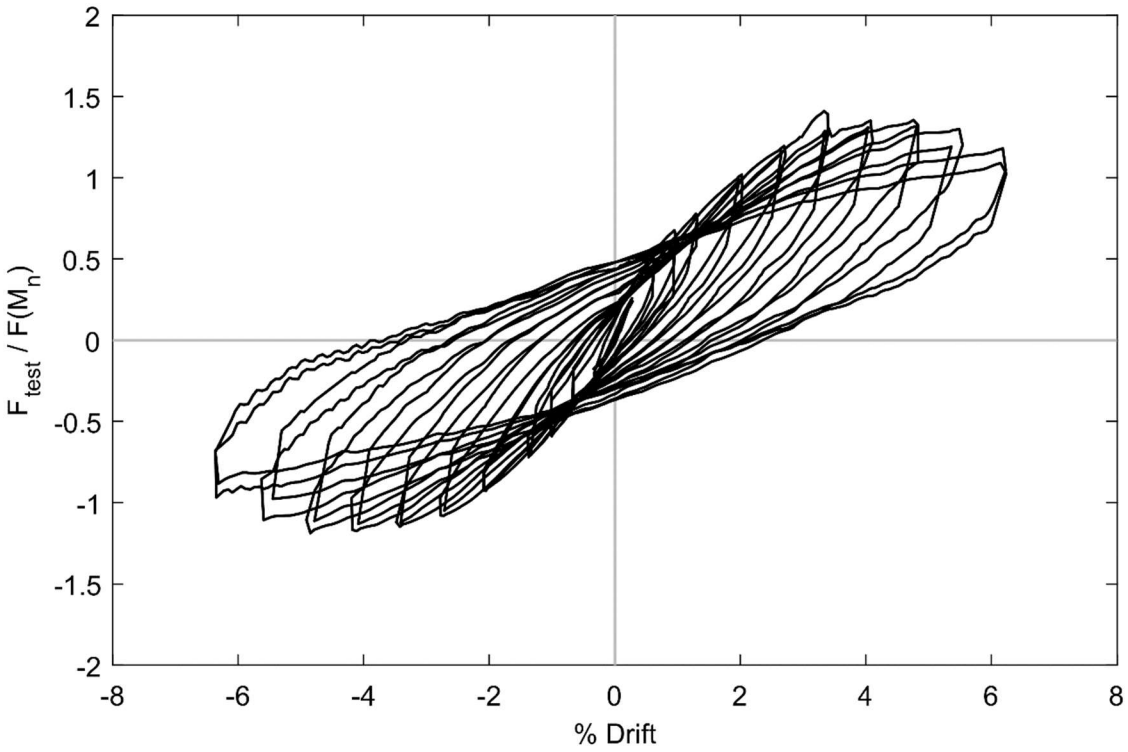

Figure 4.9. Normalized Drift Response with $P-\Delta$ Effects Removed (PTB_4.5_1_0_6)

4.2.2 *Specimen Performance State Summary*

Table 4.4 provides the approximate drift levels at which the damage states are observed in specimen PTB_4.5_1_0_6.

Table 4.4. Summary of Damage (PTB_4.5_1_0_6)

Damage State	Drift (%)
Cracking	0.73 – 2.90
Yielding (initial-final)	2.18 – 6.53
Spalling	3.63
Crushing	5.08
Bar Buckling	5.81

4.2.3 *Low Drift Cycles (0.0% - 1.5% Target Drift)*

Each target drift consisted of two cycles. The first of which was run without stopping, while the second was stopped to observe damage during the cycle. To clarify the different cycles, a naming convention consisting of the target drift and a number indicating the cycle at that drift.

0.5-1 reached drifts of +0.34/-0.36 and was run without interruption. During 0.5-2 tested to +0.33/-0.35 drift cracking had not extended across the full width of the slab. Most of the initial cracking observed during 0.5-2 was due to shrinkage. The maximum crack widths measured were on the bottom face of the slab. Maximum crack width measurements were 0.3-0.35 mm. The typical crack sizes during low drift cycles can be found in Table 4.5.

Table 4.5. Typical Crack Opening at Peaks: Low-Drift Cycle

Cycle	Drift (%)		Bottom (mm)		Top (mm)		Side (mm)	
	South	North	South	North	South	North	South	North
0.5-2	0.33	-0.35	0.20	0.18	0.10	0.10	0.10	0.12
1.0-2	0.66	-0.70	0.23	0.23	0.13	0.15	0.13	0.13
1.5-2	1.01	-1.01	0.21	0.20	0.15	0.18	0.13	0.13
2.0-2	1.34	-1.39	0.13	0.22	0.18	0.15	0.2	0.15

1.0-1 (+0.67/-0.70 drift) was run without interruption. During 1.0-2 to +0.66/-0.70 drift cracking Stage 1 was observed and is shown in Figures 4.10 and 4.11. The cracking was more extensive on the bottom face of the slab, but is mostly symmetric between the north and south ends. There is asymmetry between the east and west sides where one side shows more radial cracking than the other. This behavior is the opposite for the bottom face of the slab. The maximum crack widths were found on the bottom face of the slab with the largest being 0.35 mm on the North side of the slab during the North peak displacement.

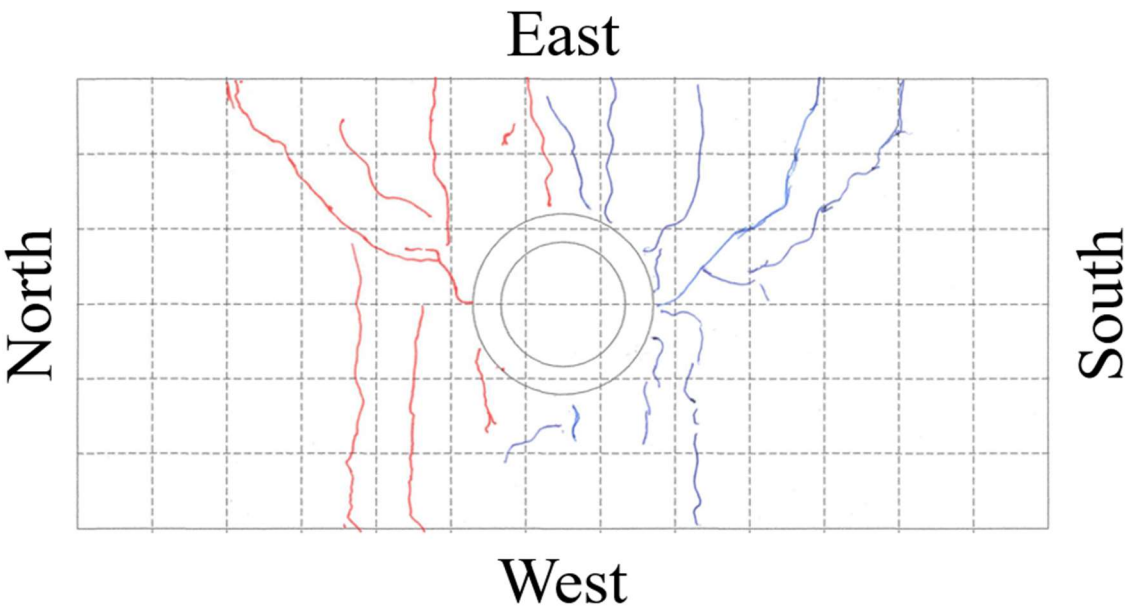

Figure 4.10. Top of Slab Crack Map – 0.70% Drift (PTB_4.5_1_0_6)

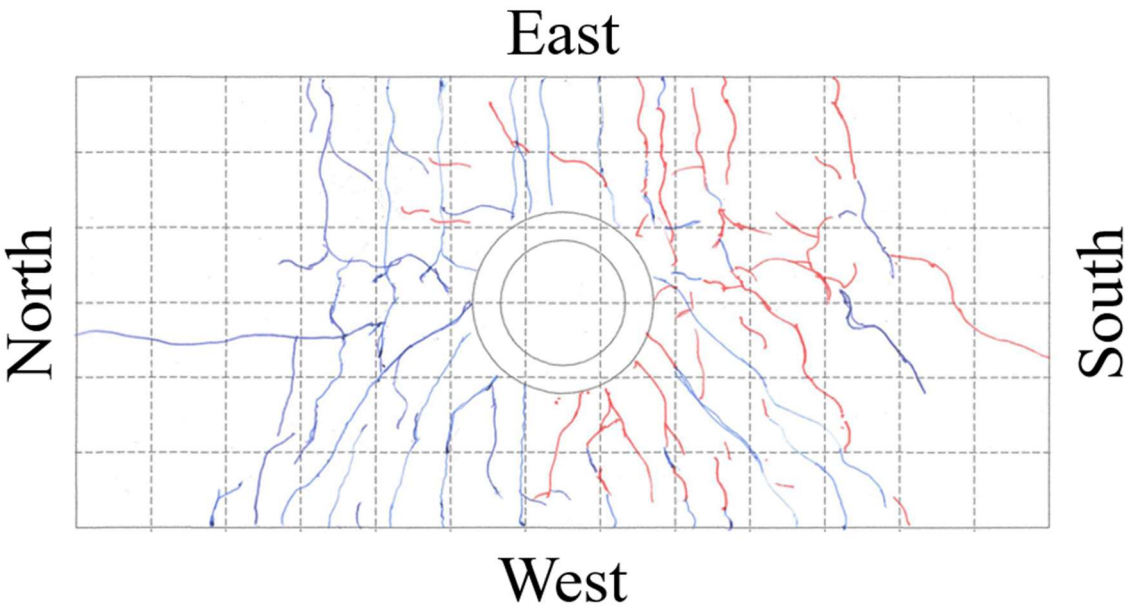

Figure 4.11. Bottom of Slab Crack Map – 0.70% Drift (PTB_4.5_1_0_6)

At 1.5-2 the developed extended transversely across the slab. The radial cracks noticed during 0.5-2 and 1.0-2 do not show further development indicating they were a result of shrinkage that occurred before testing. Cracking also occurred along the flexural reinforcement within the column width in the north-south direction. The maximum crack widths were found on the bottom

face of the slab. There was a crack with a width of 0.3 mm on the North side and a crack with a width of 0.35 mm on the South side.

During 2.0-2 (+1.34/-1.39 drift) the cracks along the flexural reinforcement in the north south direction developed to the edges of the slab on the top face. Diagonal cracking occurs in the region to the east and west of the column in which the red cracks denoting the MTS actuator was in tension occur in the area that typically blue cracks were forming. Cracking of the grout pad underneath the upper column occurred during 2.0-2. These cracks closed when the direction of loading was reversed. The maximum crack widths were on the bottom face of the slab. The controlling crack on the North side of the slab increased to 0.35 mm while the crack on the South side of the specimen didn't increase in size.

During the low drift cycles there was no indication of yielding of the flexural reinforcement. The crack patterns that occurred show a development of flexural cracks extending in the direction transverse to loading, as well as some longitudinal cracking along the flexural reinforcement within the column width. There was development of some diagonal cracking in the region to the east and west of the column.

4.2.4 *Moderate Drift Cycles (1.5% - 3.6% Target Drift)*

3.0-2 (+2.09/-2.06 drift) was not paused at the South peak due to a controller error that completed the cycle rather than pause at the peak. Due to the error development of cracks at the South peak were not able to be recorded. The new cracks observed during the North peak were primarily formed near the edge roller supports. More flexural cracks developed transverse to the direction of loading. On the bottom face a crack along the flexural reinforcement outside of the slab and ring flange width developed showing engagement of the flexural reinforcement extending across the slab. The maximum crack measured on the north side of the bottom face of the slab, did not increase in width at this target drift. Table 4.6 provides the typical crack widths for the moderate drift cycles.

Table 4.6. Moderate Drift Cycle Typical Crack Opening at Peaks

Cycle	Drift (%)		Bottom (mm)		Top (mm)		Side (mm)	
	South	North	South	North	South	North	South	North
10	2.09	-2.06	-	0.23	-	0.15	-	0.20
12	2.71	-2.74	0.52	0.28	0.35	0.28	0.3	0.25
14	3.41	-3.42	0.70	0.67	0.75	0.51	0.3	0.3

Observations made during 4.0-2 showed a slight increase in cracking near the connection at this target drift level provided by figures 4.12 and 4.13. Most of the new cracks were radial. A large crack around the perimeter of the ring flange seemed to be the only crack with a significant change due to its increasing crack width. The maximum measured crack width on the north side of the bottom face of the slab was 0.45 mm. On the south side it was 0.75 mm a significant increase from the previous drift level. During 4.0-2 there was minimal development of the crack pattern resulting in it meeting Cracking Stage 2 criteria. The rest of the discussion about concrete damage will focus on spalling and crushing. The top and bottom flexural reinforcement reach yielding at this target drift level as shown in Figure 4.14 and Figure 4.15. The strain summaries of the slab are shown below.

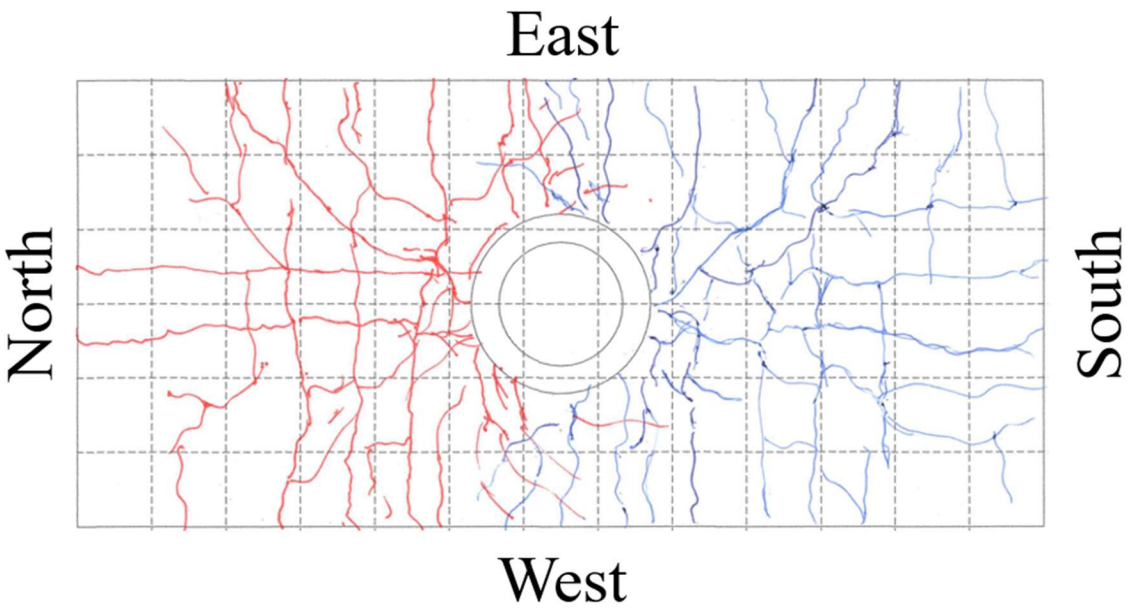

Figure 4.12. Top of Slab Crack Map – 2.74% Drift (PTB_4.5_1_0_6)

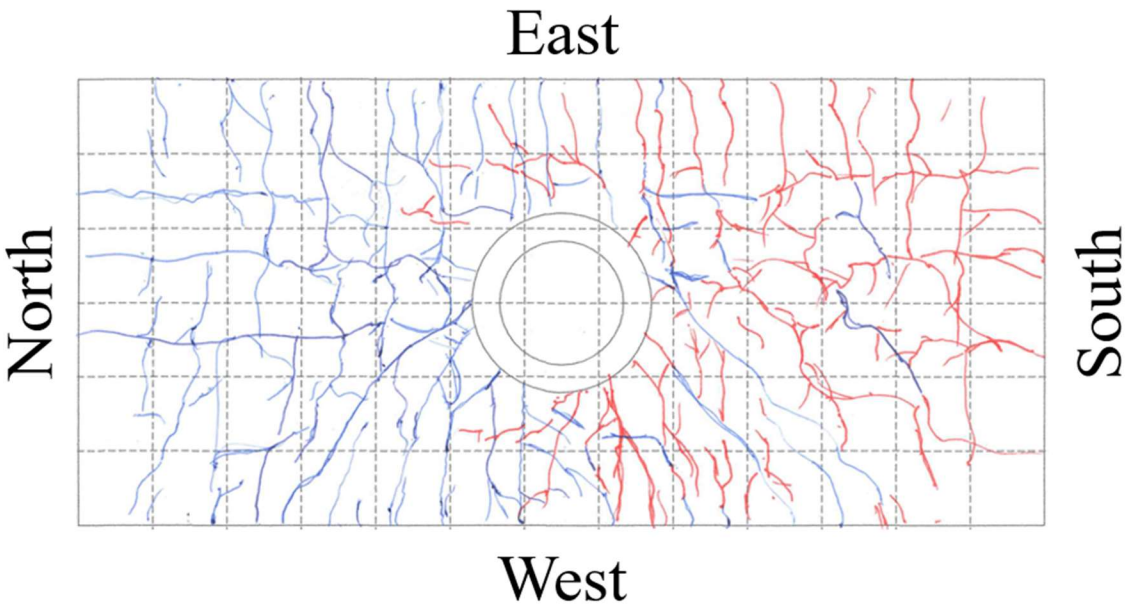

Figure 4.13. Bottom of Slab Crack Map – 2.74% Drift (PTB_4.5_1_0_6)

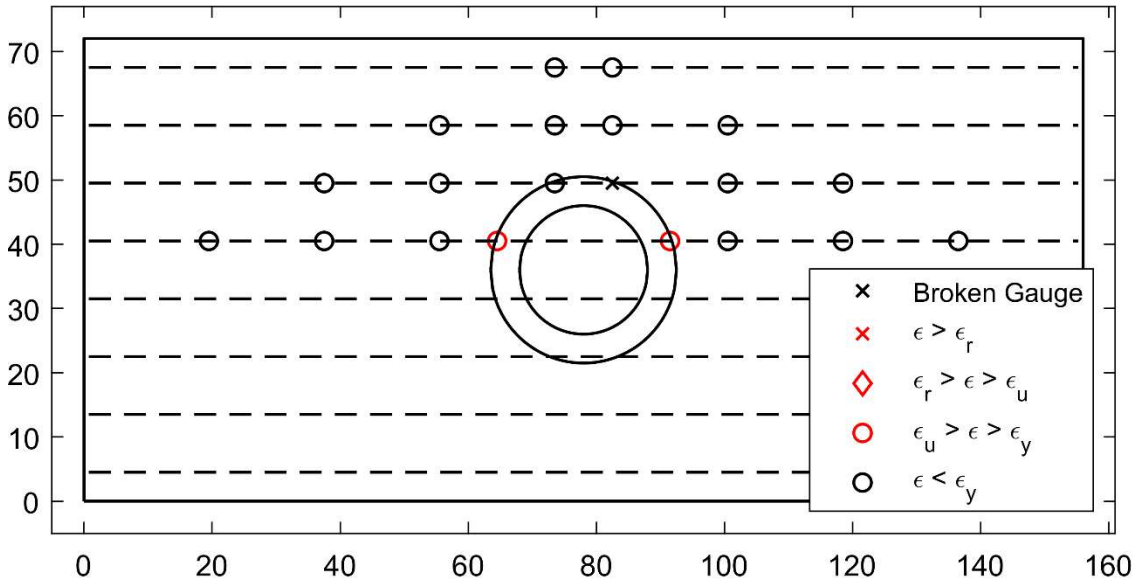

Figure 4.14. Top Reinforcement Strain Summary – 2.80% Drift (PTB_4.5_1_0_6)

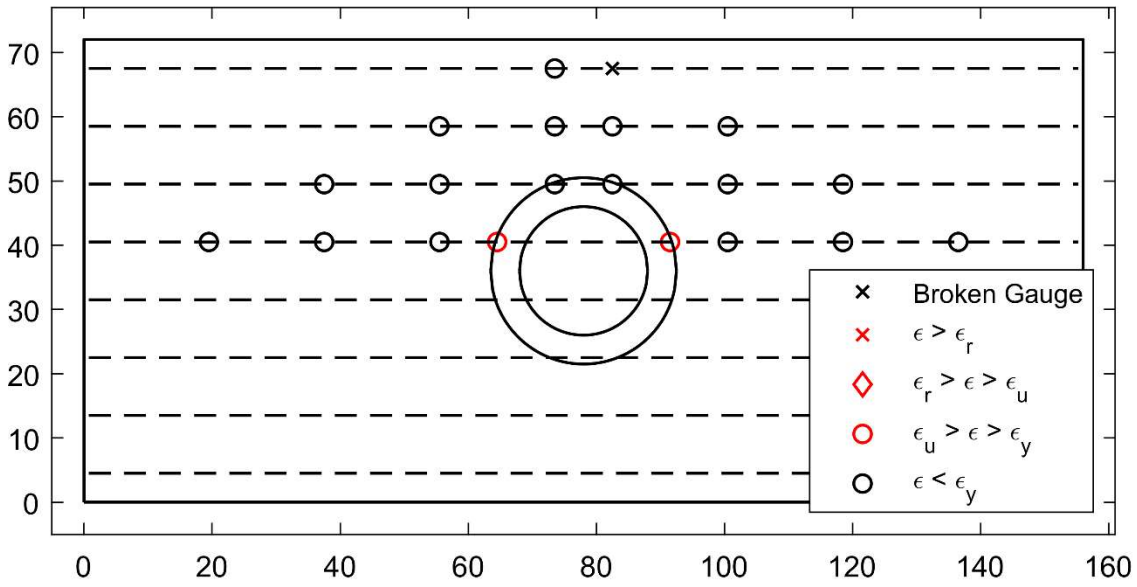

Figure 4.15. Bottom Reinforcement Strain Summary – 2.80% Drift (PTB_4.5_1_0_6)

During 5.0-2 large cracks were measured on the top face of the slab near the connection. The cracking around the ring edge gave way to spalling seen in Figure 4.16. The spalling occurred on the northeast edge of the ring and extended roughly 2.5 in. from the edge. A crack width of 4.5 mm was measured on the south edge of the ring flange during the north peak displacement and 4.5 mm on the north edge during in the reverse direction. A few more strain gauges recorded yielding around the ring flange or along the reinforcement within the column width. The lateral load began to plateau at this load step.

Figure 4.16. Spalling on North Side of Bottom Face – 3.48% Drift (PTB_4.5_1_0_6)

4.2.5 *High Drift Cycles (3.6% - Final Target Drift)*

During 6.0-2 (+4.09/-4.11 drift) the amount of spalling increased as shown in Figure 4.17 and Figure 4.18. The spalling is kept mostly to the north and south edges of the ring flange. The maximum crack measured was at the South edge of the connection on the top face of the slab measuring 11.0 mm. Table 4.7 provides the typical crack widths for the high drift cycles. At this drift level the top and bottom reinforcement indicate yielding of bars beyond the bar intersecting

the column. Showing how the yield stress is expanding to different bars. The strain summaries are given in Figures 4.19 and 4.20. The lateral force was similar.

Figure 4.17. Spalling on North Side of Bottom Face – 4.11% Drift (PTB_4.5_1_0_6)

Figure 4.18. Spalling on South Side of Bottom Face – 4.11% Drift (PTB_4.5_1_0_6)

Table 4.7. High Drift Cycle Typical Crack Opening at Peaks

Cycle	Drift (%)		Bottom (mm)		Top (mm)		Side (mm)	
	South	North	South	North	South	North	South	North
16	4.09	-4.11	0.80	0.56	0.80	0.54	0.50	0.61
18	4.79	-4.89	1.50	0.90	0.80	1.00	0.65	0.50
20	5.45	-5.44	1.00	-	0.50	-	0.50	0.50

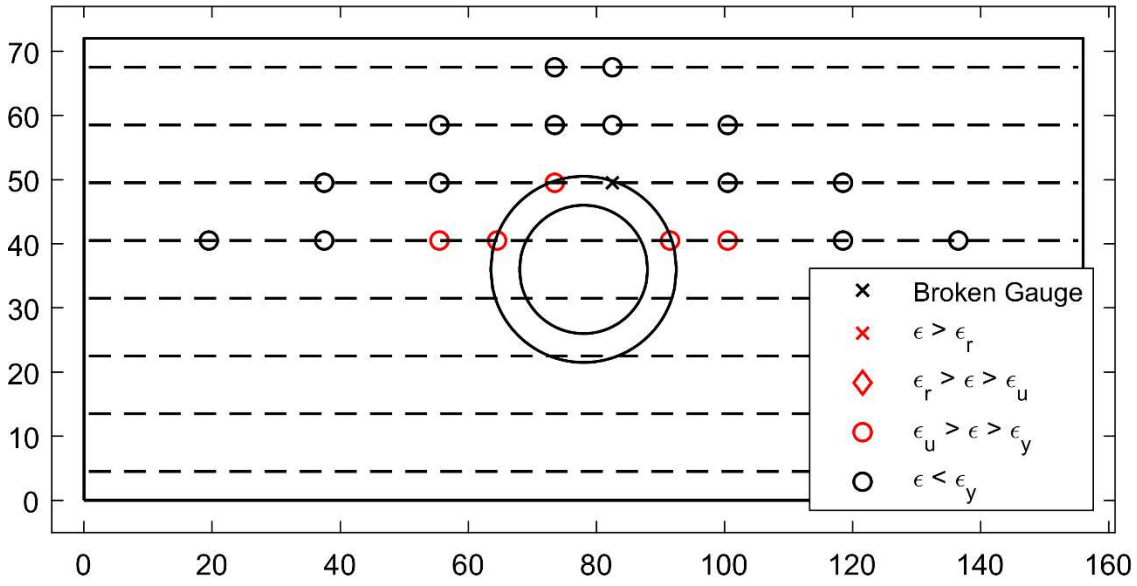

Figure 4.19. Top Reinforcement Strain Summary – 4.11% Drift (PTB_4.5_1_0_6)

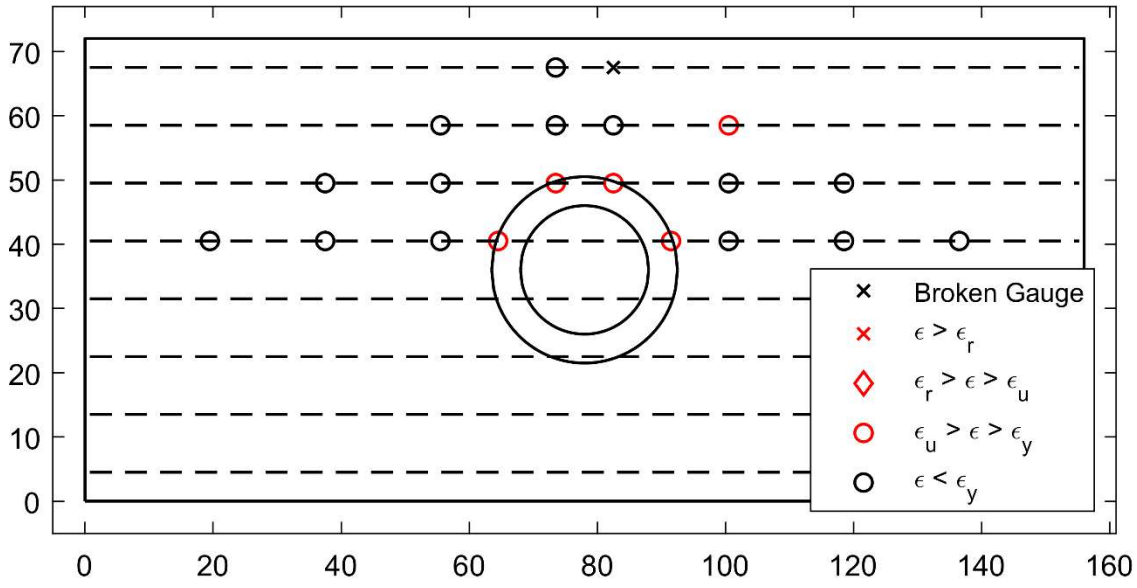

Figure 4.20. Bottom Reinforcement Strain Summary – 4.11% Drift (PTB_4.5_1_0_6)

During 7.0-2 (+4.79/-4.89 drift) spalling increased and was measured extending approximately 4 in. away from the edge of the ring flange. The spalling is still mostly focused on the north and south edges of the connection. At this drift level crushing occurred on the north and south edges of the ring. It extended approximately 2 in. out from the ring on the north edge of the connection and approximately 2.5-3 in. on the south edge of the connection. The crushing on the south side is shown in Figure 4.21. The initiation of crushing begins the degradation of strength of the specimen. Yielding of the flexural reinforcement continues to extend further across the slab. The top and bottom reinforcement both indicate yielding of three bars. The yielded strain gauge of the third bar was located to the south of the ring flange edge and could indicate a high deformation demand at this location due to formation of a flexural hinge.

Figure 4.21. Crushing on South Side of Bottom Face – 4.91% Drift (PTB_4.5_1_0_6)

8.0-2 (+5.45/-5.44 drift) resulted in a significant increase in the amount of crushing in the slab. Multiple reinforcing bars were exposed. The resulting damage due to crushing is shown in Figures 4.22 and 4.23. The extent of crushing was concentrated on the east side of the connection, with small increases in the amount of crushing developed to the north and south of the connection. The top face of the slab shows no signs of crushing, but the concrete around the connection has spalled. The third bar of the top flexural reinforcement did not record yielding during this drift level. There was a significant loss in lateral force resistance during 8.0-2 as a result of the damage to the slab.

Figure 4.22. Crushing on North Side of Bottom Face – 5.63% Drift (PTB_4.5_1_0_6)

Figure 4.23. Crushing on South Side of Bottom Face – 5.63% Drift (PTB_4.5_1_0_6)

9.0-2 (+6.31/-6.31 drift) was the last cycle of testing. The cycle was run uninterrupted since inspection of the specimen at the peaks was considered dangerous. The lateral force resistance measured the 40% strength loss criteria signifying end of testing. The top bars show yielding of

the bar closest to the east face of the slab. Since there is no indication of yielding on the third bar of the top reinforcement, the yielding of the outermost bar is likely due to the amount of crushing on the bottom face causing the load to be redistributed. The bottom bars do no show this same yielding of the outermost bar. The yielding of the outermost bar occurred after degradation of strength had begun.

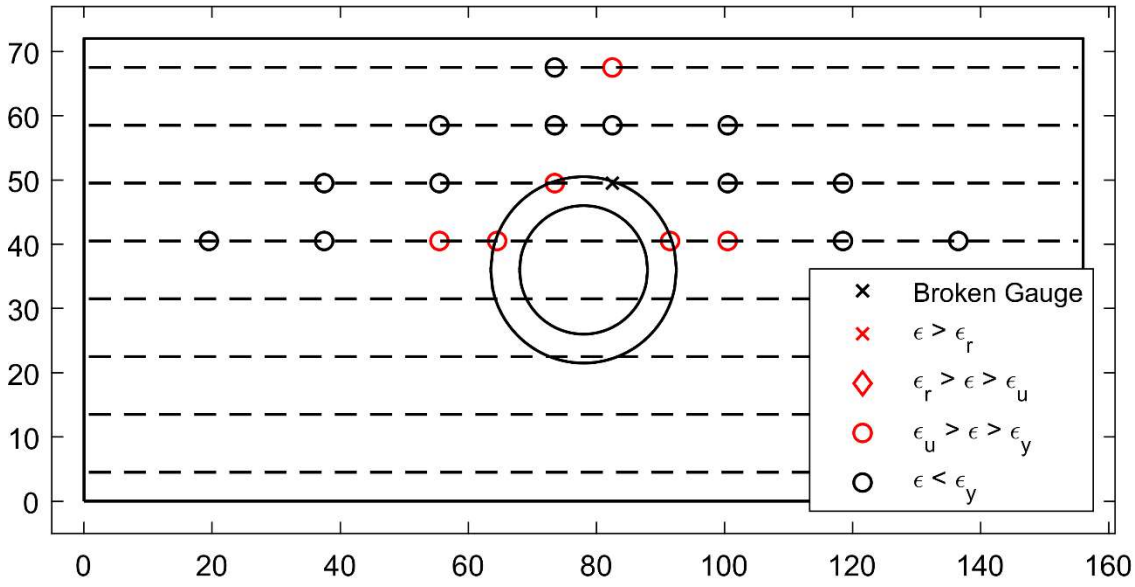

Figure 4.24. Top Reinforcement Strain Summary – 6.35% Drift (PTB_4.5_1_0_6)

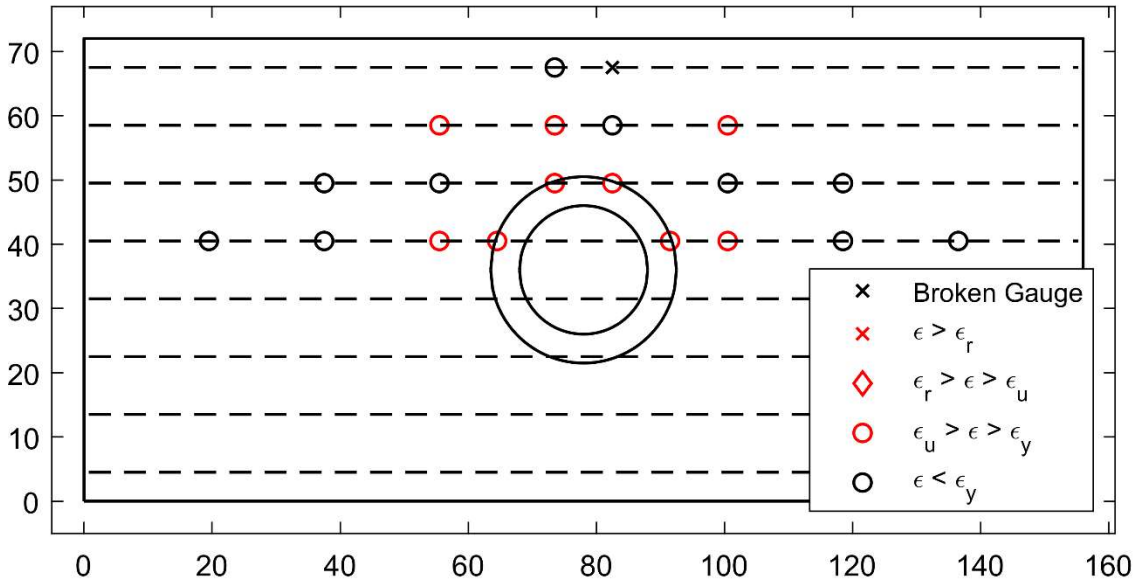

Figure 4.25. Bottom Reinforcement Strain Summary – 6.35% Drift (PTB_4.5_1_0_6)

4.2.6 *Post Test*

Since 9.0-2 was run without interruption, the photos of the resulting damage were not taken until after the test. The column was returned to a displacement of zero and measures were taken to secure the specimen before inspection of the damage. Damage to the top face of the slab is provided by Figure 4.26. Extensive crushing near the base of the ring flange was found. The crushing extended 3-4 in. from the north and south edge of the ring flange. Large cracks to the east and west of the connection indicate larger areas of spalling/delamination of the concrete that were not visible. The cracks extend approximately 1 ft. in both directions.

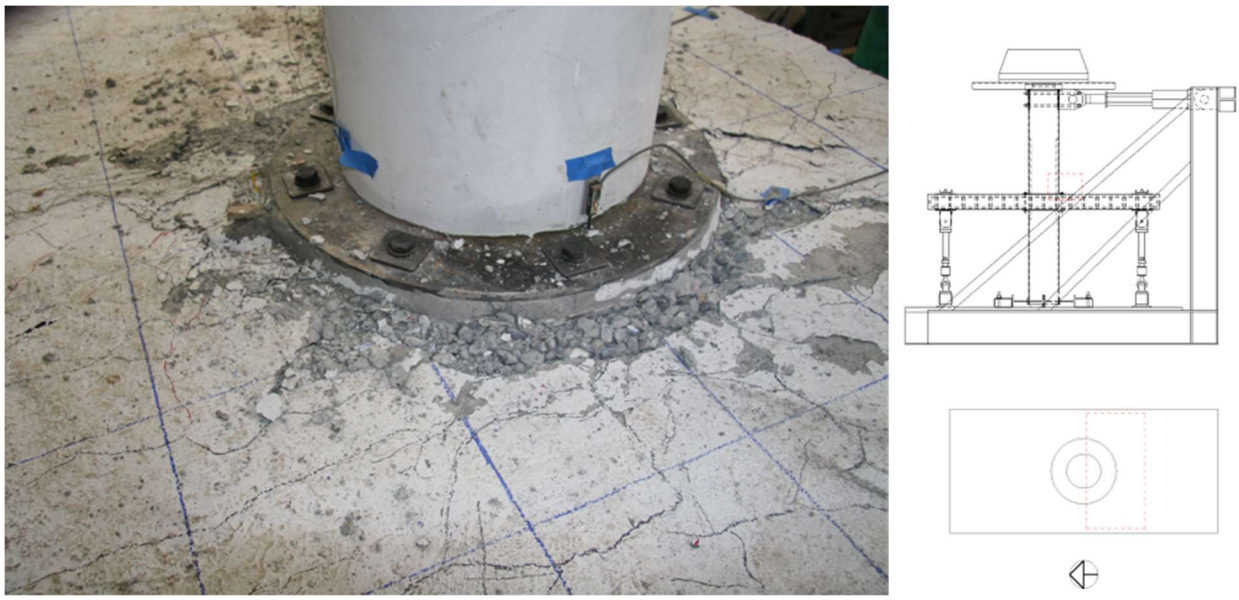

Figure 4.26. Damage on South Side of Top Face – 6.35% Drift (PTB_4.5_1_0_6)

On the bottom face of the slab, the crushing and spalling damage increased as shown in Figures 4.27 to 4.29. Looking at the North side of the slab, there is spalling to the West of the connection that appears to be in a direction radial to the column. The South side of the slab shows increased spalling South of the ring flange, but the majority of the crushing is concentrated to the East of the connection. One bar just within the confinement zone of the ring flange shows complete debonding from the interior concrete. While it is difficult to determine from the shape of the bar at a displacement of zero, it likely would have buckled at the target displacement since the concrete could no longer confine the bar.

Figure 4.27. Damage on North Side of Bottom Face – 6.35% Drift (PTB_4.5_1_0_6)

Figure 4.28. Exposed Bar on North Side of Bottom Face – 6.35% Drift (PTB_4.5_1_0_6)

Figure 4.29. Damage on South Side of Bottom Face – 6.35% Drift (PTB_4.5_1_0_6)

In addition to damage on the top and bottom faces of the slab, there were significant cracks formed on the side of the specimen shown in Figure 4.30. The photo was taken of the west face at a north-south location even with the column. The crack showed spalling around the mid-height of the slab, then extend diagonally up to a height that is approximately in line with the North-South flexural reinforcement. The damage could be a result of extensive spalling in the regions directly east and west of the column extending across the width of the slab.

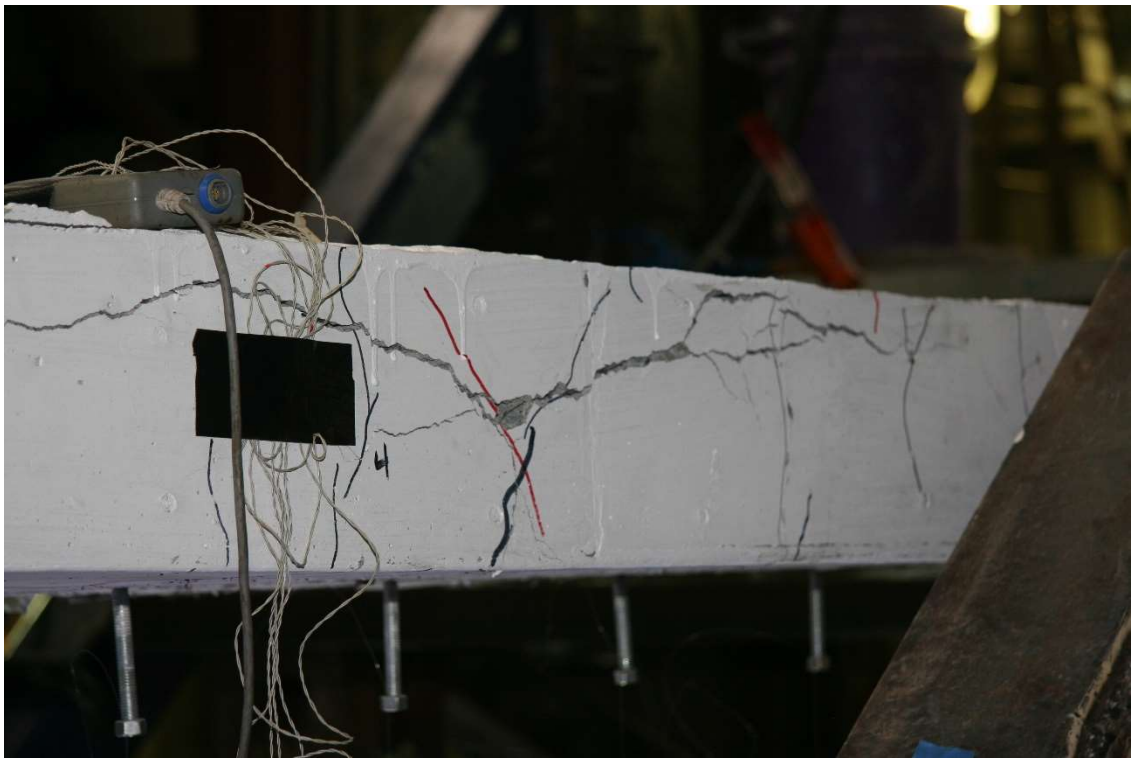

Figure 4.30. Damage on West Face – 6.35% Drift (PTB_4.5_1_0_6)

4.2.7 *Test Summary*

PTB_4.5_1_0_6 reached a maximum drift of 6.35%. Initial cracking across the width of the slab was noticed early into testing at a drift of 0.70%. Yielding of the slab first occurred in the reinforcement passing through the slab column joint at 2.11% drift. The maximum lateral force of -25.6 kips occurred at a drift of -3.48%. This correlated to the initiation of spalling. The spalling first occurs in on the north and south sides of the ring flange. Crushing began at 5.08% followed by the beginning of strength degradation. Testing was stopped at 6.35% drift after the strength had degraded by at least 40% of the peak measured resistance.

4.3 SPECIMEN PTB_9_2_0_6

Testing of PTB_9_2_0_6 was performed on June 18, 2021 in the University of Washington Structural Engineering Laboratory. The following section provides the global measured response of the test specimen as well as the crack patterns, reinforcement yield status, and other damage observations. The cycles are separated into drift level ranges of low, moderate, and high.

4.3.1 *Global Response and Specimen Geometry*

PTB_9_2_0_6 had a 9 in. wide ring flange with two rows of bolts within the ring flange. The slab is thin at a depth of 6 in.. A more thorough description of the specimen can be found in Chapter 3. The test was run smoothly without unexpected interruptions. The induced drift and the resulting lateral loading can be seen in Figure 4.31 and Figure 4.32 respectively.

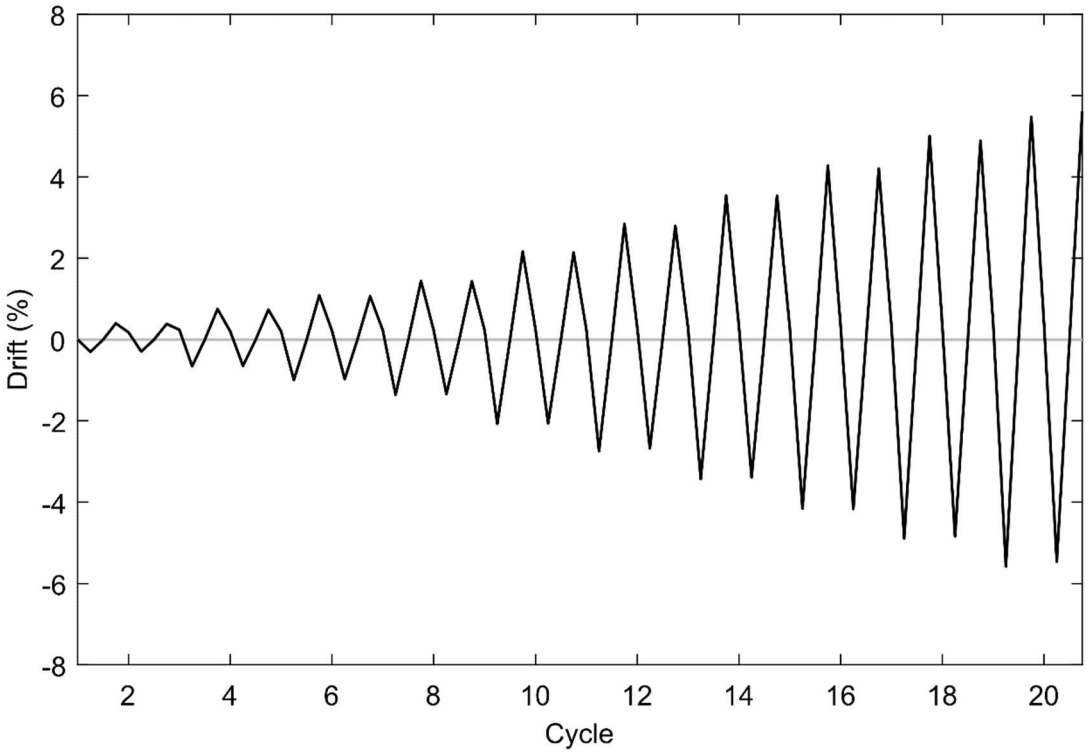

Figure 4.31. Induced Drift (PTB_9_2_0_6)

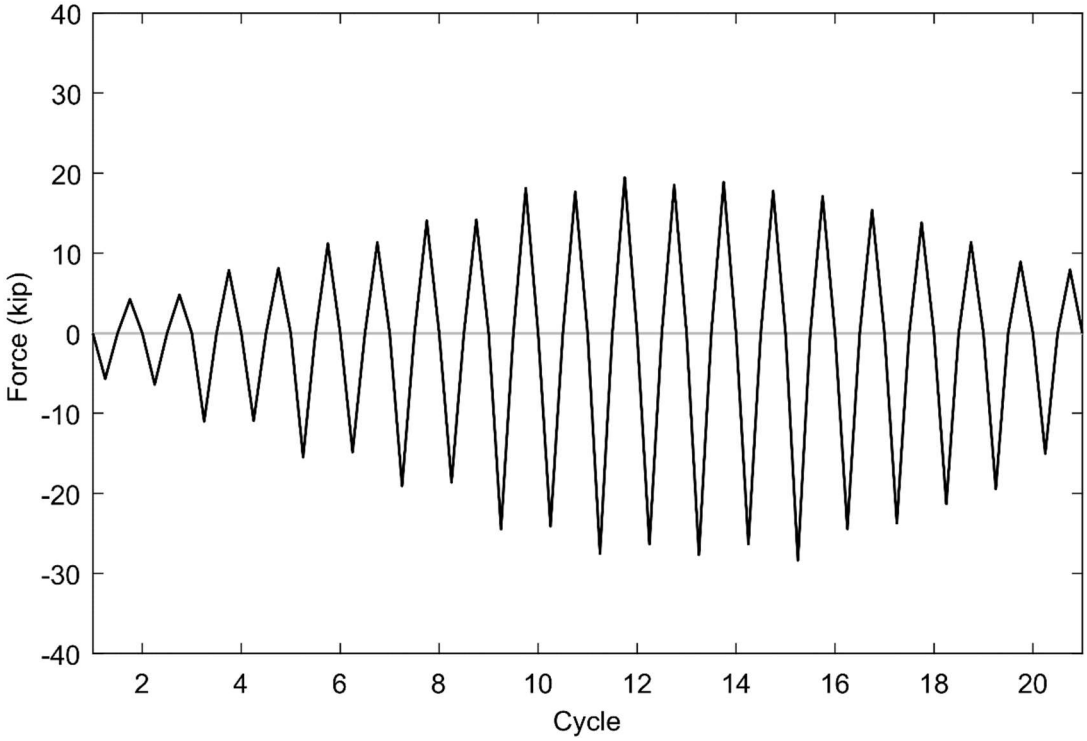

Figure 4.32. Applied Lateral Load (PTB_9_2_0_6)

The maximum drift reached by PTB_9_2_0_6 was 5.61%. The maximum measured lateral force of 28.4 kips occurred at the north peak during the 15th cycle. At the end of testing the force in the north direction drops significantly to 8.9 kips. This decrease in force is approximately a 54% loss of peak measured strength in the north direction. One additional cycle was run to complete the target drift. The tabulated maximum measured lateral response and the corresponding drift are provided in Table 4.8.

Table 4.8. Maximum Resistances and Drifts in Each Cycle (PTB_9_2_0_6)

Cycle	Maximum Measured Resistance (kips)		Maximum Drift (%)	
	Tension	Compression	Tension	Compression
1	4.2	-5.7	0.40	-0.30
2	4.8	-6.4	0.38	-0.29
3	7.9	-11.0	0.75	-0.66
4	8.1	-10.9	0.73	-0.65
5	11.2	-15.5	1.08	-0.99
6	11.3	-14.8	1.06	-0.97
7	14.0	-19.1	1.44	-1.36
8	14.2	-18.6	1.43	-1.34
9	18.1	-24.5	2.16	-2.07
10	17.7	-24.1	2.14	-2.06
11	19.5	-27.5	2.84	-2.74
12	18.5	-26.3	2.79	-2.68
13	18.9	-27.7	3.54	-3.43
14	17.8	-26.3	3.53	-3.39
15	17.1	-28.4	4.28	-4.16
16	15.4	-24.4	4.20	-4.16
17	13.8	-23.7	5.00	-4.89
18	11.3	-21.3	4.89	-4.84
19	8.9	-19.5	5.47	-5.58
20	7.9	-15.0	5.61	-5.46

The tabulated values show that the measured peak lateral resistance was reached during the 15th cycle. The measured resistance gradually decreases after cycle 15. The hysteretic response of the specimen is shown in Figure 4.33. The response has been normalized by the ACI flexural strength across the full width of the specimen. This calculated moment is then converted to a

corresponding MTS actuator force. Figure 4.34 shows the response with the $P - \Delta$ effects removed.

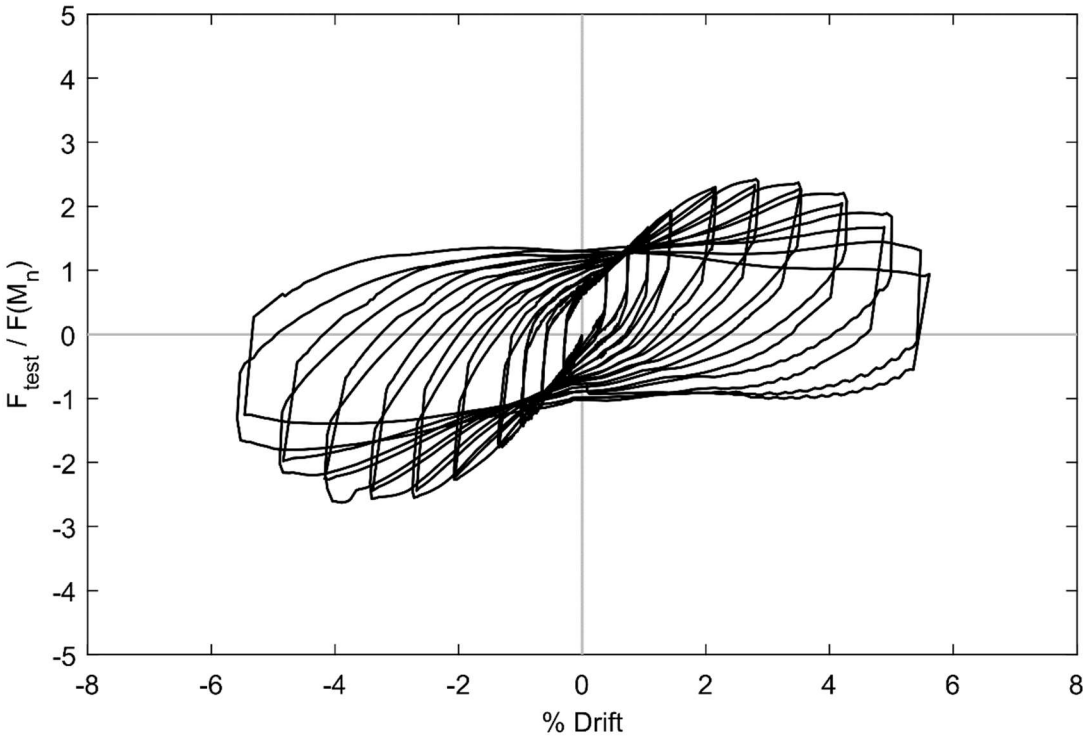

Figure 4.33. Normalized Drift Response (PTB_9_2_0_6)

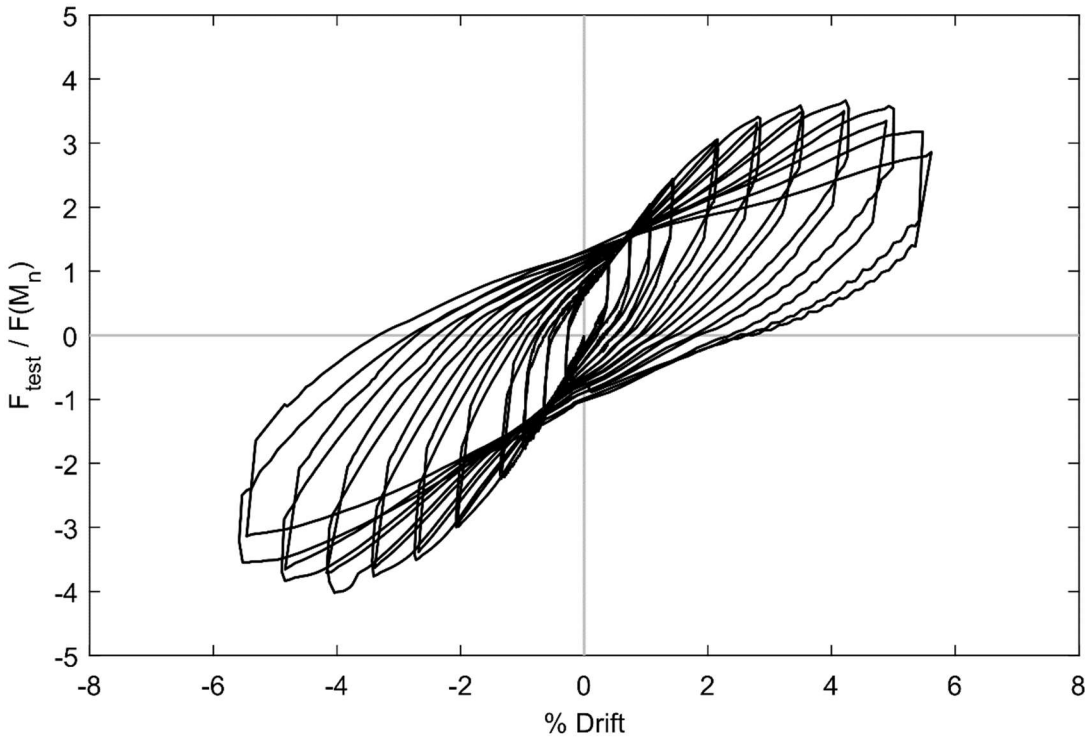

Figure 4.34. Normalized Drift Response with $P-\Delta$ Effects Removed (PTB_9_2_0_6)

4.3.2 *Specimen Performance State Summary*

Table 4.9 provides the summary of the damage states observed by during testing and the corresponding drift at which the damage states were observed.

Table 4.9. Summary of Damage (PTB_9_2_0_6)

Damage State	Drift (%)
Cracking	0.75 – 3.54
Yielding (initial – final)	2.84 – 5.61
Spalling	2.84
Crushing	5.00
Bar Buckling	5.61

4.3.3 *Low Drift Cycles (0.0% - 1.5% Target Drift)*

Inspection of the specimen during 0.5-2s showed cracks on the bottom face of the slab that were mostly due to shrinkage. When compared to the cracks on the top face of the slab it is apparent that the cracking had not yet extended across the width of the slab. The cracks were primarily around the edges of the ring flange and were transverse to the direction of loading. The orientation and location of the cracks resemble flexural cracking. Cracks widths at this drift level were small. The max measured crack widths were 0.15 mm found on the bottom face of the slab. Below is a table showing the average of the largest flexural and radial cracks measured during low cycle drifts. The table separates the cracks based on which face of the slab they are found on bottom, top, or side. Within those categories the table distinguishes which directional peak the crack widths were measured at. North corresponds with the compressive MTS force alternatively south corresponds with the tensile MTS force.

Table 4.10. Low Drift Cycle Typical Crack Opening at Peaks

Cycle	Drift (%)		Bottom (mm)		Top (mm)		Side (mm)	
	South	North	South	North	South	North	South	North
2	0.38	-0.29	0.15	0.15	0.10	0.10	0.10	0.10
4	0.73	-0.65	0.375	0.23	0.10	0.10	0.20	0.15
6	1.06	-0.97	0.50	0.33	0.28	0.35	0.25	0.20
8	1.43	-1.34	0.53	0.45	0.60	0.55	0.20	0.20

1.0-2 (+0.73/-0.65 drift) showed flexural cracks spanning the width of the slab on the top and bottom faces of the slab as shown in Figures 4.35 and 4.36. The cracking satisfied the definition of Cracking Stage 1. The cracking is more extensive on the bottom side of the slab. This is a result of shrinkage as well as increased loading due to the weight of the slab. There were some cracks parallel to the direction of loading along the flexural reinforcement passing through the column. The parallel cracks were found mostly on the bottom face of the slab. The location of them aligned with the slab flexural reinforcement indicating cracking due to engagement of the reinforcement. The cracks widths increased for every face of the slab. The bottom slab showed the

greatest change with a maximum flexural crack of 0.35 mm and maximum radial crack of 0.40 mm during the South peak. However the cracks were not large enough to show a significant change in the stiffness of PTB_9_2_0_6 at this drift level.

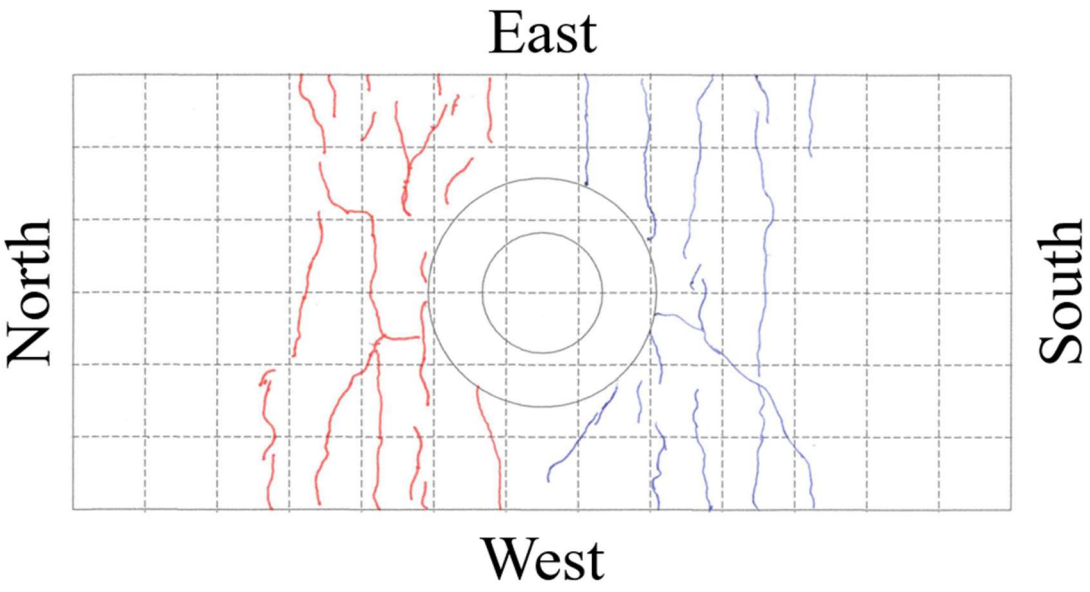

Figure 4.35. Top of Slab Crack Map – 0.75% Drift (PTB_9_2_0_6)

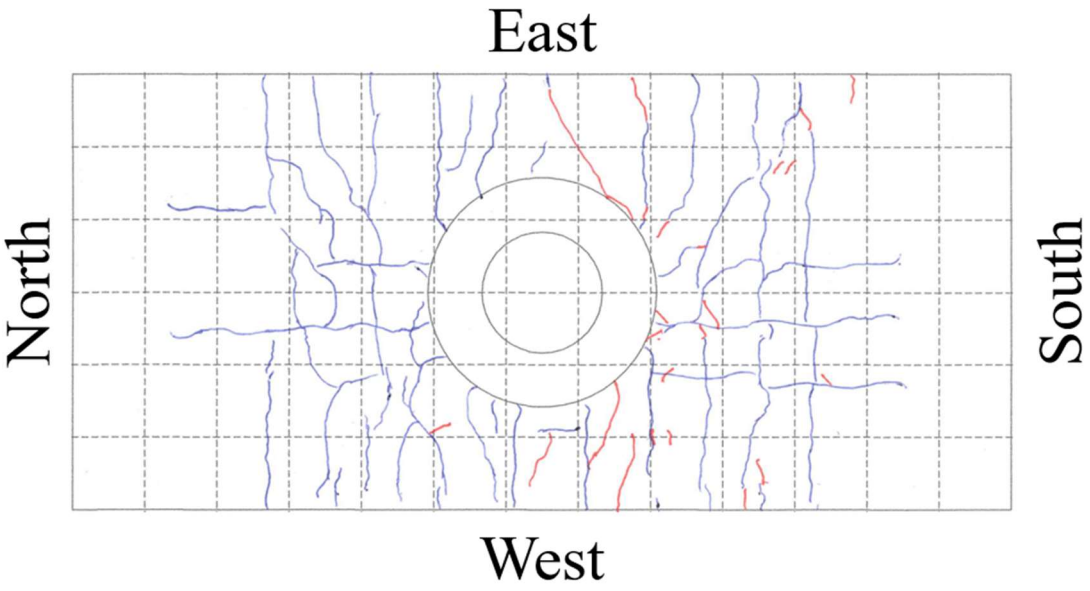

Figure 4.36. Bottom of Slab Crack Map – 0.75% Drift (PTB_9_2_0_6)

1.5-2 (+1.06/-0.97 drift) showed minimal increase in new flexural cracks. The majority of new cracks were parallel to the direction of loading along the flexural reinforcement. There was

also cracking to the east and west of the ring flange. The cracks were not perpendicular to the direction of load, they were approximately 45° to the direction of loading. The more extreme angles of this cracking are on opposite edges of the slab for the different faces which may indicate the diagonal cracking is a result of torsion. The maximum crack widths found during 1.5-2 were on average 0.5 mm on the south side of the bottom face of the slab during peak south loading. In contrast the maximum cracking on the north side of the bottom face of the slab during the north peak was 0.33 mm. Cracking on the top side of the slab followed a similar trend with it being larger during the south peak than the north peak. The cracking on the side face increased slightly from the previous drift level.

2.0-2 (+1.43/-1.34 drift) the cracking on the bottom face of the slab showed new flexural cracks forming further away from the column. In addition some of the already existing flexural cracks near the ring flange developed connecting cracks. On the top face of the slab there was an increase in cracks in the direction of loading aligned with the flexural reinforcement. New diagonal cracks also formed on the east side of the ring flange. The top slab also showed new flexural cracks distant from the ring flange as well as many small connecting cracks for the already existent flexural cracks near the ring flange. The crack widths continued to increase. The largest crack was found on the top slab near the edge of the ring flange measuring 0.85 mm. The other crack widths on the top face of the slab were smaller in comparison to the bottom of the slab, but the large crack skewed the reported average. The crack widths on the side face did not show any significant change during this drift level.

4.3.4 *Moderate Drift Cycles (1.5% - 3.6% Target Drift)*

3.0-2 (+2.14/-2.06 drift) showed a similar increase in flexural cracks near the slab end roller supports for both top and bottom faces of the slab. There was also an increase in the amount of diagonal cracks to the east and west of the column. Both top and bottom of the slab showed a slight increase in flexural cracks forming near the east and west edges of the slab at about the same north south location as the ring flange edges. There were also cracks parallel aligning with all of the bars within the column and ring flange width. On the bottom slab face there was cracking parallel to the direction of load along the middle six bars. This included one bar from outside the column and ring flange width in both east and west direction showing the spreading of engaged reinforcement.

The crack widths also show significant increase during this drift level. Cracks were largest during the south loading where the bottom face of the south side of the slab had two cracks widths measure 1.0 mm. The top face of the north side of the slab had a maximum crack width of 1.0 mm. The side cracking also showed significant increase measuring 0.35-0.40 mm. A summary of the crack widths during the moderate drift cycles is given in Table 4.11. It is apparent that the cracking is reducing the stiffness of the specimen at this point from the change in slope of the hysteretic response, however it is not a significant change in stiffness yet. At this drift level there is no indication of yielding of the flexural reinforcement.

Table 4.11. Moderate Drift Cycle Typical Crack Opening at Peaks

Cycle	Drift (%)		Bottom (mm)		Top (mm)		Side (mm)	
	South	North	South	North	South	North	South	North
10	2.14	-2.06	1.00	0.75	0.93	0.60	0.40	0.35
12	2.79	-2.68	1.25	1.25	1.25	1.00	0.40	0.40
14	3.53	-3.39	2.00	1.35	1.75	1.35	0.45	0.40

4.0-2 (+2.79/-2.68 drift) did not result in significant new damage due to cracking. The new cracks on the top face of the slab were diagonal cracks to the west of the column and flexural cracking near the east edge of the slab. There was also some new cracks along the reinforcing bar to the west of the ring flange. The bottom face of the slab showed some development of existing flexural cracks and a bit more cracking along the bar west of the ring flange. Crack widths continued to increase on the top and bottom faces. The largest crack was found during the south peak loading on the south side of the bottom face of the slab. The crack width measured 1.5 mm. During this drift level the top and bottom flexural reinforcement yielded for the first time at the locations shown in Figures 4.37 and 4.38. The yield resulted in a loss of stiffness and therefore the slope of the hysteresis decrease at this drift level.

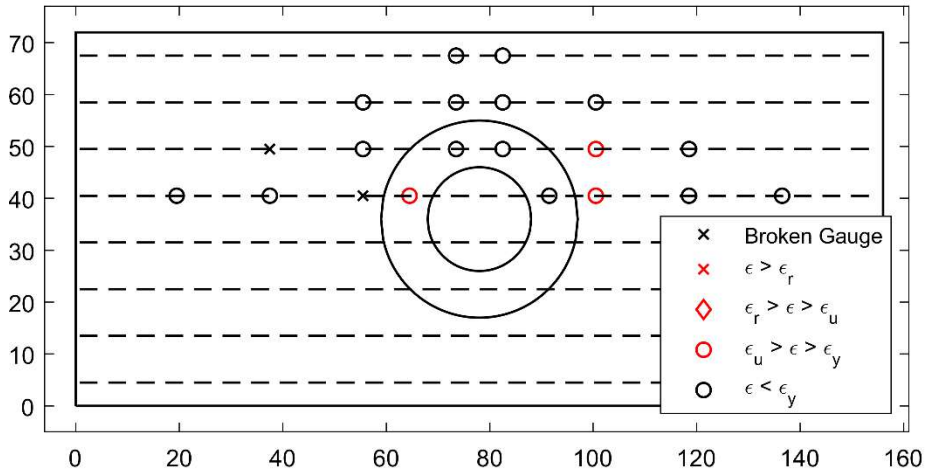

Figure 4.37. Top Reinforcement Strain Summary – 2.84% Drift (PTB_9_2_0_6)

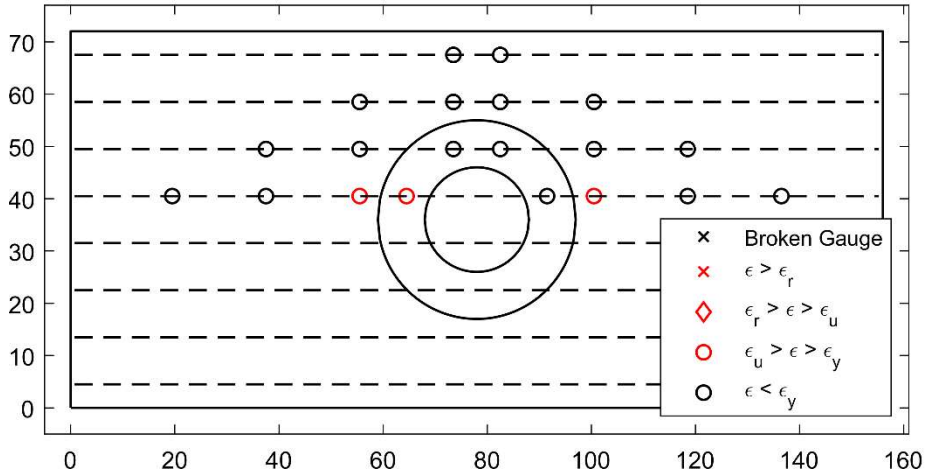

Figure 4.38. Bottom Reinforcement Strain Summary – 2.84% Drift (PTB_9_2_0_6)

5.0-2 (+3.53/-3.39 drift) showed insignificant difference in the crack pattern from the previous drift level. The majority of the crack development was on the top slab to the east and west of the column. The maximum crack widths at the north peak displacement were measured at 1.5 mm on both the top and bottom face of the slab. During the south peak displacement the maximum measured crack widths are 2.0 mm on both the top and bottom face of the slab. Initial spalling occurred at the north and south edges of the ring flange. Figure 4.39 shows the minimal spalling

that measures approximately an inch in distance from the ring flange. The yielding of the flexural reinforcement began to spread further across the width of the specimen as shown in Figures 4.40 and 4.41. The bottom reinforcement shows yielding of the bar just outside the ring flange. Some of the strain gauges within the ring flange did not show yielding, showing that confinement of the ring reduced the strain they experienced.

Figure 4.39. Spalling on North Side of Bottom Face– 3.54% Drift (PTB_9_2_0_6)

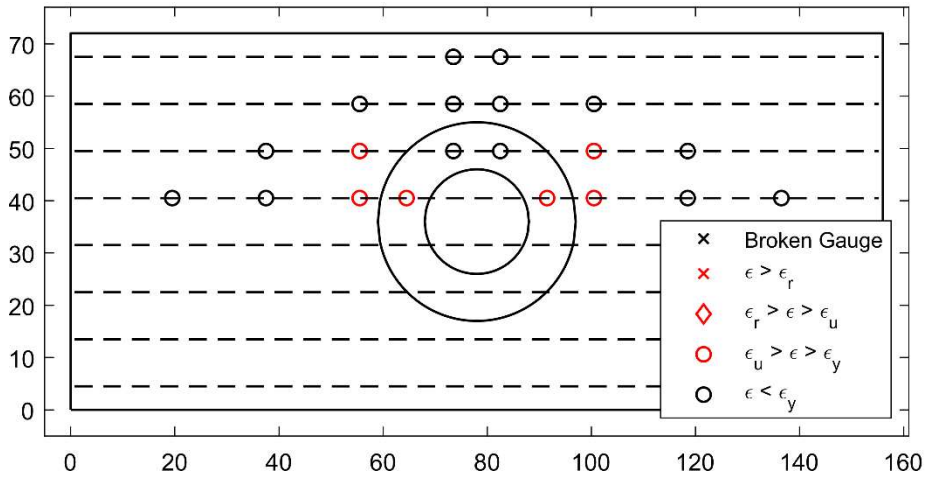

Figure 4.40. Top Reinforcement Strain Summary – 3.54% Drift (PTB_9_2_0_6)

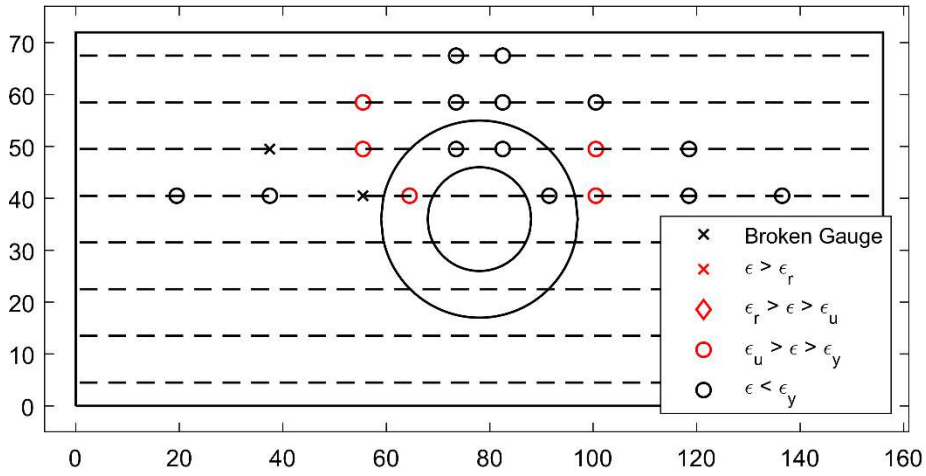

Figure 4.41. Bottom Reinforcement Strain Summary – 3.54% Drift (PTB_9_2_0_6)

4.3.5 *High Drift Cycles (3.6% - Final Target Drift)*

6.0-2 (+4.20/-4.16 drift) showed minimal crack development. The spalled region increased but is still primarily near the north and south edges of the ring flange. The crack sizes continued to increase. At the south peak the maximum crack widths were 2.5 mm on both the top and bottom faces of the slab. At the north peak the maximum measured crack widths were 3.0 mm and 3.5 mm on the bottom and top face of the slab respectively. Tabulated values of the measured crack widths for the high drift cycles are provided by Table 4.12. Cycle 20 was not measured due to safety precautions. The yielding had spread to the bar outside the confined ring flange region as shown in Figures 4.42 and 4.43. The line of yielded strain gauges seems to indicate that the hinging due to flexure forms at or near the edge of the ring flange.

Table 4.12. Moderate Drift Cycle Typical Crack Opening at Peaks

Cycle	Drift (%)		Bottom (mm)		Top (mm)		Side (mm)	
	South	North	South	North	South	North	South	North
16	4.20	-4.16	2.75	2.25	3.25	2.25	0.45	0.45
18	4.89	-4.84	3.25	2.75	5.00	2.75	0.50	0.50
20	5.61	-5.46	-	-	-	-	-	-

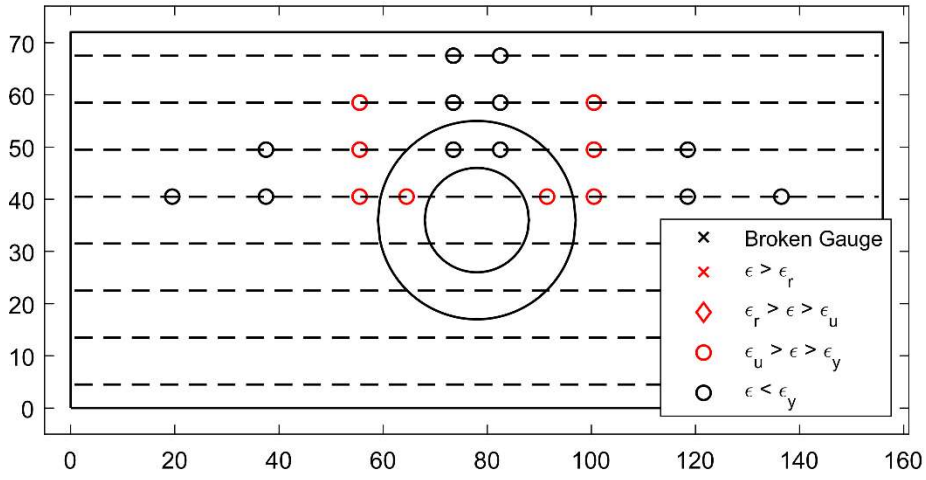

Figure 4.42. Top Reinforcement Strain Summary – 4.28% Drift (PTB_9_2_0_6)

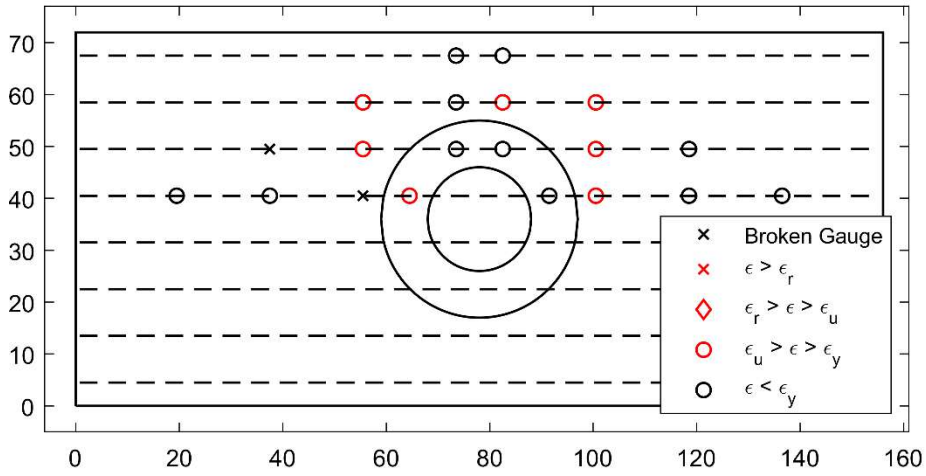

Figure 4.43. Bottom Reinforcement Strain Summary – 4.28% Drift (PTB_9_2_0_6)

During 7.0-2 (+4.89/-4.84 drift) PTB_9_2_0_6 showed significant increase in spalling on the top and bottom faces of the slab. Spalling occurring on the top face was primarily around the north and south edges of the ring. Spalling on the bottom face is shown in Figure 4.44. In addition to the spalling at the north and south edges of the ring, spalling occurred along the flexural reinforcement west of the ring flange. During 7.0-2 crushing was noticed on the bottom face of the slab shown in Figures 4.45 and 4.46. The extent of crushing measured approximately 2 in. from the north edge of the ring. The crushing on the south side occurred at roughly 1 ft from the ring edge and had a length of about 3 in.. The flexural reinforcement strain summary did not change for the top bars. The bottom bars changed slightly.

Figure 4.44. Spalling on North Side of Bottom Face– 5.00% Drift (PTB_9_2_0_6)

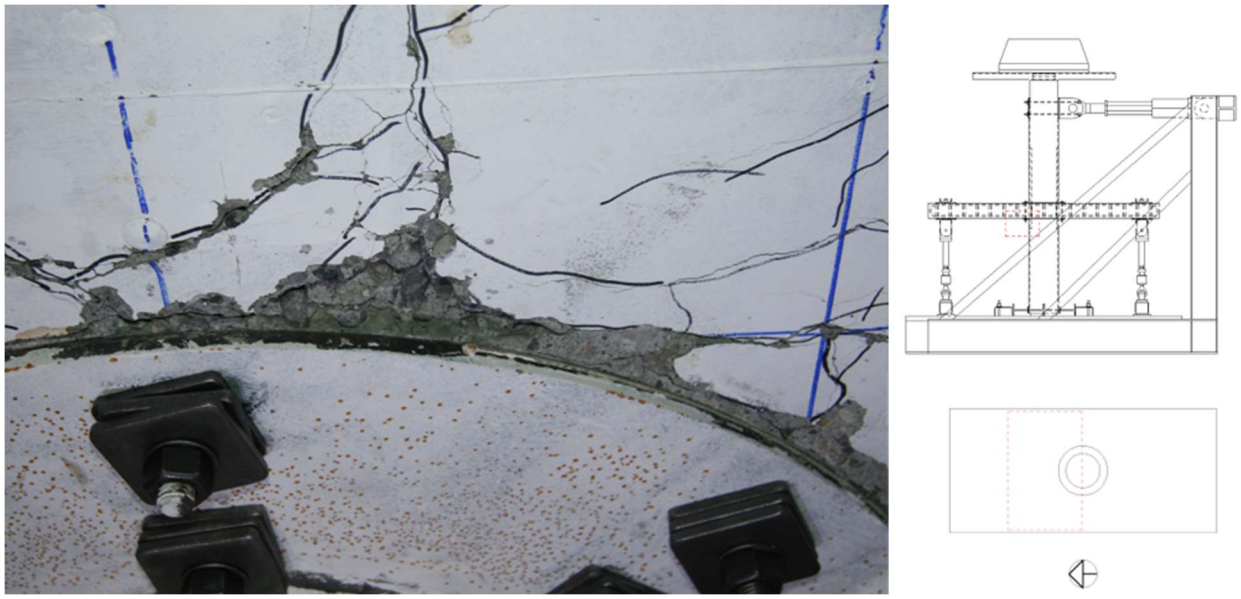

Figure 4.45. Crushing on North Side of Bottom Face– 5.00% Drift (PTB_9_2_0_6)

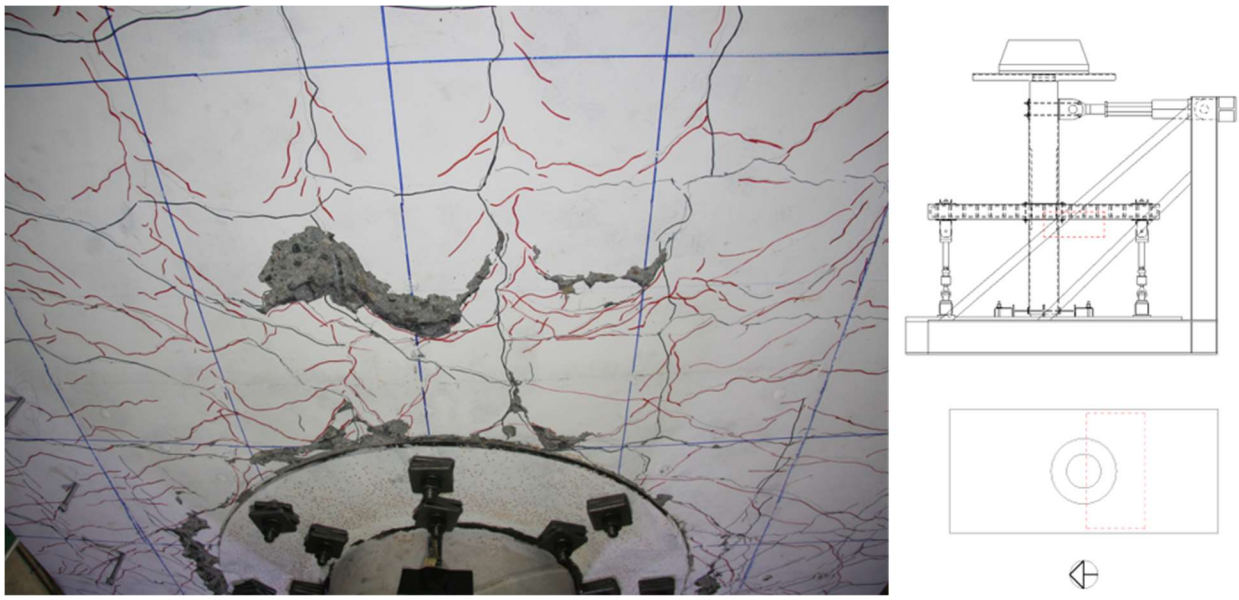

Figure 4.46. Spalling on South Side of Bottom Face– 5.00% Drift (PTB_9_2_0_6)

8.0-2 (+5.61/-5.46 drift) was paused at the north peak. The strength loss was high enough that for safety precautions the specimen was not inspected in the same manner as the other drift levels. The cycle was the completed without further interruption. Figures 4.47 and 4.48 show the concrete damage increased significantly. The spalled regions expanded in the north and south. Much of the spalled region showed significant crushing of the concrete near the north and south edge of the ring. The two reinforcing bars passing through the column buckled and can be seen on the south side of the specimen. In addition a crack on the west face of the slab similar to PTB_4.5_1_0_6 formed as shown in Figure 4.49. The strain status of the reinforcement can be seen in Figures 4.50 and 4.51. The bottom bars show yielding of the outermost bar. Based on the location of the strain gauges not being in line with the north and south edge of the ring flange, they may yield at a higher drift than if the outermost bar had four gauge locations. The strength loss was large enough to satisfy the end of testing criteria.

Figure 4.47. Damage on North Side of Bottom Face– 5.61% Drift (PTB_9_2_0_6)

Figure 4.48. Bar Buckling on South Side of Bottom Face– 5.61% Drift (PTB_9_2_0_6)

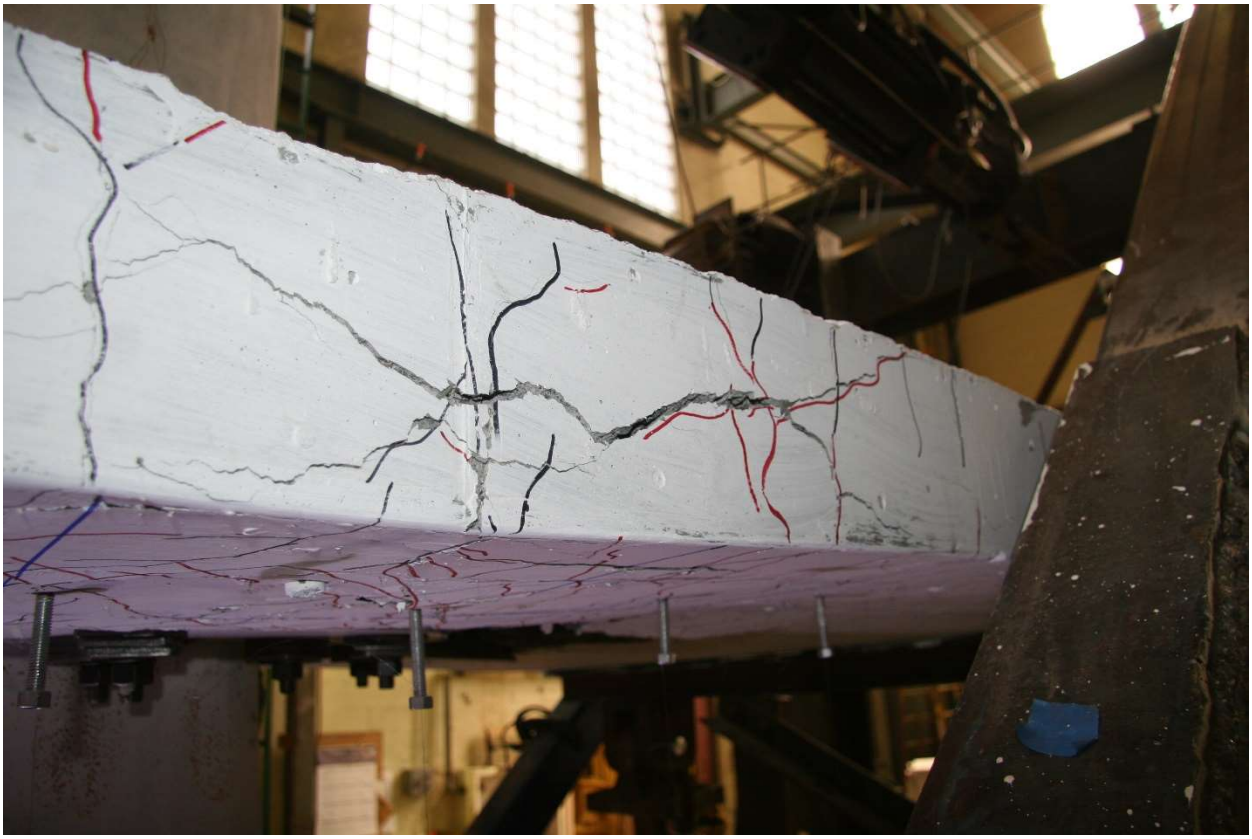

Figure 4.49. Cracking on West Face– 5.61% Drift (PTB_9_2_0_6)

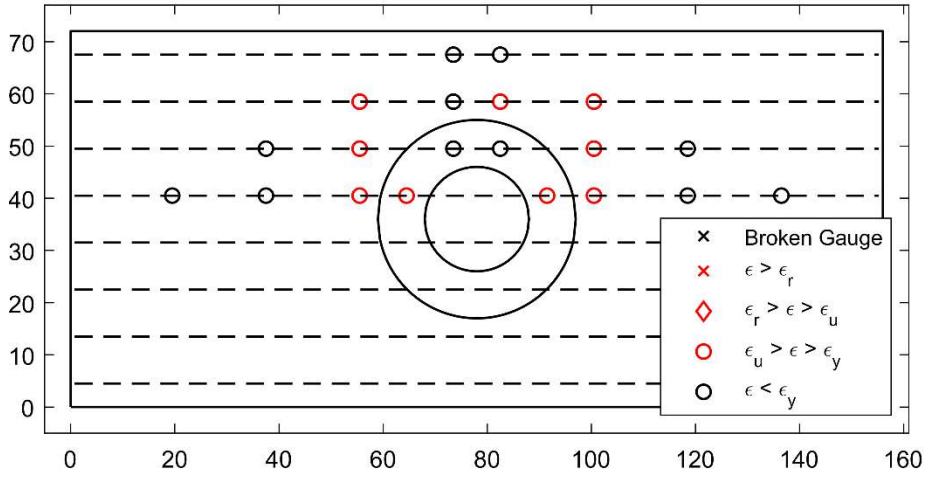

Figure 4.50. Top Reinforcement Strain Summary – 5.61% Drift (PTB_9_2_0_6)

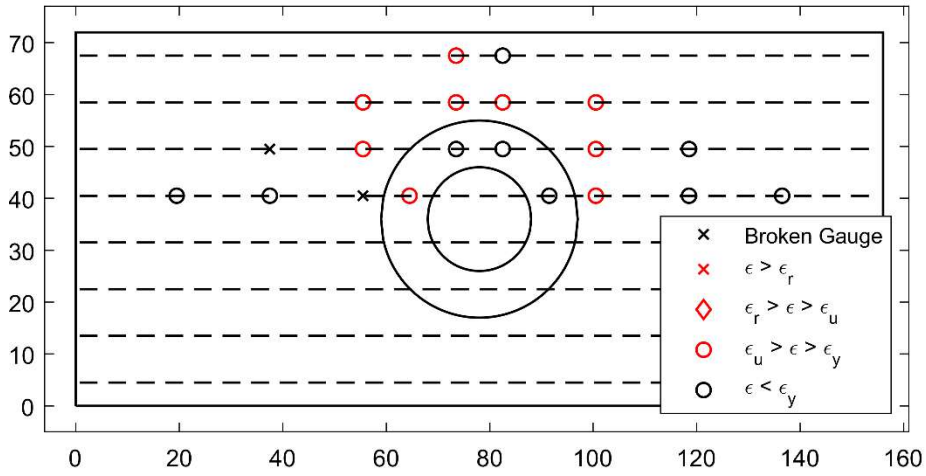

Figure 4.51. Bottom Reinforcement Strain Summary – 5.61% Drift (PTB_9_2_0_6)

4.3.6 *Test Summary*

PTB_9_2_0_6 reached a maximum drift of 5.61%. Cracking Stage 1 occurred at approximately 0.73% drift. During 4.0-2 initial yielding of the flexural reinforcement was observed. Cracking Stage 2 and initiation of spalling both occurred at approximately 3.6% drift. This also corresponded to the beginning of a strength plateau which continued until initiation of crushing around 5.1% drift. The initiation of crushing lead to loss of strength which resulted in the test ending during the next target drift level.

Chapter 5. DATA ANALYSIS OF COMBINED-LOADING SPECIMENS

This chapter discusses the measured responses from testing of the combined-loading specimens and compares them to the first phase of the experimental test program conducted by Yeutter (2020) to investigate the impact of slab depth on connection response and design. The comparisons are comprised of global behavior, local behavior, and observation of damage. Global behavior is examined by investigating the force-displacement response of the specimens. Local behavior is studied using the displaced shape and reinforcing bar strain distributions in the slab. The observational damage is quantified reporting the drift levels at which the specimens exhibited damage described by the damage states given in Chapter 4.

In this chapter, the stud rail specimen, SR_4_10_5_10, is used as the reference specimen since it most closely simulates current engineering practice. Two of the 10 in. slab specimen tests by Yeutter, specifically PTB_4.5_1_0_10 and PTB_9_2_0_10, are compared to the reference specimen. The thin slab specimens, PTB_4.5_1_0_6 and PTB_9_2_0_6, are then presented to investigate the difference in the connection behavior with the change in slab depth.

5.1 SYSTEM BEHAVIOR

The system response of the specimens is characterized by the hysteretic response, peak and 10% loss of peak strength drift values, and energy dissipation. The hysteretic responses of the specimens are given with $P - \Delta$ removed and normalized by the ACI 318-19 predicted flexural strength. The predicted strength uses the ACI approach with a modification defining the effective depth to include the ring flange in the definition of the column diameter (e.g., the specimens with a 4.5 in. ring would use a column of 26.7 in.).

5.1.1 *Hysteretic Response Including Energy Dissipation*

Figures 5.1 to 5.5 show the hysterestic responses of Specimens SR_4_10_5_10, PTB_4.5_1_0_10, PTB_9_2_0_10, PTB_4.5_1_0_6, and PTB_9_2_0_6 respectively. Pinching, the degradation of stiffness of the hysteretic curve due to bond slippage and cracking, is observed

in all cases. SR_4_10_5_10 reached peak strength at approximately 2.9% drift followed by a gradual degradation of the peak strength. The spike in strength near the end of testing of SR_4_10_5_10 at the negative (North) half cycle was attributed to the behavior of the MTS Actuator's electronic instrumentation as it approached maximum stroke. The following summarizes the responses of the new connections.

- PTB_4.5_1_0_10 reached peak strength at 3.6% drift. The strength degrades gradually until a sudden loss of strength at 5.1% drift.
- PTB_9_2_0_10 reached peak strength at approximately 3.6% drift and maintains this strength until approximately 5.8% drift. At that point it begins to gradually lose strength, but the test was stopped before the specimen had lost 10% of its peak strength due to limitations of the test setup.
- PTB_4.5_1_0_6 had a much lower initial stiffness than the 10 in. slab specimens. The peak strength was reached at roughly 3.6% drift. The strength plateaued for a few cycles before beginning to gradually degrade at 5.1% drift.
- PTB_9_2_0_6 reached peak strength at 3.6% drift. The strength began to deteriorate at approximately 5.1% drift.

The proposed connection specimens were able to maintain the maximum strength at higher drifts than the reference specimen. The deterioration of strength was ductile for all specimens excluding PTB_4.5_1_0_10. This indicates better ductility for the proposed connection specimens when the ring flange width is at least equal to the effective depth of the slab.

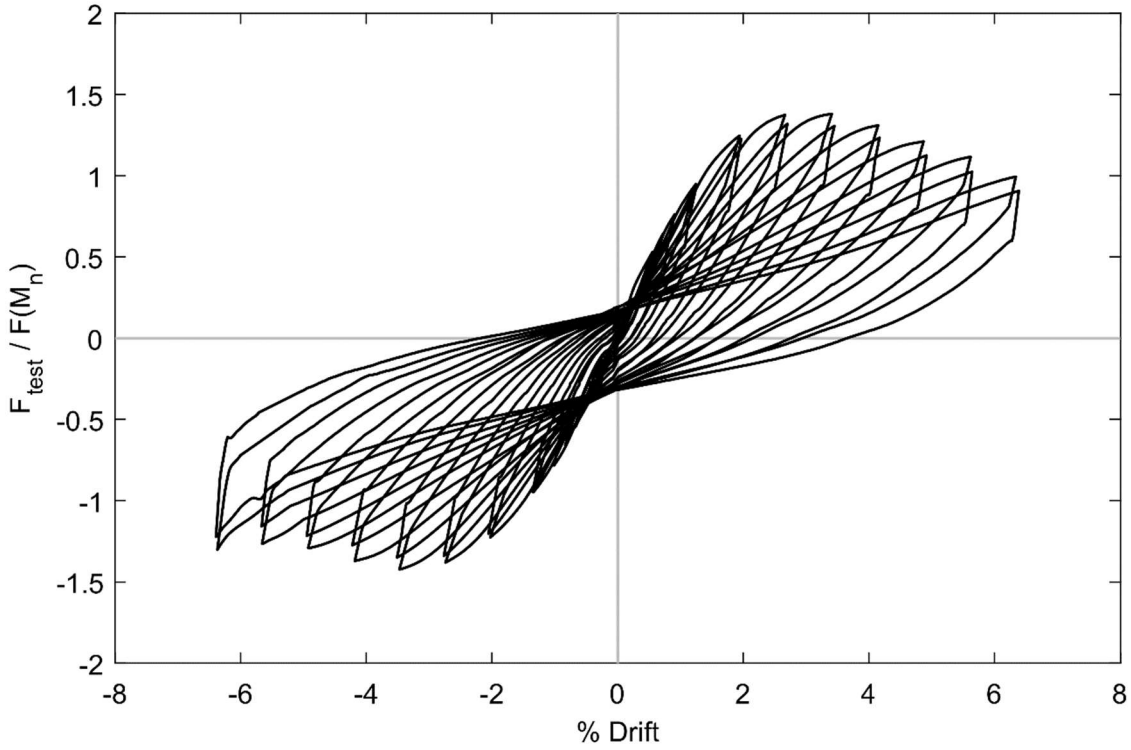

Figure 5.1. Normalized Drift Response with $P-\Delta$ Effects Removed (SR_4_10_5_10)

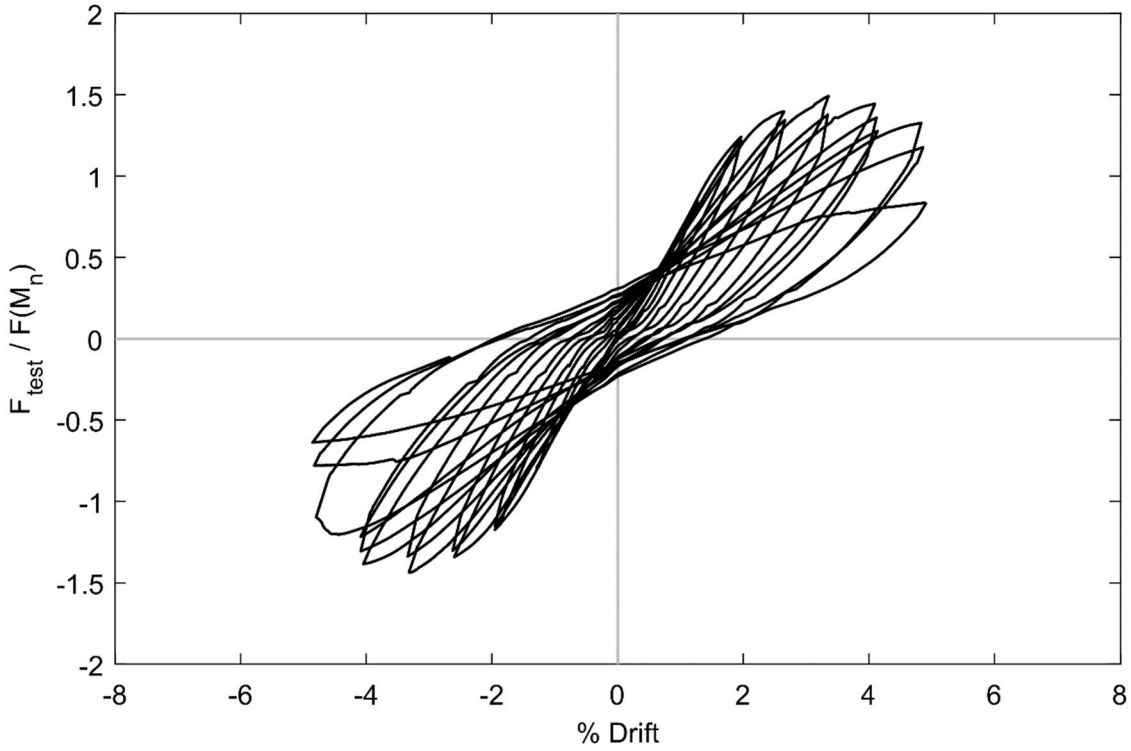

Figure 5.2. Normalized Drift Response with $P-\Delta$ Effects Removed (PTB_4.5_1_0_10)

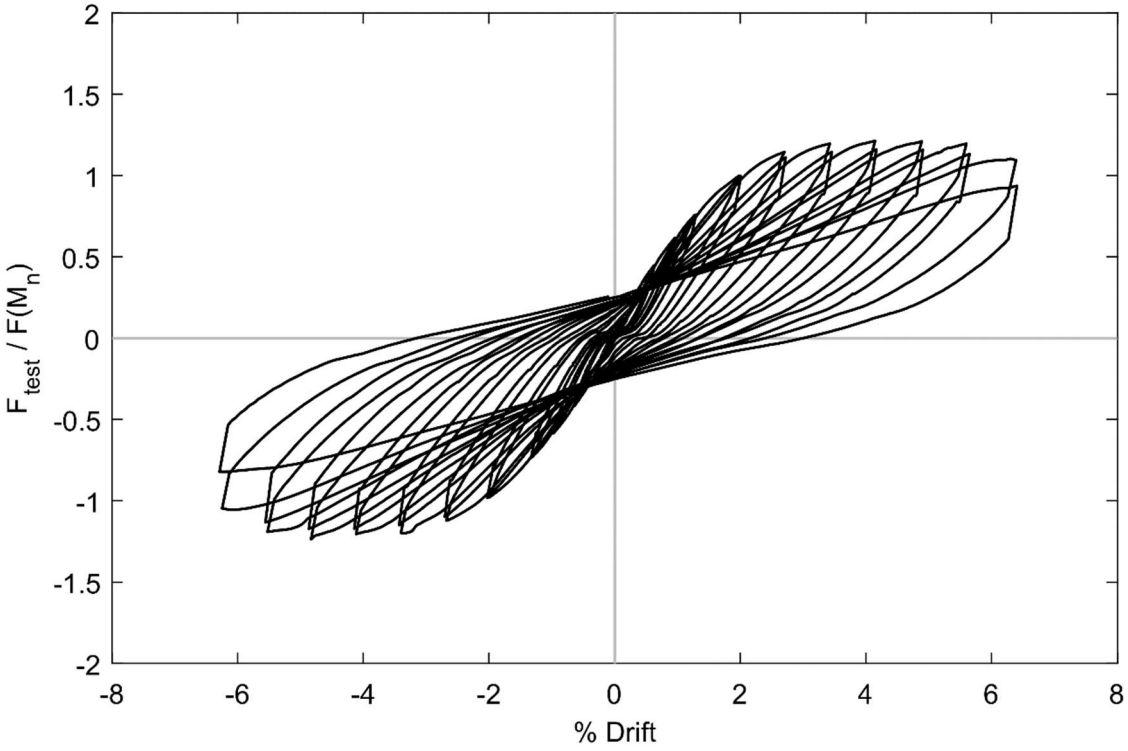

Figure 5.3. Normalized Drift Response with $P - \Delta$ Effects Removed (PTB_9_2_0_10)

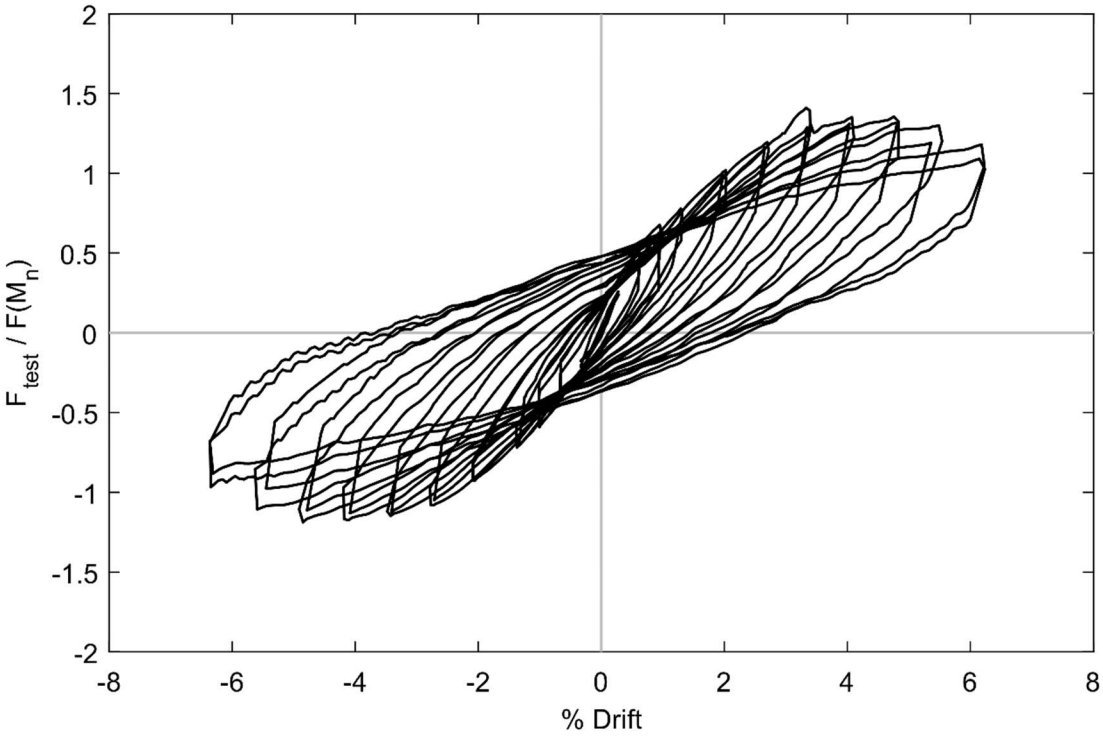

Figure 5.4. Normalized Drift Response with $P - \Delta$ Effects Removed (PTB_4.5_1_0_6)

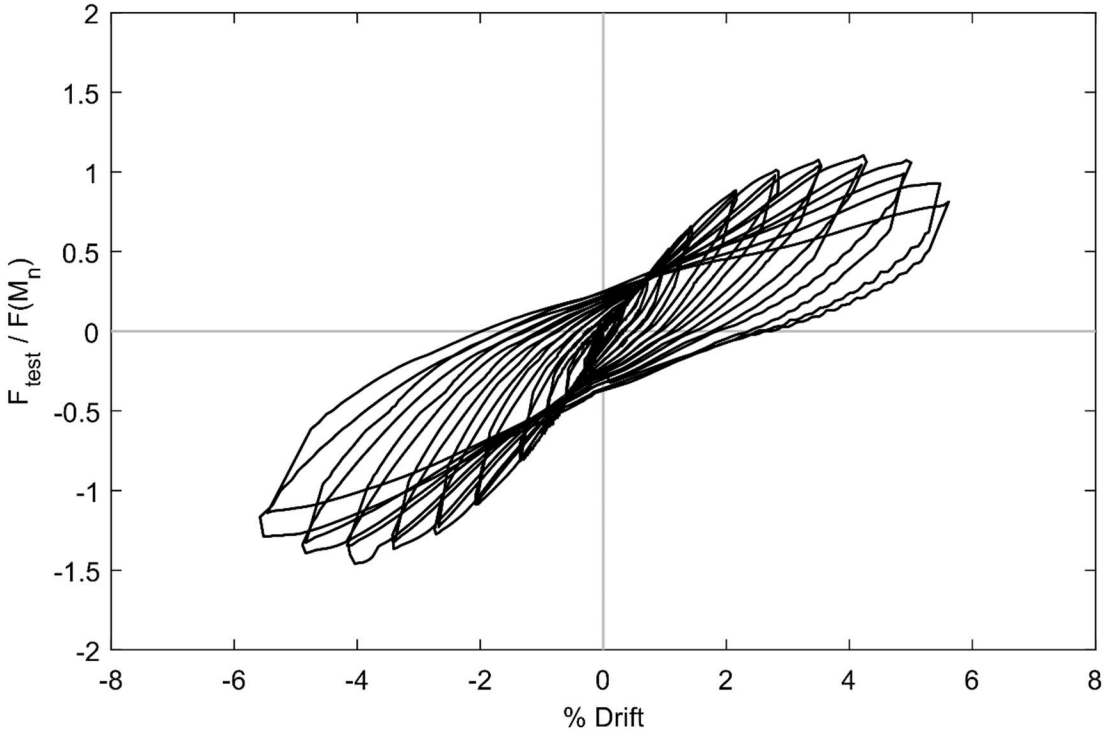

Figure 5.5. Normalized Drift Response with $P-\Delta$ Effects Removed (PTB_9_2_0_6)

5.1.2 *First Cycle Force-Drift Envelopes*

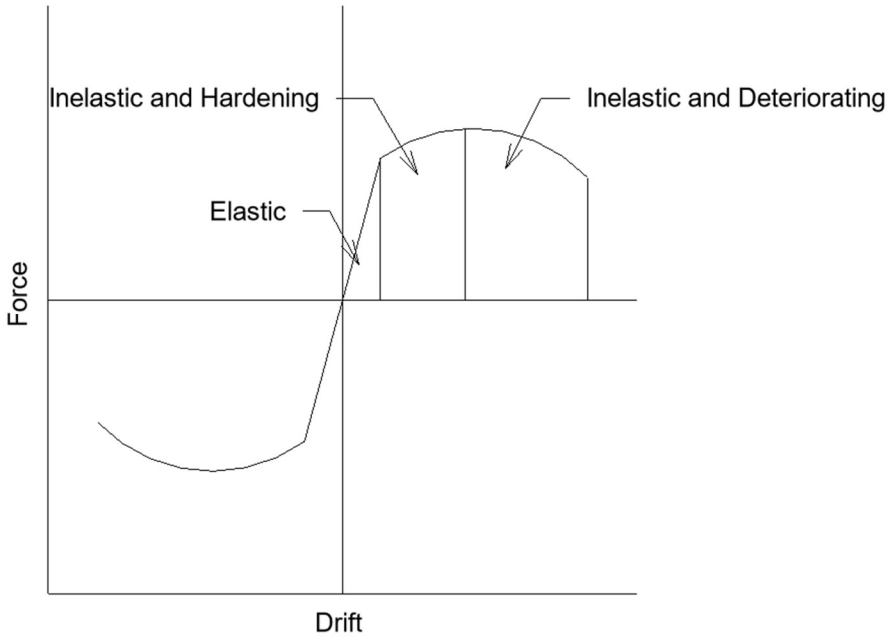

Figure 5.6. Stages of Hysteretic Behavior

The hysteretic response of the specimens can be categorized into three different stages of behavior shown in Figure 5.6. Figures 5.7 and 5.8 show the measured hysteretic response and the hysteretic response with $P - \Delta$ effects retained and removed, respectively.

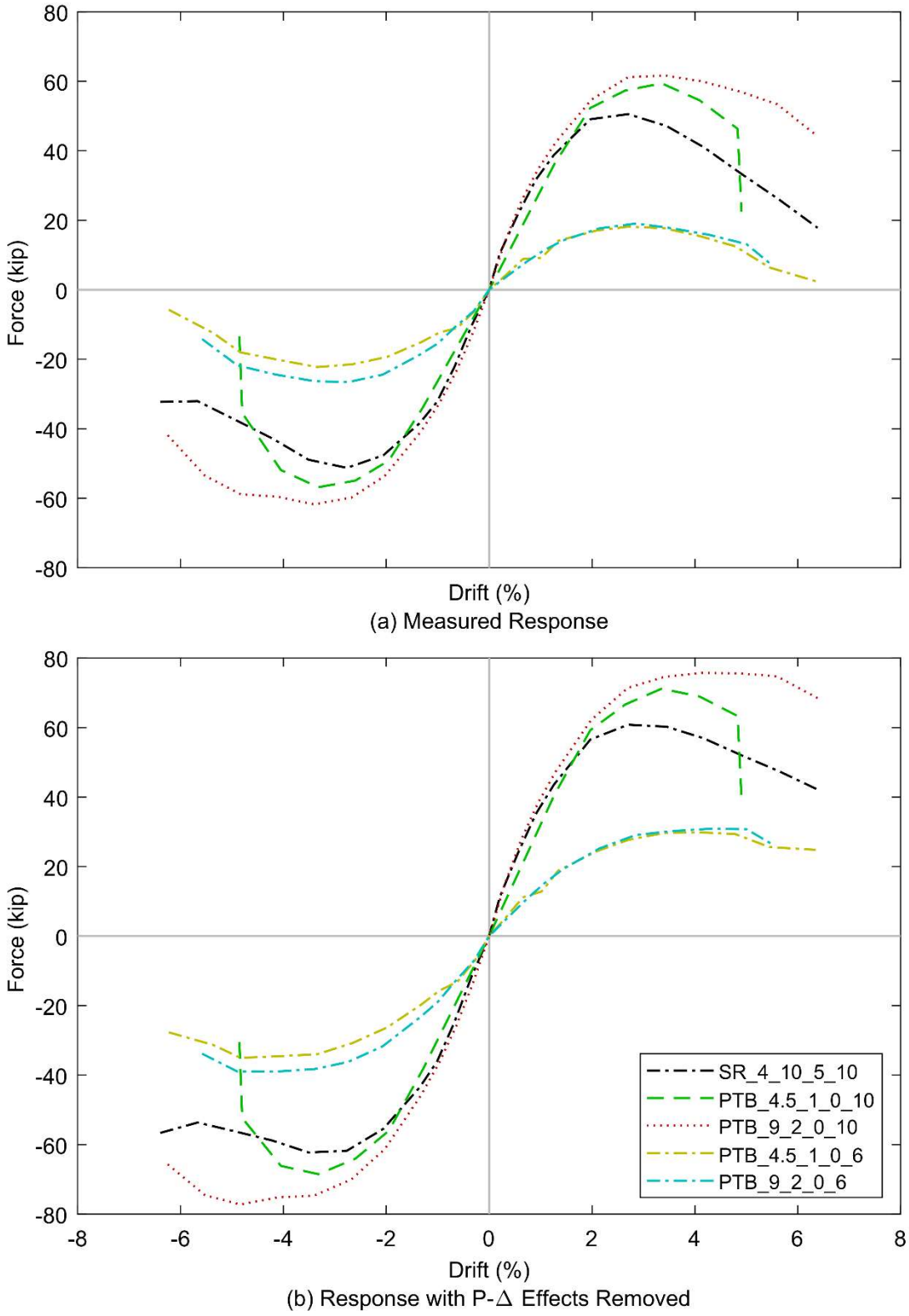

Figure 5.7. Hysteretic Envelopes

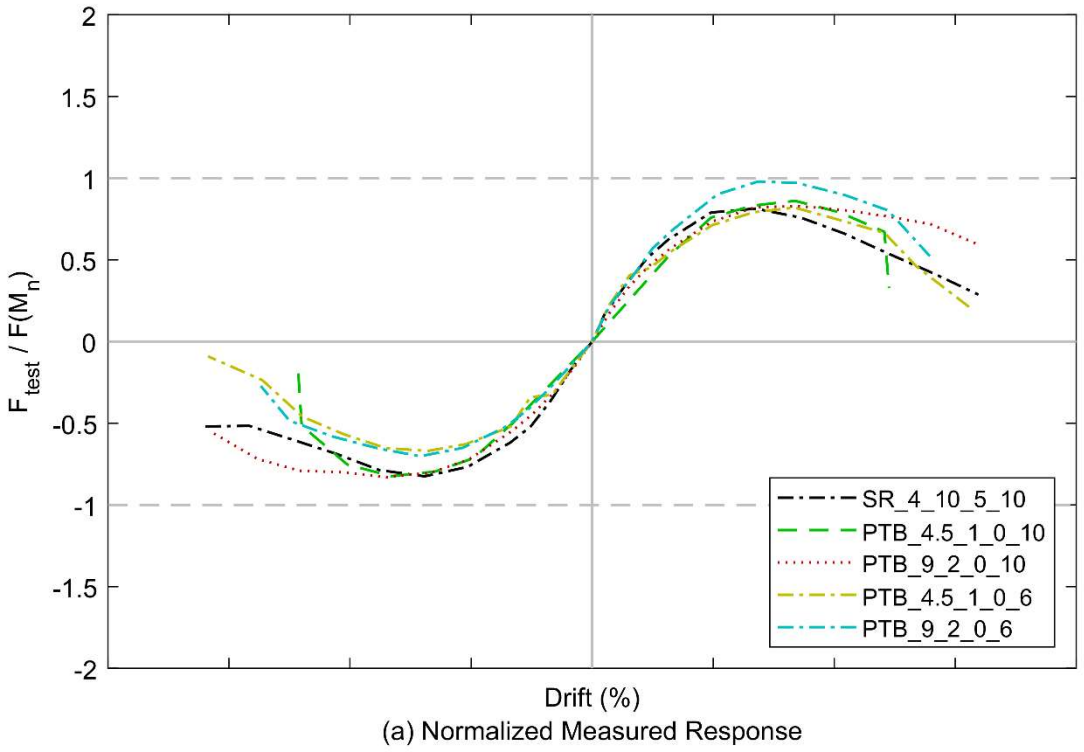

(a) Normalized Measured Response

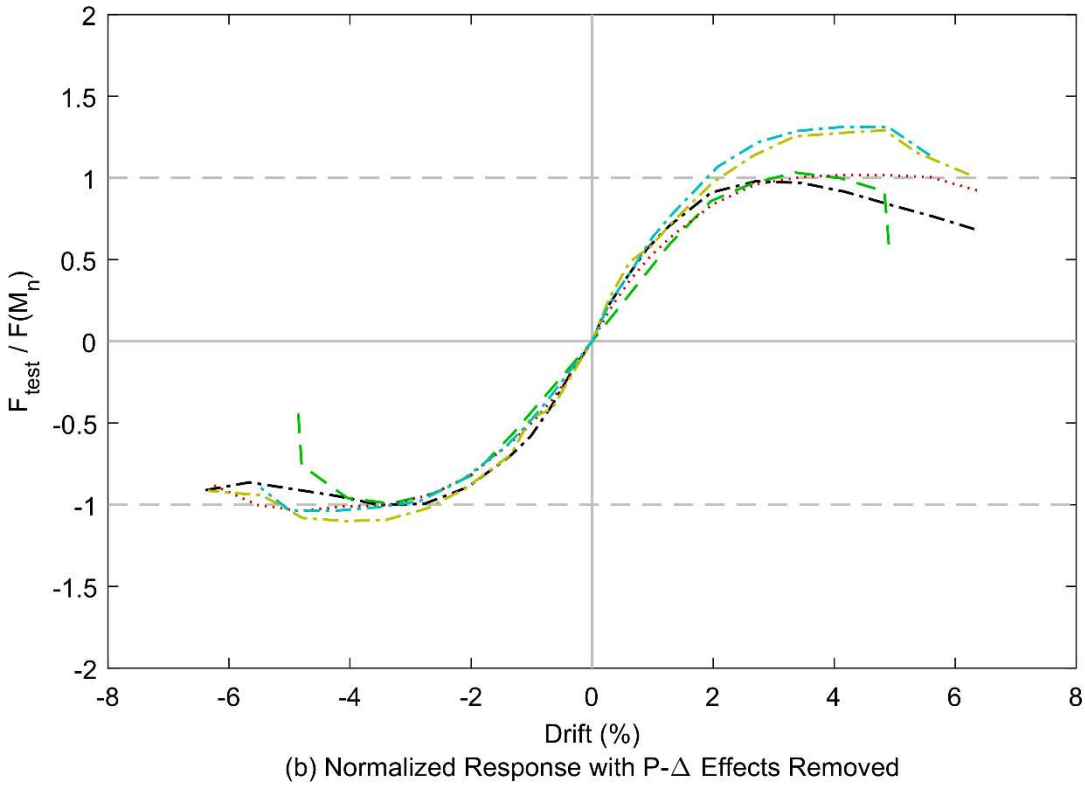

(b) Normalized Response with P-Δ Effects Removed

Figure 5.8. Normalized Hysteretic Envelopes

Figure 5.7 shows that PTB_4.5_1_0_10 and PTB_9_2_0_10 had higher peak loadings than SR_4_10_5_10 and the new connection specimens reached their peak strength at a higher drift. As expected the lateral forces are higher than the 6 in. slab specimens. In Figure 5.8 when the normalized responses are compared the normalized strength is near 1 for all of the specimens since they had flexural responses. After $P-\Delta$ effects are accounted for, most of the new connections are shown to plateau at their peak strength while the reference specimen and PTB_4.5_1_0_10 begin to loss strength after the peak force is reached. All of the specimens with plateauing strength have a ring flange width that is equal to or greater than the effective depth of the slab.

5.1.3 *Peak and Ultimate Resistance and Drift Values*

The initial yield and peak strengths are shown in Table 5.1. The values are provided with the $P-\Delta$ effects removed. The values are normalized by the normalized by the nominal ACI moment calculated using the full width of the slab.

Table 5.1 shows that ACI does well with predicting the peak strengths of the specimen, although there is some under prediction of the strength for the 6 in. slab specimens. Although looking at Figure 5.8 shows that this under prediction is not evident in the negative direction. The initial yield shows that PTB_9_2_0_6 delayed initial yield to a higher percentage of its peak strength than PTB_4.5_1_0_6.

Table 5.1. Key Strengths with $P-\Delta$ Effects Removed (Normalized by $F(M_n)$)

Specimen	Initial Yield Strength		Peak Strength	
	kip	F/F(M_n)	kip	F/F(M_n)
SR_4_10_5_10	56.5	0.91	62.3	1.00
PTB_4.5_1_0_10	59.2	0.86	71.2	1.03
PTB_9_2_0_10	62.2	0.84	77.2	1.04
PTB_4.5_1_0_6	26.3	0.97	35.0	1.29
PTB_9_2_0_6	36.2	1.22	39.0	1.31

The drift at which the peak force is reached and the drift at 10% loss of peak strength are given in Table 5.2. The values provided are based off strengths after $P-\Delta$ effects are removed.

The table shows that the stud rail specimen reaches peak strength at a lower drift than the specimens with the new connection other than PTB_9_2_0_6. The 10% loss of peak strength is given to show when the specimens strength starts to deteriorate significantly. For post-tensioned bolt connections with a ring flange equal to or greater than the effective depth we see than this occurs at a higher drift level than the stud rail specimen. This is expected following the behavior shown in the backbone comparison curves.

Table 5.2. Peak and 10% Loss of Peak Measured Drifts

Specimen	Drift (%)					
	Peak			10% Loss of Peak		
	Positive	Negative	Range	Positive	Negative	Range
SR_4_10_5_10	2.70	-2.77	5.47	4.50	-4.99	9.49
PTB_4.5_1_0_10	3.36	-3.32	6.68	4.73	-4.29	9.02
PTB_9_2_0_10	3.42	-3.40	6.82	6.39*	-5.94	11.89
PTB_4.5_1_0_6	2.72	-3.42	6.14	5.23	-5.33	10.56
PTB_9_2_0_6	2.84	-2.74	5.58	5.35	-5.41	10.76

5.1.4 *Energy Dissipation*

The energy dissipation of the specimens is compared in Figures 5.9 and 5.10. The energy dissipation was calculated by integrating the area under the hysteretic curve. In Figure 5.9 the energy dissipation is a sum of the integrated cycles of only the first cycle of each drift level. Figure 5.10 shows the total energy dissipation during the test.

From the figures PTB_9_2_0_10 dissipates the most energy. PTB_4.5_1_0_10 and SR_4_10_5_10 dissipate similar amounts of energy the same displacements, although testing was stopped for PTB_4.5_1_0_10 with a smaller amount of energy dissipated than SR_4_10_5_10. The 6 in. specimens do not reflect the difference in amount of energy dissipated for different ring sizes as seen in the 10 in. specimens. This shows that a ring that is twice the size of the effective depth found in PTB_9_2_0_6 does not offer a benefit in dissipating more energy. However, there is a disadvantage in energy dissipation for using a ring less than the effective depth like the 4.5 in. ring in PTB_4.5_1_0_10.

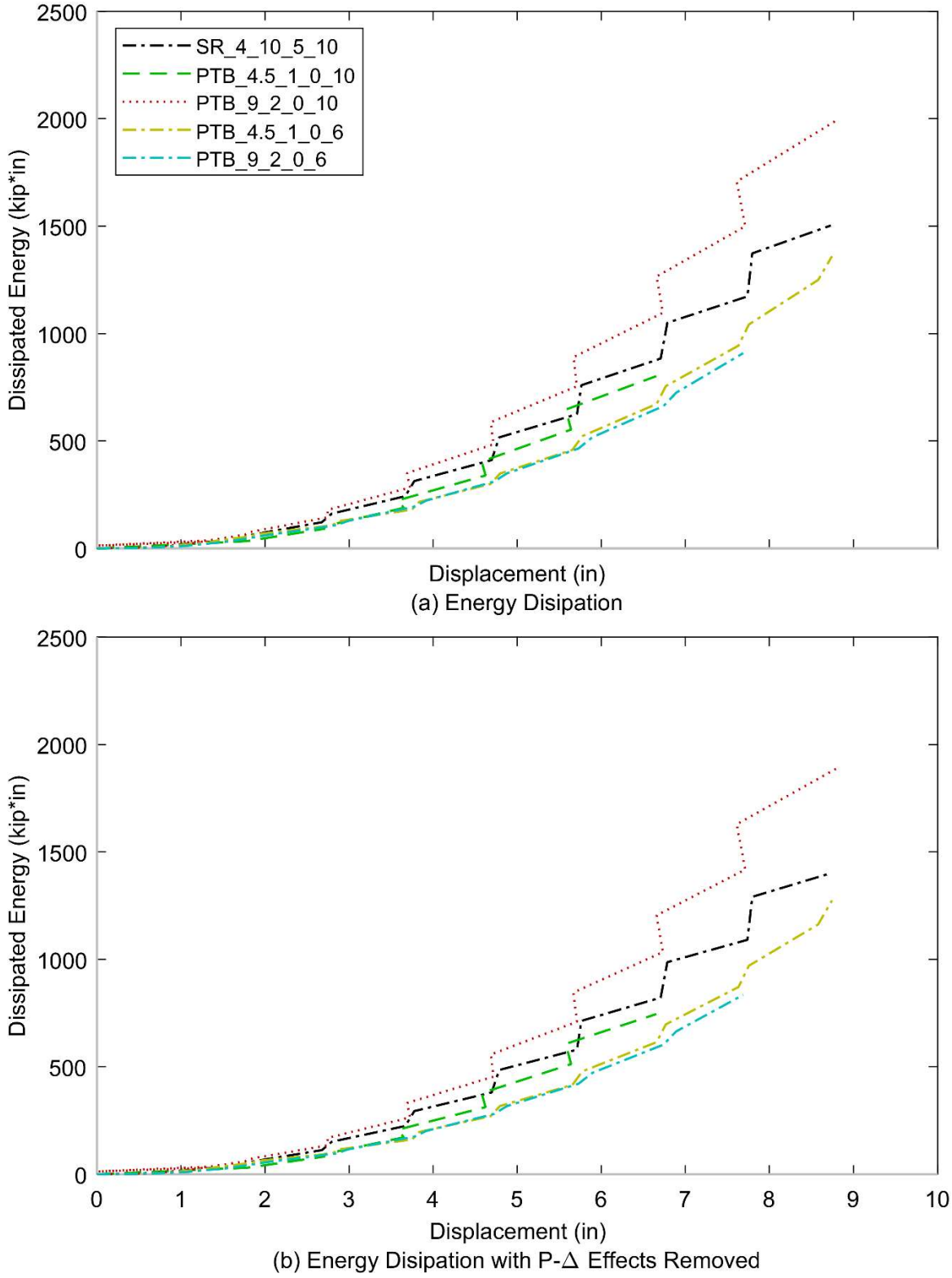

Figure 5.9. Single Cycle Energy Dissipation vs. Displacement

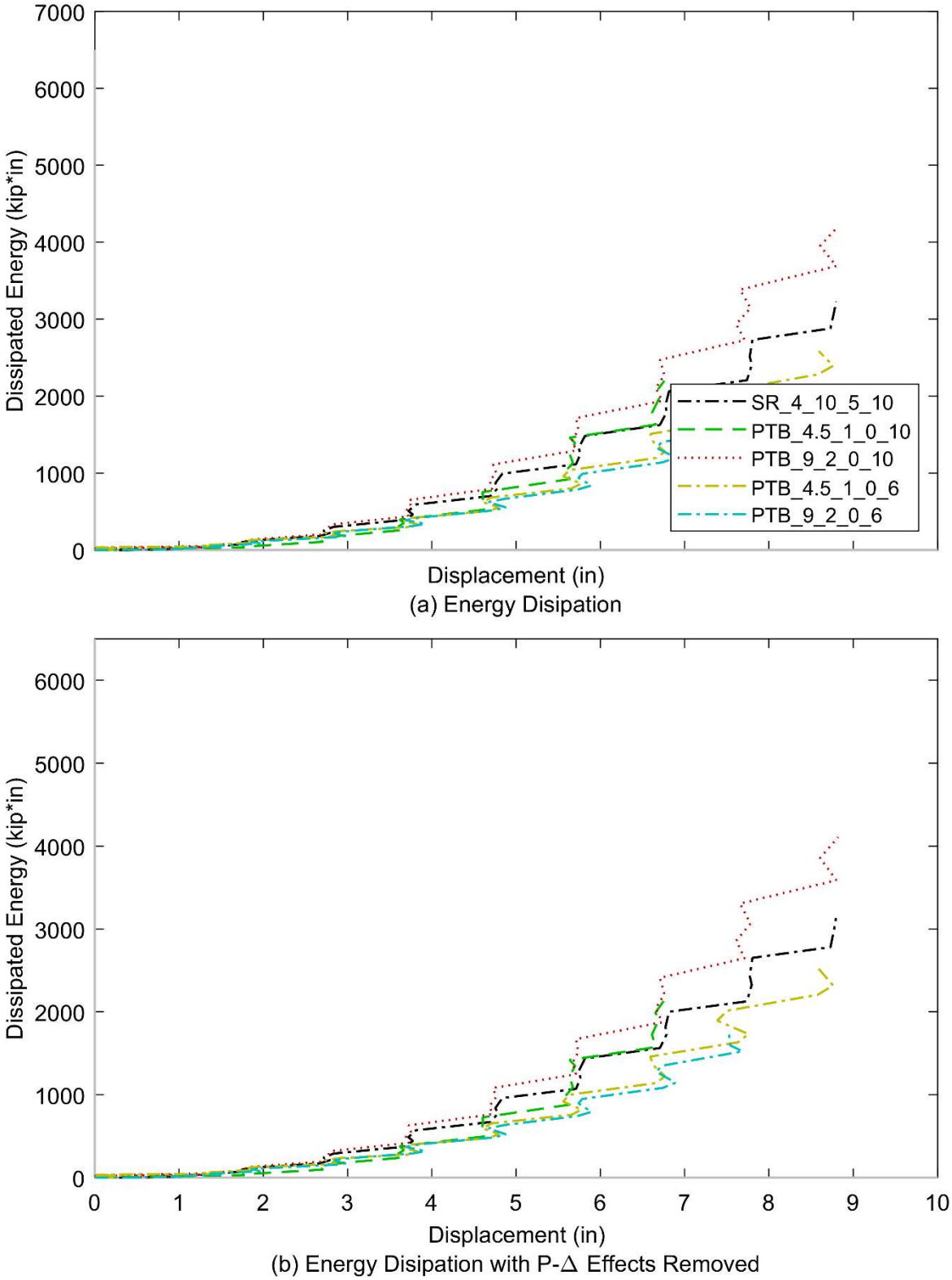

Figure 5.10. Total Energy Dissipation vs. Displacement

5.2 LOCAL BEHAVIOR

This section provides information about the local displacements and reinforcement strains in the specimens. The displacements of the slabs are used to visualize the inelastic behavior of the test specimens. Strain visualization provides insight into where the concentration of strain is in each of the reinforcing bars of each specimen during testing. For plotting of the displacements and strains a coordinate system with the column centerline at zero is used. Negative values along the x-axis indicate locations to the north of the column centerline, positive values indicate locations to the south of the column centerline. To summarize the behavior of the specimens throughout the tests, plots are provided at the drifts associated with peak force and initiation of strength loss.

5.2.1 *Slab Displacements*

This sections describes the maximum slab displacements and their locations for the first cycle at each drift level. It also provides displaced shapes at the target drifts discussed previously.

Slab vertical displacements were measured using string potentiometers attached to the underside of the slab and anchored to the reaction block of the testing frame at the locations shown in Figure 5.11. Figure 5.12 shows the measured response of Specimen SR_4_10_5_10 at low drift cycles. Due to both slop and deformation of the slab end roller supports the ends of the slab are not at zero. The deformations were recorded and removed. The displaced shapes are presented with the top subplot in the figure occurring during the south peak (positive) and the bottom subplot occurring during the north peak (negative). The following discussion refers to the corrected slab displacements. The measured responses can be found in Appendix D. The displacements were used to determine rotations along the specimens as well, the rotation plots can be found in Appendix E.

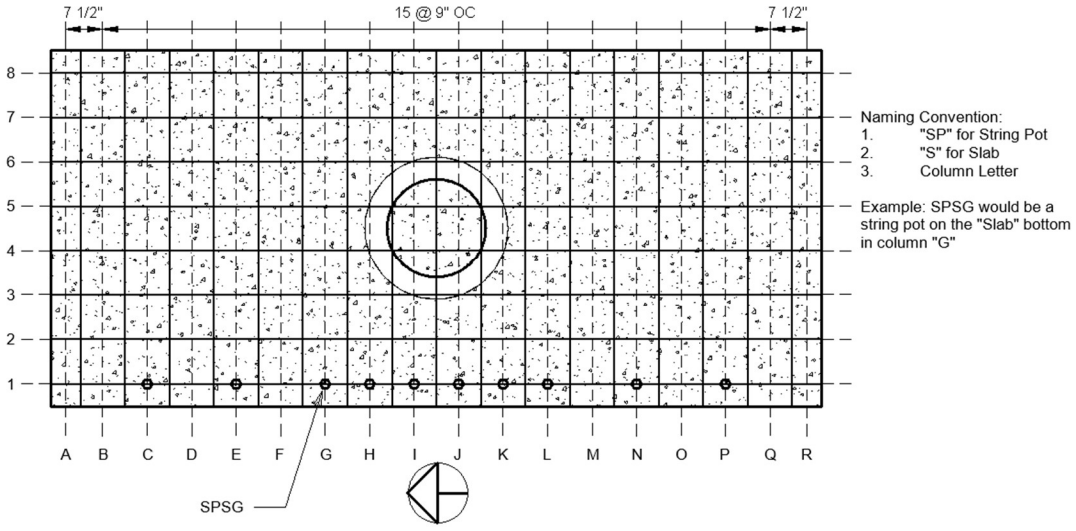

Figure 5.11. Location of Vertical Potentiometers on Slab (Indicated with Circles)

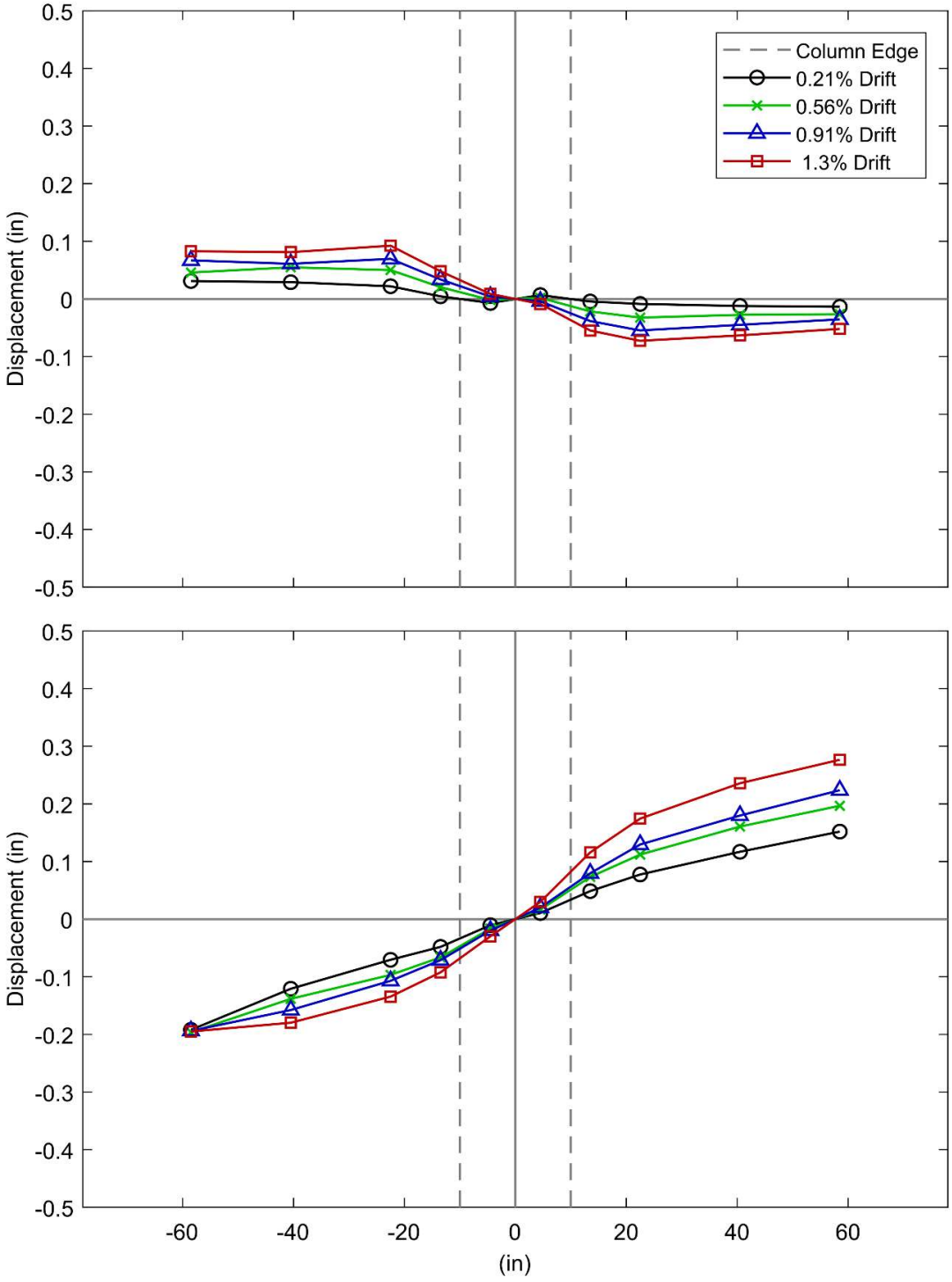

Figure 5.12. Low Drift Cycles Measured Slab Displaced Shape (SR_4_10_5_10)

Table 1.3 shows the maximum slab displacement during the first cycle at each target drift and the location at which the maximum displacement occurred. Negative values refer to a location

north of the centerline of the column, positive values are south of the specimen. Values marked with an asterisk are questionable due to damage of the concrete possibly dislodging the string pots.

Table 5.3. Maximum Corrected Displacement by Target Drift Cycle

Specimen			SR_4_10_5_10	PTB_4.5_1_0_10	PTB_9_2_0_10	PTB_4.5_1_0_6	PTB_9_2_0_6
Target Drift (%)	0.36	Disp. (in.)	-0.031	-	0.027	0.099	0.059
		Loc. (in.)	-58.5	-	-58.5	-58.5	58.5
	0.73	Disp. (in.)	0.045	-	0.077	0.116	0.127
		Loc. (in.)	22.5	-	-13.5	-58.5	58.5
	1.1	Disp. (in.)	0.062	-	0.095	0.137	0.142
		Loc. (in.)	-22.5	-	40.5	-40.5	40.5
	1.5	Disp. (in.)	0.098	0.125	0.120	0.211	0.185
		Loc. (in.)	40.5	40.5	40.5	58.5	40.5
	2.2	Disp. (in.)	0.131	0.150	0.140	0.228	0.220
		Loc. (in.)	-22.5	22.5	22.5	22.5	22.5
	2.9	Disp. (in.)	0.171	0.200	0.220	0.286	-0.292
		Loc. (in.)	-22.5	22.5	22.5	-22.5	22.5
	3.6	Disp. (in.)	0.203	0.259	0.313	0.353	0.368
		Loc. (in.)	-22.5	22.5	22.5	-22.5	22.5
	4.4	Disp. (in.)	0.221	0.361	0.367	0.413	0.447
		Loc. (in.)	-22.5	-22.5	22.5	-22.5	22.5
	5.1	Disp. (in.)	0.246	0.781	2.777*	0.538	0.550
		Loc. (in.)	-22.5	22.5	4.5	-22.5	22.5
	5.8	Disp. (in.)	0.280	1.108	2.728*	0.615	0.924
		Loc. (in.)	-22.5	-22.5	22.5	-22.5	22.5
	6.5	Disp. (in.)	0.314	-	4.353*	0.575	-
		Loc. (in.)	-22.5	-	4.5	-22.5	-
	6.9	Disp. (in.)	-	-	-	-	-
		Loc. (in.)	-	-	-	-	-

Figure 5.13 shows that PTB_4.5_1_0_6 stands out. The displacements to the south of the column centerline look incorrect during the south column displacement. During the north column displacement the displacements for PTB_4.5_1_0_6 look more like the displacements that would be expected and the magnitude is similar to PTB_9_2_0_6. Both string potentiometers near the slab end roller supports read positive for both directions of column displacement. Due to this the

displaced shape of PTB_4.5_1_0_6 does not contribute to the discussion. PTB_9_2_0_6 shows higher slab displacements than the 10 in. specimens as expected due to the more flexible slab.

Figure 5.14 shows the slab displacements at drift corresponding to loss of strength of the specimens. PTB_9_2__0_10 did not begin to lose strength until 5.8% at which point there was extensive spalling damage near the string pots causing higher displacements than the slab actually experienced. Figure 5.15 shows displacements at the same drift level but with PTB_9_2_0_10 removed. As expected the thin slab specimen shows higher displacements than the stiffer 10 in. slabs. This displacement peaks at 22.5 in. north or south of the centerline of the column which would be outside the diameter of the column and 9 in. ring flange; however, there is no correlation between peak displacement location and ring size.

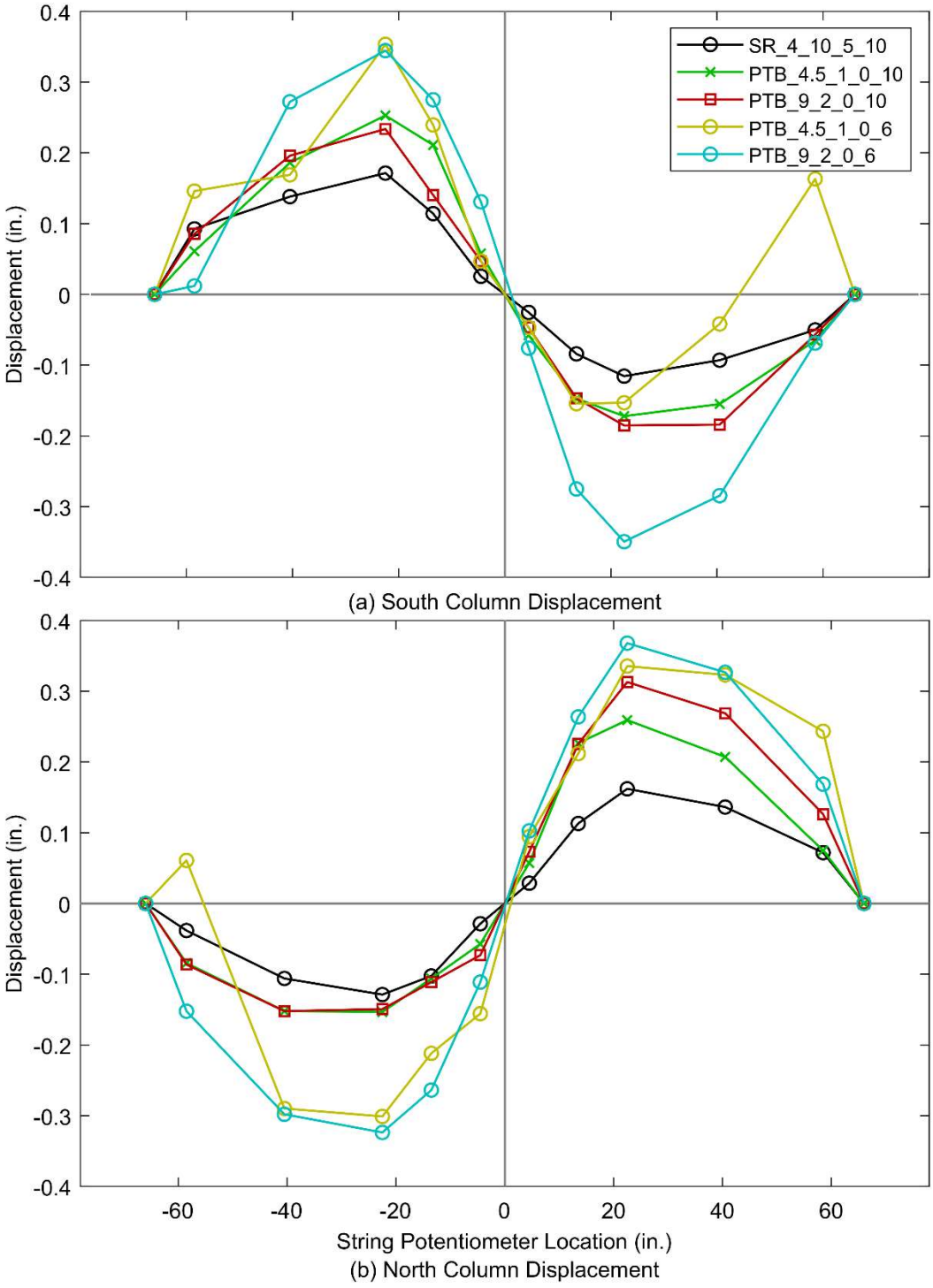

Figure 5.13. Corrected Slab Displaced Shape at Drift Corresponding to Peak Force

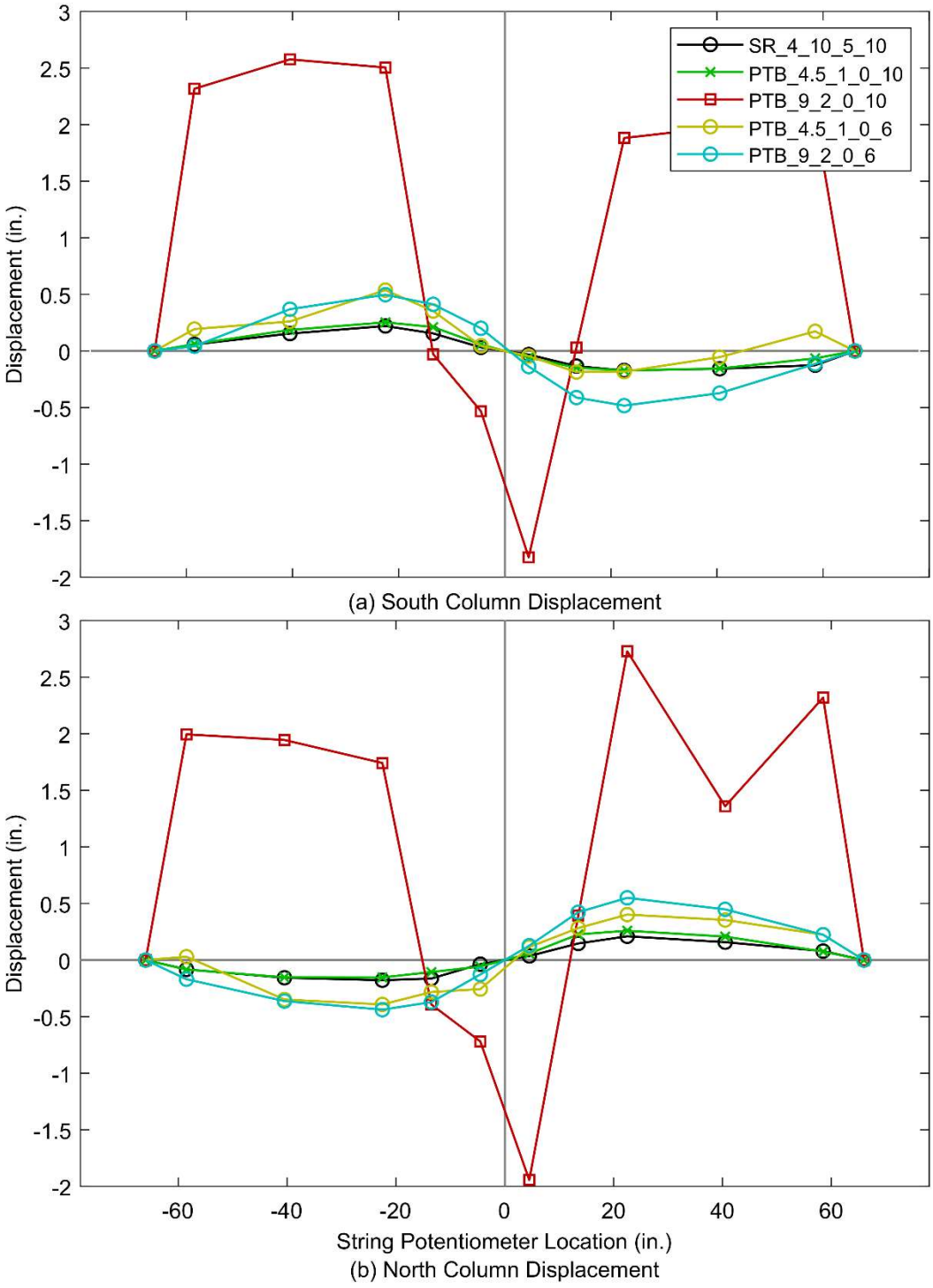

Figure 5.14. Corrected Slab Displaced Shape at Drift Corresponding to Loss of Strength

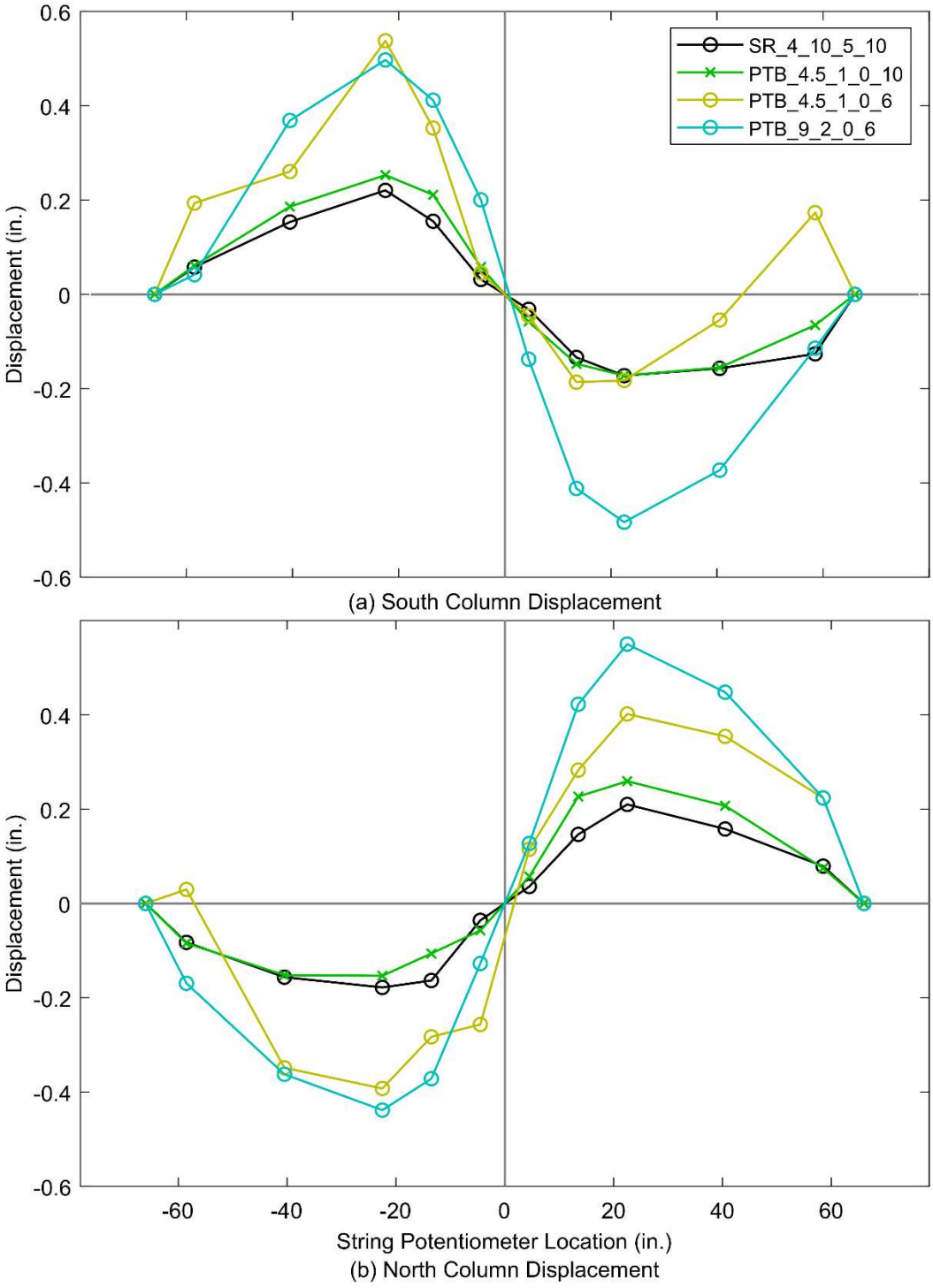

Figure 5.15. Corrected Slab Displaced Shape at Drift Corresponding to Strength Loss with PTB_9_2_0_10 removed

5.2.2 *Reinforcement Strain Profile*

This section provides the strain distribution along the length of the slab for the bottom reinforcing bars, which tended to have higher strains. The maximum strains measured during the first cycle of each target drift are used for this discussion. Tabulated values are given for the peak strain and the bar on which the strain occurred.

Figure 5.16 shows the strain gauge layout for the specimens. The naming convention is explained in the figure as well as section 3.5.4.

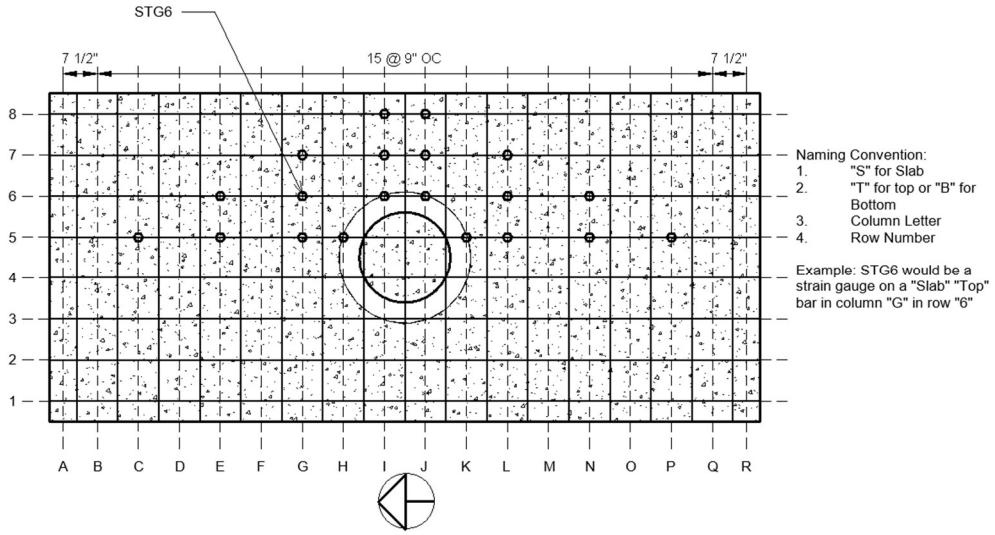

Figure 5.16. Location of Strain Gauges (Indicated with Circles)

The peak strains from the first cycle at each target drift level are given in Table 5.4. Asterisks are used for strains that read the maximum for that drift cycle, but are most likely a result of a gauge that has previously broken.

Table 5.4. Maximum Corrected Displacement by Target Drift Cycle

Specimen			SR_4_10_5_10	PTB_4.5_1_0_10	PTB_9_2_0_10	PTB_4.5_1_0_6	PTB_9_2_0_6
Target Drift (%)	0.36	Strain (10^{-3})	0.38	-	0.30	0.86	0.71
		Loc.	SBK5	-	SBG5	SBK5	SBL5
	0.73	Strain (10^{-3})	1.36	-	1.25	1.49	1.27
		Loc.	SBK5	-	SBH5	SBK5	SBH5
	1.1	Strain (10^{-3})	0.203	-	1.94	2.01	1.71
		Loc.	SBK5	-	SBH5	SBK5	SBH5
	1.5	Strain (10^{-3})	2.58	2.06	2.52	2.43	2.16
		Loc.	SBK5	SBG5	SBH5	SBK5	SBL5
	2.2	Strain (10^{-3})	4.68	10.36	8.30	13.13	3.14
		Loc.	SBH5	SBG5	SBK5	SBK5	SBL5
	2.9	Strain (10^{-3})	11.19	72.66	13.75	15.29	4.35
		Loc.	SBK5	SBG5	SBK5	SBK5	SBL5
	3.6	Strain (10^{-3})	13.39	72.66*	61.90	18.23	10.28
		Loc.	SBK5	SBG5	SBJ6	SBK5	SBH5
	4.4	Strain (10^{-3})	15.22	72.66*	64.49	21.44	63.11
		Loc.	SBK5	SBG5	SBI7	SBK5	SBJ7
	5.1	Strain (10^{-3})	14.75	72.66*	64.49*	62.56	63.11*
		Loc.	SBK5	SBG5	SBI7	SBJ6	SBJ7
	5.8	Strain (10^{-3})	13.56	-	64.49*	62.56*	65.51
		Loc.	SBG5	-	SBI7	SBJ6	SBI8
	6.5	Strain (10^{-3})	12.61	-	64.49*	62.56*	-
		Loc.	SBG5	-	SBI7	SBJ6	-
	6.9	Strain (10^{-3})	-	-	-	-	-
		Loc.	-	-	-	-	-

The strain distribution of the bottom reinforcing bars, which tended to have higher strains, are given in Figures 5.17 to 5.21 for drifts corresponding to peak strength. Figures 5.22 to 5.26 provide the strain distributions for the bottom reinforcing bars at initiation of loss of strength. Plots of individual gauges vs. drift are found in Appendix F.

The figures show that at peak strength the 10 in. slabs cause yield strain measurements in the gauges across the full width of the slab. The 6 in. slabs only engage 2-3 bars east of the column centerline enough to measure yield strains. This behavior seems independent of ring size, but it

should be noted that the strain measurements in PTB_9_2_0_6 read higher along the 3rd bar from the column centerline than PTB_4.5_1_0_6 at peak strength.

For the plots at initiation of strength loss the most of the specimens still measure yield strains across the width of the slab except PTB_4.5_1_0_10. The 6 in. specimens measure yield through the 3 bars to the east of the column centerline, with higher strain measurements in the 3rd bar for PTB_9_2_0_10. This is reflected in the higher strength measurements in the hysteretic response of the thin slab specimen. It is also apparent that the 9 in. ring flange specimens measure higher strains in the gauges located approximately 40 in. north and south of the column centerline. The depth of the slab effects the distribution of strains through the slab, and to a lesser extent so does the ring width.

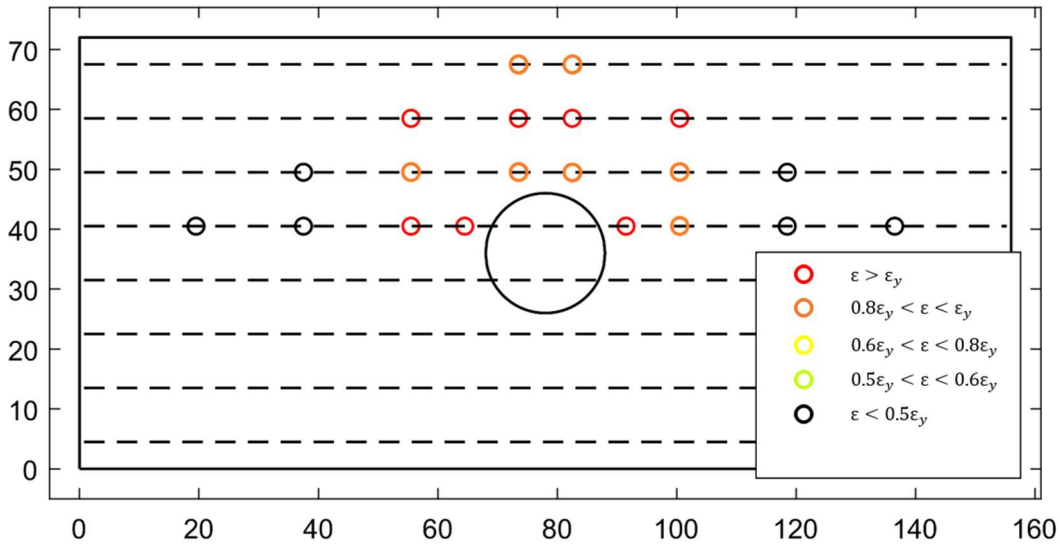

Figure 5.17. Strain Distribution at Drift Corresponding to Peak Strength (SR_4_10_5_10)

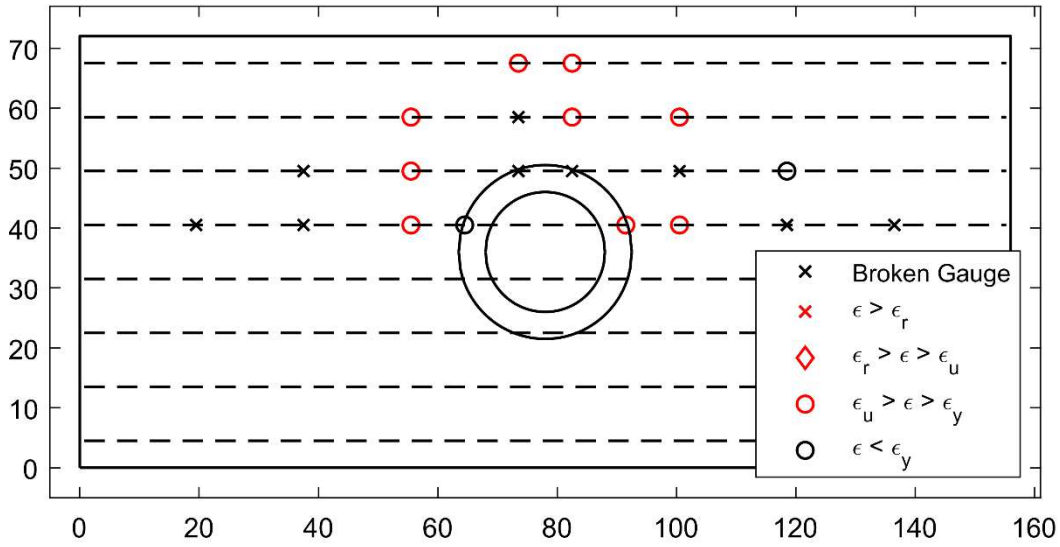

Figure 5.18. Strain Distribution at Drift Corresponding to Peak Strength (PTB_4.5_1_0_10)

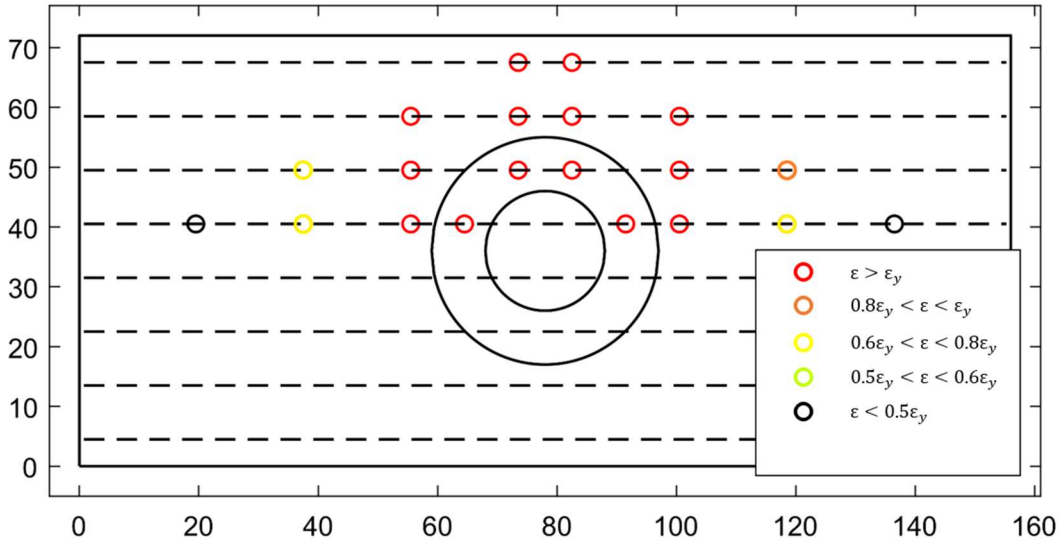

Figure 5.19. Strain Distribution at Drift Corresponding to Peak Strength (PTB_9_2_0_10)

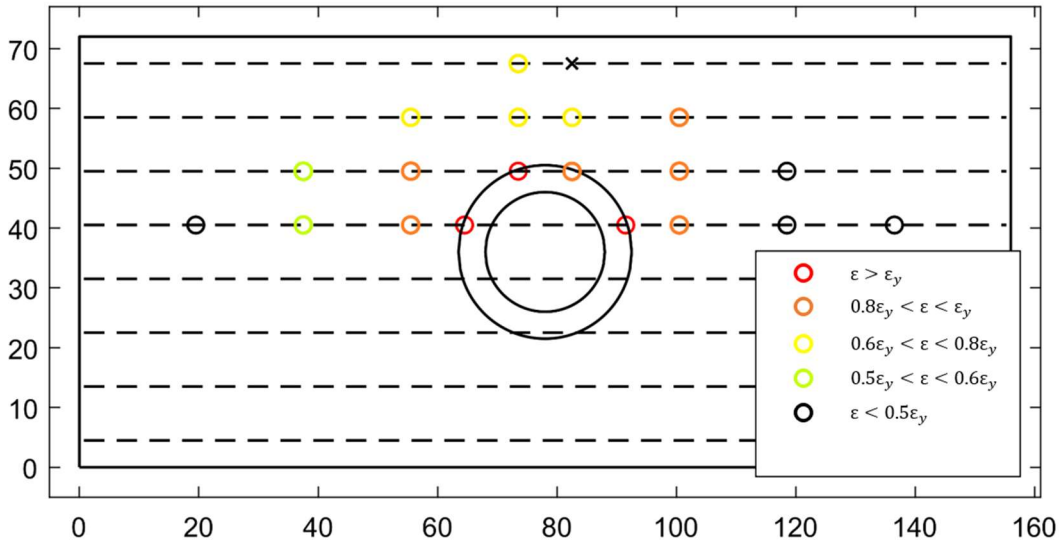

Figure 5.20. Strain Distribution at Drift Corresponding to Peak Strength (PTB_4.5_1_0_6)

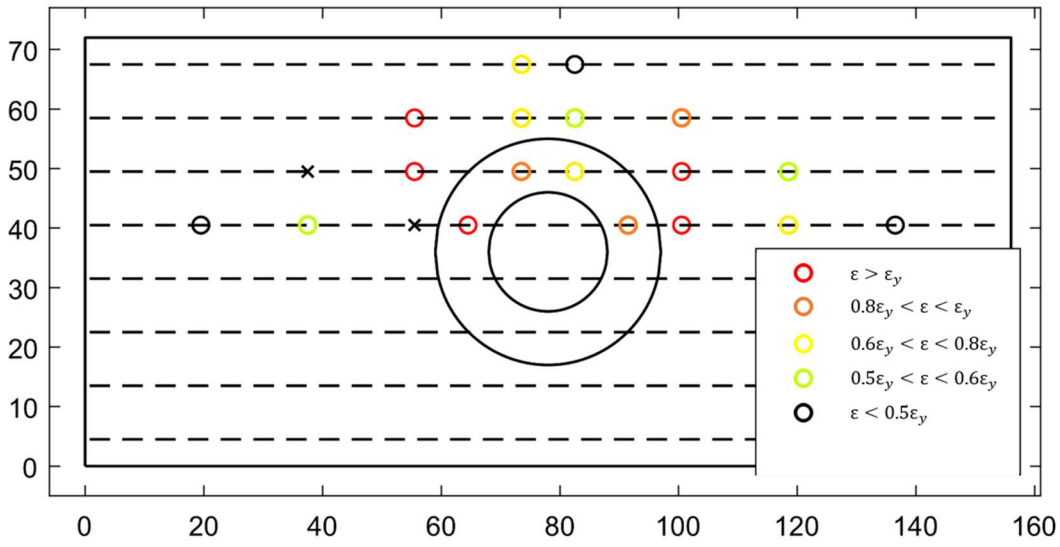

Figure 5.21. Strain Distribution at Drift Corresponding to Peak Strength (PTB_9_2_0_6)

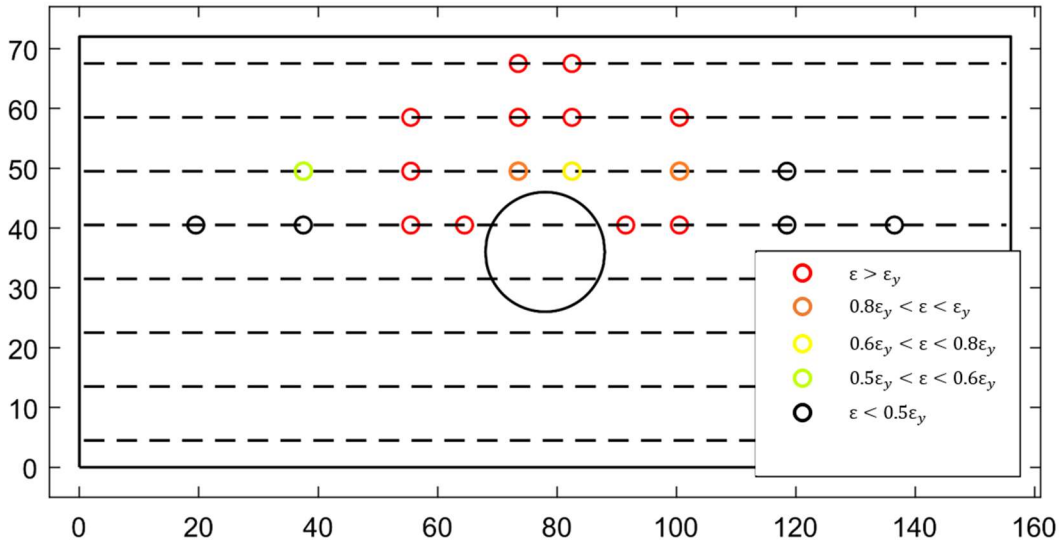

Figure 5.22. Strain Distribution at Drift Corresponding to Loss of Strength (SR_4_10_5_10)

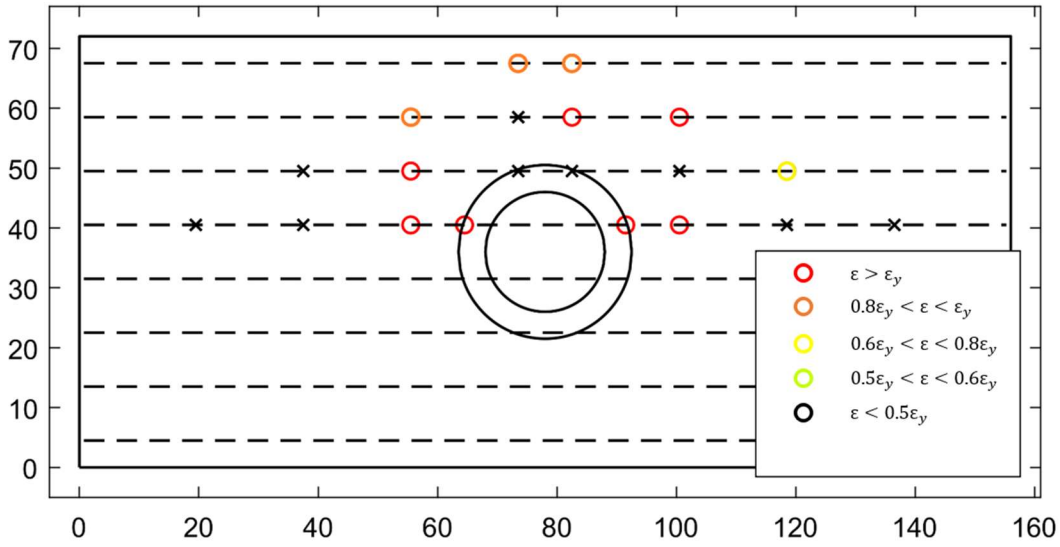

Figure 5.23. Strain Distribution at Drift Corresponding to Loss of Strength (PTB_4.5_1_0_10)

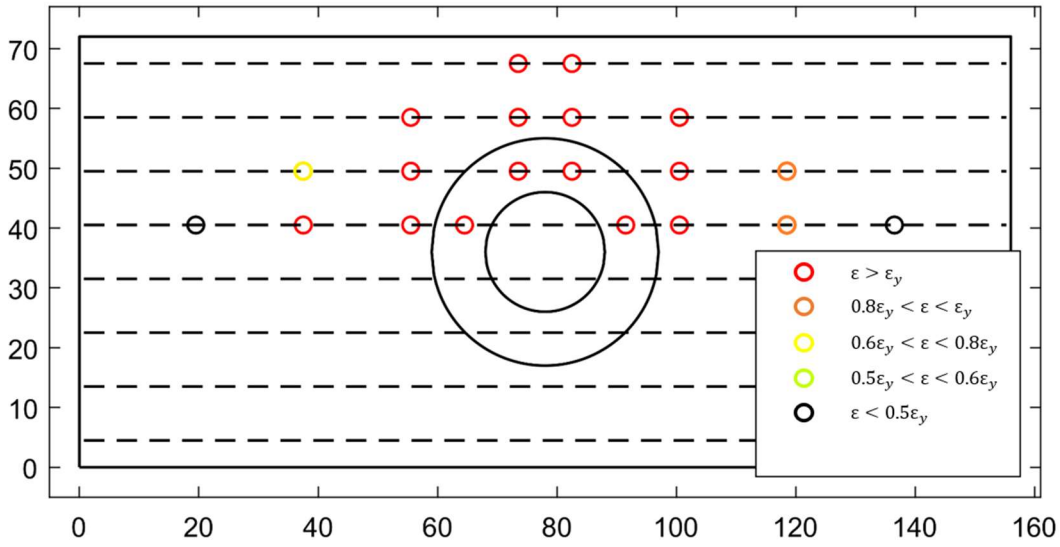

Figure 5.24. Strain Distribution at Drift Corresponding to Loss of Strength (PTB_9_2_0_10)

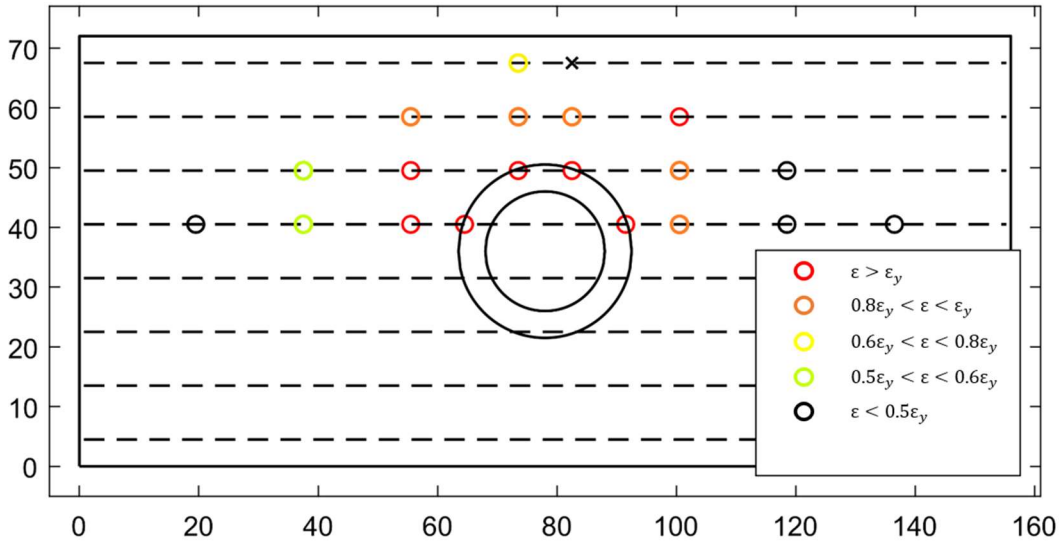

Figure 5.25. Strain Distribution at Drift Corresponding to Loss of Strength (PTB_4.5_1_0_6)

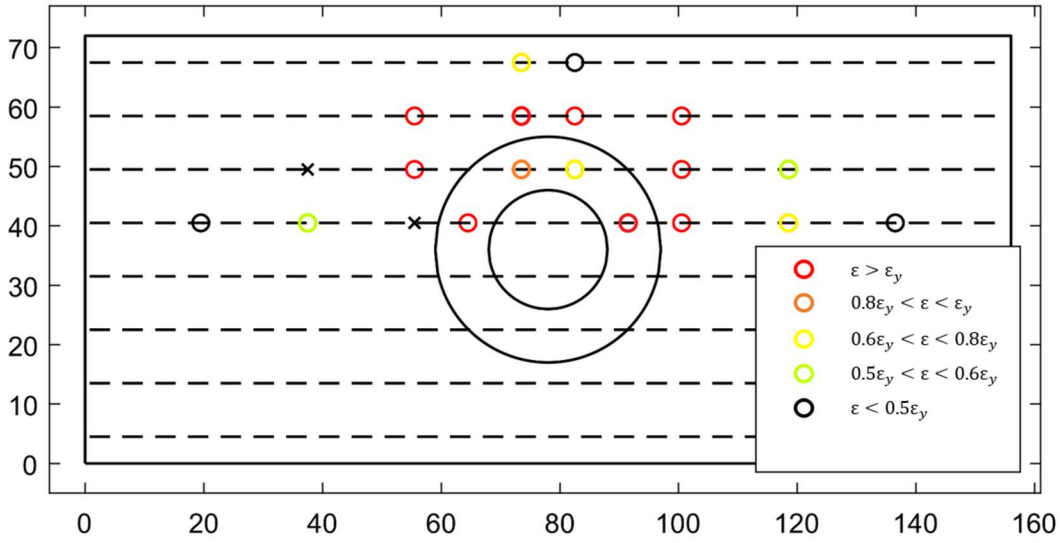

Figure 5.26. Strain Distribution at Drift Corresponding to Loss of Strength (PTB_9_2_0_6)

5.3 DAMAGE

This chapter provides the drift at which the specimens reach the damage states defined in Chapter 4. Figures 5.27 to 5.31 show the backbones of the specimens with points at which they reached specific damage states to relate the damage states to the response behavior. For damage states with 2 stages, the second stage is denoted by the shape being filled. The backbones show that the peak strength of SR_4_10_5_10 and PTB_4.5_1_0_10 occurred at the same time as the initial of spalling or Cracking Stage 2. PTB_4.5_1_0_10 spalled early due to previous tests that had to be restarted due to issues with the slab end supports. For specimens with a ring flange equal to or greater than the effective depth of the slab, there is a strength plateau. This plateau begins at the initiation of spalling in the slab and ends at approximately the initiation of crushing, although PTB_9_2_0_10 maintains strength for a drift level beyond crushing.

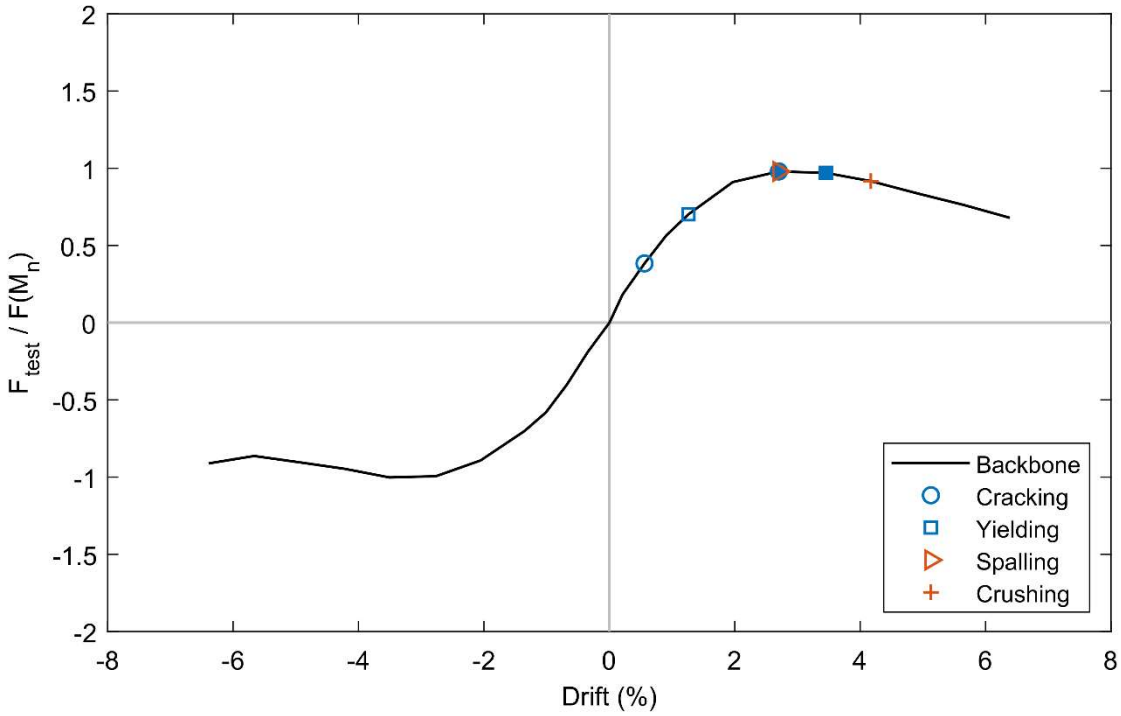

Figure 5.27. Backbone with Damage States (SR_4_10_5_10)

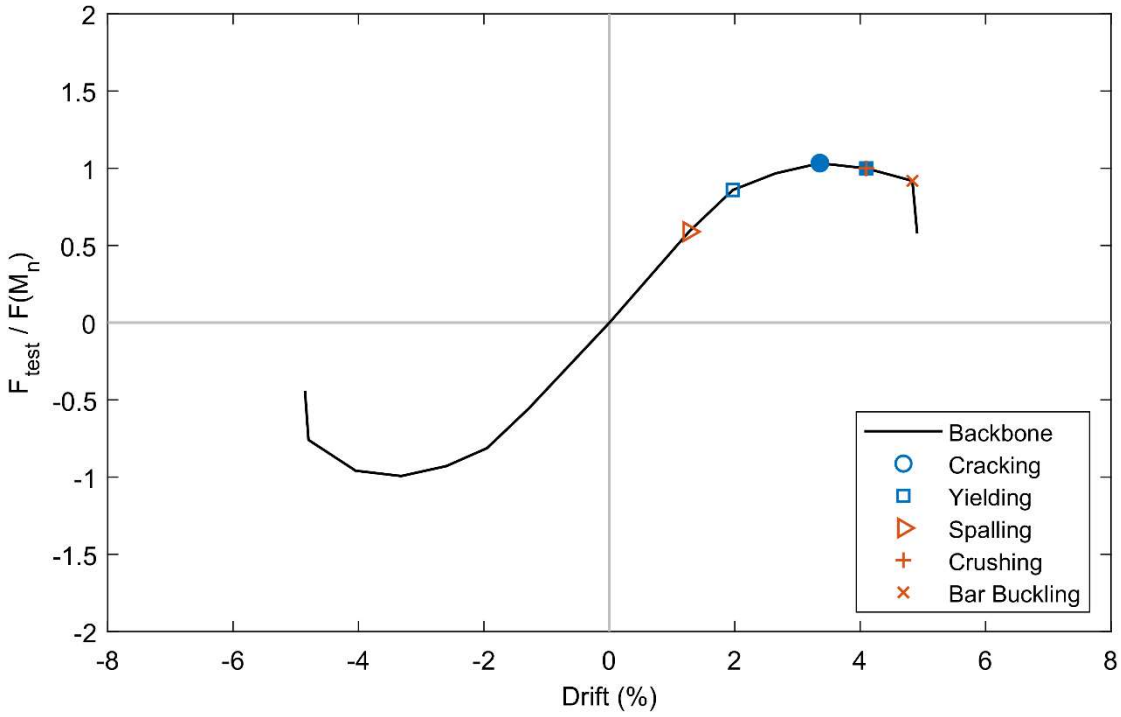

Figure 5.28. Backbone with Damage States (PTB_4.5_1_0_10)

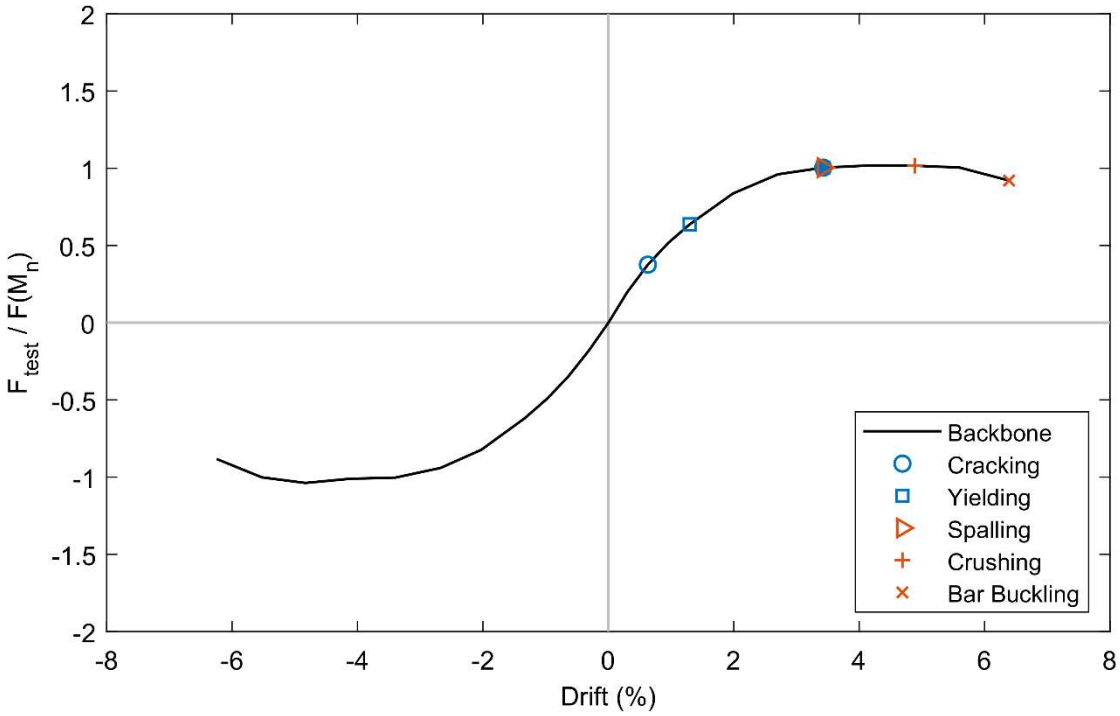

Figure 5.29. Backbone with Damage States (PTB_9_2_0_10)

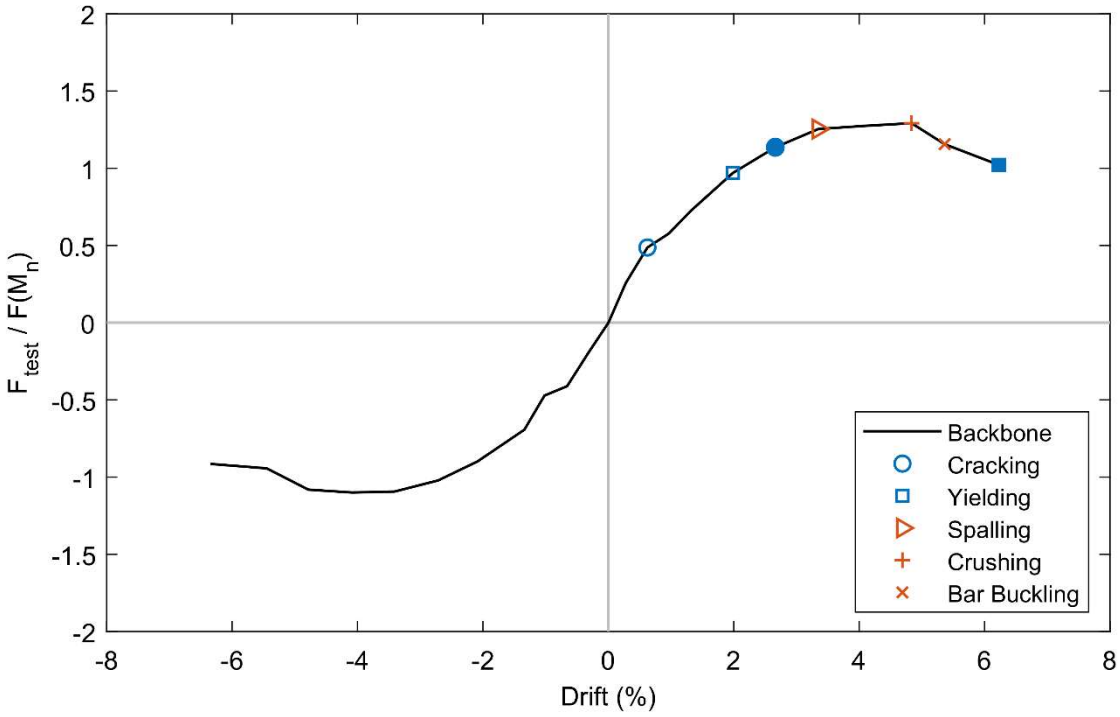

Figure 5.30. Backbone with Damage States (PTB_4.5_1_0_6)

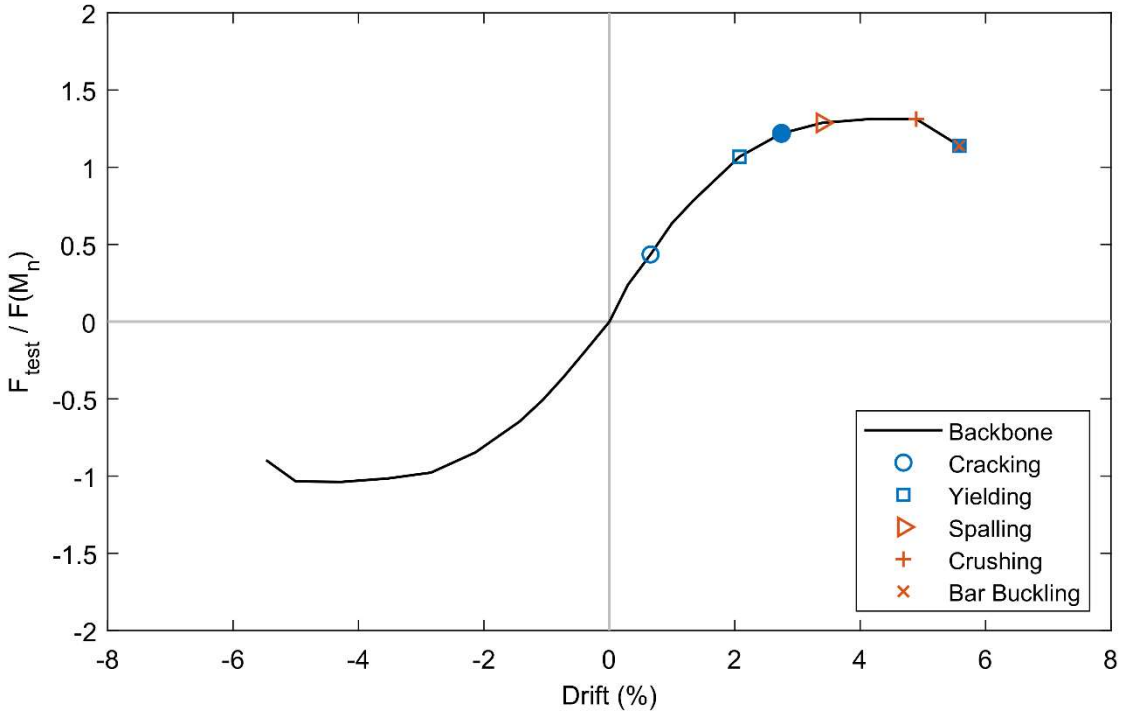

Figure 5.31. Backbone with Damage States (PTB_9_2_0_6)

Figures 5.32 and 5.33 show a comparison of the different damage states and at which drift levels they occurred for the different specimens. Figure 5.32 shows that Cracking Stage 1 occurred at the same drift for all the test specimens. Yielding Stage 1 and Cracking Stage 2 do not show a pattern for different ring widths to effective depth ratio, so those damage states are not dependent upon the ratio. The 9 in. ring specimens reach Yielding Stage 2 before the 4.5 in. ring specimens of the same slab depth, showing that the ring impacts the width of flexural reinforcement effected by the lateral loading. However, the 10 in. specimens reach Yielding Stage 2 at a much lower drift than the 6 in. specimens. Yielding Stage 2 does not occur in the 6 in. specimens until after the end of their strength plateaus. This shows that the depth of the slab is more a prominent factor in the width of slab engaged by lateral loading of the column than the ring flange width.

Figure 5.33 shows the other damage states. Recall from the backbone curves, the peak strength or beginning of a strength plateau occurred at the initiation of spalling and strength

plateaus ended at the initiation of crushing. Figure 5.33 shows that for specimens with a ring flange equal to or greater than the effective depth of the slab these key damage states occur at higher drifts.

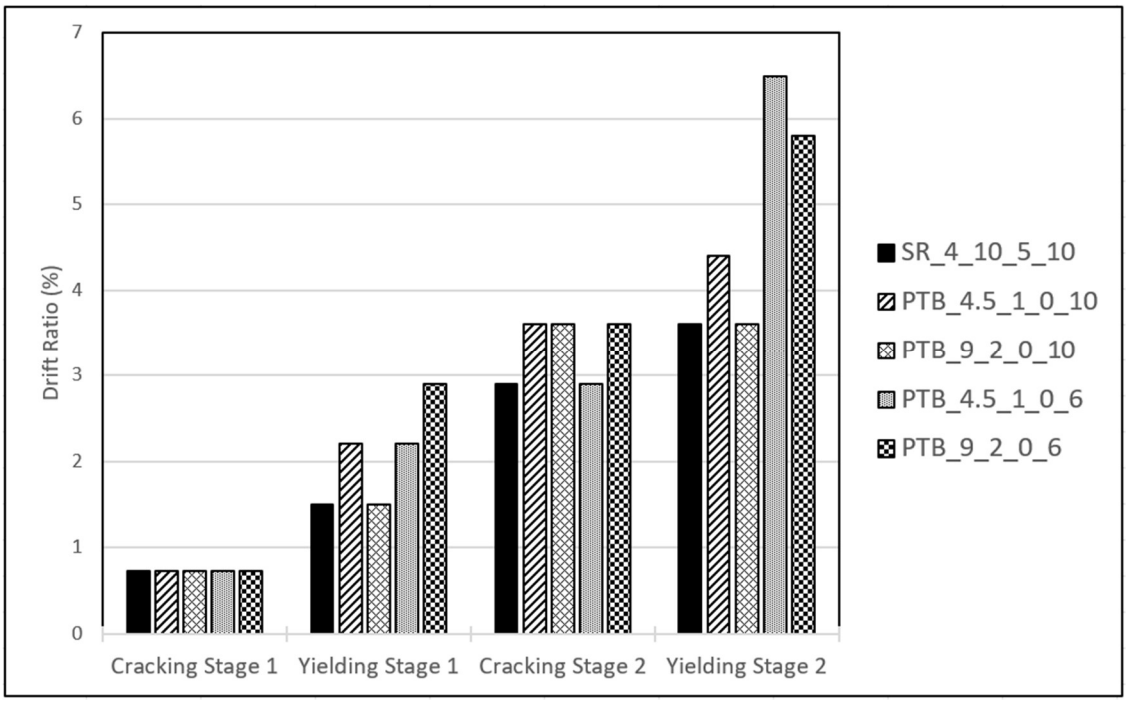

Figure 5.32. Damage Summary (1/2)

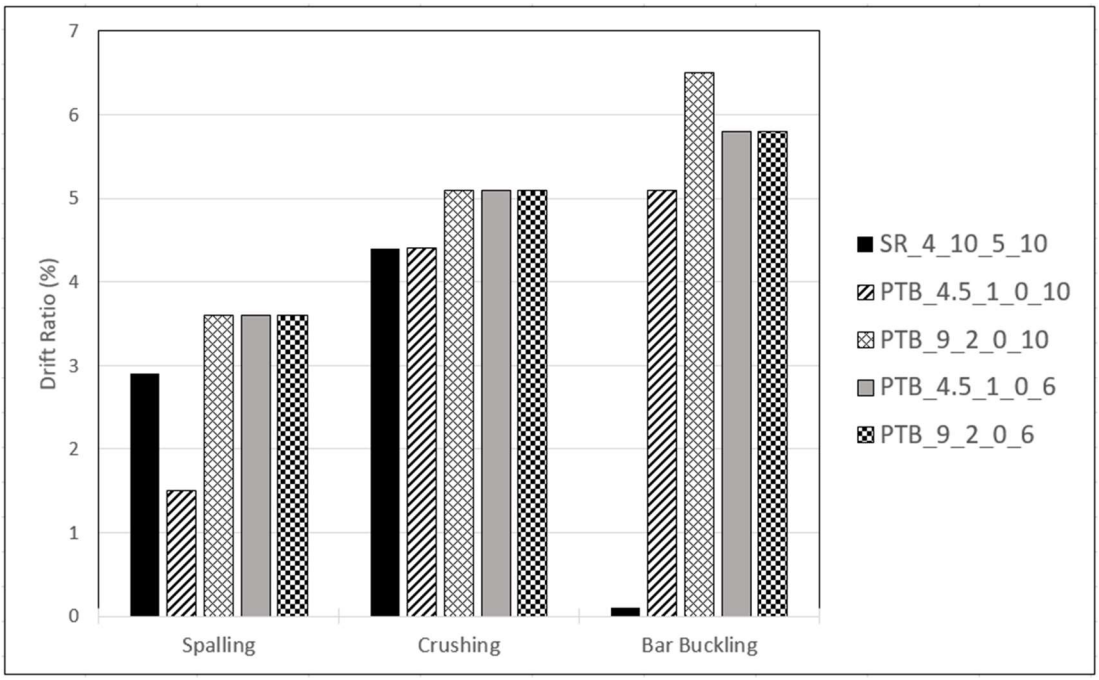

Figure 5.33. Damage Summary (2/2)

Chapter 6. EXPERIMENTAL OBSERVATIONS AND DATA ANALYSIS OF PUNCHING SPECIMENS

This chapter provides observations of the punching specimens during testing and investigates the behavior of the connection when subjected to punching. To separate the stages of testing, the observations will be discussed in three sections:

- Before Peak Loading: The specimen is experiencing an increasing applied load
- After Peak Loading: Test specimen has reached the peak load and begins to lose strength
- After Testing: The specimen has completed testing and the load has been removed

The observations will focus on the two typical failure types: (1) Failure due to punching shear, (2) Flexural failure due to plastic hinging.

Punching shear failure produces a conical crack begins to form when the shear stress along the shear plane is higher than the capacity that the concrete, along with other variables, can support. As the crack opens the specimen loses strength and depending on the amount of reinforcement in the slab the strength loss can be very sudden.

Failure due to flexure is characterized by yielding of the flexural reinforcement. The failure should be a more ductile response than that of punching shear. Due to the ductile behavior of flexural failure there should be various cracks to give warning of failure before loss of strength.

6.1 EXPERIMENTAL OBSERVATIONS OVERVIEW

This section will focus on the observations discussed previously. The sections will be broken into the three sections discussed early and each of those sections will be broken into 100 kip load steps to give insight into what was happening to the specimen during each of those load steps. During testing of the specimen the cracking on the bottom side of the slab was difficult to observe. Photos of the bottom side of the slab and north edge were taken at 10 second intervals, but the lighting and angles limited the quality of the photos. Therefore the discussion of cracking will be most prevalent in the after testing section. Force vs. Displacement curves along with the

status of the strain gauges will give the best indication of what is happening to the specimens during testing.

6.2 SPECIMEN PTB_4.5_1_0_P EXPERIMENTAL OBSERVATIONS

Specimen PTB_4.5_1_0_P had ring flange was 4.5 in. wide and 0.5 in. thick. The slab dimensions were 72 x 72 x 10 in. with a flexural reinforcement ratio of 1.79%.

The specimen was loaded initially at a load rate of 20 kips/min.. At 250 kips the Baldwin press was switched from load controlled to displacement controlled. This was done to prevent the Baldwin from trying to increase loading after the specimen began experiencing loss of strength. Under displacement control displacement the displacement increased at 0.03 in./min. Figure 6.1 shows the Force vs. Displacement relationship.

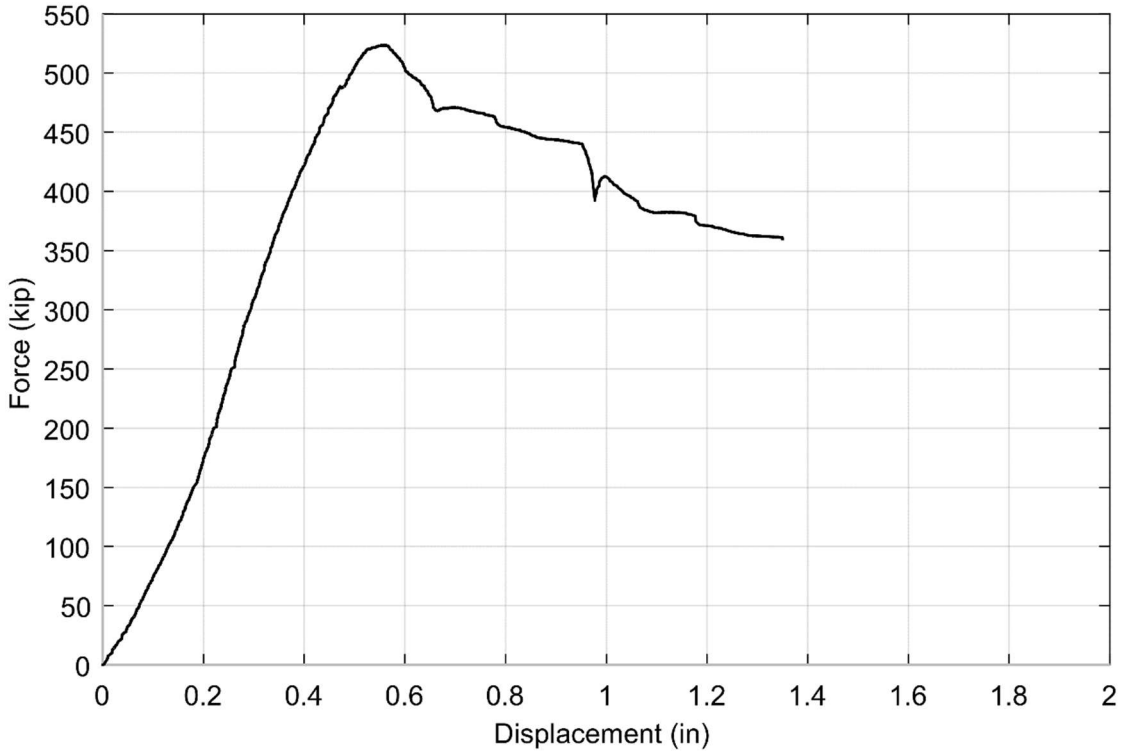

Figure 6.1. Force vs. Displacement (PTB_4.5_1_0_P)

6.2.1 *Before Peak Loading*

Load step 1 (0-100 kips) ran smoothly. The initial stiffness changed slightly as seen by the change in slope. This is most likely due to deformation of the test setup including the deformation of the cotton duck pads the edges of the slab rested upon. The photos of the underside of the specimen show no signs of cracking. The strain gauges during this load step showed no sign of yield strains.

During load step 2 (100-200 kips), the test had been paused a few times to calculate the rate of displacement of the column during the current load rate of 20 kips/min.. The displacement rates were decreasing during this period, which can be seen by the change in slope of Figure 6.1. Due to this the constant load rate was continued for the entire load step. There was no significant signs of cracking during the load step. The strain gauges showed no sign of yielding.

During load step 3 (200-300 kips), the Baldwin press was changed from load controlled to displacement controlled loading. During the load step the underside of the slab showed no signs of cracking. There was no sign of yielding in the flexural reinforcement either. A sound was noted to occur at approximately 300 kips and was attributed to settlement of the test frame. At around 300 kips the stiffness of the specimen begins to decrease slowly.

Load step 4 (300-400 kips) showed a continuation the specimen's stiffness decreasing. There was no significant change in cracking from the test photos, but loss in stiffness is likely caused by new cracks forming or existing cracks increasing in size. At 400 kips there was no indication of yielding of the flexural reinforcement. All strains are near or below 50% of the yield strain.

Cracking developed significantly during the load step 5 (400-500 kips) which can be seen in Figure 6.2. The circumferential crack formed around the perimeter of the ring flange is outlined in blue. Cracks emanating from the ring flange aligned with the flexural reinforcement. Cracks began to appear on the north face of the specimen that were mostly vertical and appeared to originate from the bottom face of the slab. The cracks are highlighted in Figure 6.3. At 500 kips the flexural reinforcement indicated yielding as shown in Figure 6.4.

Figure 6.2. Cracking on Bottom Face of Northeast Slab – 500 kips (PTB_4.5_1_0_P)

Figure 6.3. Cracking on North Face of Slab –500 kips (PTB_4.5_1_0_P)

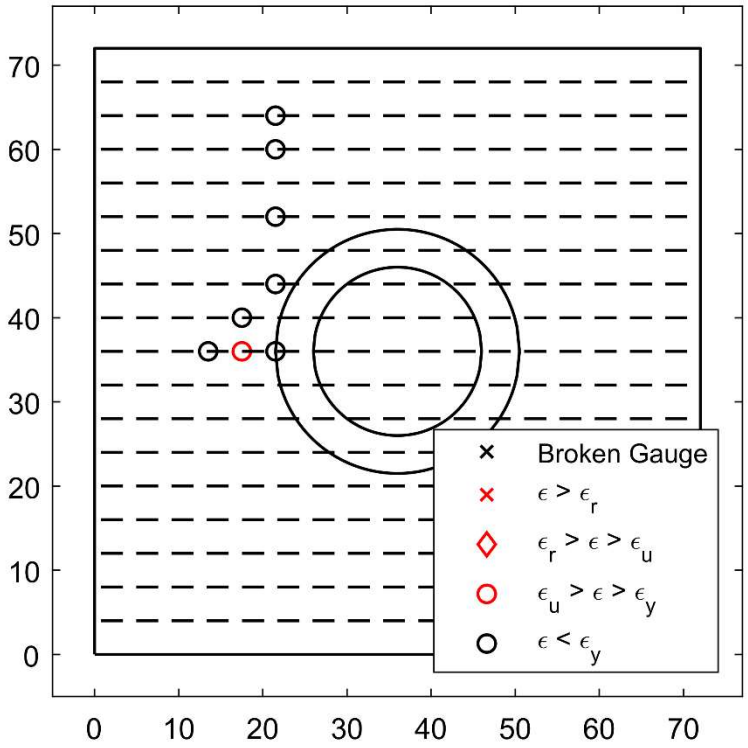

Figure 6.4. East-West Bottom Reinforcement Strain Summary –500 kips (PTB_4.5_1_0_P)

During load step 6 (500-523 kips) the specimen reached peak force. There was a noticeable change in stiffness at approximately 519 kips. The load increased from 519 kips to the peak force of 523 kips over a displacement of 0.04 in.. There was no noticeable increase in cracking during load step 6. A few of the strain gauges attached to the east-west bars have yielded seen in Figure 6.5. The east-west bars within the column width had all very nearly yielded if not fully yielded. The three bars west of the column width recorded strains of 75-90% of the yield strength of the reinforcement. In the north-south reinforcement there were no signs of yielding of the reinforcement. The strain gauges attached to bars within the column region experienced least 72-90% of the yield strain. The reinforcement outside of the column region experienced a maximum strains of 64% of the yield strain.

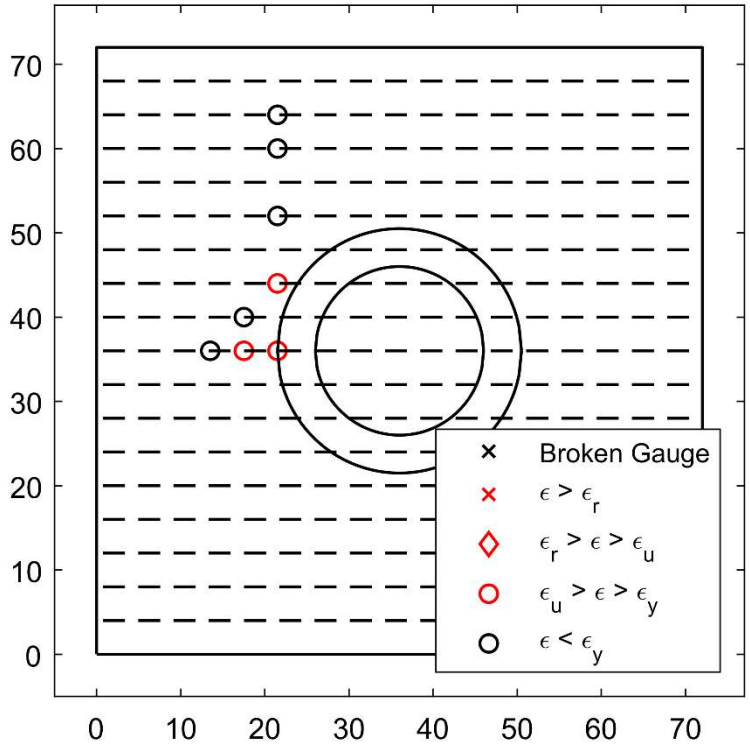

Figure 6.5. East-West Bottom Reinforcement Strain Summary –523 kips (PTB_4.5_1_0_P)

6.2.2 *After Peak Loading*

After the peak was reached the test continued to load the specimen at the same displacement rate of 0.03 in./min.. The test was paused once after the peak force was reached to increase the displacement rate of the Baldwin to reach 40% of peak strength loss signaling end of test.

Load step 7 (523-500 kips) was a quick step that did not result in much change in the crack pattern. More vertical cracks formed on the north face. The strain in the east-west reinforcement decreased below yield strain. Strains for the bars in the north-south direction continued to increase, which may indicate that the force was redistributed to rely more heavily on the reinforcement in the non-yielded direction.

During load step 8 (500-400), the rate of resistance loss decreased in comparison with that of load step 7. The resistance loss plateaued around 470 kips. During the plateau the grout pad underwent significant damage as the ring flange was pressed into the slab shown in Figure 6.6. The circumferential crack width grew significantly during this load step. Cracks between the inner

and outer circumferential cracks began to develop. The vertical cracks on the north face of the slab increased in crack width, but did not increase in the number of cracks visible. Many of the bars that pass within the critical perimeter of the connection had yielded in both the east-west and north-south directions to accommodate the high deformation demands. The gauges attached to east-west bars passing through the critical perimeter of the connection that did not register yield strain had decreased in strain. The north-south bars within the critical perimeter of the connection that showed no yielding at 400 kips post peak were either broken before testing or reached yield strain during load step 8, but decreased below yield before the end of the load step.

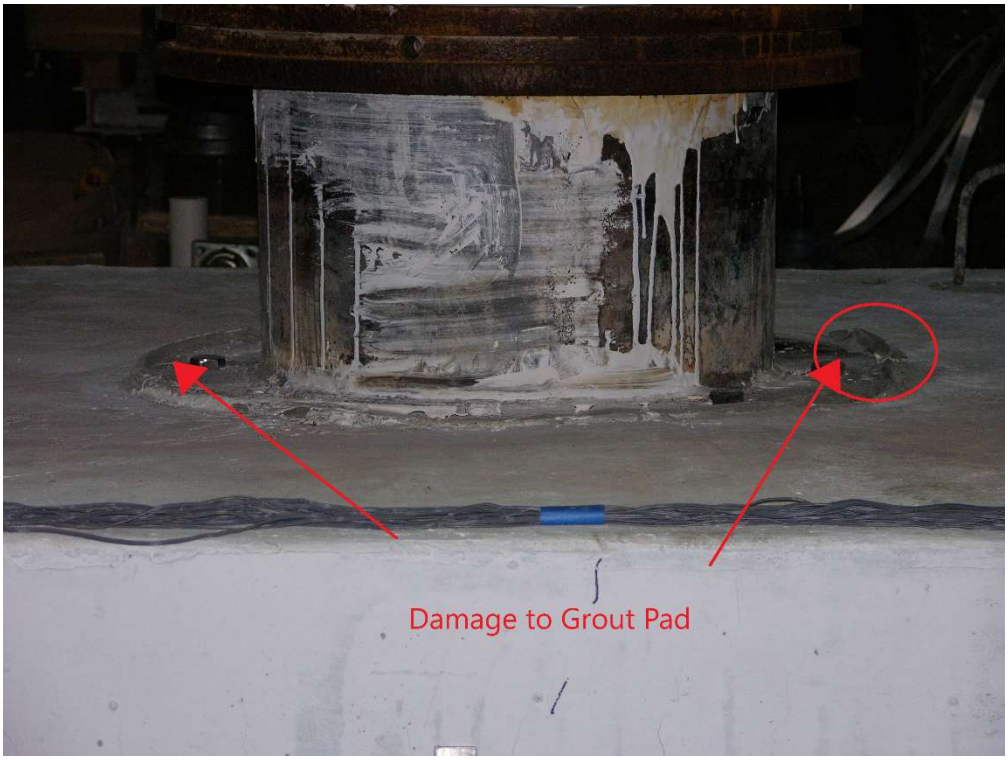

Figure 6.6. Crushing of Grout Pad North Side of Slab – 470 kips (PTB_4.5_1_0_P)

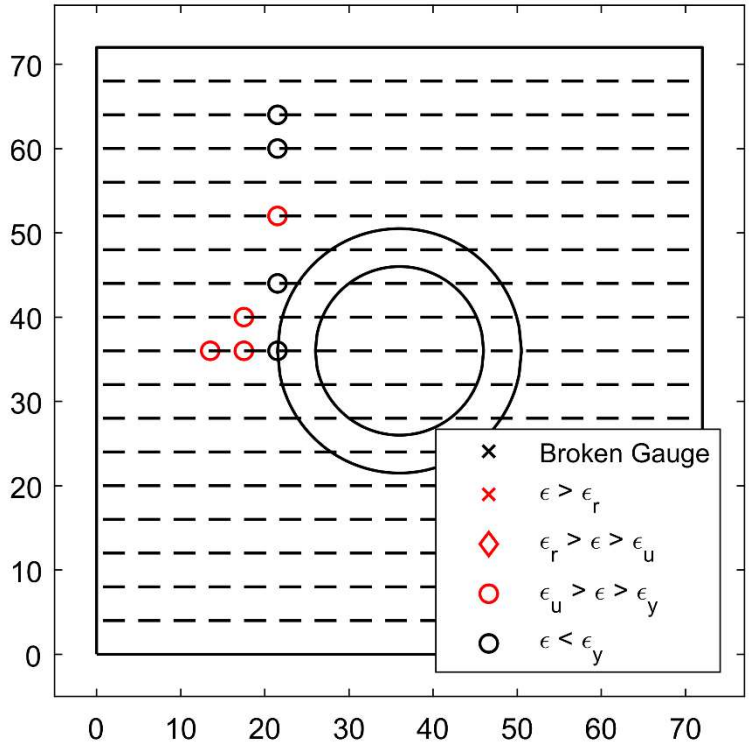

Figure 6.7. East-West Bottom Reinforcement Strain Summary – 400 kips (PTB_4.5_1_0_P)

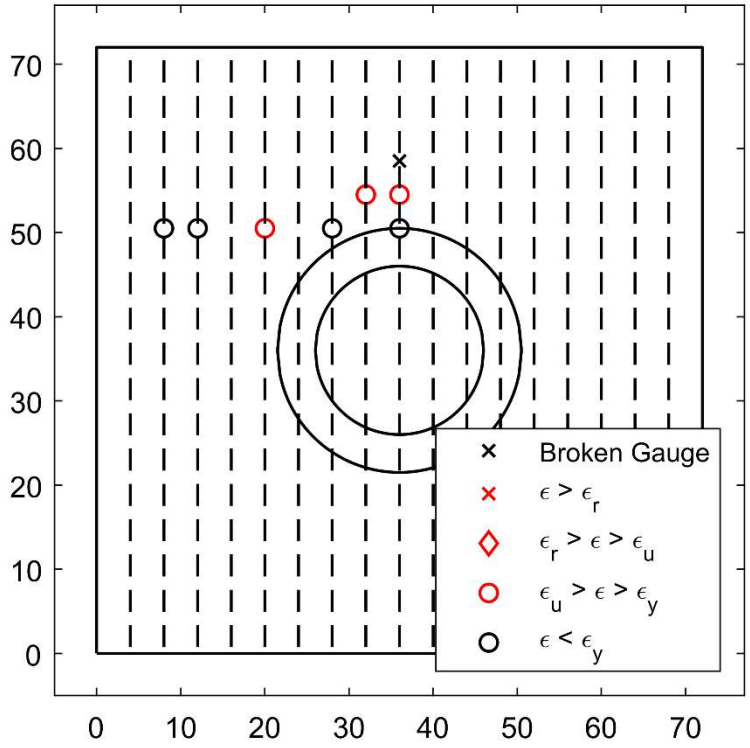

Figure 6.8. North-South Bottom Reinforcement Strain Summary – 400 kips PTB_4.5_1_0_P

Near the end of load step 8 the test was paused briefly to adjust the displacement rate. During the pause the Baldwin press relaxed causing the force to drop approximately 22 kips. This resulted in a large drop shown in Figure 6.1. Once testing was resumed the strength increased but the slopes did not lineup, indicating that there was some form of deterioration at this point.

In load step 9 (400-358 kips) the specimen gradually lost strength until reaching end of test. Figure 6.9 shows the inner circumferential crack width increased greatly. The circumferential cracks grew a significant amount more than any of the radial cracks. Significant damage near the middle of the north support was noticed and is shown in Figure 6.10. Both the large increase in crack width, and damage of the concrete near the support are believed to be due to significant increase in deflection during load step 9. The circumferential cracks and displacement of the top column and ring flange into the top of the slab is indicate the formation of a shear cone. The strain gauges did not indicate yielding across the full width of the specimen at end of test.

Figure 6.9. Cracking on Bottom Face of Northeast Slab – 358 kips (PTB_4.5_1_0_P)

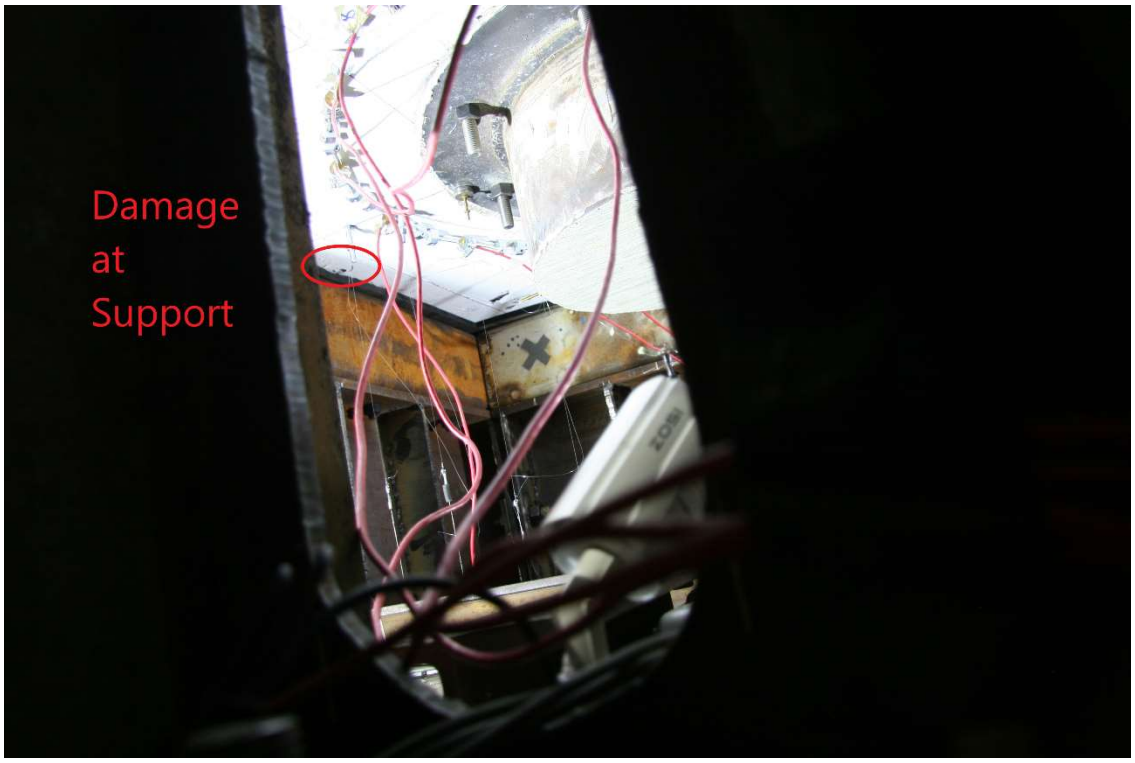

Figure 6.10. Initiation of Damage Near North Support – 358 kips (PTB_4.5_1_0_P)

6.2.3 *After Testing*

After completion of the test, the load was removed. The specimen was raised slightly on the North side to allow for the removal of the North support. This allowed better access underneath the specimen to investigate the damage post-test.

Beginning with the top face of the slab, the top column had noticeably sunk into the slab. The discontinuity is apparent on the northeast side of the ring in Figure 6.11. The gap between the top surface of the slab and the top of the ring show a displacement of the top of the connection that is not seen underneath the specimen. Figure 6.12 shows that the top face of the ring is flush with the bottom of the slab.

Figure 6.11. Deformation at Ring Edge of Top Column – Post Test (PTB_4.5_1_0_P)

Figure 6.12. Deformation of Concrete around Ring Flange on Bottom Face – Post Test (PTB_4.5_1_0_P)

Cracks are noticed on the top surface of the slab originating from the edge of the ring. They are located in the cardinal directions. Outside of the small amount of cracking and the damage around the ring there are no other signs of damage on the top face of the slab.

The extent of the cracking on the bottom face of the slab is shown in Figure 6.13. The blue lines denote the largest crack widths, and form a clear circumferential crack. The shape

mostly follows a circular pattern as expected, but the southeast corner shown in the bottom left of the figure is square. This is most likely due to the influence of the shape of the test frame. The circumferential crack was measured in the four cardinal directions and the average distance was found to be approximately 6.75 in.. Along the supports there is significant damage. Where the specimen rested on the supports can be seen by the discoloration as well as spall damage to the concrete. Removal of the North support allowed for observation of the damage of the concrete at the support shown in Figure 6.14.

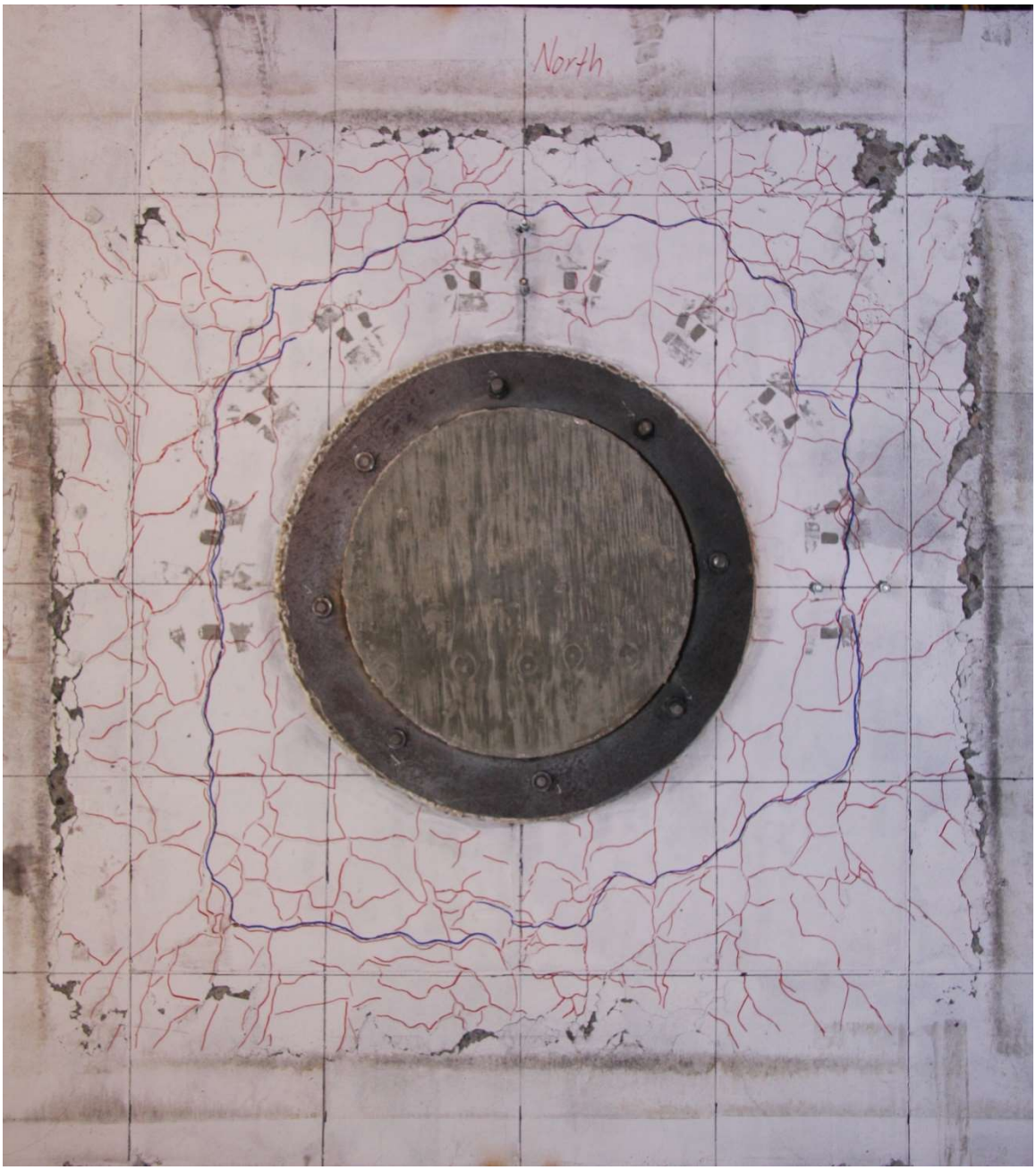

Figure 6.13. Cracking of Bottom Face – Post Test (PTB_4.5_1_0_P)

Figure 6.14. Spalling at North Support – Post Test (PTB_4.5_1_0_P)

From the photos during the test the spalling is approximated to have started during the final load step. During the final load step the specimen displaced approximately 0.37 in. which is 27.6% of the total test displacement. The spalling is a result of the supports restricting the displacement of the bottom face of the slab. From 470 kips post peak there is a relatively consistent rate of strength loss. Which does not indicate that the spalling was the result of a large drop in strength..

6.2.4 *Displaced Shape*

This section provides the displaced shapes of specimen along the middle of the slab in the west-east and north-south directions. In Figure 6.15 the displaced shape is plotted with the origin at the center of the slab. Along the x-axis negative values indicate locations north of the column centerline, and positive values indicate locations south of the column centerline. There were no instruments to measure the deformation of the slab at the supports, so a curve fit was applied. To denote that the value was not a measurement it is marked by an x. The displacement at the supports

was determined by fitting second order polynomial to the four negative values given in the displaced shape.

During the first load step there was a larger change in displaced due to the deformation of the supports and cotton duck pads. As the load is increased Figure 6.15 and Figure 6.16 show a consistent increase in the deflections of the slab to approximately 400 kips. At 400 kips the string pots attached to the column and ring at -10 and -14 in. deflect slightly more than the string pots at the locations off the ring. From 400 to 500 kips, there is a larger increase in deflection as a result of the specimen losing stiffness from cracks forming. When the load peaks the differences in deflections between the string pots on the ring and off the ring become more pronounced. Approximately 40% of the deformation occurs during the load step from 500-400 past peak force. During this load step that grout pad crushes and the spalling at the middle of the supports begins.

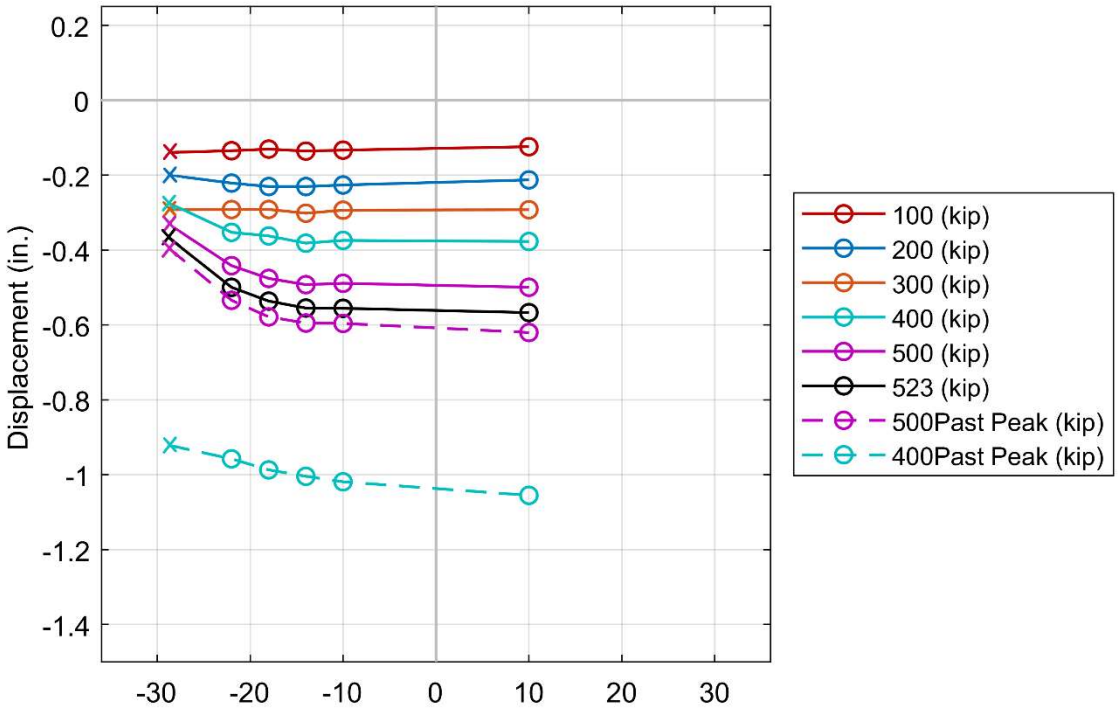

Figure 6.15. Displaced Shape North-South (PTB_4.5_1_0_P)

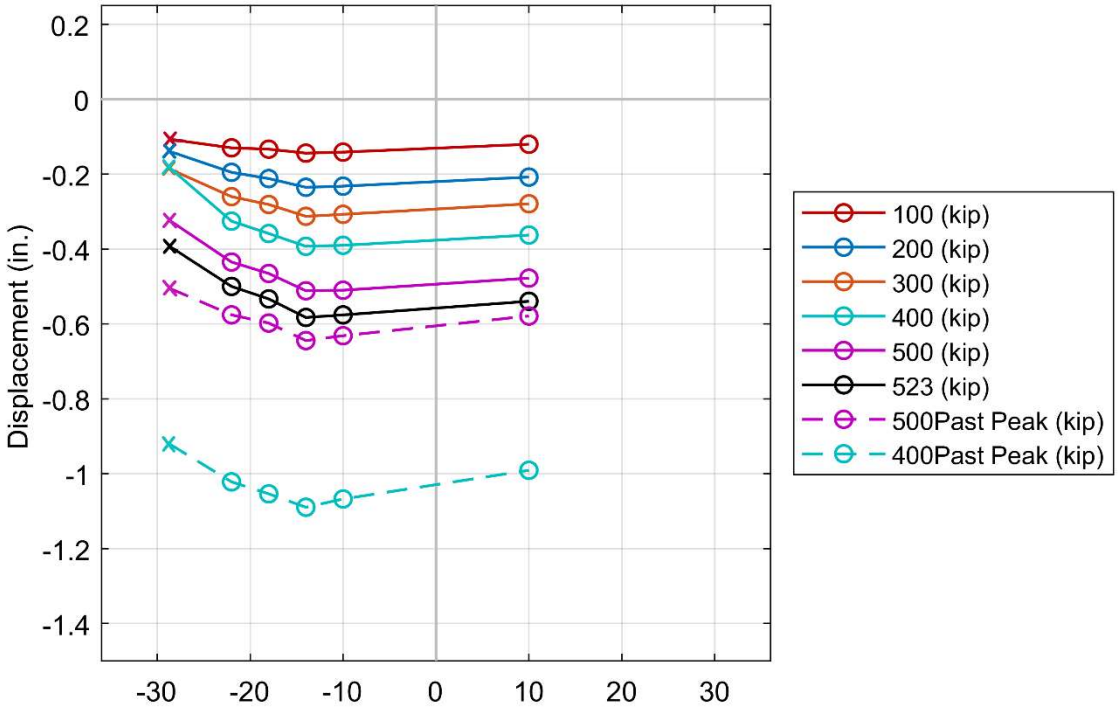

Figure 6.16. Displaced Shape West-East (PTB_4.5_1_0_P)

6.3 SPECIMEN PTB_9_2_0_P EXPERIMENTAL OBSERVATIONS

Specimen PTB_9_2_0_P is designed with the proposed connection. Slab geometry is 72 x 72 x 10 in.. The connection consists of a 20 in. diameter CFST column with a 3/8 in. wall thickness of the tube. PTB_9_2_0_P has a 9 in. ring flange that is 1/2 in. thick. There were two peripheral sets of ¾ in. bolts within the ring. The slab had a 1.79% flexural reinforcement ratio.

The punching load was initially applied at a controlled load rating of 20 kips/min. At 150 kips the Baldwin Press was converted to displacement controlled loading rate at 0.06 in./min. The global response is shown below. The column displacement was calculated from an average of four vertical string pots attached to the bottom column.

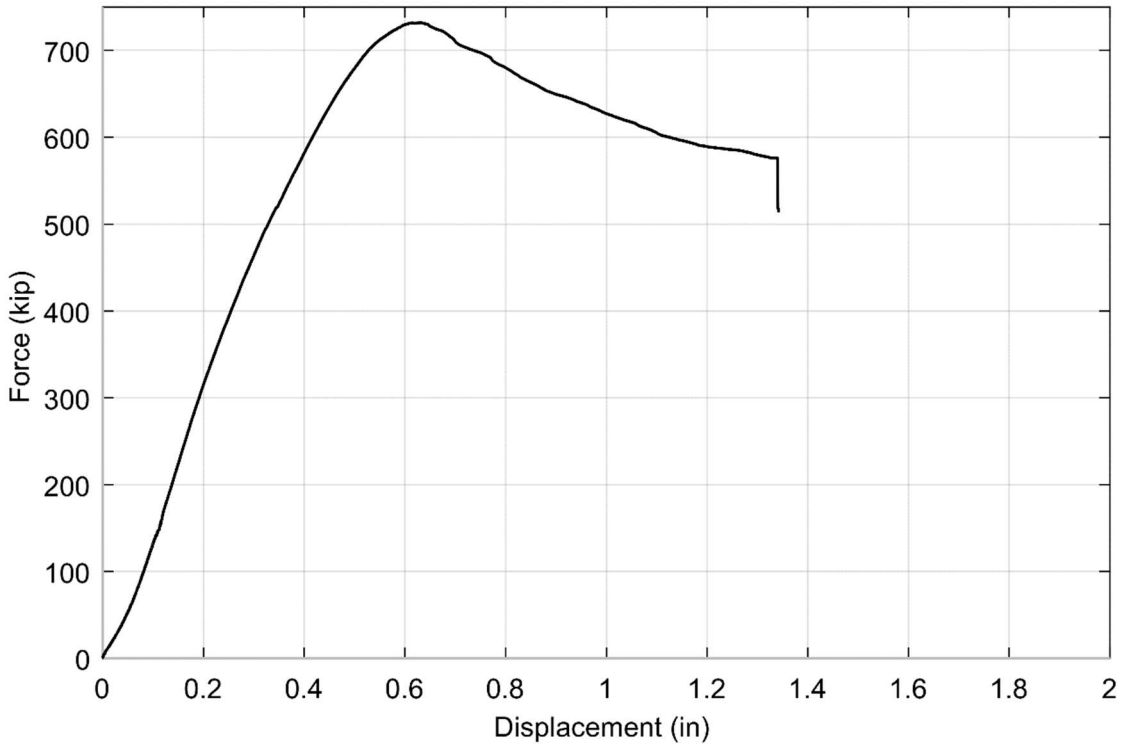

Figure 6.17. Force vs. Displacement (PTB_9_2_0_P)

The specimen reached a peak strength of 731.86 kips at approximately 0.61 in. displacement. Due to the test setup some of the displacement is artificial and includes deformation of the edge supports and cotton duck.

6.3.1 *Before Peak Loading*

Load step 1 (0-100 kips) ran smoothly. Noises due to be settling of the test frame or the specimen shifting in relation to the test frame were heard during this test. There was no apparent cracking in the slab during this load step. The strains were less than $142\mu\varepsilon$ during this load step.

Load step 2 (100-200 kips) was paused at 141 kips due to an issue with the Baldwin. The effects of this delay were removed from the global response. The test was paused at 150 kips to switch the Baldwin controller from force controlled to displacement controlled. The stiffness of increased in comparison to the initial stiffness. This is most likely due to displacements of the test frame and cotton duck pad similar to the behavior observed in PTB_4.5_1_0_P. There were no significant signs of cracking during this load step. The strains were insignificant.

During load step 3 (200-300 kips) the stiffness stayed constant during this load step. This was consistent with the lack of cracking in the bottom of the slab. The strains were all below 50% of yield strain of the flexural reinforcement. The highest strains were located on reinforcing bars passing through the column and within the critical perimeter.

During load step 4 (300-400 kips) the stiffness began to decrease indicating that cracking had started but there was no visible signs of cracking from the cameras. A few of the strain gauges recorded strains of over 50% of yield during this load step. All were located on the bar passing through the center of the column and within critical perimeter.

Load step 5 (400-500 kips) the cameras underneath the slab were out of focus so the development of cracking was inconclusive. Figure 6.18 shows cracking on the north edge of the slab at approximately 470 kips. The cracks highlighted in black were there before the start of testing. The cracks highlighted in red show the cracks developed during testing. In the previous test these cracks seemed to be a result of similar cracks along the reinforcement on the underside of the slab, which helps to give some information about the cracking beneath the slab, but it is not definitive. None of the strain gauges indicated yielding of the flexural reinforcement, many of the gauge readings had surpassed 50% of the yield strain. The few gauges that had strain readings below 50% of the yield strain were on bars in the east-west direction far from the ring flange, and in the north-south direction the strain gauge on the bar passing through the center of the column but at 8 in. from the edge of the ring flange.

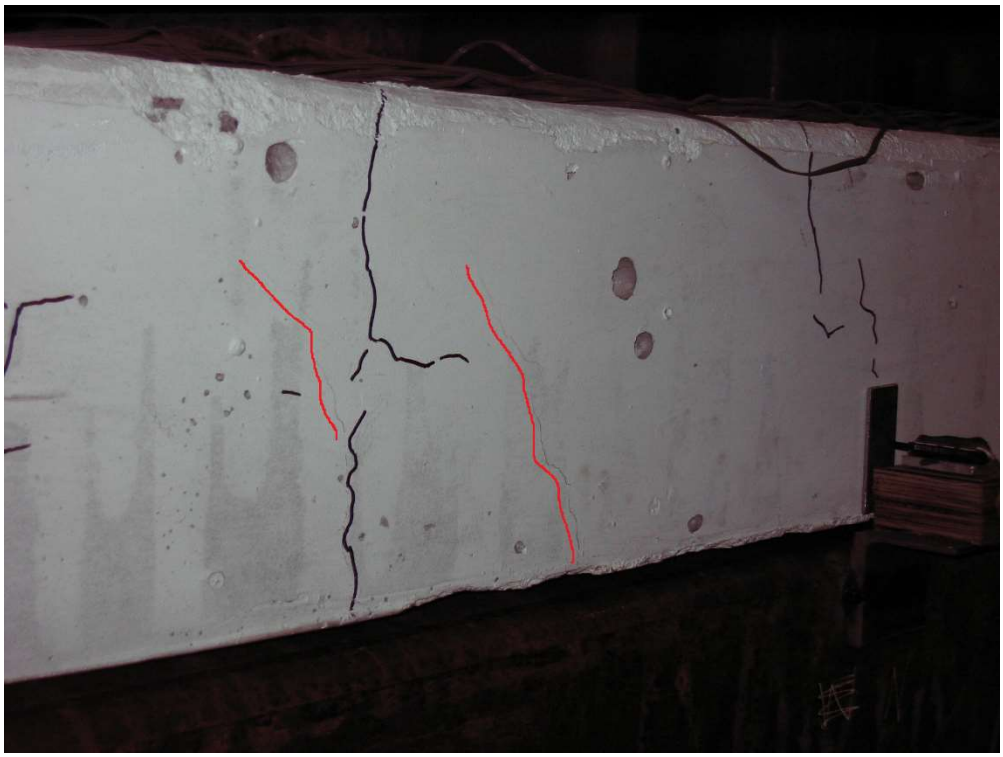

Figure 6.18. Cracking on North Face of Slab – 470 kips (PTB_9_2_0_P)

Load step 6 (500-600 kips) ran smoothly. The specimen stiffness continued to decrease likely due to increased cracking and expansion of already existing cracks. The cameras were still out of focus so this cannot be confirmed. At 600 kips a few strain gauges report yielding of the reinforcement as seen in Figure 6.19 and Figure 6.20. All of the strain gauges on the north-south bars are at least above 50% of the yield strain with the majority of strain gauges reading above 70%. The only gauge recording strain lower than this on the north-south bars is the gauge located on the reinforcing bar passing through the center of the column at 8 in. away from the ring flange. The general trend in strain magnitude is decreasing as the gauges move away from the center of the column as expected. The strain gauges on the east-west reinforcing bars show a similar trend, but with lower magnitudes. The strain gauges on the bars closest to the north face of the slab read less than 50% of the yield strain.

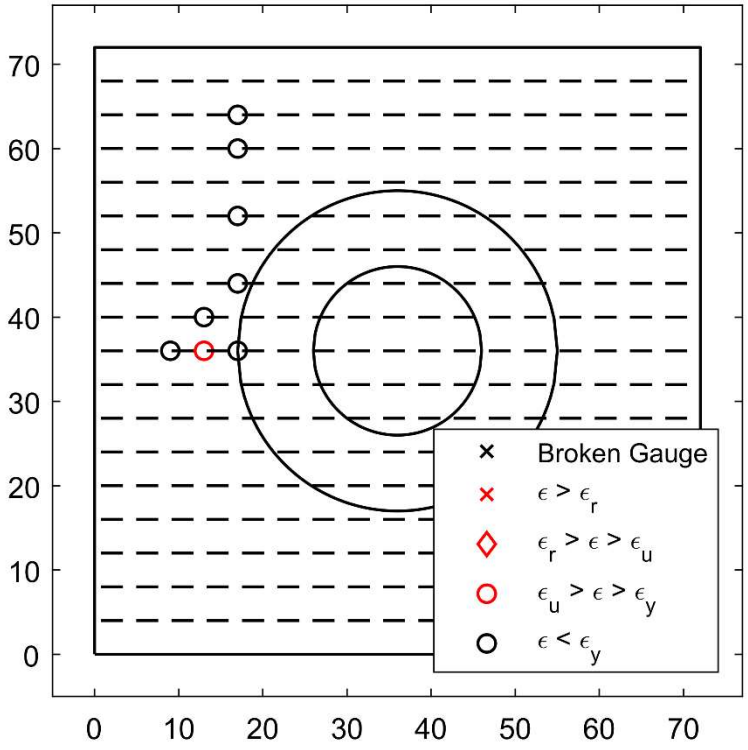

Figure 6.19. East-West Bottom Reinforcement Strain Summary – 600 kips (PTB_9_2_0_P)

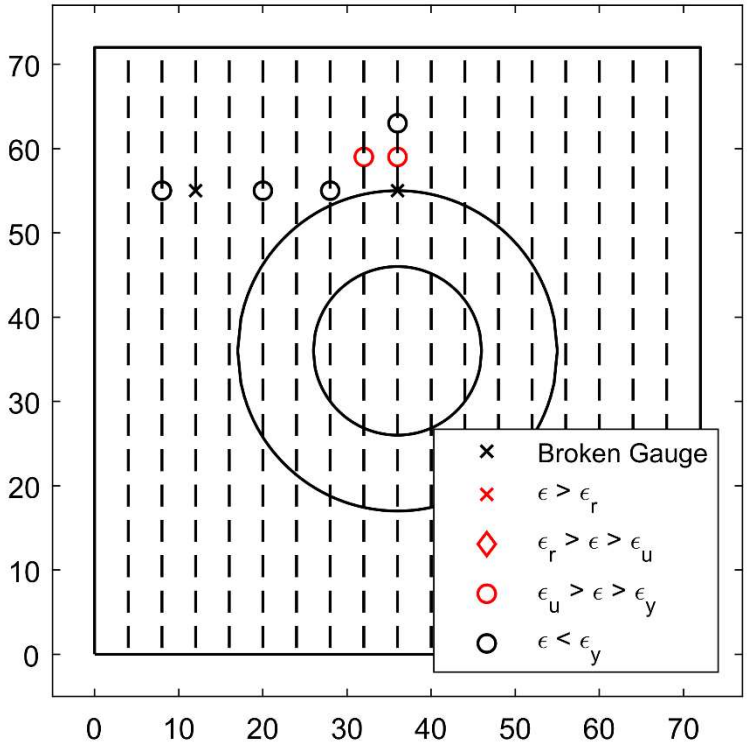

Figure 6.20. North-South Bottom Reinforcement Strain Summary – 600 kips (PTB_9_2_0_P)

During load step 7 (600-700 kips) the stiffness continued to decrease as the load approached the peak measured load. The decrease in stiffness is attributed to yield of flexural reinforcement as well as large cracks formed on the bottom of the slab. Cracking near the middle of the north support was noticed during this load step and is shown in Figure 6.21. Figure 6.22 shows the changes in strain for the east-west bars during this load step. All of the strain gauges on the east-west bars record strains of higher than 50% of the yield strain following the similar pattern of highest strains being the bars near the column within $d/2$ from the edge of the ring flange. The strains decrease as the gauges move further away from the column. Strain gauges on the north-south bars showed increase in strain magnitudes, however there were no new instances of gauges recording strains above the yield strain.

Figure 6.21. Cracking on Bottom Face of Slab near North Support – 670 kips (PTB_9_2_0_P)

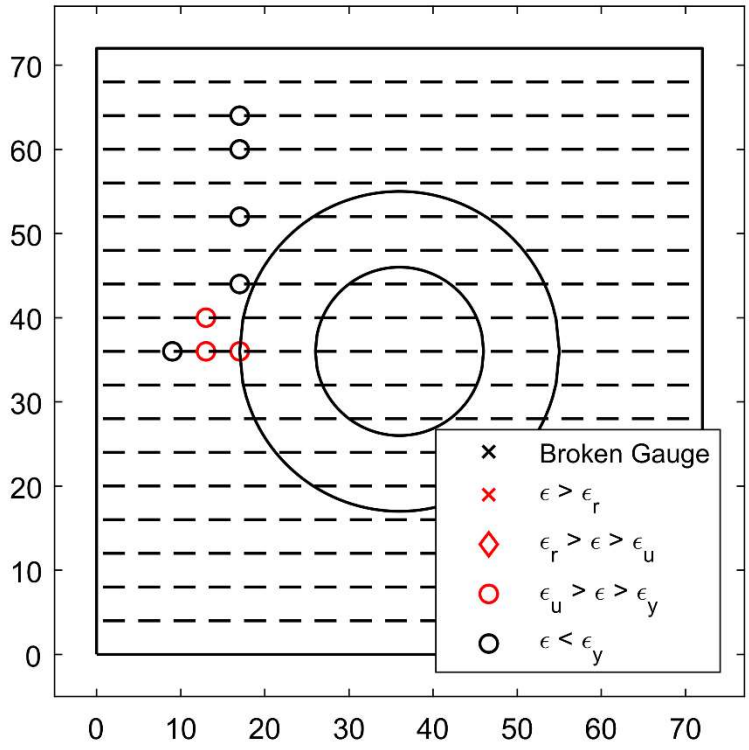

Figure 6.22. East-West Bottom Reinforcement Strain Summary – 700 kips (PTB_9_2_0_P)

During load step 8 (700-731 kips) the specimen reached the peak force of 731.86 kips at a displacement of 0.63 in.. The camera looking at the east side of the bottom of the slab was still out of focus during this load step. The camera looking at the north side of the slab was in focus but aimed at the support so it did not give reliable observations to cracking of the slab at this point. The strain gauges indicated three new strain gauges reached yield strain which are shown in Figure 6.23 and Figure 6.24. They show the strain in the reinforcing is extending across the majority of the reinforcing bars passing through the column. The extent of yielding of PTB_9_2_0_P was greater than PTB_4.5_1_0_P at peak strength. The majority of the strain gauges were above or near yielding, with the exceptions being the strain gauges on the reinforcing bars passing through the center of the column located 8 in. from the ring flange, and the two strain gauges on east-west reinforcing bars located outside the confined region.

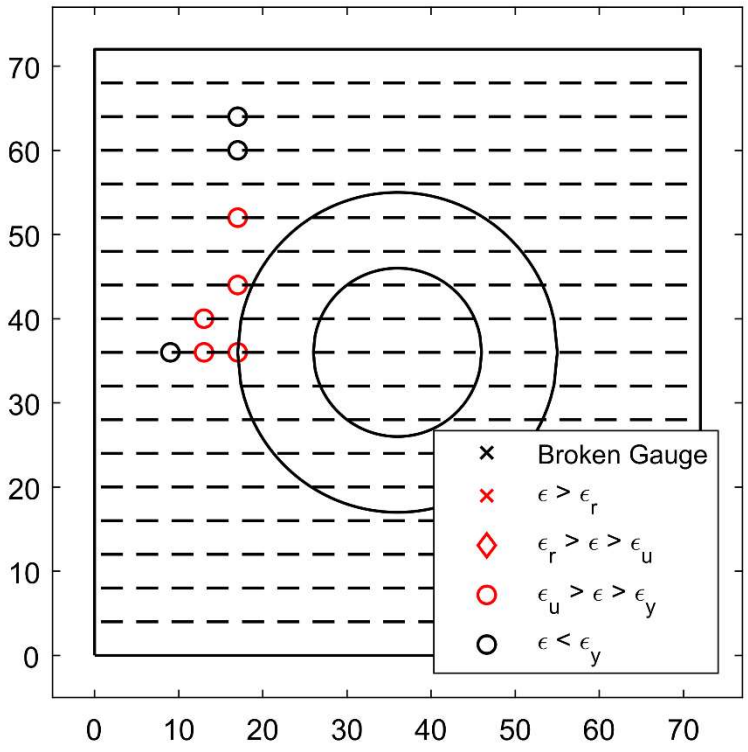

Figure 6.23. East-West Bottom Reinforcement Strain Summary – 732 kips (PTB_9_2_0_P)

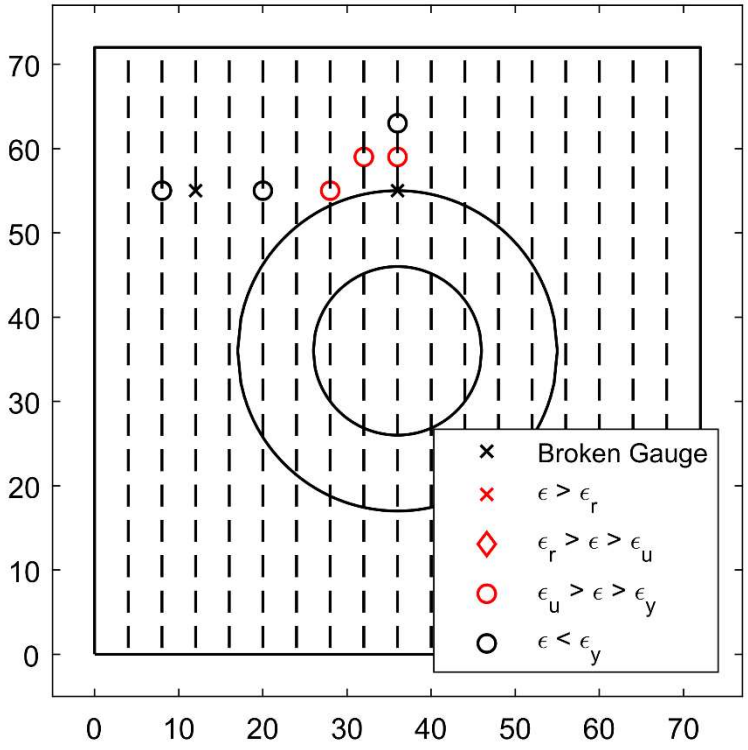

Figure 6.24. North South Bottom Reinforcement Strain Summary – 732 kips (PTB_9_2_0_P)

6.3.2 *After Peak Loading*

During load step 9 (731-700 kips) the specimen began to gradually lose strength. The damage to bottom surface of the slab consists of cracking around the column and middle of the support with some radial cracking that extends towards the corner of the supports shown in Figure 6.25 and 6.26. Figure 6.25 shows cracking on the north edge of the slab that originated from the bottom side and aligned with the location of flexural reinforcement as well as shrinkage cracking noticed before testing. The strain gauges showed no new locations at which yield strain was reached. Strain gauges attached to east-west reinforcement continued to increase strain magnitudes with the exceptions being at the locations on the bar passing through the center of the column at the edge of the ring flange and 8 in. from the ring flange and the reinforcing bar furthest from the column. The strains on reinforcing bars in the north-south direction within the critical perimeter continued to increase in strain. The strain gauge located along the east-west bar closest to the north

edge of the specimen reached yield strain during this load step, but decreased below yield strain before the specimen reached 700 kips post peak.

Figure 6.25. Bottom Face of Slab near North Support – 700 kips Post Peak (PTB_9_2_0_P)

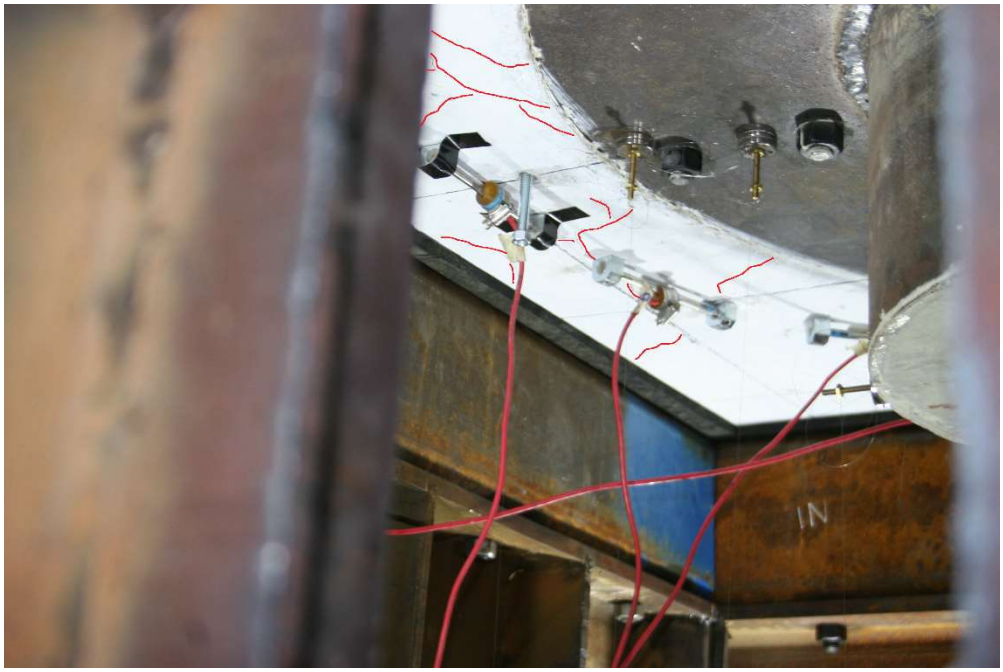

Figure 6.26. Bottom Face of Slab near West Support – 700 kips Post Peak (PTB_9_2_0_P)

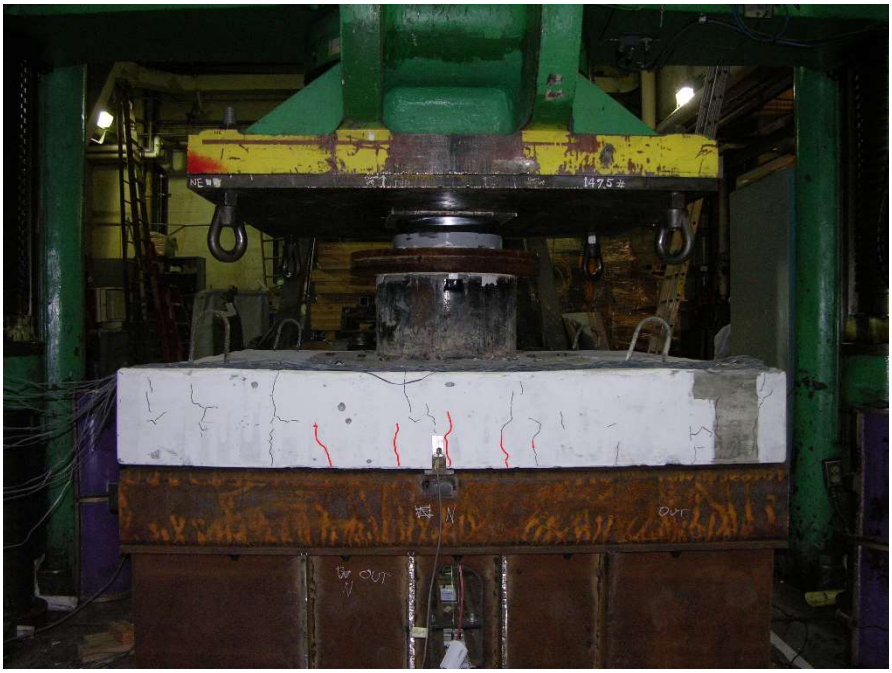

Figure 6.27. North Face of Slab – 700 kips Post Peak (PTB_9_2_0_P)

During load step 10 (700-600 kips) the rate of resistance degradation decreased in comparison to load step 9. Cracks highlighted in Figures 6.25 and 6.26 continued to increase in width. The top ring flange bends upward as the top column is pressed into the top of the slab. The deformation is seen in the movement of the top column relative to the top face of the slab as the grout pad begins to crush. Figures 6.28 and 6.29 show that all of the strain gauges other than the north most gauge on the east-west bars recorded strains above yield.

Figure 6.28. Deformation of Top Ring Flange – 600 kips Post Peak (PTB_9_2_0_P)

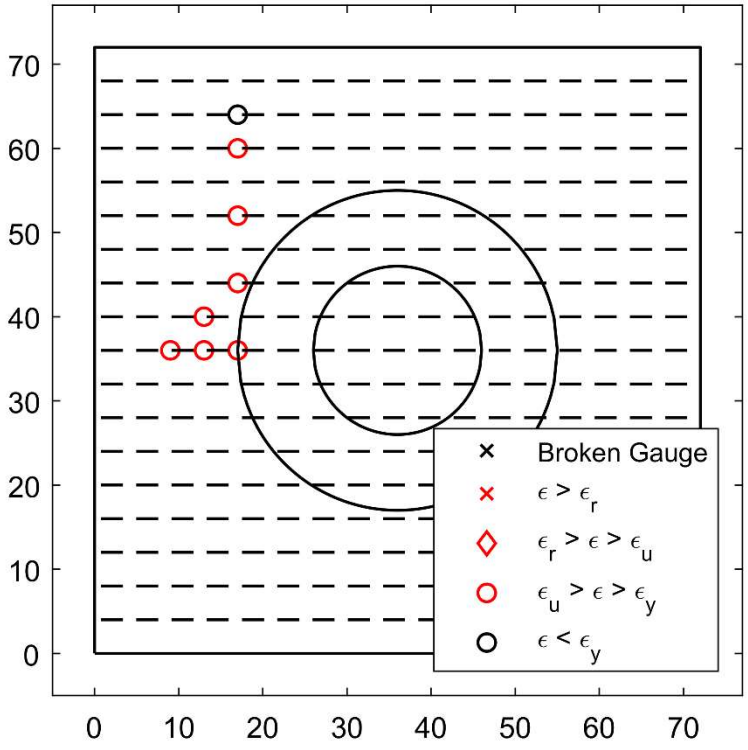

Figure 6.29. East-West Bottom Reinforcement Strain Summary – 600 kips Post Peak (PTB_9_2_0_P)

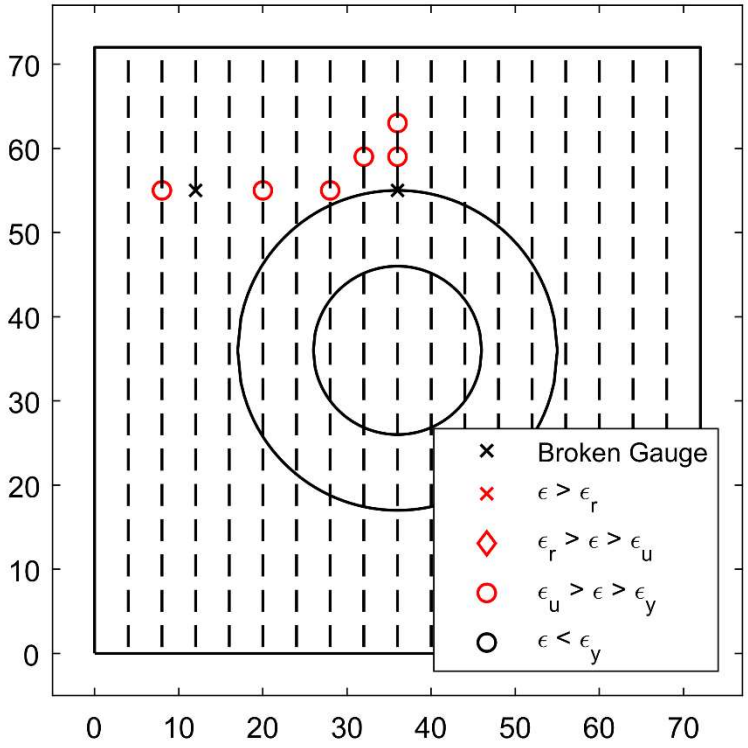

Figure 6.30. North-South Bottom Reinforcement Strain Summary – 600 kips Post Peak (PTB_9_2_0_P)

During the final load step 11 (600-513 kips) the rate of degradation of resistance continued to decrease until there was a sudden drop in force at approximately 1.34 in.. The strength dropped from 576 to 513 kips. The sudden drop in strength was due to a post-tensioned bolt fracture located on the second periphery at the north most bolt location seen in Figure 6.33. Figure 6.31 shows the continuation of damage near the North support. The slab crack widths continued to increase and are shown in Figure 6.32.

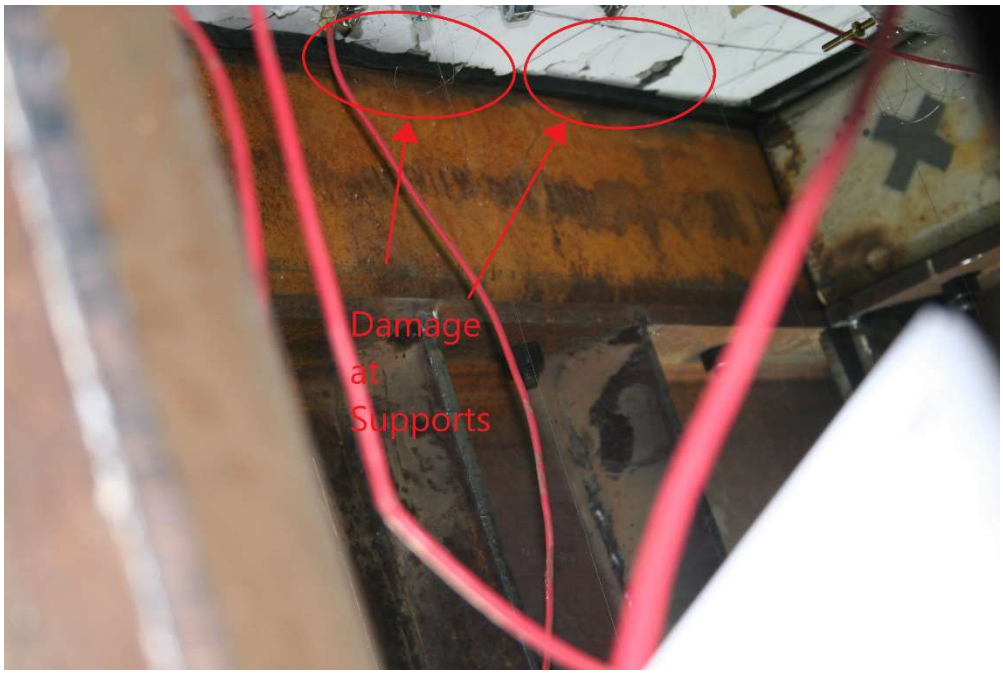

Figure 6.31. Bottom Face of Slab near North Support – 513 kips Post Peak (PTB_9_2_0_P)

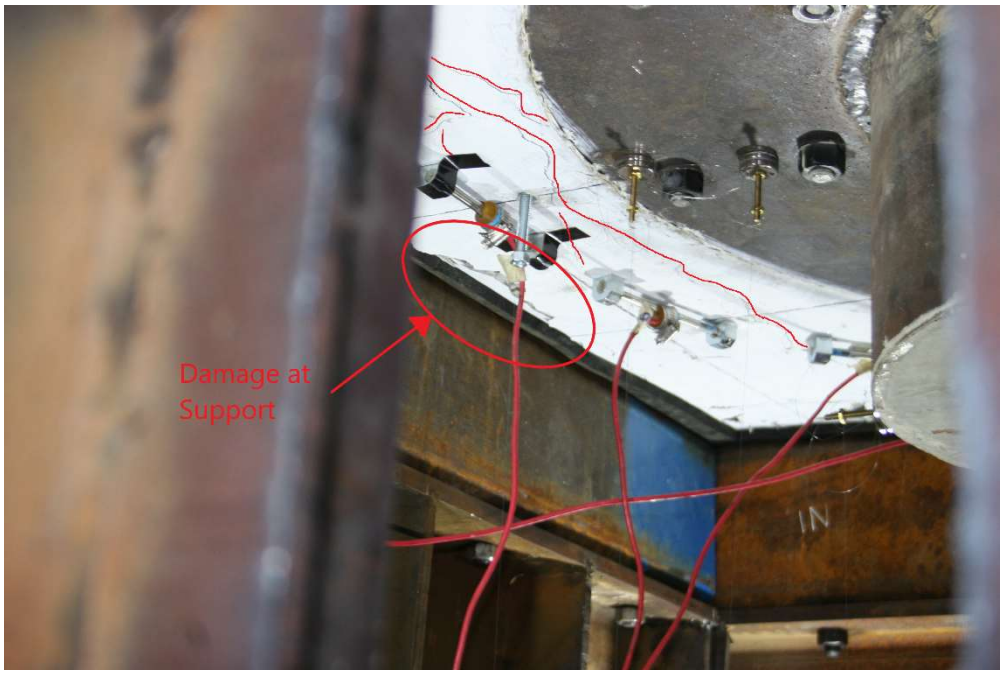

Figure 6.32. Bottom Face of Slab near West Support – 513 kips Post Peak (PTB_9_2_0_P)

Figure 6.33. North Side of Top Column – 513 kips Post Peak (PTB_9_2_0_P)

6.3.3 *After Testing*

After testing was completed the Baldwin press was held at a constant displacement. Photos were taken during this configuration to observe the cracking and damage at the maximum displacement of the specimen. With the load in place it was difficult to take photos of the bottom of the specimen, so the photos were used to determine the damage to the top of the slab around the ring flange. Figure 6.34 highlights damage to the grout pad and concrete at the edge of the ring. A large crack formed at the edge of the ring flange. Figure 6.33 and Figure 6.34 show the width of the crack at different locations. The damage to the concrete around the ring flange allowed the top column to displace into the top surface of the slab. At the start of test, the bottom of the top ring flange was flush with the top of the slab. At end of test the top of the ring flange was flush with the top of the slab at a few points along the ring.

Figure 6.34. North Side of Top Column – After Test (PTB_9_2_0_P)

Figure 6.35. North Side of Ring Flange – After Test (PTB_9_2_0_P)

Figure 6.36. Southwest Side of Ring Flange – After Test (PTB_9_2_0_P)

The load was then removed from the specimen to allow for easier inspection of the specimen. During inspection of the top surface of the specimen, some small cracks were found extending in the cardinal directions of the ring flange to the closest edge of the specimen. These cracks mostly aligned with the flexural reinforcement within the column region and are highlighted for the north side of the specimen in Figure 6.37. Vertical cracks were formed on the side edges of the specimens and are shown in Figure 6.38. The east edge of the slab had a small horizontal crack highlighted in Figure 6.39. Additionally there was warping of the top ring flange. The regions of the ring that were confined by the post-tensioned bolts moved to nearly level with the top surface of the slab when the column was pressed into the slab. The regions in between the bolts began to lift and the effect can be seen in Figure 6.39. The prying effect of the ring resulted in high stress on the post-tensioned bolt that caused it to fracture. The ring itself is not strong in resisting the bending due to this prying effect. The best way to increase the bending strength would be to increase the thickness of the ring.

Figure 6.37. Cracking North Side of Top Face – Load Removed (PTB_9_2_0_P)

Figure 6.38. Cracking South Face – Load Removed (PTB_9_2_0_P)

Figure 6.39. Cracking East Face – Load Removed (PTB_9_2_0_P)

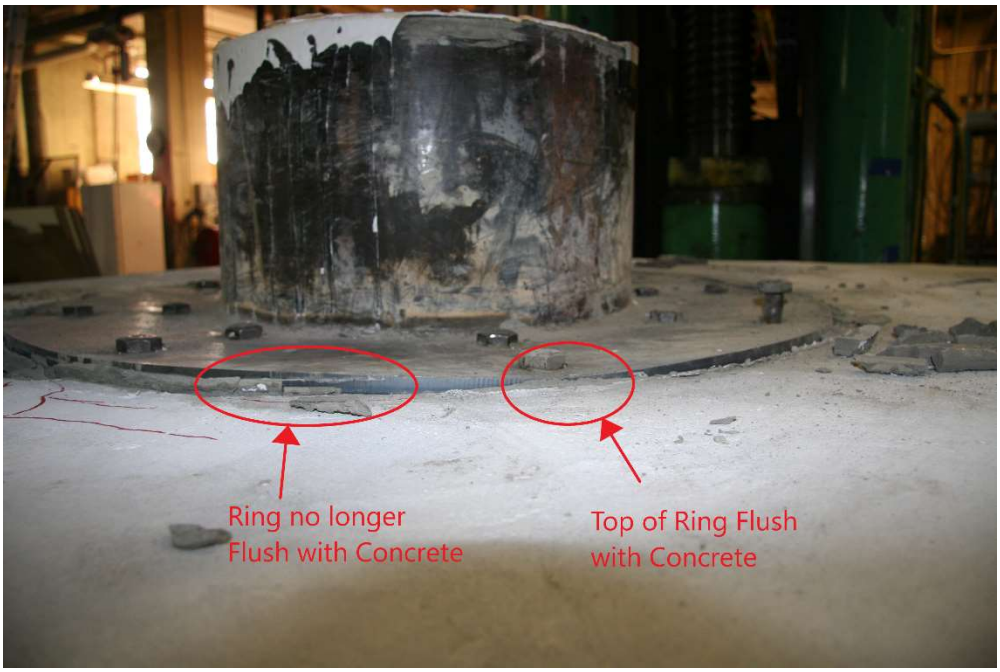

Figure 6.40. Warping of Top Ring Flange – Load Removed (PTB_9_2_0_P)

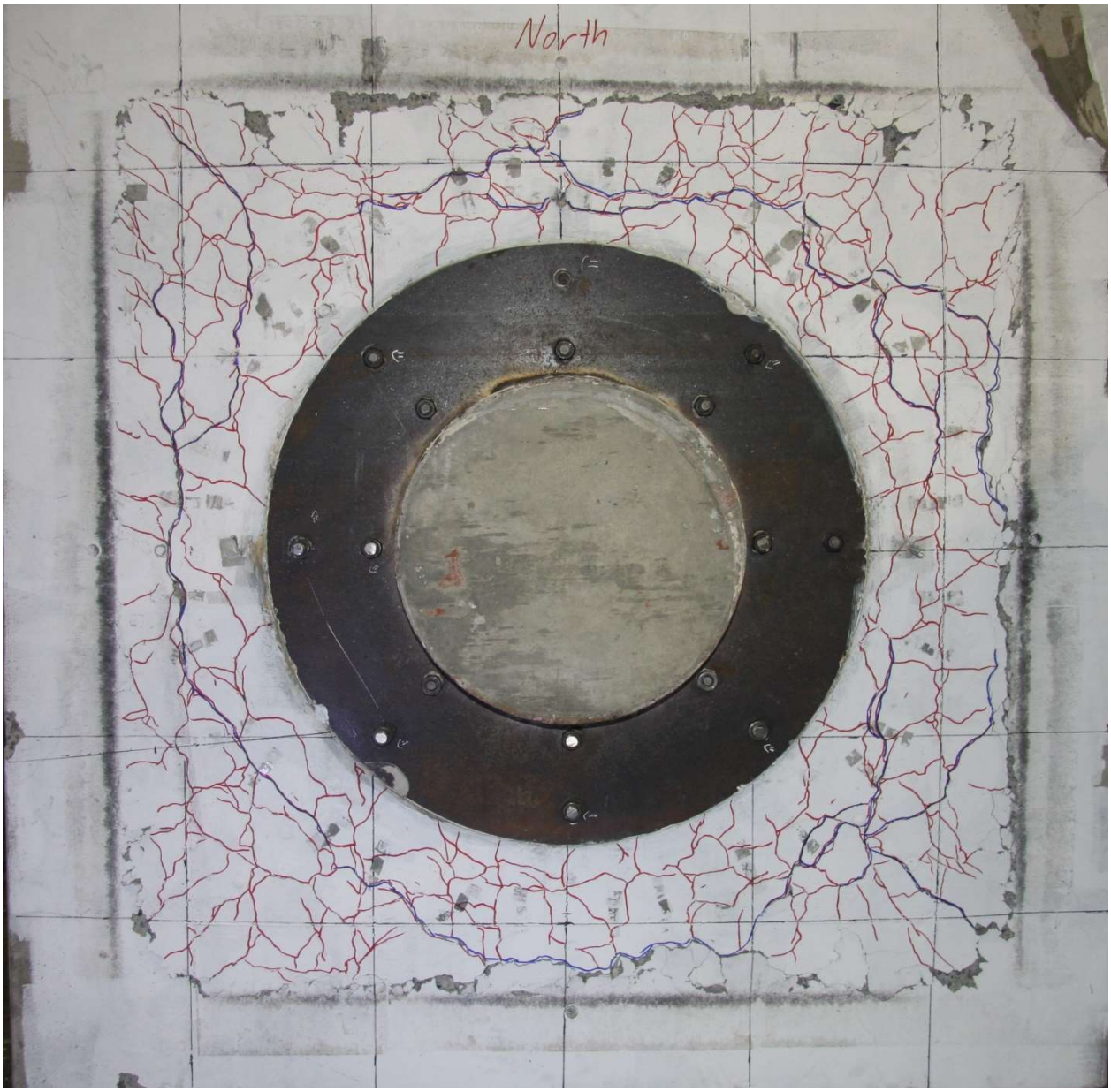

Figure 6.41. Crack Pattern – Load Removed (PTB_9_2_0_P)

The crack pattern in Figure 6.41shows the largest cracks highlighted in blue. The shape of the blue line does not follow a circumferential shape as nicely as the previous punching test. The line intersects with the support boundary on the right and bottom of the photo. It also extends to the corners of the supports in the top left and bottom right of the photo. The crack pattern was effected by the supports and likely failed at a higher strength because of this.

6.3.4 *Displaced Shape*

This section provides the displaced shapes for PTB_9_2_0_P along the centerline of the slab in the north-south and east-west direction.

The initial load step in Figures 6.42 and 6.43 show a larger change in slab displacement than the following load steps due to deformations of the test setup and cotton duck pads. Between 100 and 500 kips the increments of slab displacement are similar and show the slab behaved mostly elastically to this point. Between 500 to 600 kips the string pots attached to the column and ring which include the measurements at locations -10, -14, and -18 in. begin to move relative to each other. This shows that not only is the slab deforming, but the ring is also being engaged. This is also where we see larger deformations for similar changes in force signifying inelastic deformation of the slab. After peak strength the readings on the string pots at the edge of the column begin to move relative to each other show a tilting of the bottom column. The tilting is towards the south and west of the specimen. From 700-600 kips post peak force the largest change in displacements are recorded. Large deformations have resulted in yielding of the majority of strain gauges. At this point there is significant damage and deformations near the supports and the column and ring joint is being mostly restrained by the structural integrity of the flexural reinforcement.

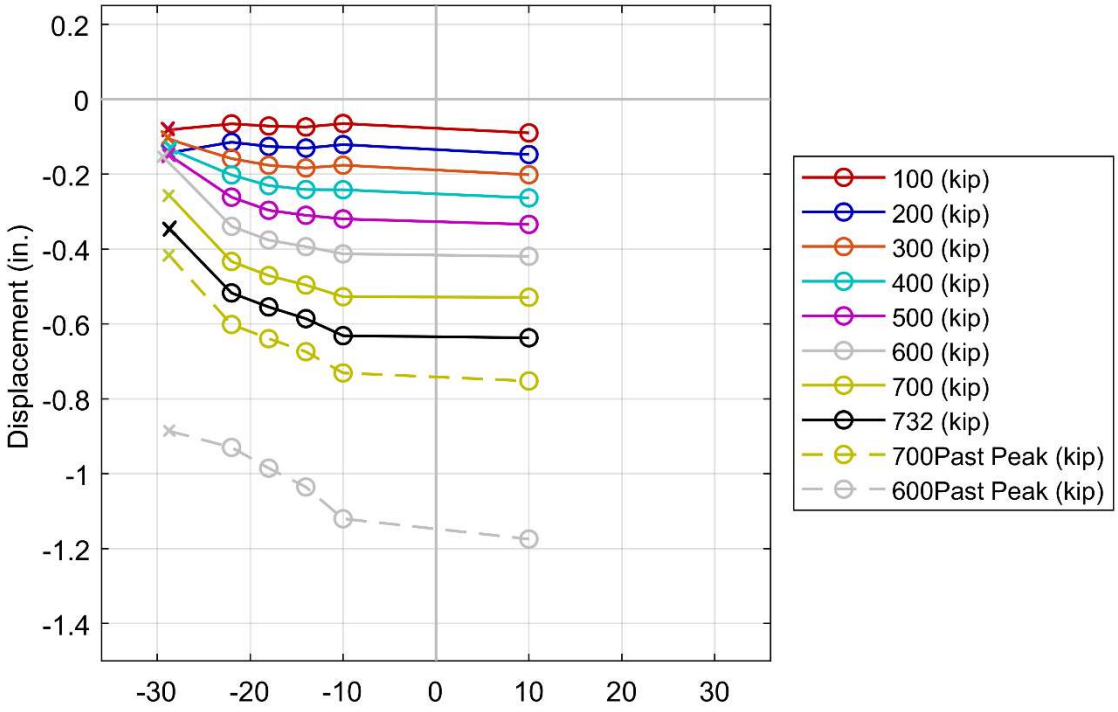

Figure 6.42. Displaced Shape North-South (PTB_9_2_0_P)

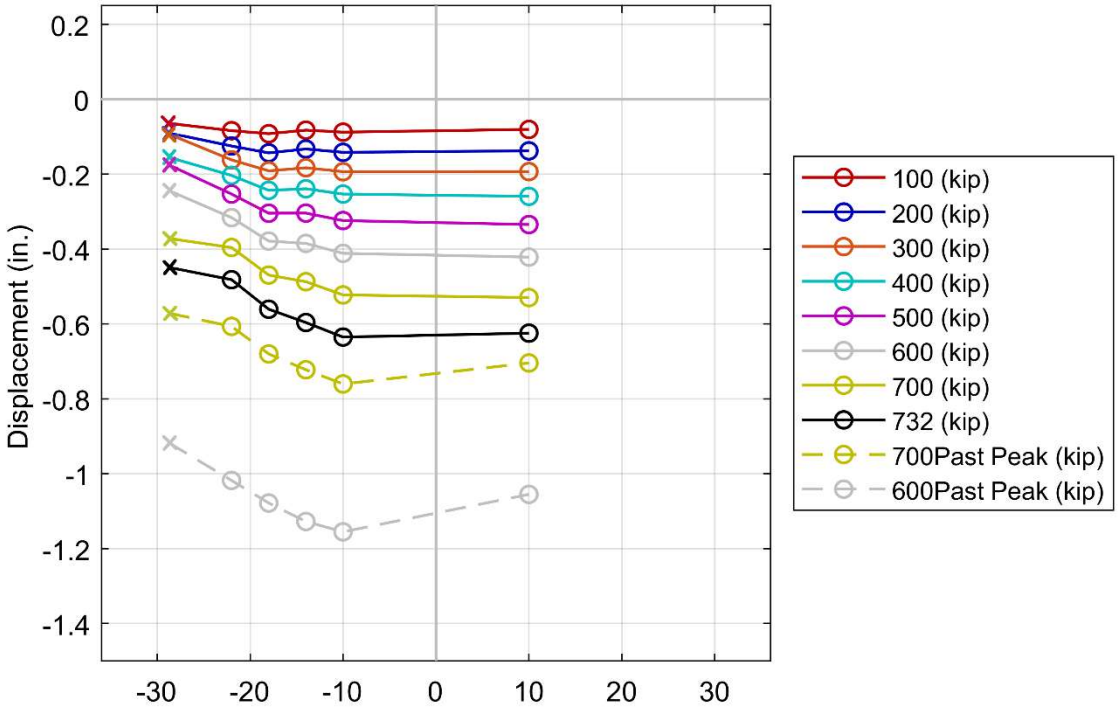

Figure 6.43. Displaced Shape East-West (PTB_9_2_0_P)

Chapter 7. EVALUATION OF RESULTS USING DESIGN EXPRESSIONS

The chapter investigates the accuracy of available codified design expressions from five different US and international codes to predict the strength of the newly proposed connection. The response of the combined-loading specimens were compared for flexure, one-way shear, and two-way shear strengths. The measured strength of the punching specimens' were compared to slab-column connection strength using both nominal punching-shear strength expressions and a shear-friction design model. This chapter is divided into two primary sections. The first compares the measured and predicted strength of the cyclic, combined-loading test specimens. The second section compares the measured and predicted strengths of the punching specimens.

7.1 COMBINED-LOADING CODE PREDICTIONS

Design expressions from five design codes were used to compare three different codified equations to specifically estimate the flexural, one-way, and two-way shear strengths. As described in Chapter 5, the specimens generally responded in a flexural mode and therefore the measured shear force is determined by the flexural strength. As such, it is expected that the shear capacity predicted by the codified equations will be larger than the shear force measured in the tests. Cases where this is not the case and the codified equation predicts a shear capacity less than the peak shear force will be deemed inaccurate.

The equations used in the codes are given in this section. Predicted strength is evaluated using the unit system of the given code and then converted to either imperial or metric units for comparison. The predicted strengths are normalized by the measured test strengths to allow for comparison across the tests. The following codes are used:

- Building Code Requirements for Structural Concrete (ACI 318-19) published by the American Concrete Institute
- Eurocode 2: Design of Concrete Structures – Part 1-1: General rules and rules for buildings (EN 1992-1-1 2004) published by the European Committee for Standardization
- Standard Specifications for Concrete Structures – 2007 (JSCE-SPCS-2007) published by the Japan Society of Civil Engineers

- Design of Concrete Structures (CSA-A23.3-04) published by the Canadian Standards Association
- Concrete Structures Standard (NZS 3101.1:2006) published by Standards New Zealand

Predicted strengths are calculated using the measured material strengths without strength-reduction (also termed resistance) factors, ϕ. To compare the predicted flexural strengths to the predicted shear strengths, the specimen geometry given in Figure 7.1 was used to equate the shear strengths to a corresponding lateral load from the actuator. The equations are given at the end of each the shear sections. In Figure 7.1 the axial load is shown for consistency, but all the measured test strengths have been adjusted to account for moment due to $P - \Delta$ effects.

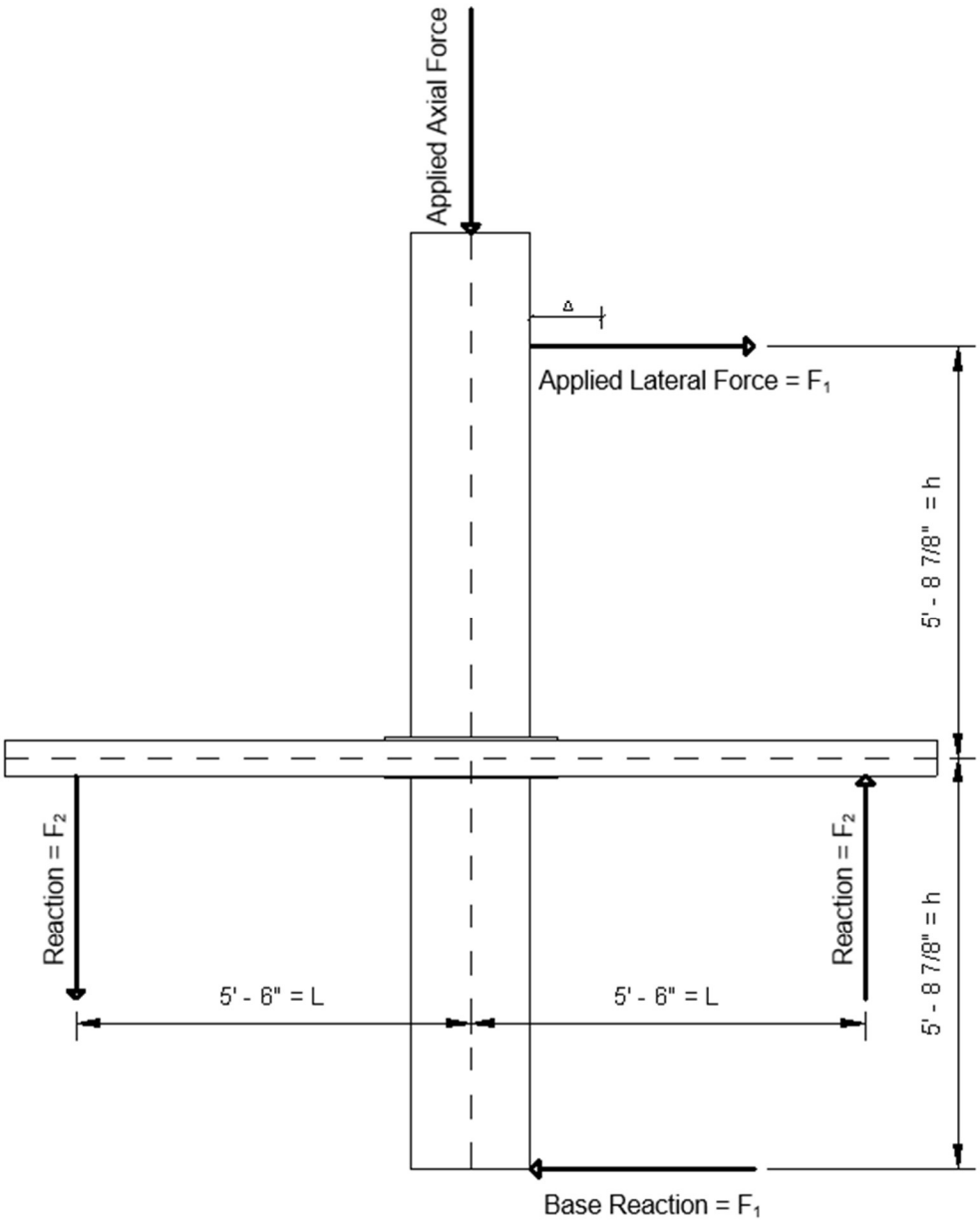

Figure 7.1. Test Geometry

7.1.1 *Combined-Loading Flexural Strength*

The calculation of the flexural capacity is similar for the different codes. They all use a variation of an equivalent rectangular concrete stress distribution to estimate strength. The

variations are provided in Section 22.2 of ACI 318-19, Section 3.1.7 of EN 1992-1-1 2004, Section 9.2.2 of JSCE-SPCS-2007, Section 10.1.7 of CSA-A23.3-04, and Section 7.4 of NZS 3101.1:2006. When determining the width of the slab that contributes to flexural resistance ACI 318-19, CSA-A23.3-04, and NZS 3101.1:2006 had a prescribed effective width that was calculated in a similar fashion. The same effective width calculated by ACI was used.

Equation 7.1 uses the nominal moment capacity, M_n, to calculate the corresponding shear force, V_{Mn}. The moment was assumed to occur at the edge of the ring flange or the column face for the reference stud-rail specimen. The value of V_{Mn} was calculated using Equation 7.2. The MTS actuator force required to reach the nominal moment capacity of each specimen is recorded in Table 7.1

Figure 7.2 uses a bar chart to compare the ratio of the measure-to-predicted strength ratios using the codified effective width. Figure 7.3 presents these ratios using the actual width of the specimen. The expressions provide a more accurate estimate for the thicker slab specimens. The results using the full width are approximately 1 for this approach suggesting that the experiemental setup influenced the flexural capacity which is expected.

$$V_{Mn} = \frac{M_n}{L-(c_1+2*Ring)/2} \tag{7.1}$$

$$F_1 = V_{Mn} * \left(\frac{L}{h}\right) \tag{7.2}$$

Where,

F_1 = MTS actuator force that results in M_n at the edge of the column or ring

M_n = nominal moment capacity of the slab

V_{Mn} = shear corresponding to M_n

h = the distance from the center line of the slab to the applied MTS force (F_1)

L = the distance from the center line of the column to the slab roller support reactions (F_2)

c_1 = dimension of the column in the direction of lateral loading for ACI this is found from assuming a rectangular column with an equivalent area as the circular columns from the test specimens.

Table 7.1. Nominal Flexural Strength

Design Code	PTB_4.5_1_0_6			PTB_9_2_0_6		
	kip	kN	$F_{1,Test}/F_{1,Code}$	kip	kN	$F_{1,Test}/F_{1,Code}$
Measured	35.0	155.8	-	39.0	173.5	-
ACI 318-19	16.5	73.3	2.12	21.3	94.9	1.83
EN 1992-1-1 2004	17.0	75.8	2.06	22.1	98.3	1.76
JSCE-SPCS-2007	16.8	74.9	2.08	21.8	97.1	1.79
CSA-A23.3-04	18.0	79.9	1.94	23.5	104.5	1.66
NZS 3101.1:2006	17.2	76.6	2.03	22.7	101.1	1.72

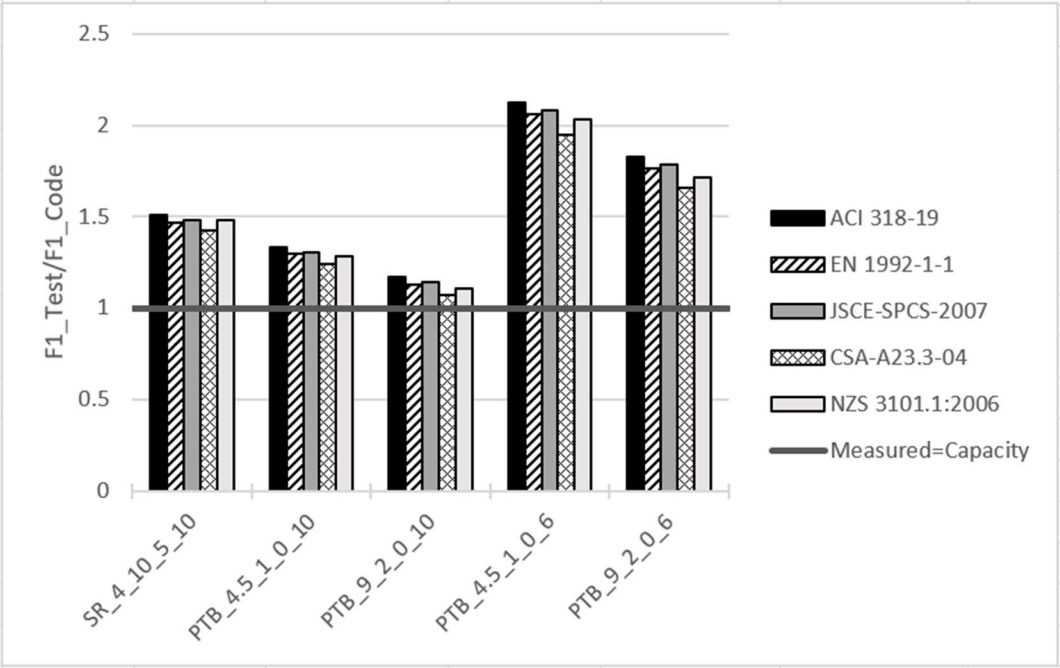

Figure 7.2. Normalized Nominal Flexural Strength – Effective Width

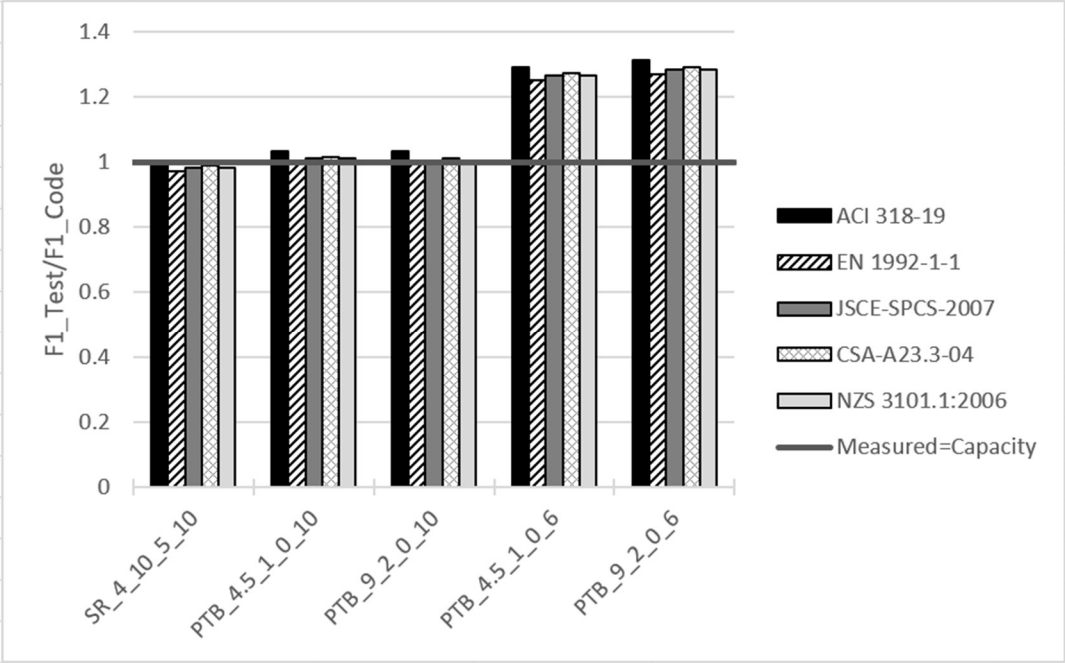

Figure 7.3. Normalized Nominal Flexural Strength – Full Width

7.1.2 *Combined-Loading One-way Shear Strength*

The one-way shear strength was calculated assuming a shear plane across the full width of the slab at the edge of the ring flange for specimens with the new connection or face of the column for the reference stud-rail specimen. The codes use different approaches to estimate this strength. Therefore each subsection describes the equation(s) used to estimate the one-way shear strength for a single code. The final section compares the ratio of the predicted to measured strength ratios. Again, it is important to recall that the code equations are expected to estimate a shear strength larger than the peak force because the specimens responded in flexure. Resulting in the ratios in the plots being less than one.

7.1.2.1 ACI 318-19 One-way Shear Strength

Nominal one-way shear strength is calculated following the provisions of Section 22.5 of ACI 318-19. The one-way shear strength is the summation of shear capacity attributed to the concrete mechanism and shear capacity attributed to transverse shear reinforcement.

$$V_n = V_c + V_s \tag{7.3}$$

Where,

V_n = nominal shear strength (lb.)

V_c = nominal shear strength provided by concrete (lb.)

V_s = nominal shear strength provided by transverse shear reinforcement (lb.)

If $A_v \geq A_{v,min}$, V_c is calculated using either of the following equations:

$$V_c = \left[2\lambda\sqrt{f'_c} + \frac{N_u}{6A_g}\right] b_w d \tag{7.4}$$

$$V_c = \left[8\lambda(\rho_w)^{1/3}\sqrt{f'_c} + \frac{N_u}{6A_g}\right] b_w d \tag{7.5}$$

If $A_v < A_{v,min}$, V_c is calculated using

$$V_c = \left[8\lambda_s\lambda(\rho_w)^{1/3}\sqrt{f'_c} + \frac{N_u}{6A_g}\right] b_w d \tag{7.6}$$

Where,

A_v = area of shear reinforcement in spacing s (in.^{2})

λ_s = factor used to modify shear strength based on the effects of member depth, commonly Referred to as the size effect factor

λ = modification factor to reflect the reduced mechanical properties of lightweight concrete relative to normalweight concrete of the same compressive strength

ρ_w = ratio of A_s to $b_w d$

f'_c = specified compressive strength of concrete (psi)

N_u = factored axial force normal to cross section occurring simultaneously with V_u or T_u; to be taken as positive for compression and negative for tension (lb.)

A_g = gross area of concrete section (in.^{2})

b_w = web width or diameter of circular section (in.)

d = distance from extreme compression fiber to centroid of longitudinal tension reinforcement (in.)

When shear reinforcement is present, V_s is calculated using Equation 7.7.

$$V_s = \frac{A_v f_{yt} d}{s} \tag{7.7}$$

Where,

A_v = area of shear reinforcement within spacing s (in.)

f_{yt} = specified yield strength of transverse reinforcement (psi)

s = center-to-center spacing transverse reinforcement (in.)

The values used in calculating the one-way shear strength are tabulated in Table 7.2.

Table 7.2. ACI 318-19 One-way Shear Strength

Design Code	PTB_4.5_1_0_6	PTB_9_2_0_6
V_n (kip)	49.5	50.1
V_c (kip)	49.5	50.1
V_s (kip)	0	0
f'_c (psi)	7430	7620
b_w (in.)	72.0	72.0
d (in.)	4.88	4.88
λ	1.0	1.0
λ_s	1.0	1.0
N_u (kip)	0	0
A_g (in.^{2})	432	432
ρ_w	0.011	0.011
A_v (in.^{2})	-	-
f_{yt} (ksi)	-	-
s (in.)	-	-

7.1.2.2 EN 1992-1-1 2004 One-way Shear Strength

The nominal one-way shear capacity is calculated using Section 6.2 of EN 1992-1-1 2004. When no shear reinforcement is present, the capacity can be calculated using Equation 7.8.

$$V_{Rd,c} = \left[C_{Rd,c}k(100\rho_l f_{ck})^{1/3} + k_1\sigma_{cp}\right]b_w \mathrm{d} \tag{7.8}$$

Where,

$V_{Rd,c}$ = the design shear resistance of the member without shear reinforcement

$C_{Rd,c}$ = value considering the constant concrete resistance factor, γ_c

k = factor related to depth of member

ρ_l = flexural reinforcement ratio for tensile steel

f_{ck} = characteristic compressive cylinder strength of concrete (MPa)

k_1 = factor accounting for axial loading of cross-section

σ_{cp} = normal stress of the cross section due to axial force (MPa)

b_w = the smallest width of the cross-section in the tensile area (mm)

d = effective depth of cross-section (mm)

The nominal one-way shear strength when shear reinforcement is present is given by Equation 7.9.

$$V_{Rd} = V_{Rd,s} + V_{ccd} + V_{td} \tag{7.9}$$

$$V_{Rd,s} = \frac{A_{sw}}{s} z f_{ywd} \cot(\theta) \tag{7.10}$$

Where,

V_{Rd} = design value of the shear force which can be sustained by the member (N)

$V_{Rd,s}$ = design value of the shear force which can be sustained by the yielding shear reinforcement (N)

V_{ccd} = design value of the shear component of the force in the compression area, in the case of an inclined compression chord (N)

V_{td} = design value of the shear component of the force in the tensile reinforcement, in the case of an inclined tensile chord (N)

A_{sw} = cross-sectional area of the shear reinforcement (mm^2)

s = spacing of shear reinforcement (mm)

z = the inner level arm, for a member with constant depth, corresponding to the bending moment in the element under consideration. In the shear analysis of reinforced concrete without axial force, the approximate value $z = 0.9d$ may normally be used (mm)

f_{ywd} = design yield strength of the shear reinforcement (MPa)

θ = angle between the concrete compression strut and the beam axis perpendicular to the shear force

The values used to calculate the one-way shear strength for the test specimens are given in Table 7.3.

Table 7.3. EN 1992-1-1 2004 One-way Shear Strength

Design Code	PTB_4.5_1_0_6	PTB_9_2_0_6
V (kN)	330	333
$V_{Rd,c}$ (kN)	330	333
V_{Rd} (kN)	0	0
$V_{Rd,s}$ (kN)	0	0
V_{ccd} (kN)	0	0
V_{td} (kN)	0	0
f_{ck} (MPa)	51.2	52.5
d (mm)	124	124
b_w (mm)	1830	1830
$C_{Rd,c}$	0.18	0.18
k	2.34	2.34
k_1	0.15	0.15
ρ_l	0.011	0.011
σ_{cp} (MPa)	0	0
A_{sw} (mm^2)	0	0
f_{ywd} (MPa)	0	0
s (mm)	0	0
z (mm)	100	100
θ (°)	45	45

7.1.2.3 JSCE-SPCS-2007 One-way Shear Strength

The nominal one-way shear resistance is calculated following Section 9.2.2.2 of the JSCE-SPCS-2007. The section calculates the sum of the strength of different components, including concrete, shear reinforcement, and prestress contributions shown in the equation below.

$$V_{yd} = V_{cd} + V_{sd} + V_{ped} \tag{7.11}$$

Where,

V_{yd} = design shear capacity

V_{cd} = design shear capacity of linear members without shear reinforcing steel

V_{sd} = design shear capacity of shear reinforcement

V_{ped} = component of effective tensile force in longitudinal tendon parallel to the shear force

The contribution of the nominal shear capacity due to concrete is given by Equation 7.12.

$$V_{cd} = \beta_d \beta_p \beta_n f_{vcd} b_w d / \gamma_b \quad (7.12)$$

Where,

β_d = factor accounting for effective depth of member

β_p = factor that is a function of the flexural reinforcement ratio of the member

β_n = factor accounting for axial force on the cross section

f_{vcd} = design compressive strength of the concrete (MPa)

b_w = width of the web (mm)

d = effective depth of member (mm)

γ_b = resistance factor usually taken as 1.3

The contribution of one-way shear capacity due to the presence of shear reinforcement is given in Equation 7.13.

$$V_{sd} = \left[\frac{A_w f_{wyd}(sin\alpha_s + cos\alpha_s)}{S_s} + A_{pw}\sigma_{pw}(sin\alpha_p + cos\alpha_p)/S_p\right] z/\gamma_b \qquad (7.13)$$

Where,

A_w = total area of shear reinforcement placed in S_s (mm^2)

f_{wyd} = design yield strength of shear reinforcement (MPa)

α_s = angle between shear reinforcement and member axis

S_s = spacing of shear reinforcement (mm)

A_{pw} = total area of prestressing steel expected to act as shear reinforcement placed in S_p (mm^2)

σ_{pw} = tensile stress in prestressing steel acting as shear reinforcement when shear reinforcing steel yields

α_p = angle between prestressing steel acting as shear reinforcement and member axis

S_p = spacing of prestressing steel expected to act as shear reinforcement (mm)

z = distance from location of compressive stress resultant to centroid of tension steel (mm)

γ_b = member resistance factor, generally taken as 1.10

The contribution of the nominal one-way shear capacity due to axial force of prestressing strand is given by Equation 7.14.

$$V_{ped} = P_{ed}\sin\alpha_p/\gamma_b \qquad (7.14)$$

Where,

P_{ed} = effective tensile force in longitudinal prestressing steel

α_p = angel between extreme compression fiber and member axis

γ_b = resistance factor, generally 1.10

The calculated values for one-way shear strength following JSCE-SPCS-2007 are given in the Table 7.4.

Table 7.4. JSCE-SPCES-2007 One-way Shear Strength

Design Code	PTB_4.5_1_0_6	PTB_9_2_0_6
V_{yd} (kN)	232	232
V_{cd} (kN)	232	232
V_{sd} (kN)	0	0
V_{ped} (kN)	0	0
f_{ved} (MPa)	0.72	0.72
d (mm)	114	114
b_w (mm)	1830	1830
β_d	1.50	1.50
β_p	1.03	1.03
β_n	1	1
γ_b	1	1
f_{ywd} (MPa)	-	-
A_w (mm^2)	-	-
α_s (°)	-	-
S_s (mm)	-	-
σ_{pw} (MPa)	-	-
A_{pw} (mm^2)	-	-
α_p (°)	-	-
S_p (m)	-	-
z (mm)	105	105
P_{ed} (kN)	0	0

7.1.2.4 CSA-A23.3-04 One-way Shear Strength

The nominal one-way shear strength for the Canadian code can be found in section 11.3.3 of CSA-A23.3-04. The nominal shear strength can be found using Equation 7.15. Since there was no prestressing of the specimen V_p is taken as zero.

$$V_r = V_c + V_s + V_p \tag{7.15}$$

Where,

V_r = factored shear resistance (N)

V_c = shear resistance attributed to the concrete factored by ϕ_c

V_s = shear resistance attributed to shear reinforcement factored by ϕ_s

V_p = component in the direction of the applied shear of the effective prestressing force factored by ϕ_p

The contribution of the nominal shear capacity due to concrete is found using Equation 7.16.

$$V_c = \phi_c \lambda \beta \sqrt{f'_c} b_w d_v \tag{7.16}$$

Where,

ϕ_c = resistance factor for concrete

λ = factor to account for low-density concrete

β = factor accounting for shear resistance of cracked concrete

f'_c = specified compressive strength of concrete

b_w = beam web width or diameter of circular cross section

d_v = effective shear depth, taken as the greater of $0.9d$ or $0.72h$

For the contribution of the nominal shear capacity due to shear reinforcement perpendicular to the longitudinal axis Equation 7.17 is used.

$$V_s = \frac{\phi_s A_v f_y d_v cot\theta}{s} \tag{7.17}$$

Where,

ϕ_s = resistance factor for non-prestressed reinforcing bars

A_v = area of shear reinforcement within a distance s

f_y = specified yield strength of non-prestressed reinforcement or anchor steel

θ = angle of inclination of diagonal compressive stresses to the longitudinal axis of the member

s = spacing of shear or torsion reinforcement measured parallel to the longitudinal axis of the member

The values used to calculate the one-way shear strength following CSA-A23.3-04 are given in Table 7.5.

Table 7.5. JSCE-SPCES-2007 One-way Shear Strength

Design Code	PTB_4.5_1_0_6	PTB_9_2_0_6
V_r (kN)	298	301
V_c (kN)	298	301
V_s (kN)	0	0
V_p (kN)	0	0
f'_c (MPa)	51.2	52.5
d_v (mm)	110	110
b_w (mm)	1830	1830
β	0.207	0.207
λ	1	1
ϕ_c	1	1
f_y (MPa)	-	-
A_v (mm^2)	-	-
s (mm)	-	-
θ (mm)	35	35
ϕ_s (kN)	1	1

7.1.2.5 NZS 3101.1:2006 One-way Shear Strength

The nominal one-way shear strength is calculated by using Section 7.5 of NZS 3101.1:2006. The shear strength is calculated using Equation 7.18.

$$V_n = V_s + V_c \tag{7.18}$$

Where,

V_n = total nominal shear strength of cross section of beam (N)

V_s = nominal shear strength provided by the shear reinforcement (N)

V_c = nominal shear strength provided by the concrete (N)

The nominal shear strength provided by concrete mechanisms is given by Equation 7.19.

$$V_c = v_c A_{cv} \tag{7.19}$$

$$v_c = k_d k_a v_b \tag{7.20}$$

Where,

v_c = shear resisted by concrete (MPa)

A_{cv} = effective shear area (mm^2)

k_d = factor allowing for the influence of member depth on shear strength

k_a = factor allowing for the influence of aggregate size on shear strength

v_b = basic shear stress (MPa)

The nominal shear resistance provided by the shear reinforcement perpendicular to the longitudinal axis of the beams is found using Equation 7.21.

$$V_s = A_v f_{yt} \frac{d}{s} \tag{7.21}$$

Where,

A_v = area of shear reinforcement perpendicular to the span within distance s (mm)

f_{yt} = lower characteristic yield strength of transverse reinforcement (MPa)

d = distance from extreme compression fiber to neutral axis at the balanced strain conditions (mm)

s = spacing of transverse reinforcement in direction parallel to longitudinal reinforcement (mm)

The resulting values for the nominal one-way shear strength using the method presented by the NZS 3101.1:2006 are tabulated below.

Table 7.6. NZS 3101.1:2006 One-way Shear Strength

Design Code	PTB_4.5_1_0_6	PTB_9_2_0_6
V_n (kN)	264	264
V_c (kN)	264	264
V_s (kN)	0	0
v_c (MPa)	1.26	1.26
A_{cv} (mm^2)	209000	209000
k_d	1	1
k_a	1	1
v_b (MPa)	1.26	1.26
A_v (mm^2)	0	0
f_{yt} (MPa)	-	-
d (mm)	114	114
s (mm)	-	-

7.1.2.6 Predicted One-way Shear Strength

The required applied horizontal force corresponding to the calculated one-way shear strength was calculated using Equation 1.22. The maximum applied force was compared with these values. The measured-to-predicted strengths are presented in Figure 7.4. As expected all predicted strengths are higher than the measured force. This is consistent with the flexural mechanism that was observed during testing.

$$F_1 = \frac{L*V_n}{h} \quad (7.22)$$

Where,

F_1 = MTS force corresponding to development of the codified one-way shear strength

L = distance from the column centerline to the slab end roller reaction force

V_n = nominal one-way shear strength of the slab

h = distance from the slab centerline to the level of the applied force

Table 7.7. MTS Force to Reach Nominal One-way Shear Strength

Design Code	PTB_4.5_1_0_6			PTB_9_2_0_6		
	kip	kN	$F_{1,Test}/F_{1,Code}$	kip	kN	$F_{1,Test}/F_{1,Code}$
Measured	35.0	155.8	-	39.0	173.5	-
ACI 318-19	47.4	210.9	0.74	48.01	213.6	0.81
EN 1992-1-1 2004	71.1	316.3	0.49	71.7	319.0	0.54
JSCE-SPCS-2007	50.0	222.4	0.70	50.0	222.4	0.78
CSA-A23.3-04	64.1	285.3	0.55	64.9	288.8	0.60
NZS 3101.1:2006	56.9	253.0	0.62	56.9	253.0	0.69

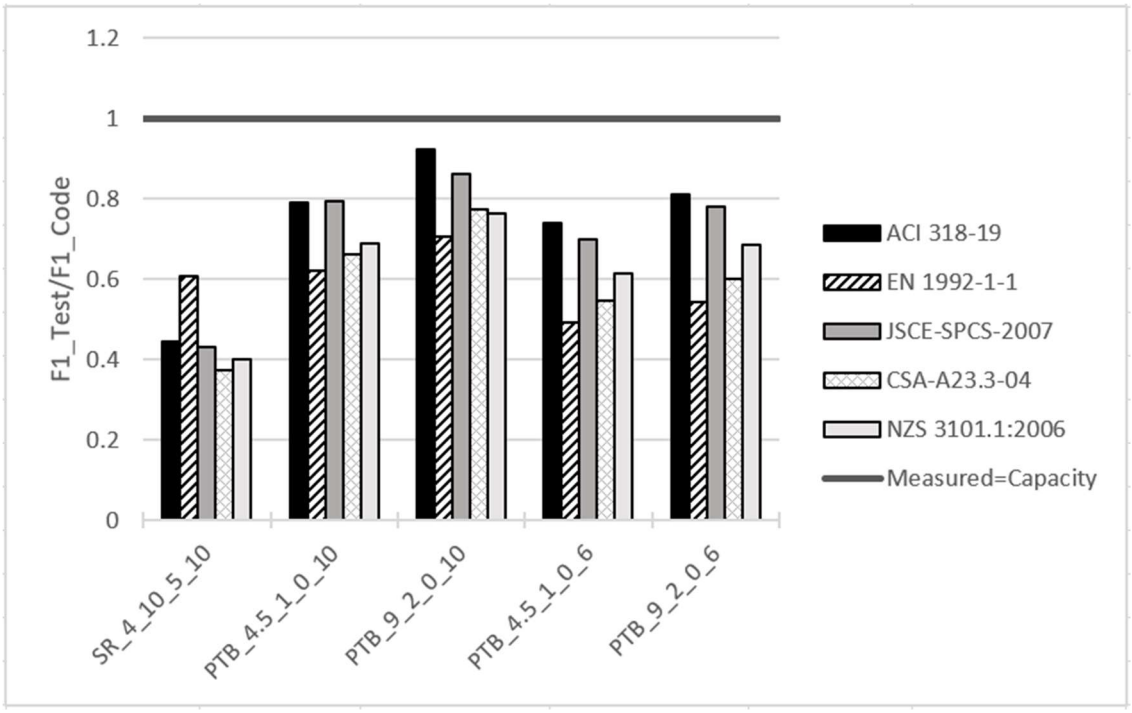

Figure 7.4. Normalized Nominal One-way Shear Strength

7.1.3 *Combined-Loading Two-way Shear Strength*

This section provides the equations used by the different codes to predict the two-way shear strength. The process includes finding a critical perimeter that allows for estimation of the area of the shear plane. For the specimens with the new connection, the confined region to the edge of the ring was as a shear cap. Therefore, the critical perimeter was outside of the ring flange. The nominal two-way shear capacity was used to calculate the force needed to reach this strength. Again, it is expected that these specimens would have a peak force less than the predicted shear strength since all of the specimens responded in flexure.

7.1.3.1 ACI 318-19 Two-way Shear Strength

The nominal two-way shear capacity is calculated using Section 22.6. When there is no shear reinforcement Equation 7.23 is used.

$$v_n = v_c \tag{7.23}$$

Where,

v_n = equivalent concrete stress corresponding to nominal two-way shear strength of slab or footing (psi)

v_c = stress corresponding to nominal two-way shear strength provided by concrete (psi)

When there is no shear reinforcement, v_c is calculated as the lesser of the following equations.

$$v_c = 4\lambda_s\lambda\sqrt{f'_c} \tag{7.24}$$

$$v_c = \left(2 + \frac{4}{\beta}\right)\lambda_s\lambda\sqrt{f'_c} \tag{7.25}$$

$$v_c = \left(2 + \frac{\alpha_s d}{b_0}\right)\lambda_s\lambda\sqrt{f'_c} \tag{7.26}$$

Where,

λ_s = factor used to modify shear strength based on the effects of member depth, commonly referred to as the size effect factor

λ = modification factor to reflect the reduced mechanical properties of lightweight concrete relative to normalweight concrete of the same compressive strength

f'_c = specified compressive strength of concrete (psi)

β = ratio of long to short dimensions: for sides of column

α_s = constant used to calculate V_c in slab footings

d = distance from extreme compression fiber to centroid of longitudinal tension reinforcement (in)

b_0 = perimeter of critical section for two-way shear in slabs and footings

The nominal two-way shear capacity when shear reinforcement is present can be calculated using Equation 7.27.

$$v_n = v_c + v_s \tag{7.27}$$

When shear reinforcement is present, v_c can be calculated using the lesser of the following equations. Equation 7.31 is used to calculate v_s.

$$v_c = 3\lambda_s\lambda\sqrt{f'_c} \tag{7.28}$$

$$v_c = \left(2 + \frac{4}{\beta}\right)\lambda_s\lambda\sqrt{f'_c} \tag{7.29}$$

$$v_c = \left(2 + \frac{\alpha_s d}{b_0}\right)\lambda_s\lambda\sqrt{f'_c} \tag{7.30}$$

$$v_s = \frac{A_v f_{yt}}{b_0 s} \tag{7.31}$$

Where,

v_s = equivalent concrete stress corresponding to nominal two-way shear strength provided by reinforcement (psi)

A_v = area of shear reinforcement within spacing s (in.^{2})

f_{yt} = specified yield strength of transverse reinforcement (psi)

s = center-to-center spacing of items, transverse reinforcement (psi)

The calculated values following ACI 318-19 for the nominal two-way shear strength are tabulated below.

Table 7.8. ACI 318-19 Two-way Shear Strength

Design Code	PTB_4.5_1_0_6	PTB_9_2_0_6
v_n (psi)	301	277
v_c (psi)	301	277
v_s (psi)	0	0
f'_c (psi)	7430	7620
d (in.)	4.88	4.88
b_0 (in.)	121	153
λ_s	1	1
λ	1	1
β	1	1
α_s	40	40
A_v (in.^{2})	-	-
f_{yt} (ksi)	-	-
s (in.)	-	-

In the commentary of Section 8.4.4.2.3, Equation 7.32 is given to account for effects of unbalanced moment transfer from the column to the slab. The unbalanced moment capacity of the slab can be set to equal the two-way shear capacity and the shear due to gravity loading is assumed to be negligible due to redistribution of the dead load to the slab end roller supports. The unbalanced moment can then be solved for and converted into a corresponding MTS load that would cause two-way shear failure. The resulting values are given in Table 7.9.

$$v_{u,AB} = v_{uv} + \frac{\gamma_v M_{sc} c_{AB}}{J_c} \quad (7.32)$$

Where,

$v_{u,AB}$ = factored shear stress along line AB, one of the sides of the critical perimeter perpendicular to direction of unbalanced moment

v_{uv} = factored shear stress on the slab critical section for two-way action, from the controlling load combination, without moment transfer (psi)

γ_v = factor used to determine the fraction of M_{sc} transferred by eccentricity of shear at slab-column connections

M_{sc} = factored slab moment that is resisted by the column at a joint (in.-lb)

c_{AB} = distance from center of column to line AB

J_c = property of assumed critical section analogous to polar moment of inertia (in.^{4})

Table 7.9. ACI 318-19 Unbalanced Moment Shear Calculation

Design Code	PTB_4.5_1_0_6	PTB_9_2_0_6
M_{sc} (kip-in.)	4140	6090
$v_{u,AB}$ (psi)	301	277
v_{uv} (psi)	0	0
γ_v	0.4	0.4
c_{AB} (in.)	15.1	19.1
J_c (in.^{4})	83100	16800

7.1.3.2 EN 1992-1-1 2004 Two-way Shear Strength

The nominal two-way shear strength is calculated following Section 6.4 of EN 1992-1-1 2004. When there is no shear reinforcement, the two-way shear strength can be found using Equation 7.33.

$$v_{Rd,c} = C_{Rd,c}k(100\rho_l f_{ck})^{1/3} + k_1\sigma_{cp} \geq (v_{min} + k_1\sigma_{cp}) \quad (7.33)$$

Where,

$v_{Rd,c}$ = design value of the punching shear resistance of a slab without punching shear reinforcement along the control section considered

$C_{Rd,c}$ = factor considering the concrete resistance factor γ_c for concrete

k = factor related to depth of member, similar to size factor

ρ_l = reinforcement ratio for longitudinal reinforcement

f_{ck} = characteristic compressive cylinder strength of concrete at 28 days (MPa)

k_1 = factor accounting for axial force on the cross-section

σ_{cp} = normal stresses on the concrete in the critical section (MPa)

v_{min} = minimum shear stress (MPa)

The nominal two-way shear resistance when shear reinforcement is present can be calculated using Equation 7.34.

$$v_{Rd,cs} = 0.75v_{Rd,c} + 1.5\left(\frac{d}{s_r}\right)A_{sw}f_{ywd,ef}\left(\frac{1}{u_1 d}\right)sin\alpha \quad (7.34)$$

Where,

$v_{Rd,cs}$ = design value of the punching shear resistance of a slab with punching shear reinforcement along the control section considered

d = mean effective depth of the slab, which may be taken as $(d_y + d_z)/2$

s_r = radial spacing of perimeters of shear reinforcement (mm)

A_{sw} = area of one perimeter of shear reinforcement around the column (mm^2)

$f_{ywd,ef}$ = effective design strength of the punching shear reinforcement (MPa)

u_1 = length of the basic control perimeter (mm)

α = angle between the shear reinforcement and the plane of the slab

The values found from calculating the nominal two-way shear strength following EN 1992-1-1 2004 for the specimens are in Table 7.10.

Table 7.10. EN 1992-1-1 2004 Two-way Shear Strength

Design Code	PTB_4.5_1_0_6	PTB_9_2_0_6
$v_{Rd,c}$ (MPa)	1.37	1.39
v_{min} (MPa)	0.708	0.717
$v_{Rd,cs}$ (MPa)	1.03	1.04
f_{ck} (MPa)	647	647
d (mm)	124	124
u_1 (mm)	3750	4470
$C_{Rd,c}$	0.18	0.18
k	2	2
k_1	0.1	0.1
ρ_l	0.011	0.011
σ_{cp} (MPa)	0	0
A_{sw} (mm^2)	-	-
$f_{ywd,ef}$ (MPa)	-	-
s_r (mm)	-	-
α (°)	-	-

In section 6.4.3 of EN 1992-1-1 2004, the relationship between the unbalanced moment and the shear stress on the critical section is described. Combining the given equations and assuming the shear due to gravity can be neglected due to redistribution of the load into the slab end roller supports results in Equation 7.37.

$$v_{ed} = \beta \frac{V_{Ed}}{u_i d} \tag{7.35}$$

$$\beta = 1 + k\frac{M_{Ed}}{V_{Ed}} * \frac{u_1}{W_1} \tag{7.36}$$

$$v_{ed} = \frac{V_{Ed}}{u_i d} + k\frac{M_{Ed}}{W_1 d} \tag{7.37}$$

Where,

v_{ed} = maximum shear stress on the perimeter (MPa)

V_{Ed} = shear force acting on the perimeter (N)

u_i = length of the control perimeter being considered (mm)

M_{Ed} = unbalanced moment being transferred from the slab to column (N-mm)

W_1 = corresponds to a distribution of shear and is a function of the basic control perimeter (mm)

The unbalanced moment capacity of the slab can be found by setting $\max(v_{Rd,c}, v_{Rd,cs}) = v_{Ed}$. In solving for the unbalanced moment capacity, the corresponding MTS force required for two-way shear failure can be found. The calculated values are tabulated below.

Table 7.11. EN 1992-1-1 2004 Unbalanced Moment Shear Calculation

Design Code	PTB_4.5_1_0_6	PTB_9_2_0_6
M_{Ed} (kN-m)	423	610
V_{Ed} (kN)	0	0
v_{Ed} (MPa)	1.37	1.39
u_i (mm)	3750	4470
d_{eff} (mm)	114	114
W_1 (mm^2)	1616000	2312000

7.1.3.3 JSCE-SPCS-2007 Two-way Shear Strength

The nominal two-way shear strength of the test specimens can be calculated using Section 9.2.2.3 of JSCE-SPCES-2007. The nominal two-way shear strength is calculated using Equation 7.38.

$$V_{pcd} = \beta_d \beta_p \beta_r f'_{pcd} u_p d / \gamma_b \quad (7.38)$$

Where,

V_{pcd} = design punching shear strength (N)

β_d = factor dependent upon the depth of the member, similar to size factor

β_p = factor dependent upon longitudinal reinforcement ratio

β_r = factor dependent upon ratio of peripheral length of loaded area to effective depth of member

f'_{pcd} = design strength of the concrete (MPa)

u_p = peripheral length of the design cross section located at a distance $d/2$ from the loaded area (mm)

d = effective depth (mm)

γ_b = member factor generally taken as 1.3

Due to the JSCE-SPCS-2007 not having a method to relate the unbalanced moment to the two-way shear capacity was not converted to a corresponding MTS force for comparison.

7.1.3.4 CSA-A23.3-04 Two-way Shear Strength

Nominal two-way shear strength is calculated following Section 13.3 of CSA-A23.3-04. When no shear reinforcement is present the predicted shear strength can be calculated using Equation 7.39 where v_c is the least of Equations 7.40, 7.41, and 7.42.

$$v_r = v_c \quad (7.39)$$

$$v_c = \left(1 + \frac{2}{\beta_c}\right) 0.19\lambda\phi_c\sqrt{f'_c} \tag{7.40}$$

$$v_c = \left(\frac{\alpha_s d}{b_0} + 0.19\right) \lambda\phi_c\sqrt{f'_c} \tag{7.41}$$

$$v_c = 0.38\lambda\phi_c\sqrt{f'_c} \tag{7.42}$$

Where,

v_r = factored shear stress resistance (MPa)

v_c = factored shear stress resistance provided by the concrete (MPa)

β_c = ratio of long side to short side of concentrated load or reaction area

λ = factor to account for low-density concrete

ϕ_c = resistance factor for concrete

f'_c = specified compressive strength of concrete (MPa)

α_s = factor that adjusts v_c for support dimensions

d = distance from extreme compression fiber to centroid of longitudinal tension reinforcement, but need not be less than $0.8h$ for prestressed members and circular sections (mm)

b_0 = perimeter of critical section for shear in slabs and footings (mm)

When shear reinforcement is present, the equations for finding the predicted two-way shear capacity are as follows.

$$v_r = v_c + v_s \tag{7.43}$$

$$v_c = 0.28\lambda\phi_c\sqrt{f'_c} \tag{7.44}$$

$$v_s = \frac{\phi_s A_{vs} f_{yv}}{b_0 s} \tag{7.45}$$

Where,

v_s = factored shear stress resistance provided by shear reinforcement (MPa)

ϕ_s = resistance factor for non-presstressed reinforcing bars

A_{vs} = cross-sectional area of headed shear reinforcement on a line parallel to the perimeter of the column (mm^2)

f_{yv} = specified yield strength of headed shear reinforcement (MPa)

s = spacing of headed shear reinforcement or stirrups measured perpendicular to b_0 (mm)

The resulting values from calculating the nominal two-way shear strength following CSA-A23.3-04 are presented below.

Table 7.12. CSA-A23.3-04 Two-way Shear Strength

Design Code	PTB_4.5_1_0_6	PTB_9_2_0_6
v_r (MPa)	2.58	2.35
v_c (MPa)	2.58	2.35
v_s (MPa)	0	0
f'_c (MPa)	51.2	52.5
d (mm)	114	114
b_0 (mm)	2670	3390
λ	1	1
β_c	1	1
α_s	4	4
ϕ_c	1	1
f_{yv} (MPa)	-	-
A_{vs} (mm^2)	-	-
s (mm)	-	-
ϕ_s	1	1

The fraction of unbalanced moment transferred by eccentricity of shear can be used to find the relationship between two-way shear capacity and unbalanced moment. This relationship is used to solve for the MTS force required to cause two-way shear failure in the specimens. The unbalanced moment relationships are given by the following equations.

$$\gamma_v = 1 - \frac{1}{1+\frac{2}{3}\sqrt{\frac{b_1}{b_2}}} \tag{7.46}$$

$$v_f = \frac{V_f}{b_0 d} + \frac{\gamma_v M_f e}{J} \tag{7.47}$$

Where,

γ_v = fraction of unbalanced moment transferred by eccentricity of shear at slab-column connections

b_1 = width of the critical section for shear measured in the direction of the span for which moments are determined (mm)

b_2 = width of the critical section for shear measured in the direction perpendicular to b_1 (mm)

v_f = factored shear stress

V_f = factored shear force

M_f = unbalanced moment about the centroid of the critical shear section (N-mm)

e = distance from centroid of section for critical shear to point where shear stress is being calculated (mm)

J = property of the critical shear section analogous to the polar moment of inertia (mm^4)

The unbalanced moment capacity can be found by setting $v_f = v_r$ and assuming that the shear force due to gravity is zero due to redistribution of the self-weight of the slab to the slab end roller supports. The values used to find the unbalanced moment capacity are given below.

Table 7.13. CSA-A23.3-04 Unbalanced Moment Shear Calculation

Design Code	PTB_4.5_1_0_6	PTB_9_2_0_6
M_f (kN-m)	525	760
V_f (kN)	0	0
v_f (MPa)	2.58	2.35
d_{eff} (mm)	114	114
b_0 (mm)	2670	3390
γ_v	0.4	0.4
e (mm)	425	540
J (mm^4)	34600000000	69700000000

7.1.3.5 NZS 3101.1:2006 Two-way Shear Strength

The nominal two-way shear strength is calculated using Section 12.7.3 of NZS 3101.1:2006. The two-way shear strength is given by Equation 7.48.

$$V_n = V_s + V_c \tag{7.48}$$

Where,

V_n = nominal shear strength of section (N)

V_s = nominal shear strength provided by the shear reinforcement (N)

V_c = nominal shear strength provided by concrete mechanisms (N)

$$V_c = v_c b_0 d \tag{7.49}$$

Where,

v_c = shear stress resisted by concrete (MPa)

b_0 = perimeter of critical section for slabs and foundations (mm)

d = distance from extreme compression fiber to centroid of tension reinforcement (mm)

When there is no shear reinforcement present the nominal two-way shear stress capacity due to concrete contribution can be found as the least of the following equations.

$$v_c = \frac{1}{6} k_{ds} \left(1 + \frac{2}{\beta_c}\right) \sqrt{f'_c} \tag{7.50}$$

$$v_c = \frac{1}{6} k_{ds} \left(\frac{\alpha_s d}{b_0} + 1\right) \sqrt{f'_c} \tag{7.51}$$

$$v_c = \frac{1}{3} k_{ds} \sqrt{f'_c} \tag{7.52}$$

Where,

k_{ds} = factor allowing for the influence of size on v_c

β_c = ratio of long side to short side of concentrated load or reaction area

f'_c = specified compressive strength of concrete (MPa)

α_s = factor accounting for columns

When shear reinforcement is present the nominal two-way shear strength can be found by adding the contribution of two-way shear strength due to shear reinforcement to the contribution of the two-way shear strength due to concrete. The contribution due to concrete can be found by taking the least of Equations 7.50, 7.51, 7.52, and 7.53. The contribution due to shear reinforcement is given in Equation 7.54.

$$v_c = \frac{1}{6}\sqrt{f'_c} \tag{7.53}$$

$$V_s = A_v f_{yv} \frac{d}{s} \tag{7.54}$$

Where,

A_v = area of shear reinforcement within a distance s (mm^2)

f_{yv} = lower characteristic yield strength of vertical (stirrup) reinforcement (MPa)

s = center-to-center spacing of shear or torsional reinforcement measured in the direction parallel to the longitudinal reinforcement (mm)

The calculated values for the nominal two-way shear strength following NZS 3101.1:2006 are tabulated below.

Table 7.14. NZS 3101.1:2006 Two-way Shear Strength

Design Code	PTB_4.5_1_0_6	PTB_9_2_0_6
V_n (kN)	730	851
v_n (MPa)	2.08	1.92
b_0 (mm)	3070	3880
d (mm)	114	114
f'_c (MPa)	51.2	52.5
k_{ds}	1	1
β_c	1	1
α_s	20	20
f_{yv} (MPa)	-	-
A_v (mm^2)	-	-
s (mm)	-	-

Section C12.7.7 discusses the unbalanced moment transfer. By setting the $v_n = v_{AB}$ Section C12.7.7 can be used to find the unbalanced moment capacity. The unbalanced moment capacity is then used to calculate the corresponding MTS force required to cause two-way shear failure of the specimen. The following equation gives the relationship between shear stress and unbalanced moment.

$$v_{AB} = \frac{V^*}{A_c} + \frac{\gamma_v M^* c_{AB}}{J_c} \tag{7.55}$$

Where,

v_{AB} = maximum design shear stress on section AB (MPa)

V^* = Design shear force at section at the ultimate limit state (N)

A_c = area of concrete section resisting shear transfer (mm^2)

γ_v = fraction of unbalanced moment considered to be transferred by eccentricity of shear

M^* = Ultimate resisting moments per unit width (N-mm)

c_{AB} = distance from centroid of loaded area to edge AB of the critical section, edge AB is perpendicular to the direction of loading

J_c = property of assumed critical section analogous to polar moment of inertia (mm^4)

V^* is assumed to be zero due to redistribution of the self-weight of the slab to slab end roller supports during testing. The calculated values in solving for the unbalanced moment capacity are given below.

Table 7.15. NZS 3101.1:2006 Unbalanced Moment Shear Calculation

Design Code	PTB_4.5_1_0_6	PTB_9_2_0_6
M^* (kN-m)	551	782
V^* (kN)	0	0
v_{AB} (MPa)	2.08	1.92
A_c (mm^2)	351000	443000
γ_v	0.4	0.4
c_{AB} (mm)	326	428
J_c (mm^4)	34600000000	69700000000

7.1.3.6 Combined Loading Two-way Predicted Shear Strength

The MTS force needed to cause two-way shear failure can be found using Equation 7.56. The calculated forces are recorded in Table 7.16. Figure 7.5 shows the predicted capacity of each code normalized by the measured maximum strength. For the two-way shear equations, many of the code capacities were similar to the measured strengths.

- EN 1992-1-1 2004 tended to predict the lowest two-way shear capacity resulting in both 6 in. slab specimens equaling or surpassing the predicted two-way shear capacity.
- From the Figure 7.5 the EN 1992-1-1 2004 is shown predicting lower strengths than ACI 318-19 in the case of the thin slab specimens and PTB_9_2_0_10. This indicates that EN 1992-1-1 2004 predicts lower strengths for specimens with thin slabs and larger critical perimeters than ACI 318-19.
- ACI 318-19, CSA A23.3-04, and NZS 3101.1:2006 follow a similar method for prediction of two-way shear strength only varying in the way the shear stress due to concrete contribution is calculated. This results in a larger difference in strength between ACI 318-19 and CSA A23.3-04 when the slabs are thinner.
- ACI 318-19 and NZS 3101.1:2006 show the biggest difference in strength predictions for the specimens with the smallest critical perimeters.

$$F_1 = \frac{0.5 * M_{unb}}{h} \quad (7.56)$$

Where,

F_1 = Applied lateral force corresponding to development of the codified two-way shear strength

M_{unb} = unbalanced moment applied to specimen to cause two-way shear failure

h = distance from the slab centerline to the level of the applied force

Table 7.16. MTS Force to Reach Nominal Two-way Shear Capacity

Design Code	PTB_4.5_1_0_6			PTB_9_2_0_6		
	kip	kN	$F_{1,Test}/F_{1,Code}$	kip	kN	$F_{1,Test}/F_{1,Code}$
Measured	35.0	155.8	-	39.0	173.5	-
ACI 318-19	30.0	133.6	1.17	44.2	196.5	0.88
EN 1992-1-1 2004	27.2	120.9	1.29	39.2	174.5	0.99
CSA A23.3-04	33.7	150.1	1.04	48.8	217.3	0.80
NZS 3101.1:2006	35.4	157.6	0.99	50.3	223.6	0.78

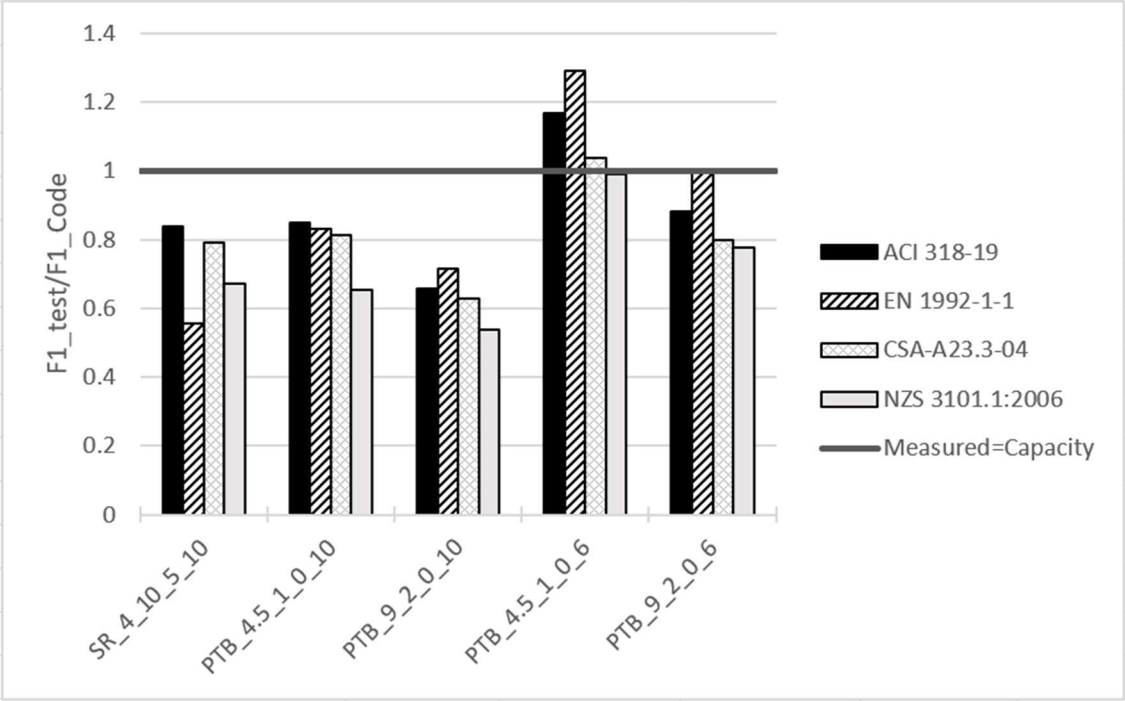

Figure 7.5. Normalized Nominal Two-way Shear Strength

7.1.4 *Predicted Failure Mode*

This section provides the predicted failure mode of each specimen. The measured MTS lateral force is normalized by the predicted strength for each of the five codes used for the combined-loading specimens. It should be noted that all specimens were observed to fail in flexure. There is a single figure for each specimen. Figures 7.6 to 7.10 provides the measured-to-predicted strength ratios for Specimens SR_4_10_5_10, PTB_4.5_1_0_10, PTB_9_2_0_10, PTB_4.5_1_0_6, PTB_9_2_0_6, respectively.

- Figure 7.6, Figure 7.7, and Figure 7.8 all predict flexural failure of the test specimens with 10 in. slabs.
- The predicted capacity of the specimens in one-way shear were greater than two-way shear with the exception of the NZS 3101.1:2006 for PTB_4.5_1_0_10, and all of the codes except EN 1992-1-1 for specimen PTB_9_2_0_10.

- When examining the 6 in. slab specimens, Figure 7.9 shows the measured-to-predicted strength ratio of PTB_4.5_1_0_6 surpassing the two-way shear capacity. However, the measured-to-predicted two-way shear strengths ratios were all less than the measured-to-predicted flexural strength ratios with the exception of EN 1992-1-1.
- PTB_9_2_0_6 shows a clear distinction between the capacities due to flexure and two-way shear.
- All codes predict a flexural failure confirming the observed behavior of the test.

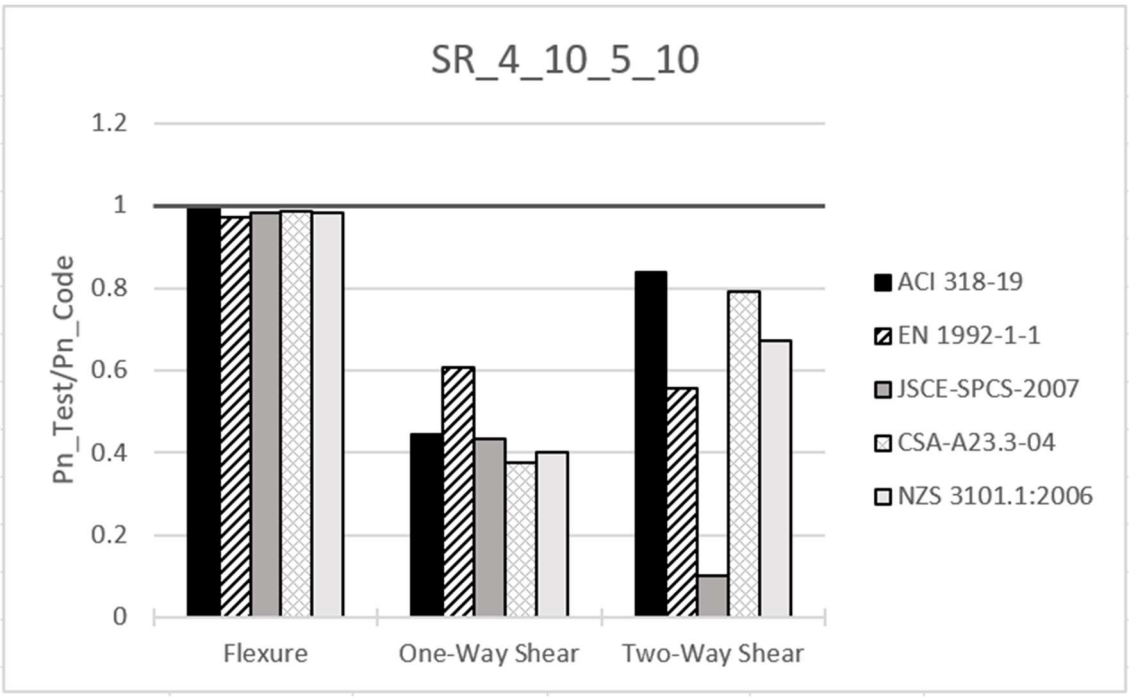

Figure 7.6. SR_4_10_5_10 Normalized Predicted Capacity

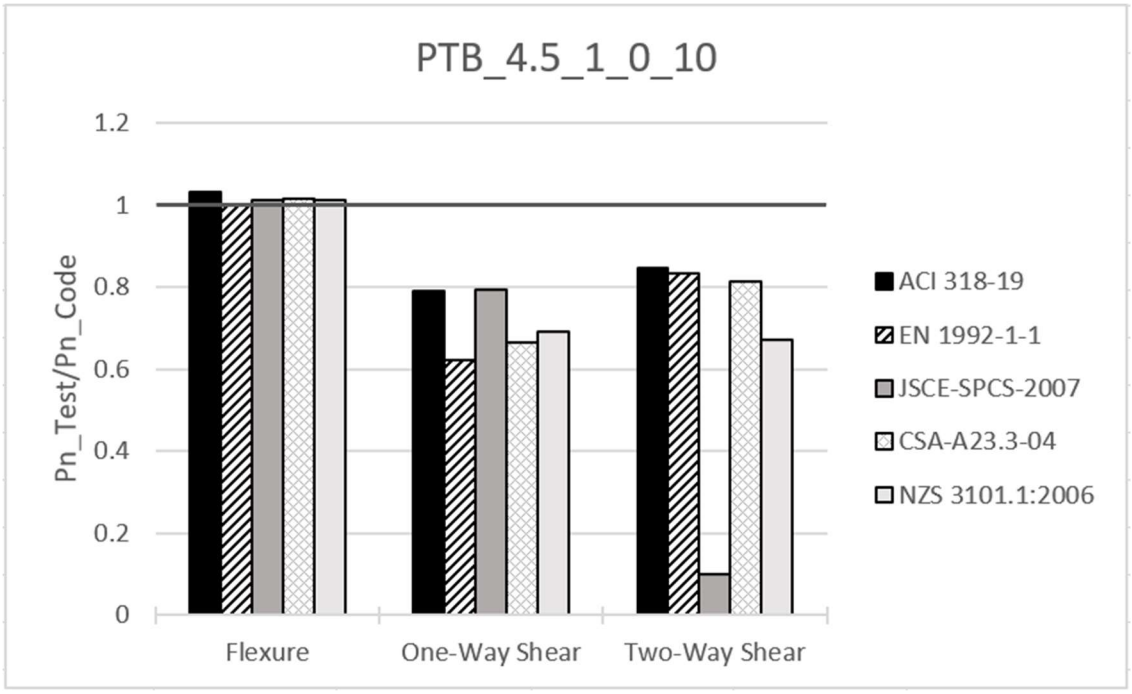

Figure 7.7. PTB_4.5_1_0_10 Normalized Predicted Capacity

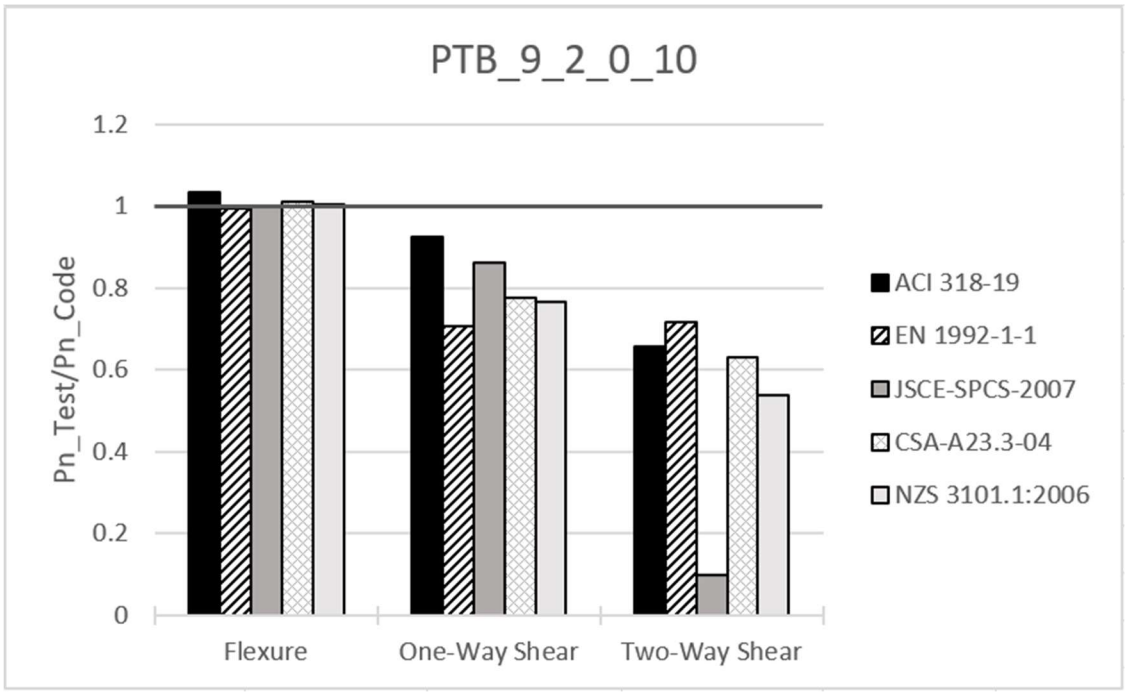

Figure 7.8. PTB_9_2_0_10 Normalized Predicted Capacity

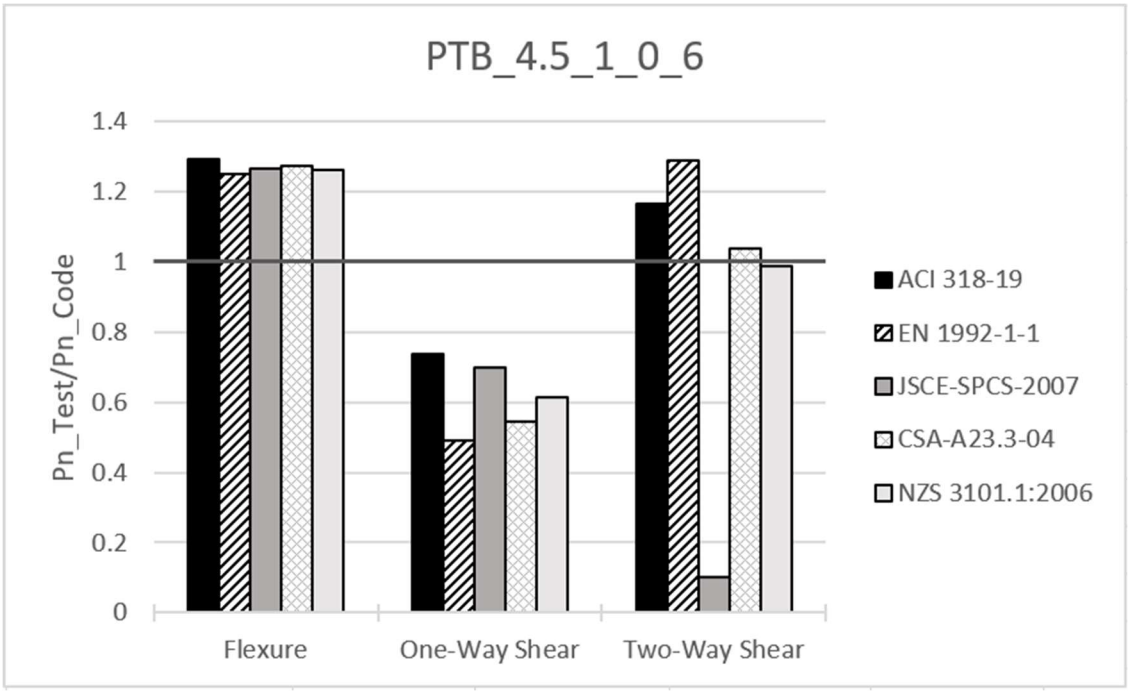

Figure 7.9. PTB_4.5_1_0_6 Normalized Predicted Capacity

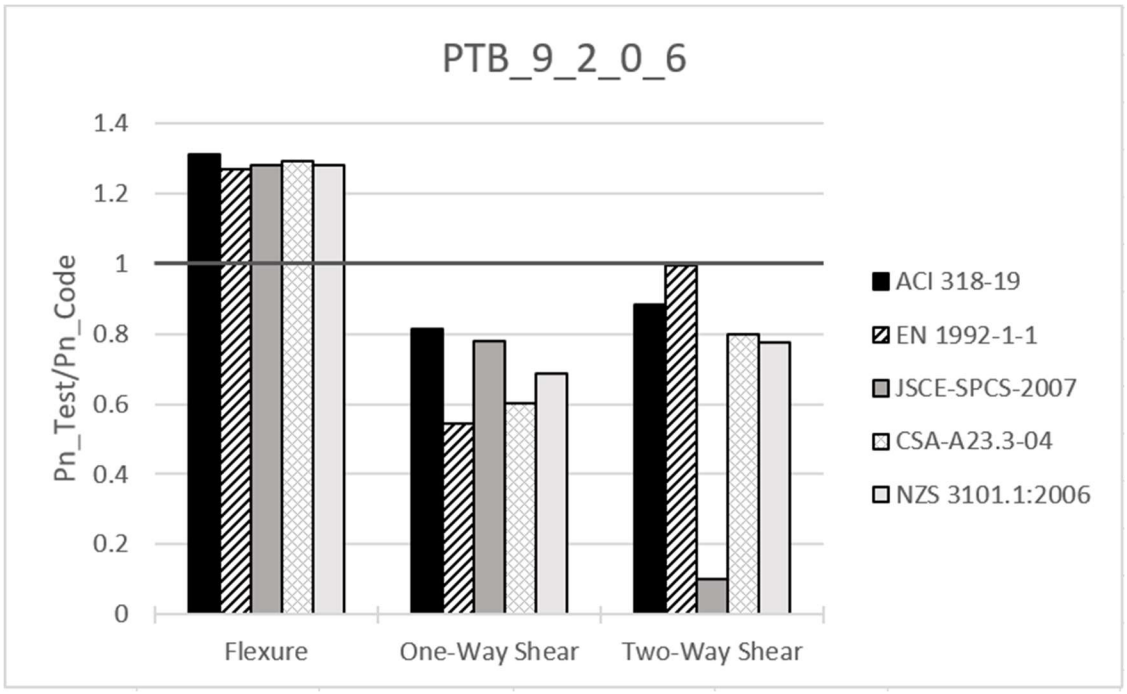

Figure 7.10. PTB_9_2_0_6 Normalized Predicted Capacity

7.2 PUNCHING SHEAR CODE PREDICTIONS

The punching shear tests were designed using equations from three codes. The following section provides the equations from the codes and compares the measured test strengths to the predicted values.

7.2.1 *Punching Shear Two-way Shear Strength*

The following section will describe the process for predicting the two-way shear capacity for three different codes/models, then provide the calculated values for each. The codes/models used where ACI 318-19, KCI 2012 provided by Jang (2019), and a shear friction model developed by Birkle (2003).

7.2.1.1 ACI 318-19 Two-way Shear Strength

The nominal two-way shear capacity can be found in Section 22.6 of ACI 318-19. It equates the nominal strength to the contribution of concrete mechanisms and shear reinforcement. The punching shear specimens have no shear reinforcement outside of the ring and therefore rely on the concrete and flexural reinforcement to resist punching failure. The critical perimeter is defined in Section 22.6.4 and allows for circular columns to be treated as square columns with an equivalent area which is the process that was used for this section. The nominal two-way capacity is found using Equation 7.57 and multiplying the resulting stress by the shear area given by $b_0 d$.

$$v_n = v_c \tag{7.57}$$

Where,

v_n = equivalent concrete stress corresponding to nominal two-way shear strength of slab or footing (psi)

v_c = stress corresponding to nominal two-way shear strength provided by concrete (psi)

The shear stress two-way shear capacity due to concrete mechanisms is taken as the least of the following equations.

$$v_c = 4\lambda_s\lambda\sqrt{f'_c} \tag{7.58}$$

$$v_c = \left(2 + \frac{4}{\beta}\right)\lambda_s\lambda\sqrt{f'_c} \tag{7.59}$$

$$v_c = \left(2 + \frac{\alpha_s d}{b_0}\right)\lambda_s\lambda\sqrt{f'_c} \tag{7.60}$$

Where,

λ_s = factor used to modify shear strength based on the effects of member depth, commonly referred to as the size effect factor

λ = modification factor to reflect the reduced mechanical properties of lightweight concrete relative to normalweight concrete of the same compressive strength

f'_c = specifies compressive strength of concrete (psi)

β = ratio of long to short dimensions: clear spans for two-way slabs, sides of column, concentrated load or reaction area, or sides of a footing

α_s = constant used to calculate V_c in slabs and footings

d = distance from extreme compression fiber to centroid of longitudinal tension reinforcement (in.)

b_0 = perimeter of critical section for two-way shear in slabs and footings (in.)

The values calculated following the methods of ACI 318-19 to find predict the nominal two-way shear capacity are tabulated below.

Table 7.17. ACI 318-19 Two-way Shear Calculation

	PTB_4.5_1_0_P	PTB_9_2_0_P
V_c (kips)	366	460
v_c (ksi)	0.321	0.326
λ_s	1	1
λ	1	1
β	1	1
α_s	40	40
d (in.)	8.38	8.38
b_0 (in.)	136	168

7.2.1.2 KCI 2012 Two-way Shear Strength

The version of KCI 2012 that was used for this research was found in a paper from Jang (2019). The paper lists the equations used by the code to predict two-way shear strength with brief descriptions of the variables. Following the process from the paper the nominal two-way shear strength according to KCI is given by the following equations.

$$V_{c,KCI} = v_{c,KCI} b_0 d \tag{7.61}$$

$$v_{c,KCI} = k_s k_{b0} f_{te} cot\psi (c_u/d) \tag{7.62}$$

$$c_u = d\left[25\sqrt{\rho/f_{ck}} - 300(\rho/f_{ck})\right] \tag{7.63}$$

Where,

$V_{c,KCI}$ = nominal two-way shear strength of the concrete determined by KCI 2012

$v_{c,KCI}$ = shear stress corresponding to the nominal two-way shear strength of the concrete determined by KCI 2012

b_0 = length of the critical shear perimeter (mm)

d = effective thickness of the slab (mm)

k_s = thickness factor

k_{b0} = effect factor of the critical section length

f_{te} = tensile strength of the compression zone in concrete

ψ = crack angle of the compression zone in concrete

c_u = average depth of the compression zone in concrete

ρ = flexural reinforcement ratio

f_{ck} = compressive strength of the concrete

The resultant values from the calculations are tabulated below.

Table 7.18. KCI 2012 Two-way Shear Calculation

	PTB_4.5_1_0_P	PTB_9_2_0_P
$V_{c,KCI}$ (kN)	1830	2067
$v_{c,KCI}$ (MPa)	2.49	2.27
d (mm)	213	213
b_0 (mm)	3460	4270
k_s	1	1
k_{b0}	0.992	0.893
f_{te} (MPa)	1.40	1.43
$cot\psi$	4.70	4.75
c_u	81.1	80.0
ρ (%)	1.79	1.79
f_{ck}	44.3	46.1

7.2.1.3 Shear Friction Model

The shear friction model was found in a paper from 2003 by Birkle et al. The model is a modification of a shear friction model for beams, developed by Loov et al. (2002), to accommodate flat plate slabs. The nominal two-way shear capacity can be found using the following equations.

$$V_{sf} = 2V_{45}\left(\sqrt{\frac{F}{V_{45}} + cot^2(\theta)} - cot(\theta)\right)\left(1 + cot^2(\theta)\right) - Fcot(\theta) + \sum V_{si} \quad (7.64)$$

$$V_{45} = \lambda\phi_c\beta_v\sqrt{f'_c}[p_0 + \pi(x_{out} + 2x_{bot})]h \quad (7.65)$$

$$\beta_v = 0.36\left(\frac{30}{f'_c}\right)^{1/4}\left(\frac{500}{h}\right)^{1/4} \quad (7.66)$$

$$F = \rho_{ave}(p_0 + 4\pi d_{ave})d_{ave}f_y \quad (7.67)$$

Where,

V_{sf} = nominal two-way shear strength of the shear friction model

V_{45} = shear strength along a plane inclined at 45°

F = force in the flexural reinforcement

θ = angle of the failure plane (for slabs without shear reinforcement assumed to be 27°)

V_{si} = force of one element of shear reinforcement crossed by the shear crack

λ = factor to account for concrete density

ϕ_c = resistance factor for concrete

β_v = calibration factor obtained from best fit analysis

f'_c = specified compressive strength of concrete

p_0 = column periphery

x_{out} = horizontal component of the failure plane

x_{bot} = distance from column at which failure plane begins to form, for slabs it is assumed to equal zero.

h = thickness of the slab

ρ_{ave} = average reinforcement ratio of the two directions

d_{ave} = average effective depth of the slab in the two directions

f_y = yield strength of reinforcement

The nominal two-way shear strength values calculated following the shear friction model are given in Table 7.19.

Table 7.19. KCI 2012 Two-way Shear Calculation

	PTB_4.5_1_0_P	PTB_9_2_0_P
V_{sf} (kN)	1064	1369
V_{45} (kN)	2730	3290
F (kN)	9680	11200
θ (°)	27	27
λ	1	1
ϕ_c	1	1
β_v	0.387	0.383
f'_c (MPa)	44.3	46.1
p_0 (mm)	2610	3420
x_{out} (mm)	499	499
h (mm)	254	254
ρ_{ave} (%)	1.79	1.79
d_{ave} (mm)	213	213
f_y (MPa)	481	481

7.2.2 *Punching Shear Predicted Strength Comparison*

This section will compare the experimental results to the predictions. Below are the tabulated results of the punching shear tests as well as the predicted two-way shear capacity for each of the methods described in the previous section.

Table 7.20. Two-way Shear Strength vs. Capacity

Design Code	PTB_4.5_1_0_6			PTB_9_2_0_6		
	kip	kN	$F_{1,Test}/F_{1,Code}$	kip	kN	$F_{1,Test}/F_{1,Code}$
Measured	523.4	2328.3	-	731.9	3255.5	-
ACI 318-19	363.6	1617.5	1.44	457.8	2036.3	1.60
KCI 2012	411.6	1831.1	1.27	464.6	2066.5	1.58
Birkle SF	239.1	1063.6	2.19	307.7	1368.8	2.38

The codes all under predict the strength of the connection. With the shear friction being the least accurate. For the shear friction model, a crack angle of 27° is assumed. Due to setup restraints the angle of cracking for the punching test was closer to 45°. When 45° is substituted into the shear friction model the following predictions are found.

Table 7.21. Two-way Shear Strength vs. Capacity (Adjusted)

Design Code	PTB_4.5_1_0_6			PTB_9_2_0_6		
	kip	kN	$F_{1,Test}/F_{1,Code}$	kip	kN	$F_{1,Test}/F_{1,Code}$
Measured	523.4	2328.3	-	731.9	3255.5	-
ACI 318-19	363.6	1617.5	1.44	457.8	2036.3	1.60
KCI 2012	411.6	1831.1	1.27	464.6	2066.5	1.58
Birkle SF	452.6	2013.1	1.16	591.2	2629.6	1.24

The strength predictions are still conservative, but improve significantly in their accuracy. The angle of cracking in ACI 318-19 and KCI 2012 are assumed to be 45.

Differences between the equations are that the KCI equation accounts for the contribution of the flexural reinforcement where ACI neglects this in calculating the strength. The shear-friction approach uses the reinforcement ratio and the strength of the reinforcement. Table 7.21 shows there is a benefit of including the flexural reinforcement as these expressions provide a better prediction of the strength than the ACI equation.

As noted in the observations of the punching test specimens in Chapter 6, PTB_9_2_0_P's behavior was likely impacted by interference at the support making the result higher than if tested in a test frame with a larger footprint. To compare this to the PTB_4.5_1_0_P the measured

strengths were used to back calculate a modifying factor of $\sqrt{f'_c}$. The results are given in Table 7.22. PTB_4.5_1_0_P was unaffected by the test setup and shows a higher factor than ACI which is accurate to how this connection would behave in punching without interference of the test setup. The difference between PTB_4.5_1_0_P and PTB_9_2_0_P is more reflective of the effects of the setup and therefore should not be considered for practical purposes.

Table 7.22. Calculated $\sqrt{f'_c}$ Modifying Factors

Specimen	$\sqrt{f'_c}$ Modifying Factor
ACI	4
PTB_4.5_1_0_P	5.72
PTB_9_2_0_P	6.35

Chapter 8. SUMMARY, CONCLUSIONS, AND FUTURE WORK

The experimental test program continued investigation into the proposed connection. Thin slab specimens were tested to investigate if slab depth was a variable to consider in design of the ring size. Additional specimens were tested to investigate the two-way shear behavior of the connection. This section will summarize the experimental testing, observed behaviors, list of conclusions, and suggestions for future research.

8.1 SUMMARY OF RESEARCH

CFSTs provide qualities beneficial allowing columns to undergo high lateral demands with minimal damage. This makes them uniquely suited to Vertical evacuation structures. The limiting factor of CFSTs are the connection to RC slabs. This experimental program builds on a previous study that showed a viable connection for CFSTs to RC slabs. The connection consists of the following:

- CFST columns above and below the slab
- Longitudinal continuity reinforcement welded to the lower CFST column extending into upper column to allow for transfer of loading
- Steel ring welded to the CFST column ends
- Steel ring has holes to allow for post-tensioned bolts to fasten columns to the slab and provide confinement of the slab-column joint

The previous study tested different variations of the connection. The current study furthered that research with the testing of four full scale tests. Two thin slab specimens subjected to gravity and lateral loading and two specimens tested in pure punching. The thin slab specimens focus on finding a relationship between the depth of the slab and the size of the ring flange. Punching tests investigate punching behavior of the connection filling in a gap in understanding from the previous tests. A summary of the specimens is as follows:

- PTB_4.5_1_0_6
    - Utilizes the post-tensioned bolt connection with a ring flange width of 4.5 in.

    - 1 row of bolts placed in the middle of the ring
    - 6 in. slab depth making the ring flange approximately equal to the effective depth of the slab
- PTB_9_2_0_6
    - Uses the proposed connection with a 9 in. ring flange
    - 2 rows of bolts placed on the ring flange spaced at 4.5 in. apart, with the first row being 2.25 in. from the column face
    - 6 in. slab depth making the ring flange approximately equal to twice the effective depth of the slab
- PTB_4.5_1_0_P
    - Proposed connection with 4.5 in. ring flange
    - 1 row of bolts placed at the middle of the ring flange
    - 10 in. slab depth making the ring flange equal to approximately half the effective slab depth
- PTB_9_2_0_P
    - Proposed connection with 9 in. ring flange
    - 2 rows of bolts spaced at 4.5 in. with the first row being 2.25 in. from the column face
    - 10 in. slab depth making ring flange approximately equal to the effective slab depth.

Testing of the connection was carried out in three phases. Phase 1 conducted by Yeutter, Phase 2 was the combined-loading tests on thin slab specimens and Phase 3 was the punching tests. Phase 2 specimens were tested under axial loading of the column by the Universal Baldwin Testing machine and cycled to different target displacements until the measured lateral force had lost 40% of the peak measured value. The axial loading and lateral displacement history were the same as tests from Phase 1 to allow for comparison of the tests. The punching specimens were supported on the edges of the slab with a load applied to center of the slab via the column. The slab edges imitate inflection points of the slab and therefore were not restrained.

During Phases 1 and 2 observations of the damage states of the combined-loading specimens were made which allowed for comparison with the previous study. The resulting points summarize the findings:

- Test specimens reach peak strength around the initiation of spalling, with the exception of PTB_4.5_1_0_10, which spalled early potentially due to two previous low drift tests.
- Specimens without a ring flange equal to or greater than the effective depth of the slab begin to loss strength after spalling. The other specimens plateau at the strength until initiation of crushing.
- Figure 8.1 shows that spalling and crushing occurred at higher drifts for post-tensioned bolt connections with a ring flange equal to or greater than the effective depth of slab
- Figures 8.2 and 8.3 show that the 10 in. slab specimens engaged more reinforcement across the slab at similar drift levels than 6 in. slab specimens.
- Figure 8.3 shows strain gauges with a strain reading of yield or higher were concentrated along the tangent to north and south edges of ring flange in 6 in. slab specimens.

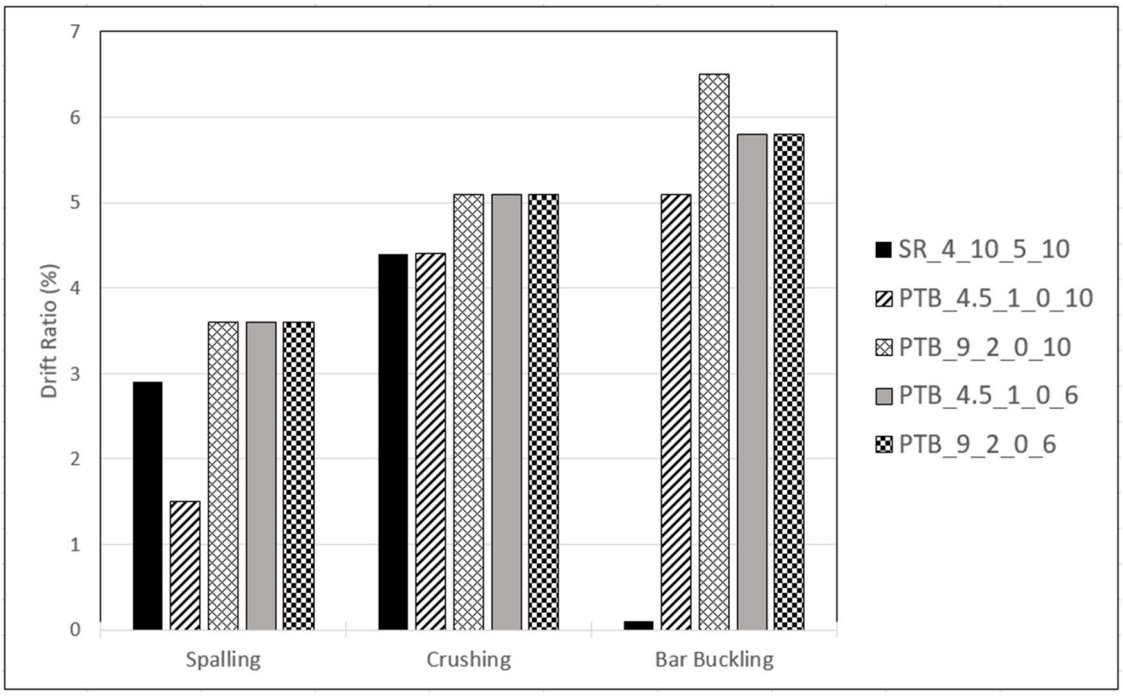

Figure 8.1. Damage Summary

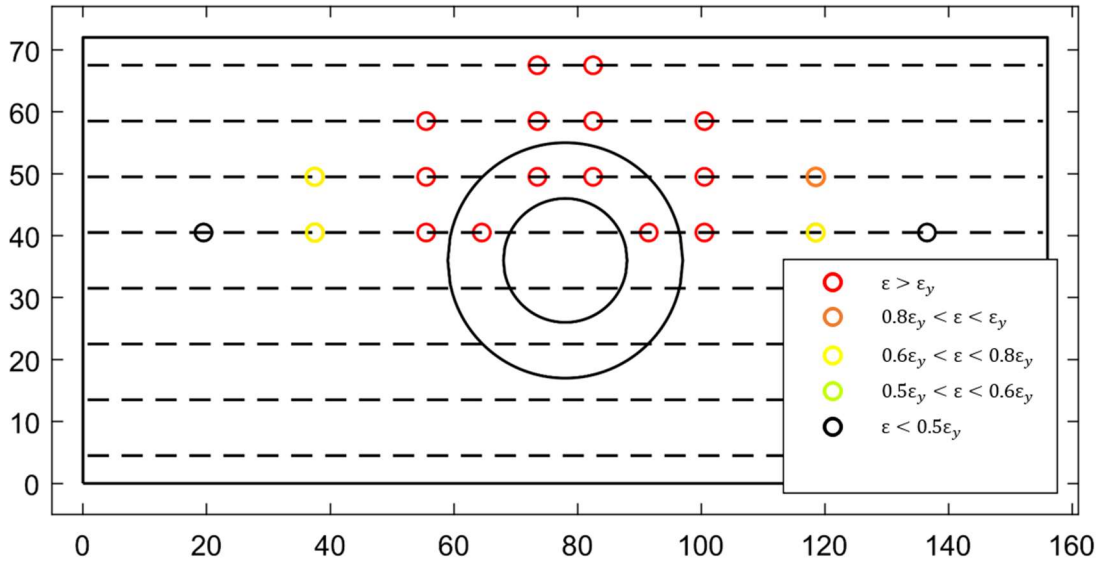

Figure 8.2. Bottom bar Stress Distribution at Peak Strength (PTB_9_2_0_10)

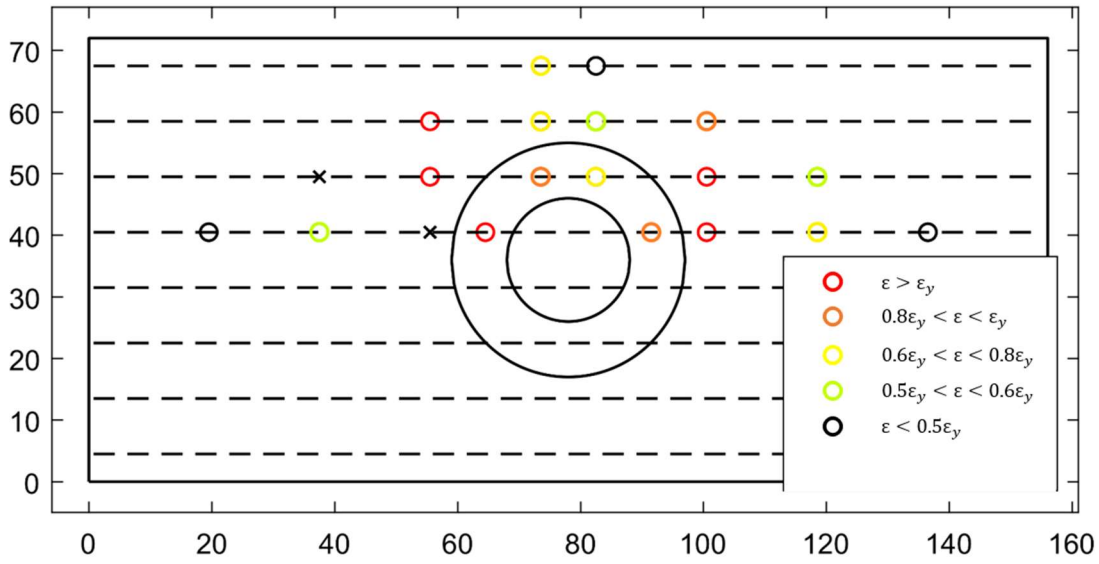

Figure 8.3. Bottom bar Stress Distribution at Peak Strength (PTB_9_2_0_6)

The observed strengths were then compared to five different design codes. Most of the codes predicted flexural failures for the responses, with the exception being EN 1992-1-1 that predicted two-way shear failure for PTB_4.5_1_0_6. Specimens were considered to have failed in flexure in all responses.

The punching specimens were more difficult to keep track of the initiation of damage states during testing. Due to this a more general response of the specimen is presented in Table 8.1. The table shows that there was a large difference in the strengths of the specimens, some of this is expected due to the larger ring increasing the critical perimeter. Figures 8.4 and 8.5 show the crack patterns. In Figure 8.5 the blue line that highlights the largest crack widths shows that the circumferential cracks interfere with the test frame which can be seen by the square discoloration at the slab edges where the slab rested upon the cotton duck pads. Due to this interference the strength of PTB_9_2_0_P was influenced by the test frame and is higher than the specimen would behave in a test setup with a larger footprint. The peak strengths were reached at similar displacements and end of testing at 40% loss of the peak strength were also similar. PTB_9_2_0_P ended testing after a post-tension bolt was fracture by prying action of the ring trying to accommodate the deformation demands due to displacement of the column.

Table 8.1. Peak and 10% Loss of Peak Measured Drifts

Observations	PTB_4.5_1_0_P	PTB_9_2_0_P
Initial Yield of Reinforcement (kips)	428	557
Peak Strength (kips)	523	732
Displacement at Peak Strength (in.)	0.56	0.63
Displacement at End of Test (in.)	1.35	1.34

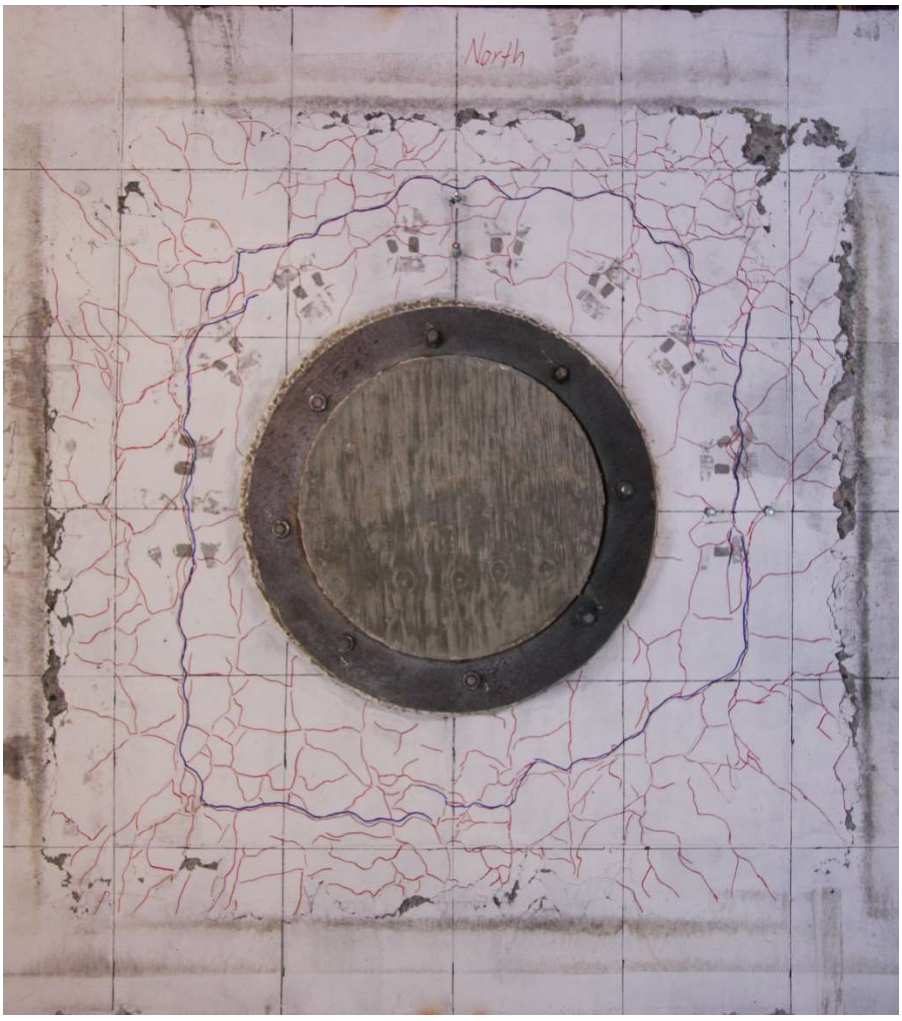

Figure 8.4. Crack Pattern (PTB_4.5_1_0_P)

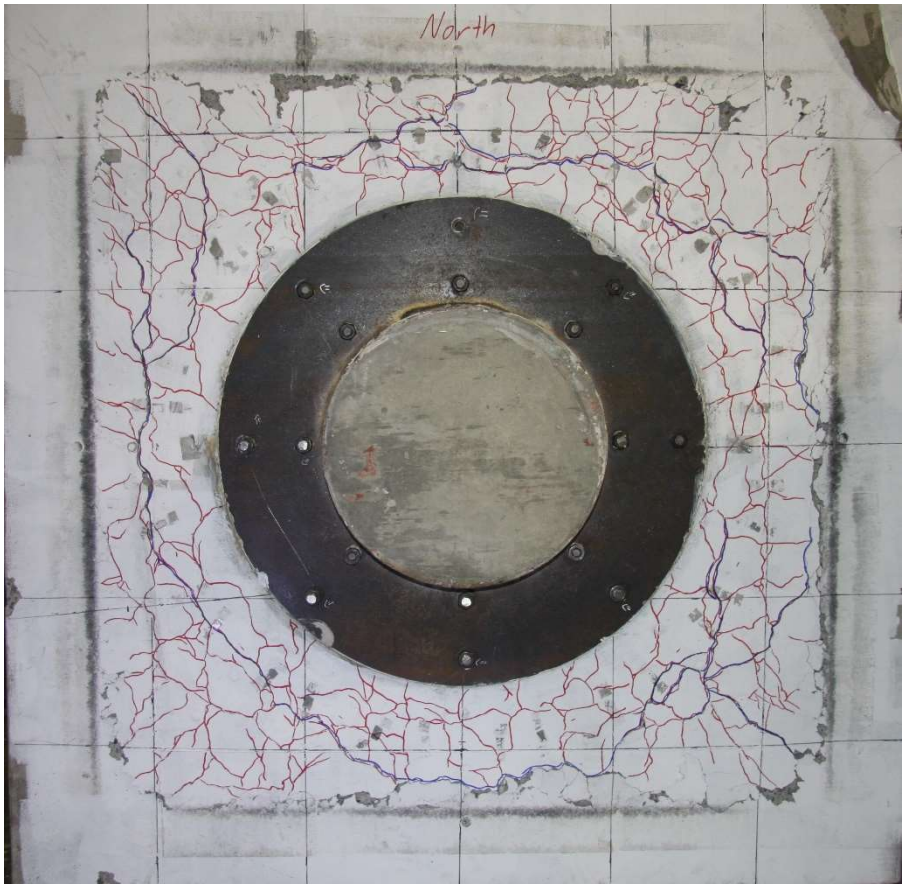

Figure 8.5. Crack Pattern (PTB_9_2_0_P)

The punching specimens were compared to three different punching expressions including ACI 318-19. The predicted strengths were calculated using the assumption that the ring flange acted as a shear cap that increased the punching strength by extending the critical perimeter of the connection. All of the models under predicted the capacity of the specimens. The most accurate model was the shear-friction model after the assumed failure angle of 27° was adjusted to 45°. The shear friction model under predicted PTB_4.5_1_0_P and PTB_9_2_0_P by 16% and 24% respectively.

8.2 Research Results and Conclusions

The following conclusions were made based on the observed damage states, measured response, and comparison to existing codes and models:

- The proposed connection delays significant damage and loss of strength of the connection due to lateral loading in comparison to the stud rail reference slab-column connection as long as it is sufficiently detailed.
- Specimens PTB_9_2_0_10, PTB_4.5_1_0_6, and PTB_9_2_0_6 began crushing and therefore losing strength at higher drifts than SR_4_10_5_10 and PTB_4.5_1_0_10. Implicating that using a ring width equal to the effective depth of the slab can provide sufficient detailing of the connection to withstand high lateral drifts without loss of strength.
- The post-tensioned bolt connection allows for accelerated construction.
- The behavior of PTB_4.5_1_0_P shows that the assumption that the shear strength of the specimen can be predicted by modeling the ring flange as a shear cap that extends the critical perimeter is conservative following ACI 318-19's two-way shear strength equations.
- Prying of the ring at high deformations can impose high stresses on the post-tension bolts causing fracture of the bolt.

8.3 Recommendations for Future Work

The proposed connection still has many aspects of its behavior that need investigating. FEM models are being validated to further the understanding of the connection, but full scale tests should examine some of these aspects to continue to validate FEM studies. Future work that would help with understanding the behavior of the connection and result in better recommendations for design include the following:

- Testing of specimens with different column sizes to see if column size should be a significant factor in design of the ring flange.
- Experimental investigation using prestressed slabs to determine the effects of prestressing on the connections behavior.
- Experimental investigation into the use of square CFST columns for use in buildings.

- Experimental studies to explore the behavior of the connection at edge and corner columns.
- Experimental investigation into the response of the connection as a part of a multi-bay structure.
- Experimental investigation into the effects of ring size on the rotational capacity of the connection.
- Testing of smaller columns for punching where the column/ring do not cause interference with the test frame to affect behavior.
- Testing with varying ring width to thickness ratio to understand the prying effect and how the ring thickness should be designed.

BIBLIOGRAPHY

[1] ACI Committee 318. (2019). Building Code Requirements for Structural Concrete (ACI 318-19): An ACI Standard: Commentary on Building Code Requirements for Structural Concrete (ACI 318R-19). American Concrete Institute.

[2] American Institute of Steel Construction. (2011). *Steel construction manual.* (Fourteenth ed.). Chicago, Illinoi]: American Institute of Steel Construction

[3] ASTM. (2014). ASTM C469: Standard test method for static modulus of elasticity and poisson's ratio of concrete in compression. West Conshohocken, PA: American Society for Testing and Materials.

[4] Birkle, G., Loov, R., Dilger, W.H. (2003). Design of slabs using Shear Friction. *Annual Conference of the Canadian Society of Civil Engineering*. Canadian Standards Association. (2004). Design of concrete structures. Mississauga, Ont.: Canadian Standards Association.

[5] Dam, X., Wight, J. (2015). Flexurally-triggered punching shear failure of reinforced concrete slab-column connections reinforced with headed shear studs arranged in orthogonal and radial layouts. *Engineering Structures*, *110*, 258-268. https://doi.org/https://doi.org/10.1016/j.engstruct.2015.11.050.

[6] Elgabry, A. A., & Ghali, A. (1987). Tests on concrete slab-column connections with stud-shear reinforcement subjected to shear-moment transfer. *Structural* Journal, 84(5), 433-442.

[7] Ghali, A., Elmasri, M. Z., & Dilger, W. (1976, October). Punching of flat plates under static and dynamic horizontal forces. In *Journal* Proceedings (vol. 73, No. 10, pp. 566-572).

[8] Hawkins, N. M., Mitchell, D., & Hanna, S. N. (1975). The effects of shear reinforcement on the reversed cyclic loading behavior of flat plate structures. *Canadian Journal of Civil* Engineering, 2(4), 572-582.

[9] Hawkins, N. M., Mitchell, D., & Sheu, M. S. (1974). *Cyclic behavior of six reinforced concrete slab-column specimens transferring moment and shear.* Division of Structures and Mechanics, Department of Civil Engineering, University of Washington.

[10] Jang, J., Kang, SM. (2019). Punching Shear Behavior of sehar Reinforced Slab-Column Connection with Varying Flexural Reinforcement. *International Journal of Concrete Structures and Materials*. https://doi.org/https://doi.org/10.1186/s40069-019-0341-4

[11] JSCE. (2007). Standard specifications for concrete structures-2007, Design. Tokyo (Japan): Japan Society of Civil Engineers.

[12] Pan, A. D., & Moehle, J. P. (1992). An experimental study of slab-column connections. *Structural Journal*, 89(6), 626-638.

[13] Robertson, I. N., Kawai, T., Lee, J., & Enomoto, B. (2002). Cyclic testing of slab-column connections with shear reinforcement. *Structural Journal*, 99(5), 605-613.

[14] Saleh, H., Kalfat, R., Abdouka, K., Al-Mahaidi, R. (2019). Punching shear strengthening of RC slabs using L-CFRP laminates. *Engineering Structures*, *194*, 274-289. https://doi.org/https://doi.org/10.1016/j.engstruct.2019.05.050.

[15] Standard, B. (2004). Eurocode 2: Design of concrete structures-. Part 1-1: *General rules and rules for buildings,* 230.

[16] Standard, New Zealand. (2006). NZS3101 Concrete Structures Standard.

[17] Stephens, M. T. (2016). *Design Expressions and Dynamic Evaluation of CFST Bridges Subjected to Seismic Hazards* (Doctoral dissertation).

[18] Symonds, D. W. (1976). *Slab-column connections subjected to high intensity shears and transferring reversed moments* (Doctoral dissertation, Division of Structures and Mechanics, Department of Civil Engineering, University of Washington).

[19] Wey, E. H., & Durrani, A. J. (1992). Seismic response of interior slab-column connections with shear capitals. *Structural Journal*, 89(6), 682-691.

[20] Yeutter. (2020). *A RC Slab to CFT Column Connection for Improved Seismic Behavior of Multi-Story Buildings*. ProQuest Dissertations Publishing.

APPENDIX A

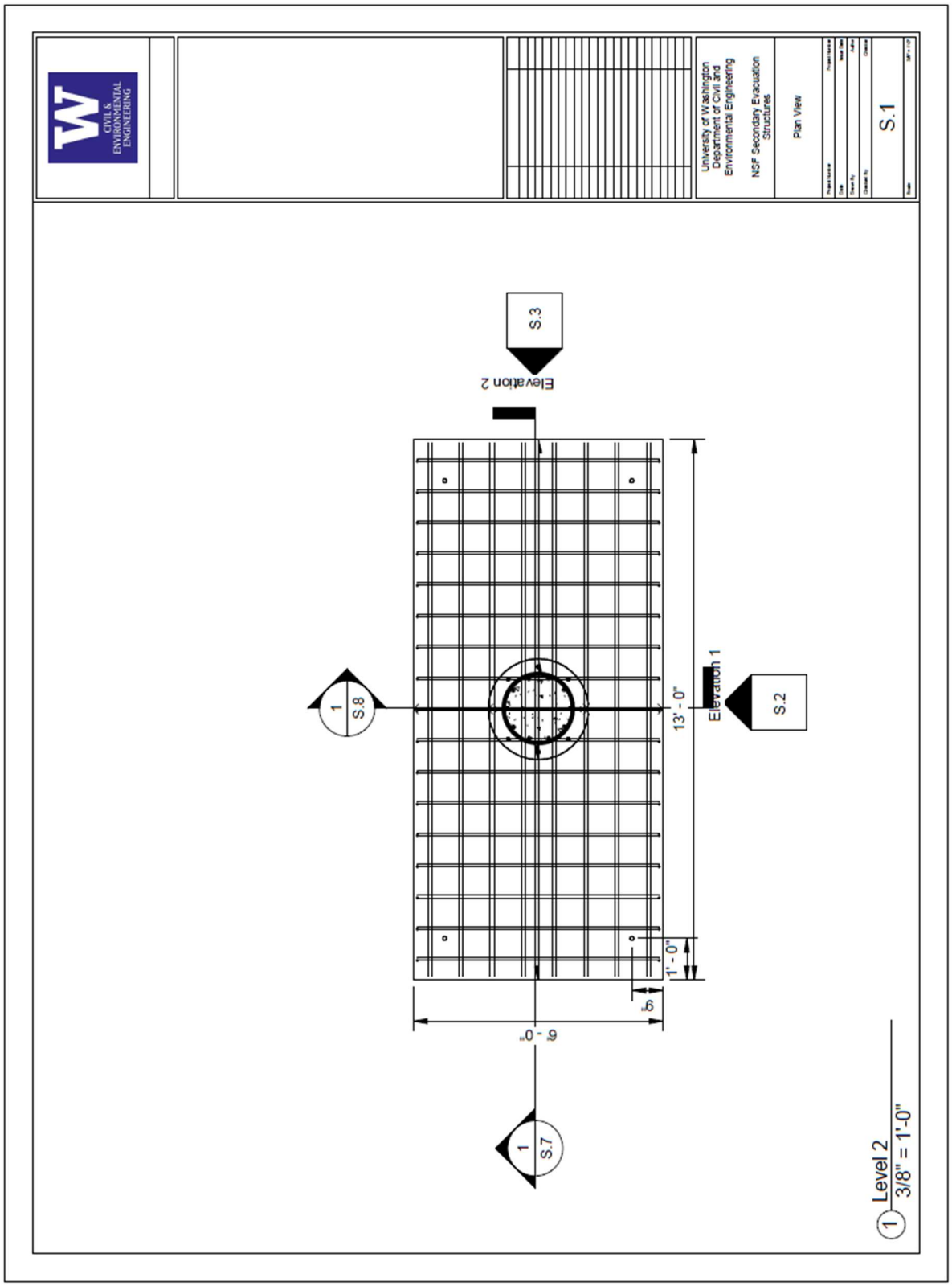
CIVIL & ENVIRONMENTAL ENGINEERING
University of Washington
Department of Civil and
Environmental Engineering
NSF Secondary Evacuation
Structures
Plan View
S.1
S.3
Elevation 2
1
S.8
13' - 0"
Elevation 1
S.2
1' - 0"
6" - 0"
1
S.7
1 Level 2
3/8" = 1'-0"

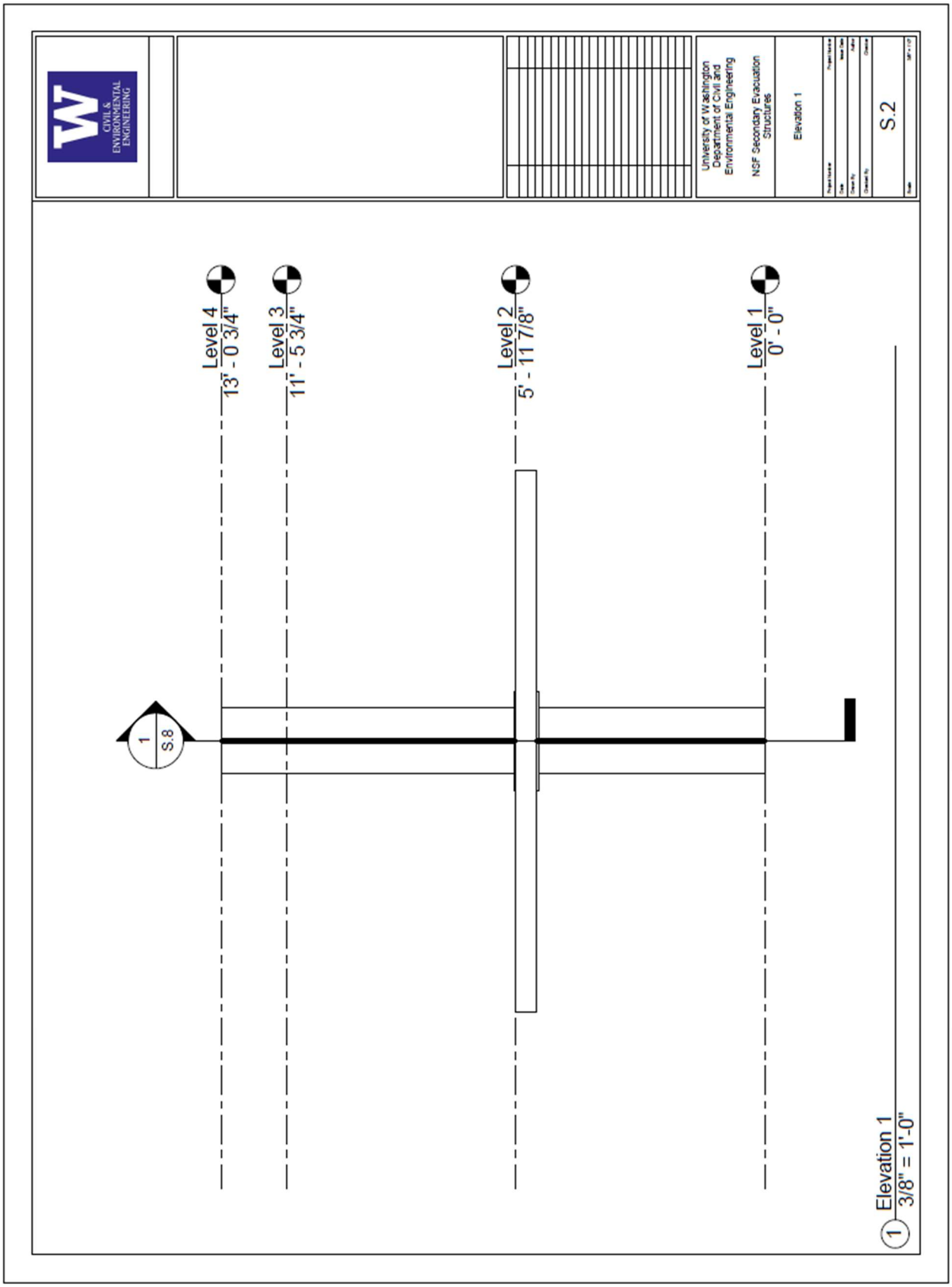
CIVIL & ENVIRONMENTAL ENGINEERING
University of Washington
Department of Civil and Environmental Engineering
NSF Secondary Evacuation Structures
Elevation 1
S.2
Level 4
13' - 0 3/4"
Level 3
11' - 5 3/4"
Level 2
5' - 11 7/8"
Level 1
0' - 0"
1
S.8
1 Elevation 1
3/8" = 1'-0"

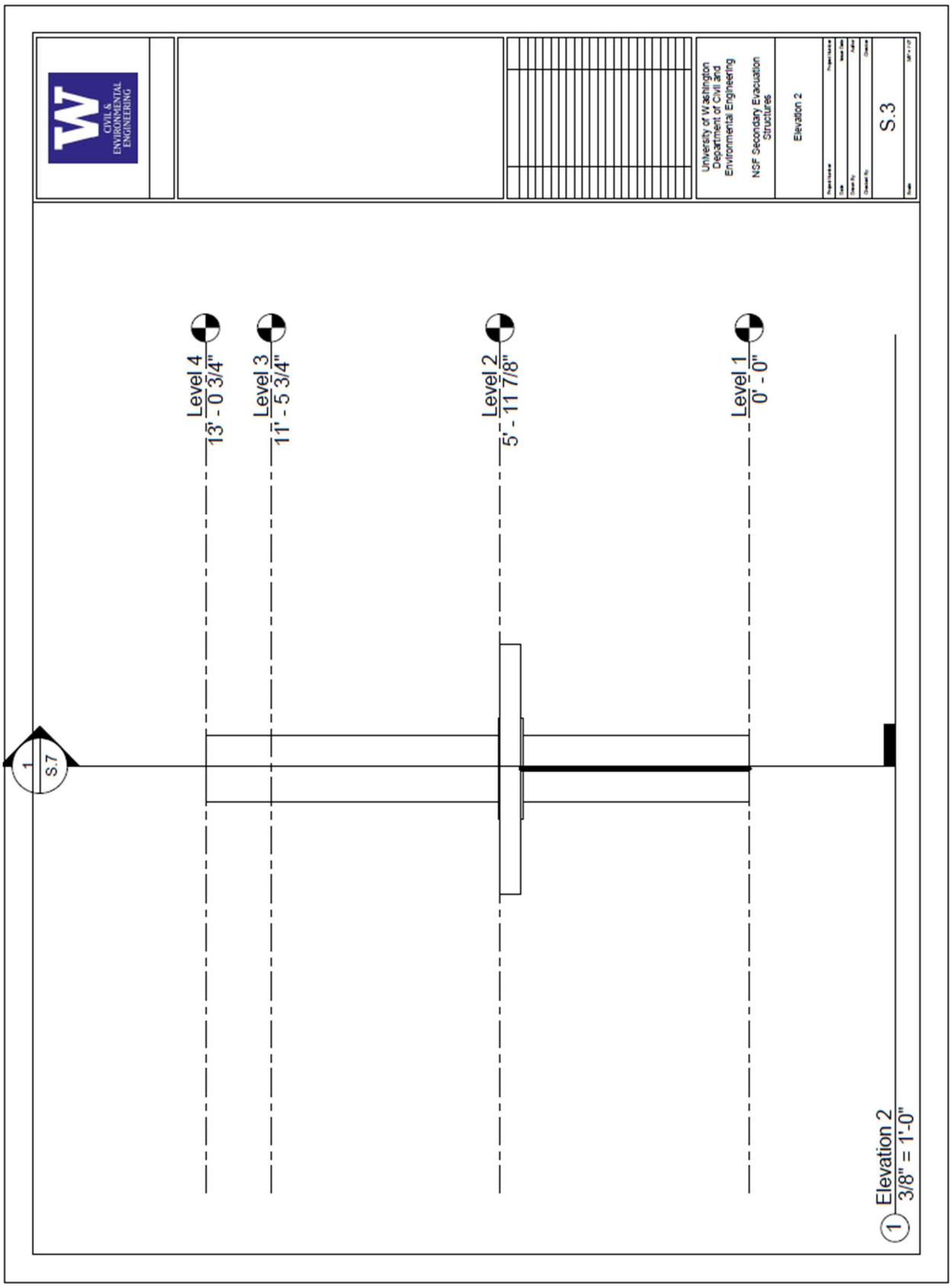
CIVIL & ENVIRONMENTAL ENGINEERING
University of Washington
Department of Civil and
Environmental Engineering
NSF Secondary Evacuation
Structures
Elevation 2
S.3
Level 4
13' - 0 3/4"
Level 3
11' - 5 3/4"
Level 2
5' - 11 7/8"
Level 1
0' - 0"
1
S.7
1 Elevation 2
3/8" = 1'-0"

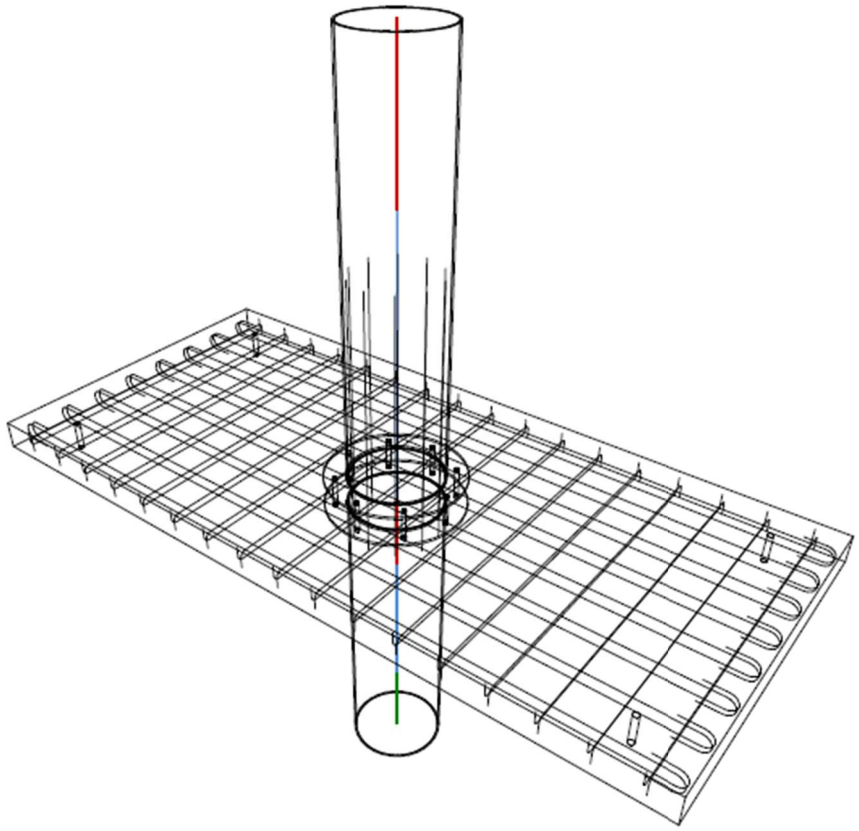

1 3D Isometric Wire Frame

CIVIL & ENVIRONMENTAL ENGINEERING

University of Washington
Department of Civil and Environmental Engineering

NSF Secondary Evacuation Structures

3D Isometric Wire Frame

S.4

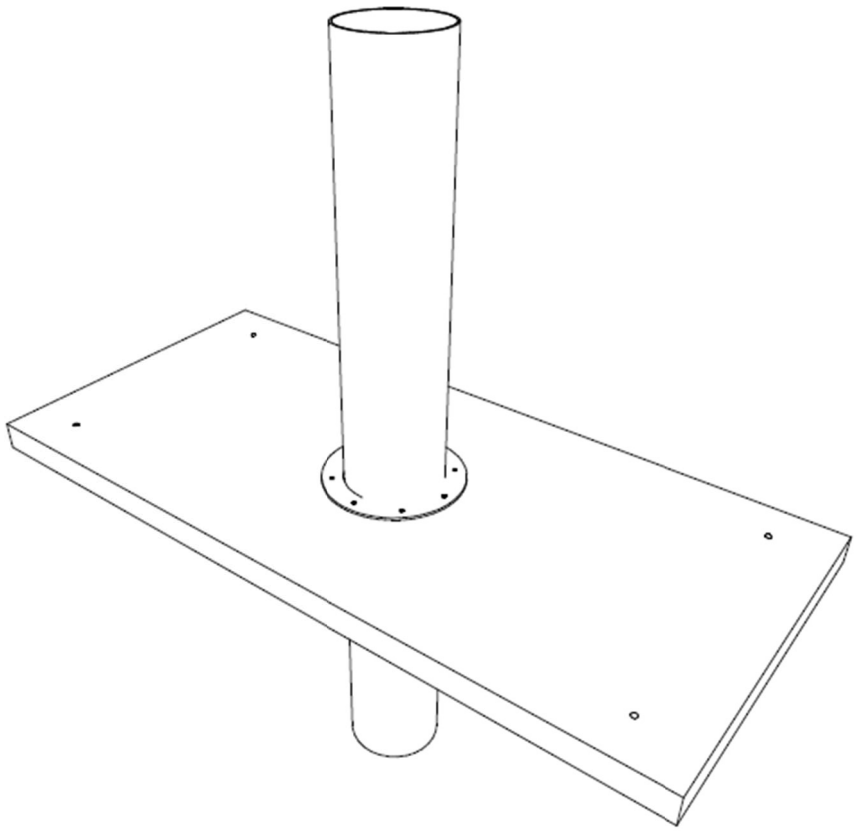

1 3D Solid Isometric View

CIVIL & ENVIRONMENTAL ENGINEERING

University of Washington
Department of Civil and Environmental Engineering

NSF Secondary Evacuation Structures

3D Solid Isometric View

S.5

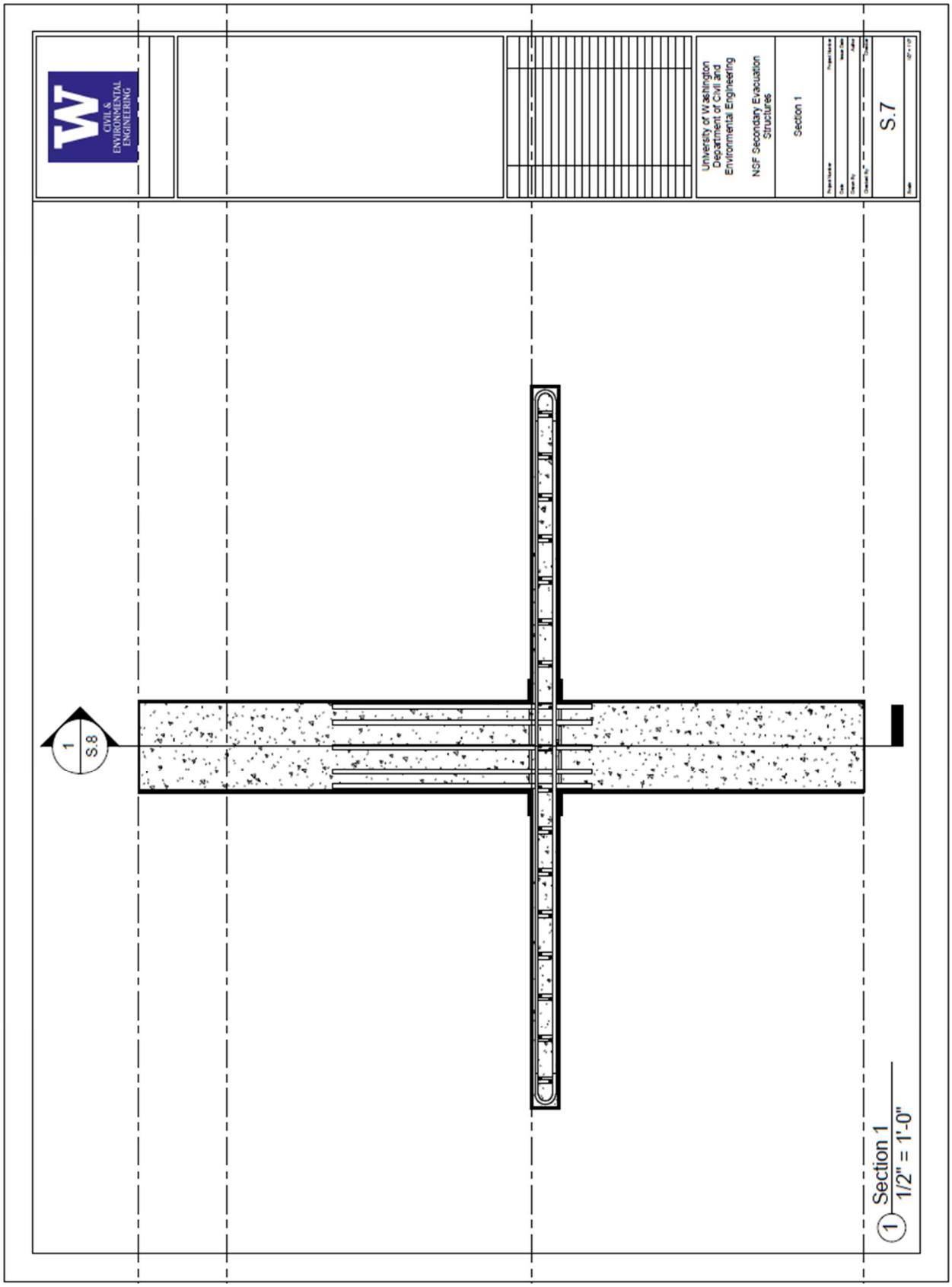
CIVIL & ENVIRONMENTAL ENGINEERING
University of Washington
Department of Civil and
Environmental Engineering
NSF Secondary Evacuation
Structures
Section 1
S.7
1
S.8
1 Section 1
1/2" = 1'-0"

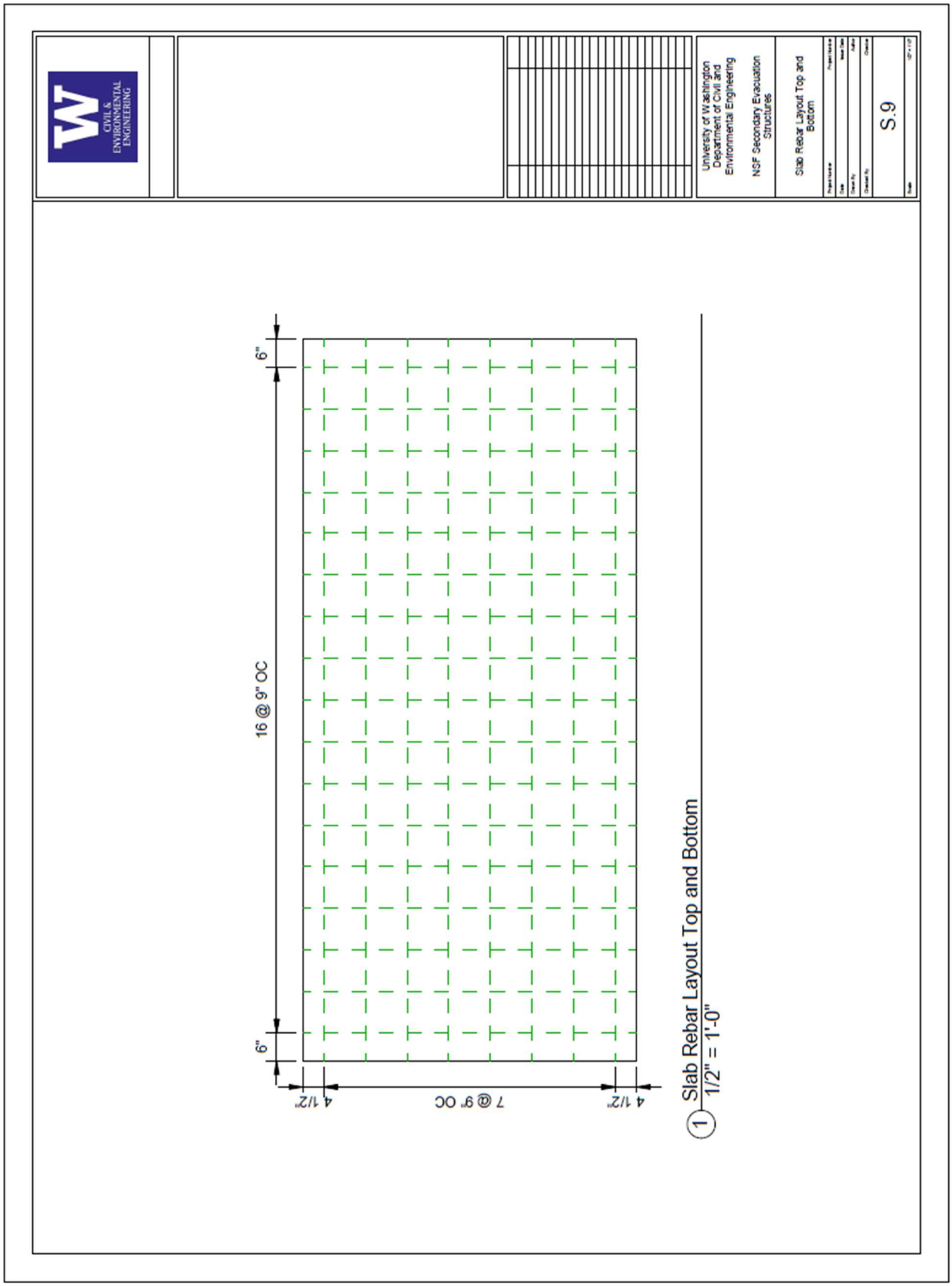
CIVIL & ENVIRONMENTAL ENGINEERING
University of Washington
Department of Civil and Environmental Engineering
NSF Secondary Evaluation Structures
Slab Rebar Layout Top and Bottom
S.9
6"
16 @ 9" OC
6"
4 1/2"
7 @ 9" OC
4 1/2"
1 Slab Rebar Layout Top and Bottom
1/2" = 1'-0"

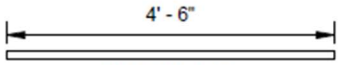

SHAPE 1: #9 Bar

① Rebar SHAPE 1
1/2" = 1'-0"

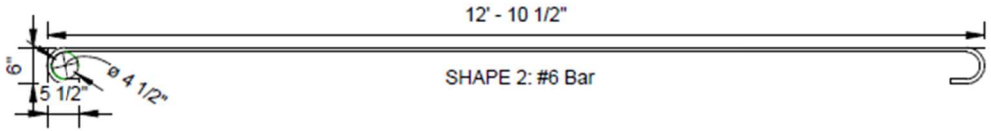

SHAPE 2: #6 Bar

② Rebar SHAPE 2
1/2" = 1'-0"

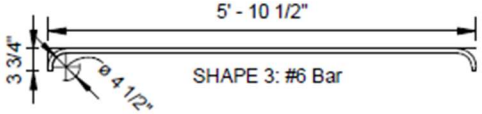

SHAPE 3: #6 Bar

③ Rebar SHAPE 3
1/2" = 1'-0"

CIVIL & ENVIRONMENTAL ENGINEERING

University of Washington
Department of Civil and Environmental Engineering

NSF Secondary Evacuation Structures

Rebar Details

S.10

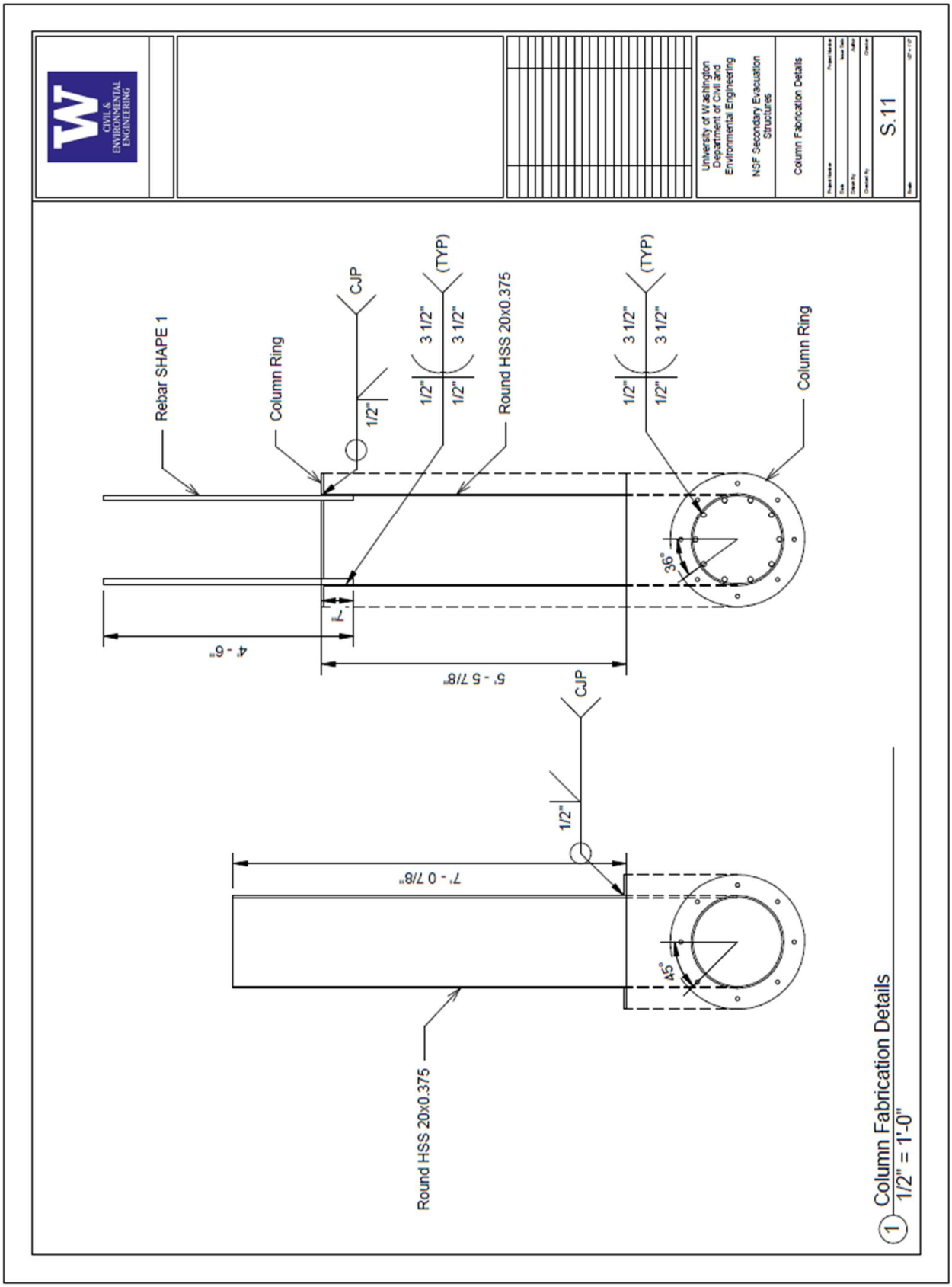
CIVIL & ENVIRONMENTAL ENGINEERING
University of Washington
Department of Civil and
Environmental Engineering
NSF Secondary Evacuation
Structures
Column Fabrication Details
S.11
Rebar SHAPE 1
Column Ring
CJP
1/2"
3 1/2"
1/2"
(TYP)
Round HSS 20x0.375
Column Ring
36°
4' - 6"
5' - 5 7/8"
7' - 0 7/8"
45°
Round HSS 20x0.375
1 Column Fabrication Details
1/2" = 1'-0"

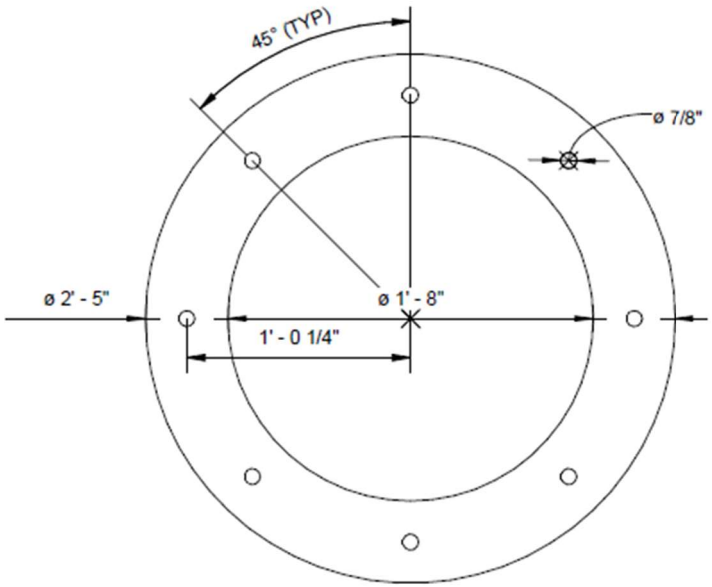

1 Ring Fabrication Detail
1 1/2" = 1'-0"

CIVIL & ENVIRONMENTAL ENGINEERING

University of Washington
Department of Civil and Environmental Engineering

NSF Secondary Evacuation Structures

Ring Fabrication Detail

S.12

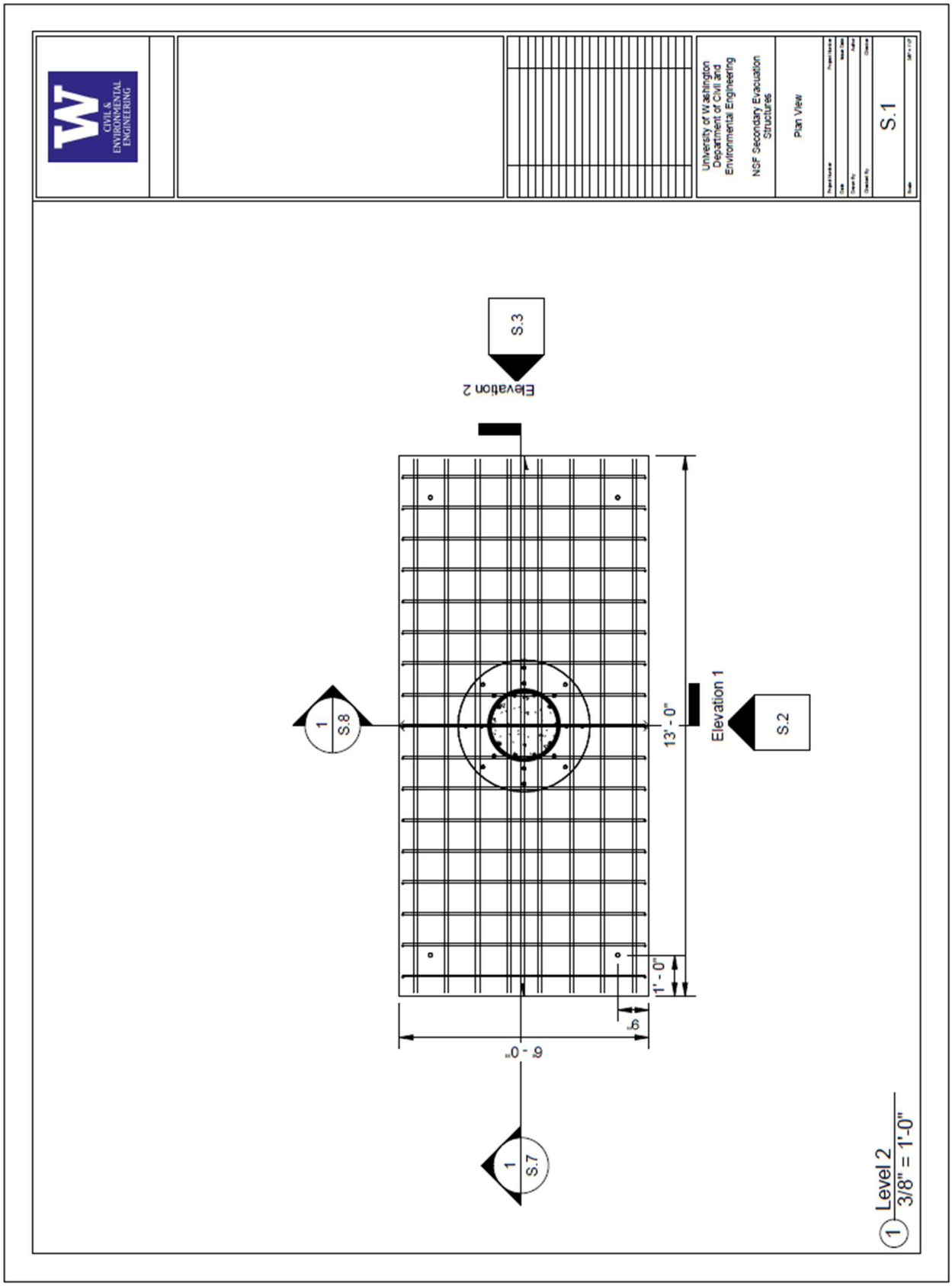
CIVIL & ENVIRONMENTAL ENGINEERING
University of Washington
Department of Civil and Environmental Engineering
NSF Secondary Evacuation Structures
Plan View
S.1
S.3
Elevation 2
1
S.8
13' - 0"
Elevation 1
S.2
1' - 0"
9"
6' - 0"
1
S.7
1 Level 2
3/8" = 1'-0"

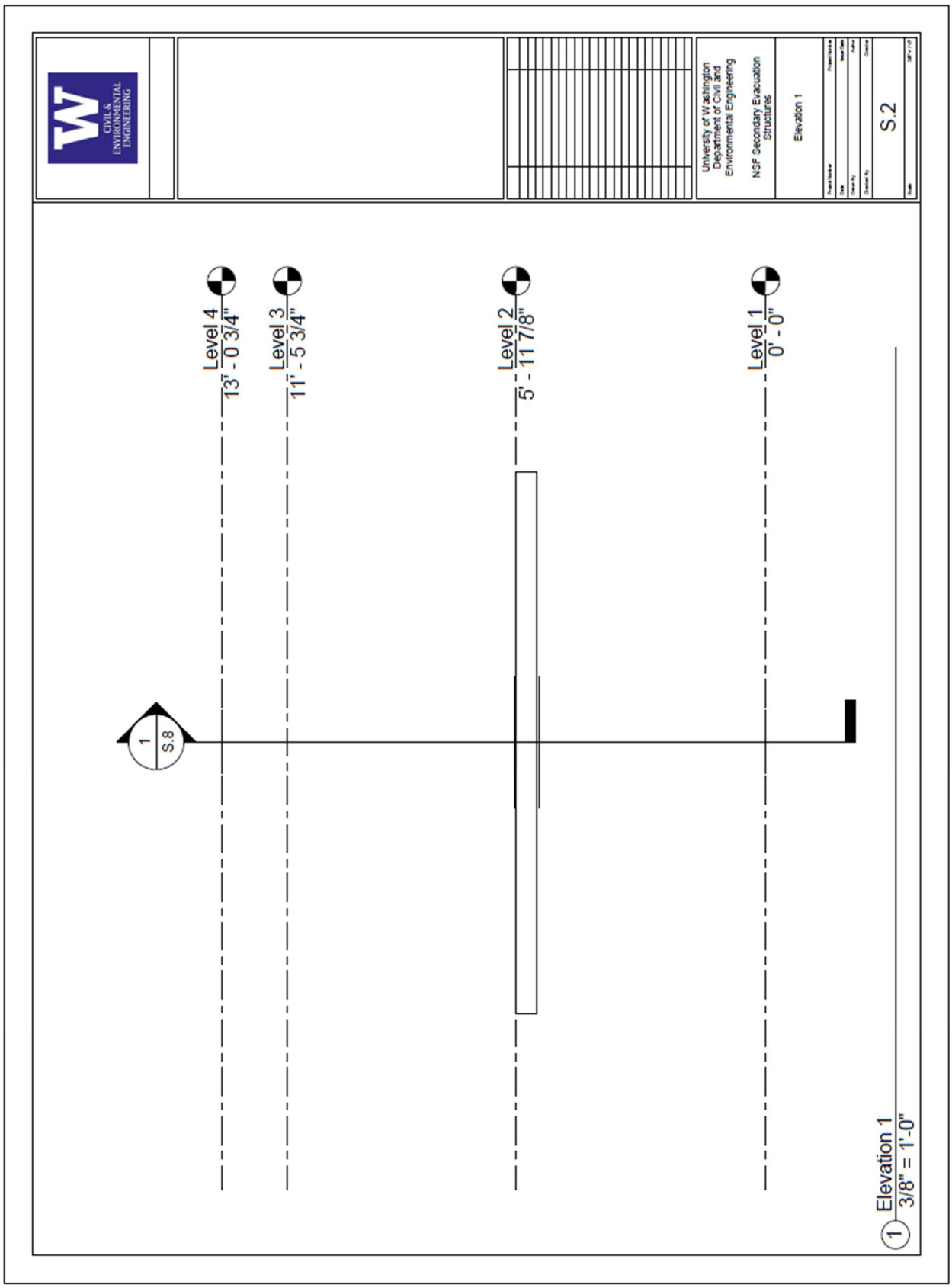
CIVIL & ENVIRONMENTAL ENGINEERING
University of Washington
Department of Civil and
Environmental Engineering
NSF Secondary Evacuation
Structures
Elevation 1
S.2
Level 4
13' - 0 3/4"
Level 3
11' - 5 3/4"
Level 2
5' - 11 7/8"
Level 1
0' - 0"
1
S.8
1 Elevation 1
3/8" = 1'-0"

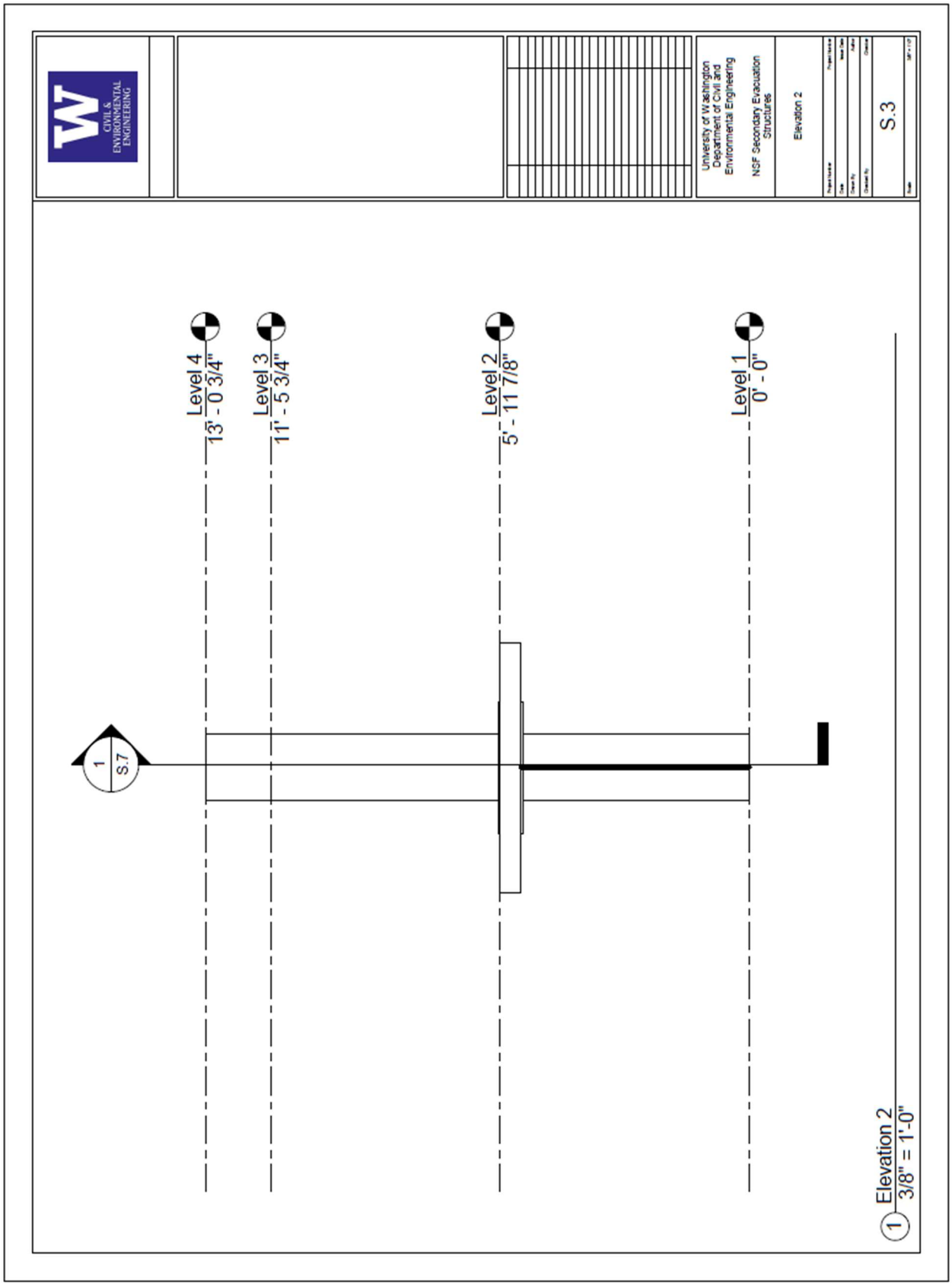
CIVIL & ENVIRONMENTAL ENGINEERING
University of Washington
Department of Civil and Environmental Engineering
NSF Secondary Evacuation Structures
Elevation 2
S.3
Level 4
13' - 0 3/4"
Level 3
11' - 5 3/4"
Level 2
5' - 11 7/8"
Level 1
0' - 0"
1
S.7
1 Elevation 2
3/8" = 1'-0"

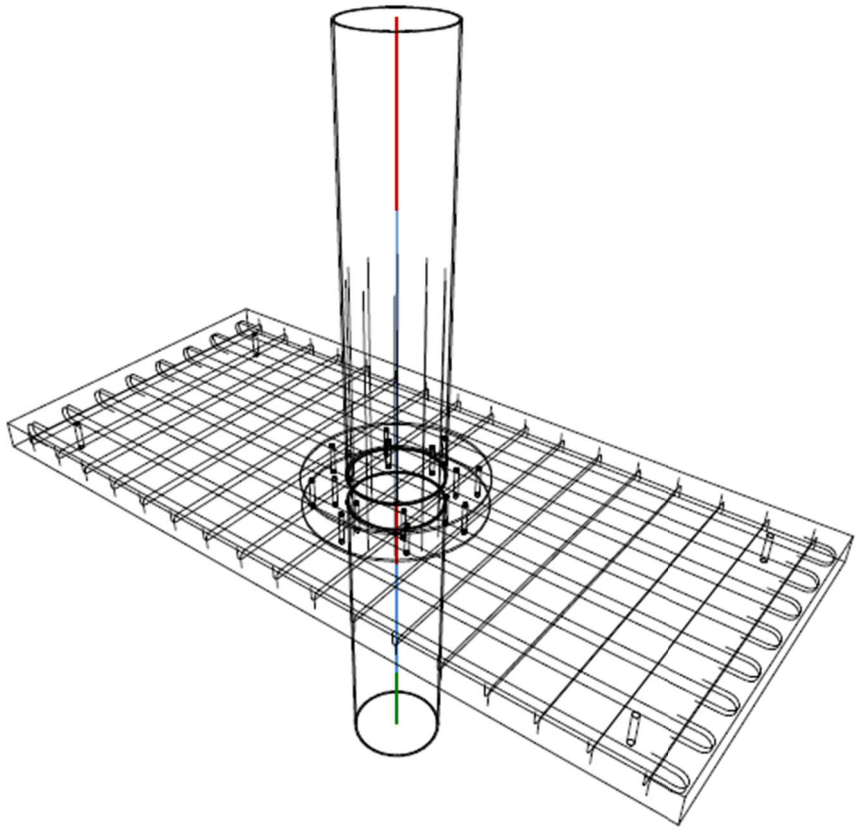

1 3D Isometric Wire Frame

CIVIL & ENVIRONMENTAL ENGINEERING

University of Washington
Department of Civil and Environmental Engineering

NSF Secondary Evacuation Structures

3D Isometric Wire Frame

S.4

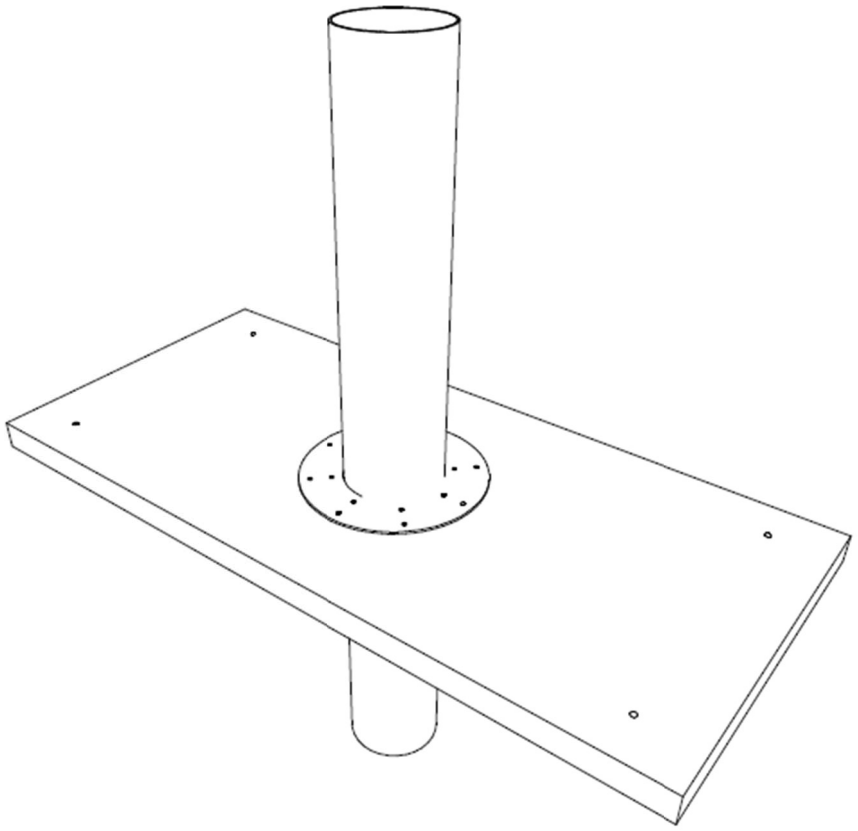

1 3D Solid Isometric View

CIVIL & ENVIRONMENTAL ENGINEERING

University of Washington
Department of Civil and Environmental Engineering

NSF Secondary Evacuation Structures

3D Solid Isometric View

S.5

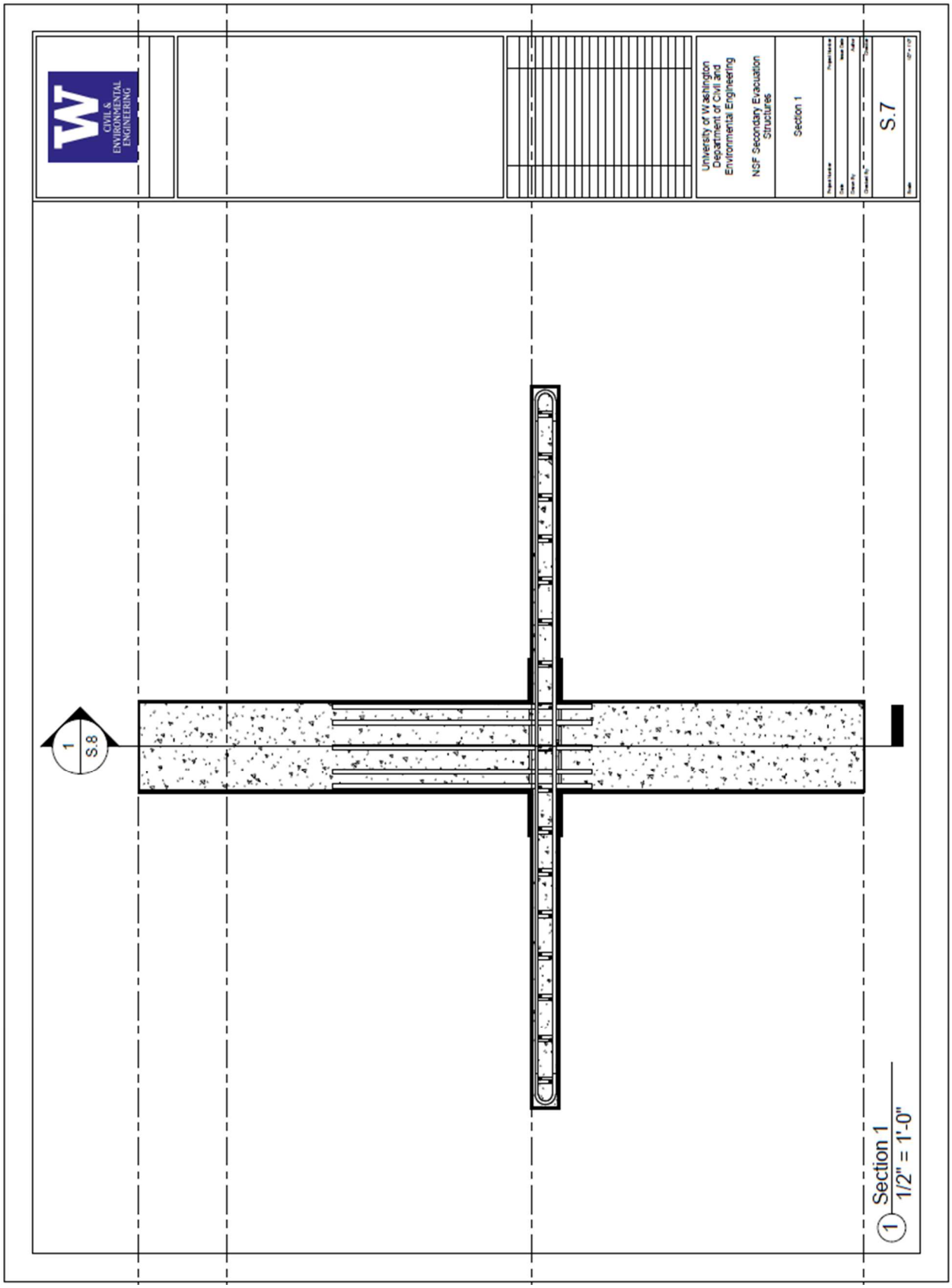
CIVIL & ENVIRONMENTAL ENGINEERING
University of Washington
Department of Civil and
Environmental Engineering
NSF Secondary Evacuation
Structures
Section 1
S.7
1
S.8
1 Section 1
1/2" = 1'-0"

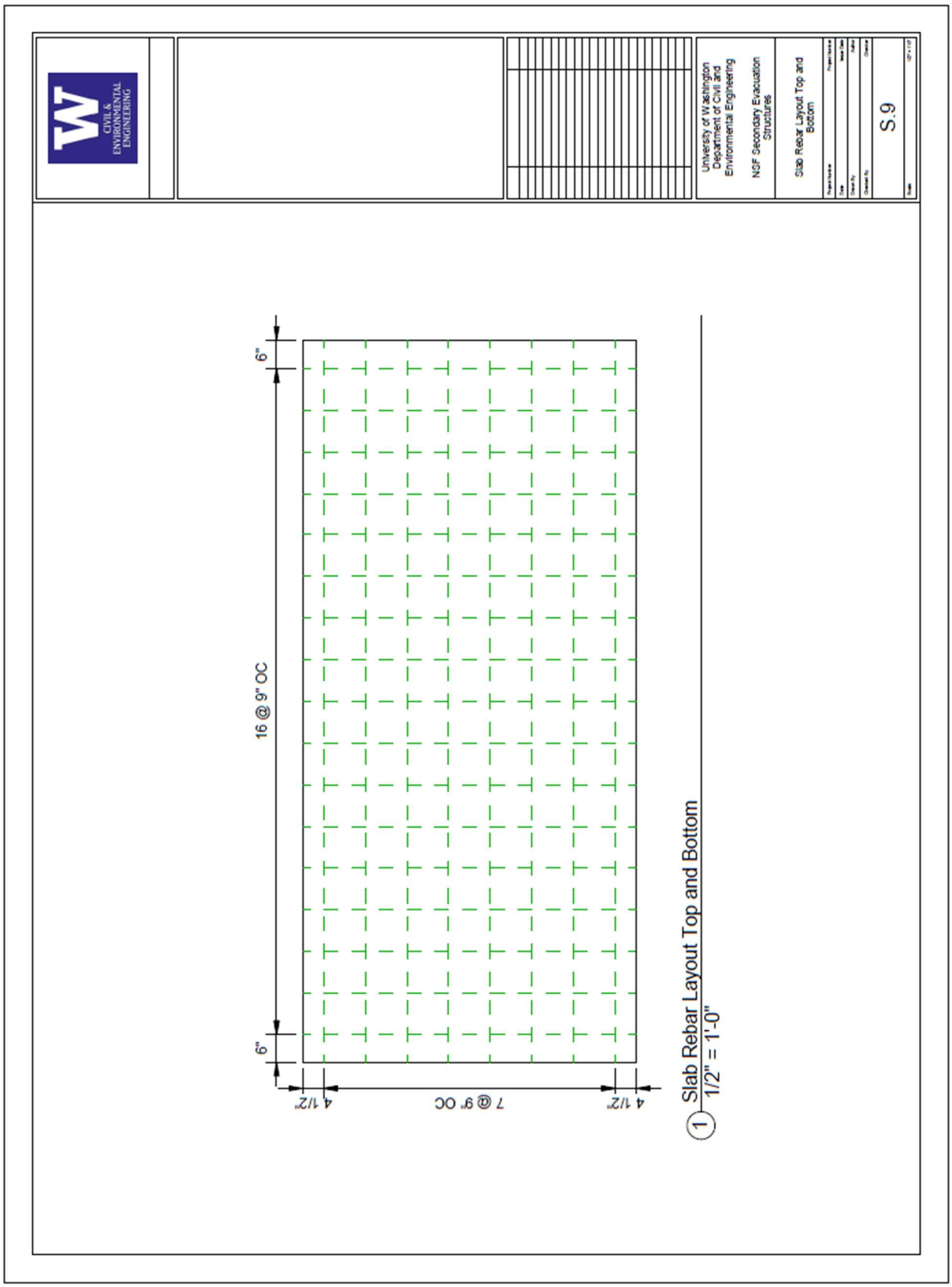
CIVIL & ENVIRONMENTAL ENGINEERING
University of Washington
Department of Civil and Environmental Engineering
NSF Secondary Evacuation Structures
Slab Rebar Layout Top and Bottom
S.9
6"
16 @ 9" OC
6"
4 1/2"
7 @ 9" OC
4 1/2"
1 Slab Rebar Layout Top and Bottom
1/2" = 1'-0"

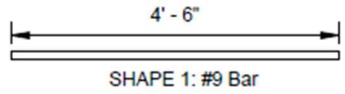

1 Rebar SHAPE 1
1/2" = 1'-0"

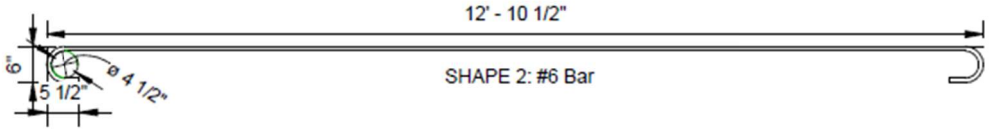

2 Rebar SHAPE 2
1/2" = 1'-0"

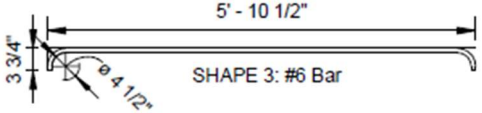

3 Rebar SHAPE 3
1/2" = 1'-0"

CIVIL & ENVIRONMENTAL ENGINEERING

University of Washington
Department of Civil and Environmental Engineering

NSF Secondary Evacuation Structures

Rebar Details

S.10

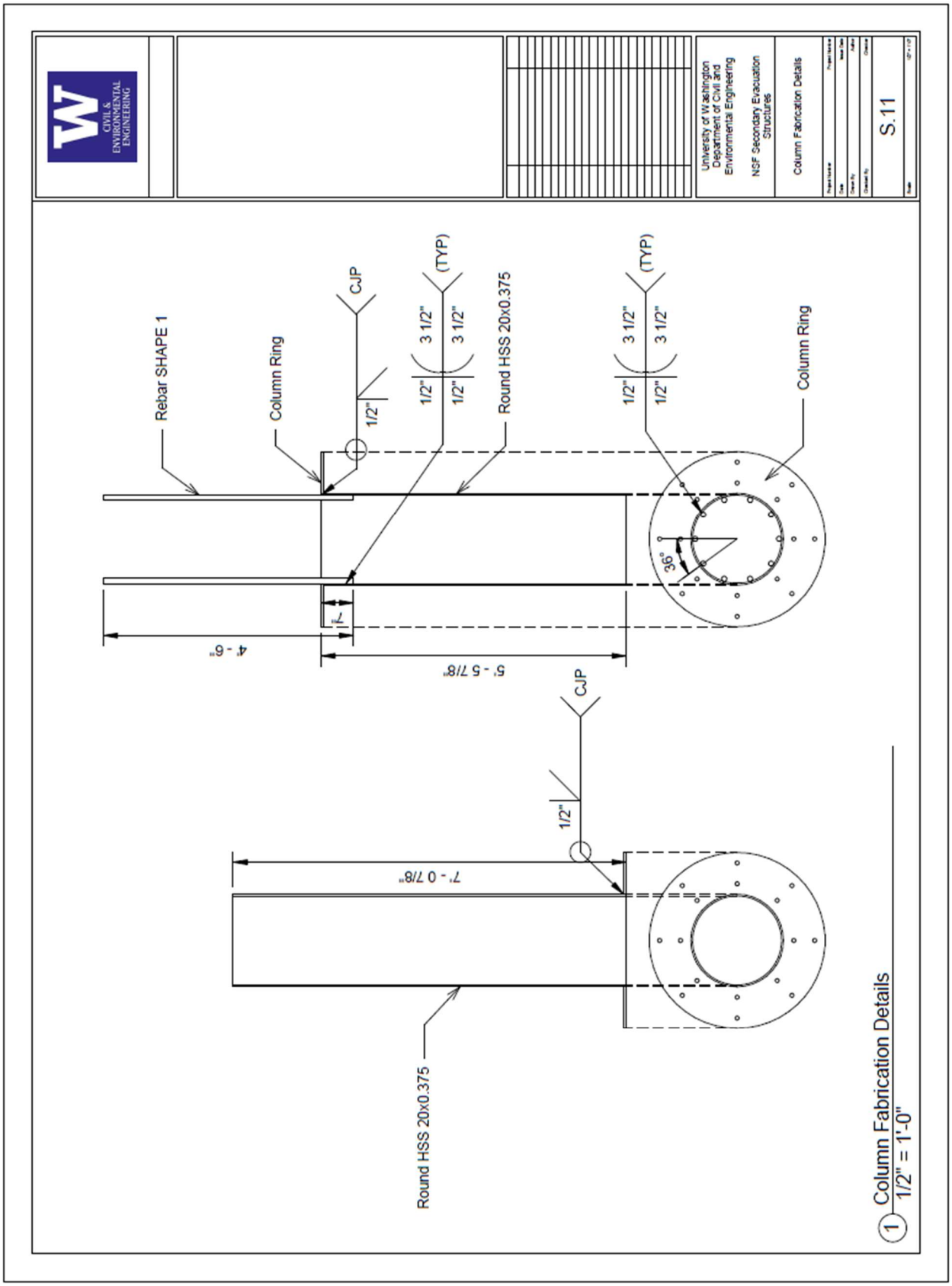
CIVIL & ENVIRONMENTAL ENGINEERING
University of Washington
Department of Civil and Environmental Engineering
NSF Secondary Evacuation Structures
Column Fabrication Details
S.11
Rebar SHAPE 1
Column Ring
CJP
1/2"
3 1/2"
1/2"
(TYP)
Round HSS 20x0.375
36°
7"
4' - 6"
5' - 5 7/8"
7' - 0 7/8"
Round HSS 20x0.375
1 Column Fabrication Details
1/2" = 1'-0"

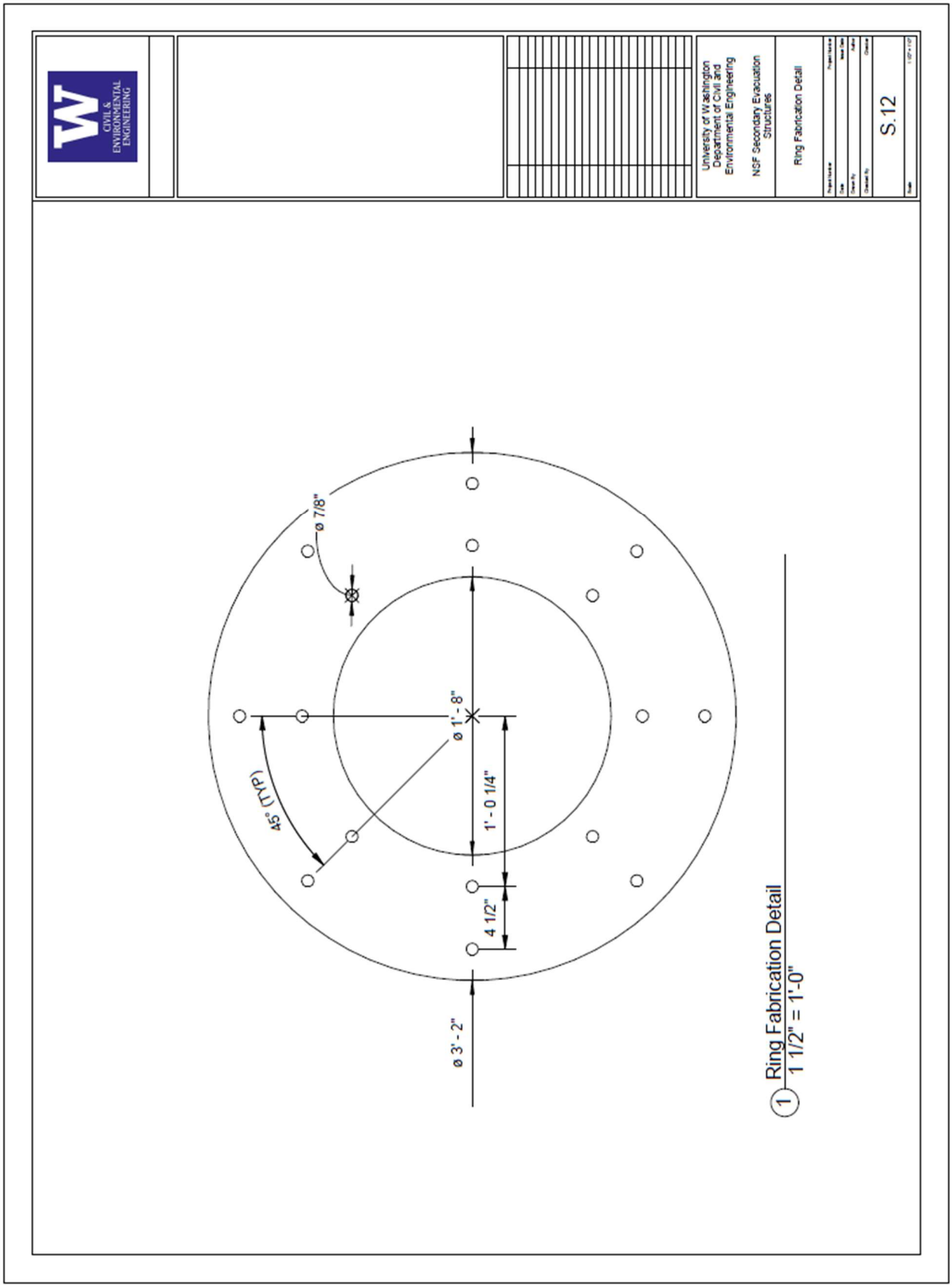
CIVIL & ENVIRONMENTAL ENGINEERING
University of Washington
Department of Civil and Environmental Engineering
NSF Secondary Evacuation Structures
Ring Fabrication Detail
S.12
ø 7/8"
ø 1' - 8"
45° (TYP)
1' - 0 1/4"
4 1/2"
ø 3' - 2"
1 Ring Fabrication Detail
1 1/2" = 1'-0"

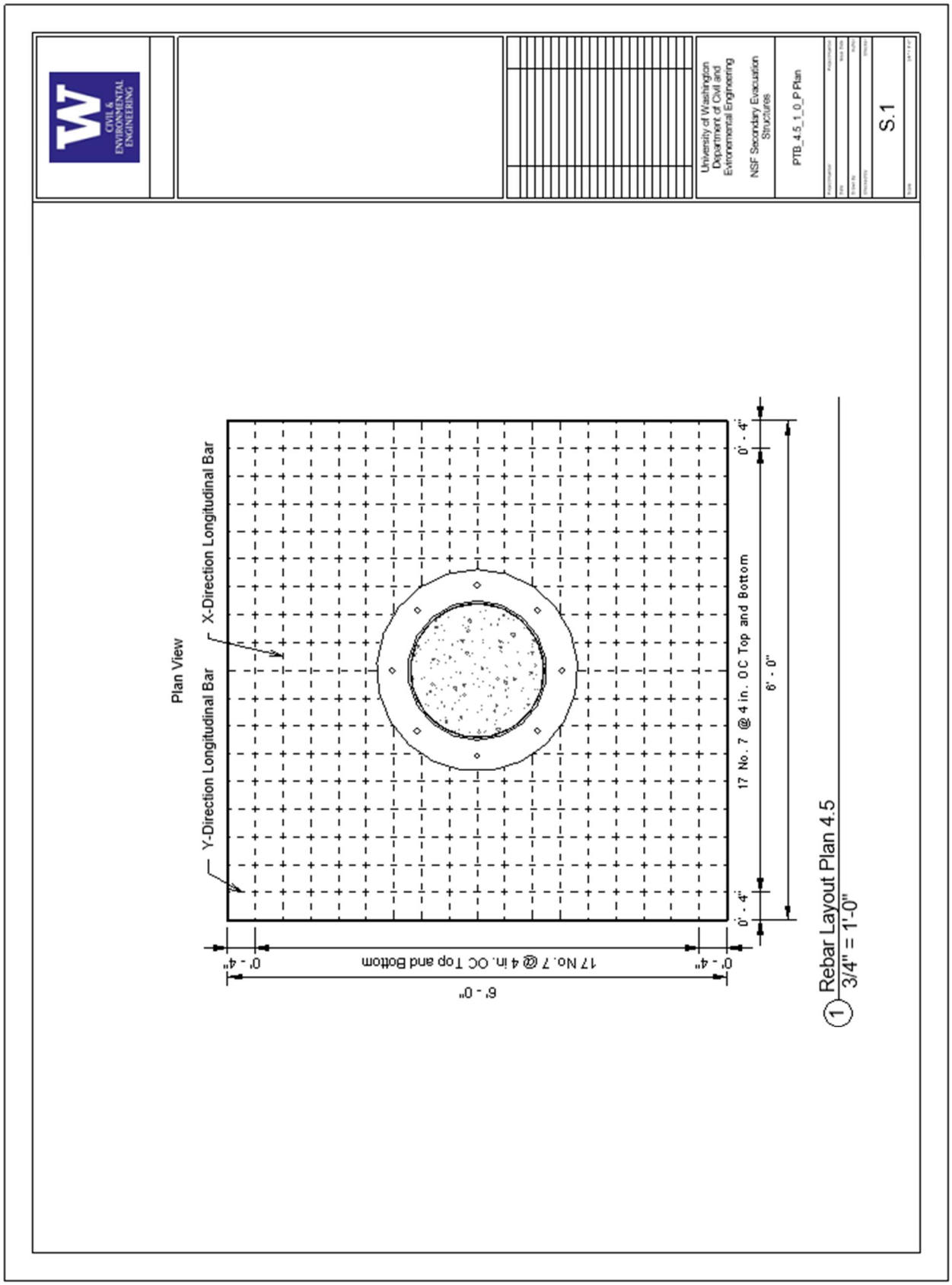
CIVIL & ENVIRONMENTAL ENGINEERING
University of Washington
Department of Civil and Environmental Engineering
NSF Secondary Evacuation Structures
PTB_4.5_1_0_P Plan
S.1
Plan View
X-Direction Longitudinal Bar
Y-Direction Longitudinal Bar
17 No. 7 @ 4 in. OC Top and Bottom
0' - 4"
6' - 0"
1 Rebar Layout Plan 4.5
3/4" = 1'-0"

Elevation

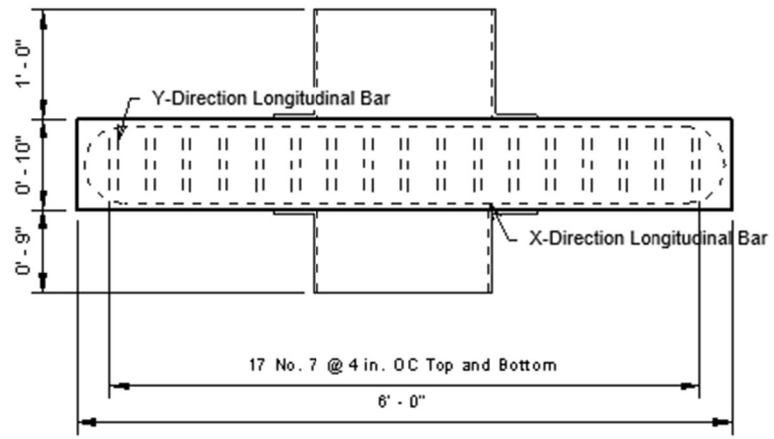

① Rebar Layout Elevation 4.5
3/4" = 1'-0"

CIVIL & ENVIRONMENTAL ENGINEERING

University of Washington
Department of Civil and Evironemental Engineering

NSF Secondary Evacuation Structures

PTB_4.5_1_0_P Elevation

S.2

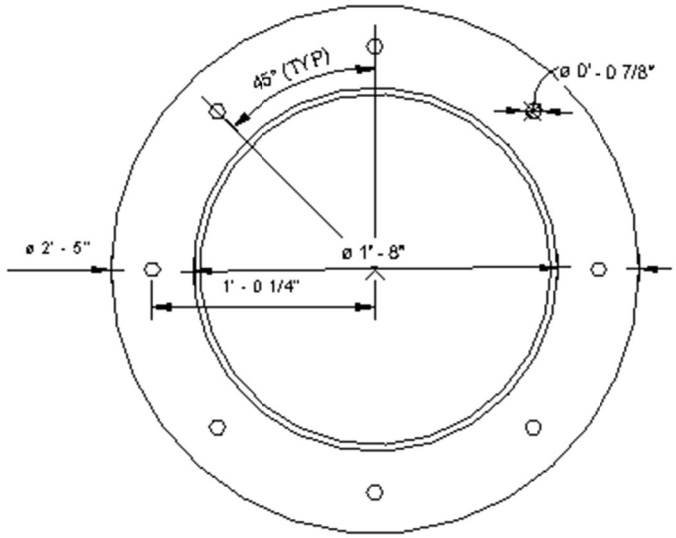

1 Ring 4.5
1 1/2" = 1'-0"

CIVIL & ENVIRONMENTAL ENGINEERING

University of Washington
Department of Civil and Evironemental Engineering

NSF Secondary Evacuation Structures

PTB_4.5_1_0_P Ring

S.3

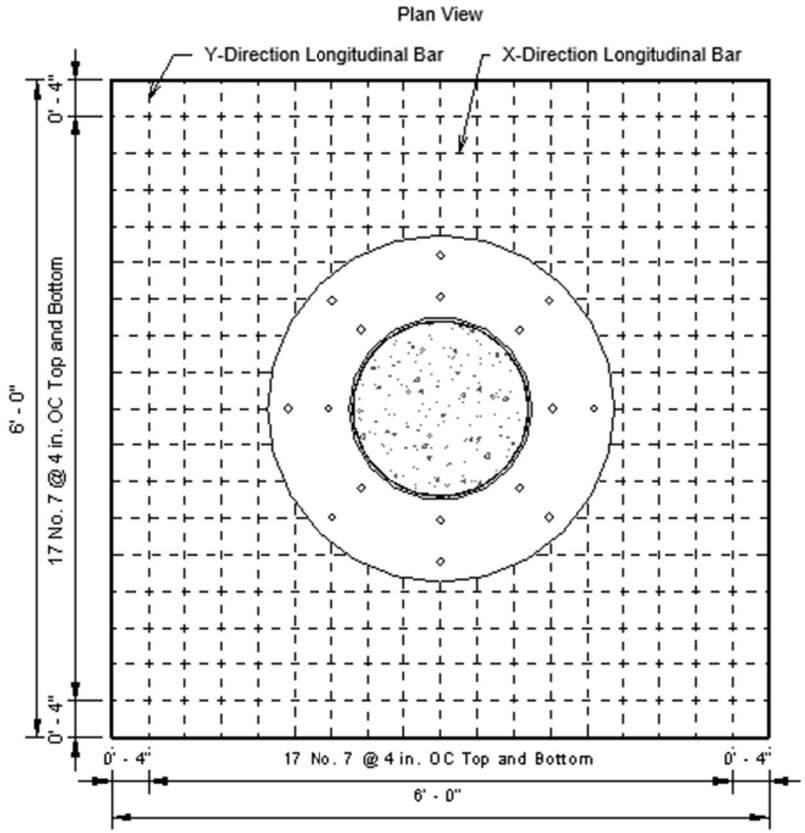

1 Rebar Layout Plan 9
3/4" = 1'-0"

CIVIL & ENVIRONMENTAL ENGINEERING

University of Washington
Department of Civil and Evironemental Engineering

NSF Secondary Evacuation Structures

PTB_9_2_0_P Plan

S.4

Elevation

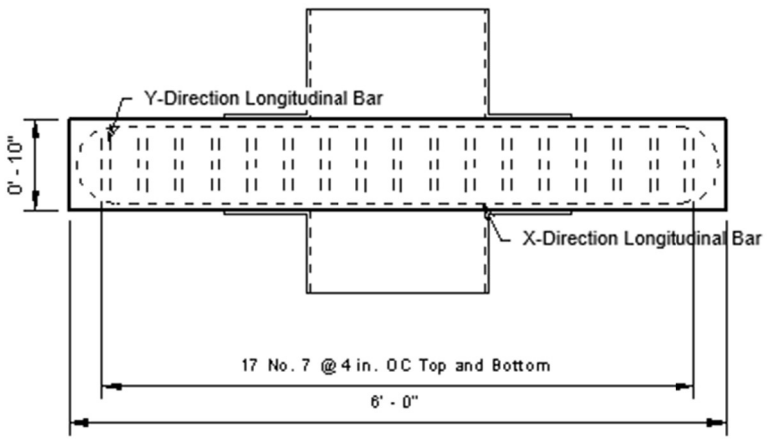

1 Rebar Layout Elevation 9
3/4" = 1'-0"

CIVIL & ENVIRONMENTAL ENGINEERING

University of Washington
Department of Civil and Evironemental Engineering

NSF Secondary Evacuation Structures

PTB_9_2_0_P Elevation

S.5

APPENDIX B

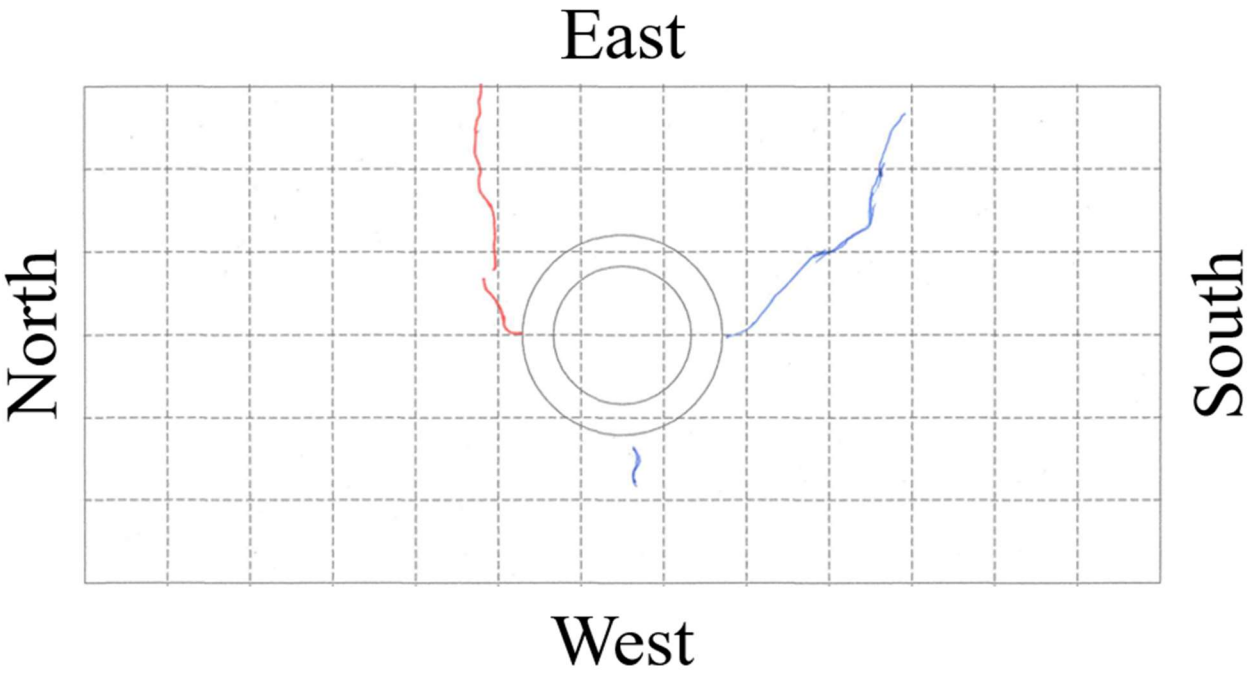

Figure 1. Top of Slab Crack Map 0.36% Drift (PTB_4.5_1_0_6)

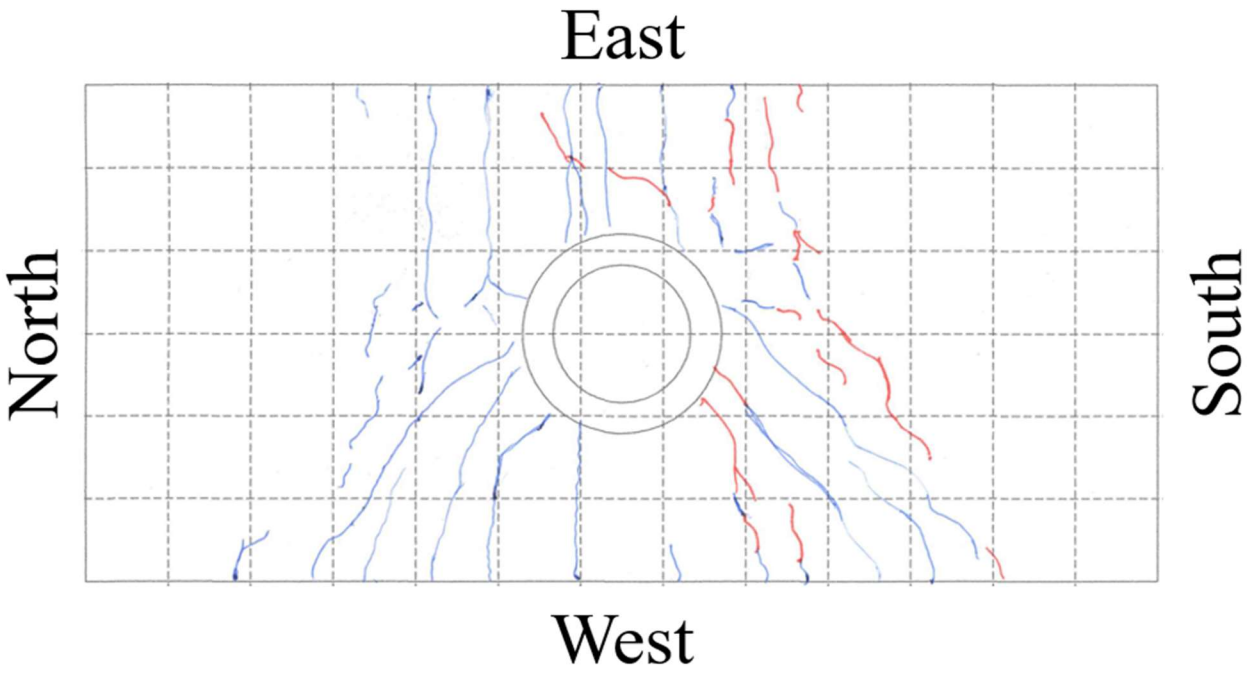

Figure 2. Bottom of Slab Crack Map 0.36% Drift (PTB_4.5_1_0_6)

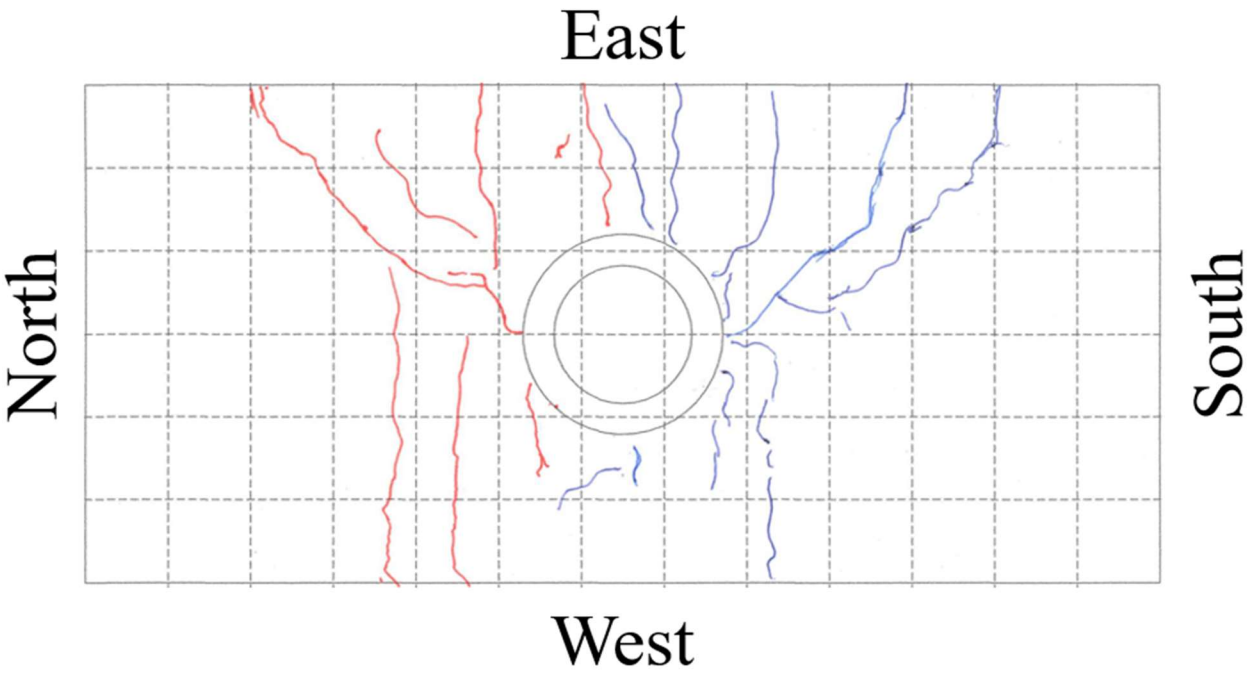

Figure 3. Top of Slab Crack Map 0.73% Drift (PTB_4.5_1_0_6)

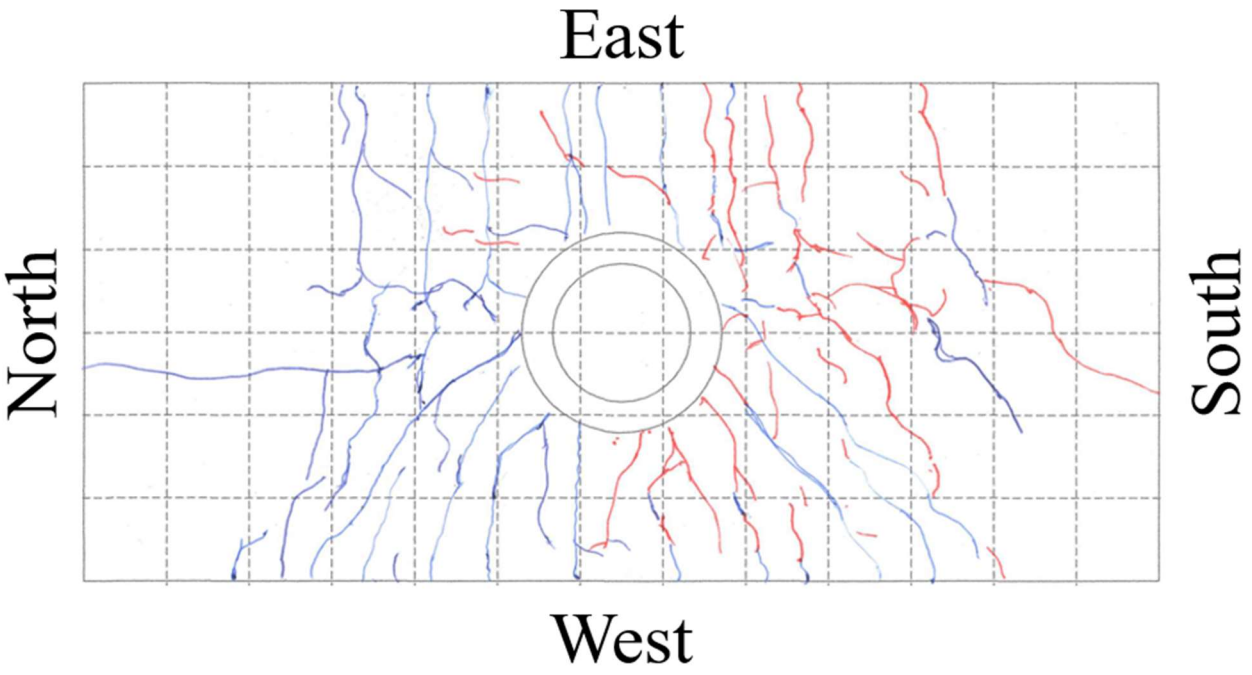

Figure 4. Bottom of Slab Crack Map 0.73% Drift (PTB_4.5_1_0_6)

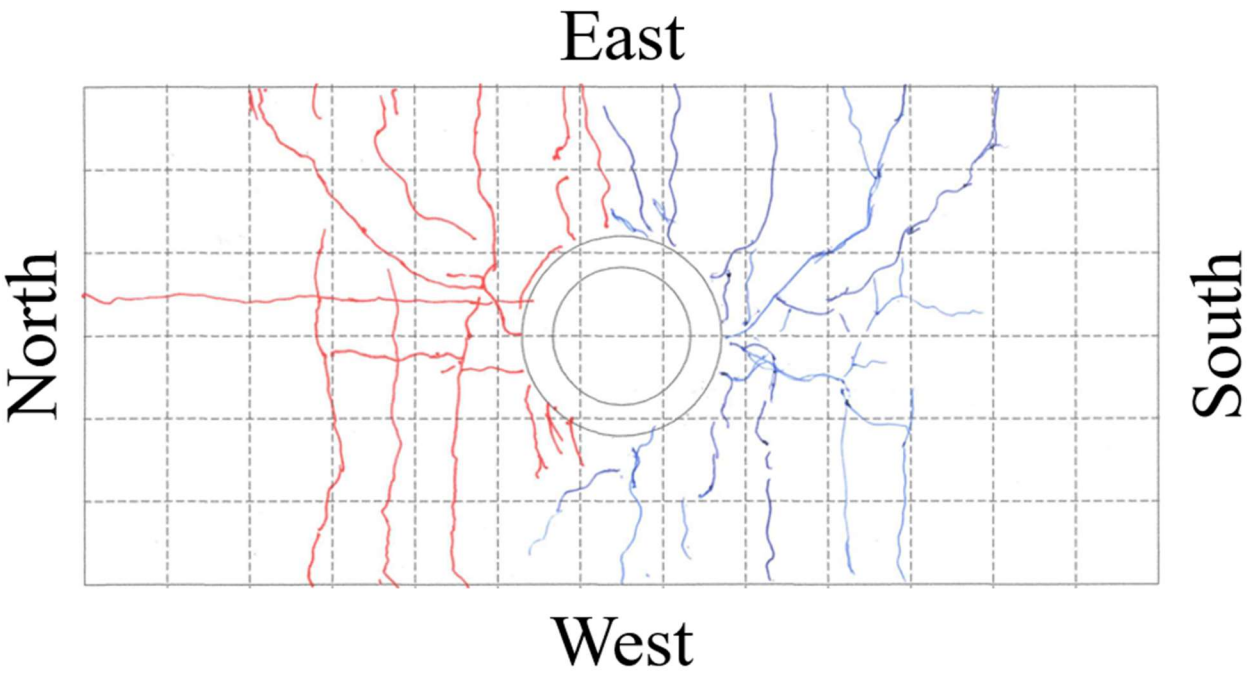

Figure 5. Top of Slab Crack Map 1.09% Drift (PTB_4.5_1_0_6)

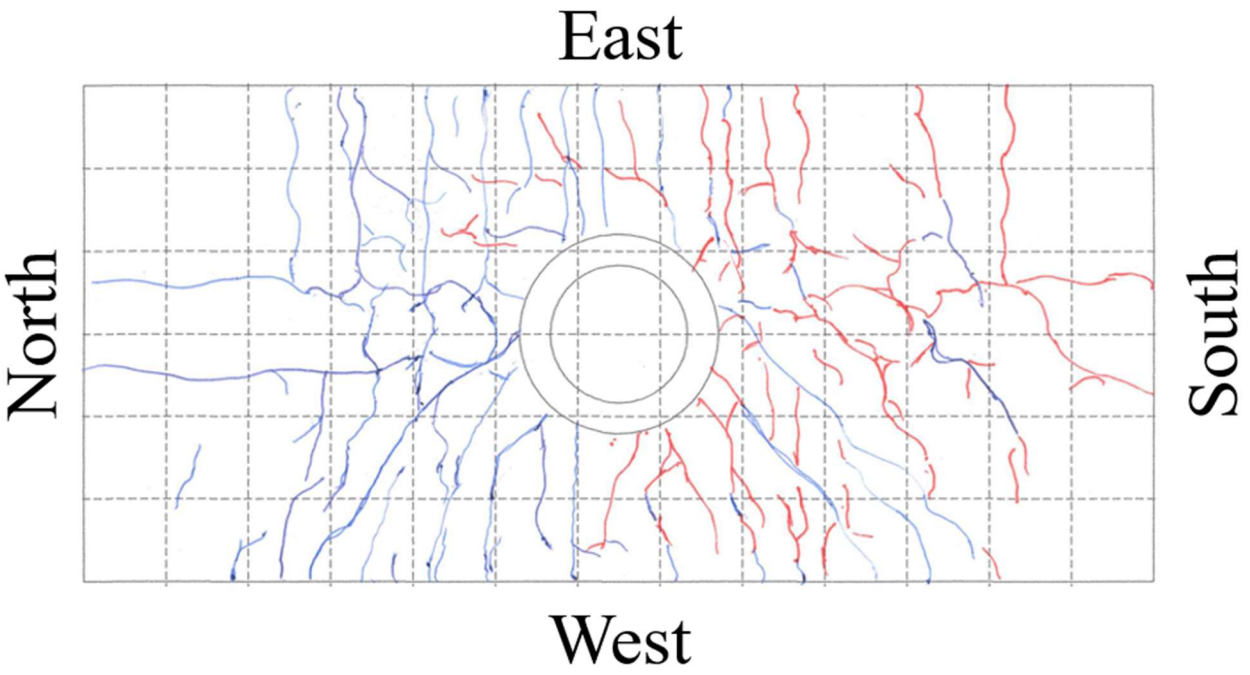

Figure 6. Bottom of Slab Crack Map 1.09% Drift (PTB_4.5_1_0_6)

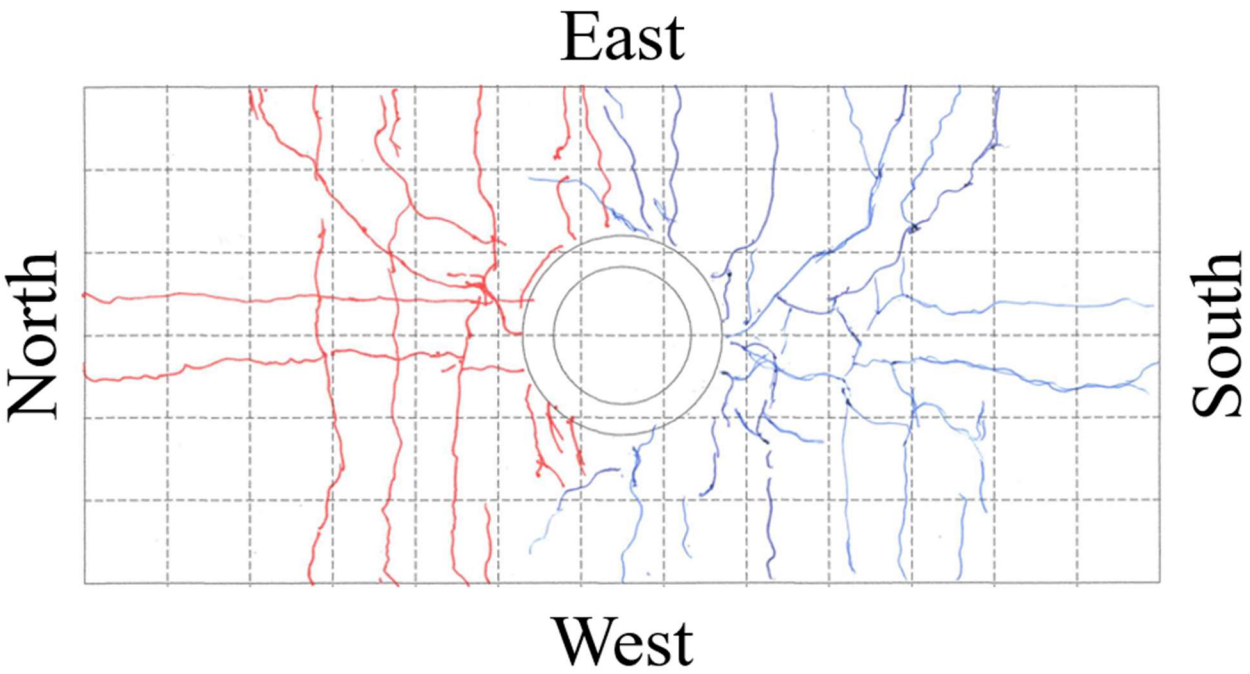

Figure 7. Top of Slab Crack Map 1.45% Drift (PTB_4.5_1_0_6)

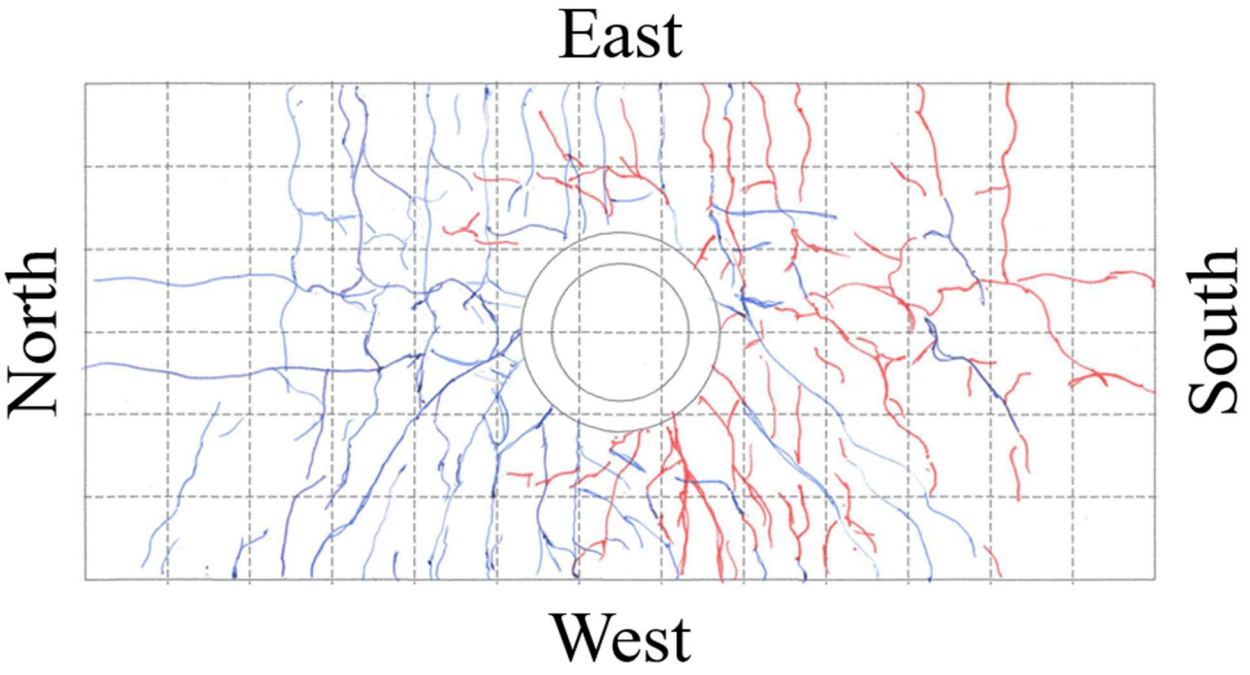

Figure 8. Bottom of Slab Crack Map 1.45% Drift (PTB_4.5_1_0_6)

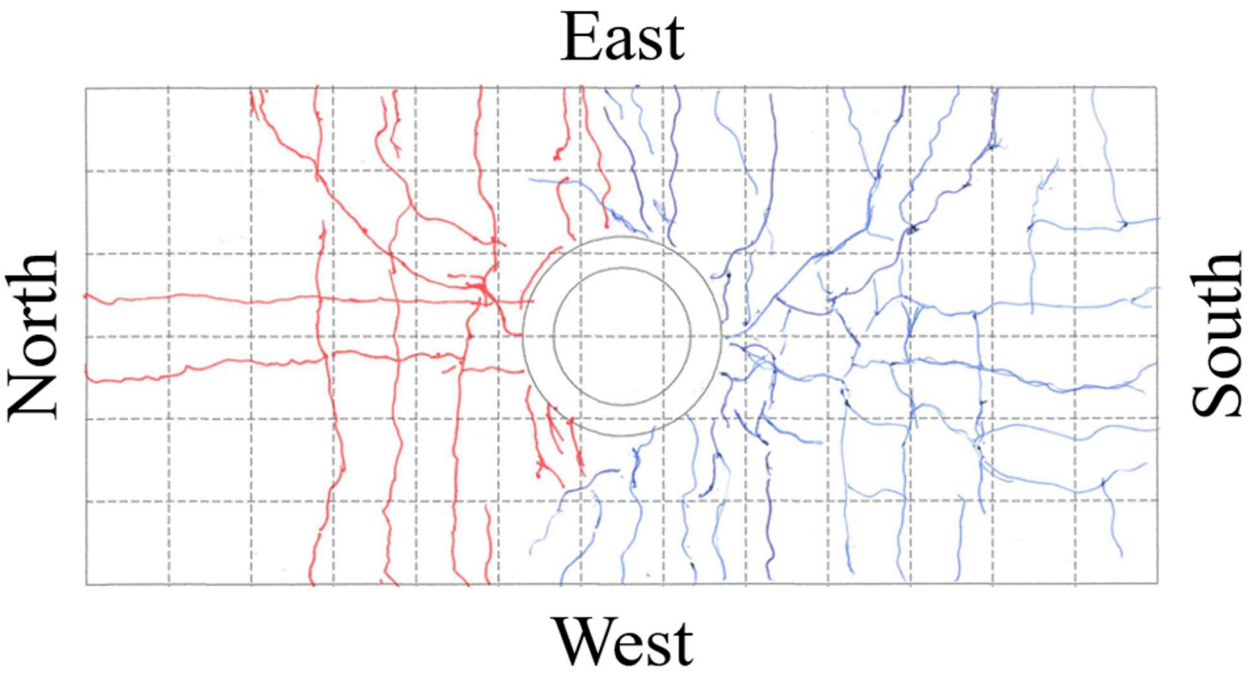

Figure 9. Top of Slab Crack Map 2.18% Drift (PTB_4.5_1_0_6)

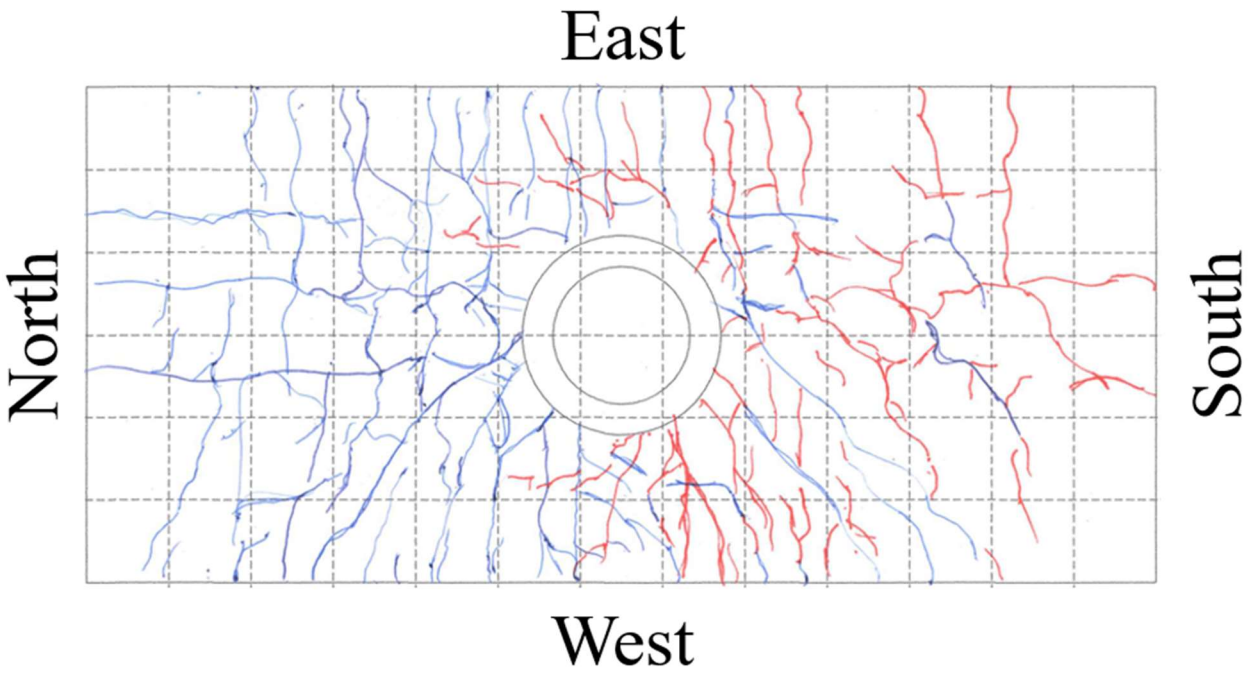

Figure 10. Bottom of Slab Crack Map 2.18% Drift (PTB_4.5_1_0_6)

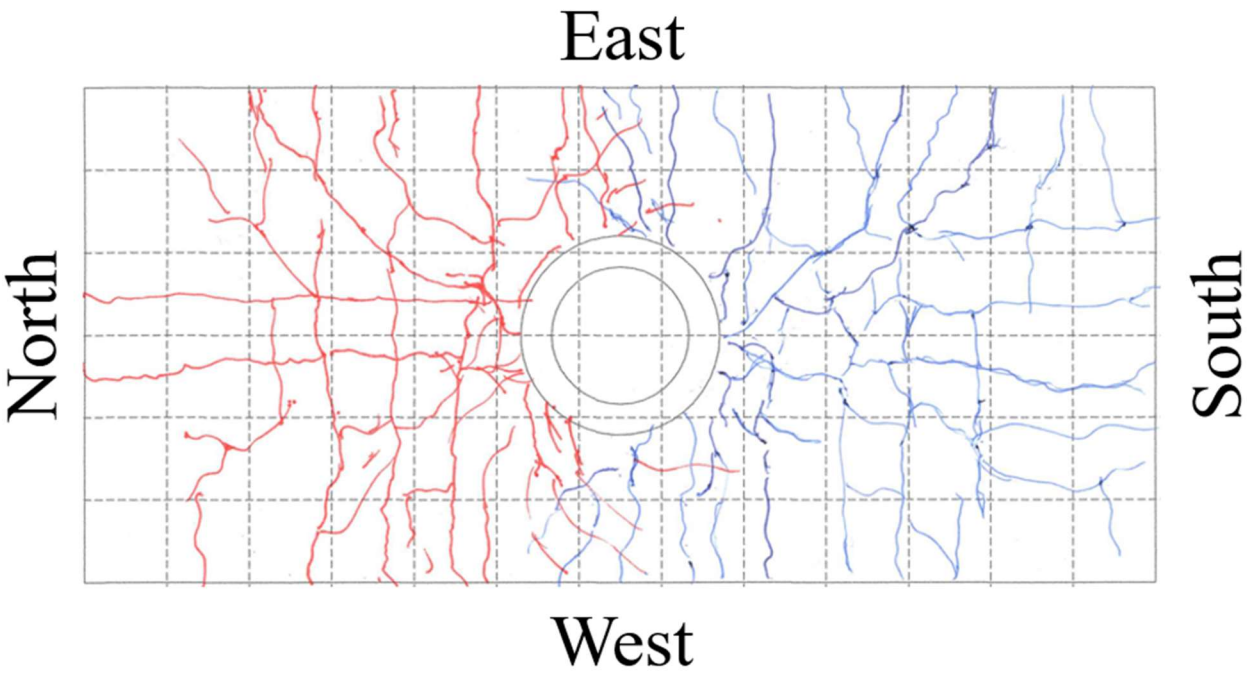

Figure 11. Top of Slab Crack Map 2.90% Drift (PTB_4.5_1_0_6)

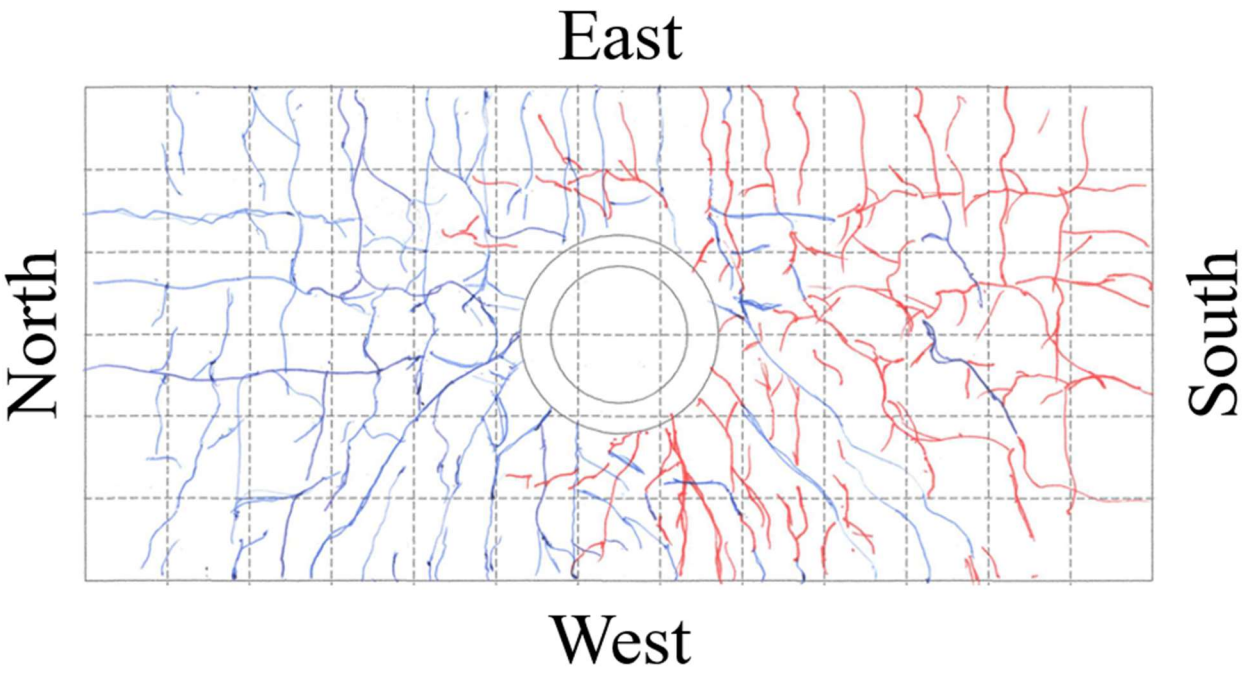

Figure 12. Bottom of Slab Crack Map 2.90% Drift (PTB_4.5_1_0_6)

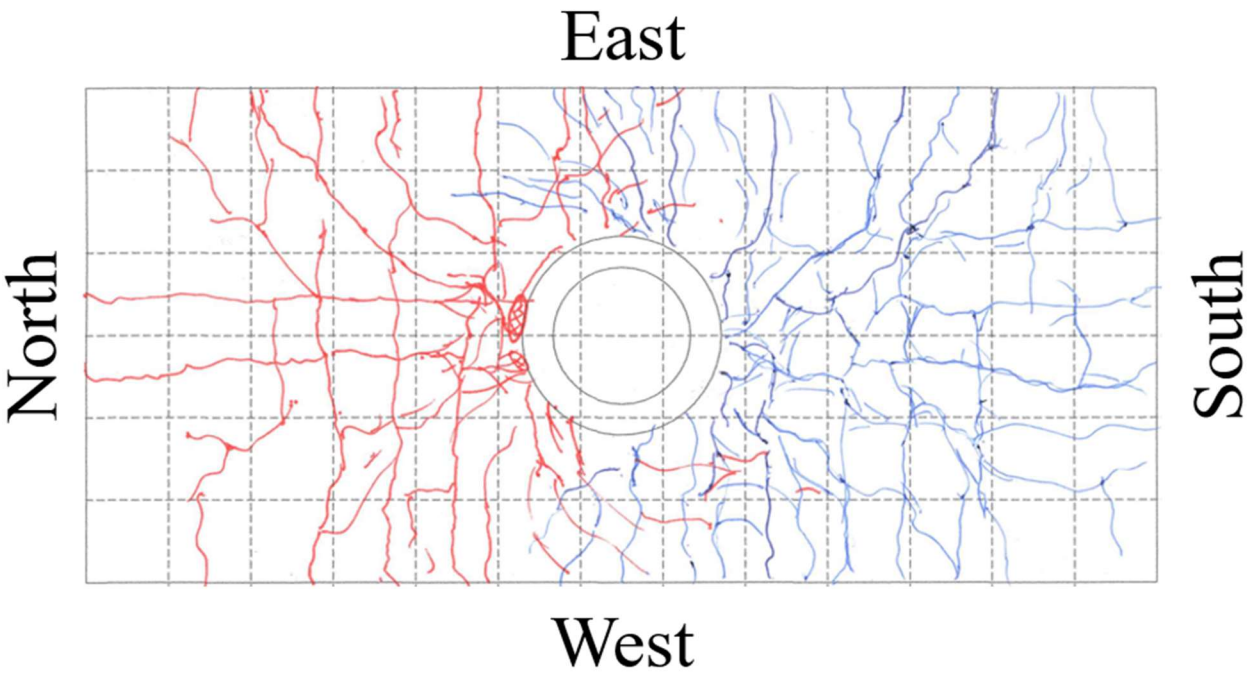

Figure 13. Top of Slab Crack Map 3.63% Drift (PTB_4.5_1_0_6)

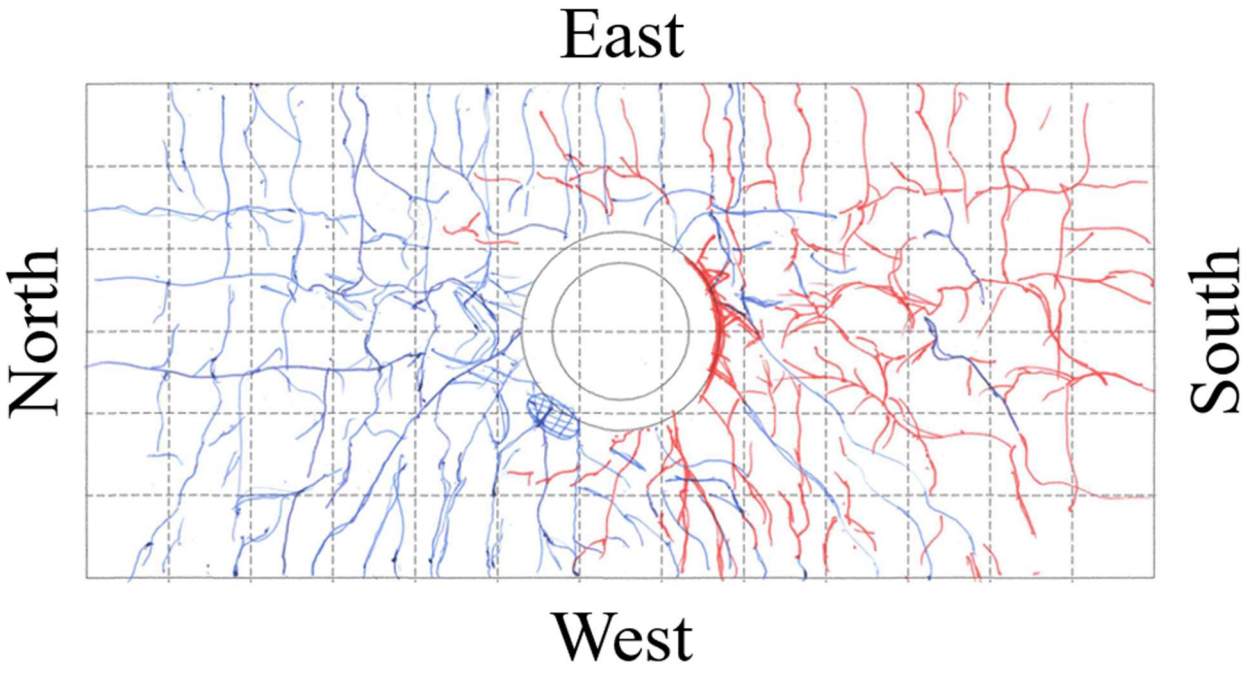

Figure 14. Bottom of Slab Crack Map 3.63% Drift (PTB_4.5_1_0_6)

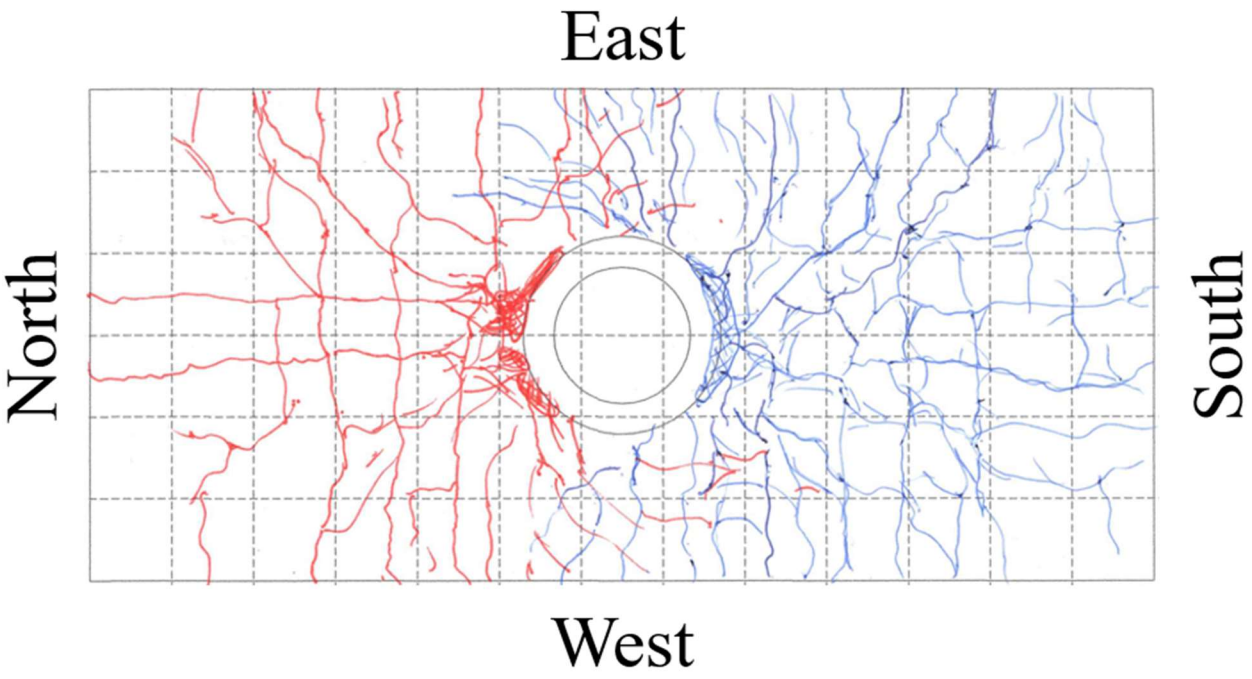

Figure 15. Top of Slab Crack Map 4.36% Drift (PTB_4.5_1_0_6)

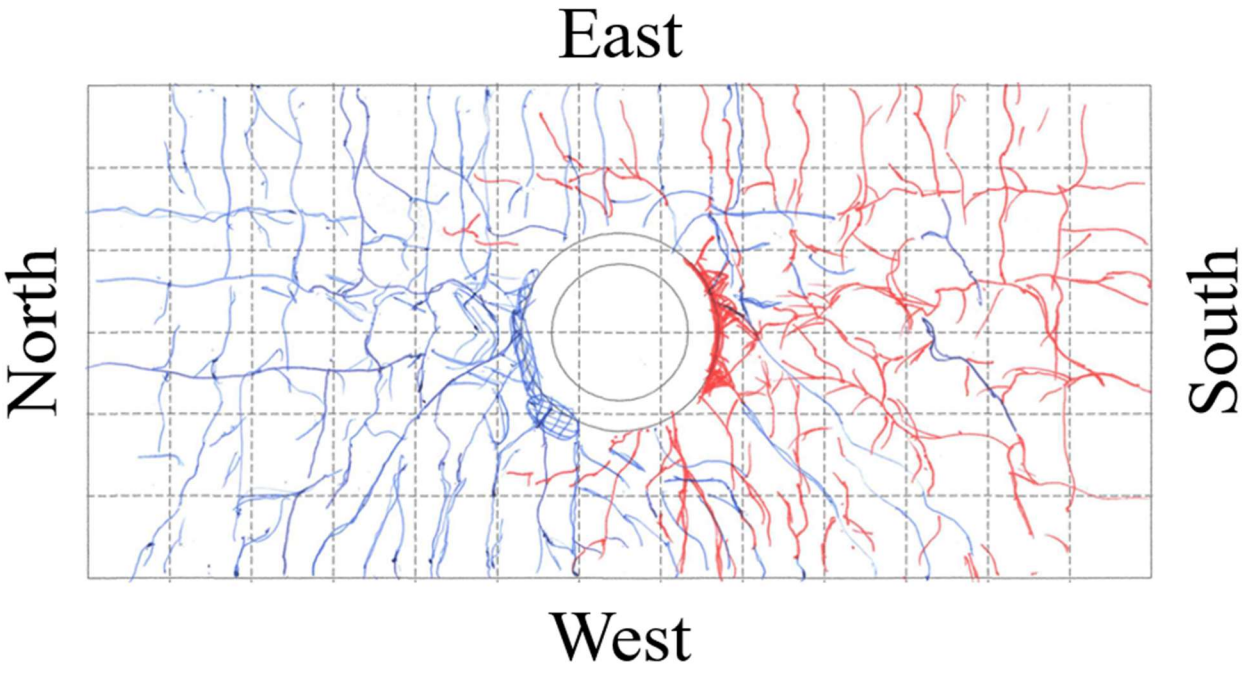

Figure 16. Bottom of Slab Crack Map 4.36% Drift (PTB_4.5_1_0_6)

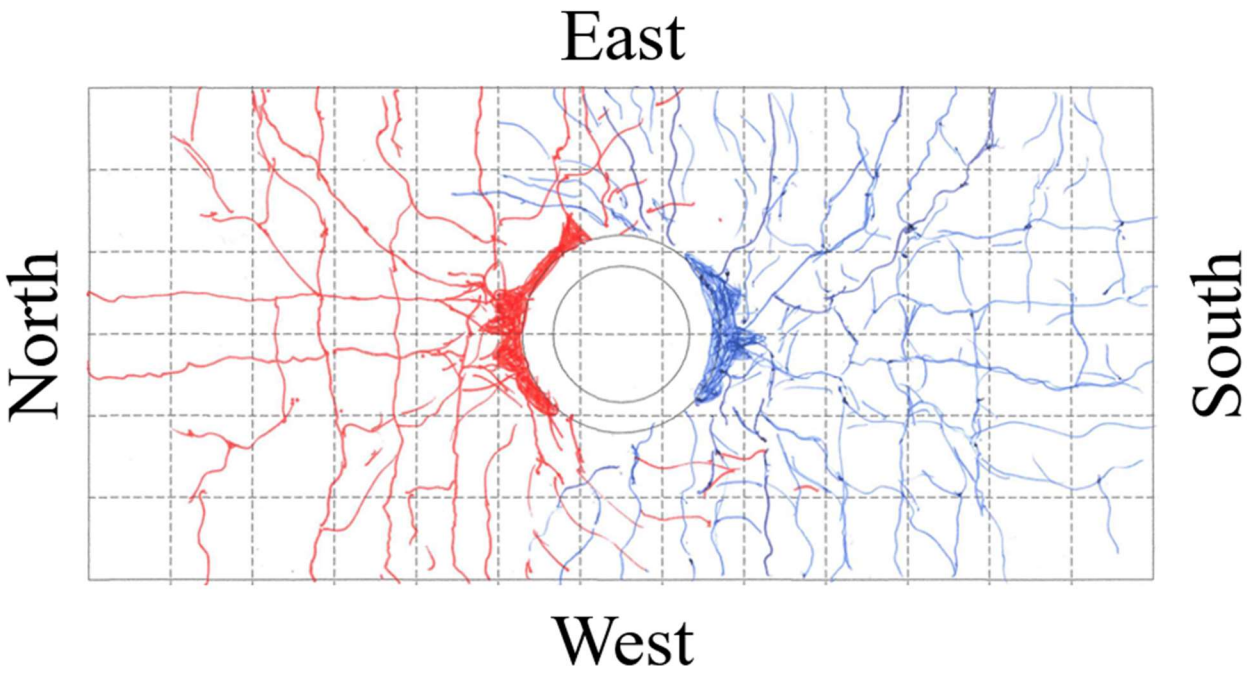

Figure 17. Top of Slab Crack Map 5.08% Drift (PTB_4.5_1_0_6)

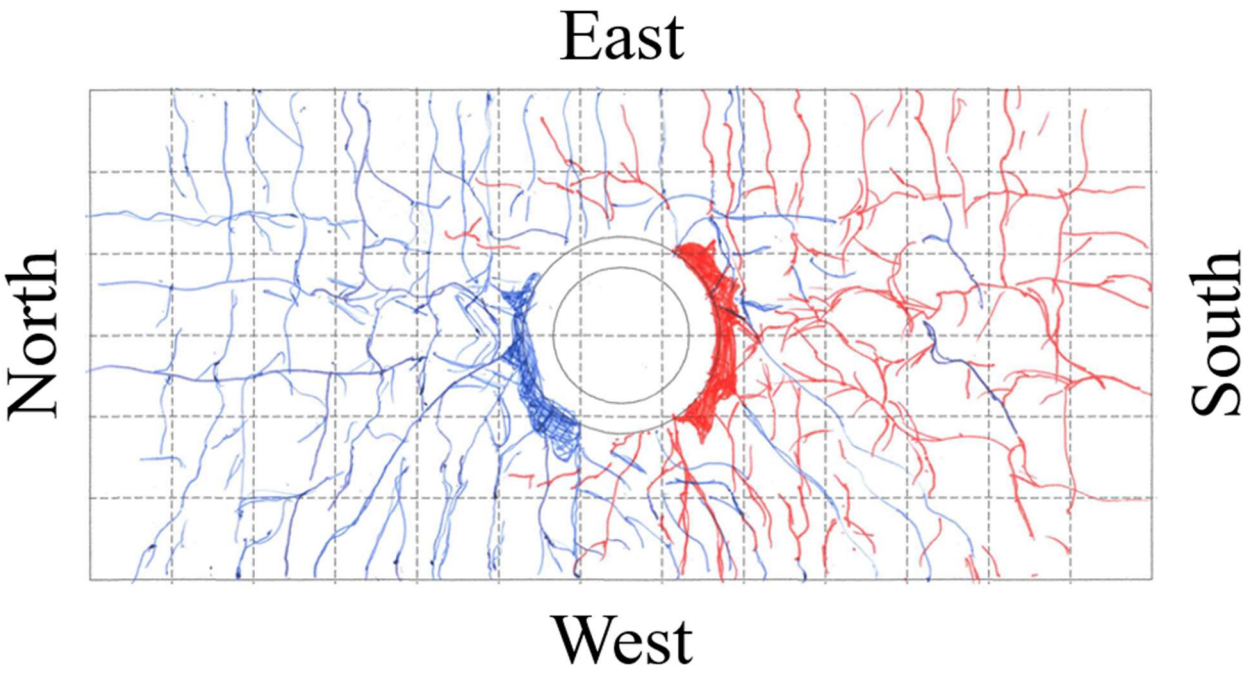

Figure 18. Bottom of Slab Crack Map 5.08% Drift (PTB_4.5_1_0_6)

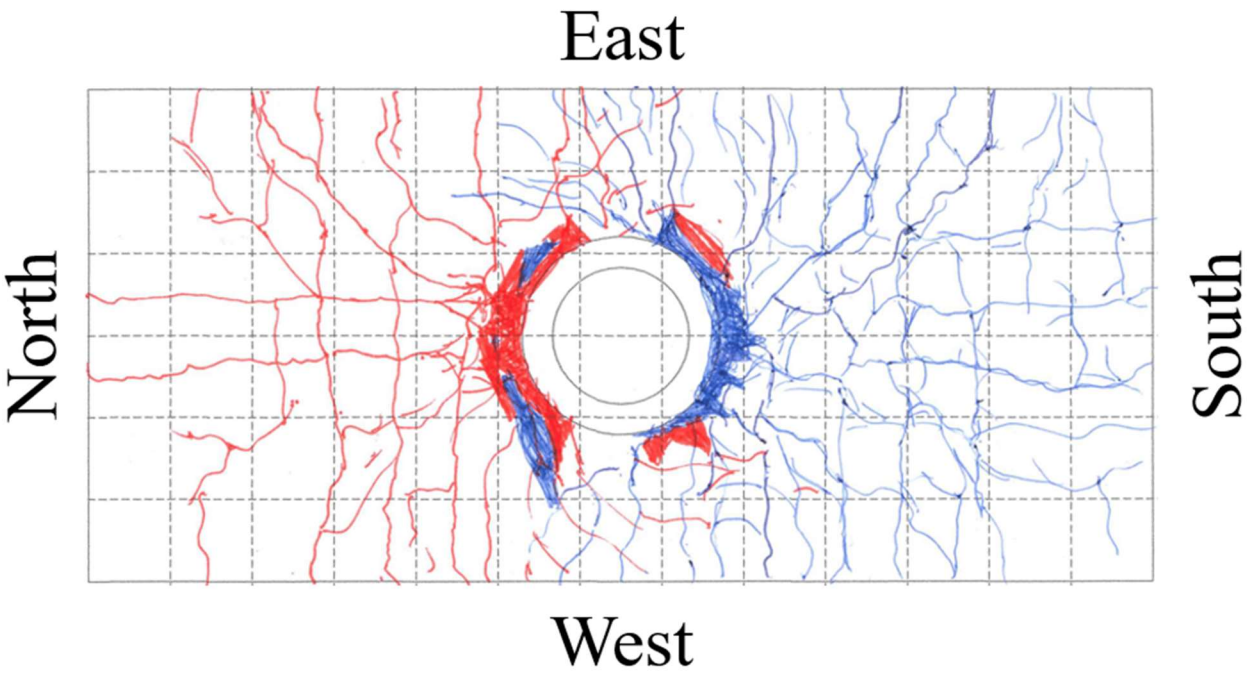

Figure 19. Top of Slab Crack Map 5.81% Drift (PTB_4.5_1_0_6)

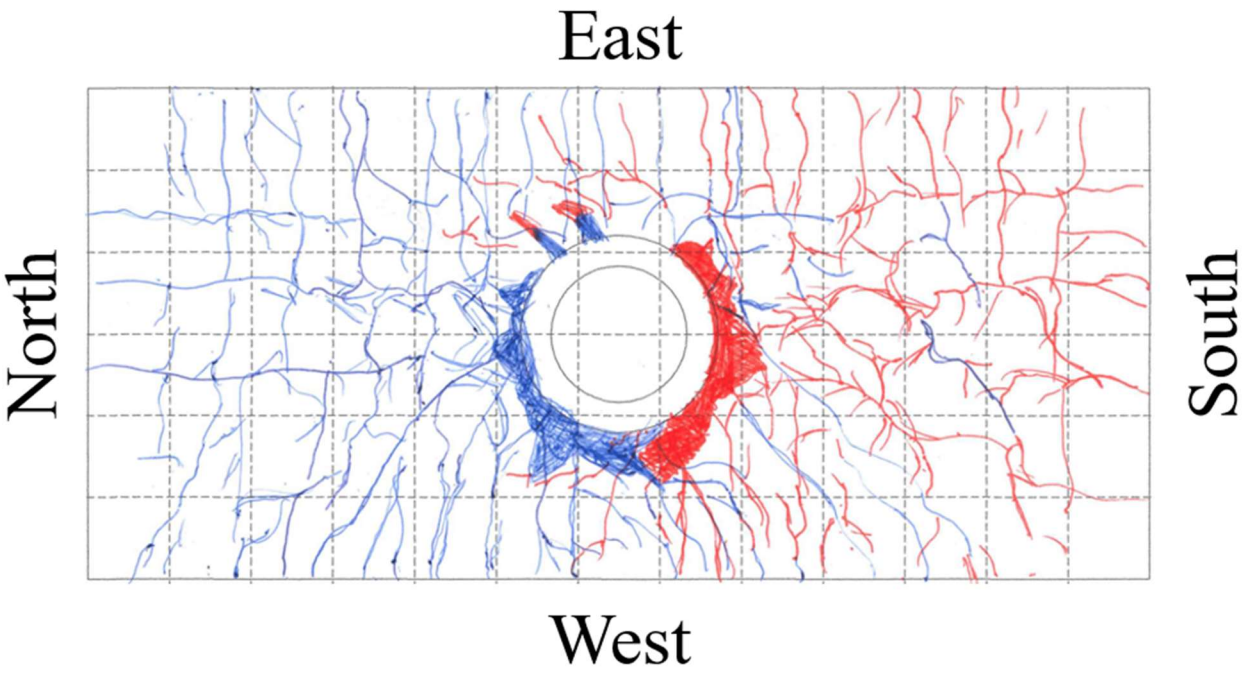

Figure 20. Bottom of Slab Crack Map 5.81% Drift (PTB_4.5_1_0_6)

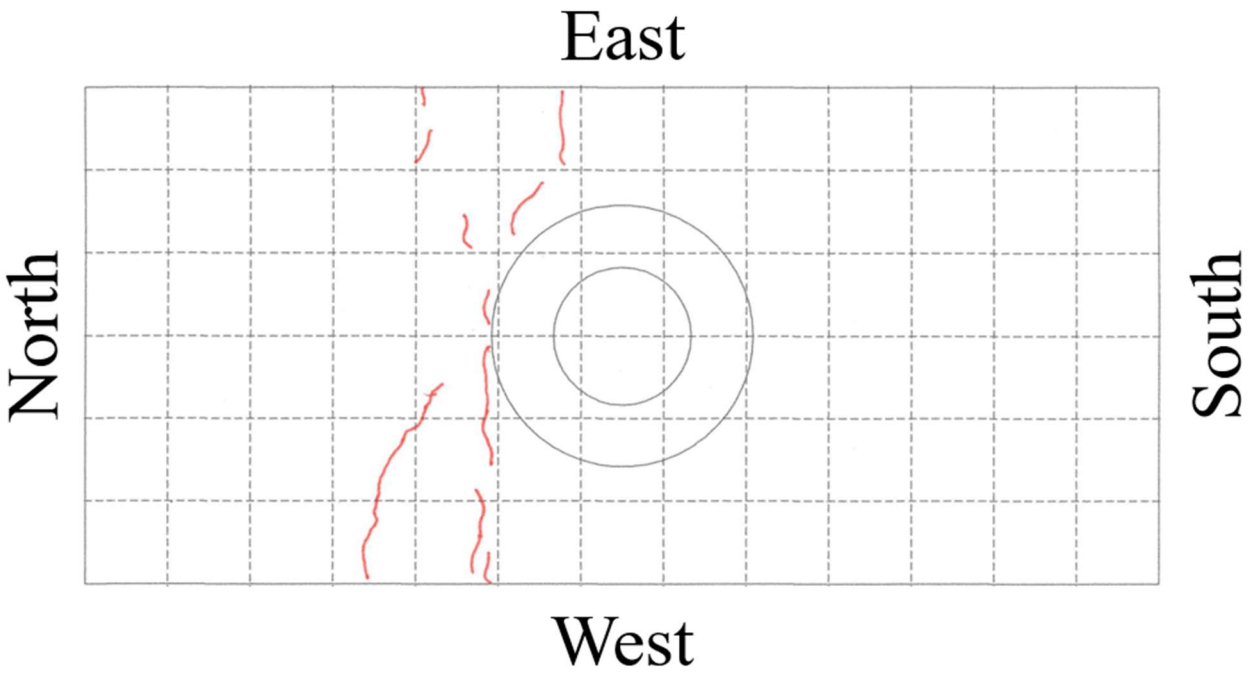

Figure 21. Top of Slab Crack Map 0.36% Drift (PTB_9_2_0_6)

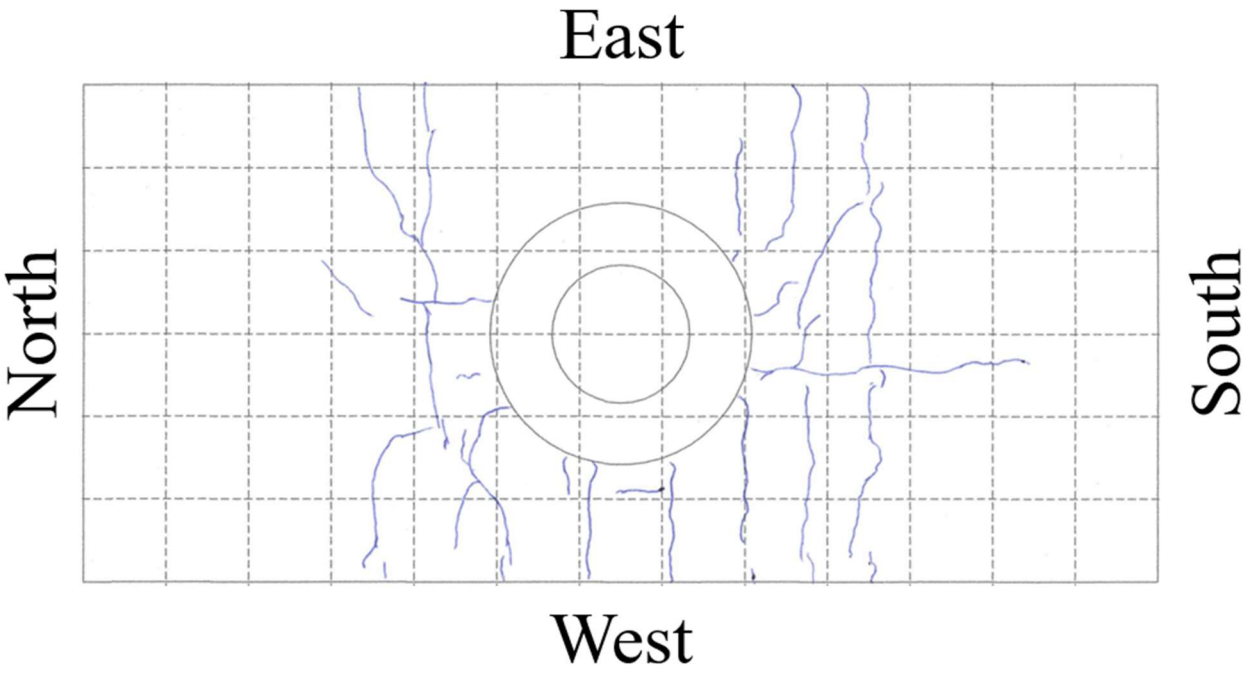

Figure 22. Bottom of Slab Crack Map 0.36% Drift (PTB_9_2_0_6)

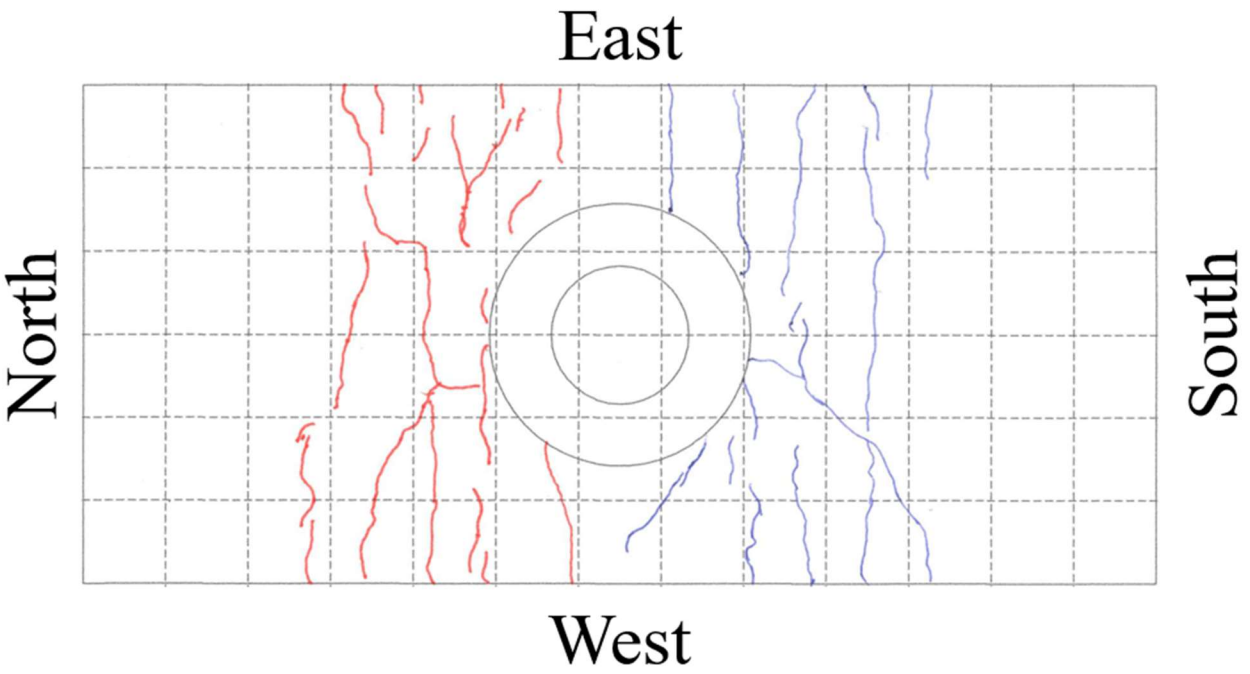

Figure 23. Top of Slab Crack Map 0.73% Drift (PTB_9_2_0_6)

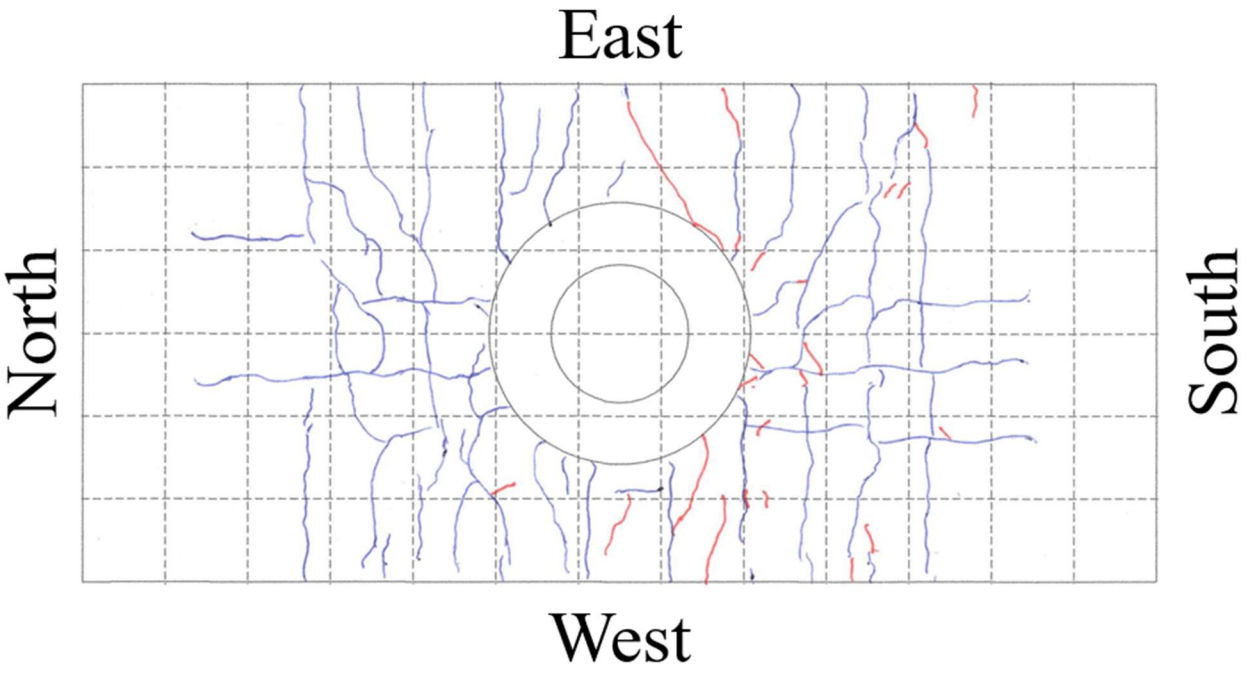

Figure 24. Bottom of Slab Crack Map 0.73% Drift (PTB_9_2_0_6)

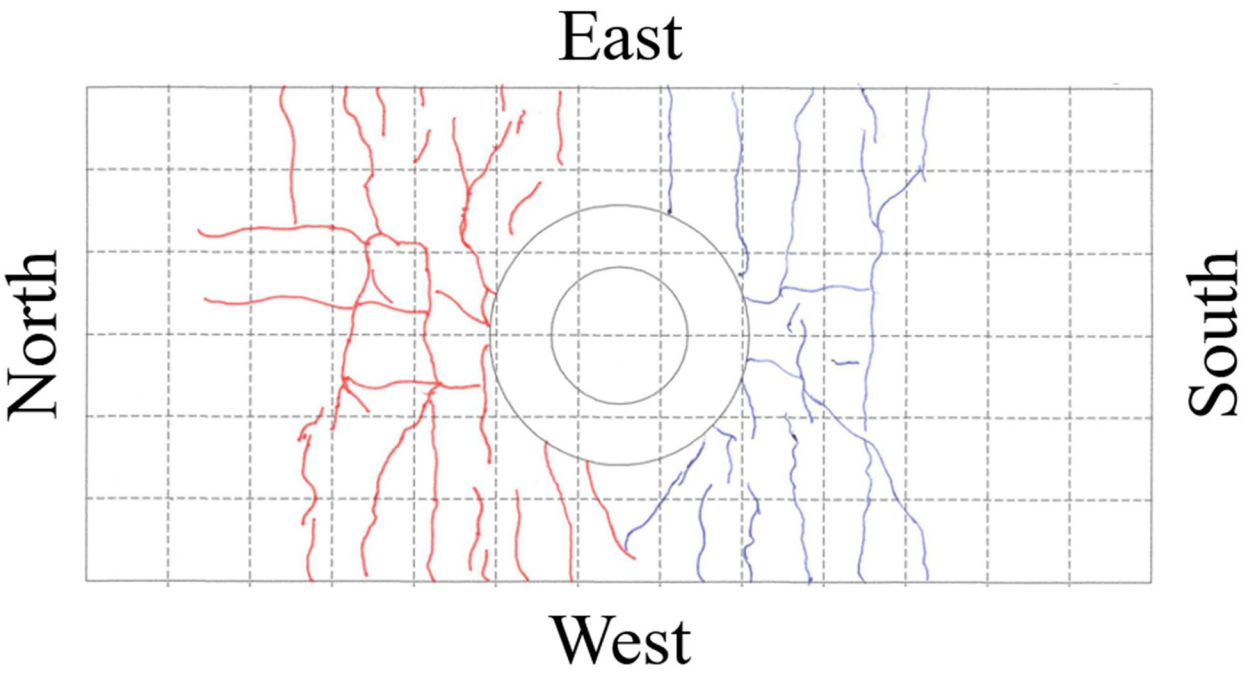

Figure 25. Top of Slab Crack Map 1.09% Drift (PTB_9_2_0_6)

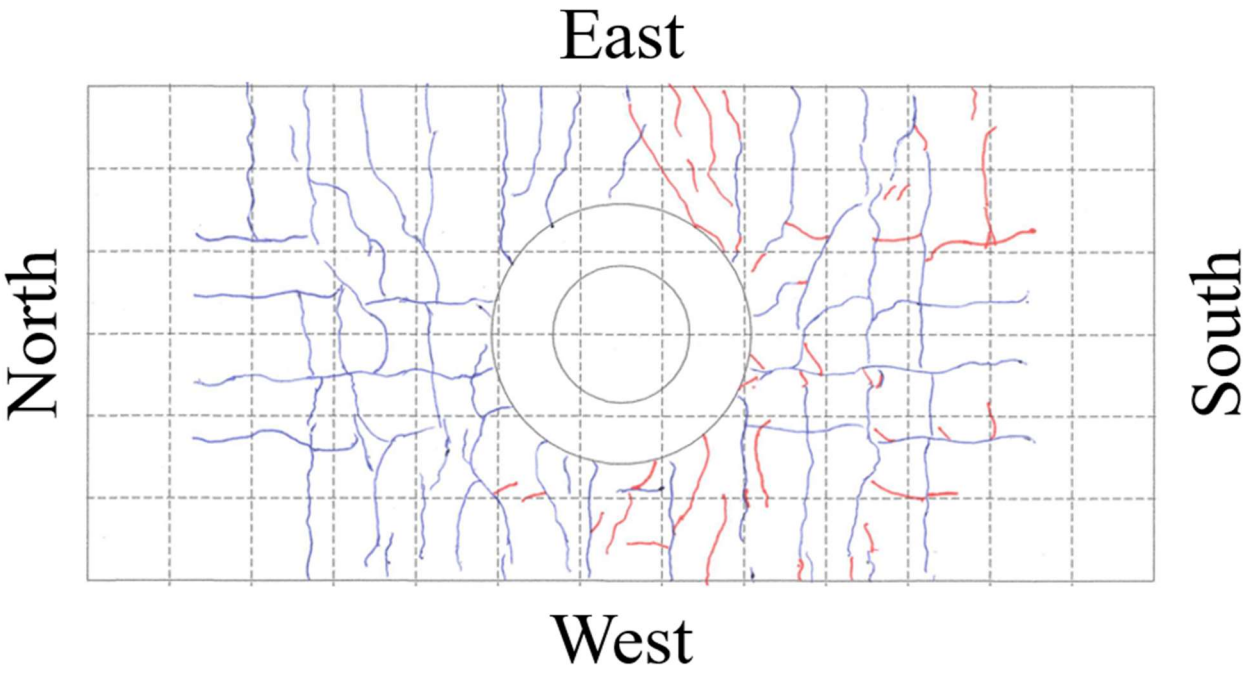

Figure 26. Bottom of Slab Crack Map 1.09% Drift (PTB_9_2_0_6)

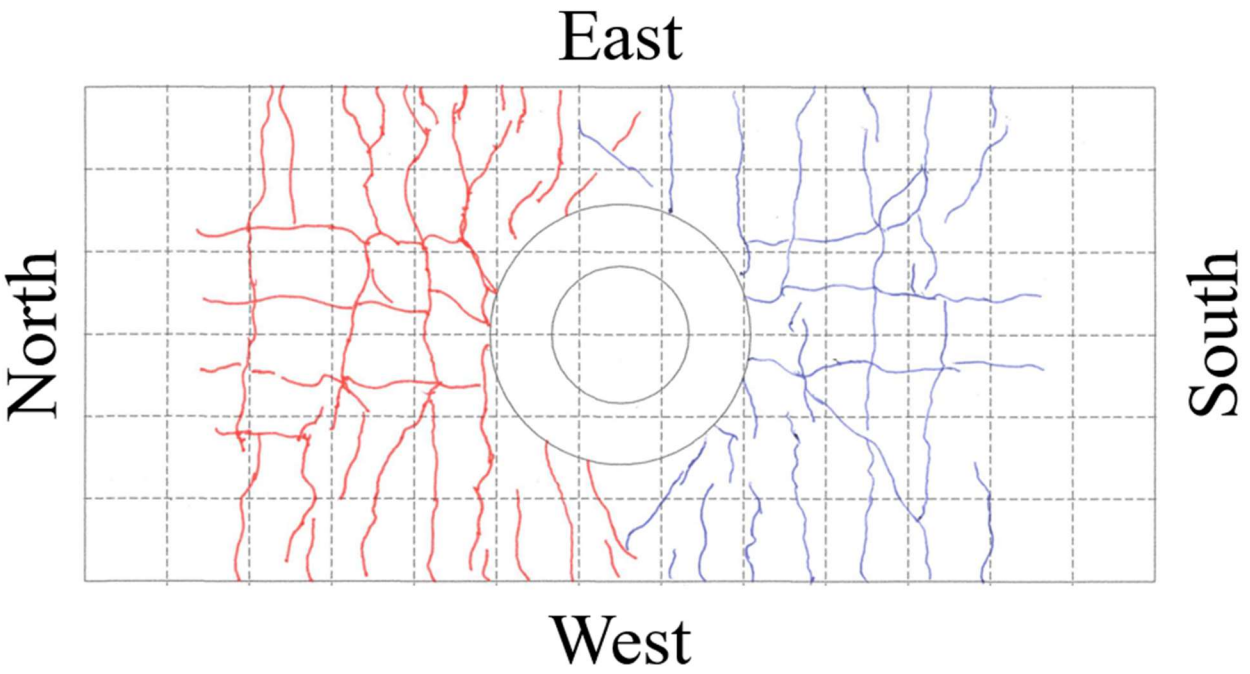

Figure 27. Top of Slab Crack Map 1.45% Drift (PTB_9_2_0_6)

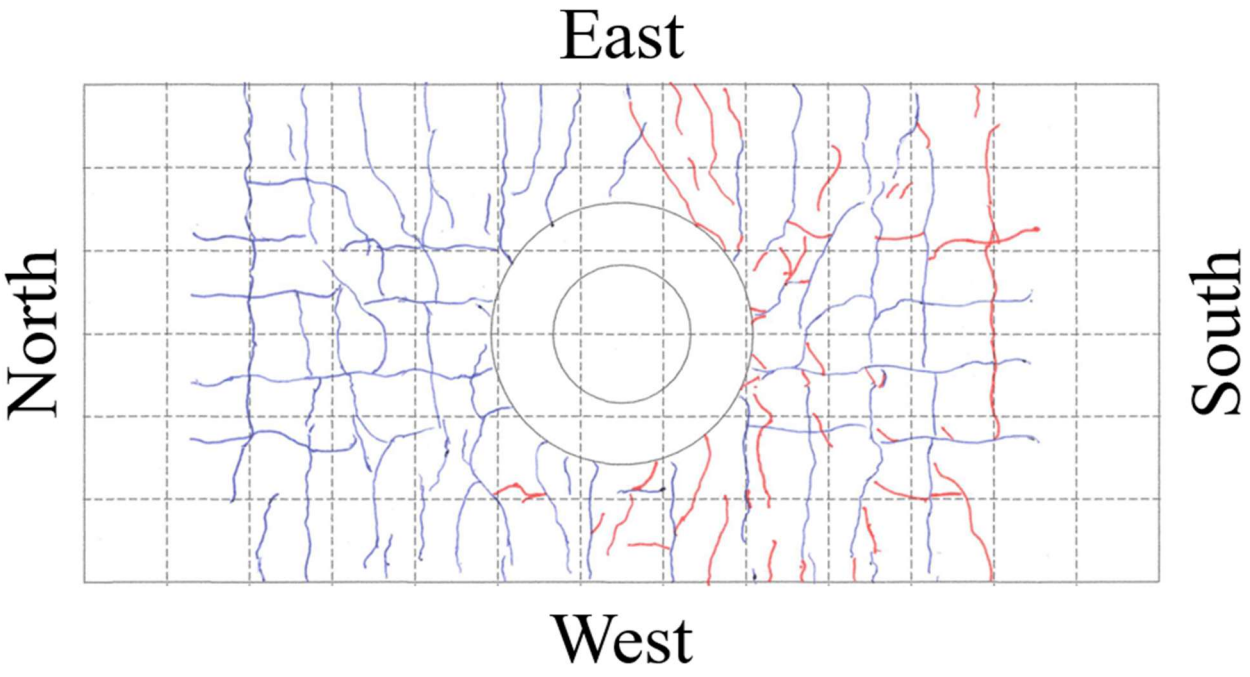

Figure 28. Bottom of Slab Crack Map 1.45% Drift (PTB_9_2_0_6)

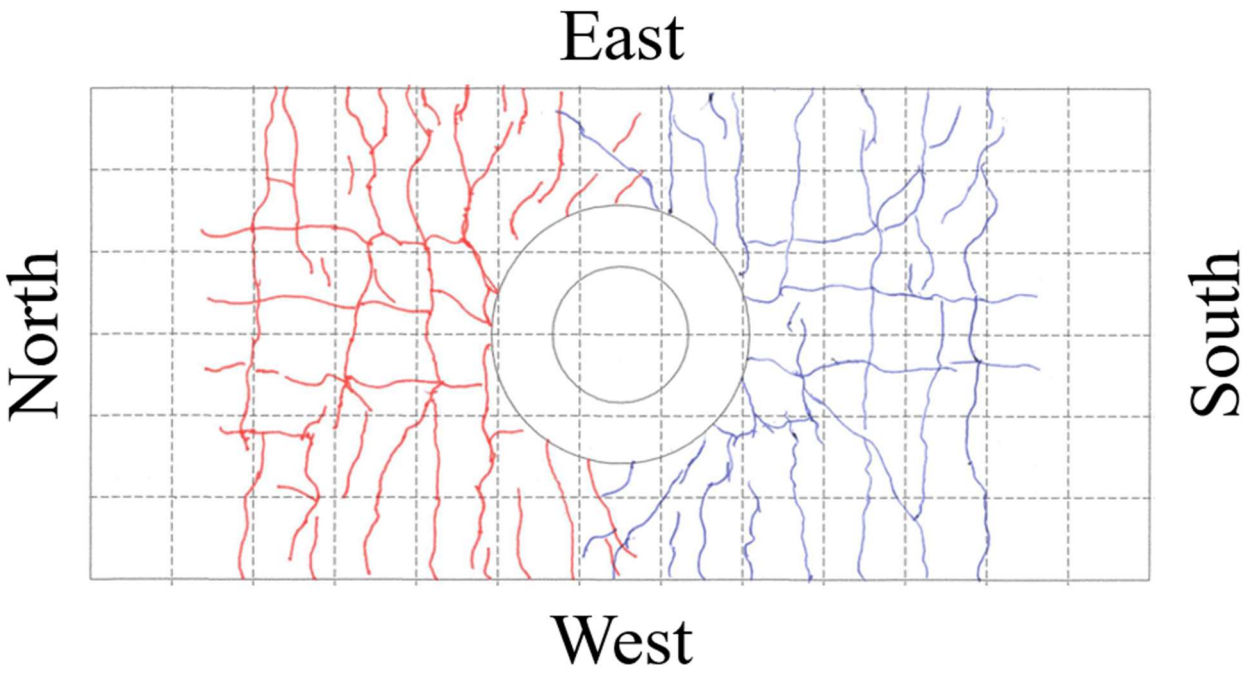

Figure 29. Top of Slab Crack Map 2.18% Drift (PTB_9_2_0_6)

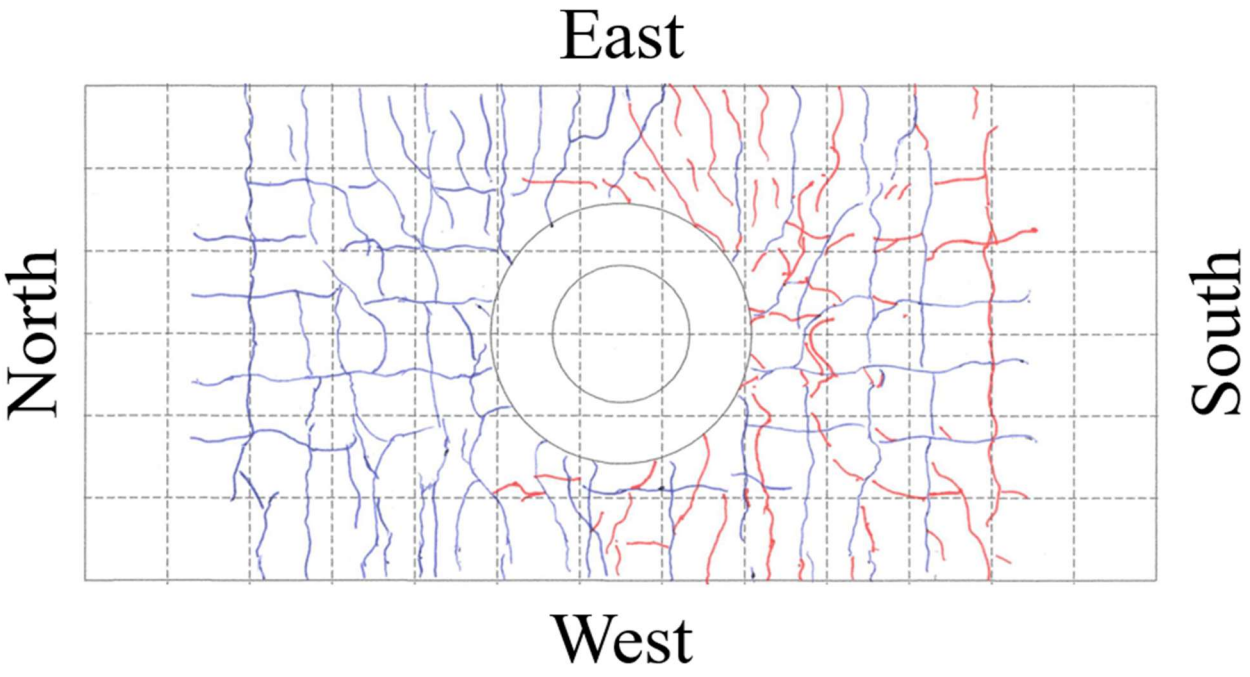

Figure 30. Bottom of Slab Crack Map 2.18% Drift (PTB_9_2_0_6)

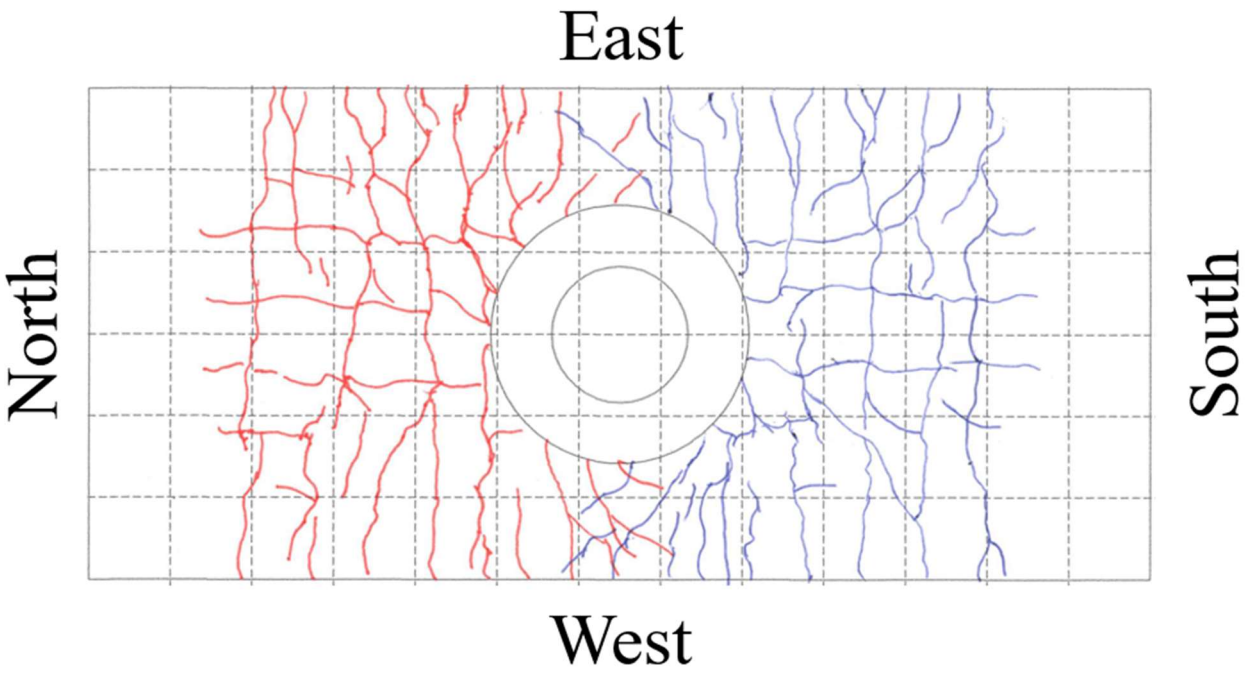

Figure 31. Top of Slab Crack Map 2.90% Drift (PTB_9_2_0_6)

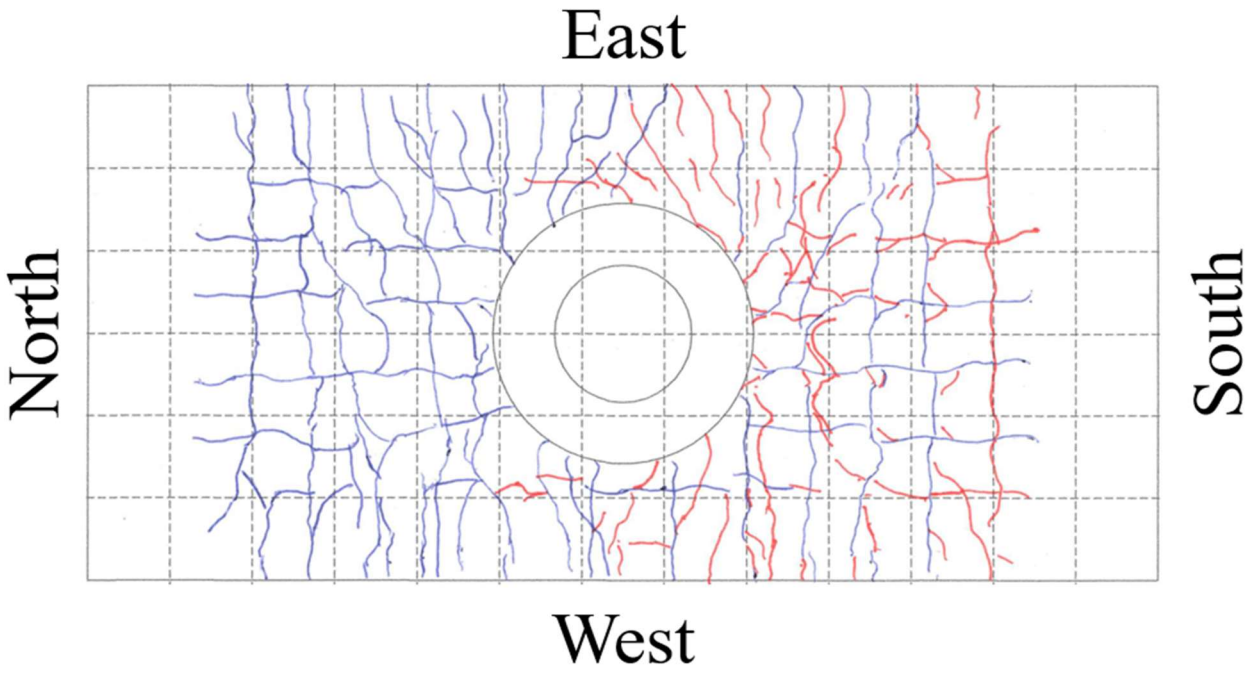

Figure 32. Bottom of Slab Crack Map 2.90% Drift (PTB_9_2_0_6)

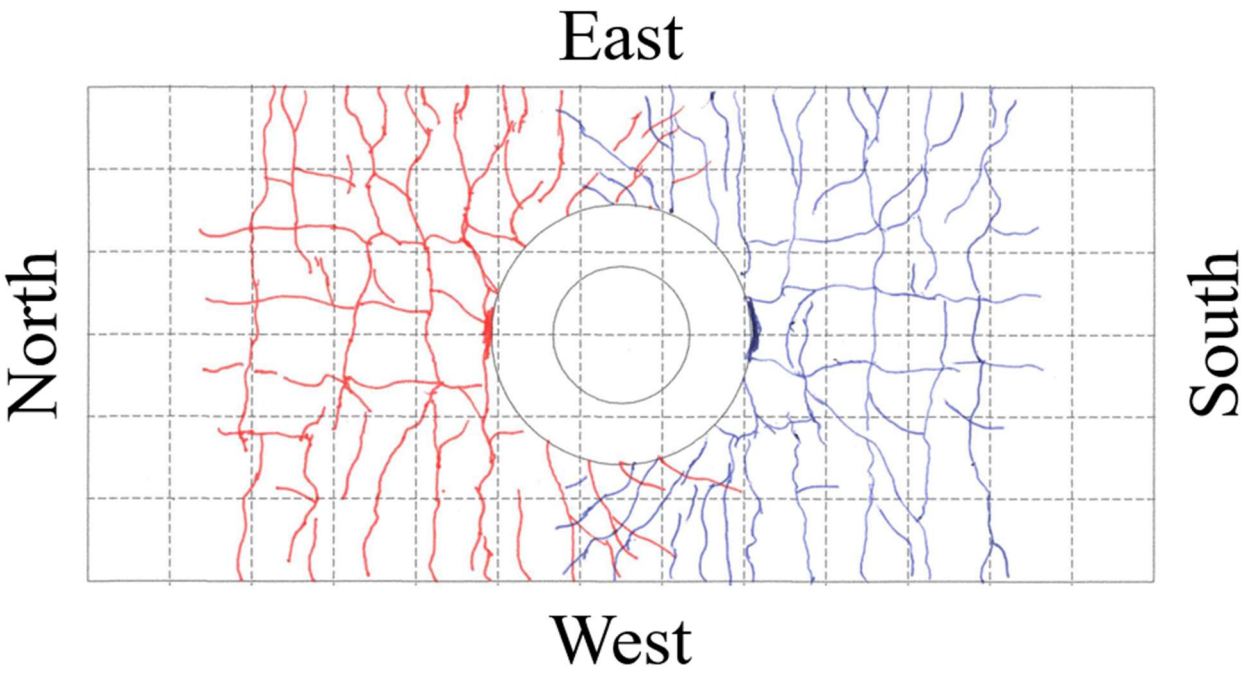

Figure 33. Top of Slab Crack Map 3.63% Drift (PTB_9_2_0_6)

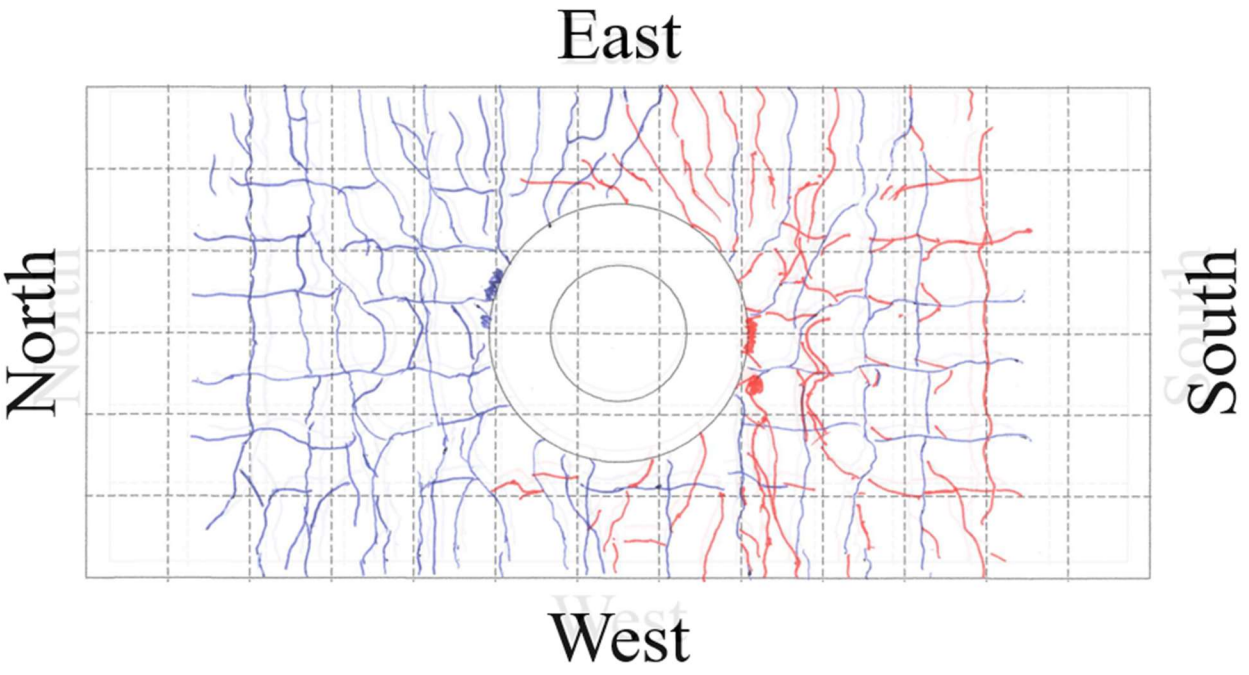

Figure 34. Bottom of Slab Crack Map 3.63% Drift (PTB_9_2_0_6)

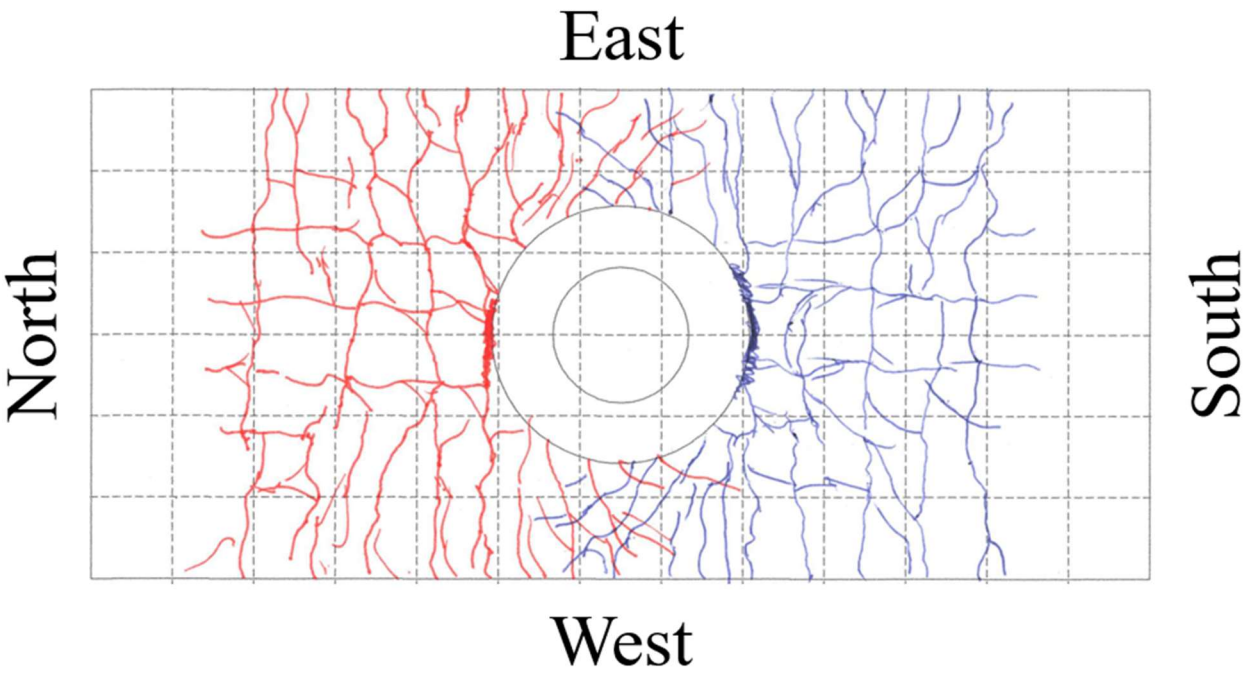

Figure 35. Top of Slab Crack Map 4.36% Drift (PTB_9_2_0_6)

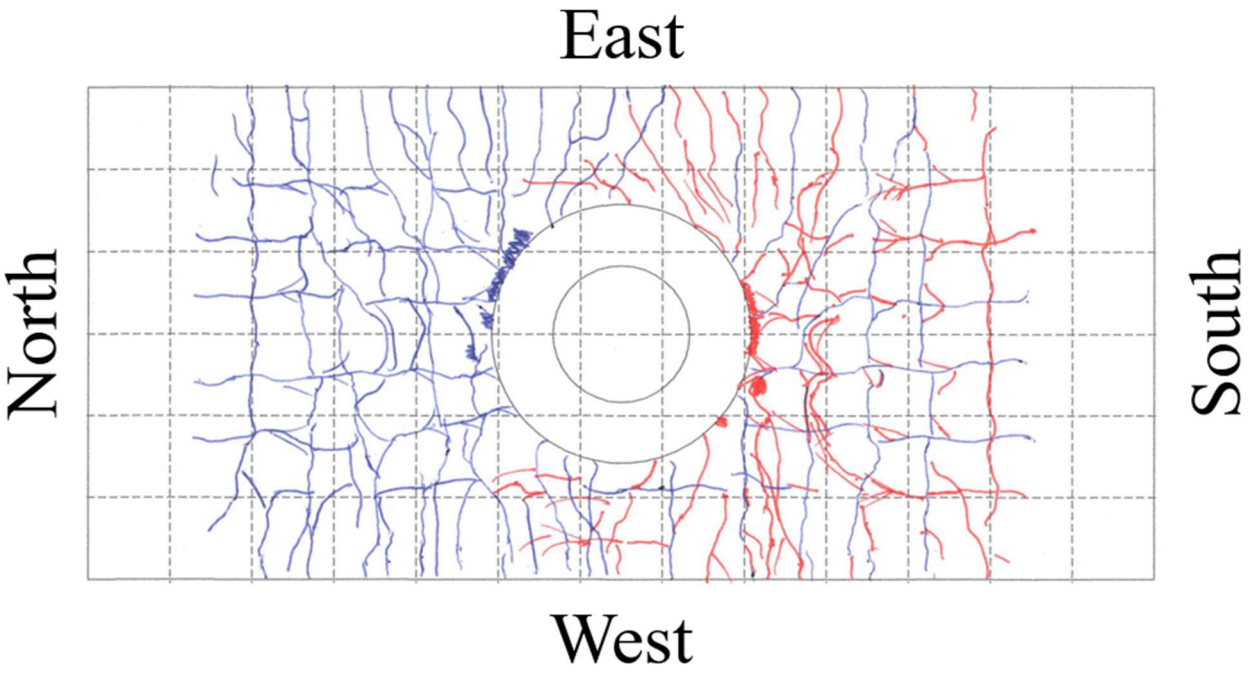

Figure 36. Bottom of Slab Crack Map 4.36% Drift (PTB_9_2_0_6)

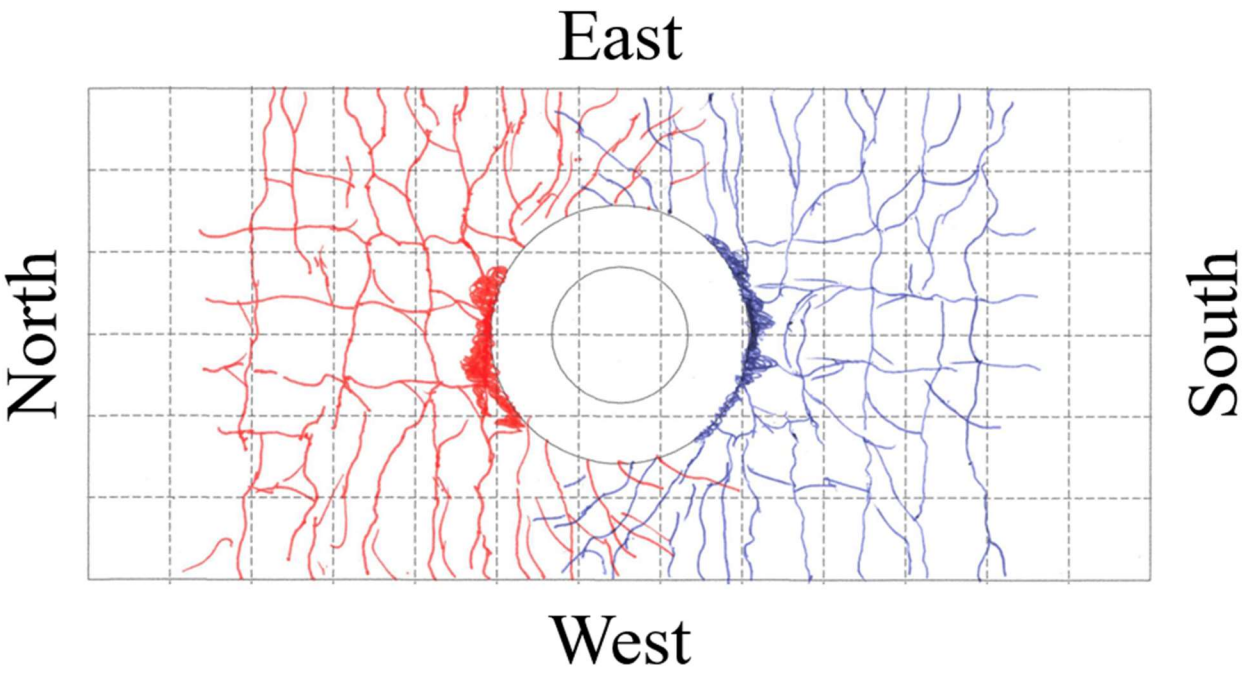

Figure 37. Top of Slab Crack Map 5.08% Drift (PTB_9_2_0_6)

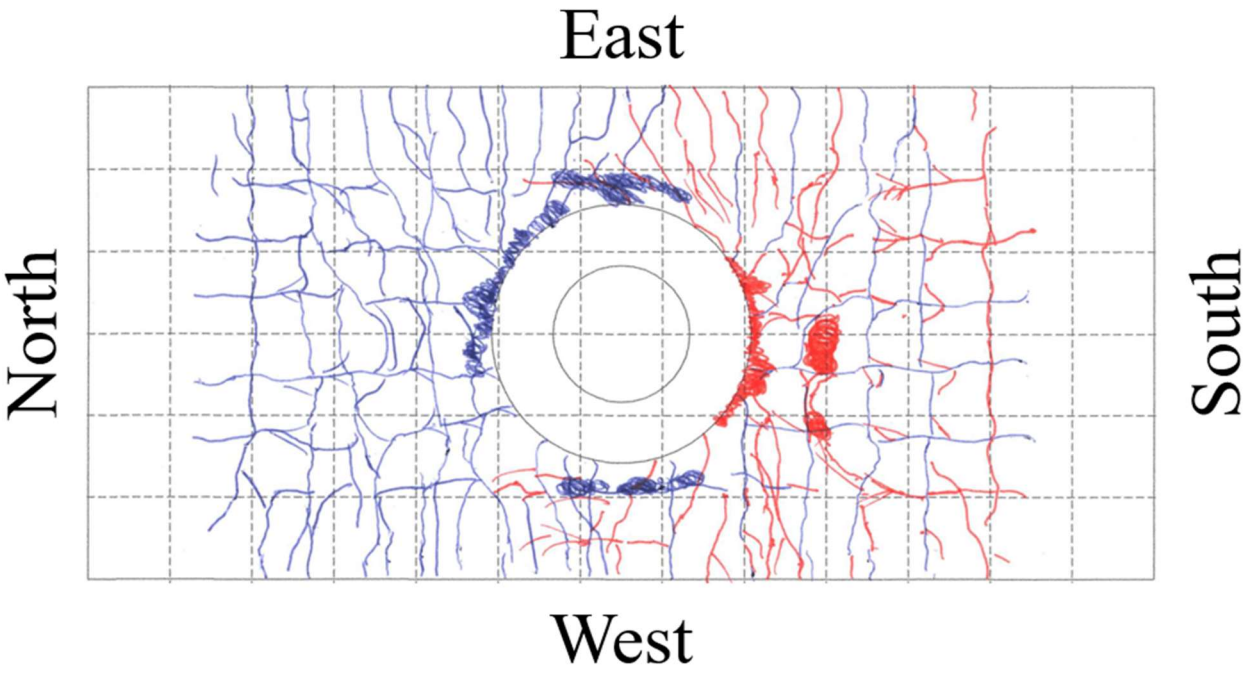

Figure 38. Bottom of Slab Crack Map 5.08% Drift (PTB_9_2_0_6)

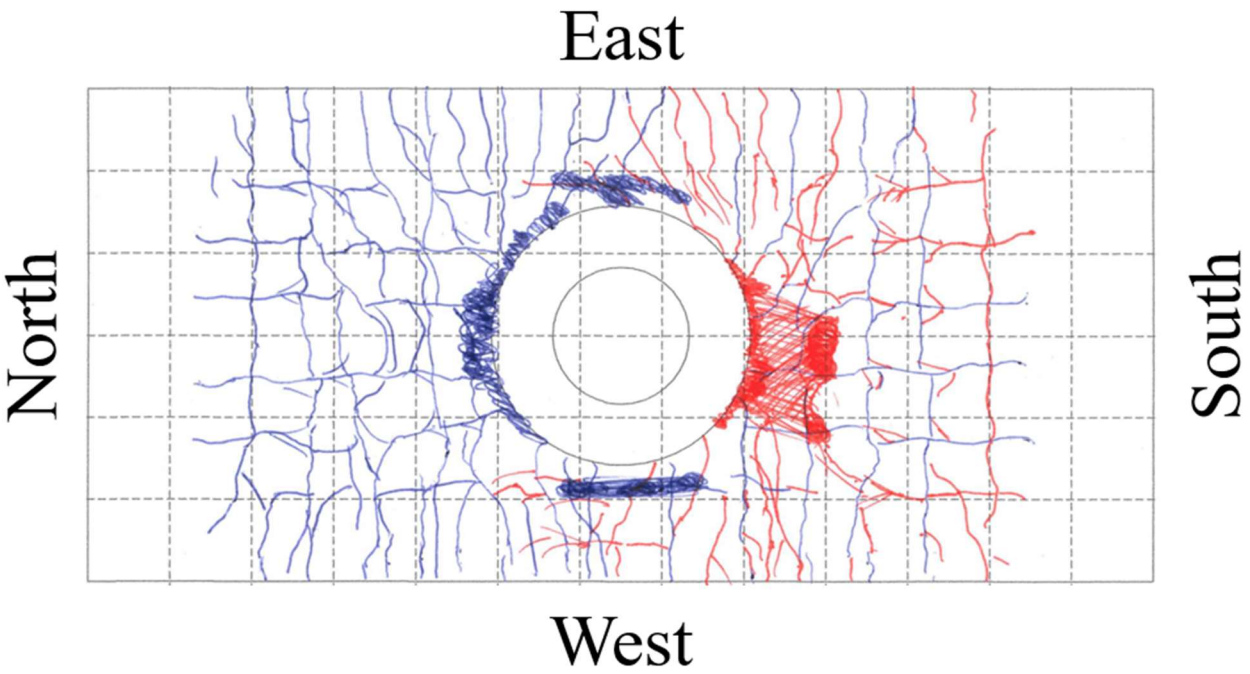

Figure 39. Top of Slab Crack Map 5.81% Drift (PTB_9_2_0_6)

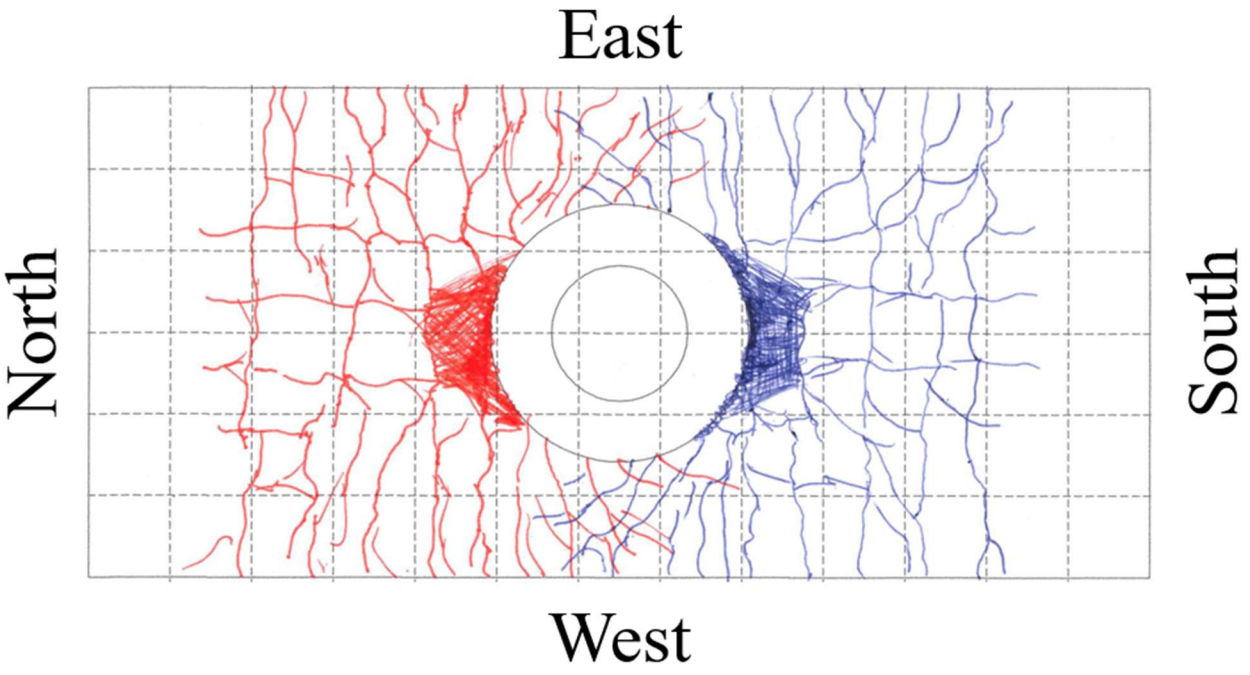

Figure 40. Bottom of Slab Crack Map 5.81% Drift (PTB_9_2_0_6)

APPENDIX C

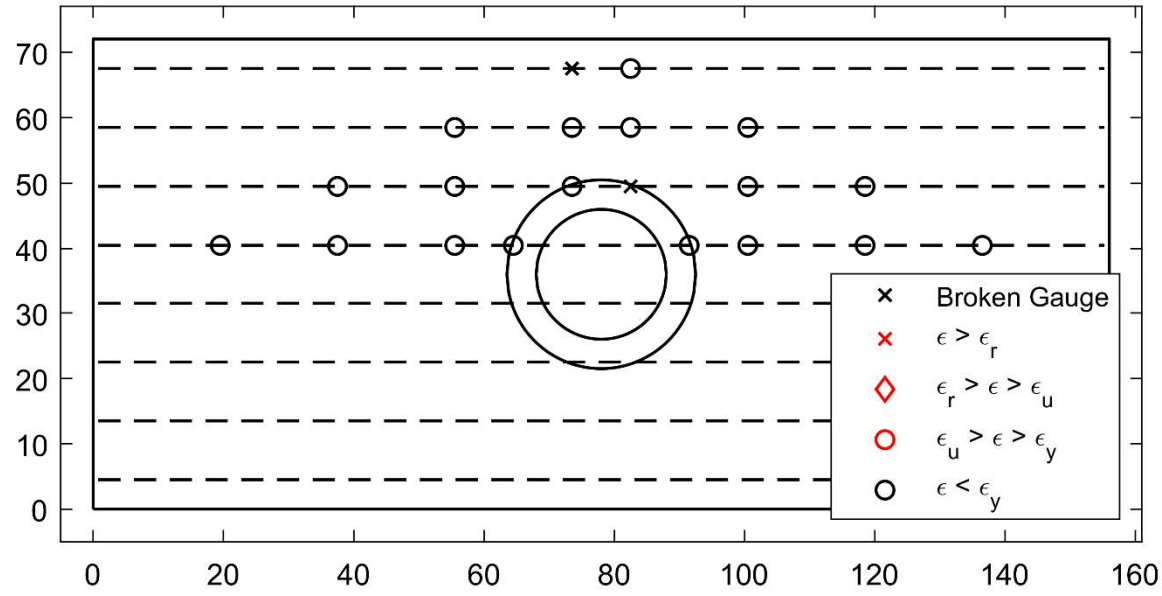

Figure 1. Top Reinforcement Strain Summary – 0.36% (PTB_4.5_1_0_6)

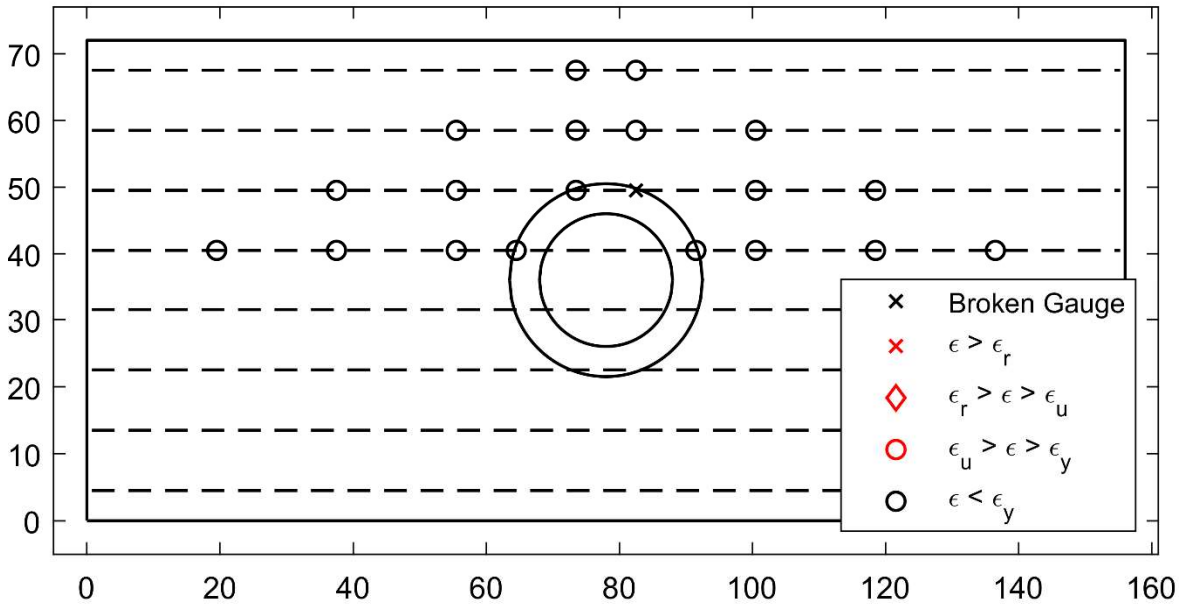

Figure 2. Top Reinforcement Strain Summary – 0.73% (PTB_4.5_1_0_6)

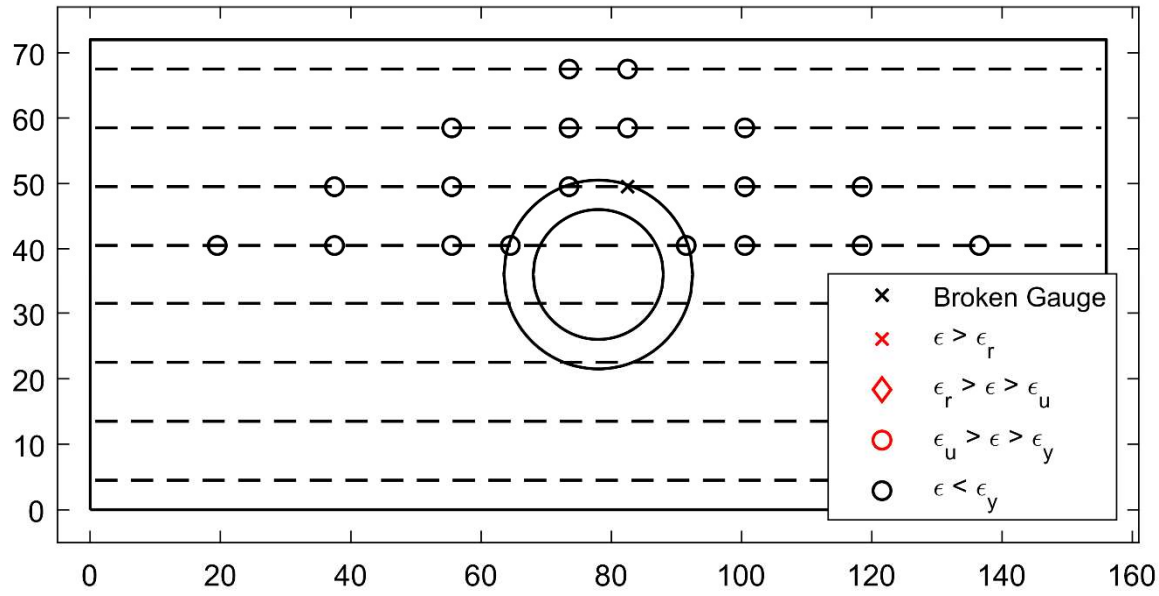

Figure 3. Top Reinforcement Strain Summary – 1.09% (PTB_4.5_1_0_6)

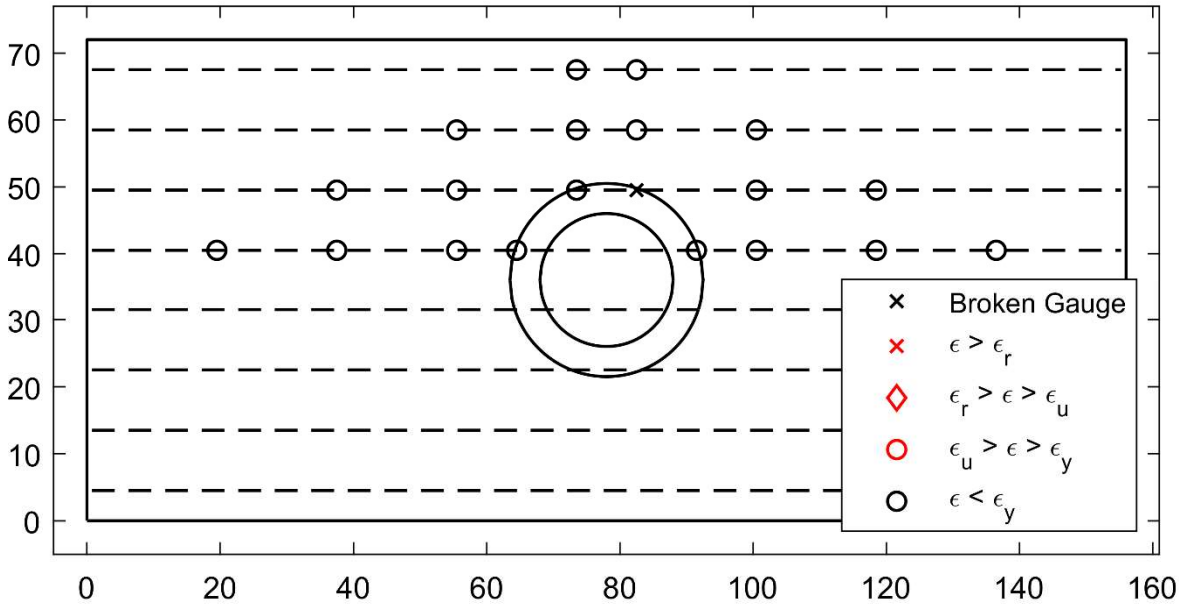

Figure 4. Top Reinforcement Strain Summary – 1.45% (PTB_4.5_1_0_6)

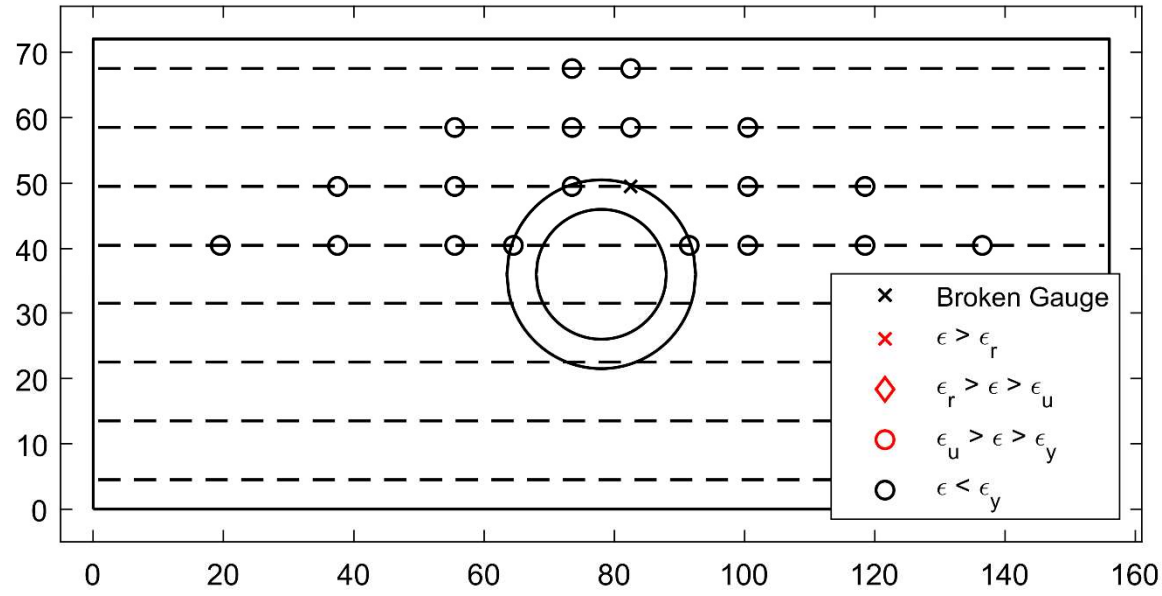

Figure 5. Top Reinforcement Strain Summary – 2.18% (PTB_4.5_1_0_6)

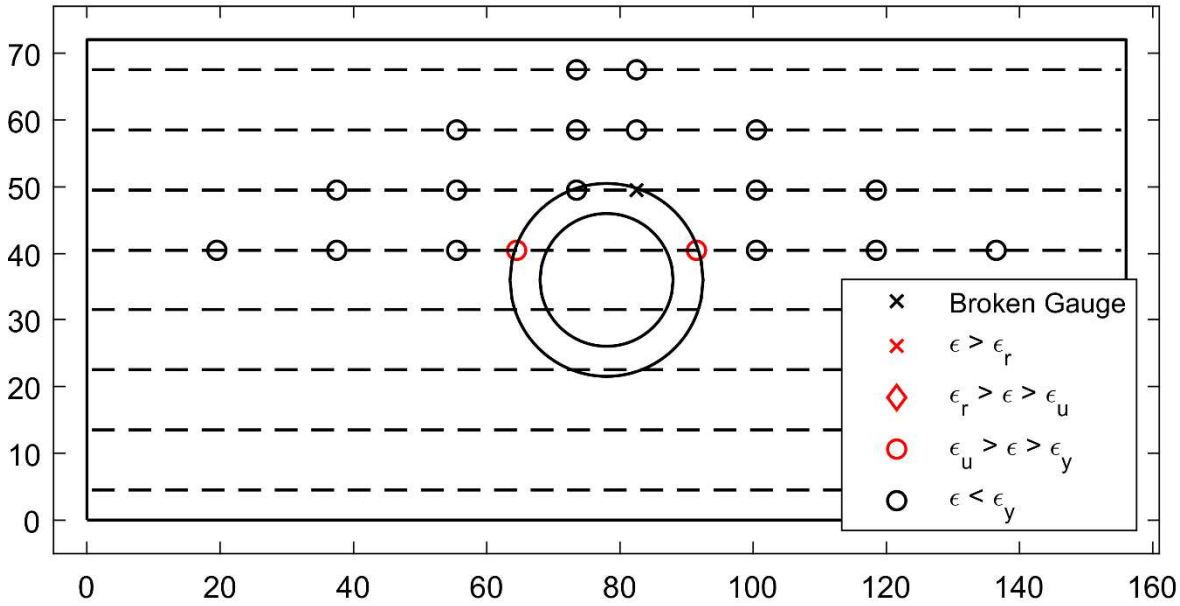

Figure 6. Top Reinforcement Strain Summary – 2.90% (PTB_4.5_1_0_6)

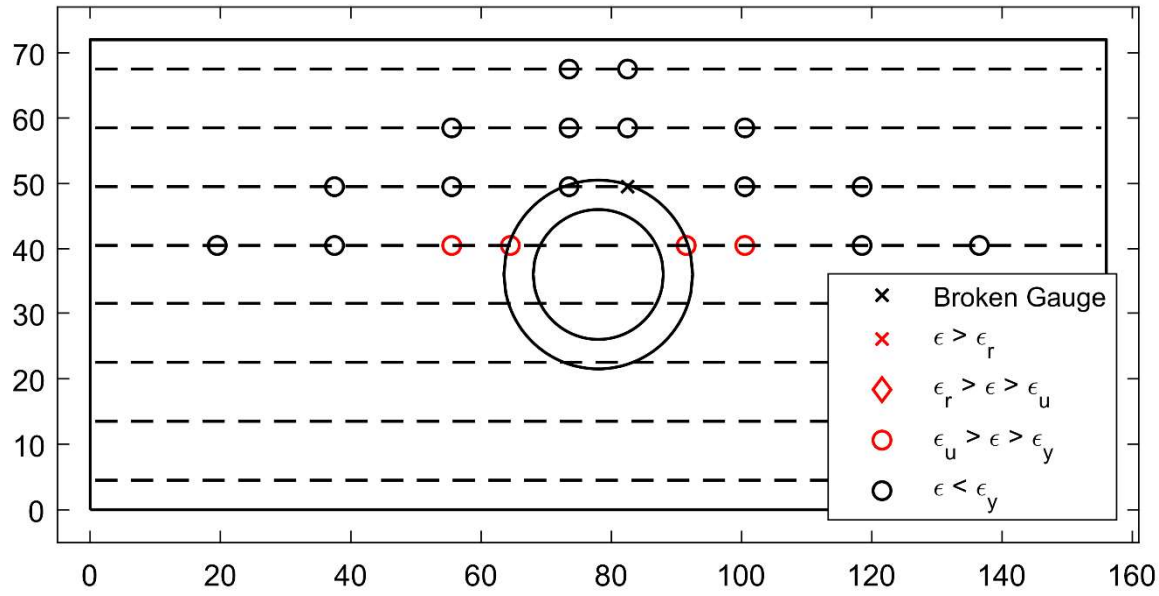

Figure 7. Top Reinforcement Strain Summary – 3.63% (PTB_4.5_1_0_6)

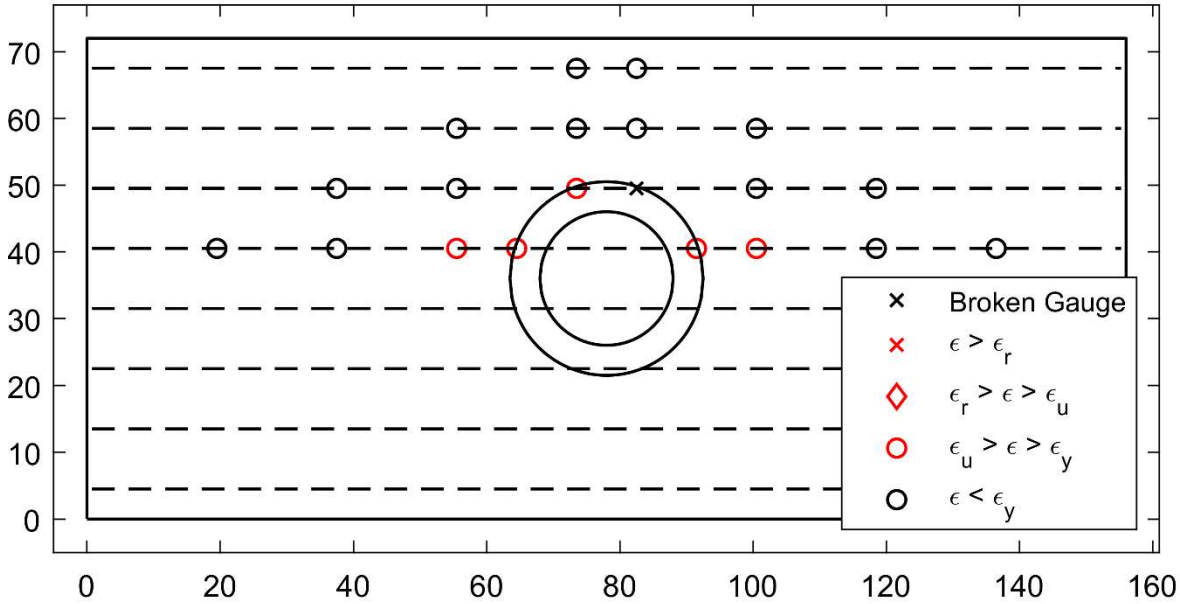

Figure 8. Top Reinforcement Strain Summary – 4.36% (PTB_4.5_1_0_6)

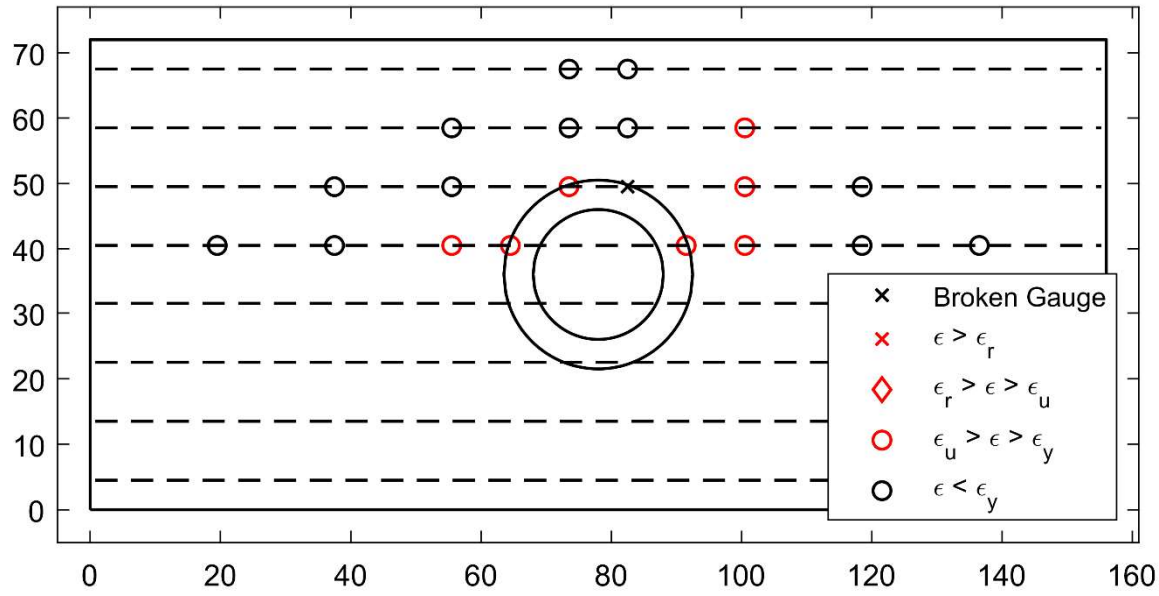

Figure 9. Top Reinforcement Strain Summary – 5.08% (PTB_4.5_1_0_6)

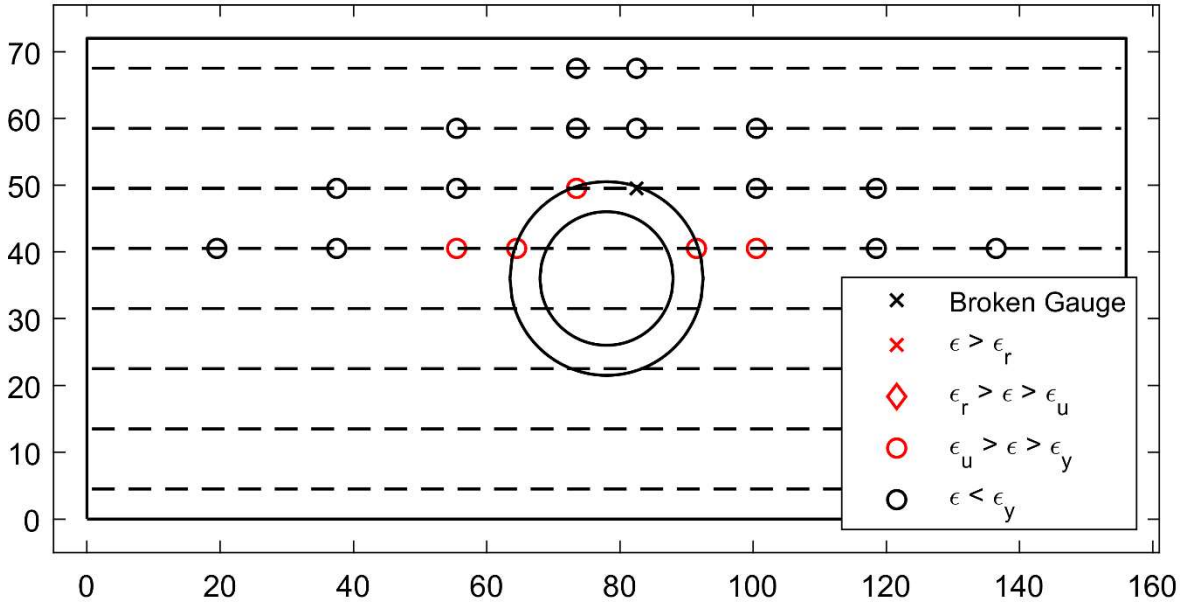

Figure 10. Top Reinforcement Strain Summary – 5.81% (PTB_4.5_1_0_6)

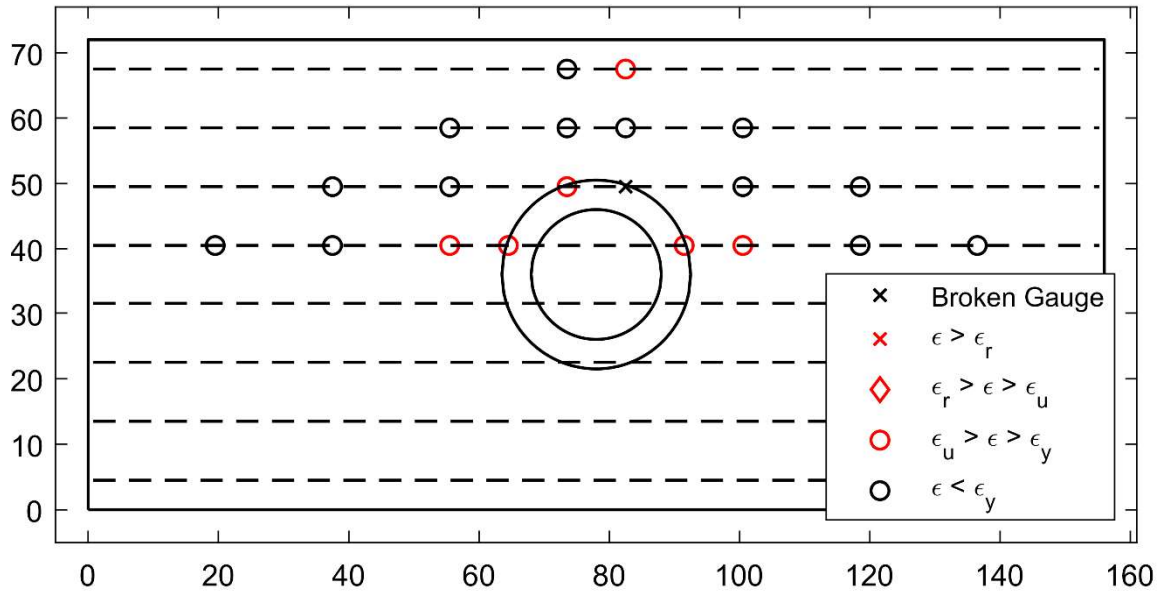

Figure 11. Top Reinforcement Strain Summary – 6.53% (PTB_4.5_1_0_6)

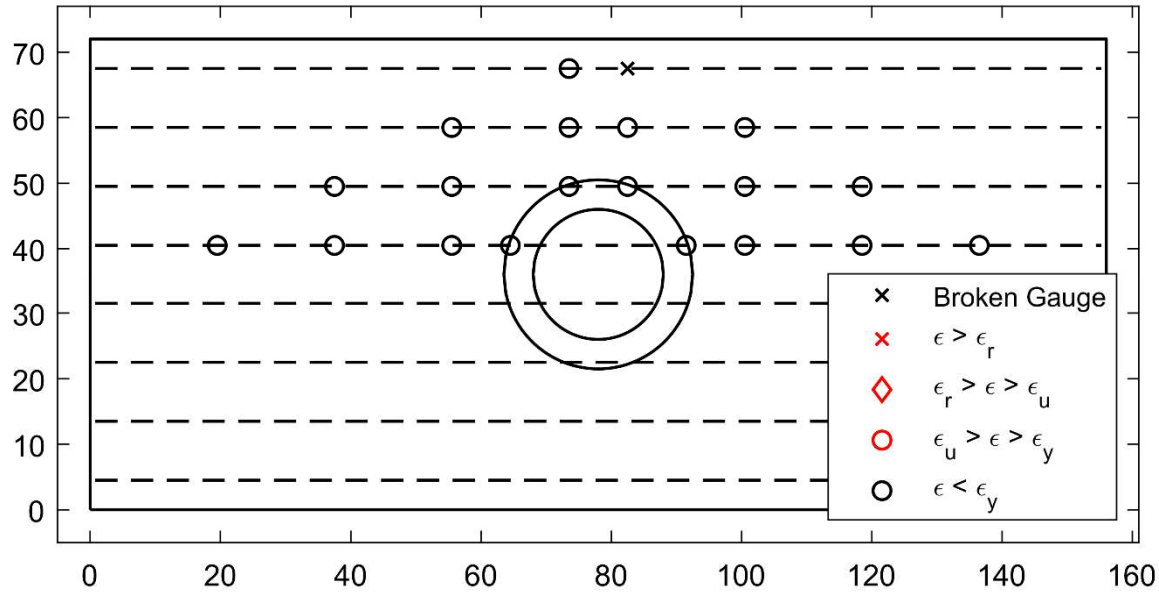

Figure 12. Bottom Reinforcement Strain Summary – 0.36% (PTB_4.5_1_0_6)

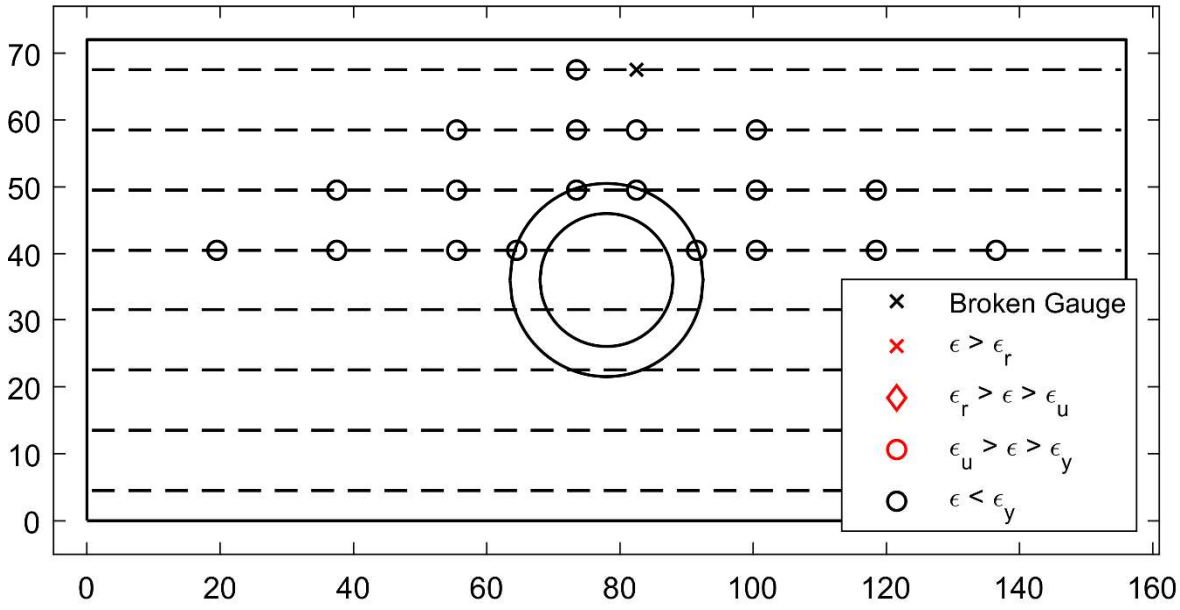

Figure 13. Bottom Reinforcement Strain Summary – 0.73% (PTB_4.5_1_0_6)

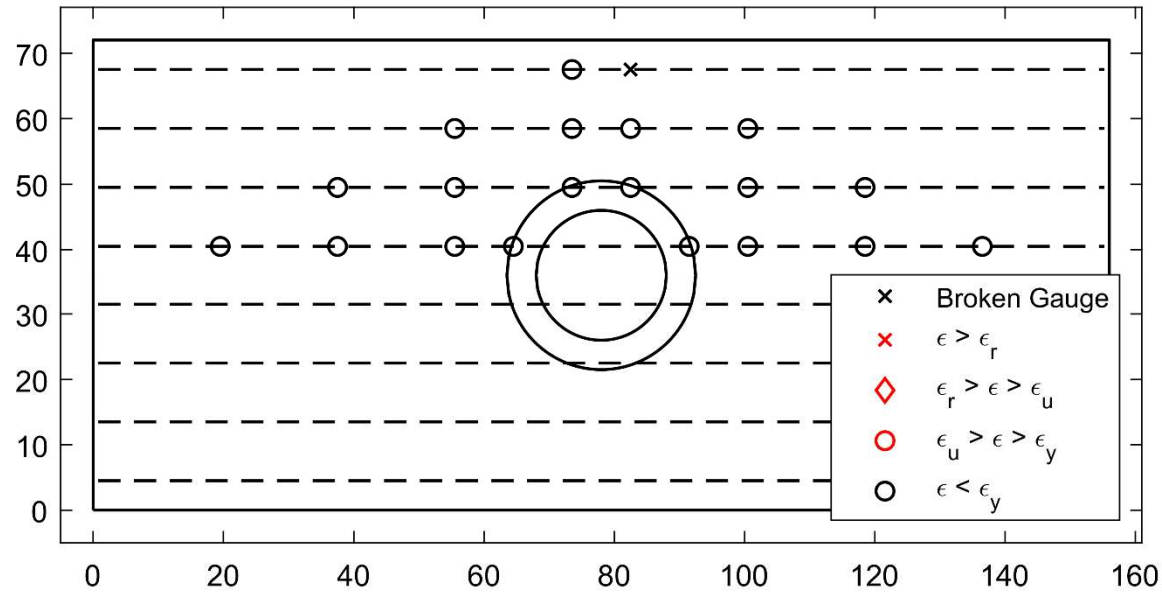

Figure 14. Bottom Reinforcement Strain Summary – 1.09% (PTB_4.5_1_0_6)

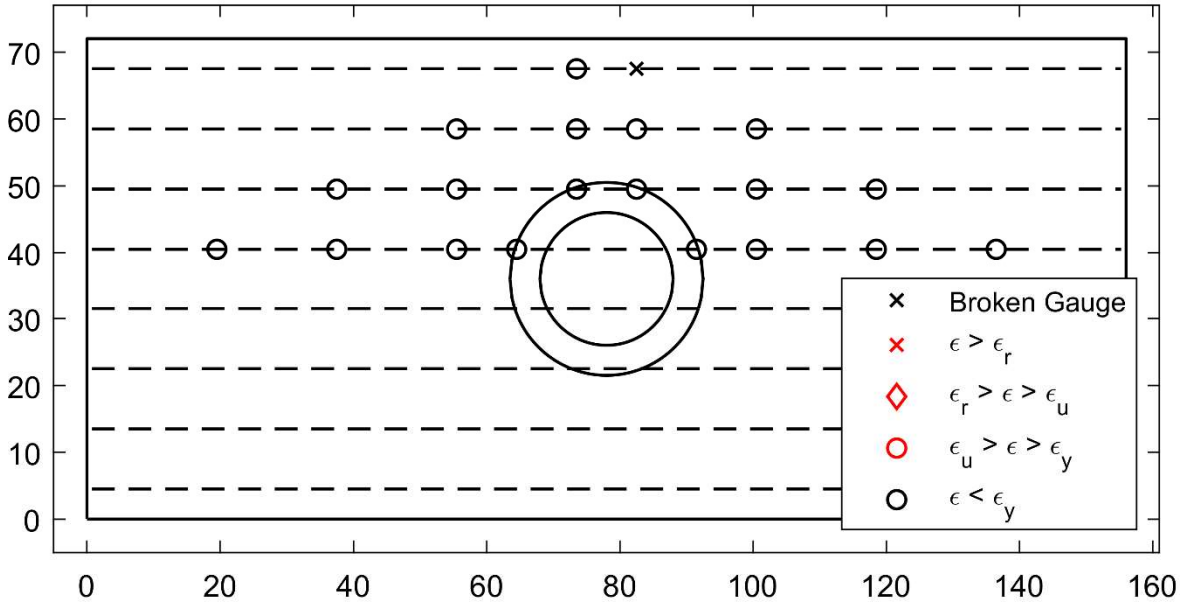

Figure 15. Bottom Reinforcement Strain Summary – 1.45% (PTB_4.5_1_0_6)

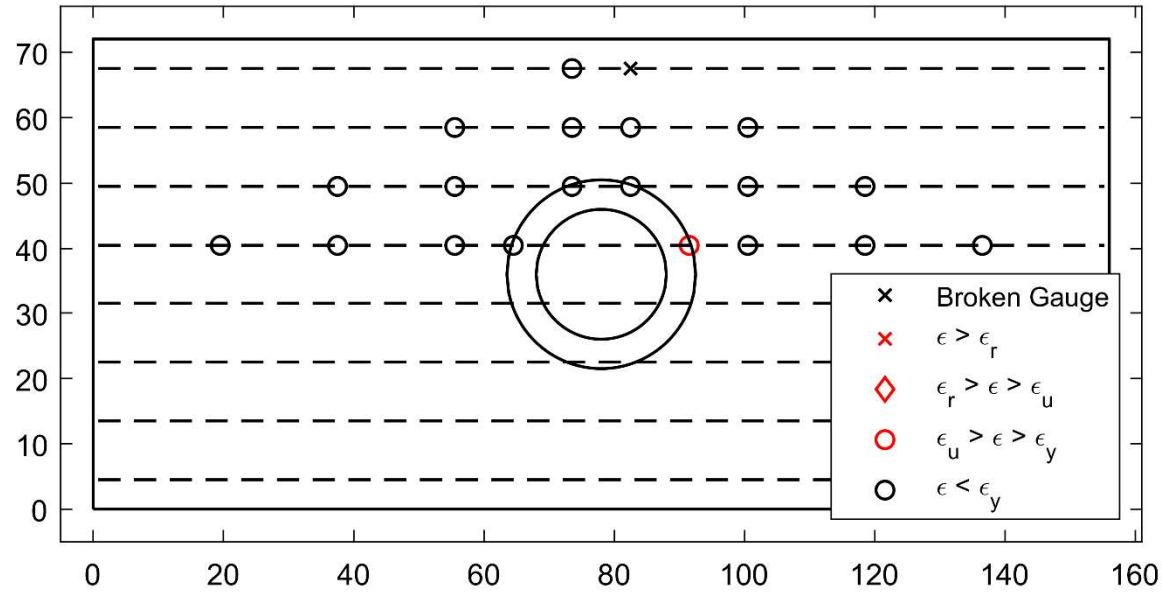

Figure 16. Bottom Reinforcement Strain Summary – 2.18% (PTB_4.5_1_0_6)

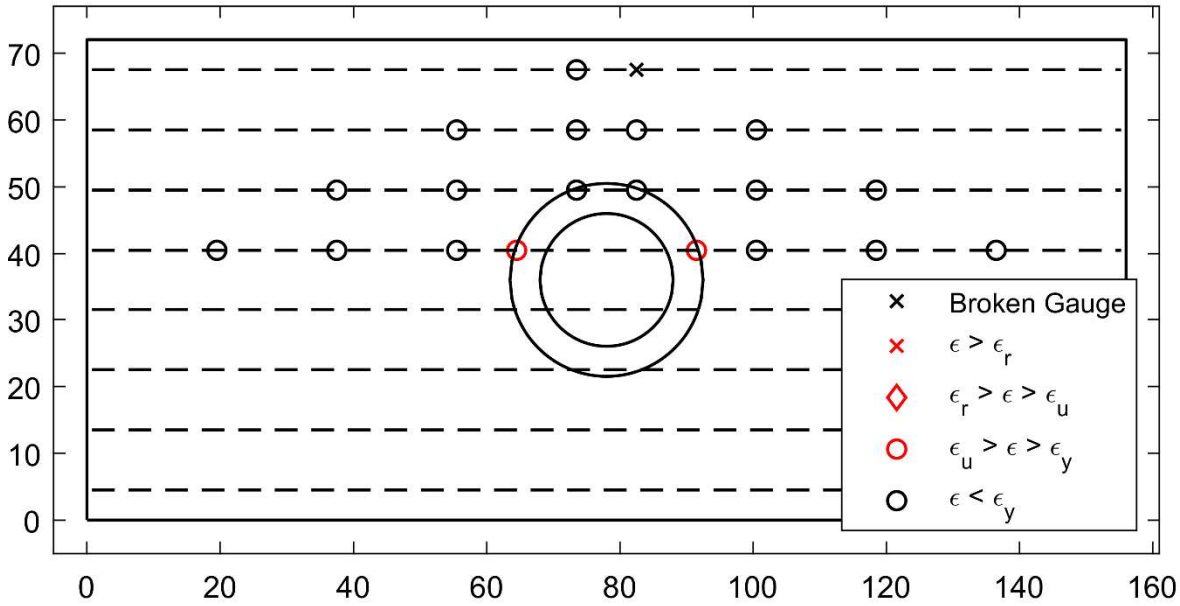

Figure 17. Bottom Reinforcement Strain Summary – 2.90% (PTB_4.5_1_0_6)

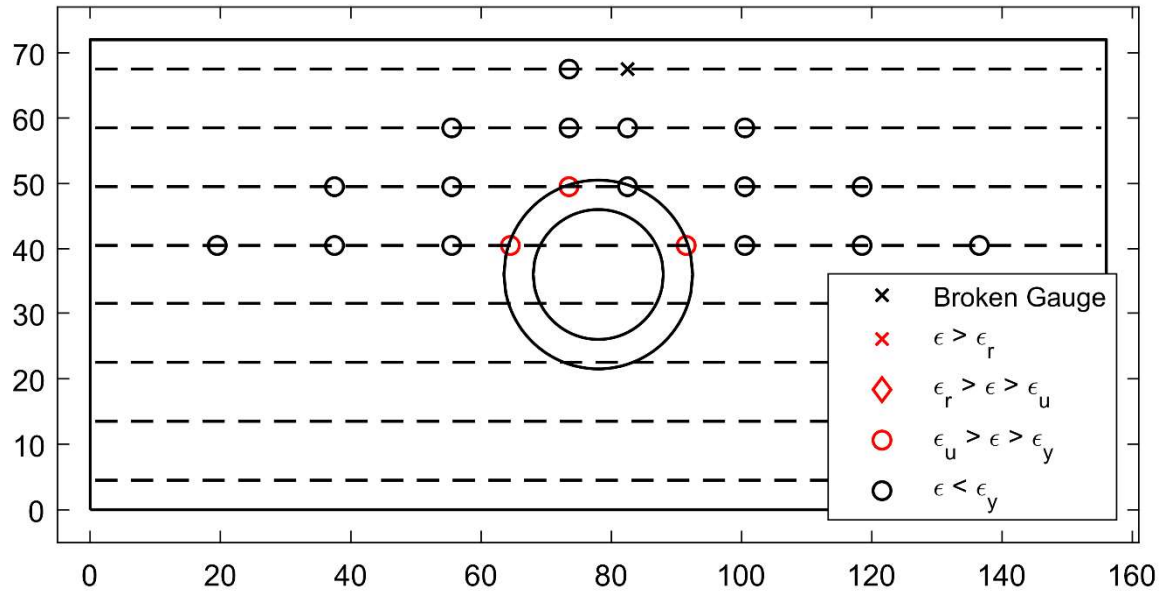

Figure 18. Bottom Reinforcement Strain Summary – 3.63% (PTB_4.5_1_0_6)

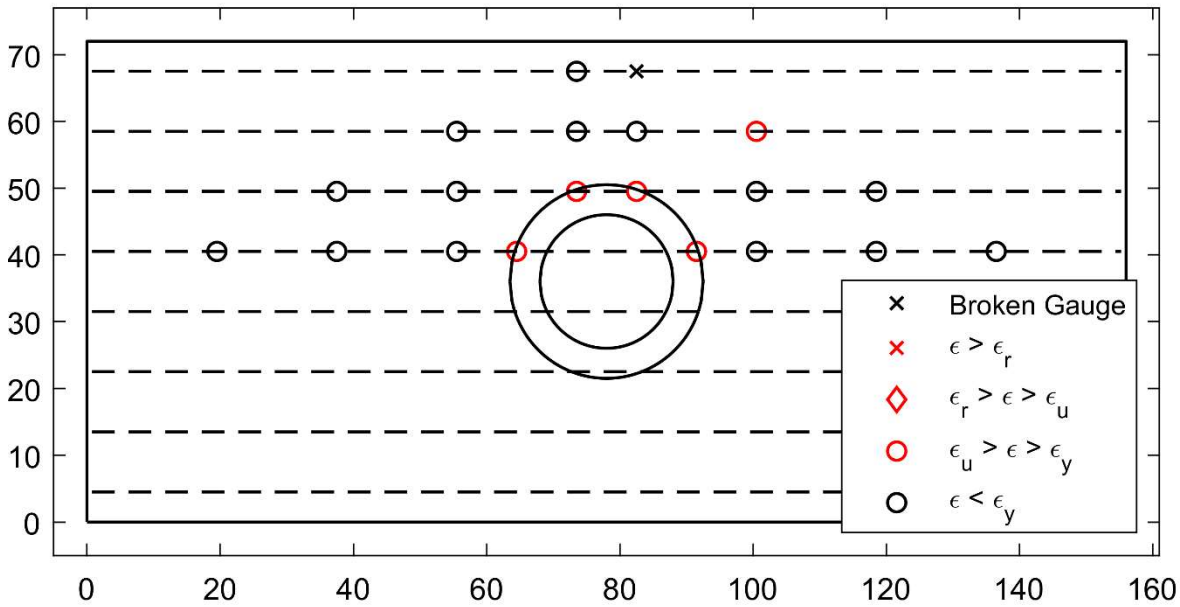

Figure 19. Bottom Reinforcement Strain Summary – 4.36% (PTB_4.5_1_0_6)

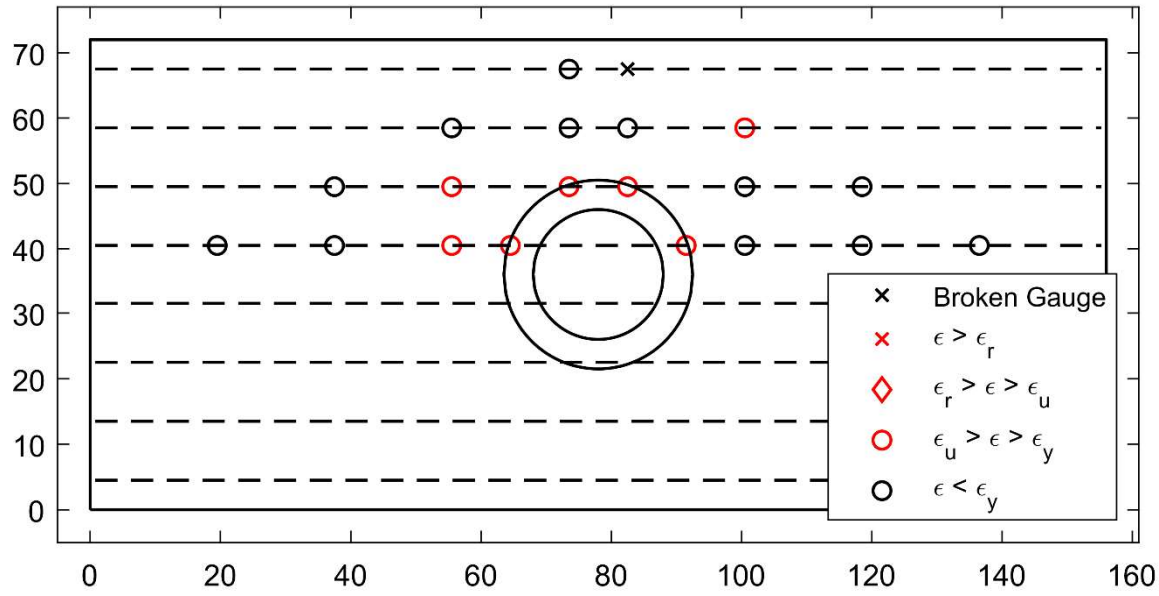

Figure 20. Bottom Reinforcement Strain Summary – 5.08% (PTB_4.5_1_0_6)

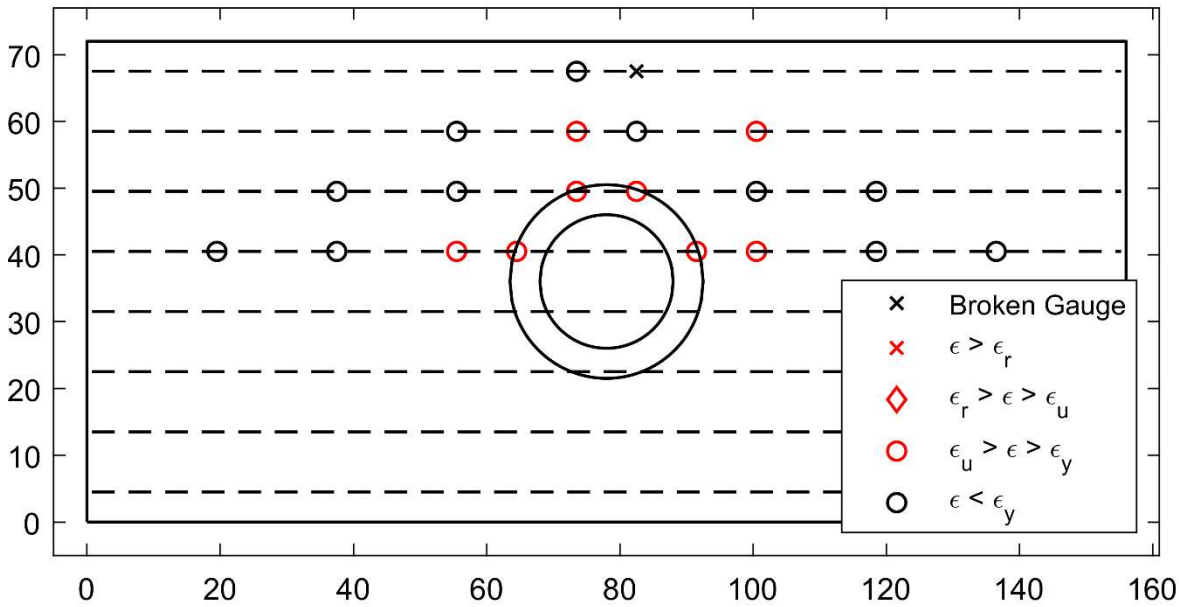

Figure 21. Bottom Reinforcement Strain Summary – 5.81% (PTB_4.5_1_0_6)

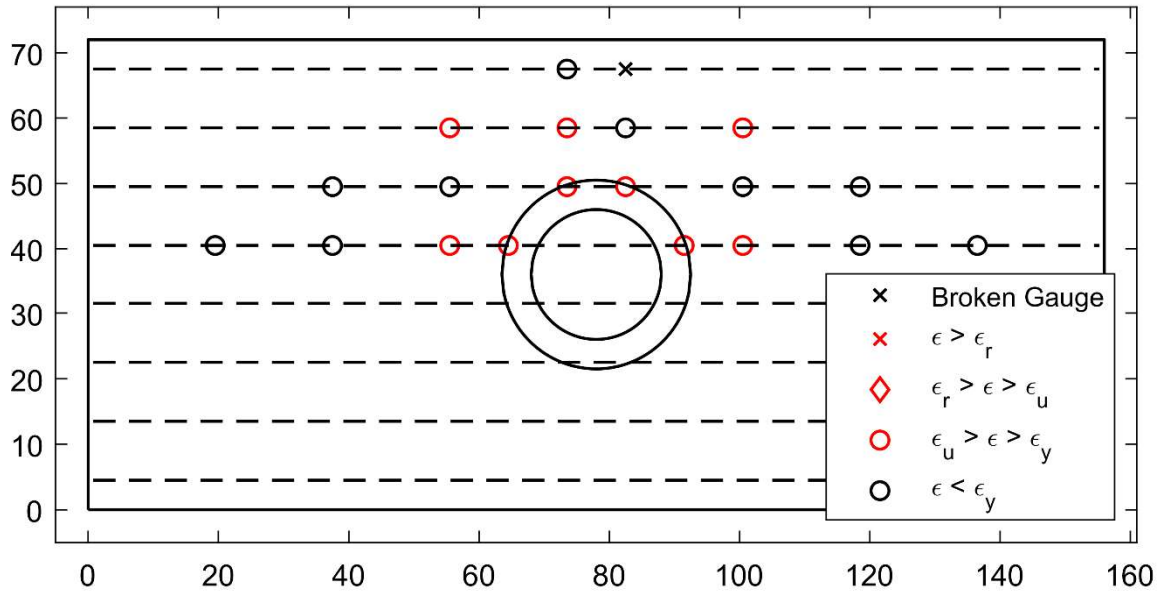

Figure 22. Bottom Reinforcement Strain Summary – 6.53% (PTB_4.5_1_0_6)

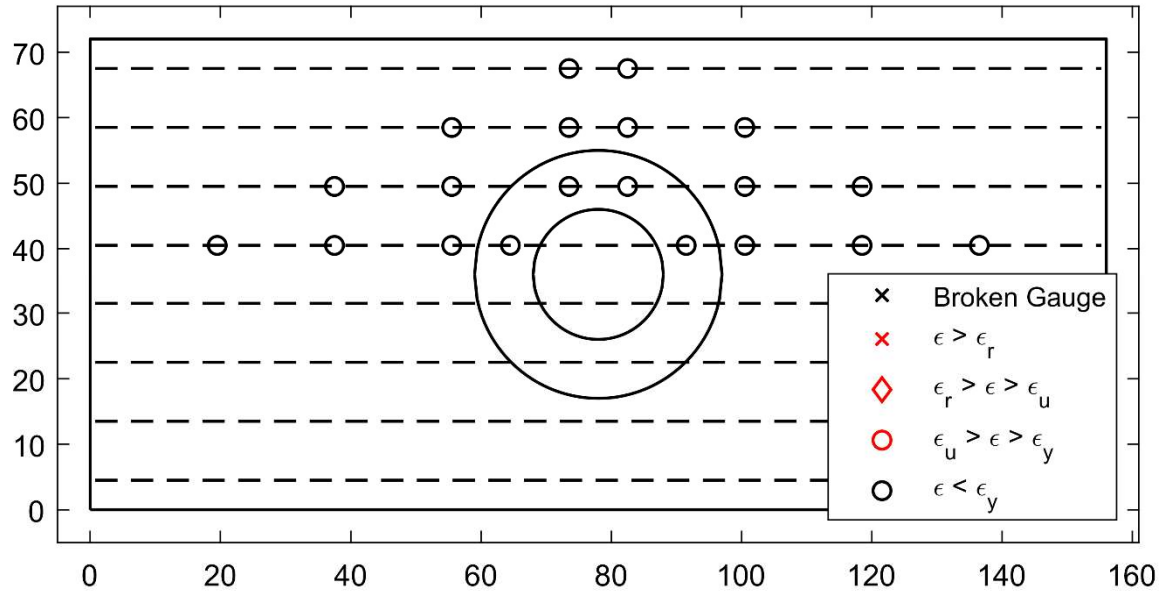

Figure 23. Top Reinforcement Strain Summary – 0.36% (PTB_9_2_0_6)

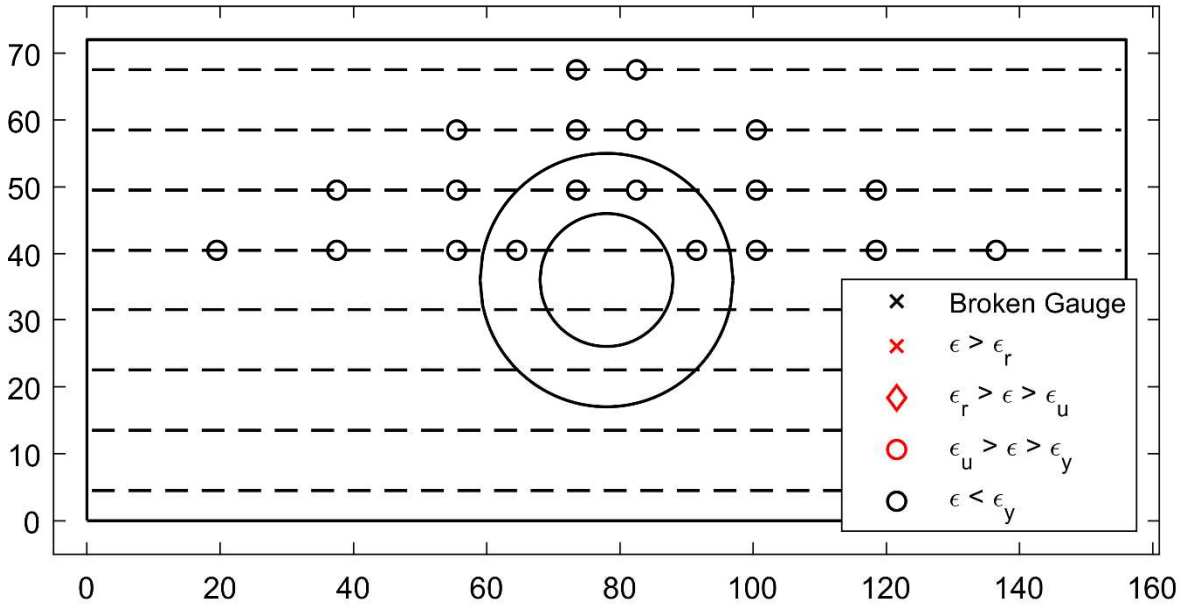

Figure 24. Top Reinforcement Strain Summary – 0.73% (PTB_9_2_0_6)

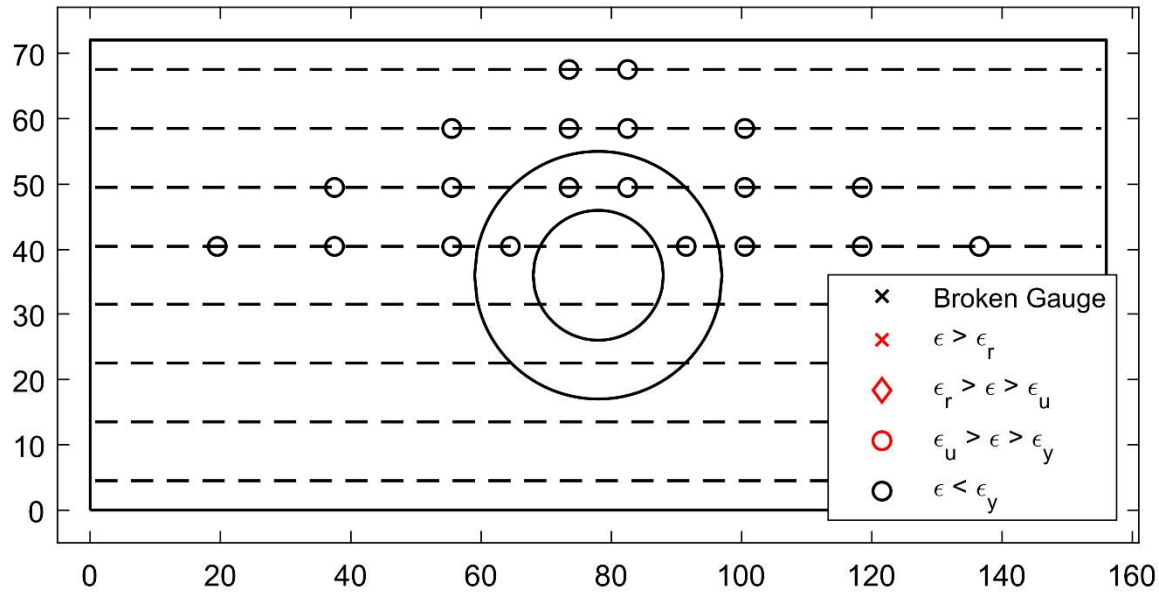

Figure 25. Top Reinforcement Strain Summary – 1.09% (PTB_9_2_0_6)

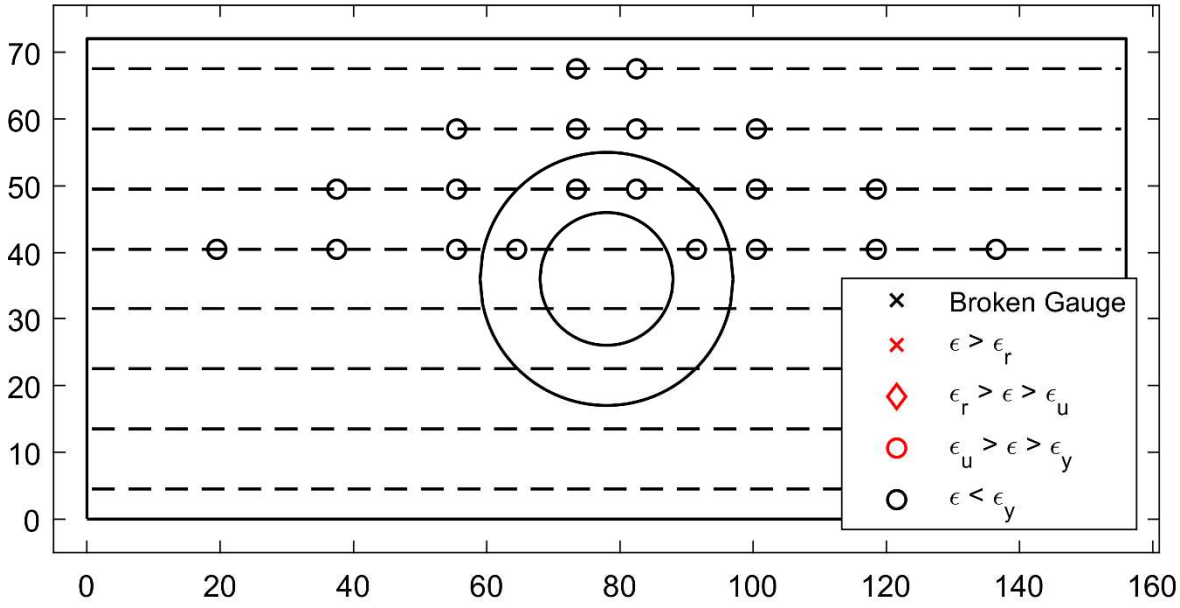

Figure 26. Top Reinforcement Strain Summary – 1.45% (PTB_9_2_0_6)

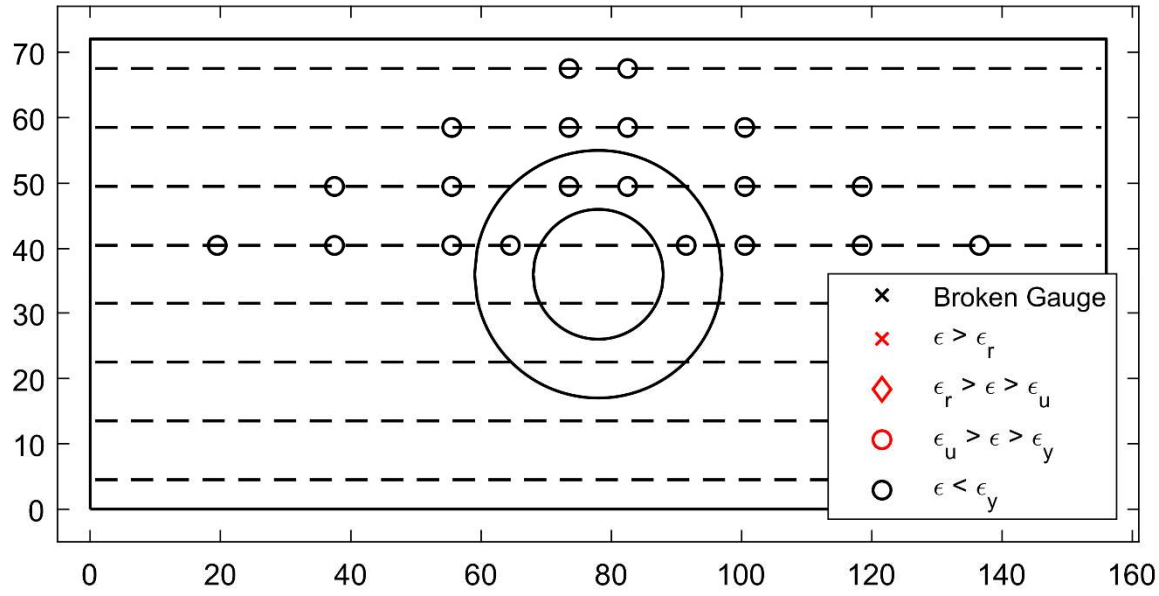

Figure 27. Top Reinforcement Strain Summary – 2.18% (PTB_9_2_0_6)

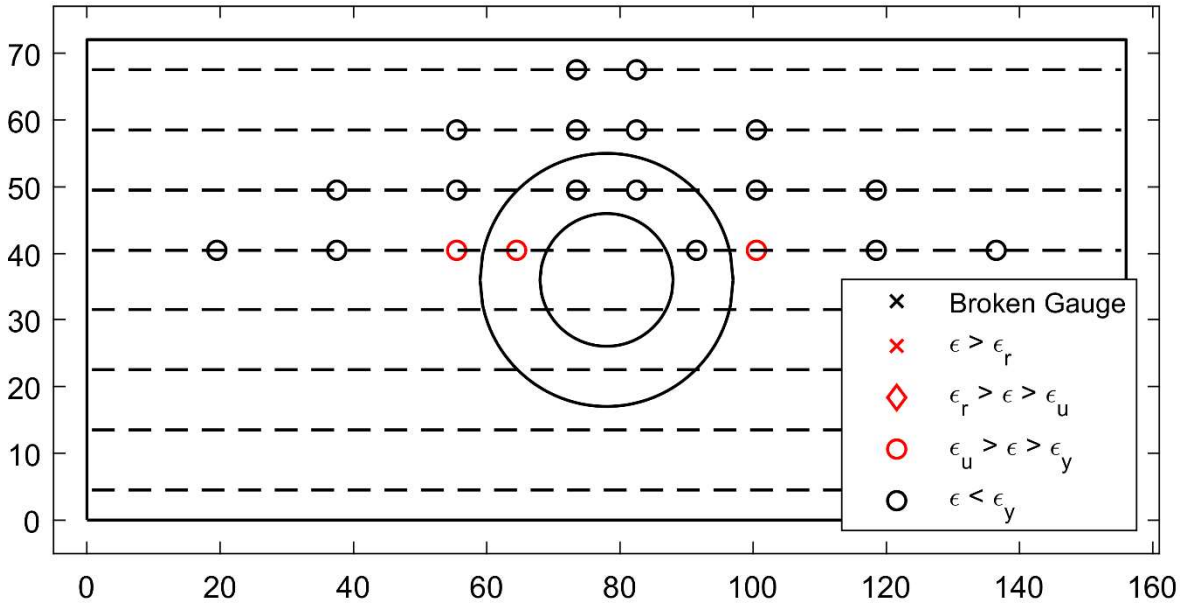

Figure 28. Top Reinforcement Strain Summary – 2.90% (PTB_9_2_0_6)

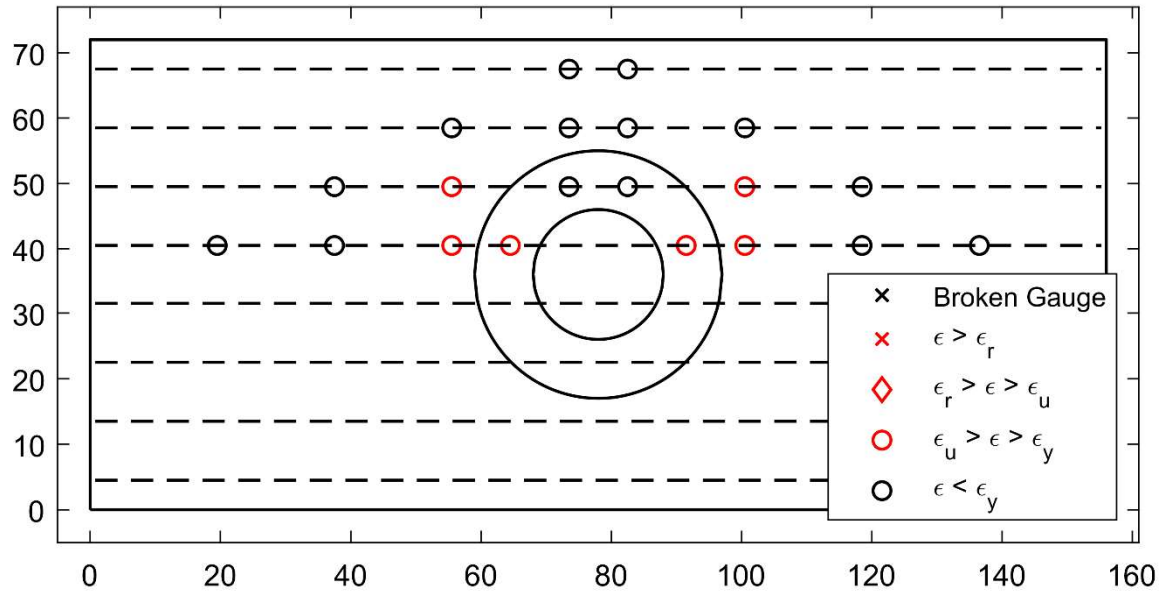

Figure 29. Top Reinforcement Strain Summary – 3.63% (PTB_9_2_0_6)

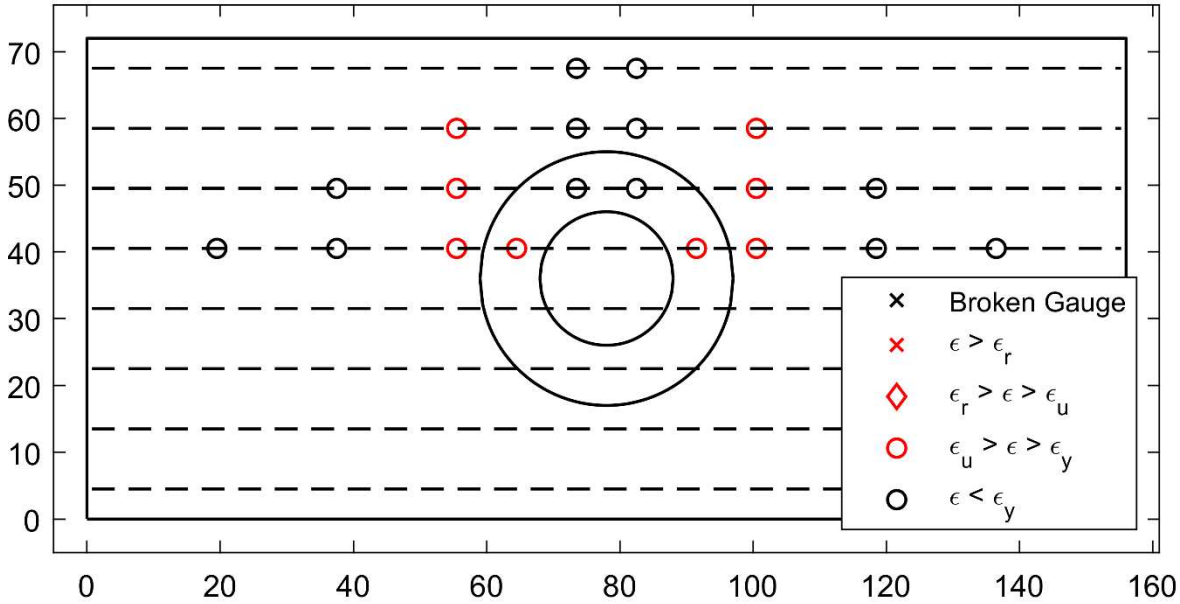

Figure 30. Top Reinforcement Strain Summary – 4.36% (PTB_9_2_0_6)

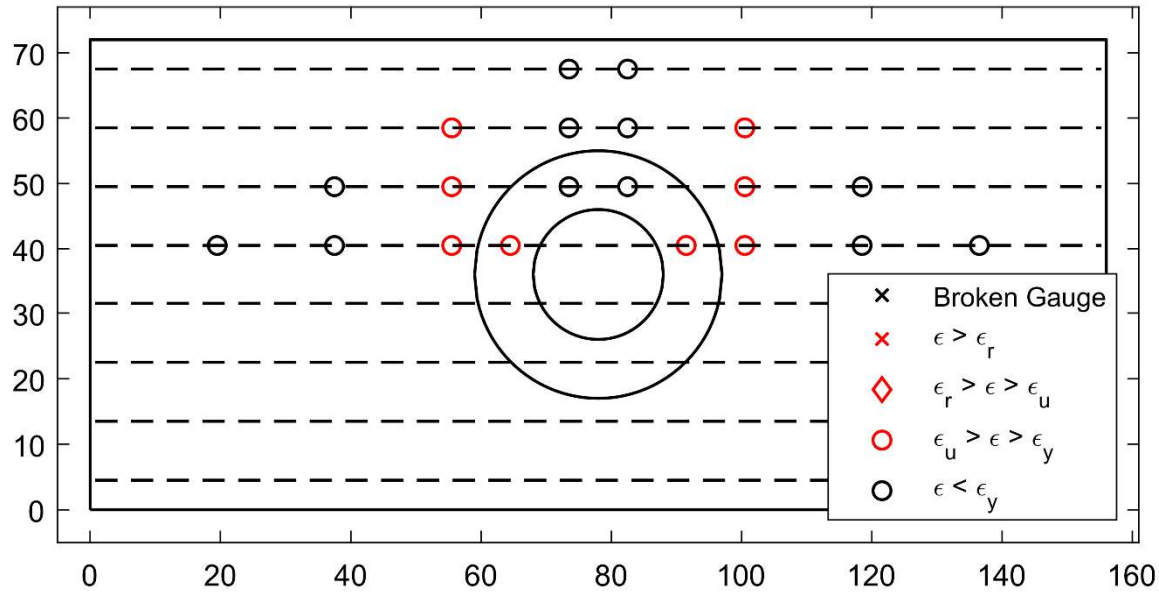

Figure 31. Top Reinforcement Strain Summary – 5.08% (PTB_9_2_0_6)

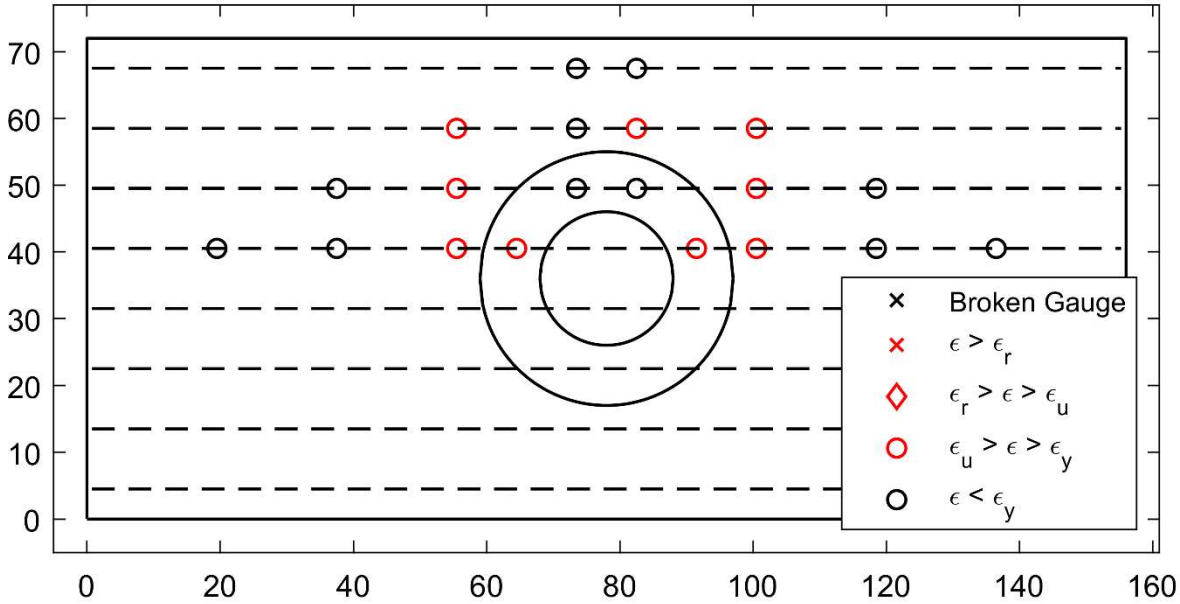

Figure 32. Top Reinforcement Strain Summary – 5.81% (PTB_9_2_0_6)

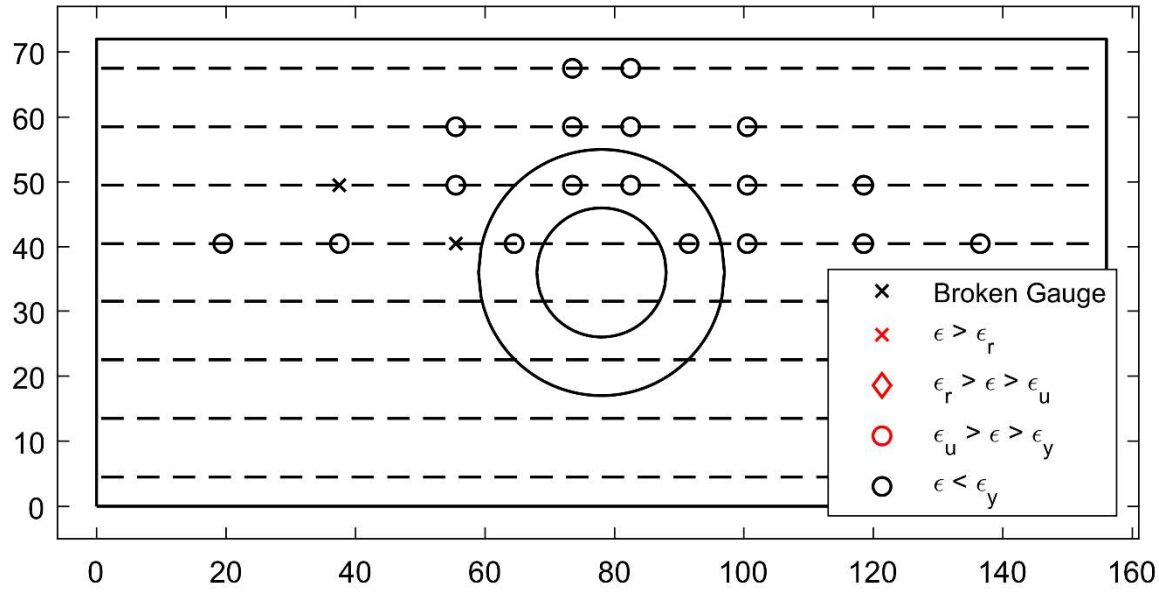

Figure 33. Bottom Reinforcement Strain Summary – 0.36% (PTB_9_2_0_6)

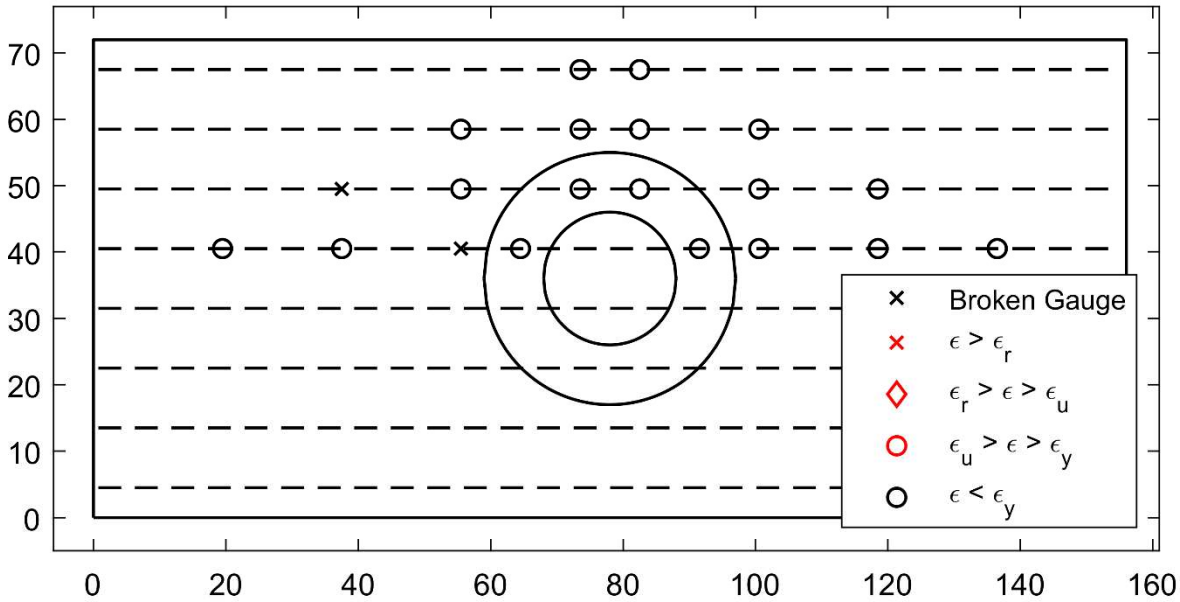

Figure 34. Bottom Reinforcement Strain Summary – 0.73% (PTB_9_2_0_6)

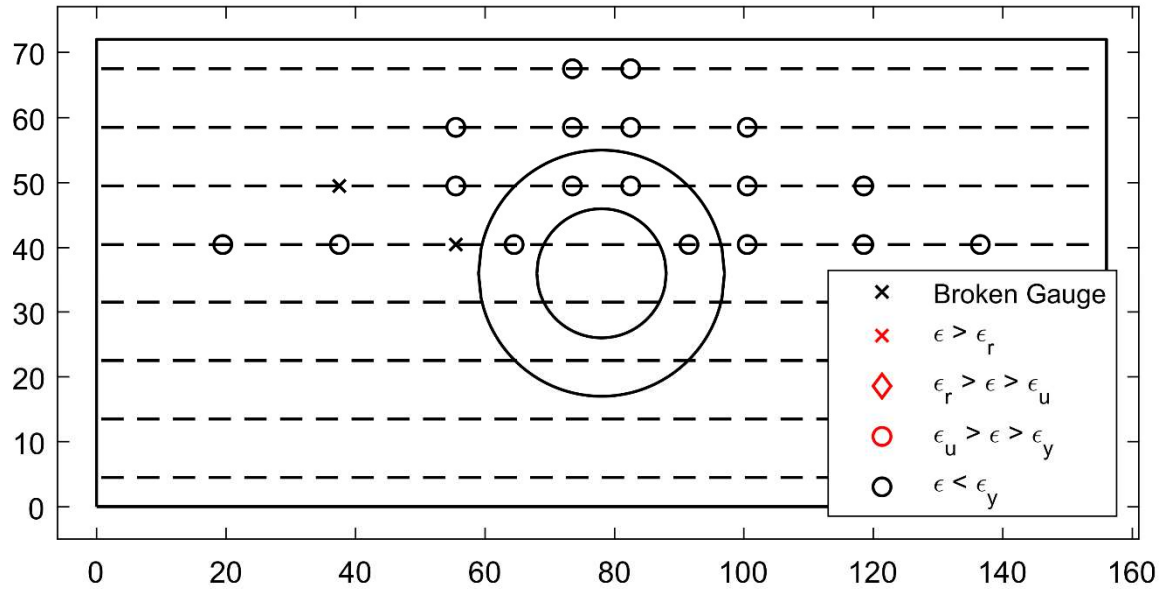

Figure 35. Bottom Reinforcement Strain Summary – 1.09% (PTB_9_2_0_6)

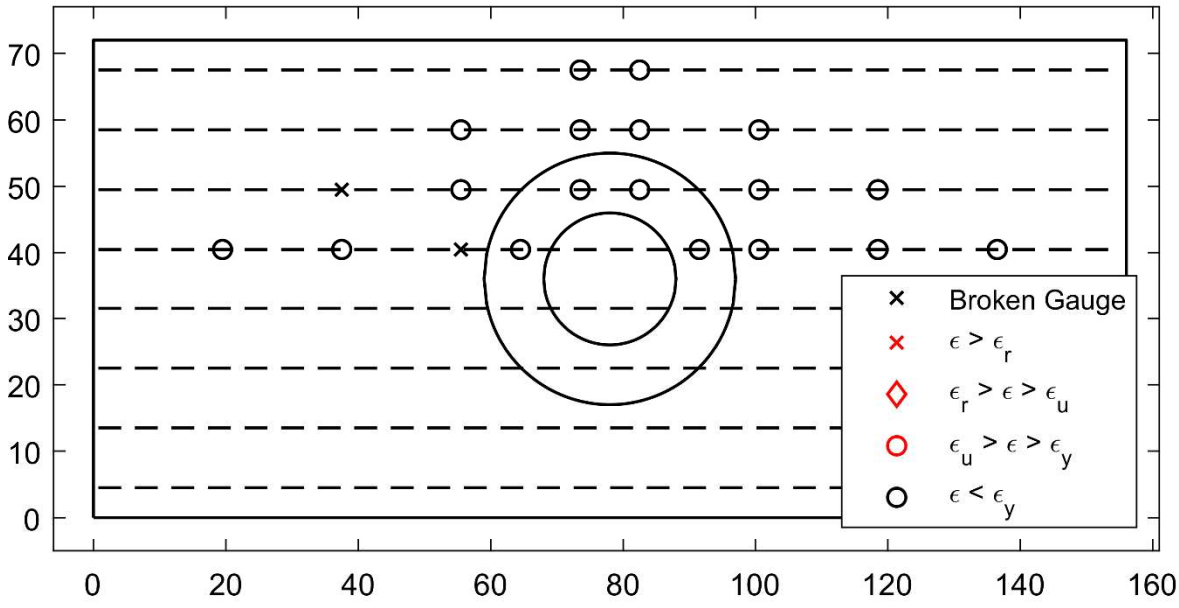

Figure 36. Bottom Reinforcement Strain Summary – 1.45% (PTB_9_2_0_6)

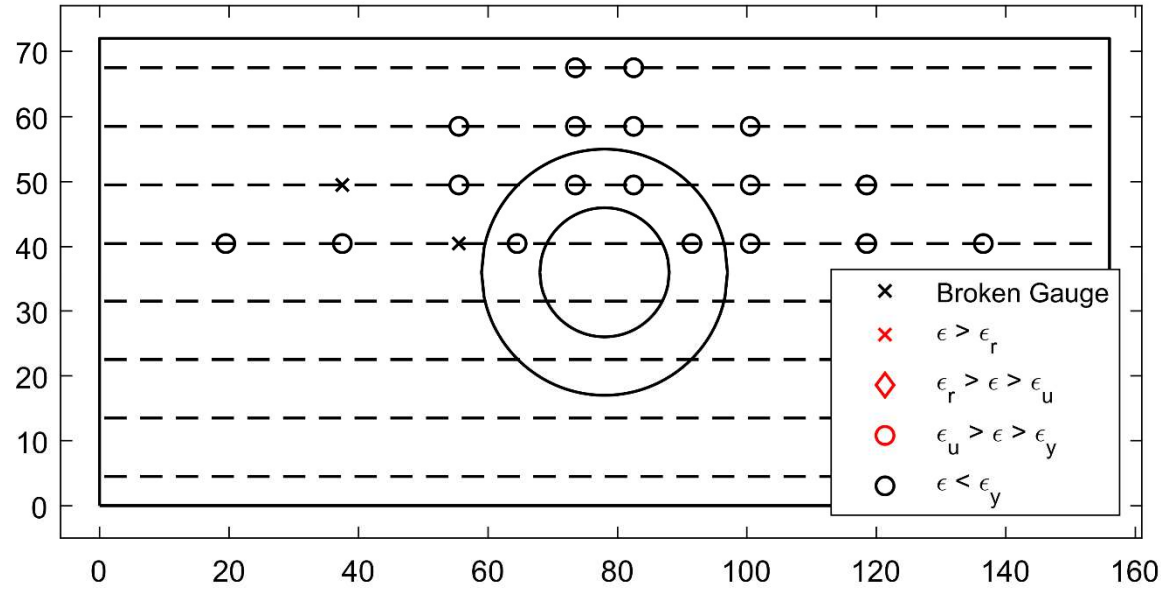

Figure 37. Bottom Reinforcement Strain Summary – 2.18% (PTB_9_2_0_6)

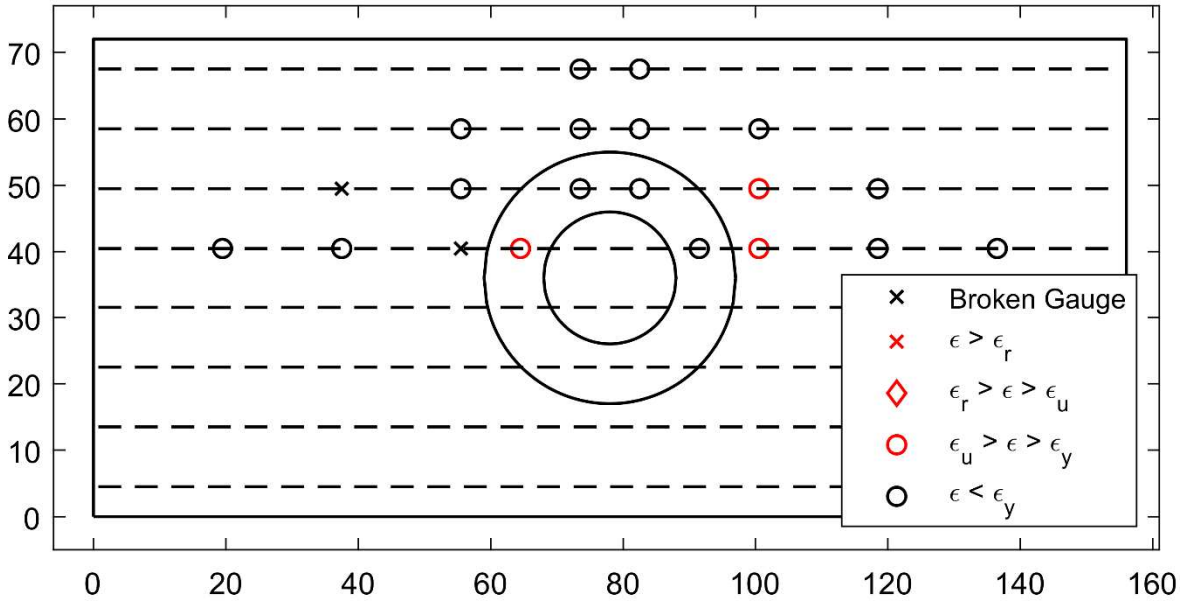

Figure 38. Bottom Reinforcement Strain Summary – 2.90% (PTB_9_2_0_6)

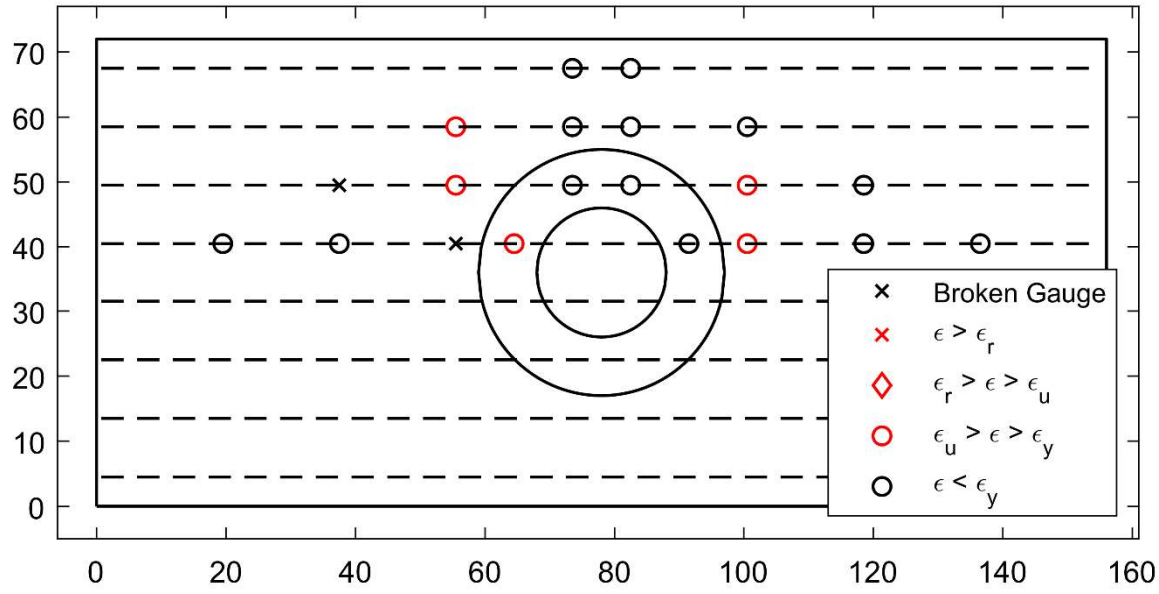

Figure 39. Bottom Reinforcement Strain Summary – 3.63% (PTB_9_2_0_6)

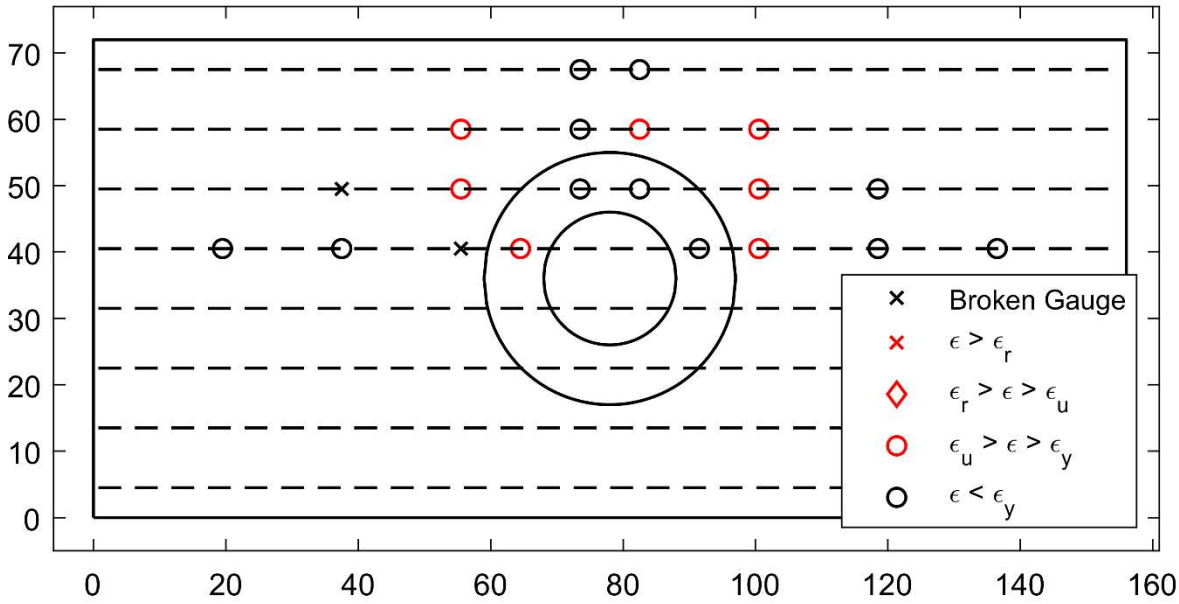

Figure 40. Bottom Reinforcement Strain Summary – 4.36% (PTB_9_2_0_6)

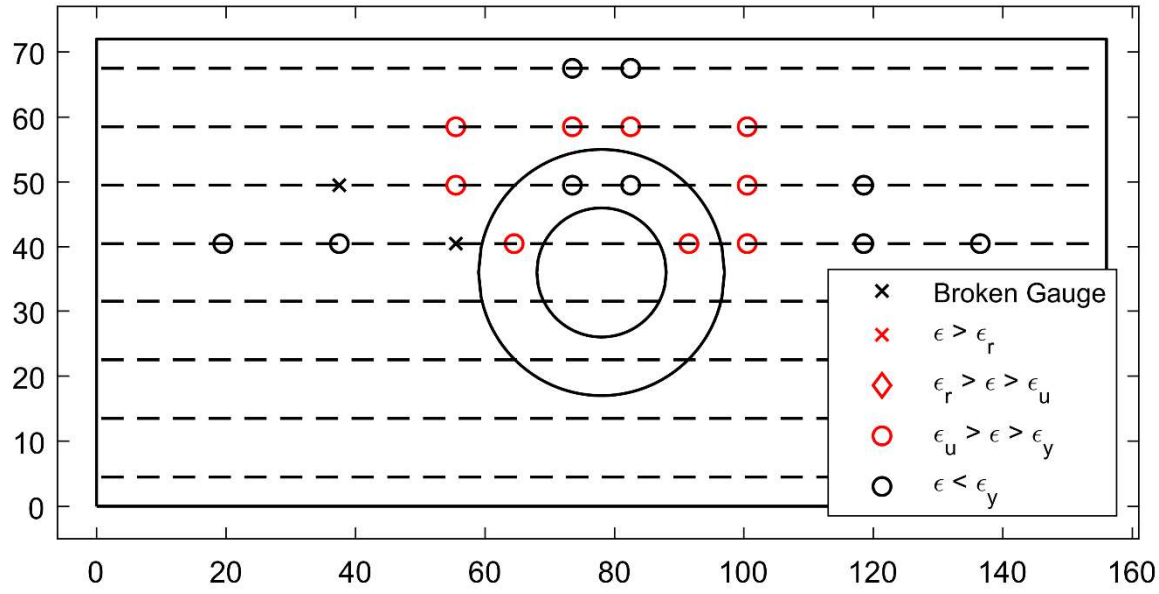

Figure 41. Bottom Reinforcement Strain Summary – 5.08% (PTB_9_2_0_6)

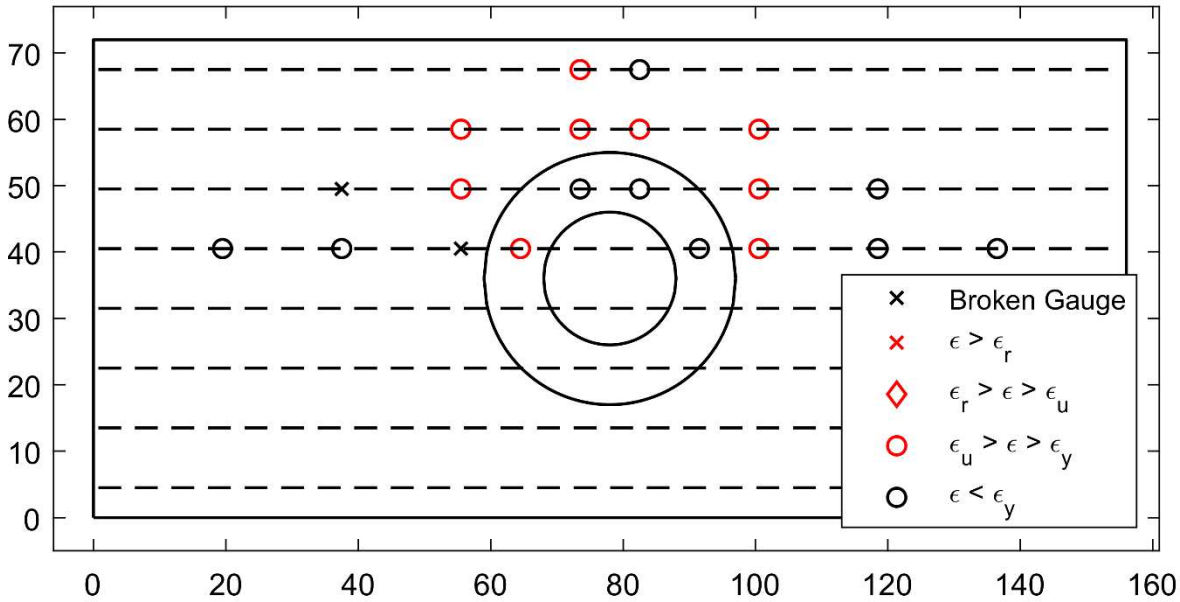

Figure 42. Bottom Reinforcement Strain Summary – 5.81% (PTB_9_2_0_6)

APPENDIX D

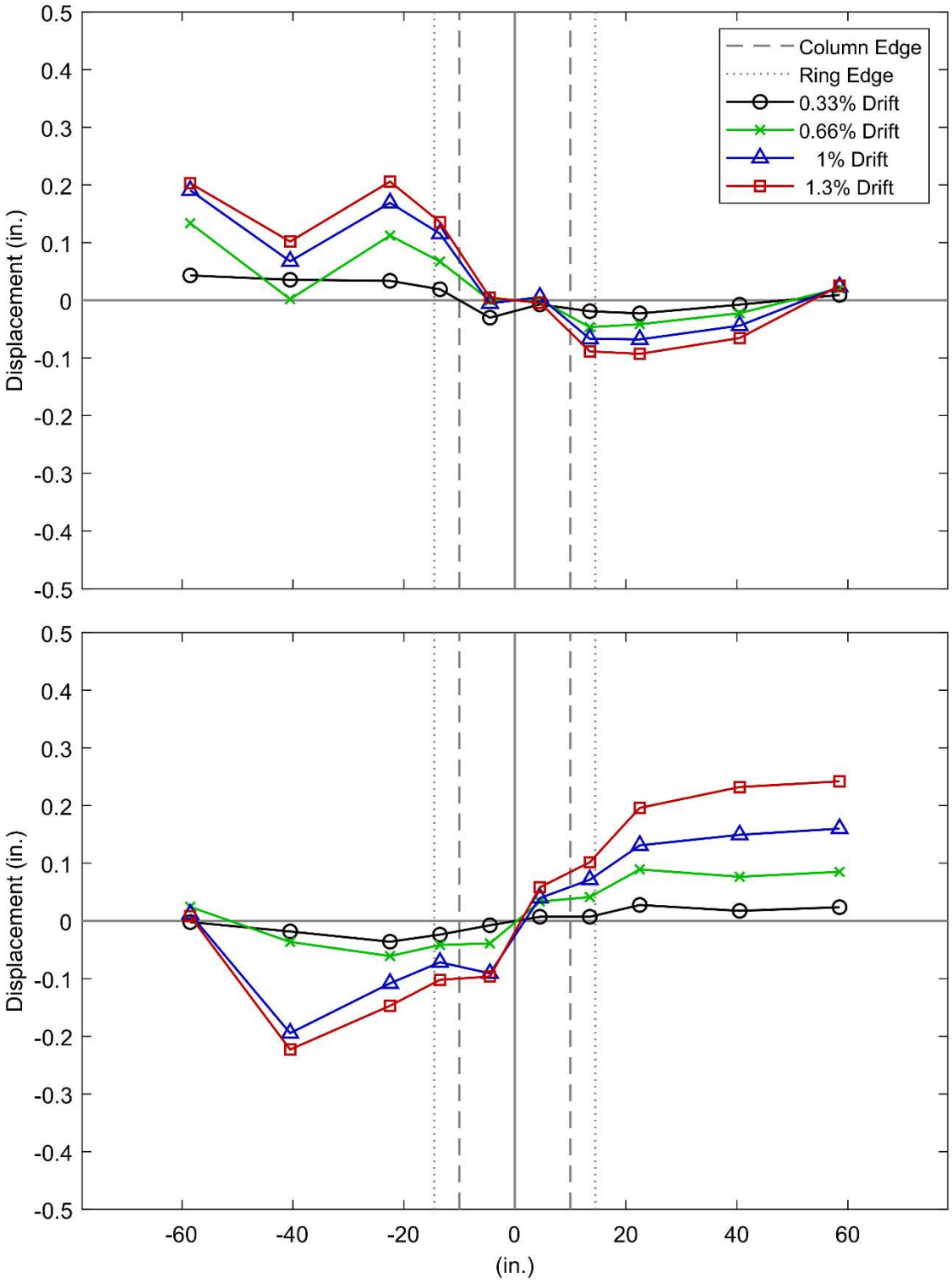

Figure 1. Low Drift Cycles Measured Slab Displaced Shape (PTB_4.5_1_0_6)

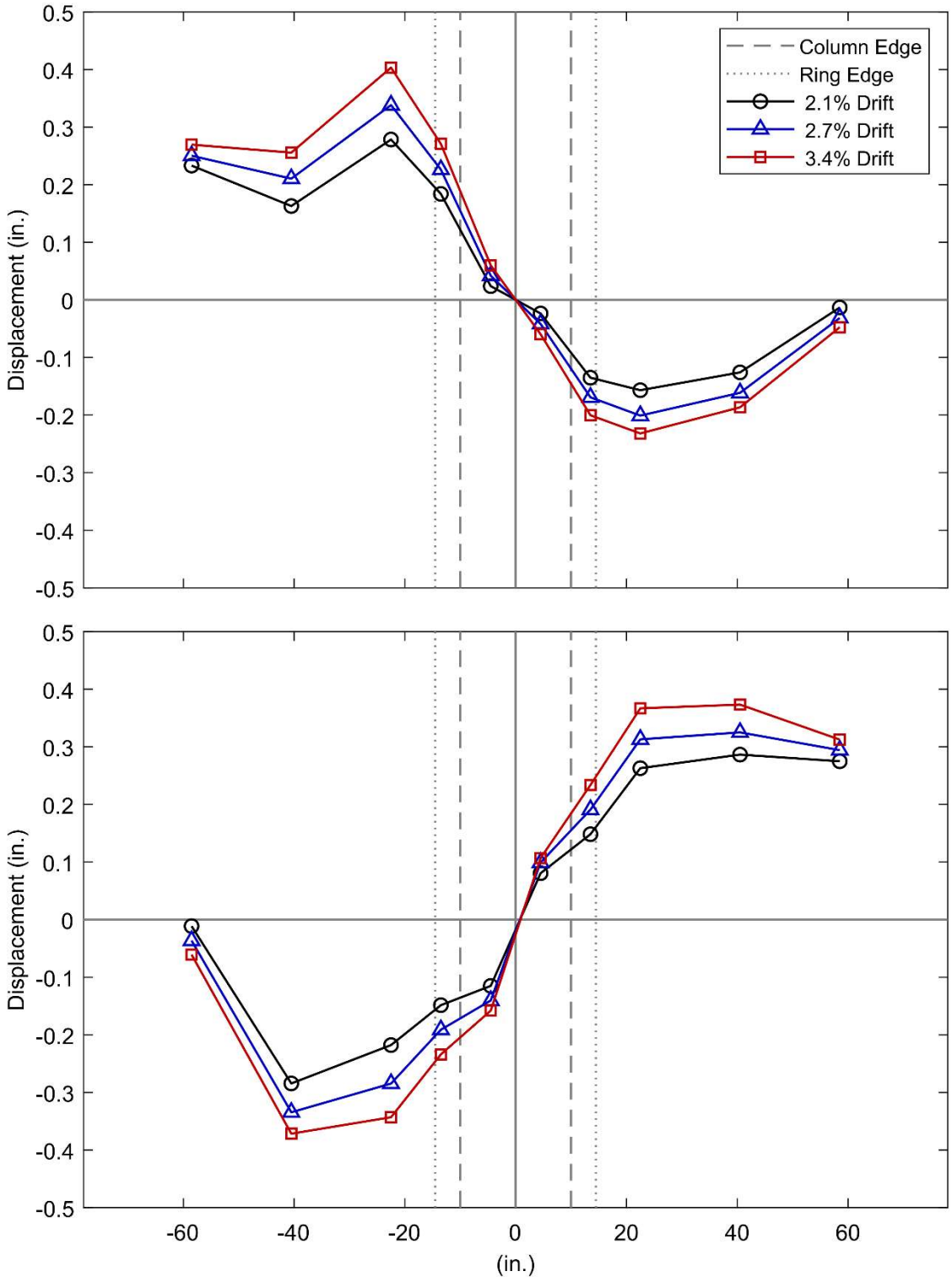

Figure 2. Moderate Drift Cycles Measured Slab Displaced Shape (PTB_4.5_1_0_6)

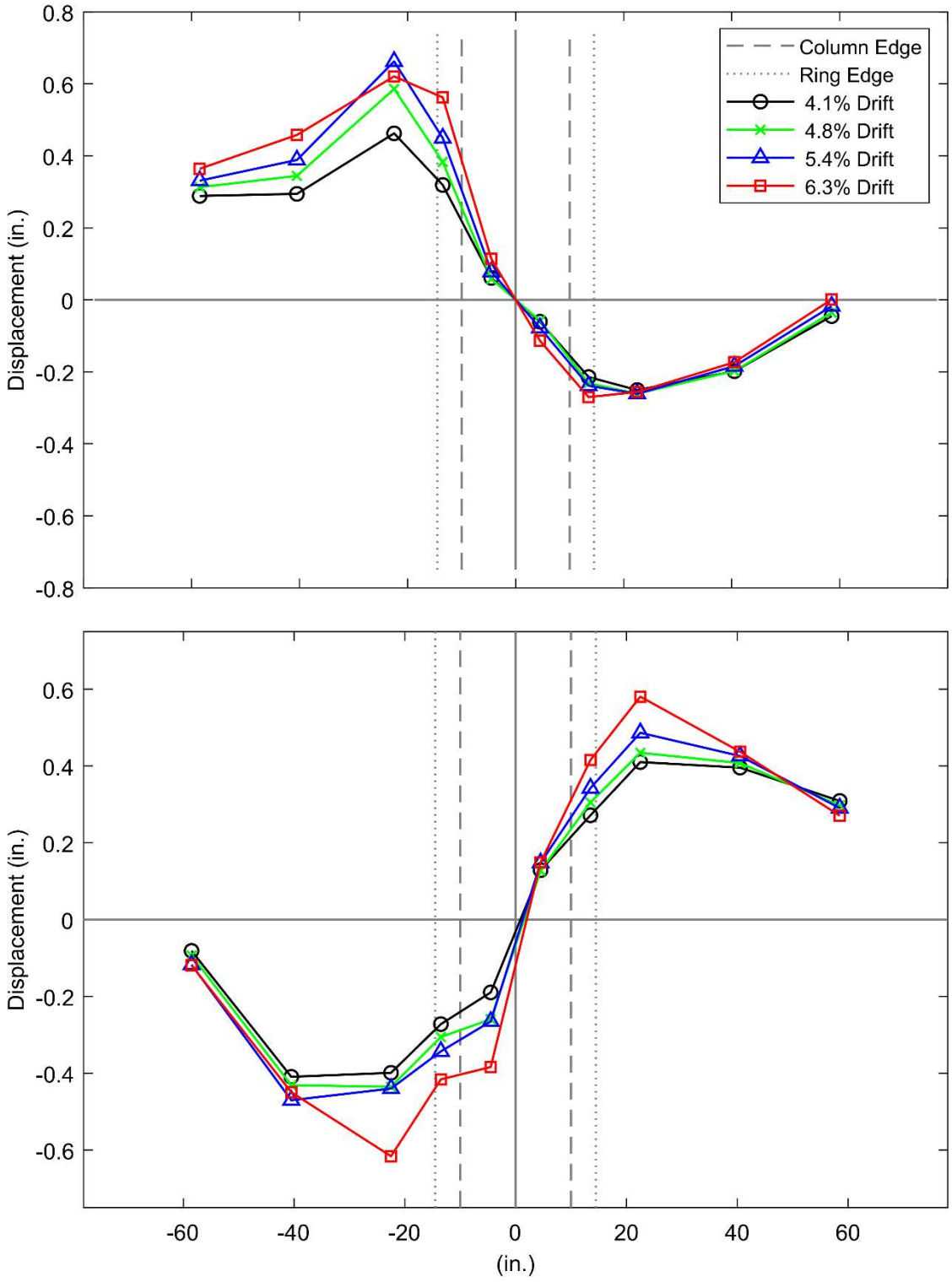

Figure 3. High Drift Cycles Measured Slab Displaced Shape (PTB_4.5_1_0_6)

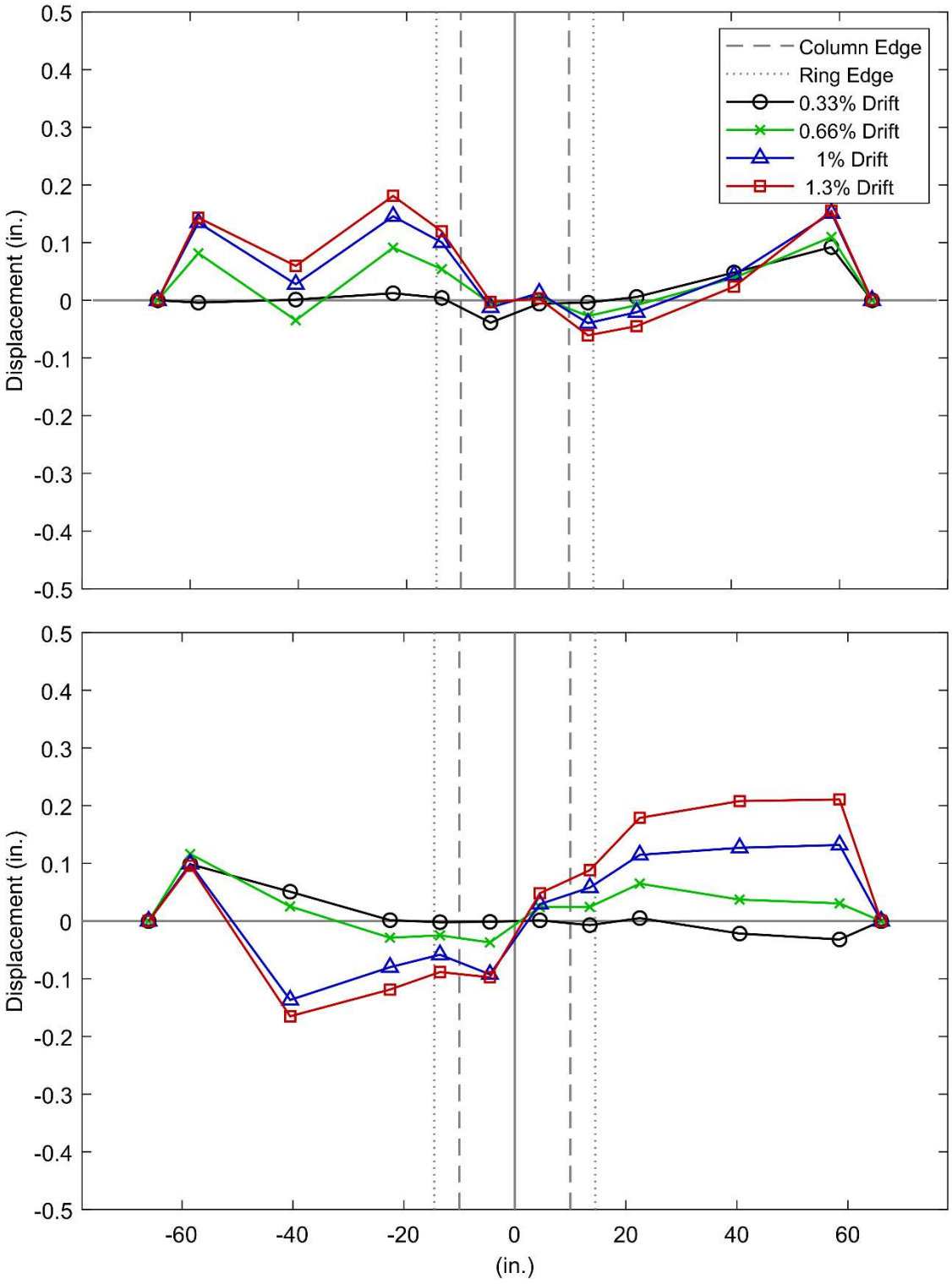

Figure 4. Low Drift Cycles Corrected Slab Displaced Shape (PTB_4.5_1_0_6)

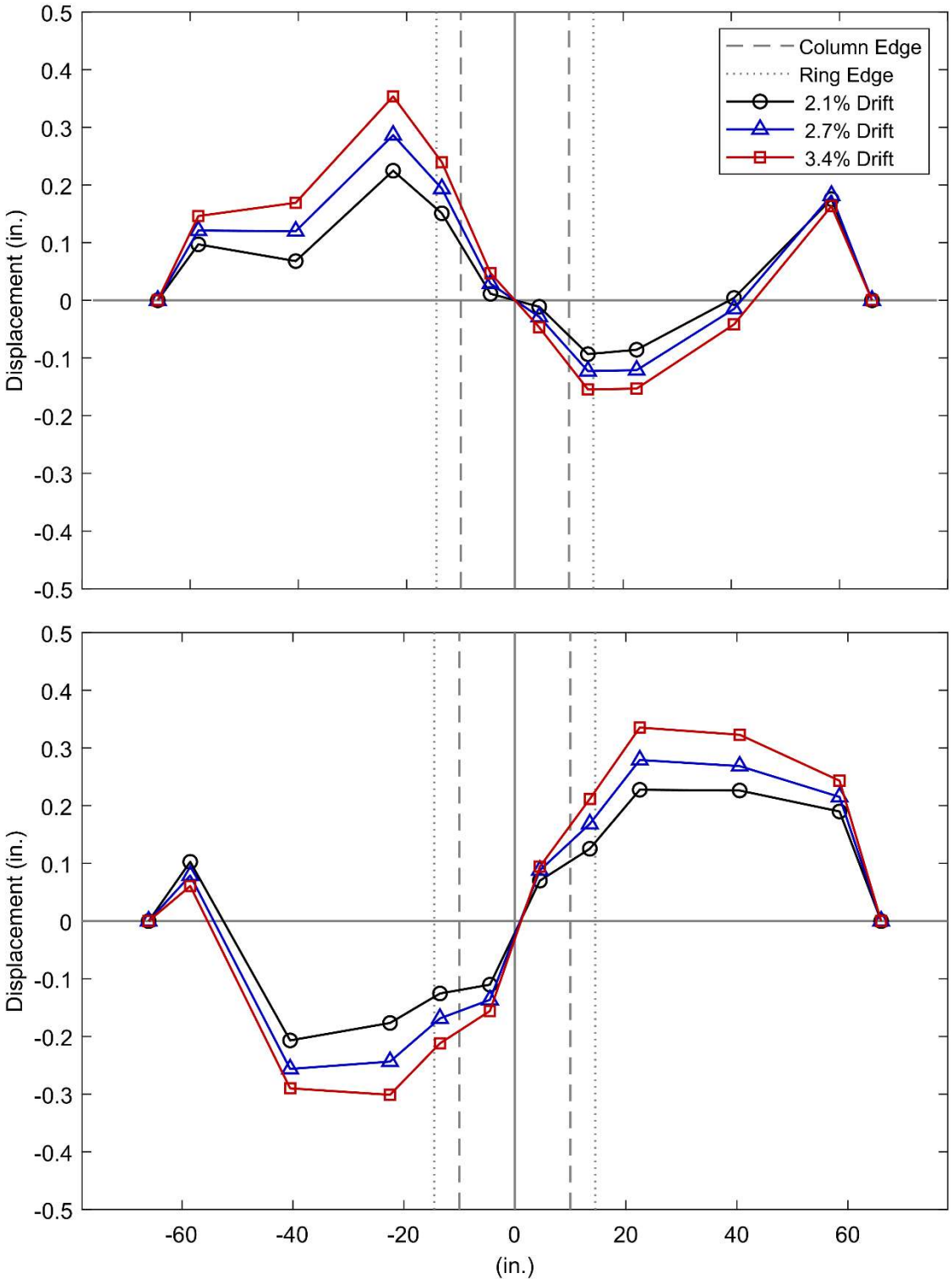

Figure 5. Moderate Drift Cycles Corrected Slab Displaced Shape (PTB_4.5_1_0_6)

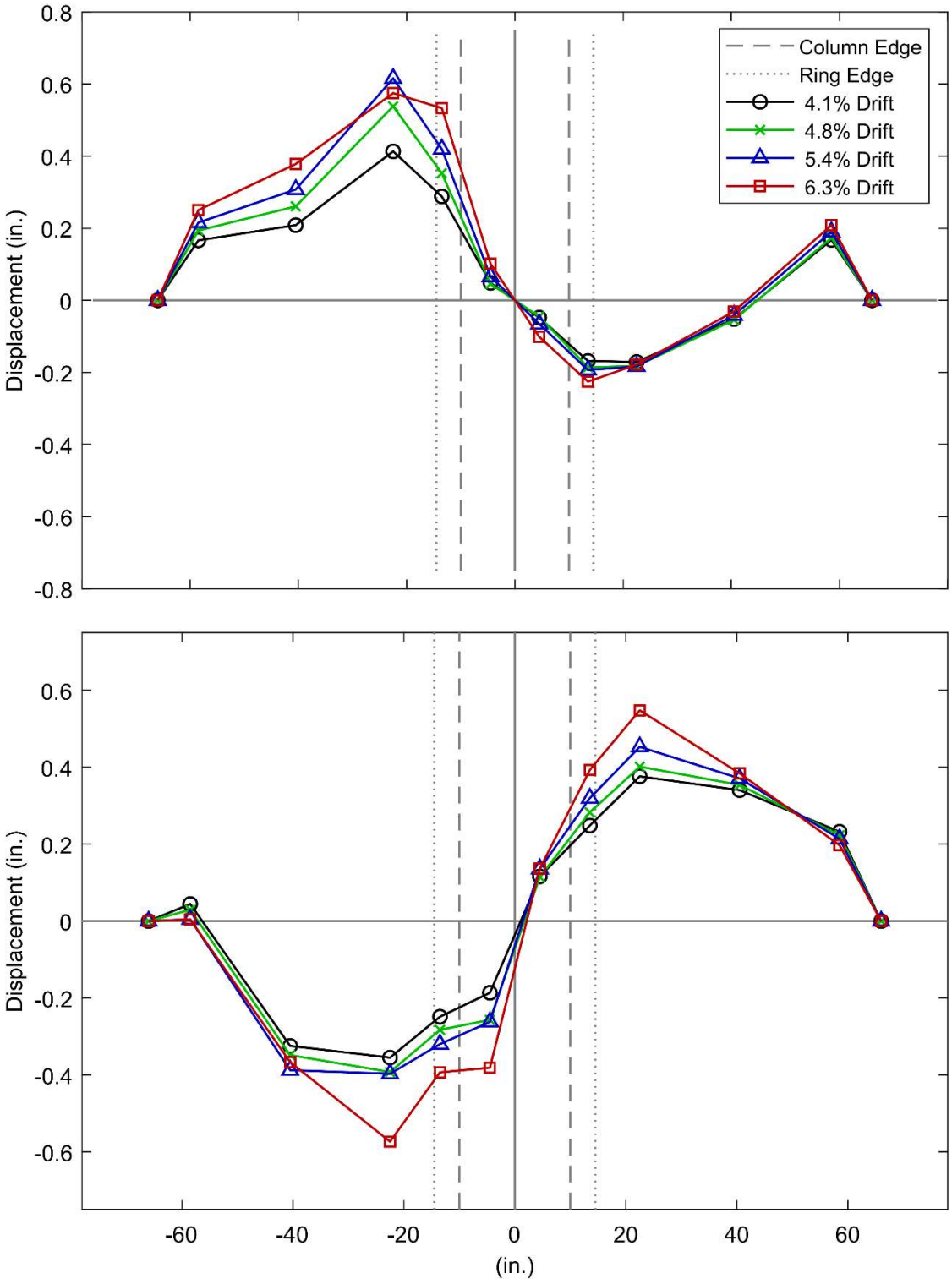

Figure 6. High Drift Cycles Corrected Slab Displaced Shape (PTB_4.5_1_0_6)

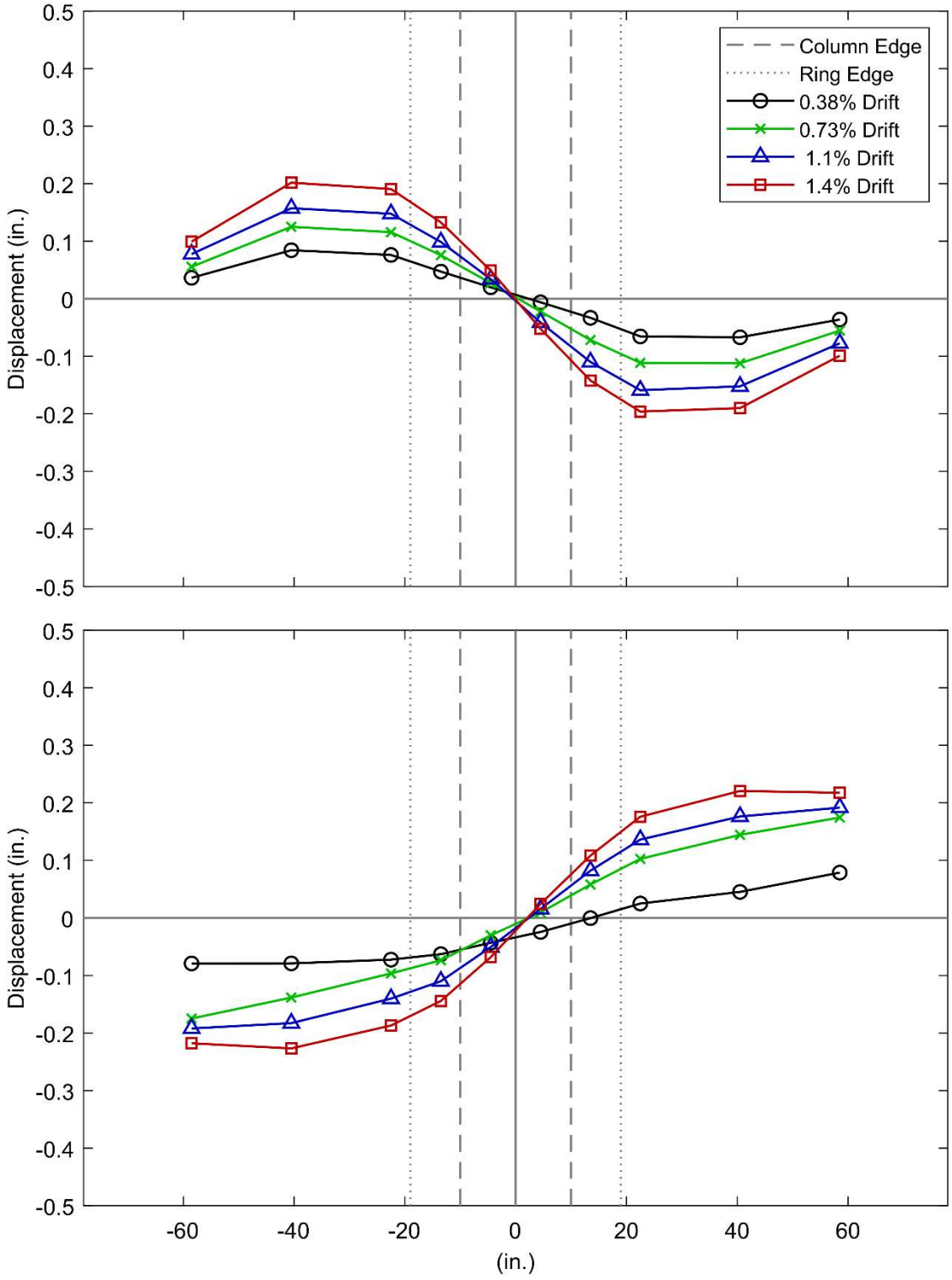

Figure 7. Low Drift Cycles Measured Slab Displaced Shape (PTB_9_2_0_6)

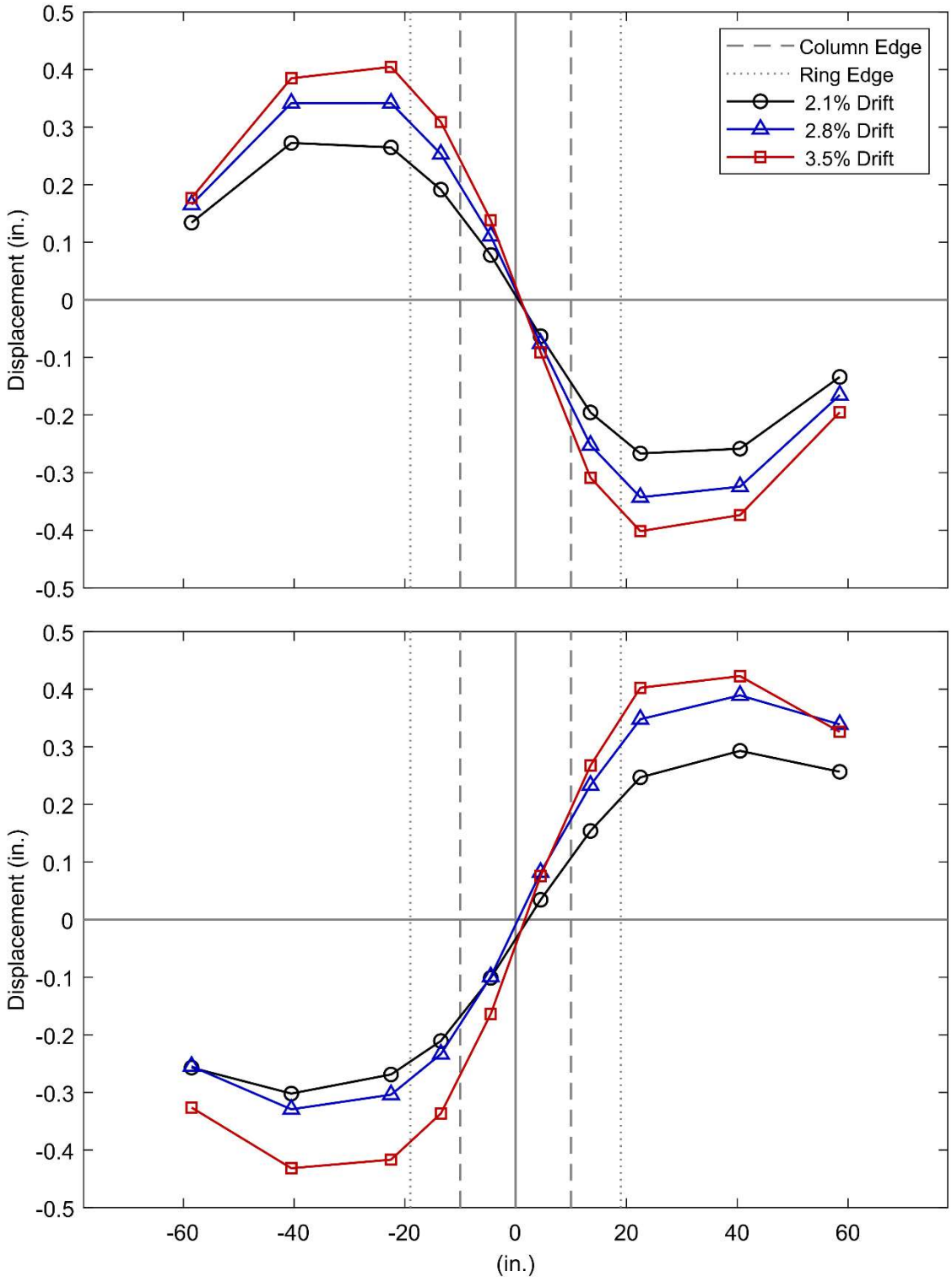

Figure 8. Moderate Drift Cycles Measured Slab Displaced Shape (PTB_9_2_0_6)

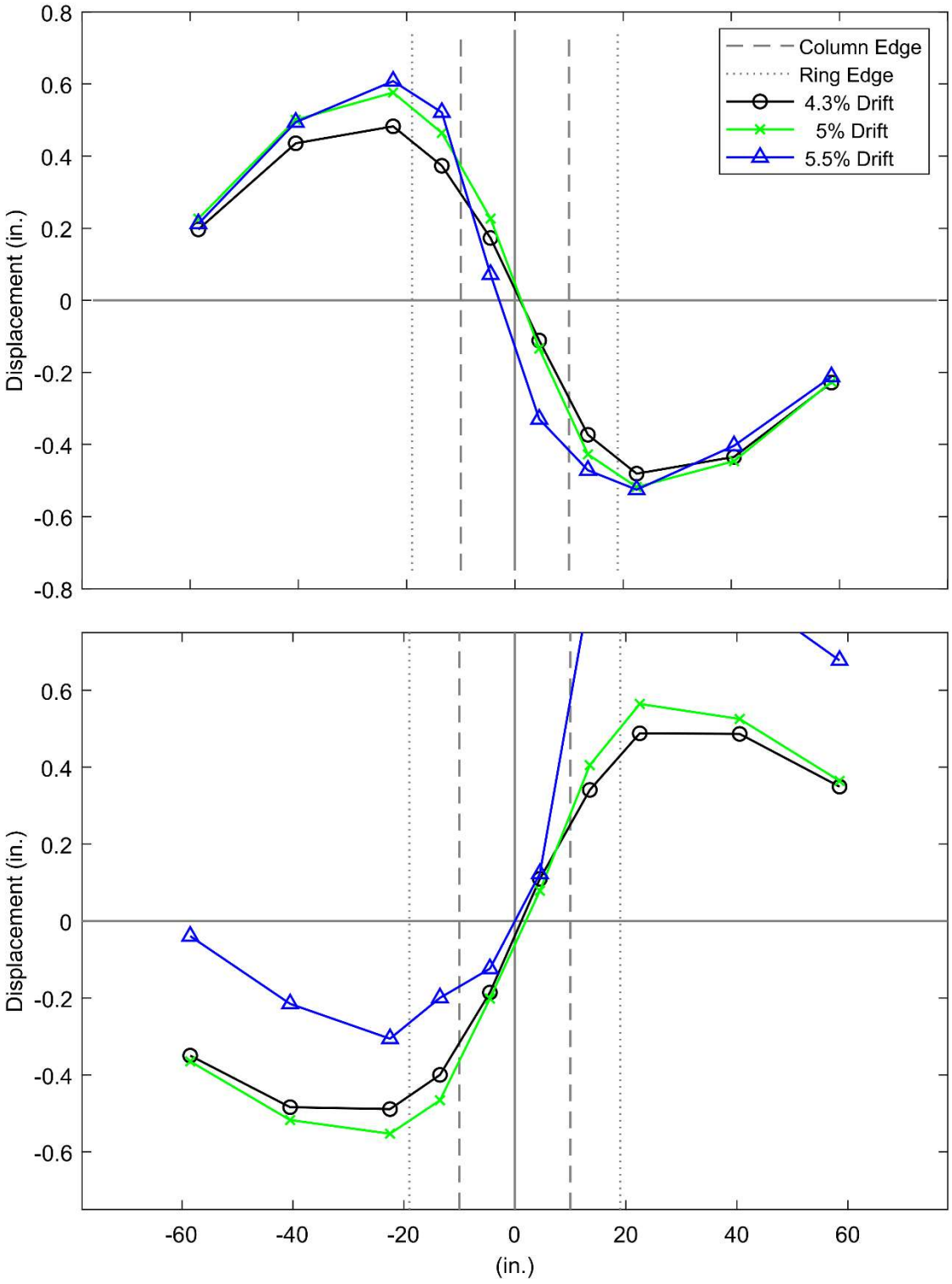

Figure 9. High Drift Cycles Measured Slab Displaced Shape (PTB_9_2_0_6)

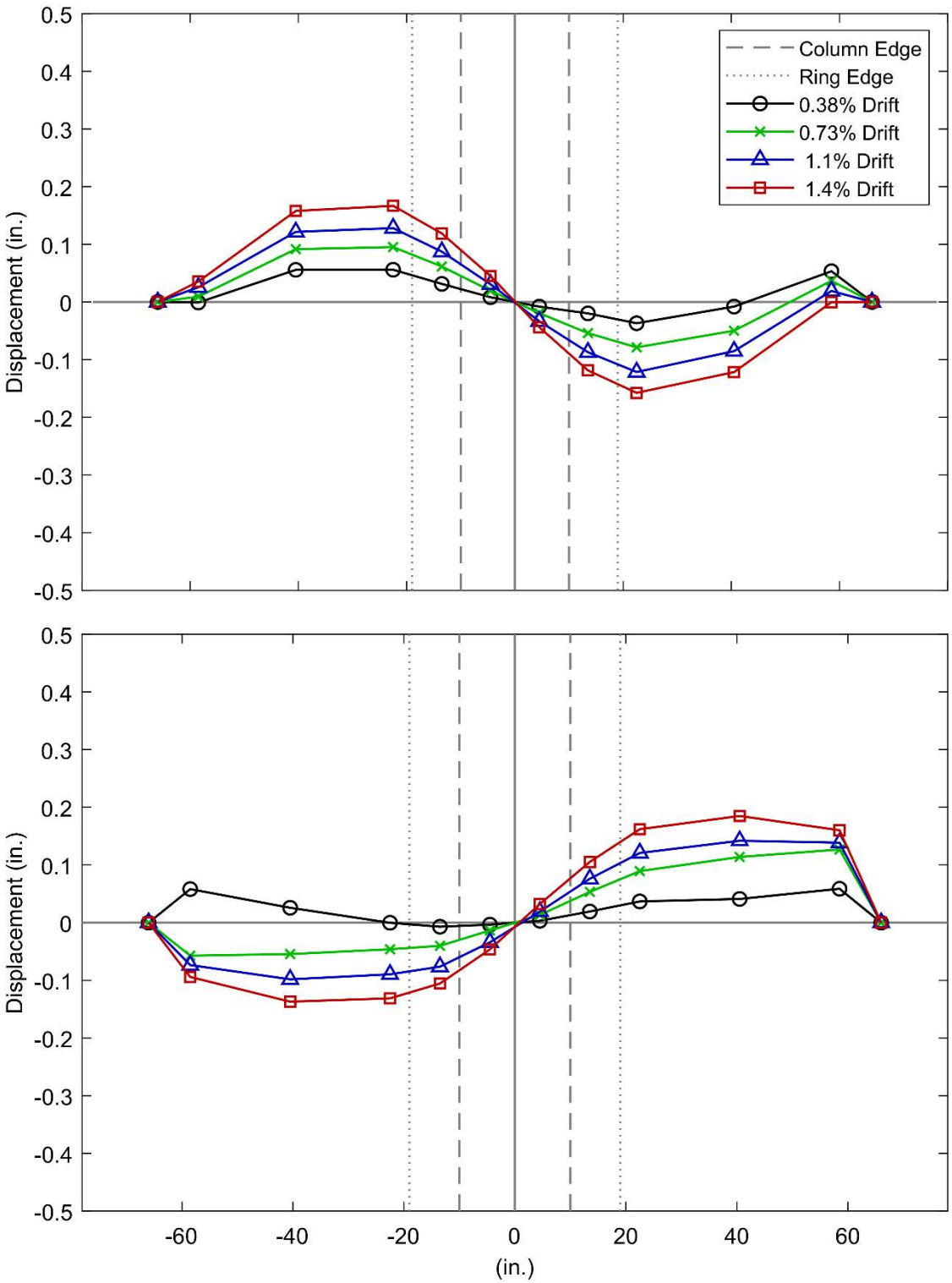

Figure 10. Low Drift Cycles Corrected Slab Displaced Shape (PTB_9_2_0_6)

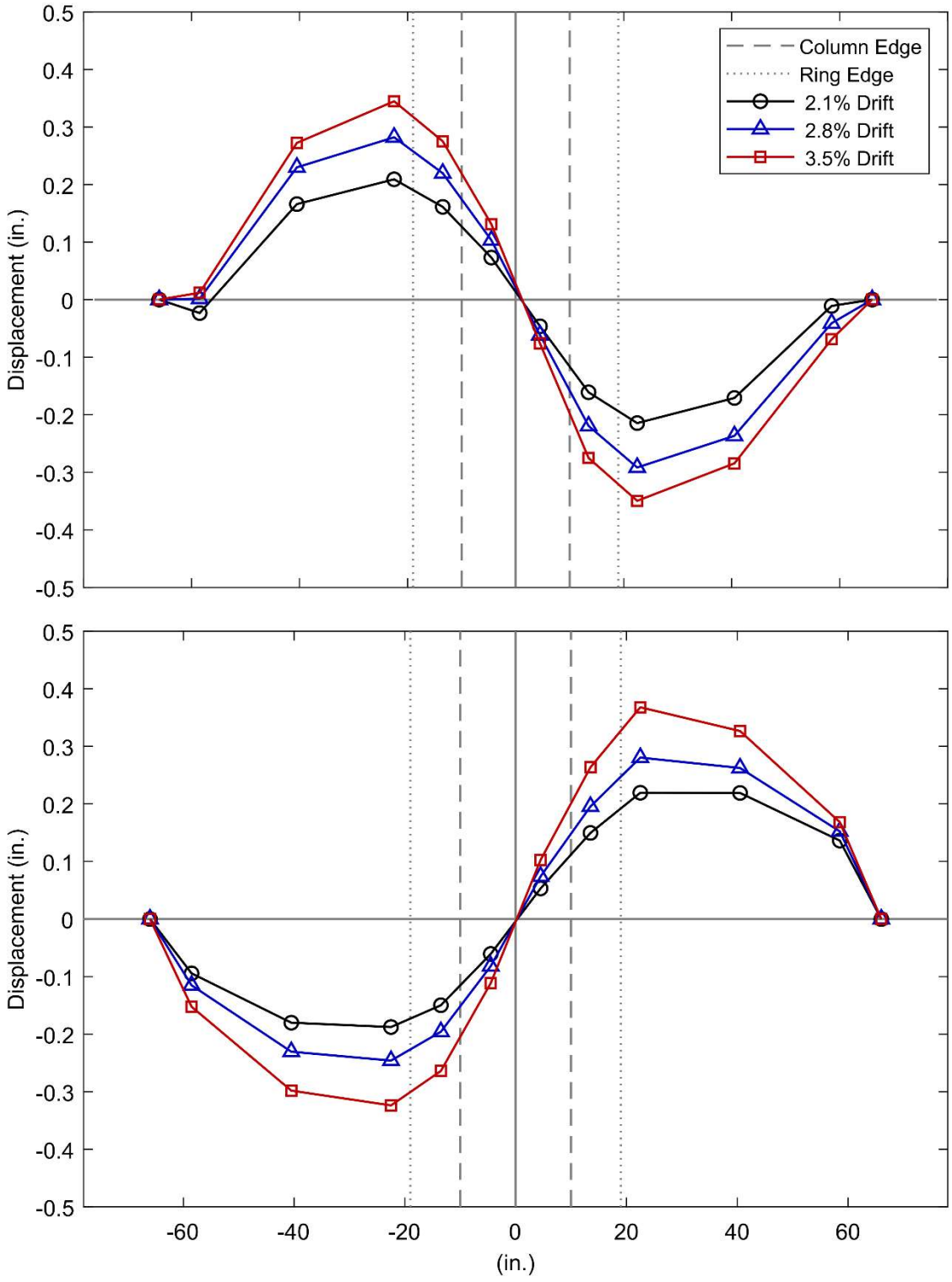

Figure 11. Moderate Drift Cycles Corrected Slab Displaced Shape (PTB_9_2_0_6)

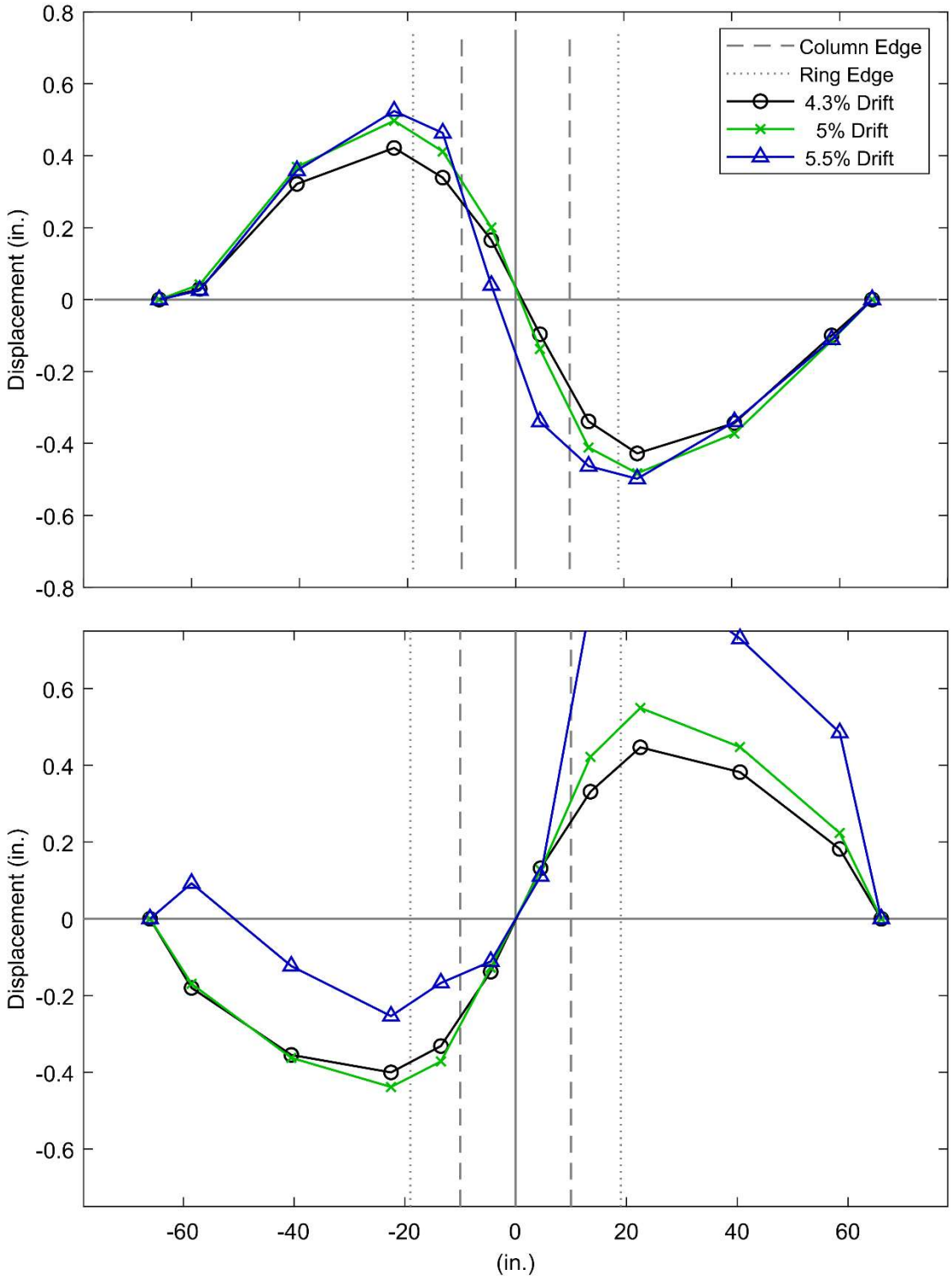

Figure 12. High Drift Cycles Corrected Slab Displaced Shape (PTB_9_2_0_6)

APPENDIX E

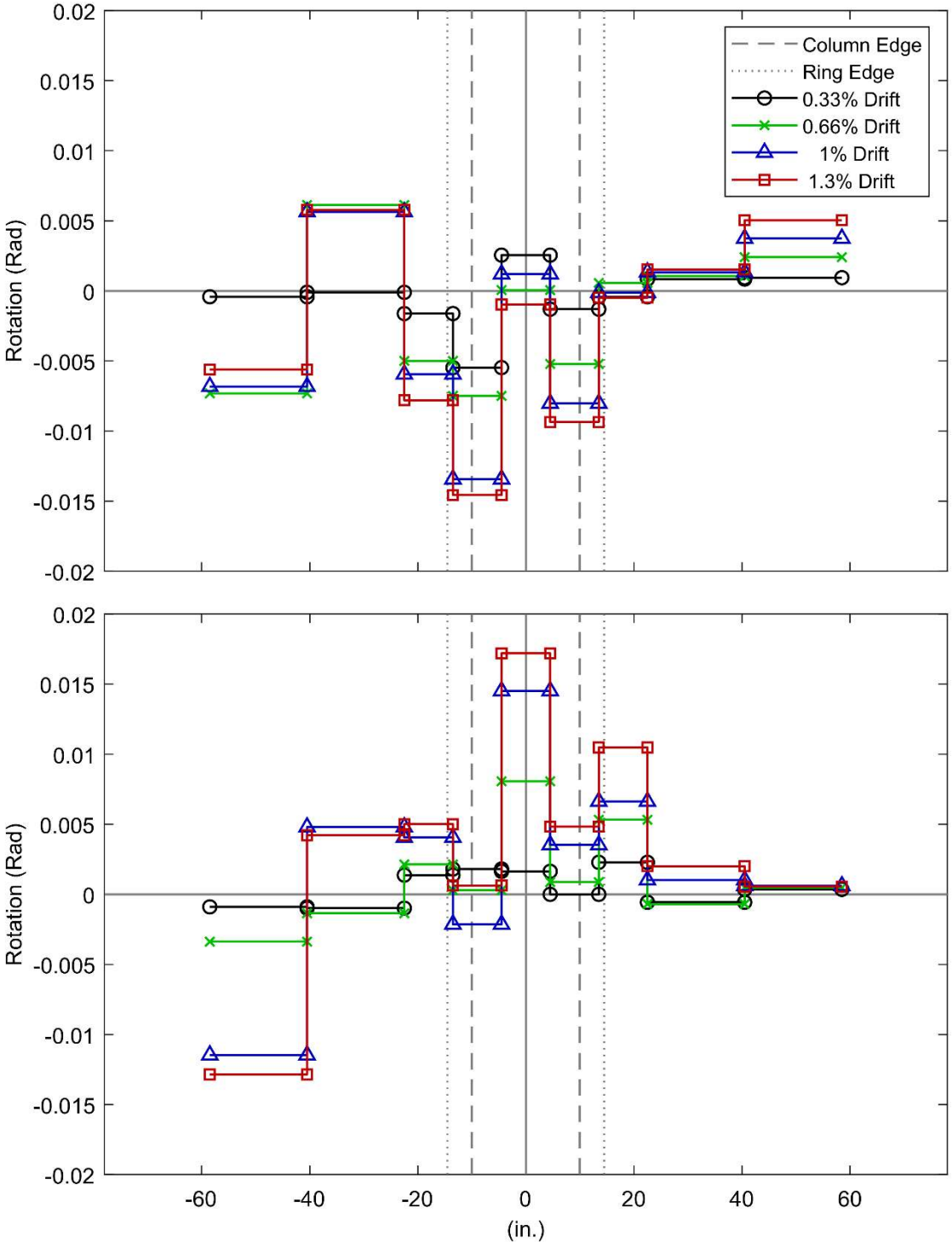

Figure 1. Low Drift Cycles Measured Slab Rotation Profile (PTB_4.5_1_0_6)

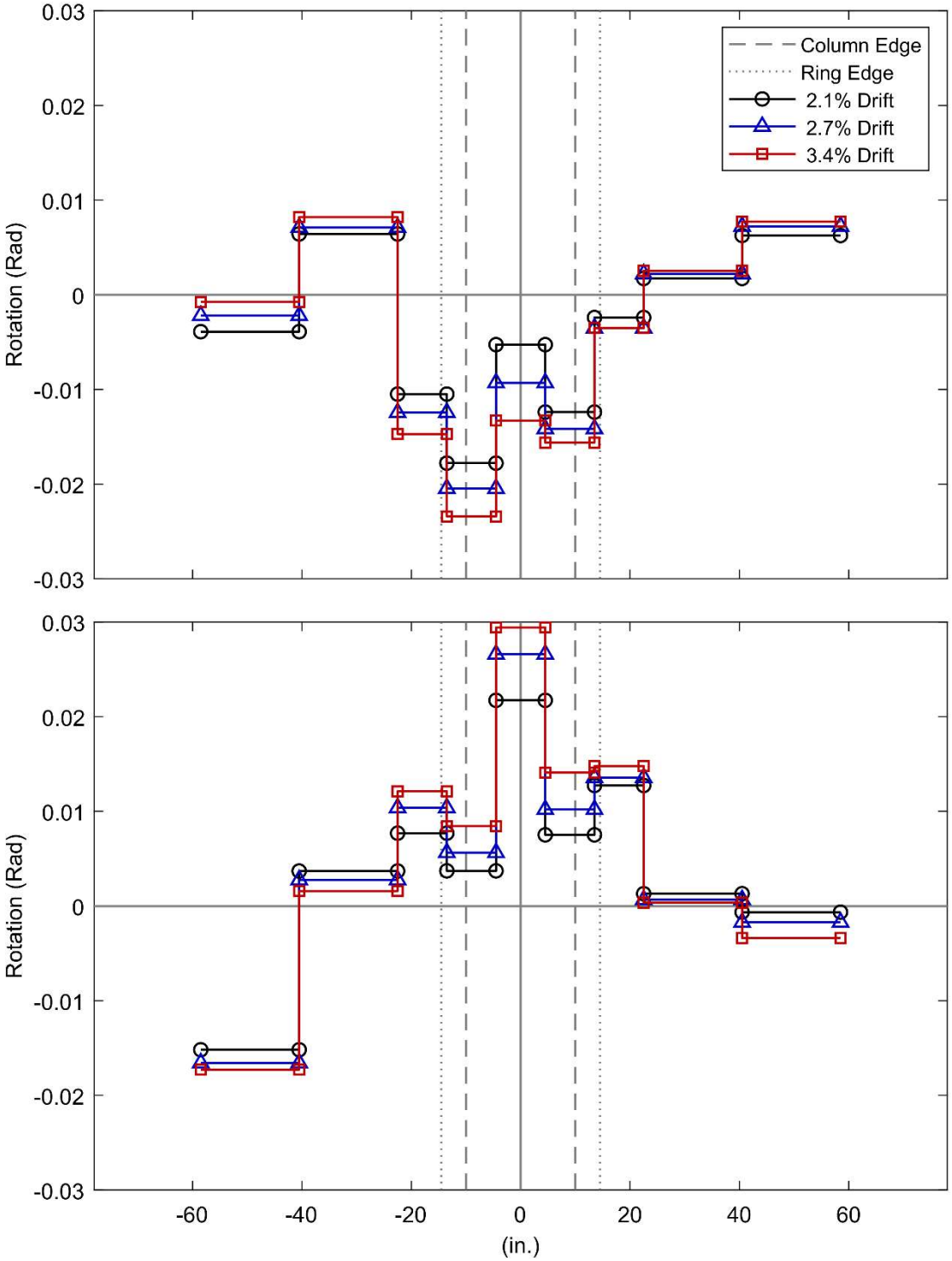

Figure 2. Moderate Drift Cycles Measured Slab Rotation Profile (PTB_4.5_1_0_6)

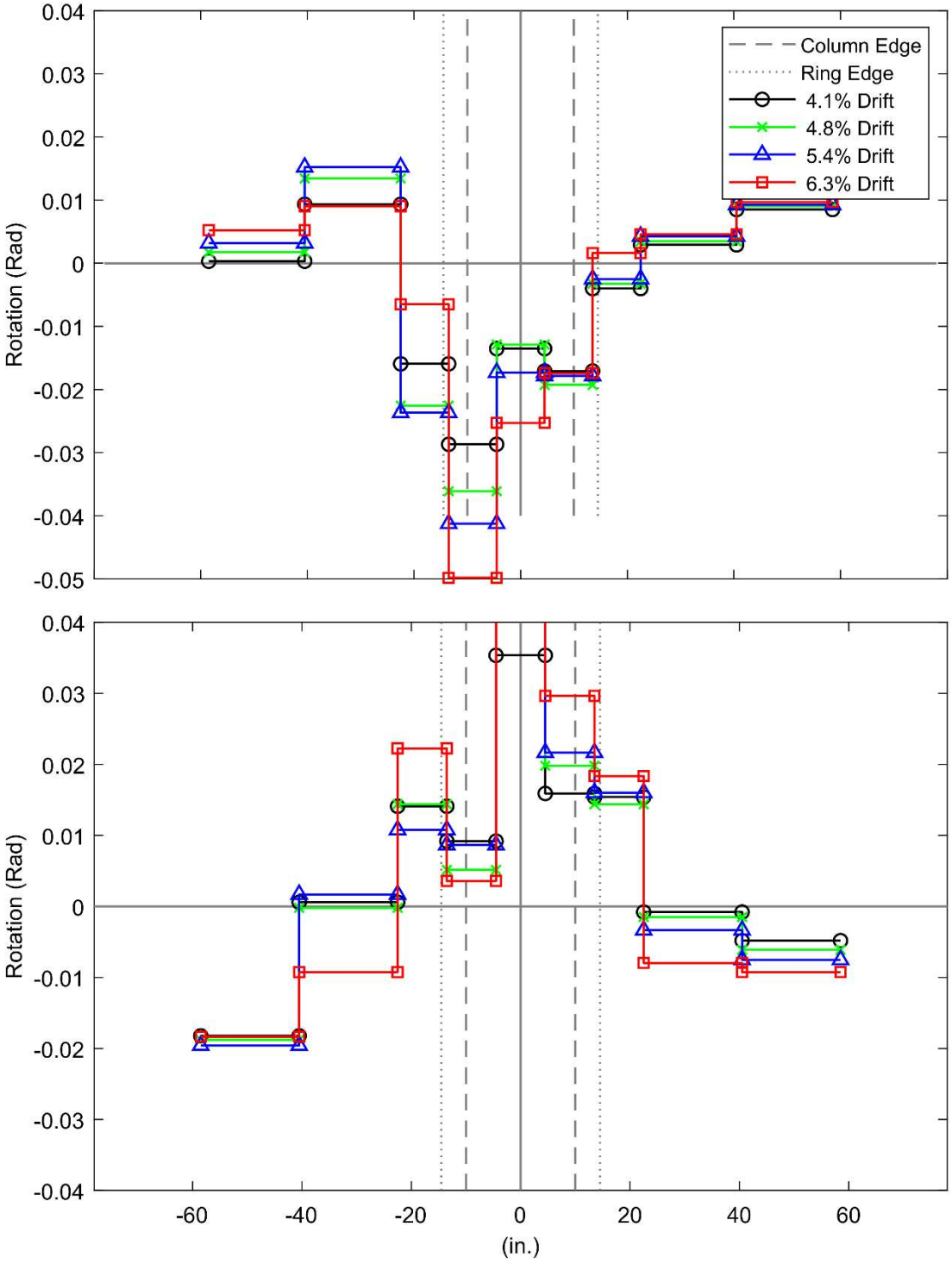

Figure 3. High Drift Cycles Measured Slab Rotation Profile (PTB_4.5_1_0_6)

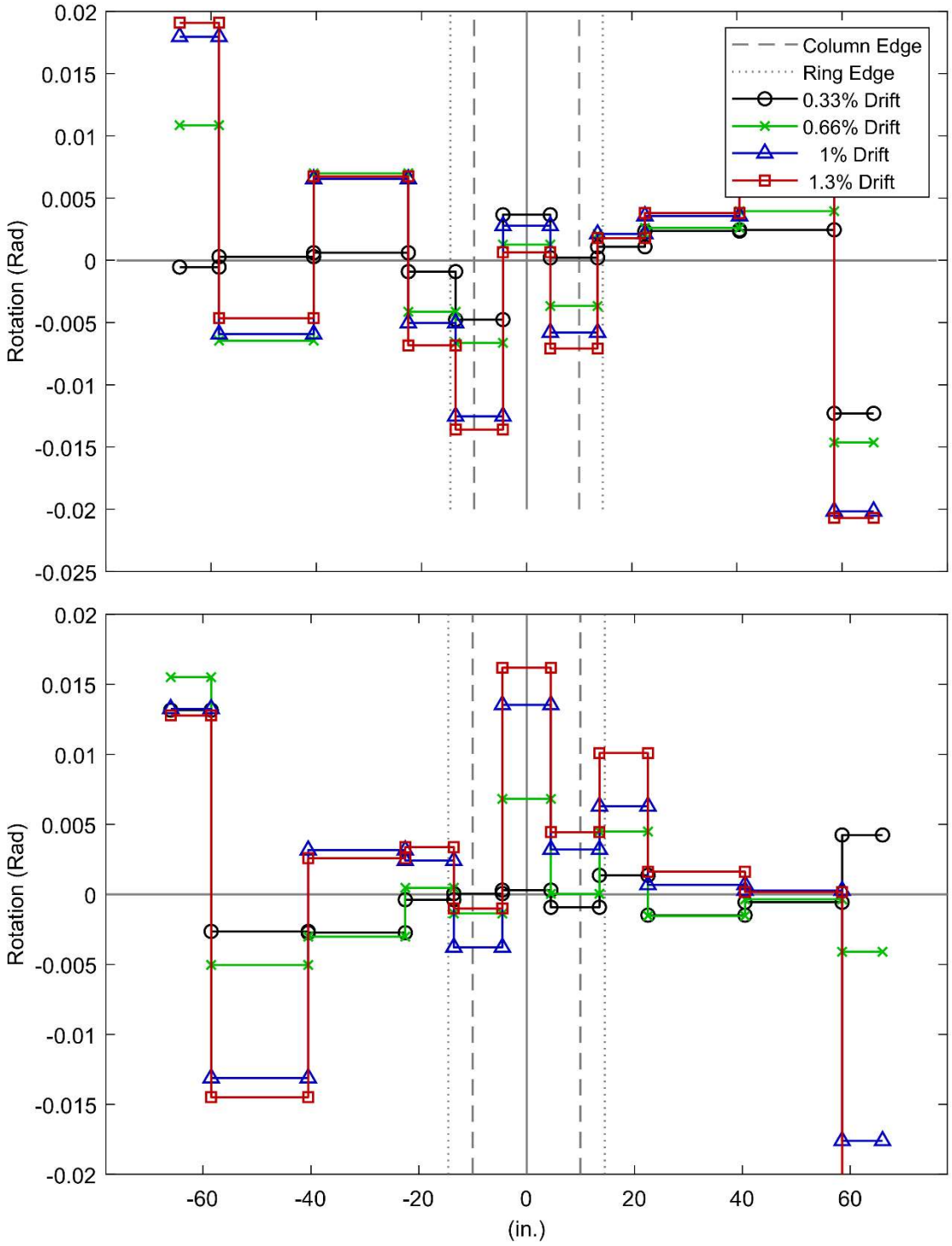

Figure 4. Low Drift Cycles Corrected Slab Rotation Profile (PTB_4.5_1_0_6)

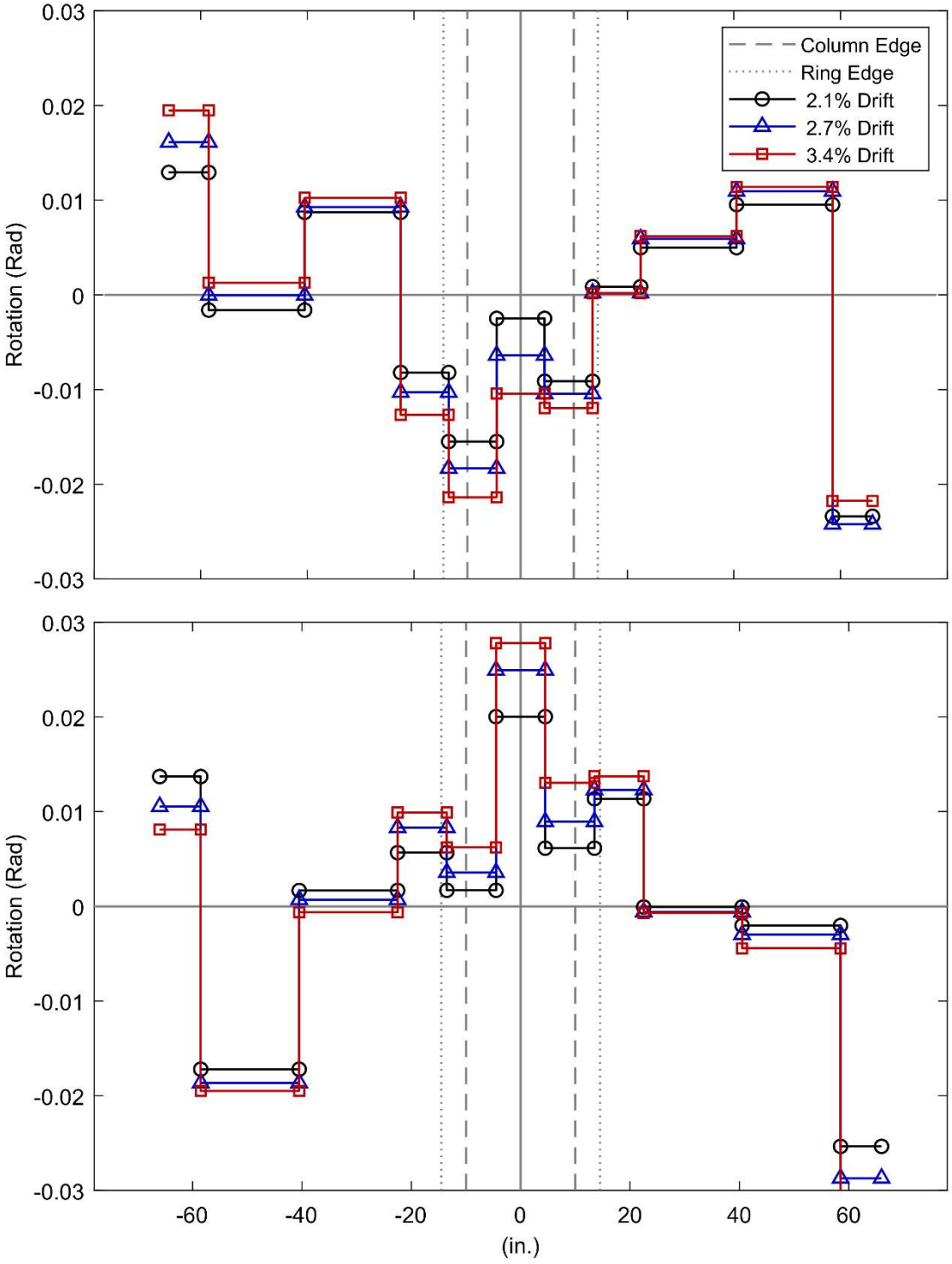

Figure 5. Moderate Drift Cycles Corrected Slab Rotation Profile (PTB_4.5_1_0_6)

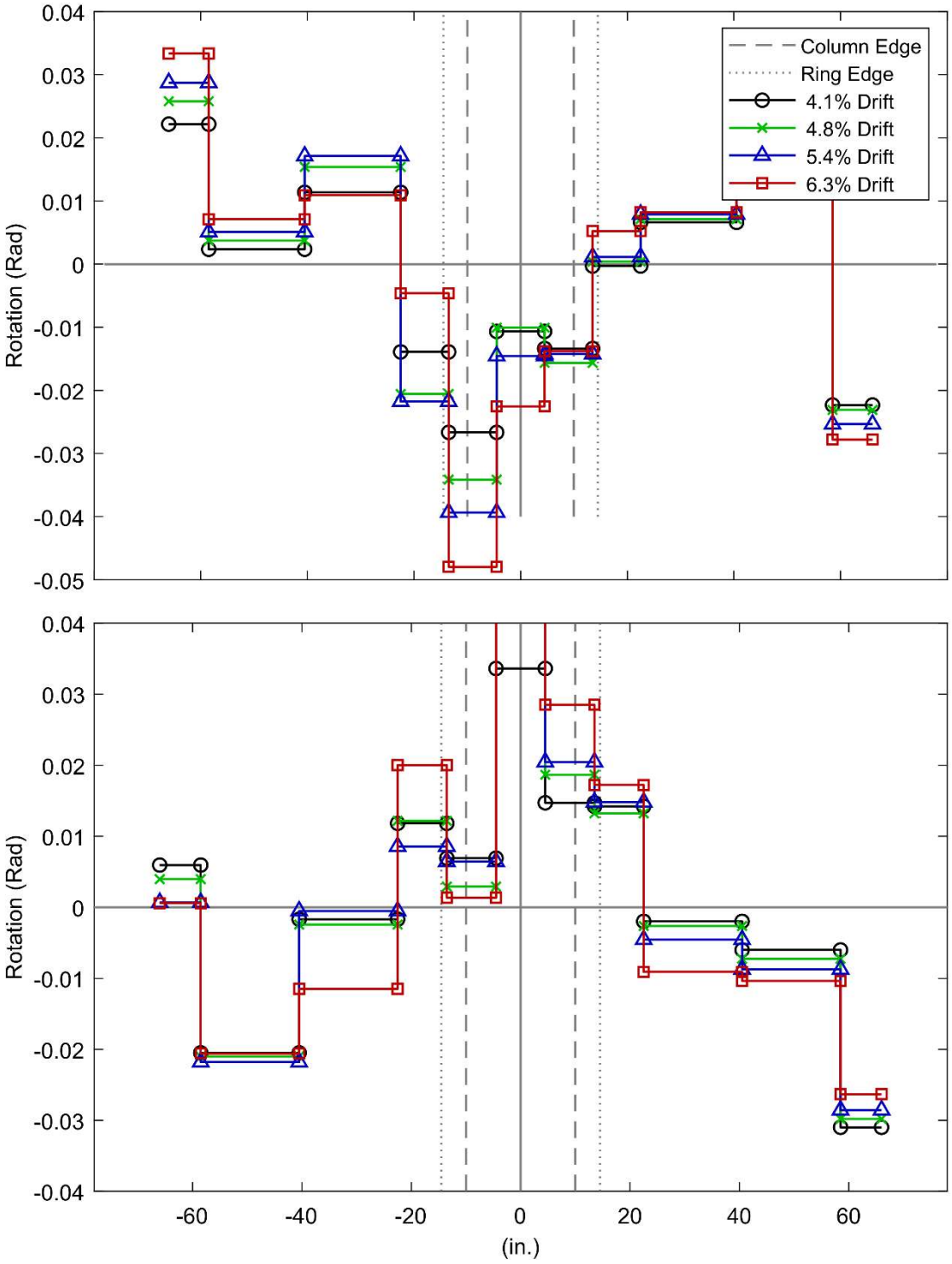

Figure 6. High Drift Cycles Corrected Slab Rotation Profile (PTB_4.5_1_0_6)

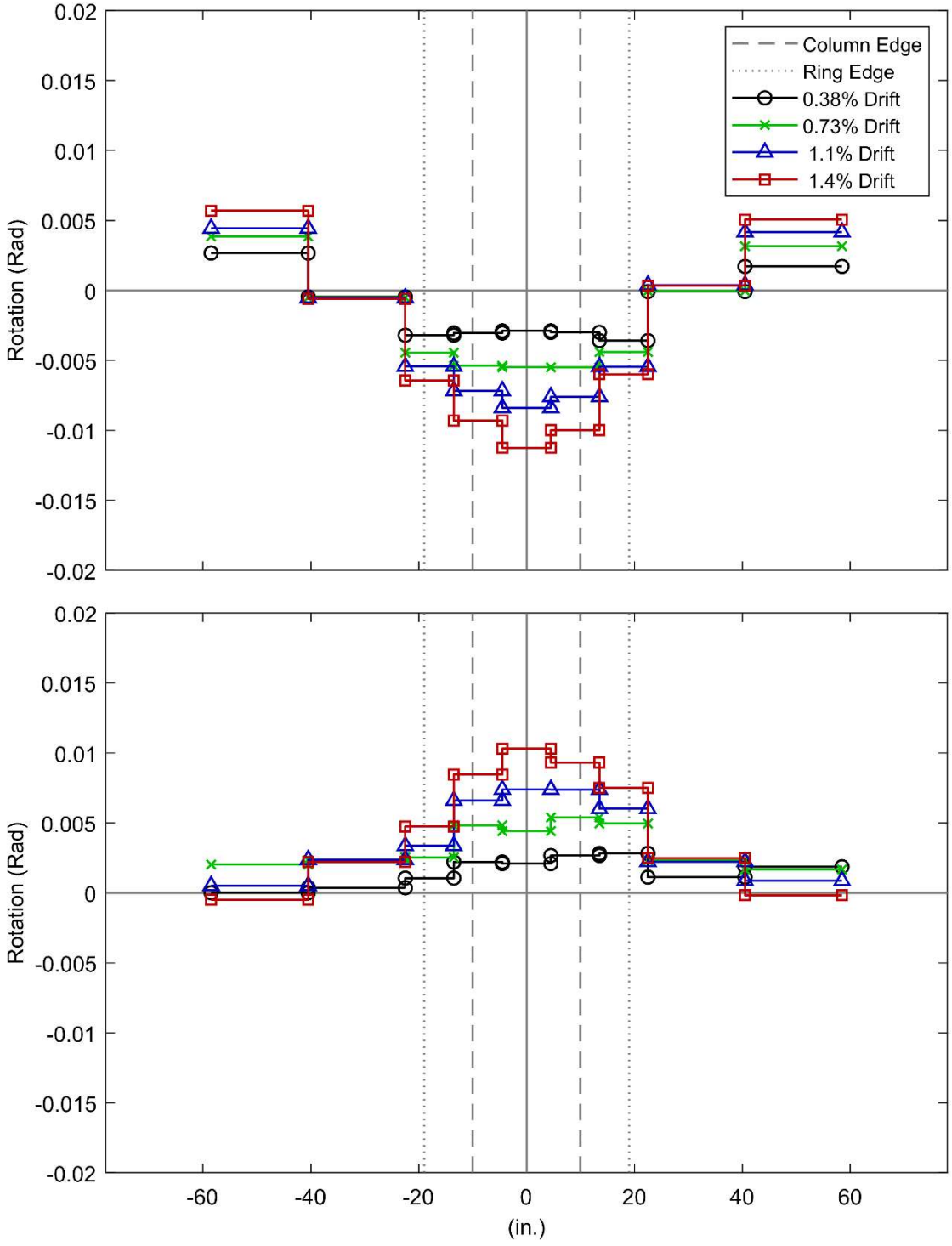

Figure 7. Low Drift Cycles Measured Slab Rotation Profile (PTB_9_2_0_6)

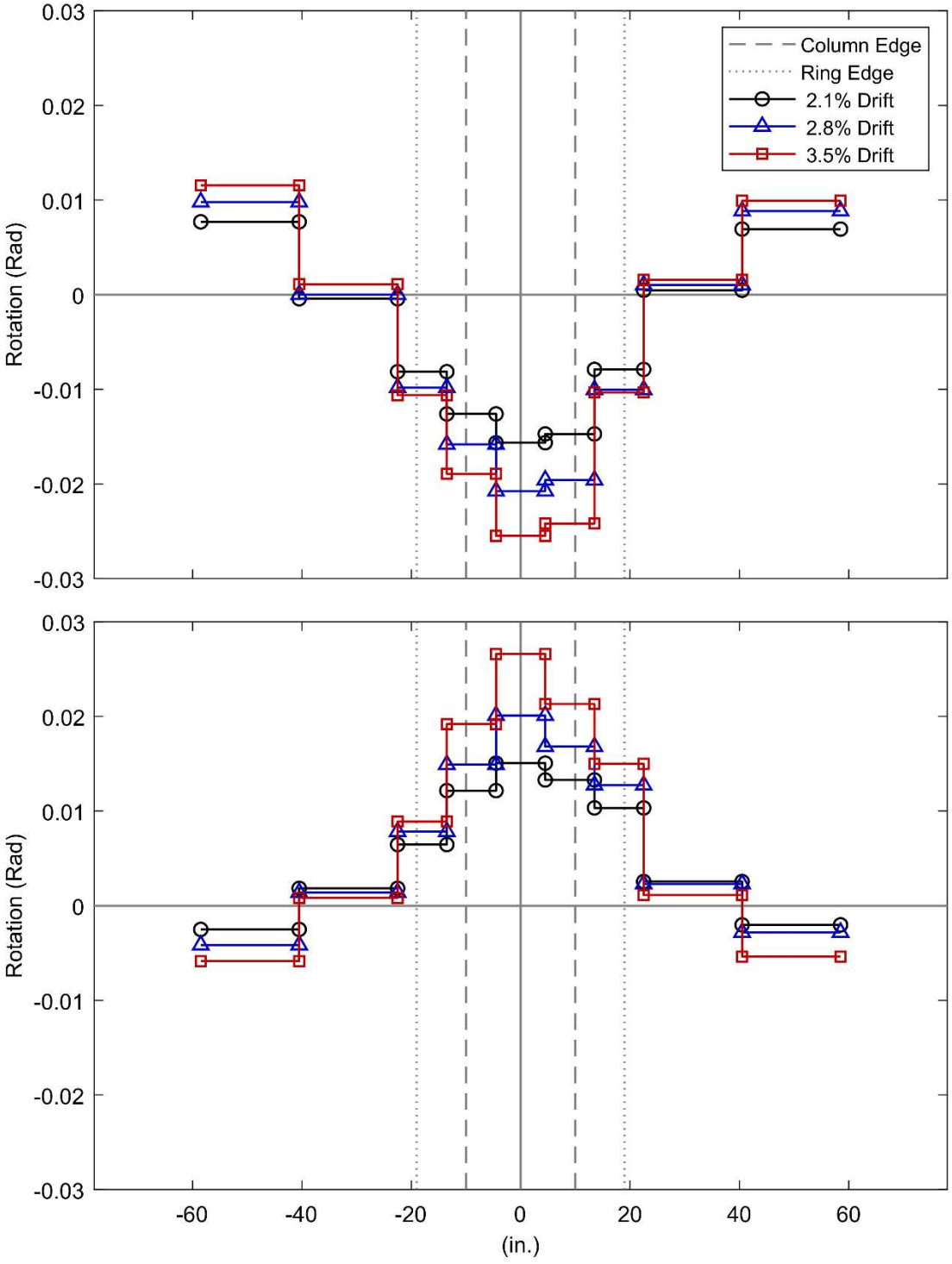

Figure 8. Moderate Drift Cycles Measured Slab Rotation Profile (PTB_9_2_0_6)

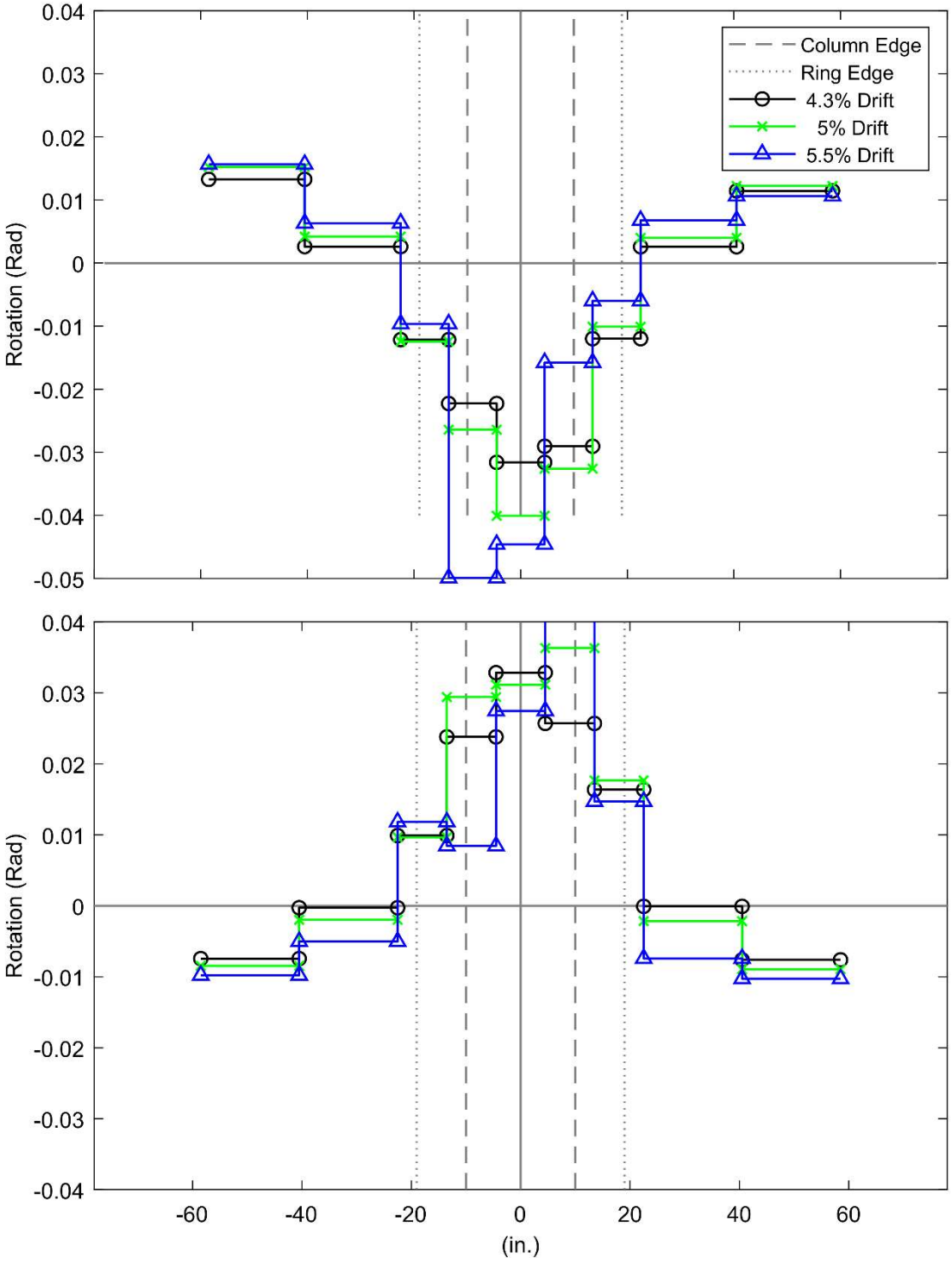

Figure 9. High Drift Cycles Measured Slab Rotation Profile (PTB_9_2_0_6)

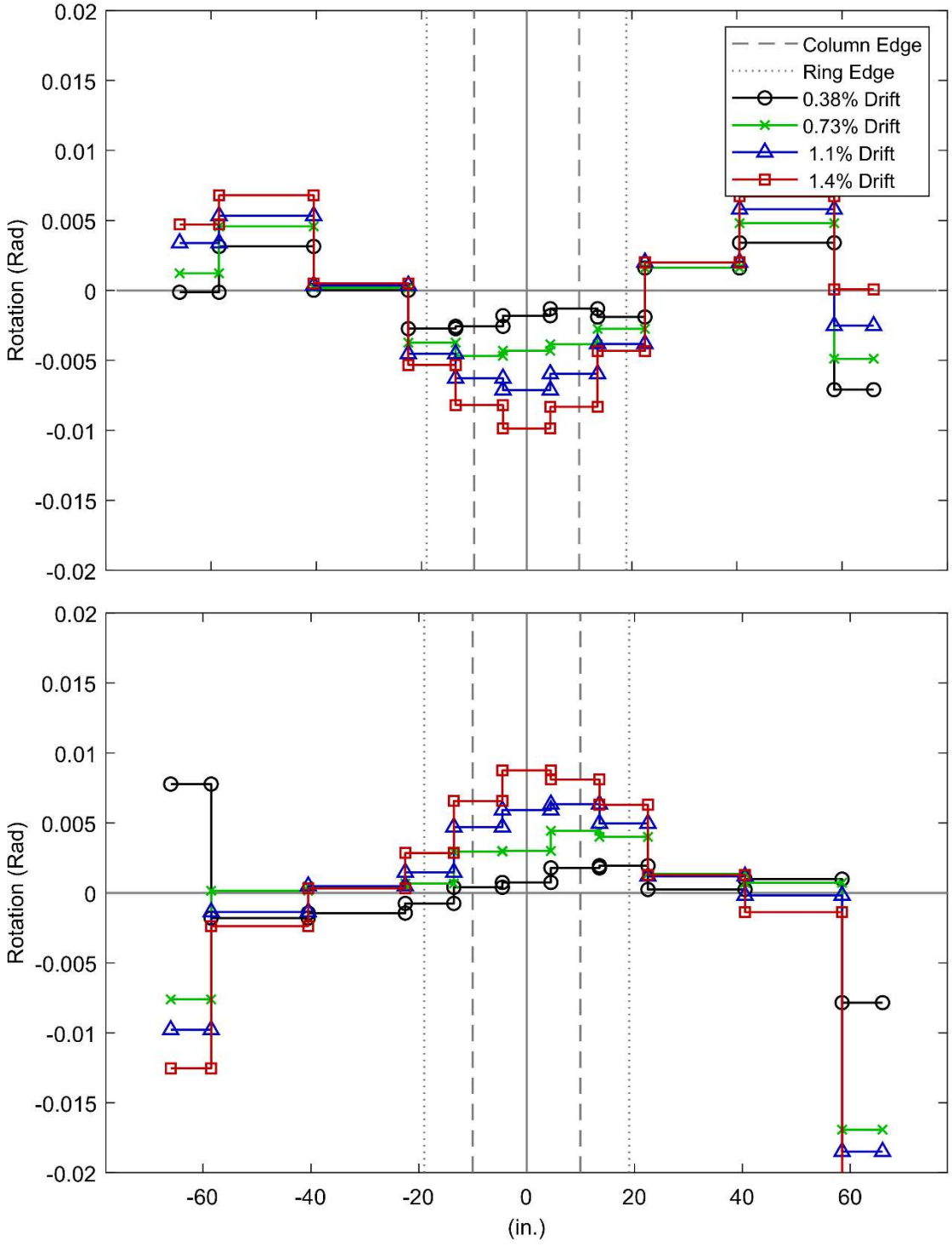

Figure 10. Low Drift Cycles Corrected Slab Rotation Profile (PTB_9_2_0_6)

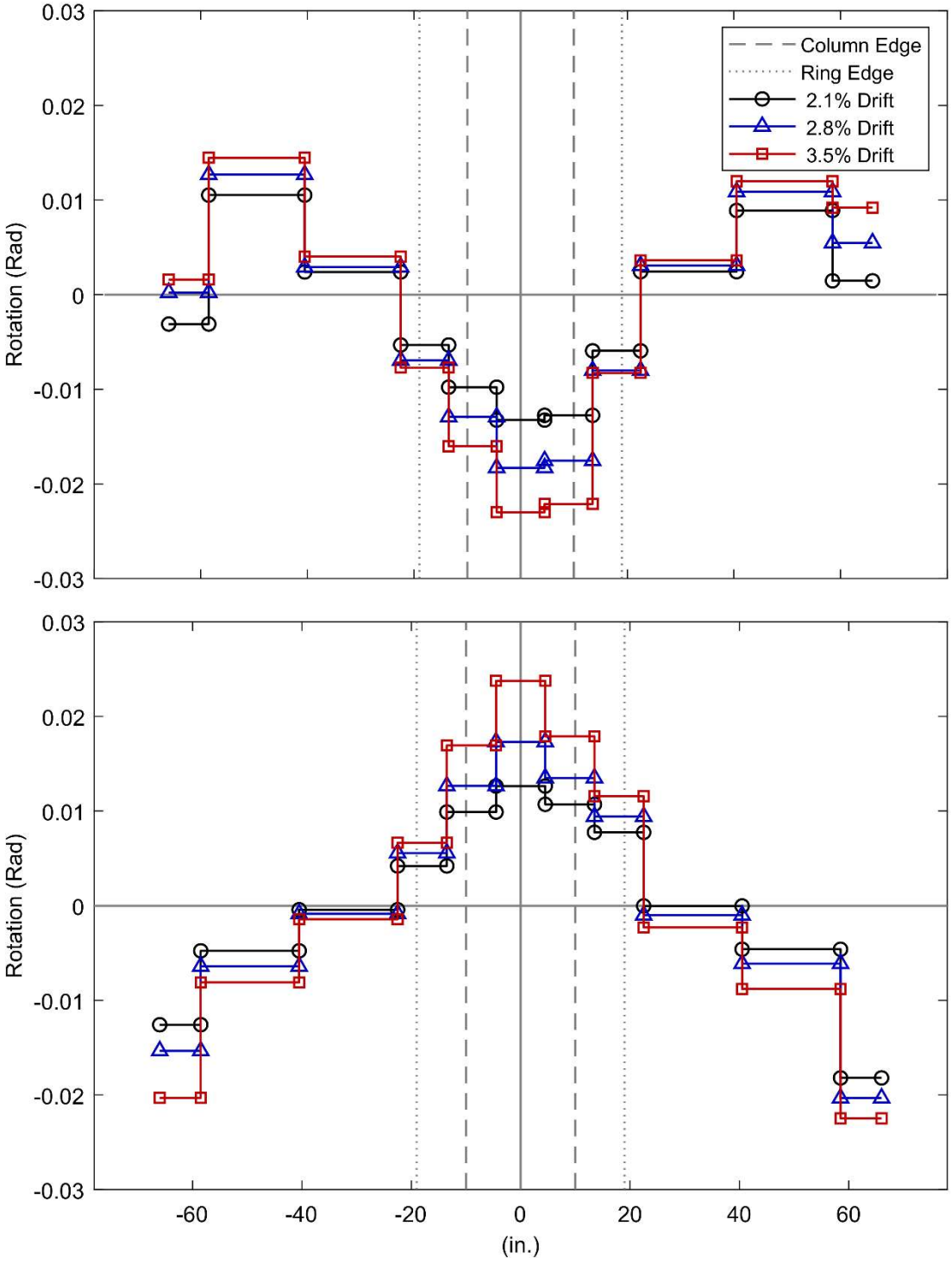

Figure 11. Moderate Drift Cycles Corrected Slab Rotation Profile (PTB_9_2_0_6)

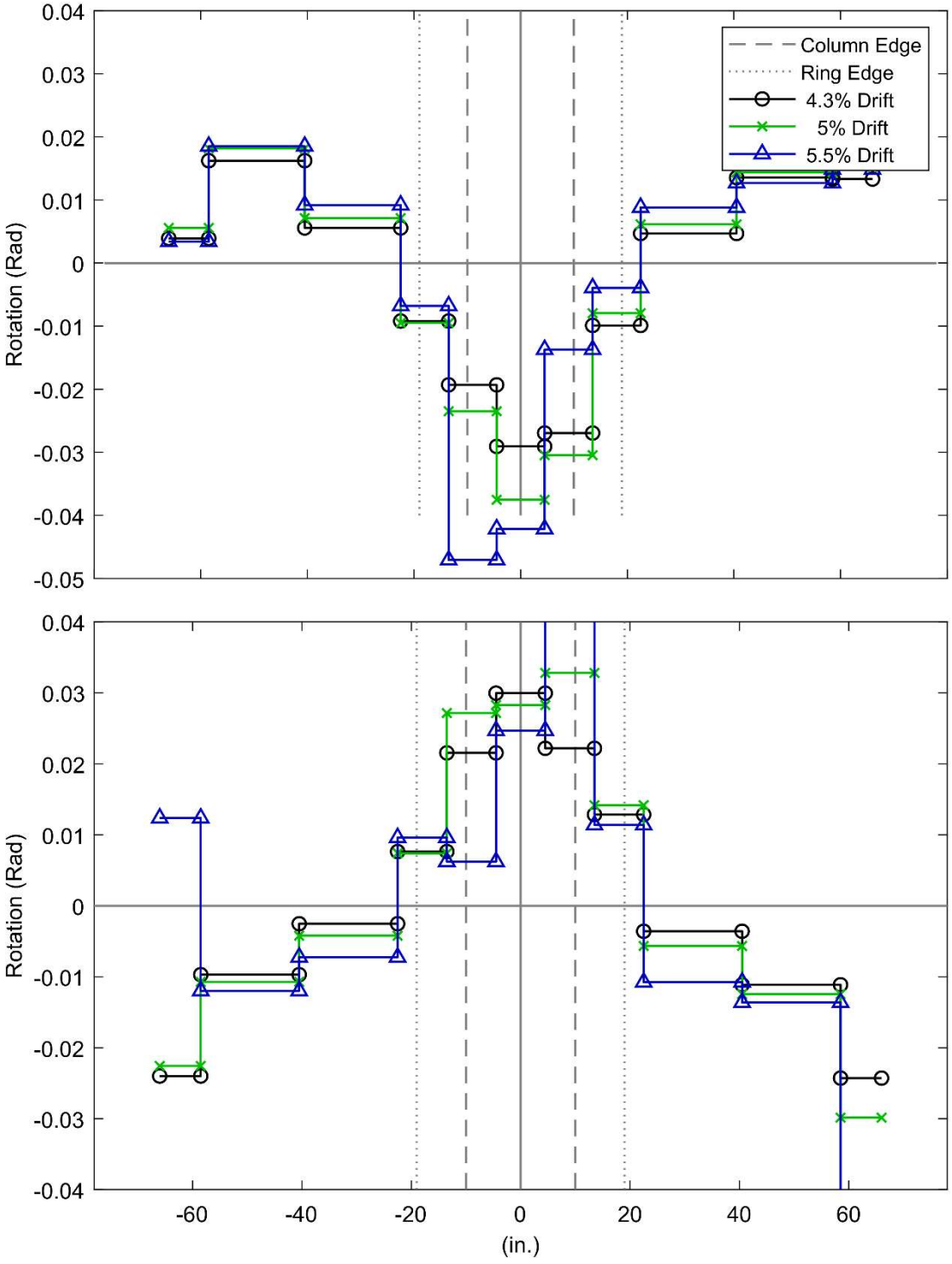

Figure 12. High Drift Cycles Corrected Slab Rotation Profile (PTB_9_2_0_6)

APPENDIX F

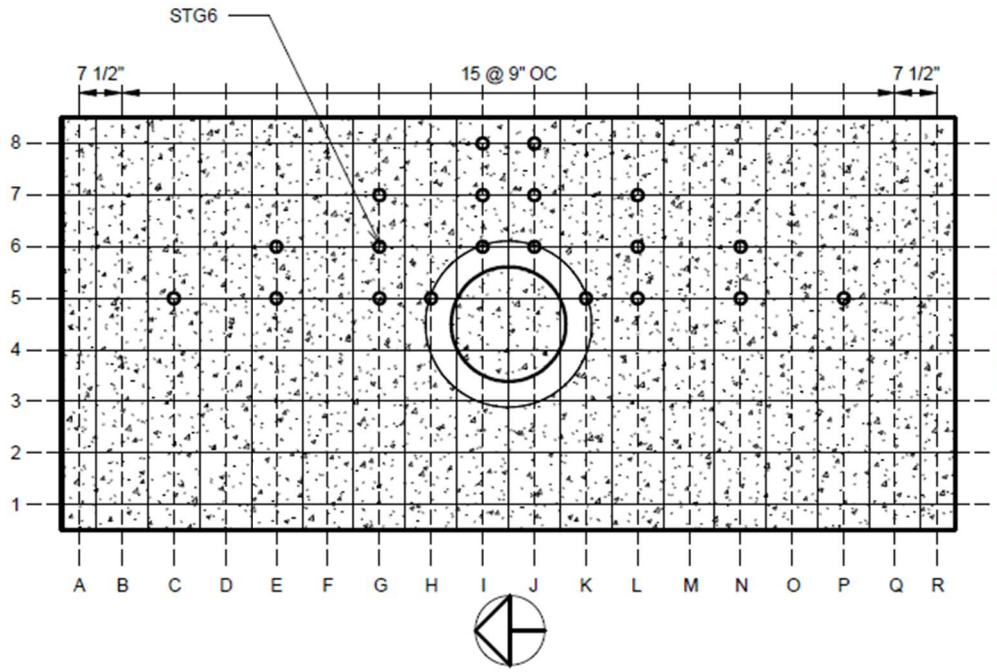

Naming Convention:
1. "S" for Slab
2. "T" for top or "B" for Bottom
3. Column Letter
4. Row Number

Example: STG6 would be a strain gauge on a "Slab" "Top" bar in column "G" in row "6"

1 Slab Strain Gauge Layout
1/2" = 1'-0"

CIVIL & ENVIRONMENTAL ENGINEERING

University of Washington
Department of Civil and Environmental Engineering

NSF Secondary Evacuation Structures

Slab Strain Gauge Layout Top and Bottom

S.13

Naming Convention:
1. "C" for Column
2. Rebar Letter
3. Level Number

Example: CI4 would be a strain gauge on "Column" bar "I" at level 4

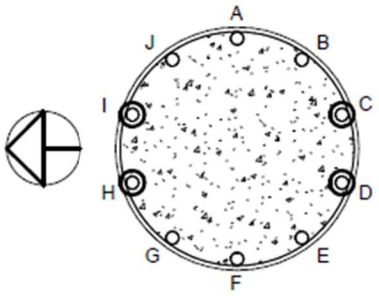

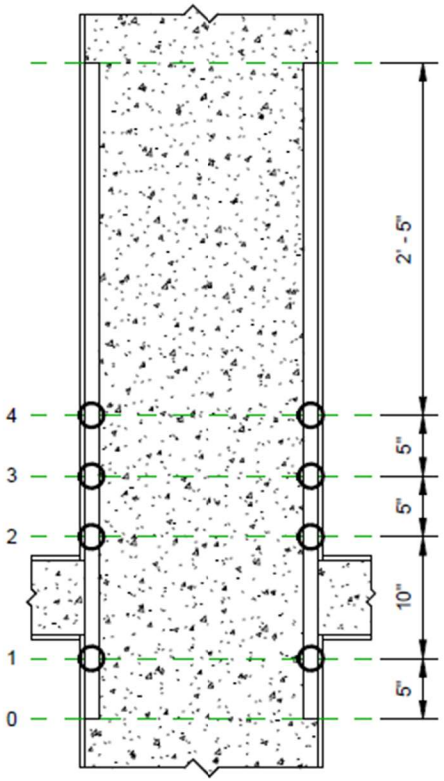

1 Column Strain Gauge Layout
1" = 1'-0"

CIVIL & ENVIRONMENTAL ENGINEERING

University of Washington
Department of Civil and Environmental Engineering

NSF Secondary Evacuation Structures

Column Strain Gauge Layout

S.14

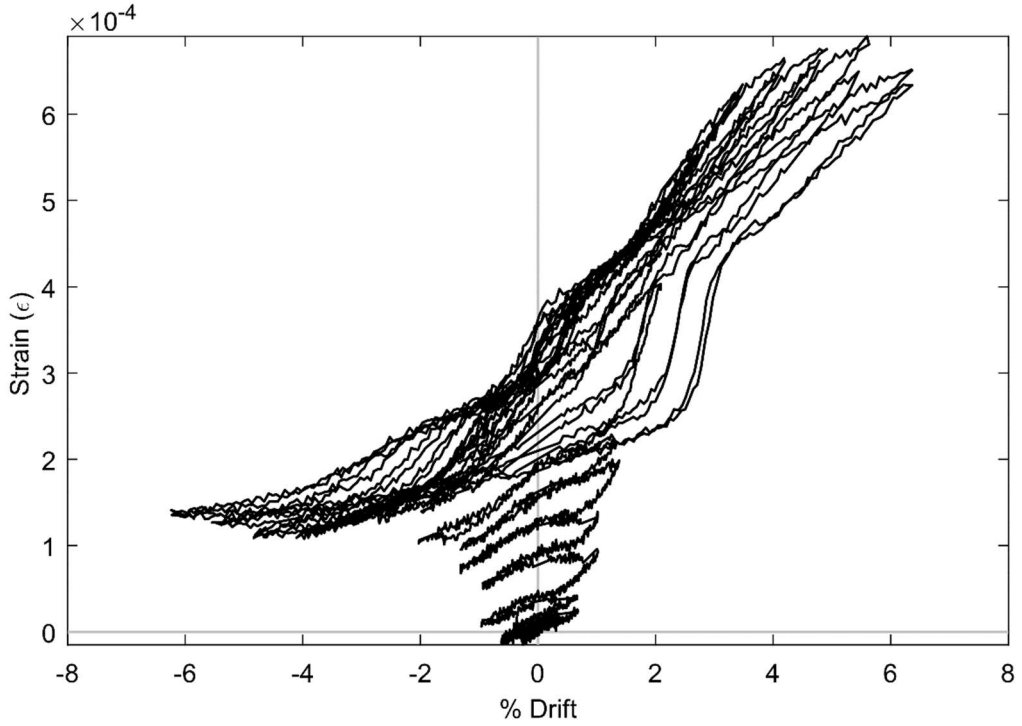

Figure 1. SG STC5 (PTB_4.5_1_0_6)

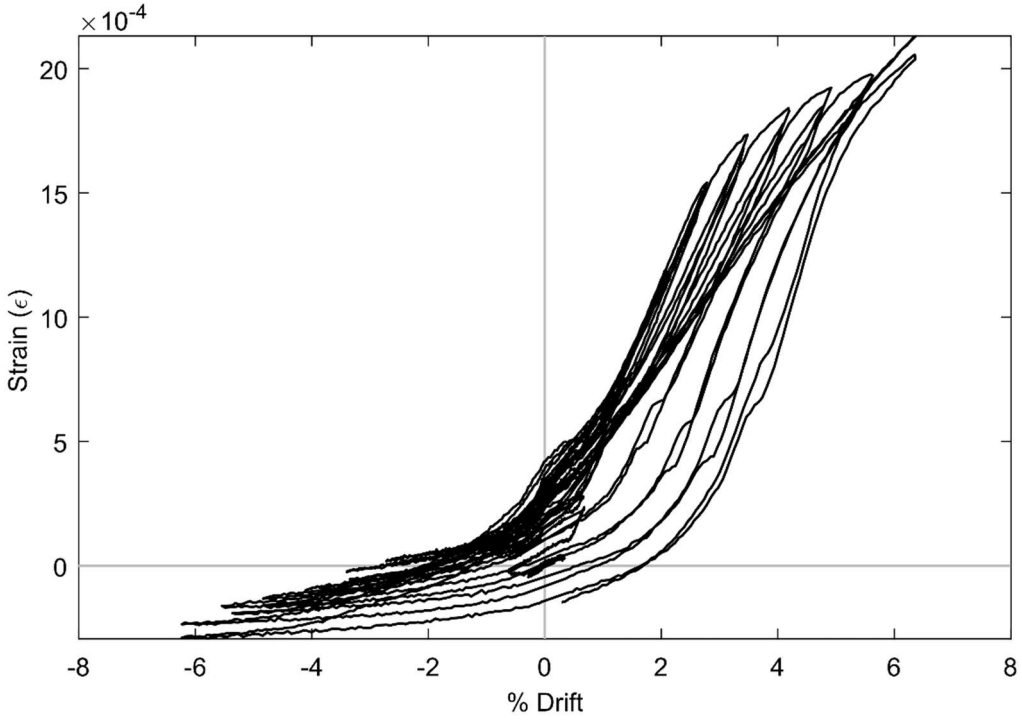

Figure 2. SG STE5 (PTB_4.5_1_0_6)

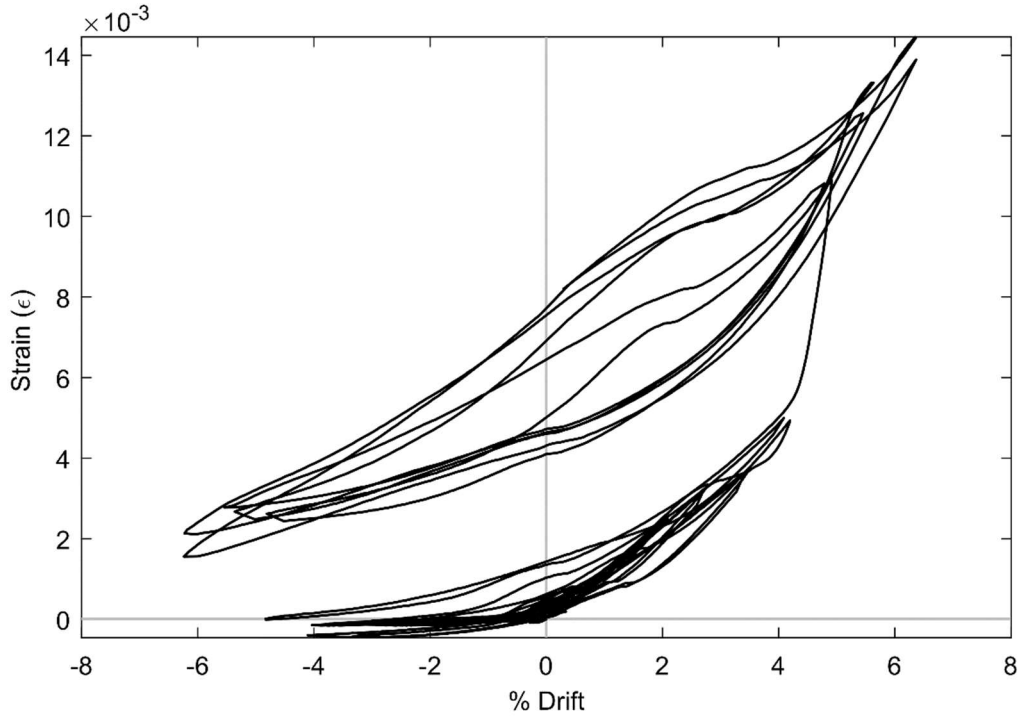

Figure 3. SG STG5 (PTB_4.5_1_0_6)

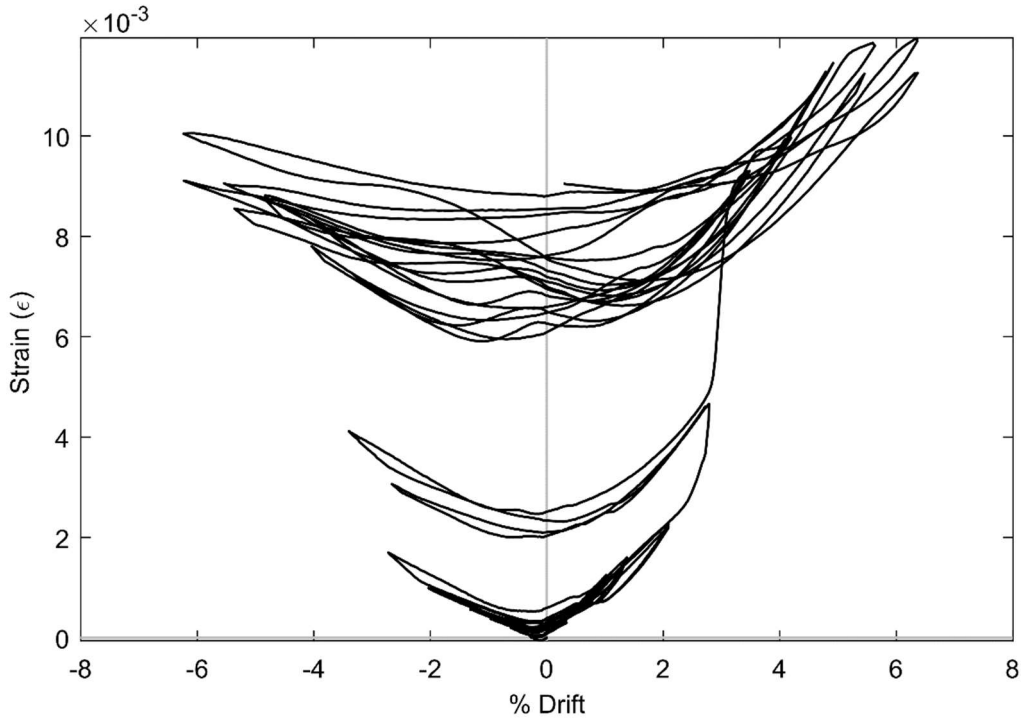

Figure 4. SG STH5 (PTB_4.5_1_0_6)

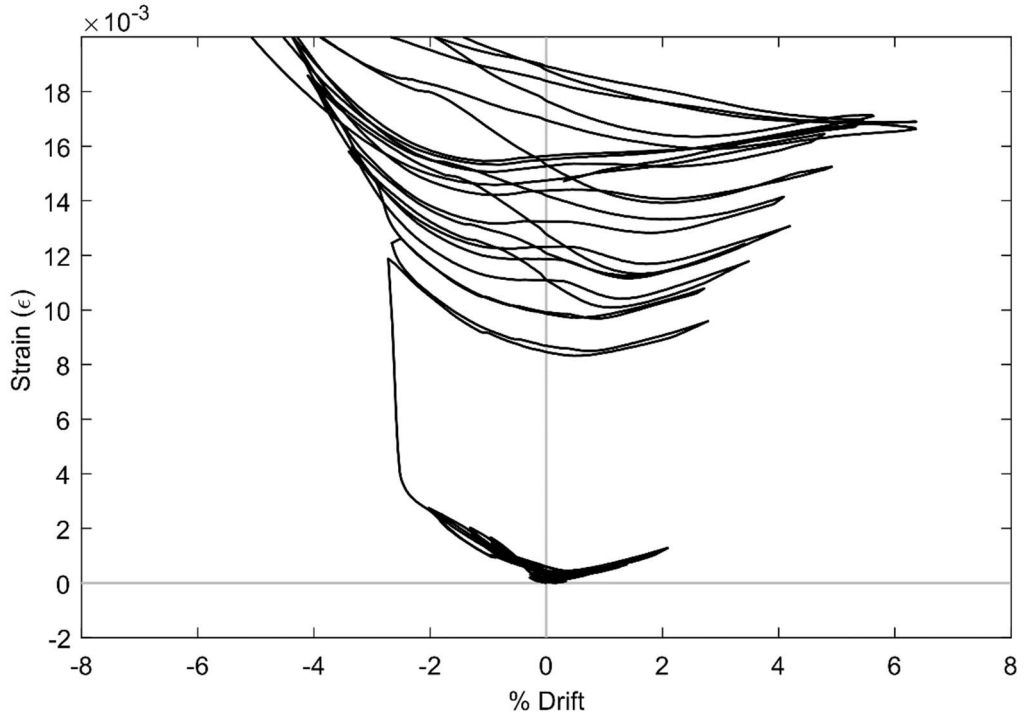

Figure 5. SG STK5 (PTB_4.5_1_0_6)

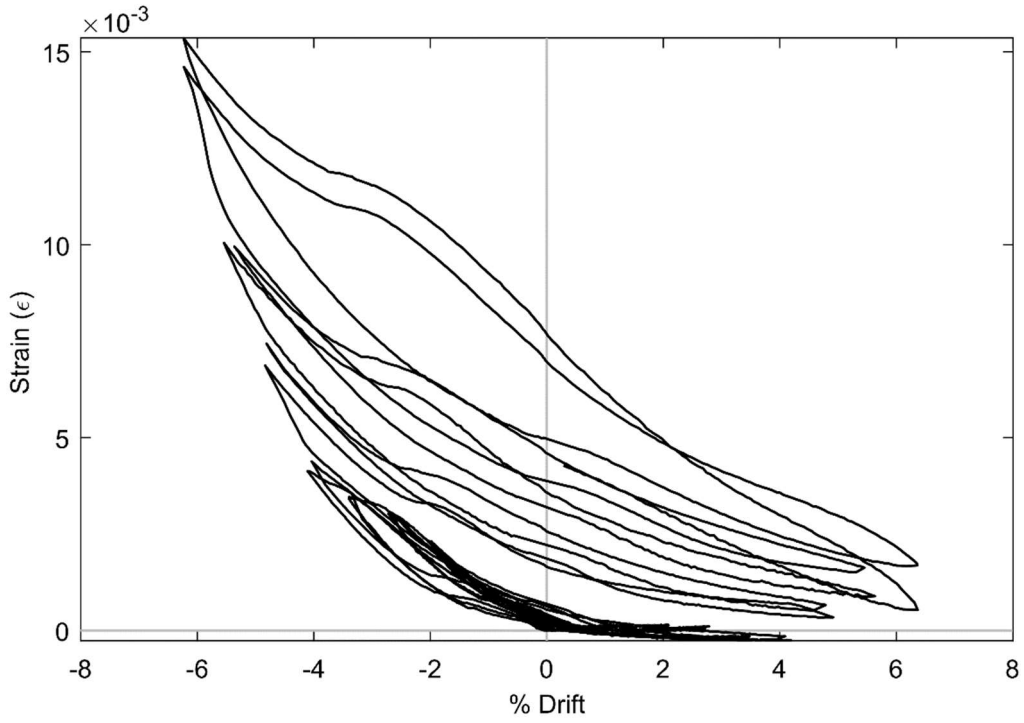

Figure 6. SG STL5 (PTB_4.5_1_0_6)

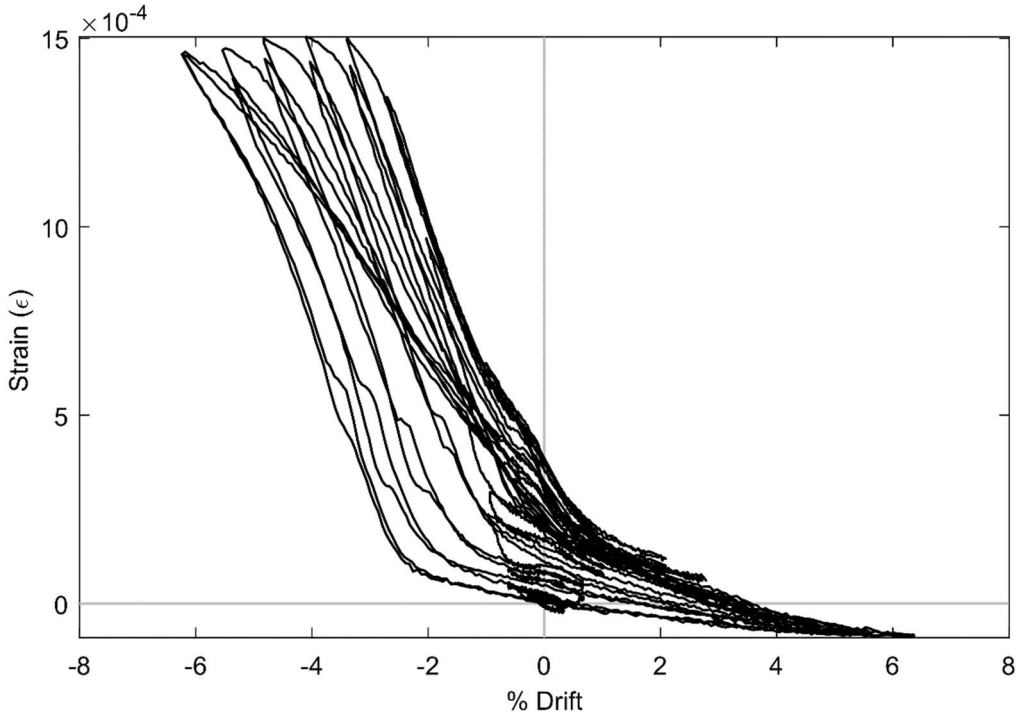

Figure 7. SG STN5 (PTB_4.5_1_0_6)

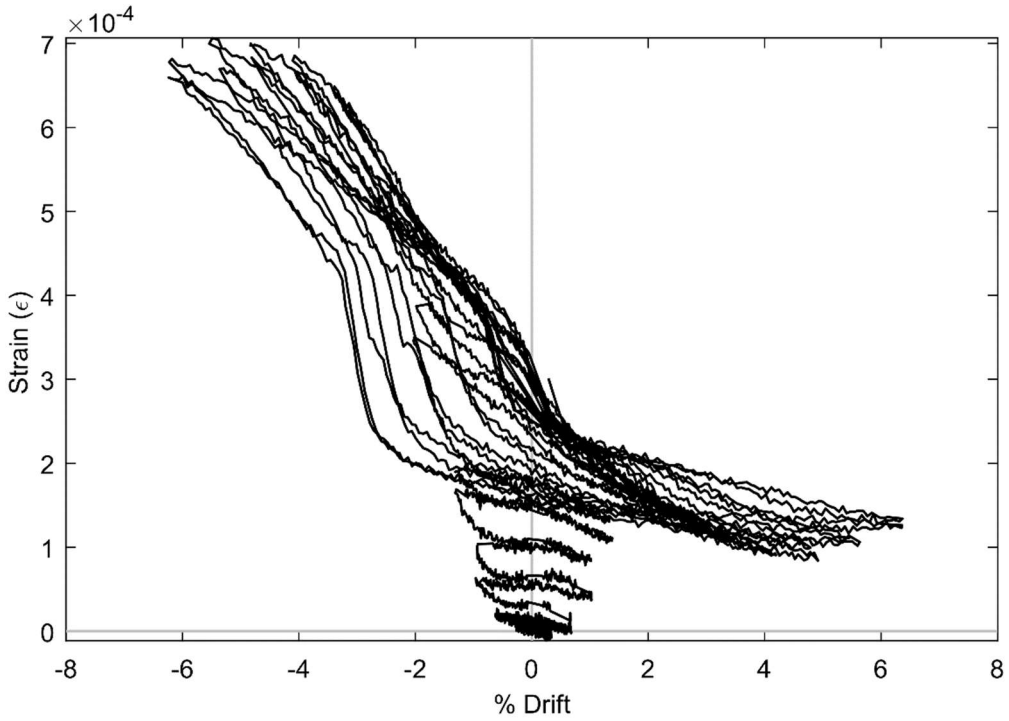

Figure 8. SG STP5 (PTB_4.5_1_0_6)

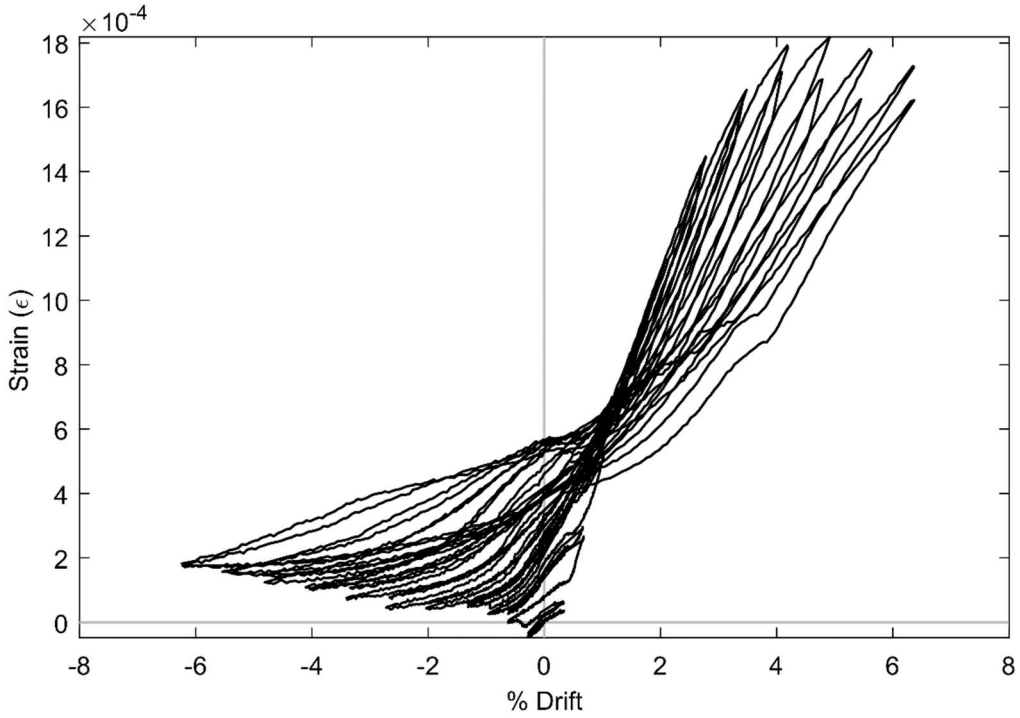

Figure 9. SG STE6 (PTB_4.5_1_0_6)

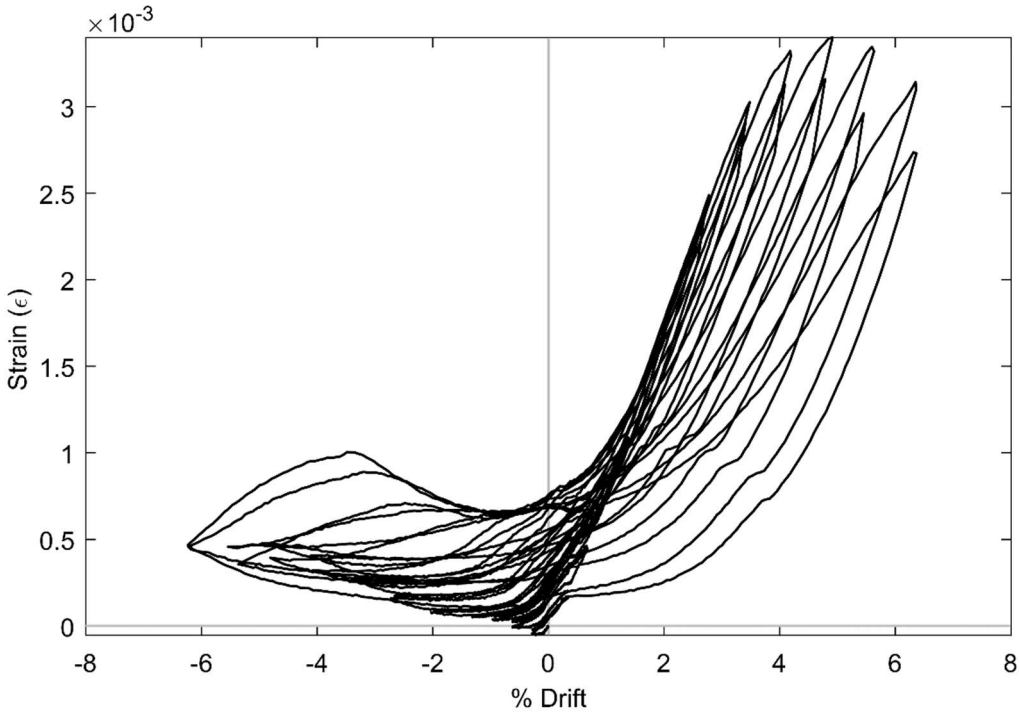

Figure 10. SG STG6 (PTB_4.5_1_0_6)

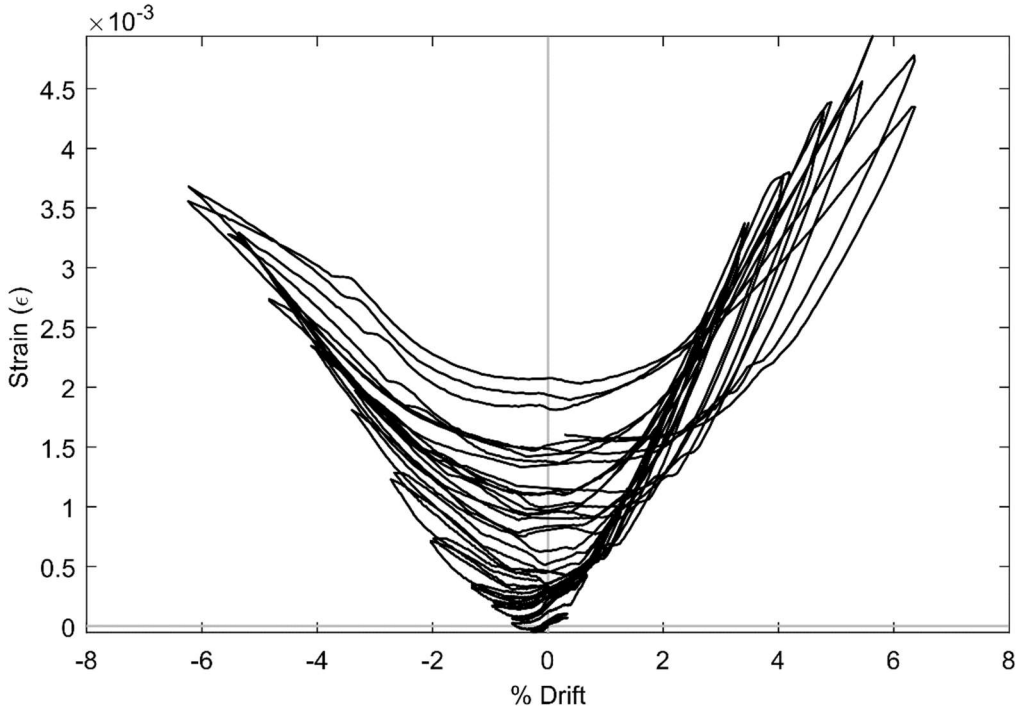

Figure 11. SG STI6 (PTB_4.5_1_0_6)

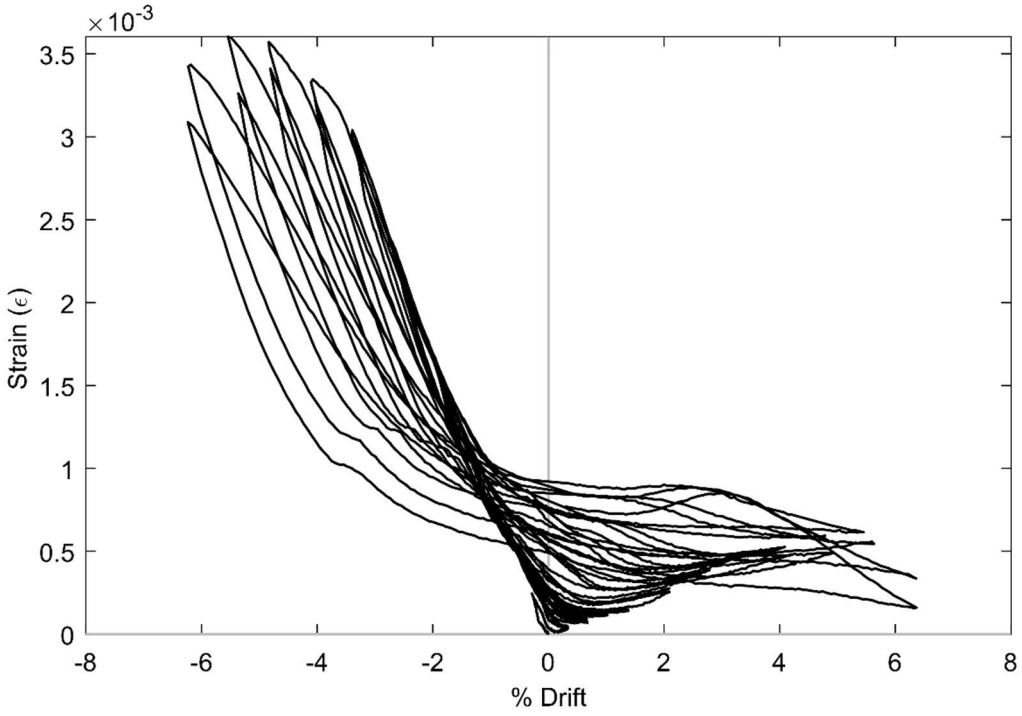

Figure 12. SG STL6 (PTB_4.5_1_0_6)

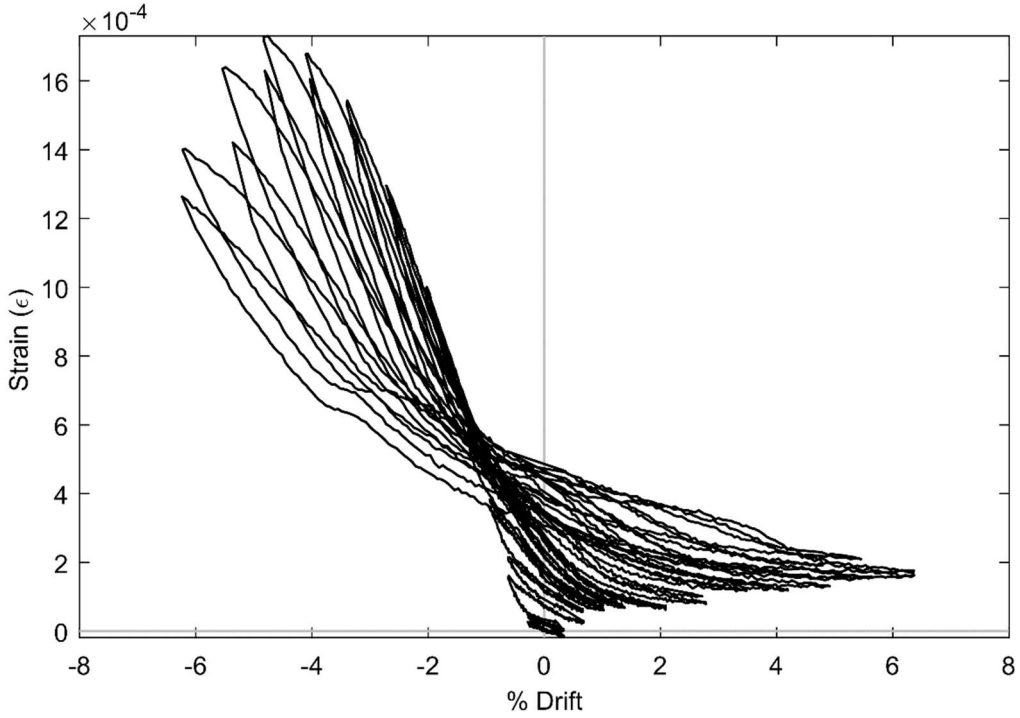

Figure 13. SG STN6 (PTB_4.5_1_0_6)

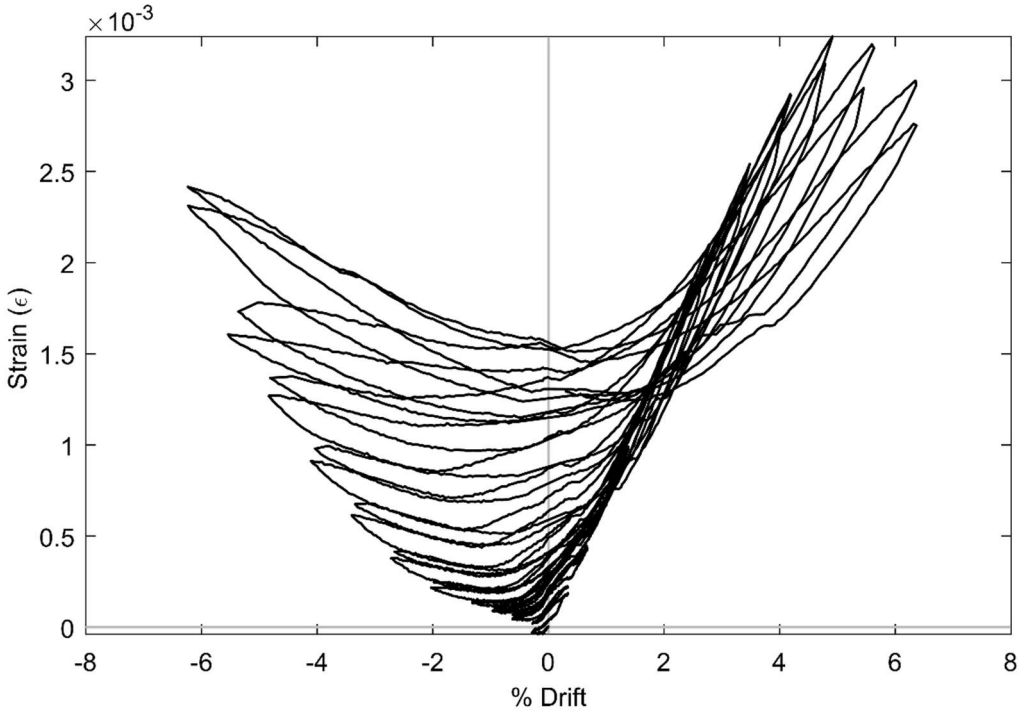

Figure 14. SG STG7 (PTB_4.5_1_0_6)

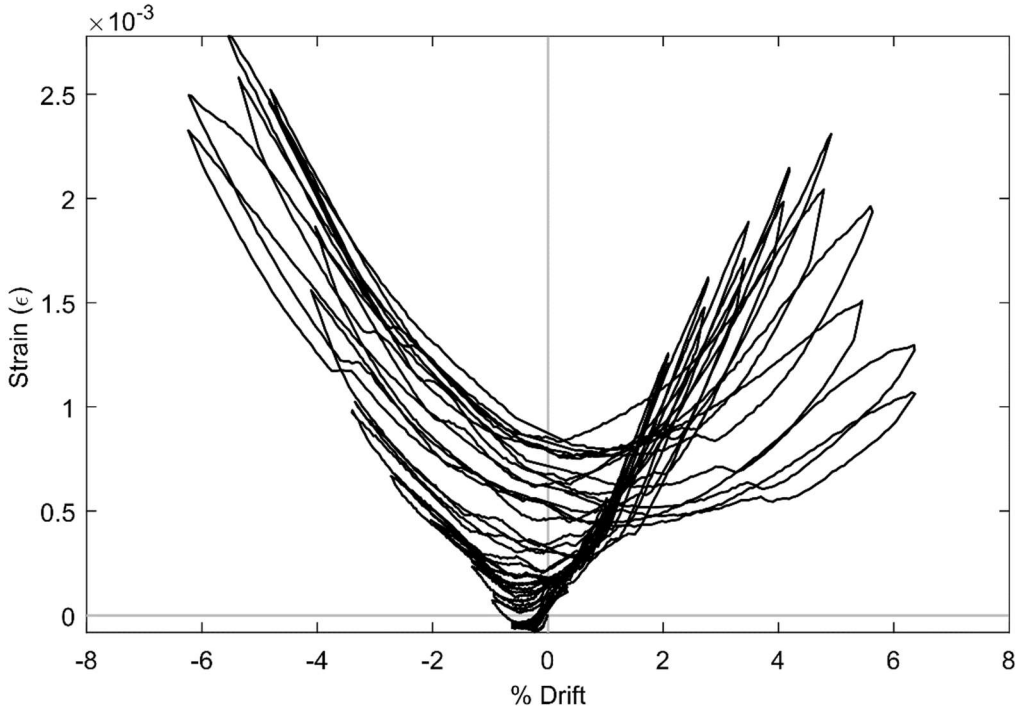

Figure 15. SG STI7 (PTB_4.5_1_0_6)

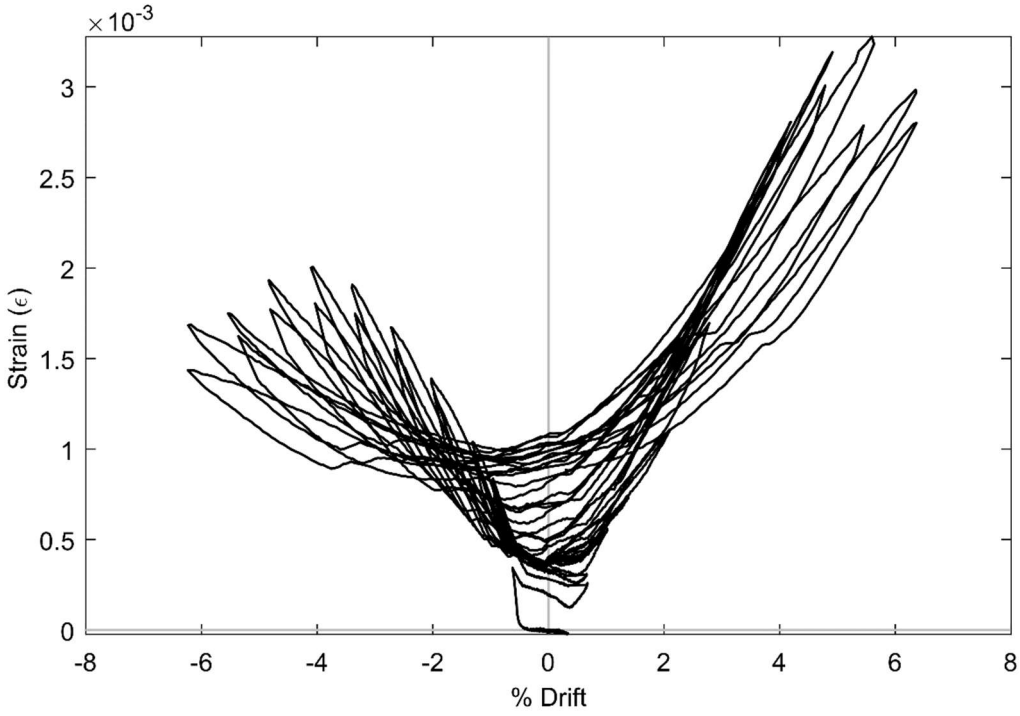

Figure 16. SG STJ7 (PTB_4.5_1_0_6)

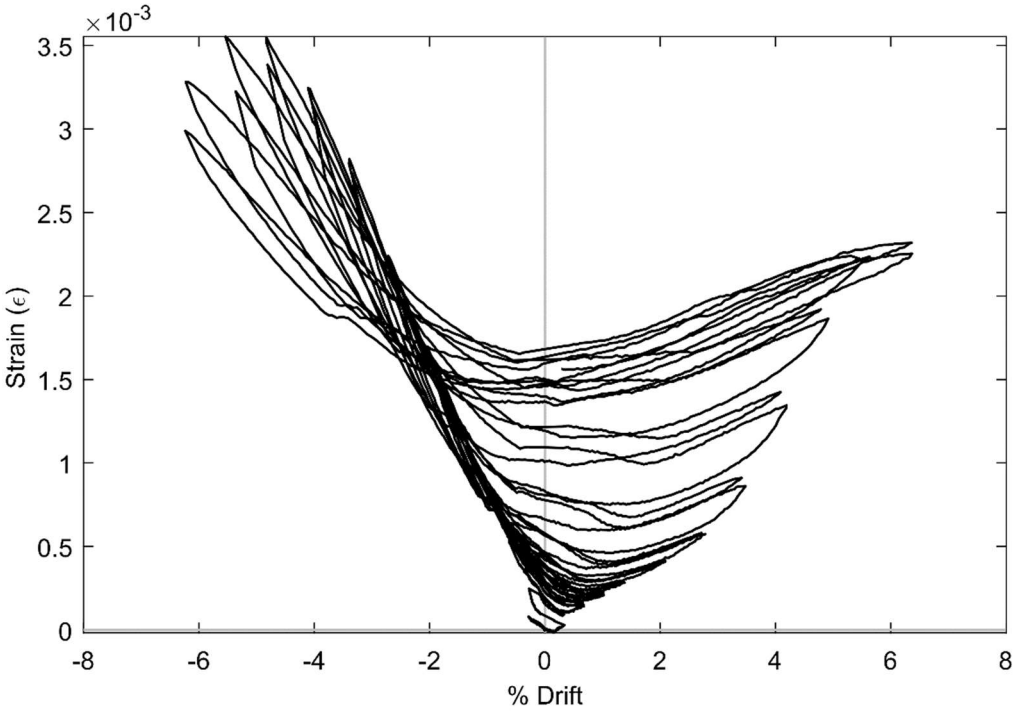

Figure 17. SG STL7 (PTB_4.5_1_0_6)

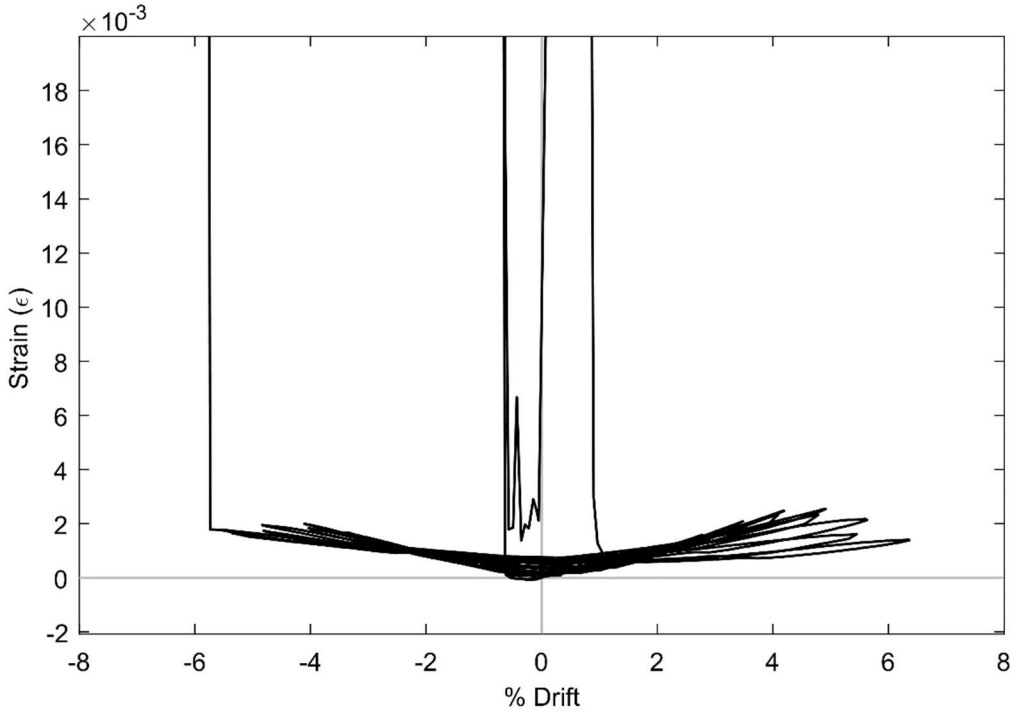

Figure 18. SG STI8 (PTB_4.5_1_0_6)

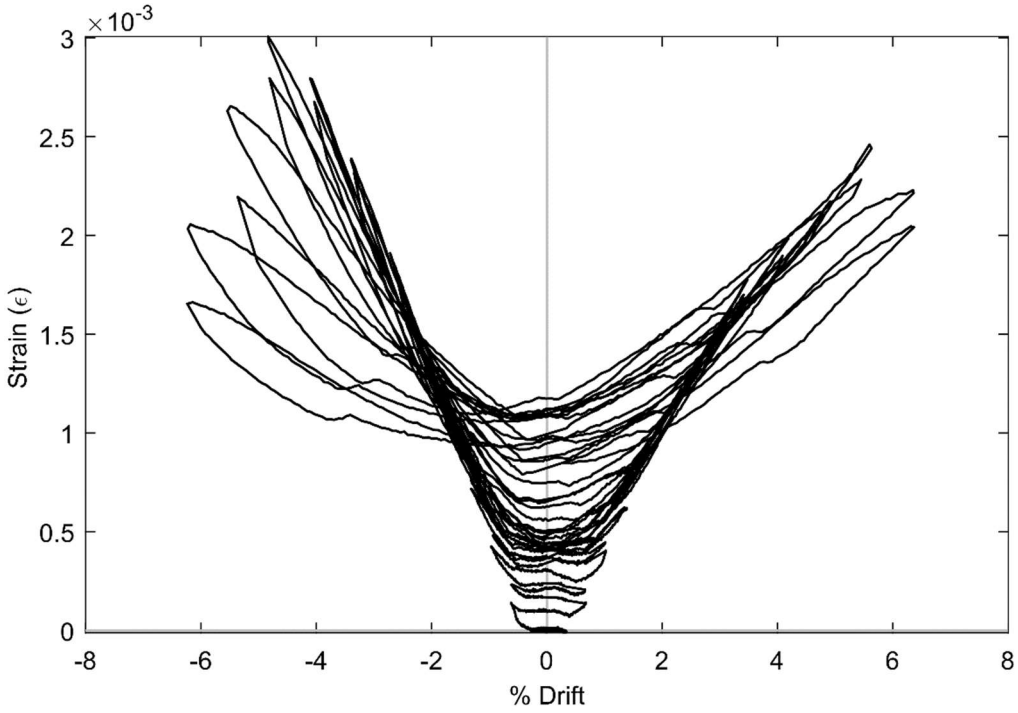

Figure 19. SG STJ8 (PTB_4.5_1_0_6)

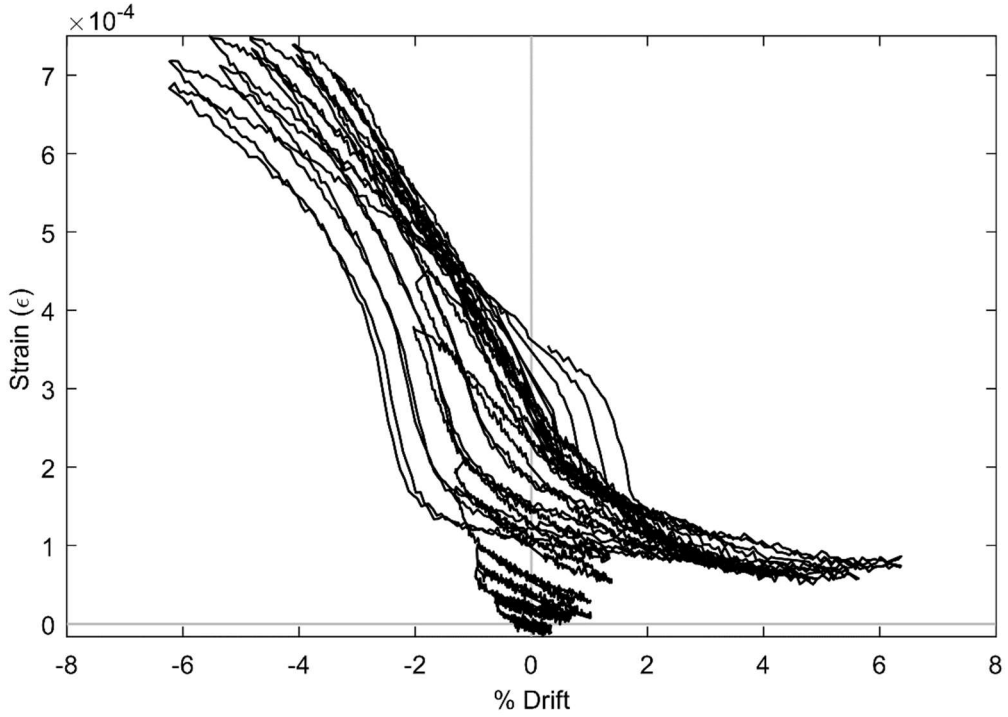

Figure 20. SG SBC5 (PTB_4.5_1_0_6)

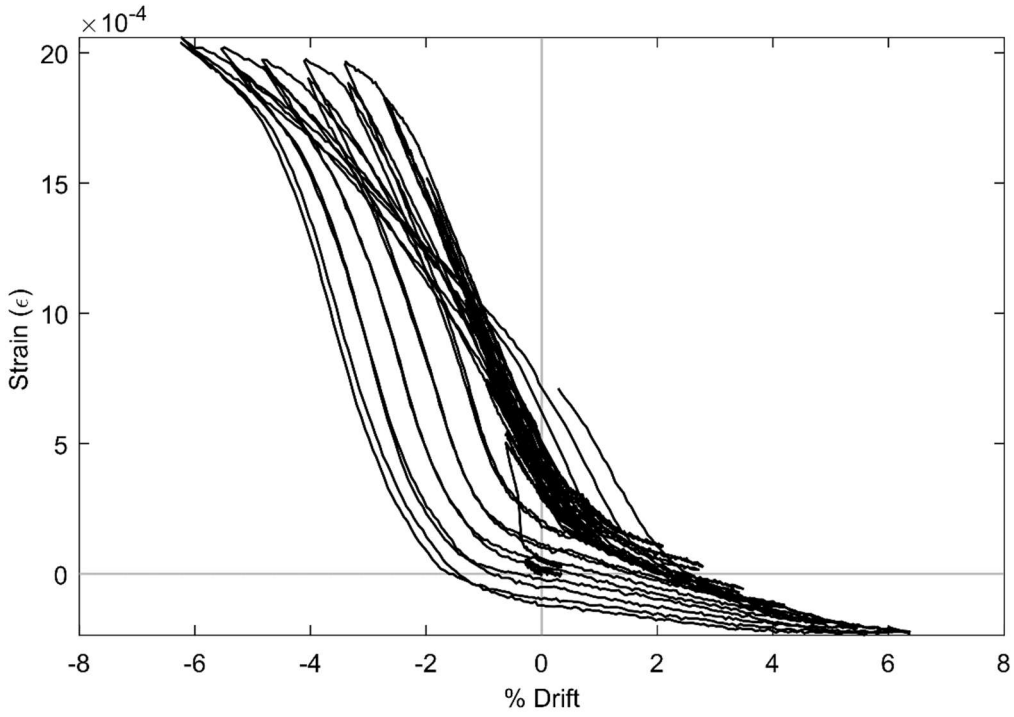

Figure 21. SG SBE5 (PTB_4.5_1_0_6)

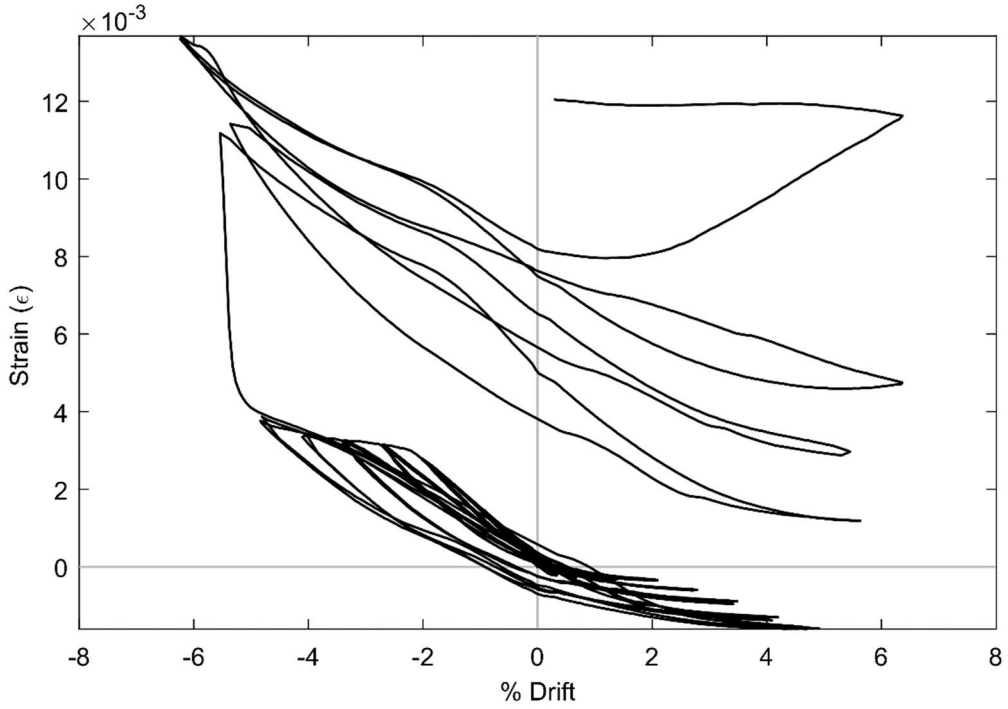

Figure 22. SG SBG5 (PTB_4.5_1_0_6)

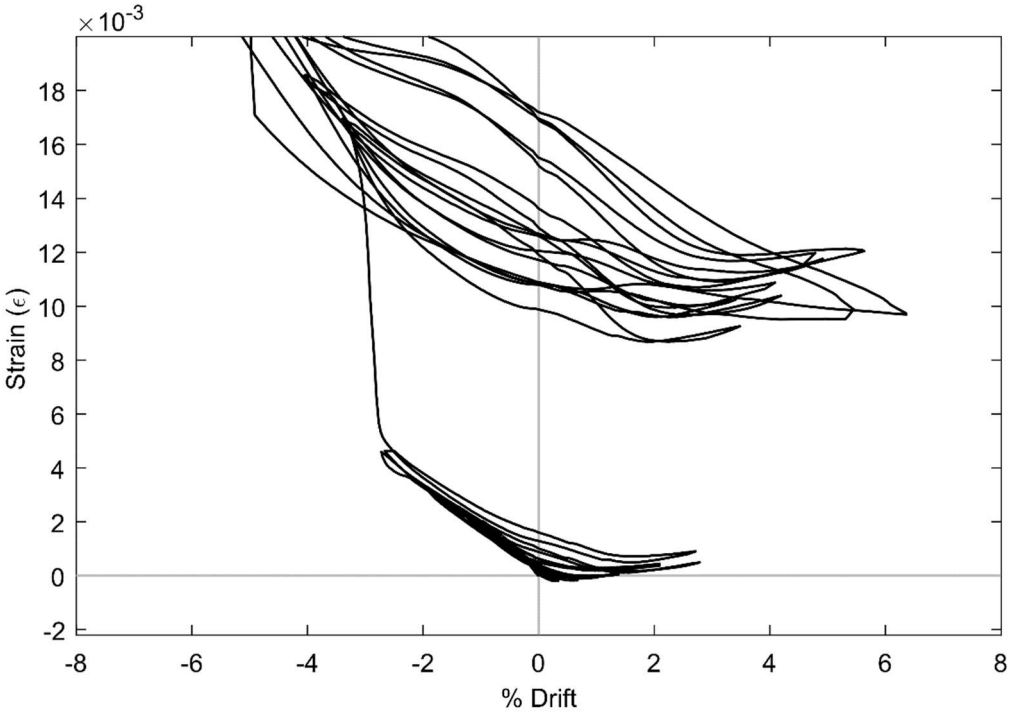

Figure 23. SG SBH5 (PTB_4.5_1_0_6)

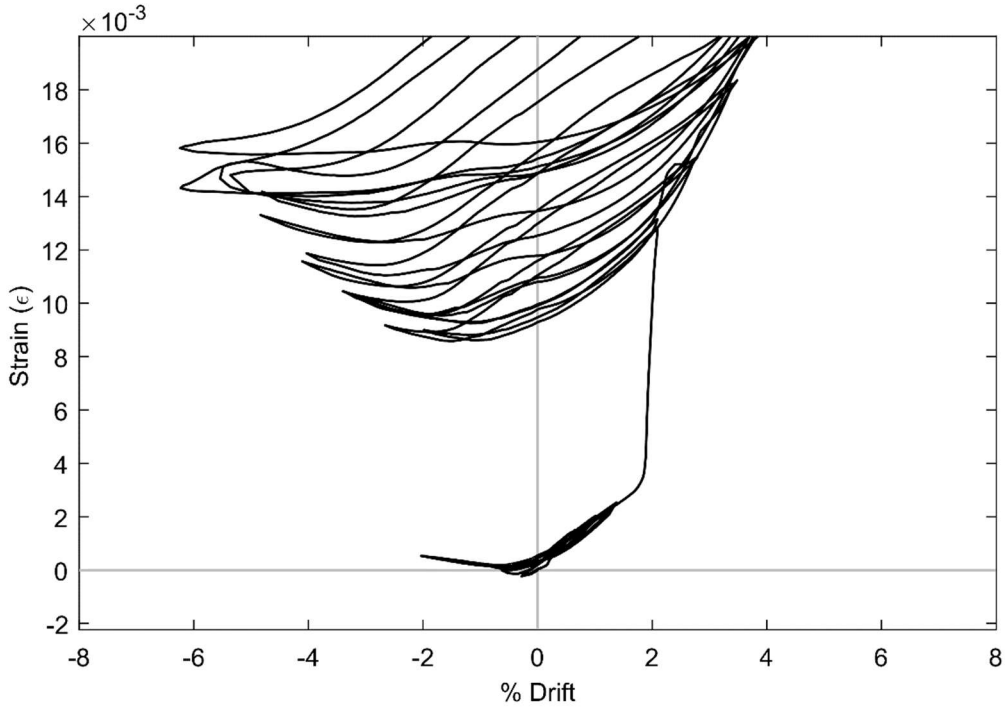

Figure 24. SG SBK5 (PTB_4.5_1_0_6)

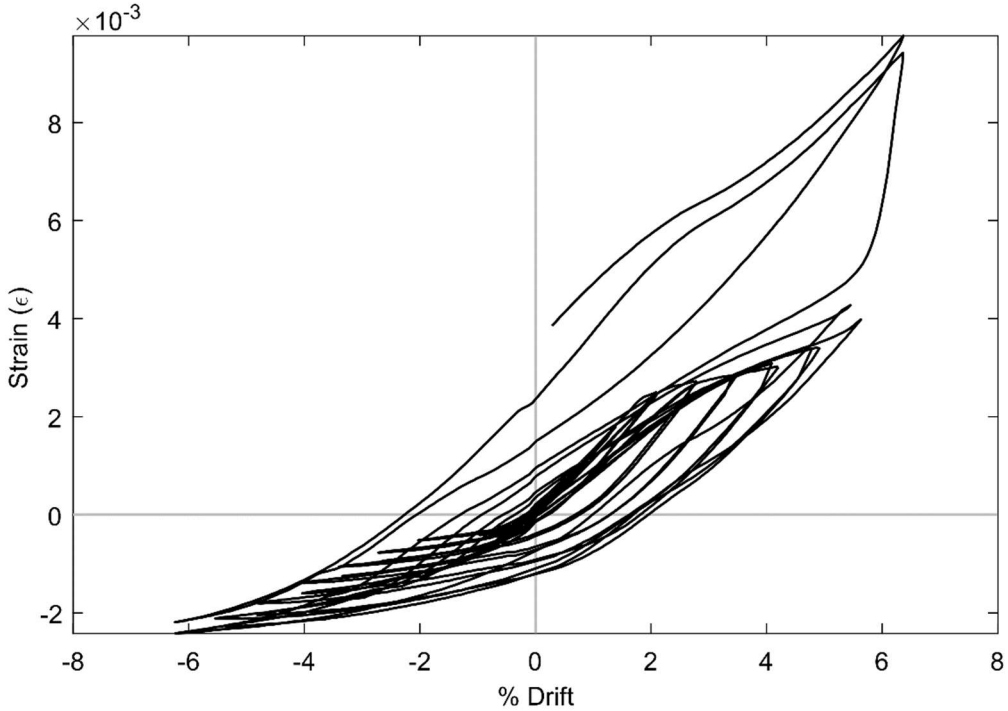

Figure 25. SG SBL5 (PTB_4.5_1_0_6)

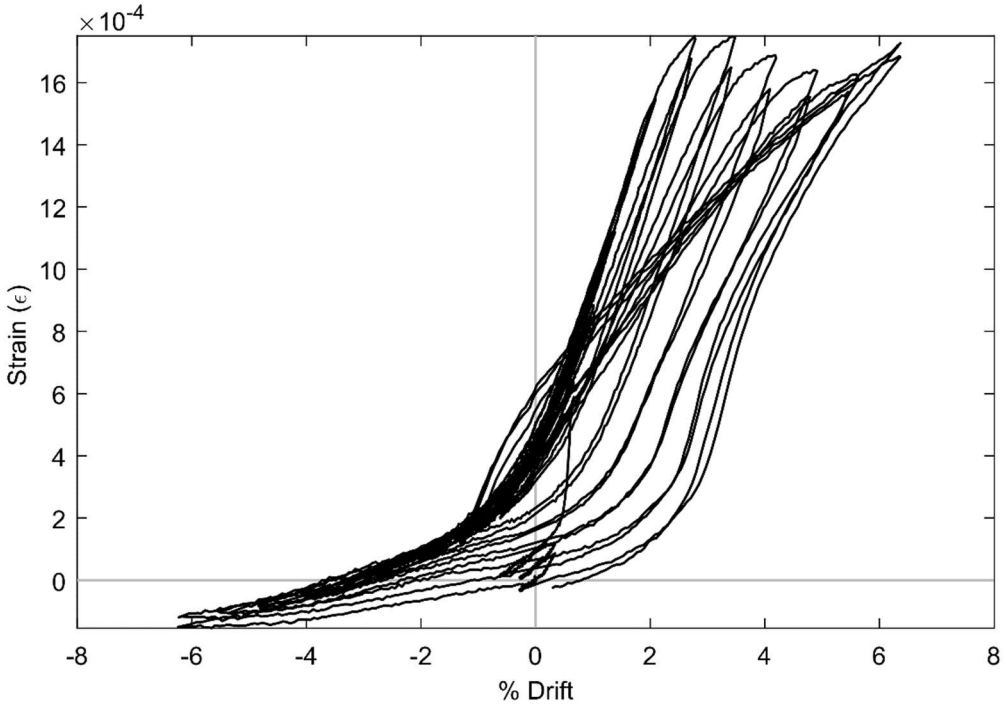

Figure 26. SG SBN5 (PTB_4.5_1_0_6)

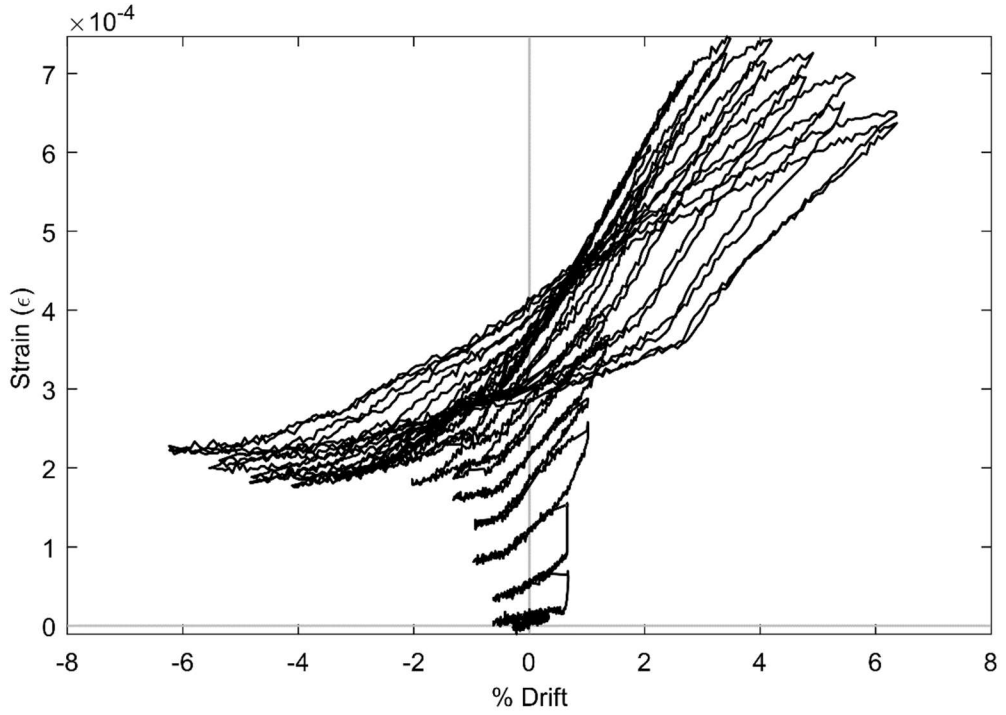

Figure 27. SG SBP5 (PTB_4.5_1_0_6)

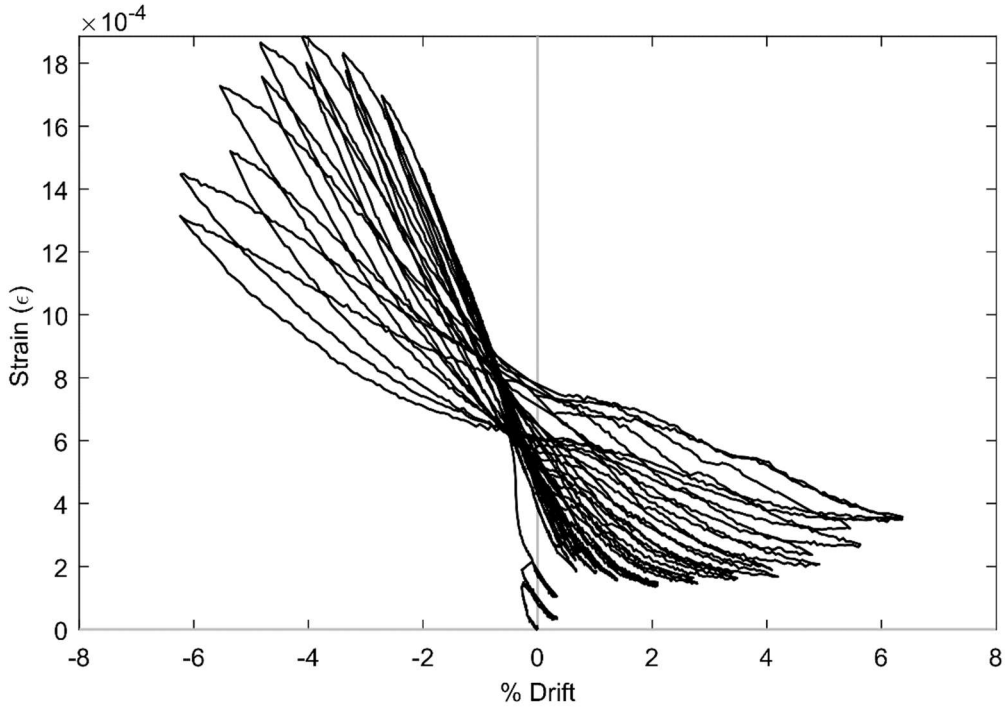

Figure 28. SG SBE6 (PTB_4.5_1_0_6)

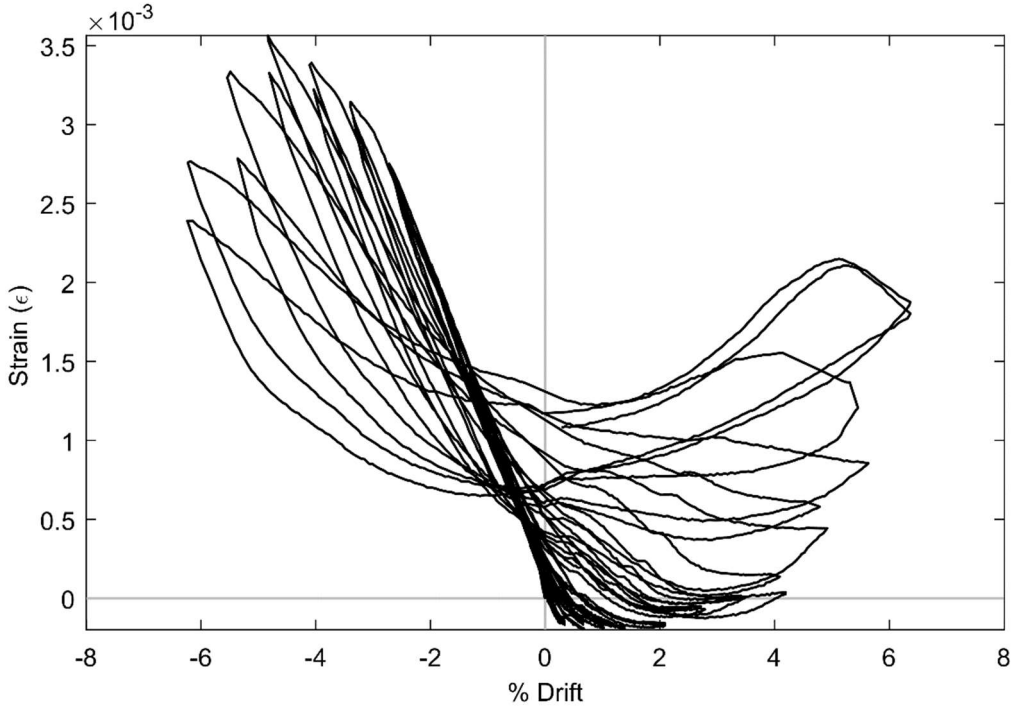

Figure 29. SG SBG6 (PTB_4.5_1_0_6)

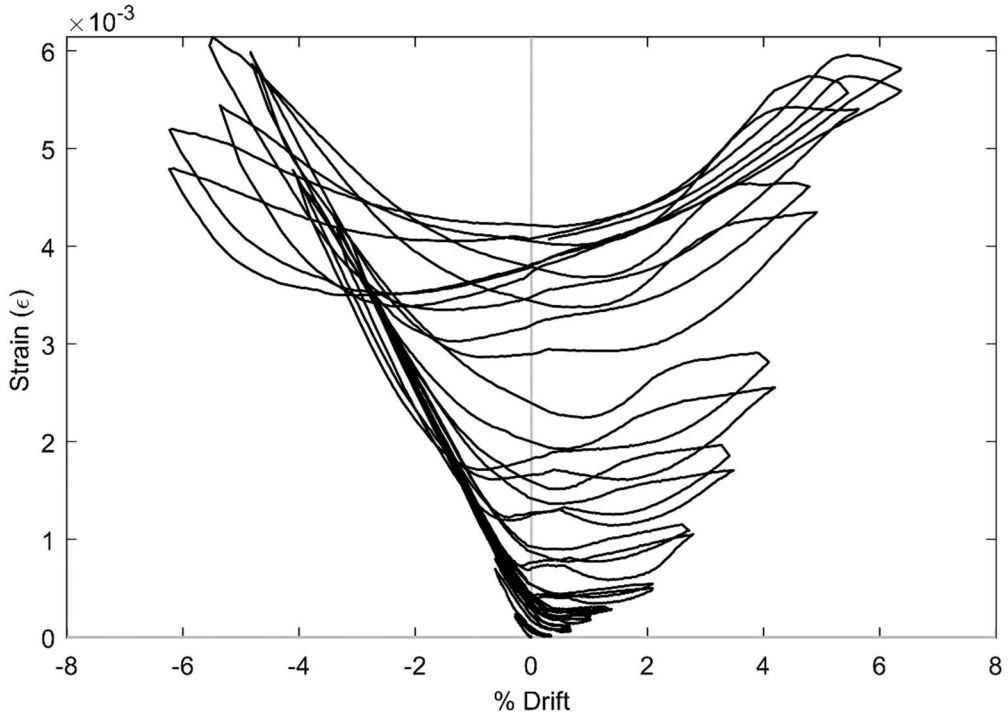

Figure 30. SG SBI6 (PTB_4.5_1_0_6)

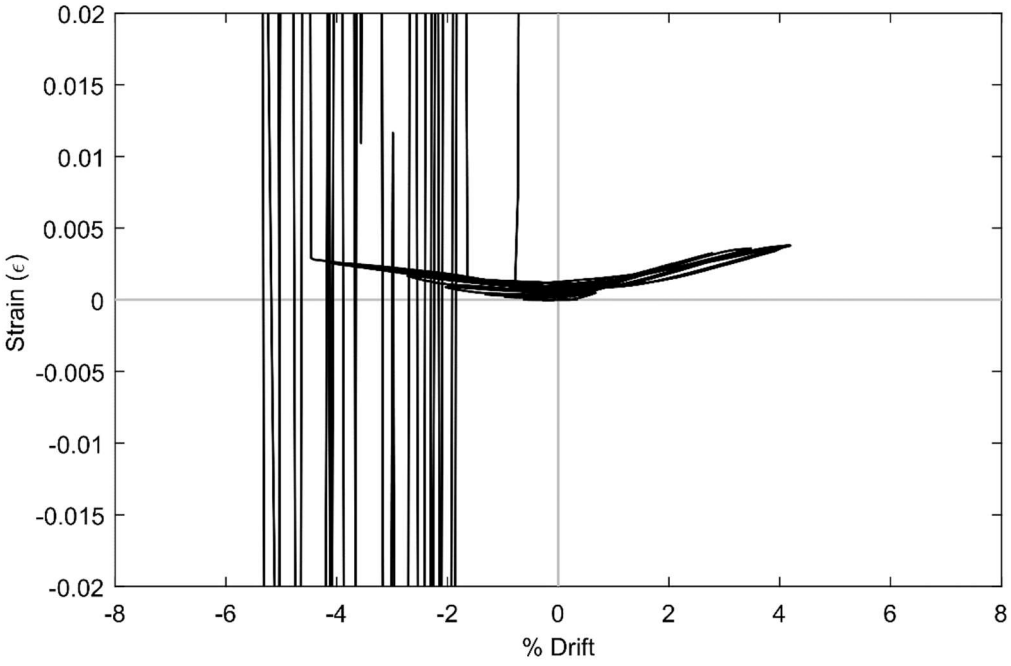

Figure 31. SG SBJ6 (PTB_4.5_1_0_6)

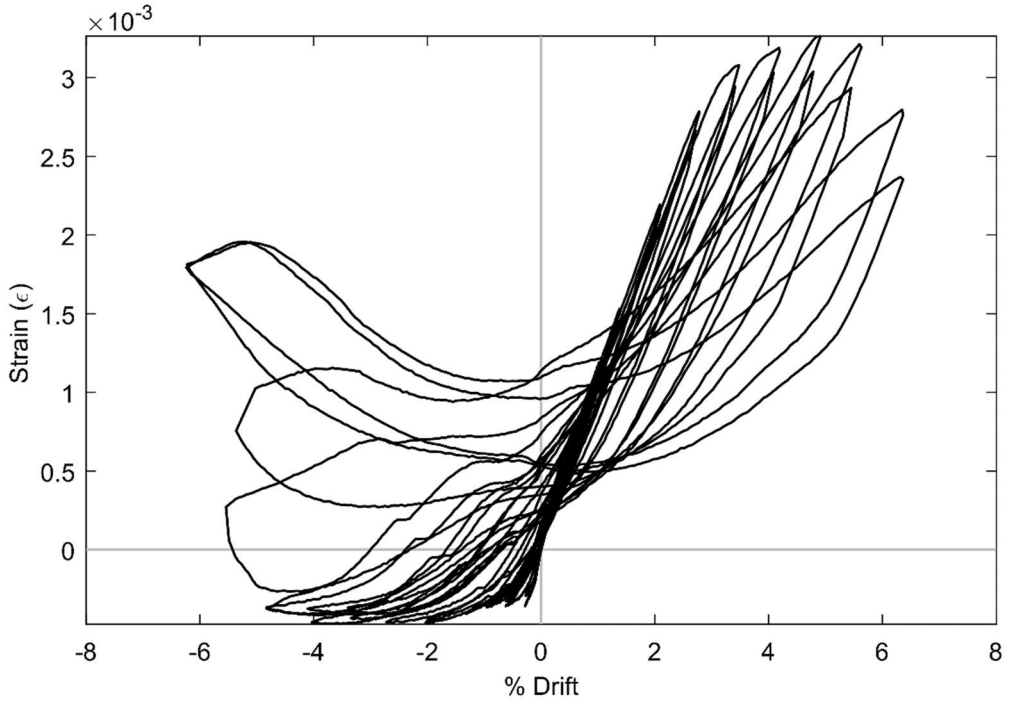

Figure 32. SG SBL6 (PTB_4.5_1_0_6)

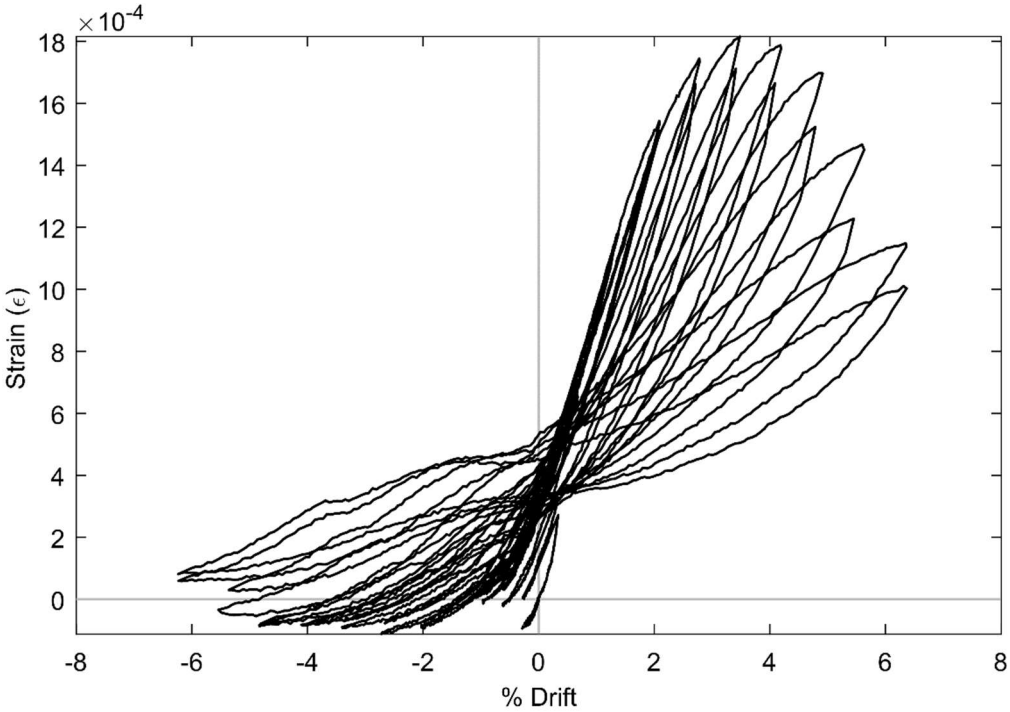

Figure 33. SG SBN6 (PTB_4.5_1_0_6)

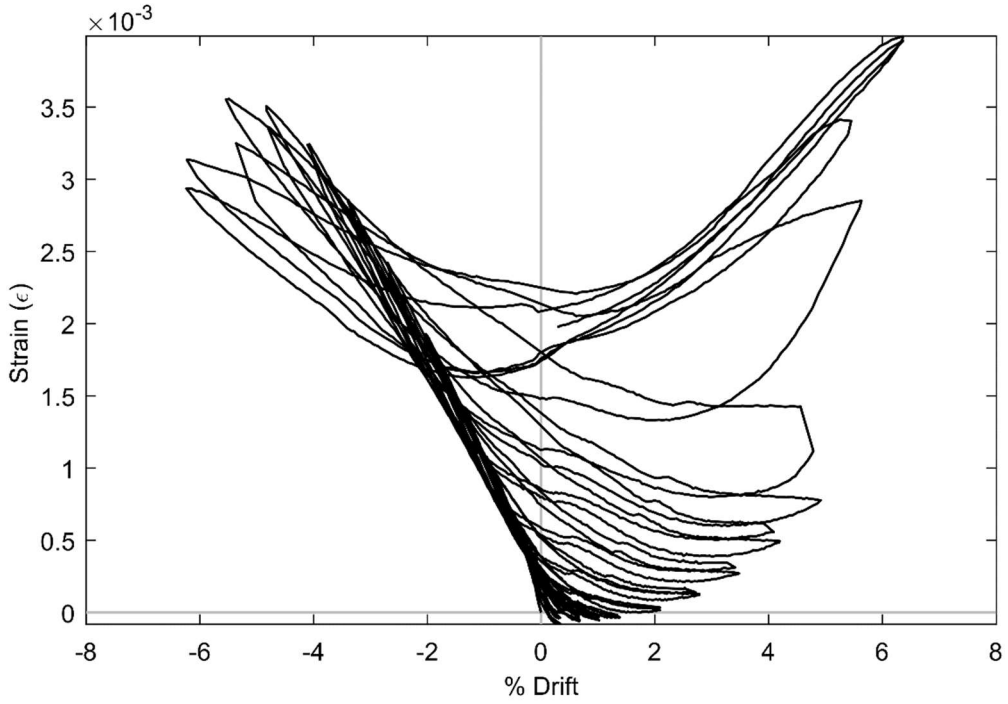

Figure 34. SG SBG7 (PTB_4.5_1_0_6)

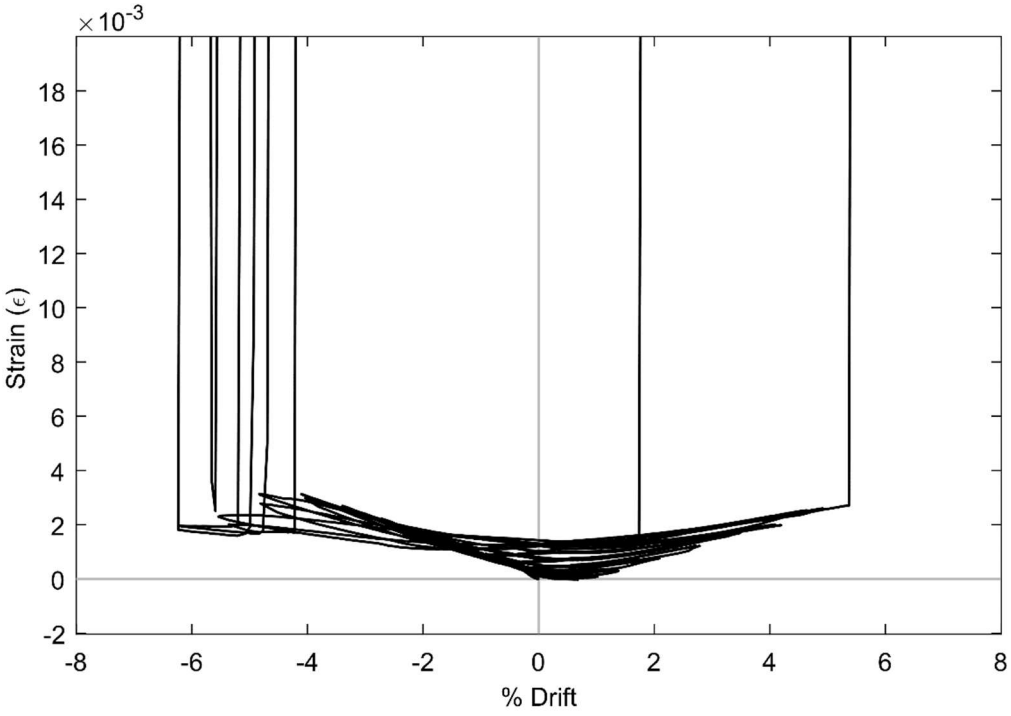

Figure 35. SG SBI7 (PTB_4.5_1_0_6)

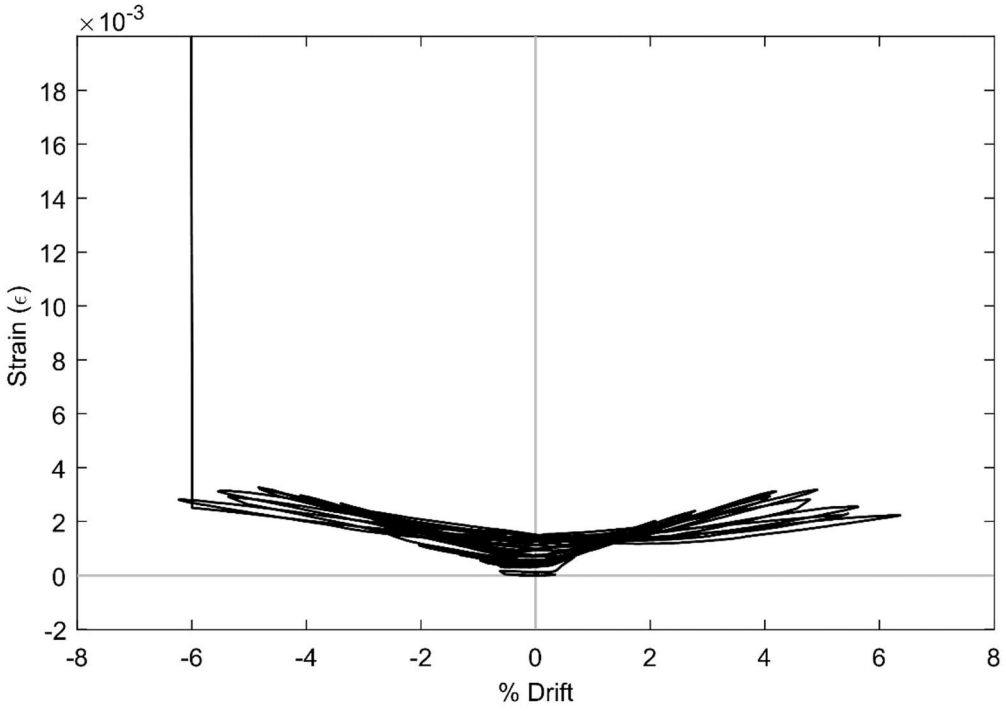

Figure 36. SG SBJ7 (PTB_4.5_1_0_6)

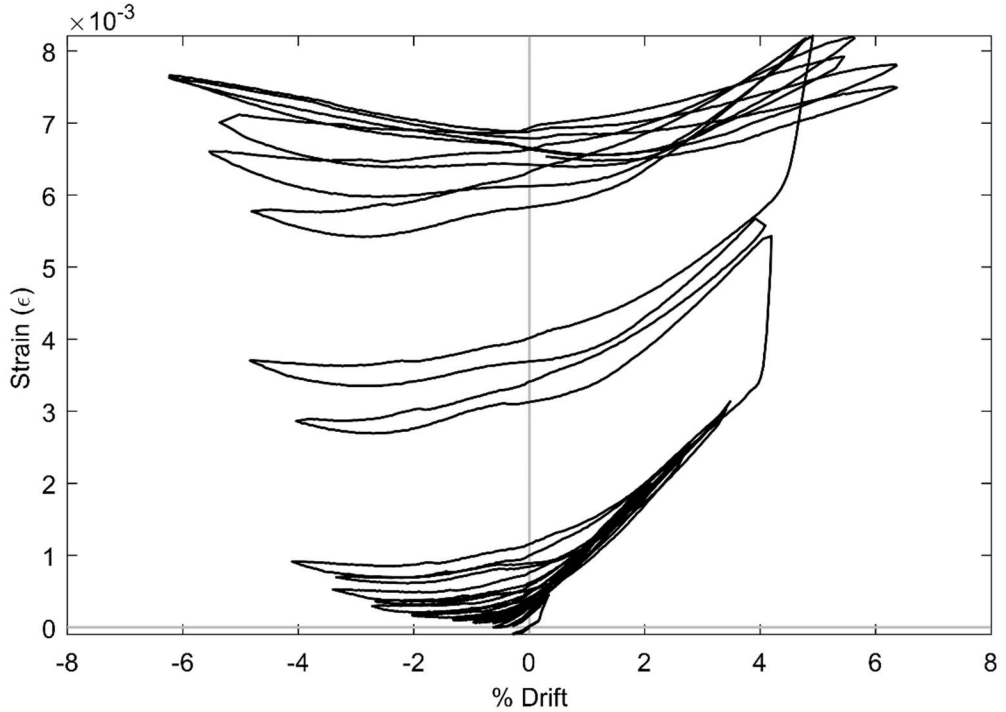

Figure 37. SG SBL7 (PTB_4.5_1_0_6)

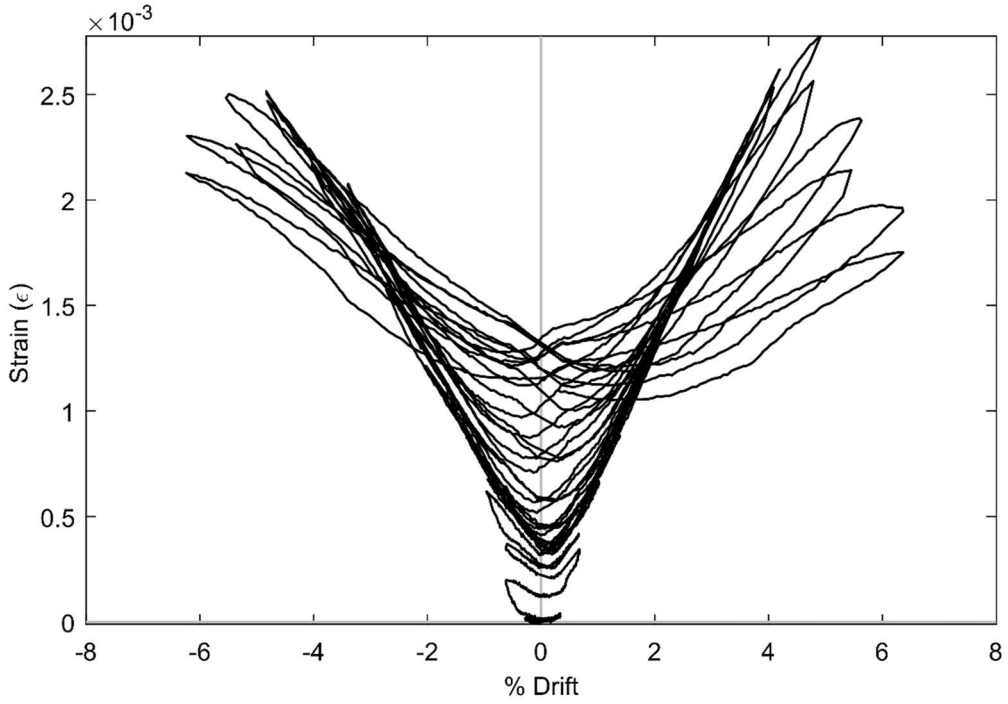

Figure 38. SG SBJ8 (PTB_4.5_1_0_6)

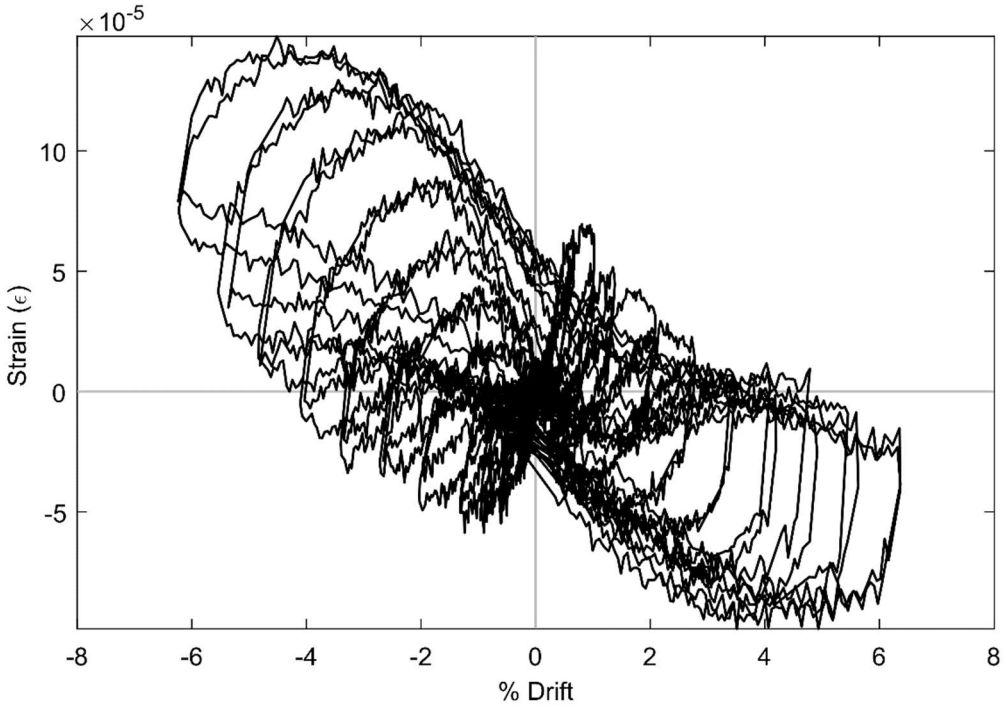

Figure 39. SG CC1 (PTB_4.5_1_0_6)

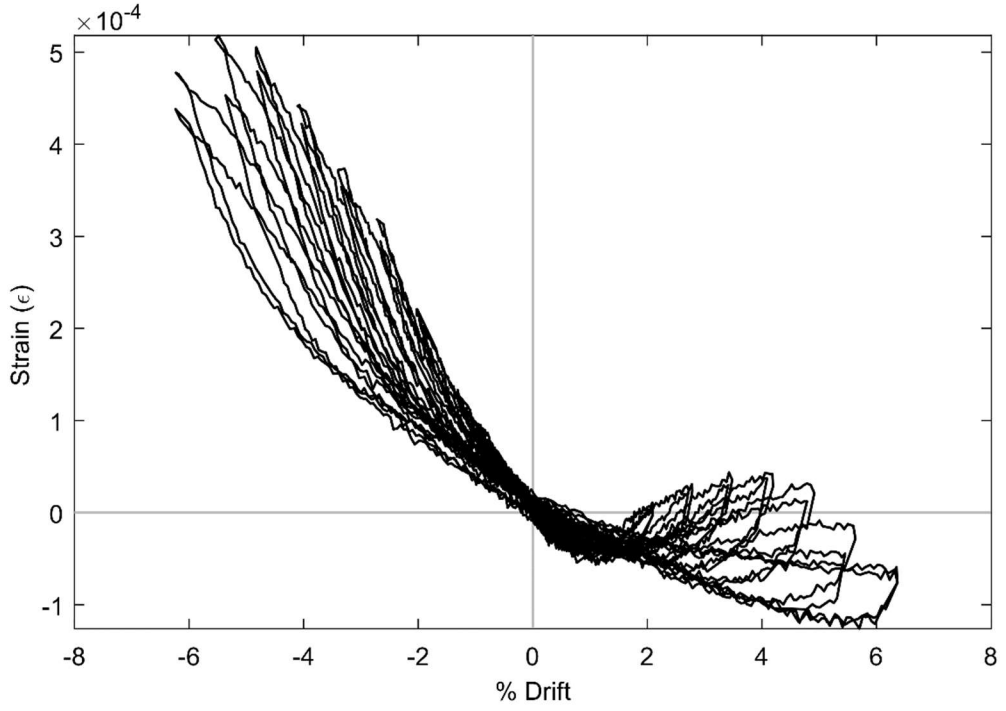

Figure 40. SG CC2 (PTB_4.5_1_0_6)

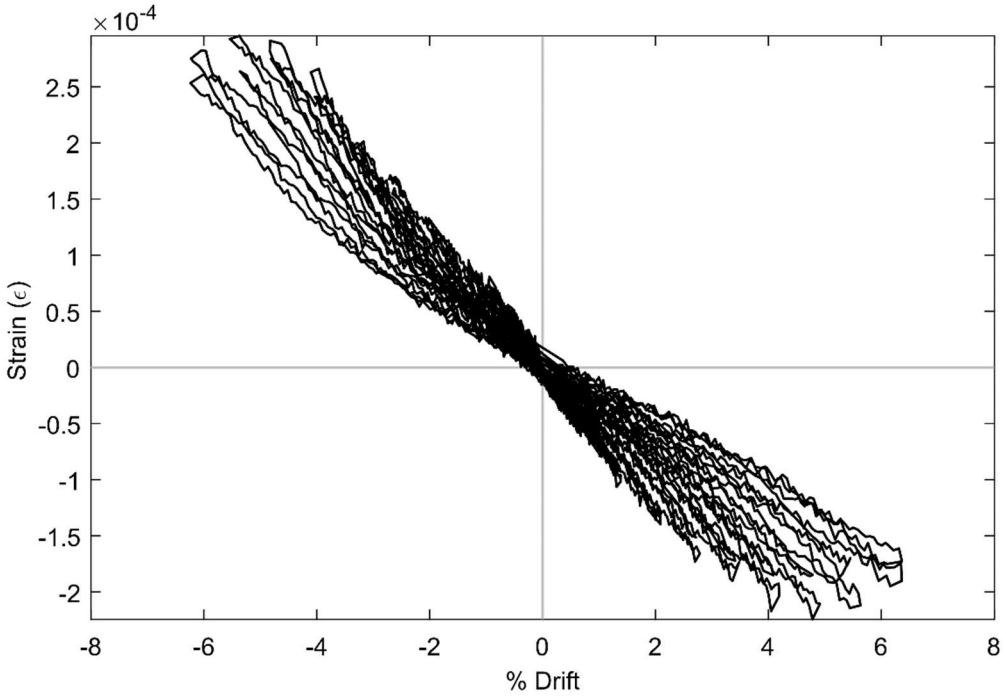

Figure 41. SG CC3 (PTB_4.5_1_0_6)

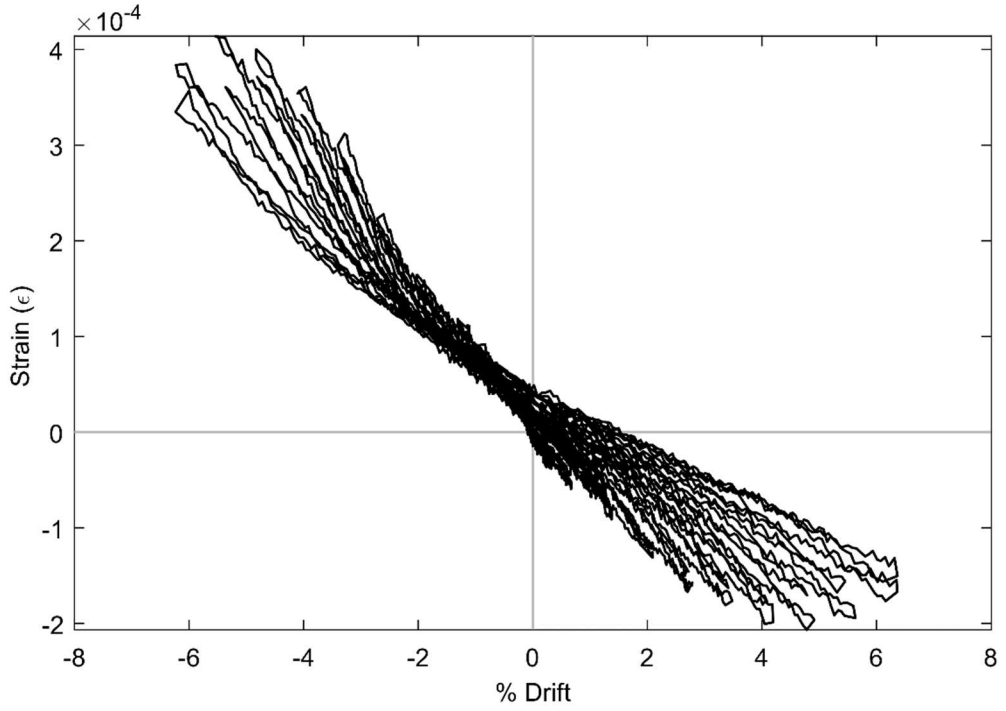

Figure 42. SG CC4 (PTB_4.5_1_0_6)

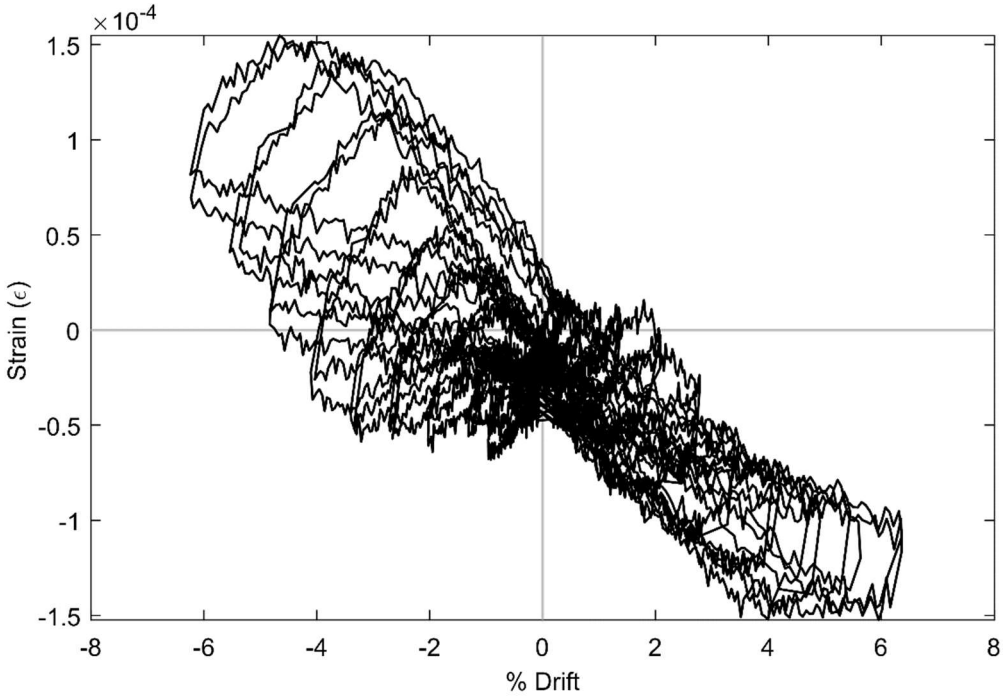

Figure 43. SG CD1 (PTB_4.5_1_0_6)

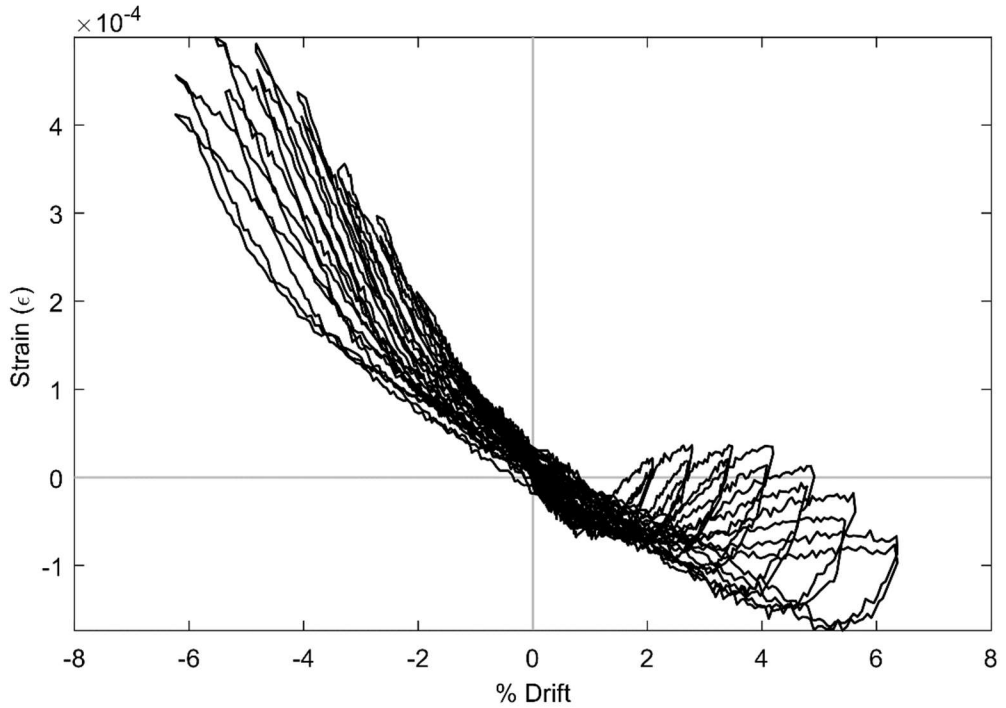

Figure 44. SG CD2 (PTB_4.5_1_0_6)

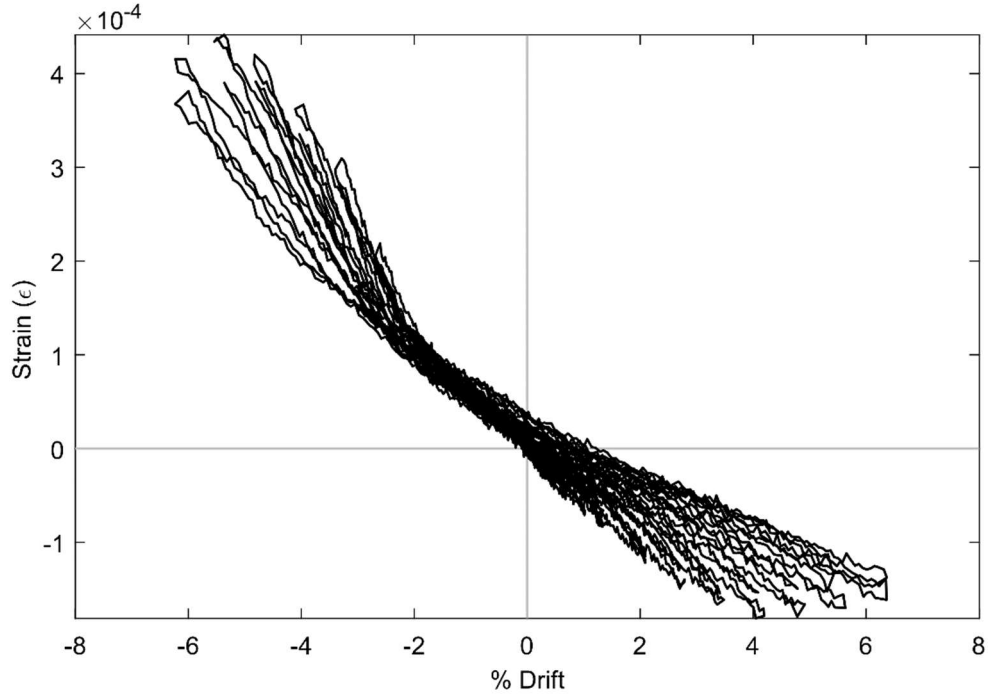

Figure 45. SG CD3 (PTB_4.5_1_0_6)

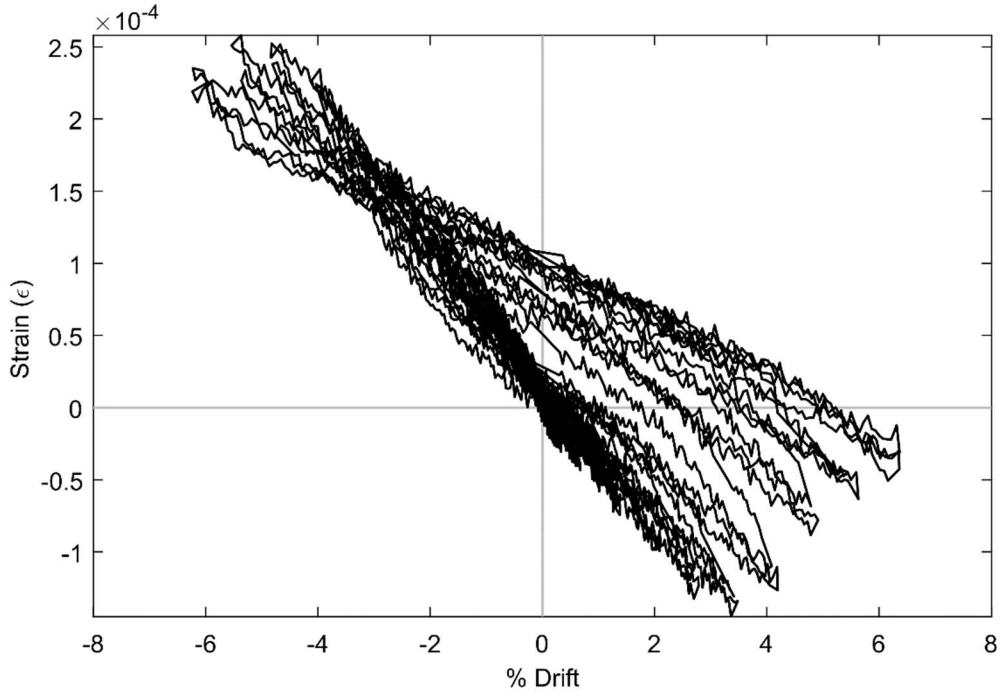

Figure 46. SG CD4 (PTB_4.5_1_0_6)

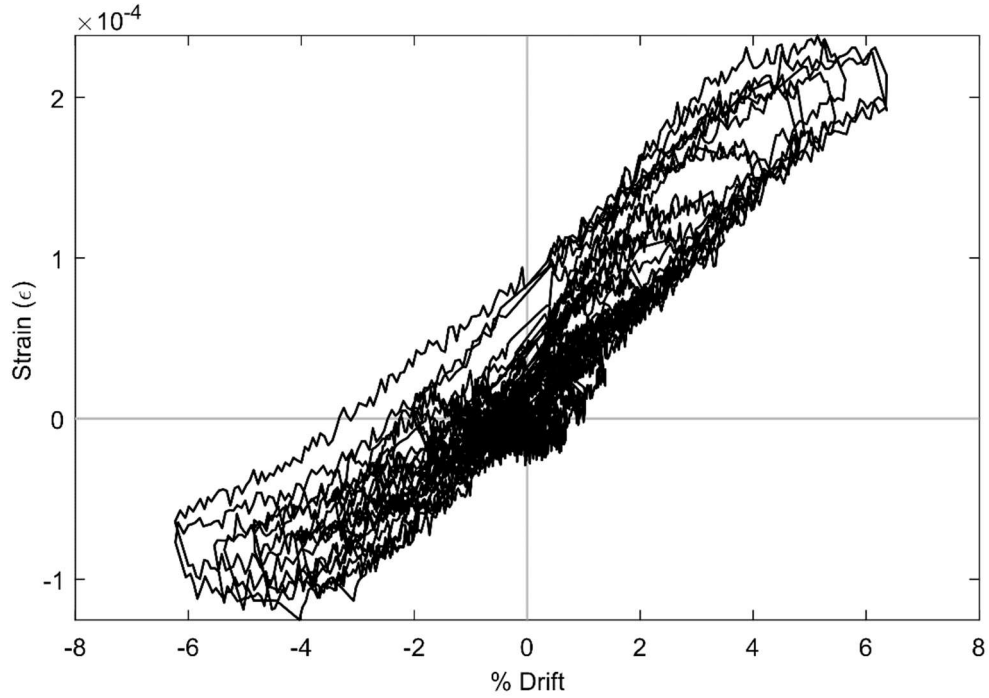

Figure 47. SG CH1 (PTB_4.5_1_0_6)

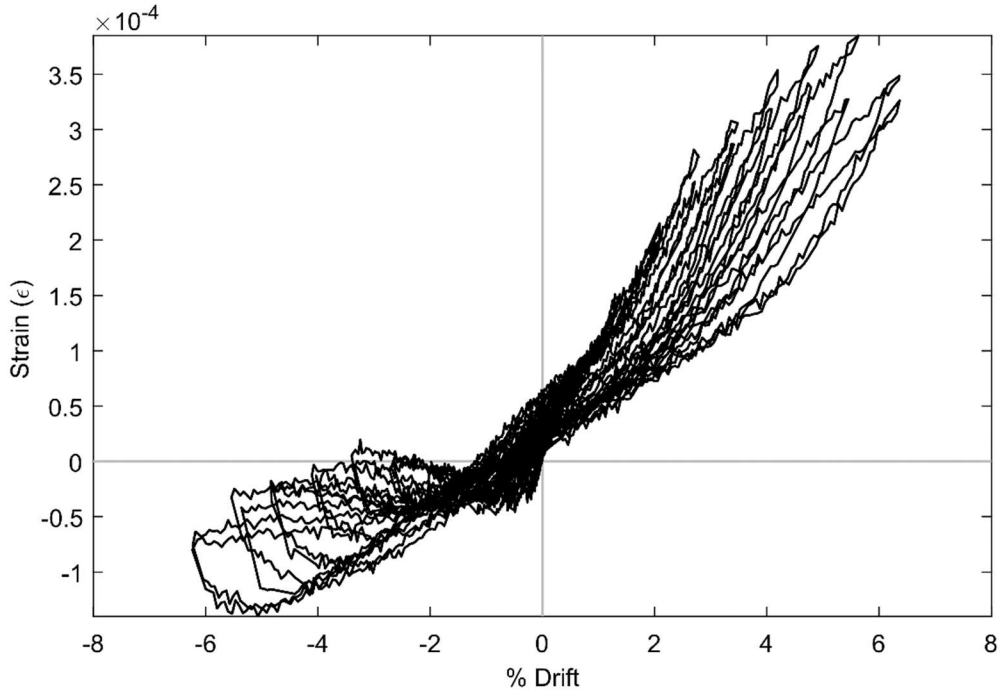

Figure 48. SG CH2 (PTB_4.5_1_0_6)

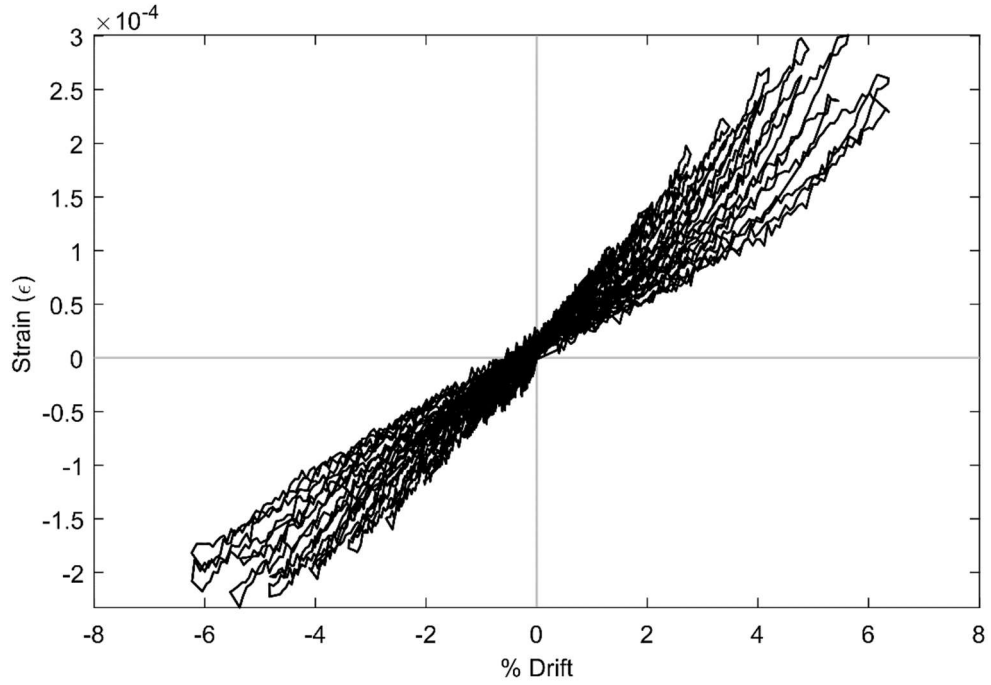

Figure 49. SG CH3 (PTB_4.5_1_0_6)

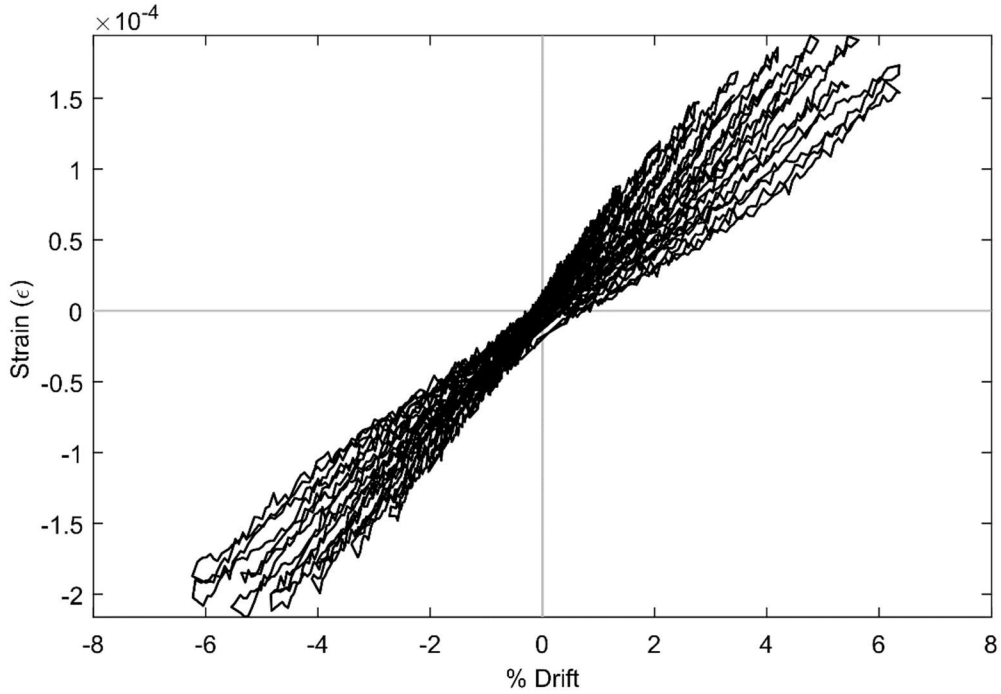

Figure 50. SG CH4 (PTB_4.5_1_0_6)

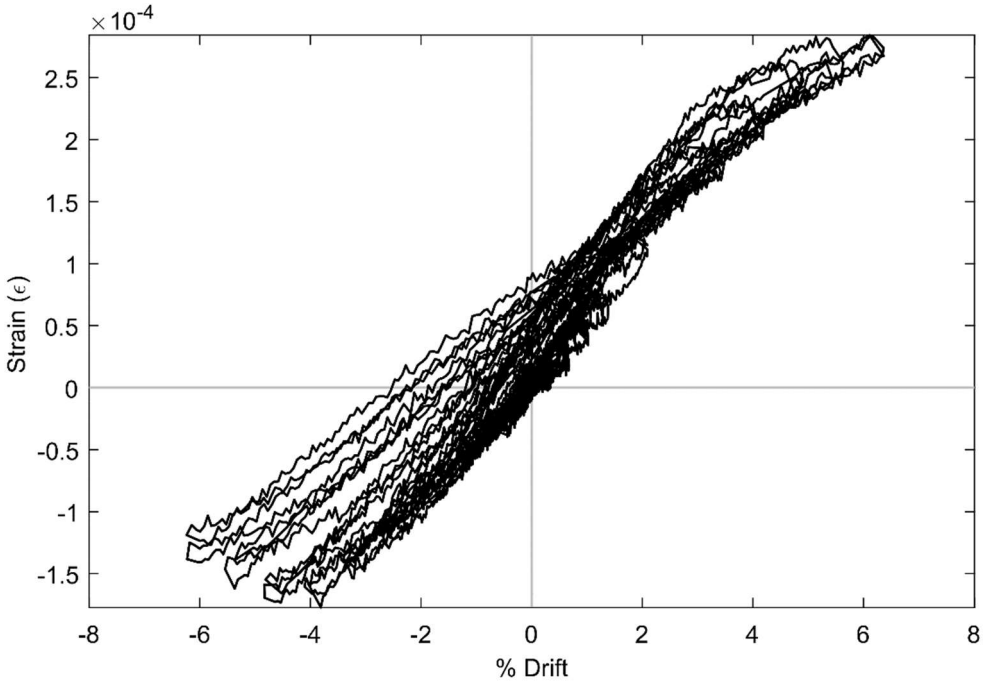

Figure 51. SG CI1 (PTB_4.5_1_0_6)

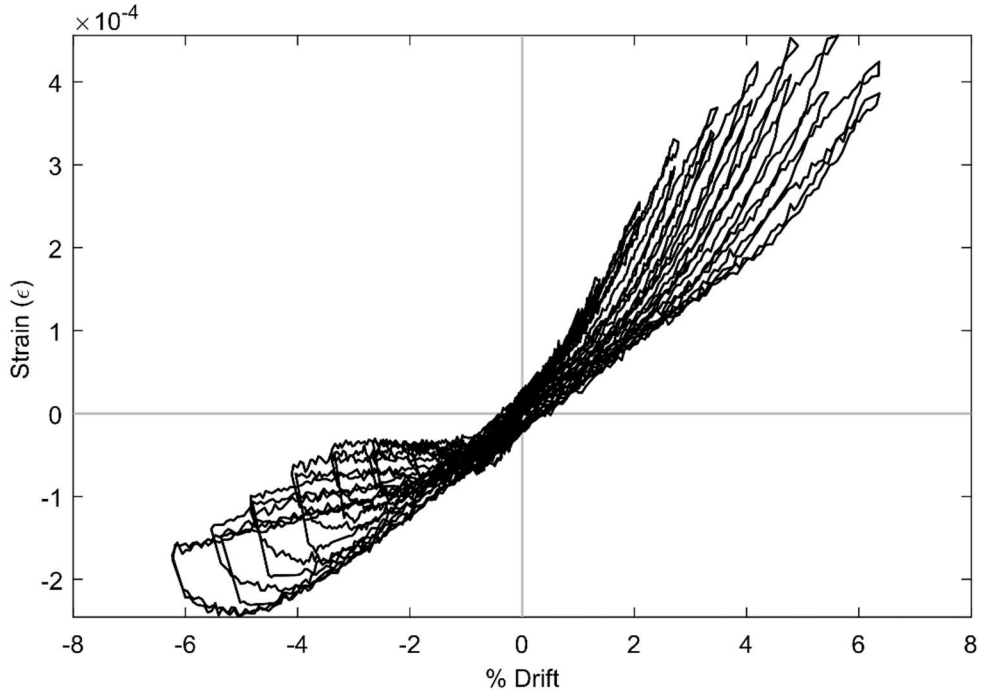

Figure 52. SG CI2 (PTB_4.5_1_0_6)

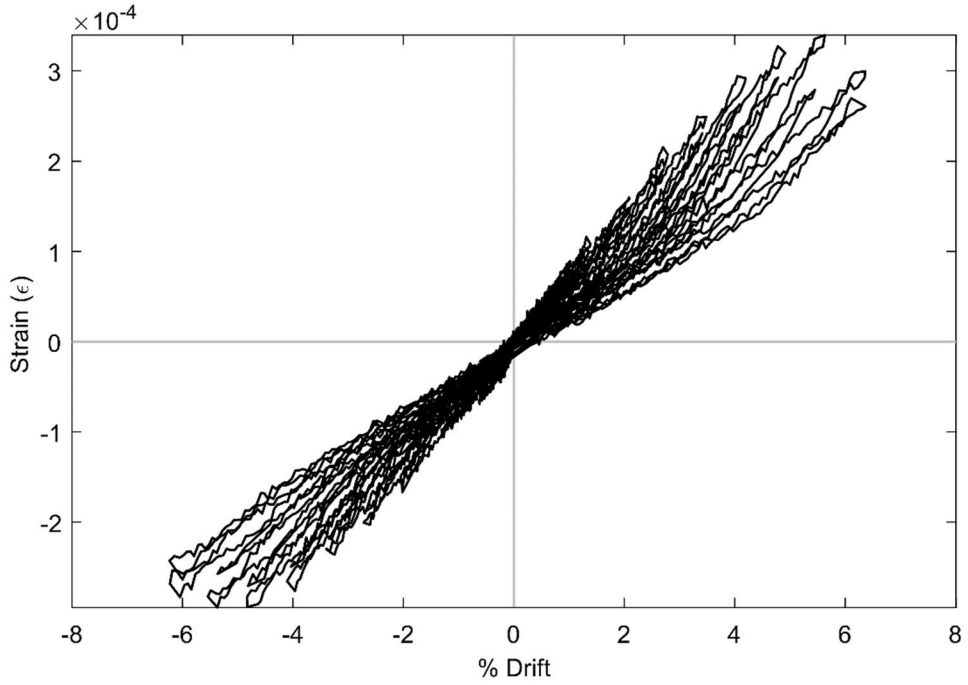

Figure 53. SG CI3 (PTB_4.5_1_0_6)

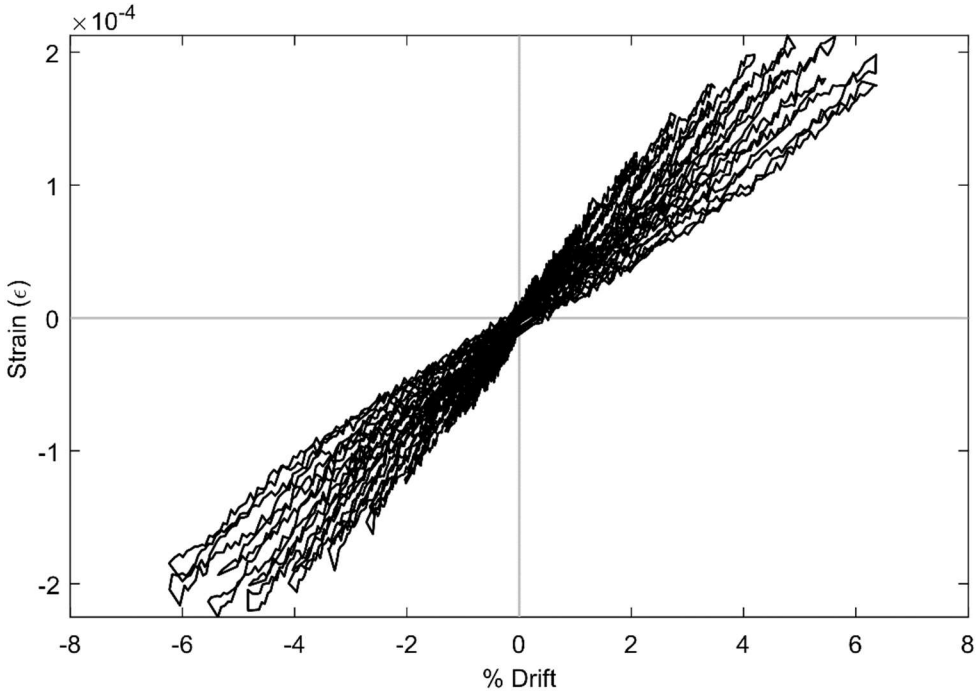

Figure 54. SG CI4 (PTB_4.5_1_0_6)

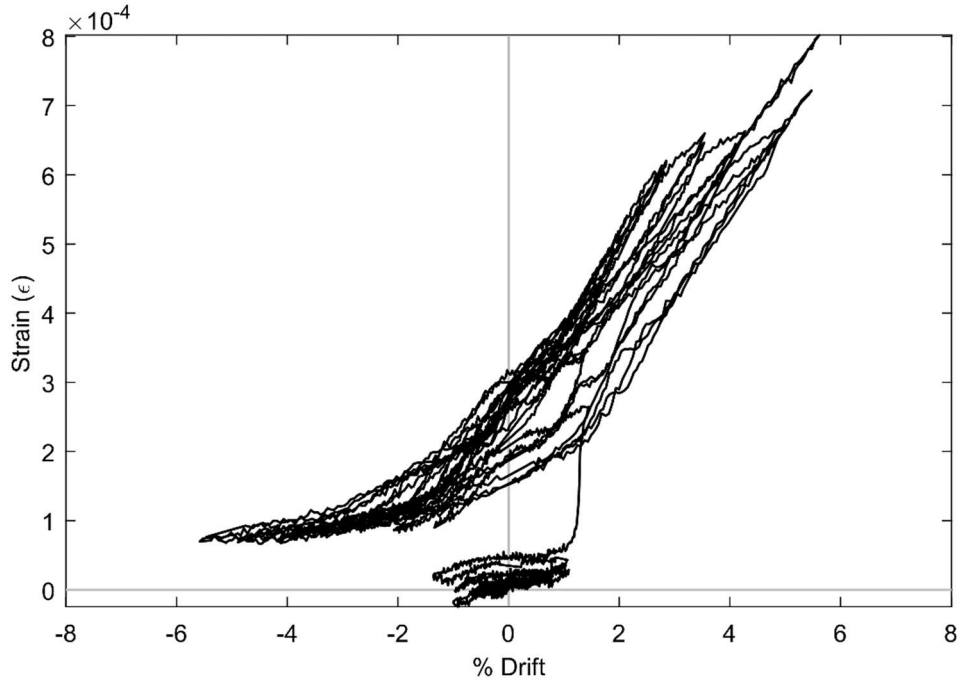

Figure 55. SG STC5 (PTB_9_2_0_6)

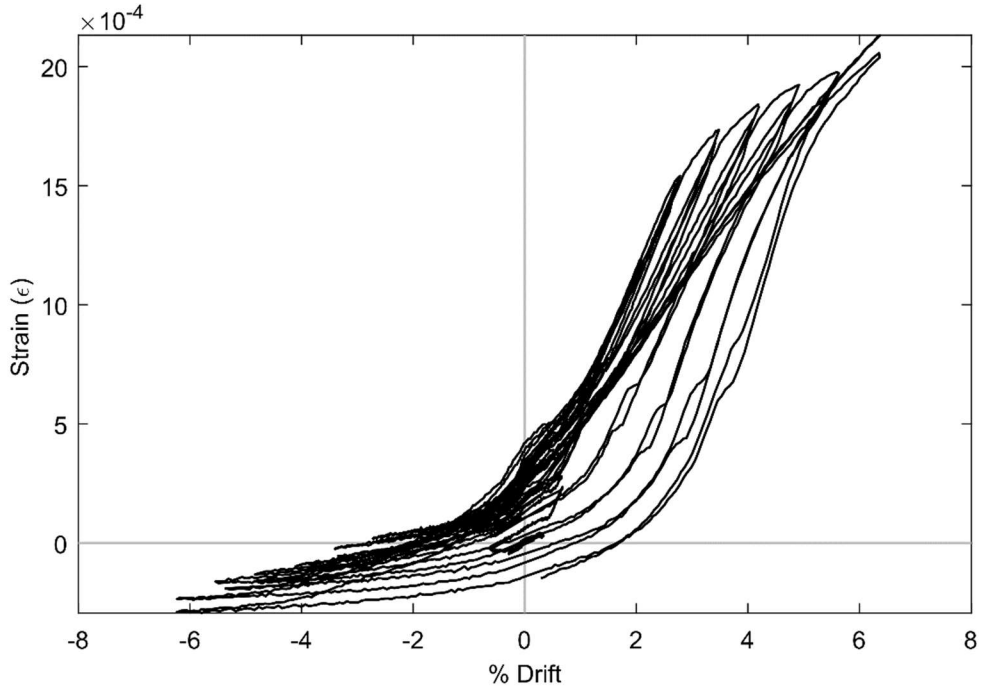

Figure 56. SG STE5 (PTB_9_2_0_6)

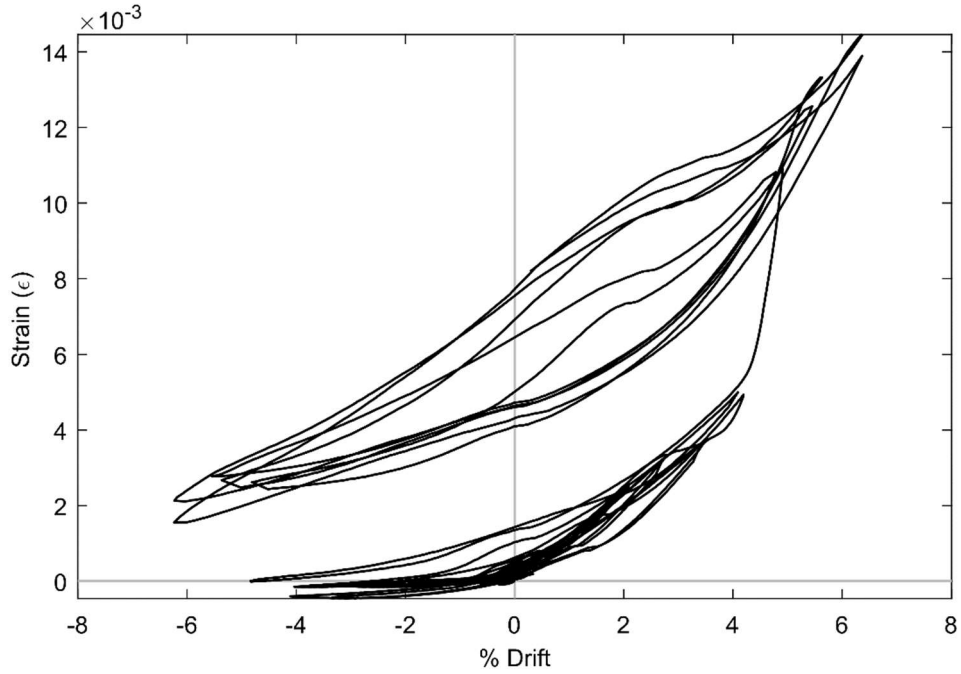

Figure 57. SG STG5 (PTB_9_2_0_6)

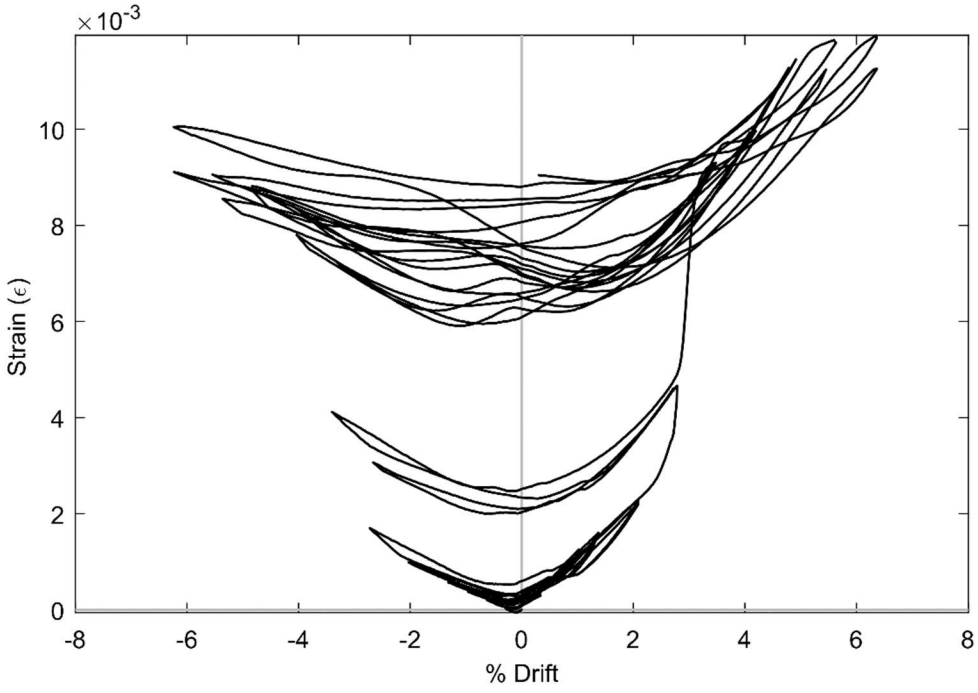

Figure 58. SG STH5 (PTB_9_2_0_6)

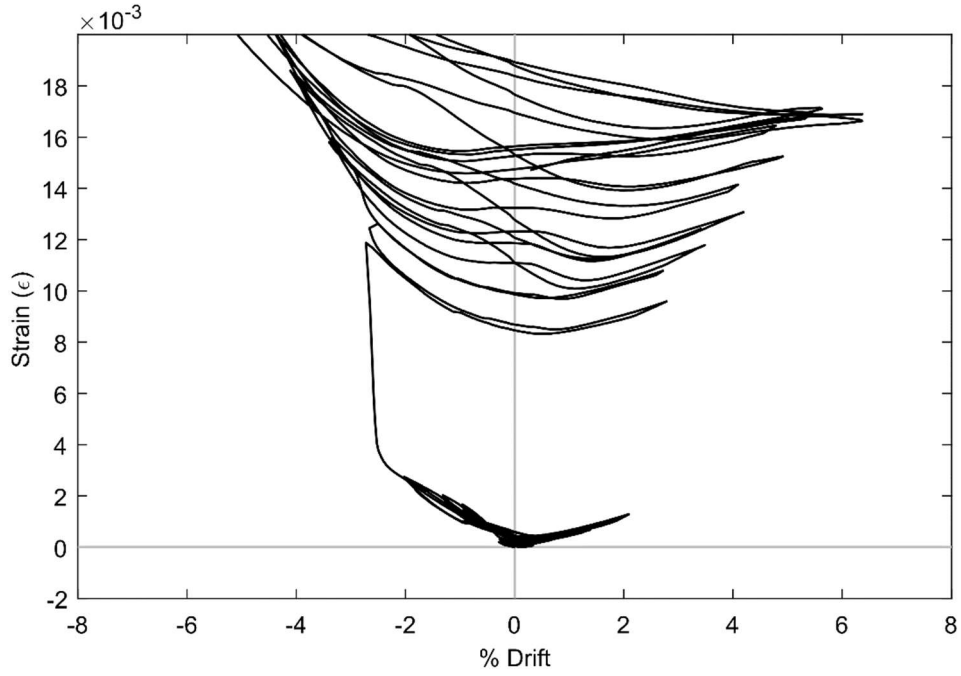

Figure 59. SG STK5 (PTB_9_2_0_6)

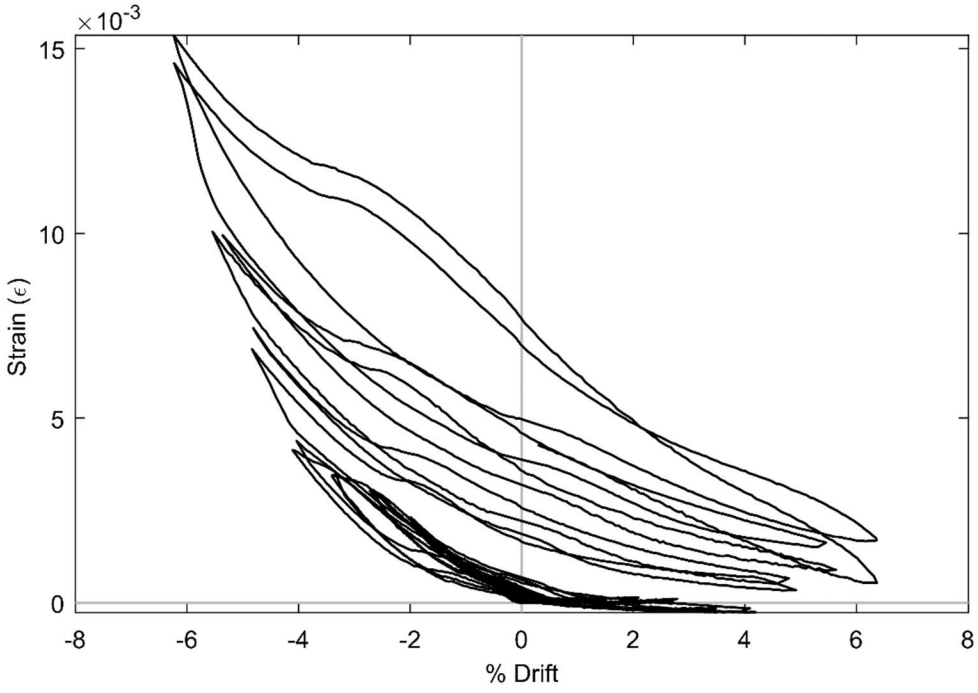

Figure 60. SG STL5 (PTB_9_2_0_6)

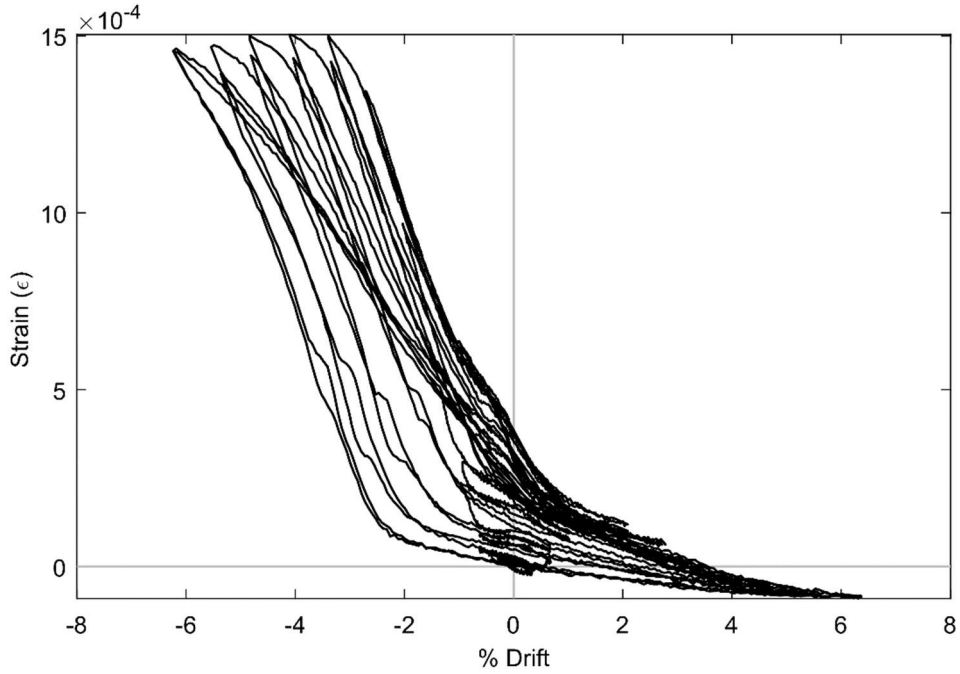

Figure 61. SG STN5 (PTB_9_2_0_6)

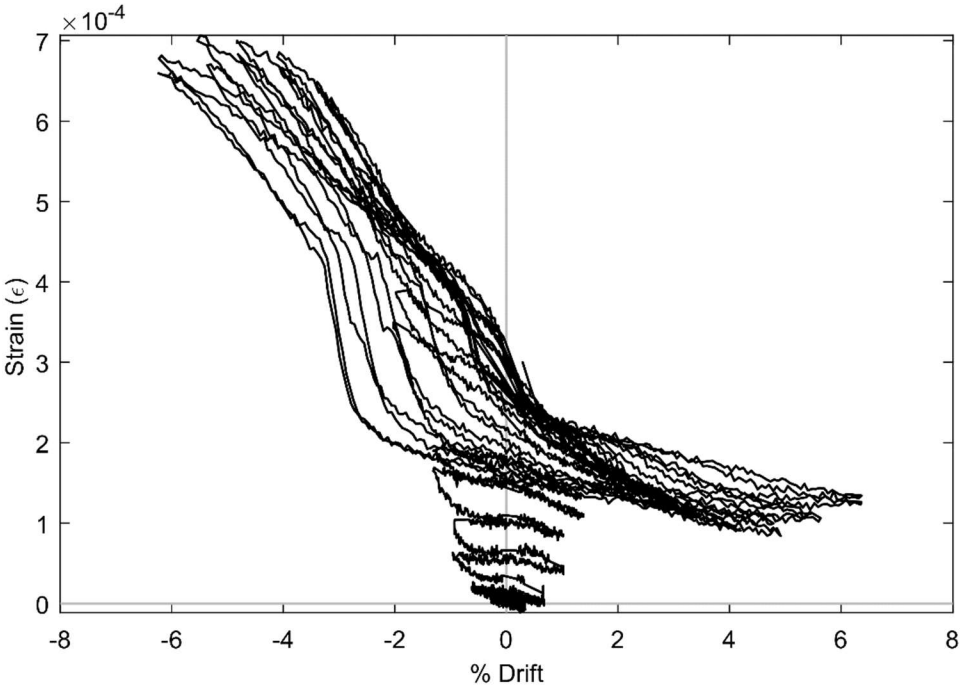

Figure 62. SG STP5 (PTB_9_2_0_6)

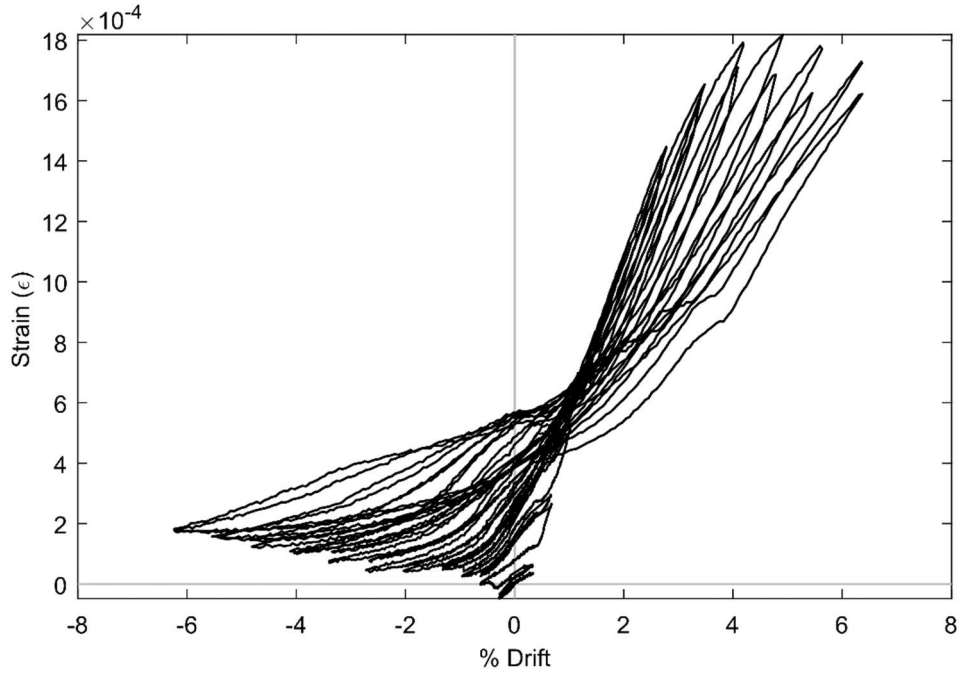

Figure 63. SG STE6 (PTB_9_2_0_6)

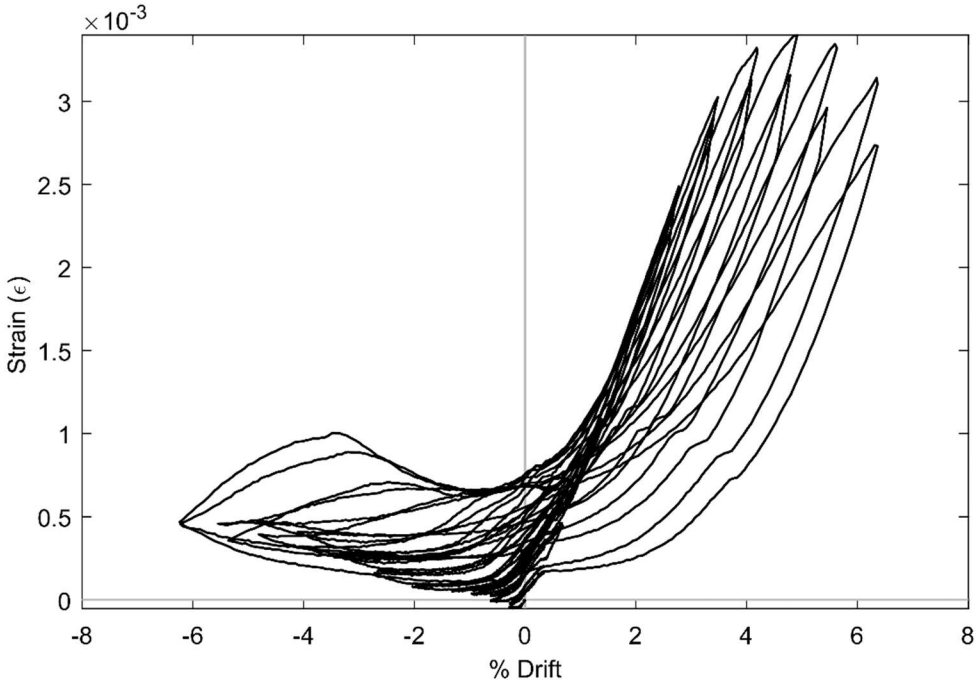

Figure 64. SG STG6 (PTB_9_2_0_6)

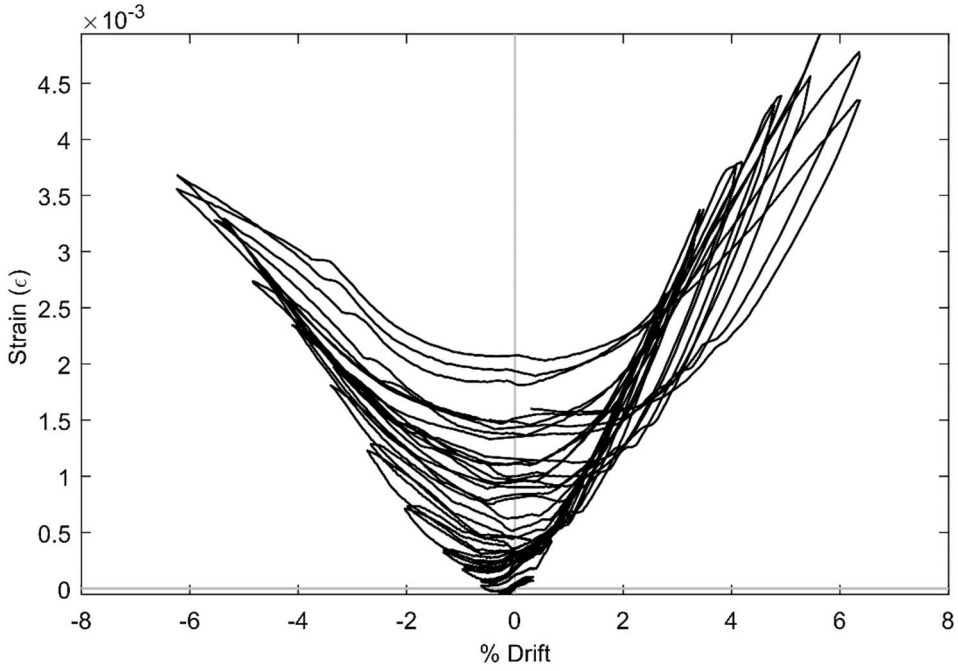

Figure 65. SG STI6 (PTB_9_2_0_6)

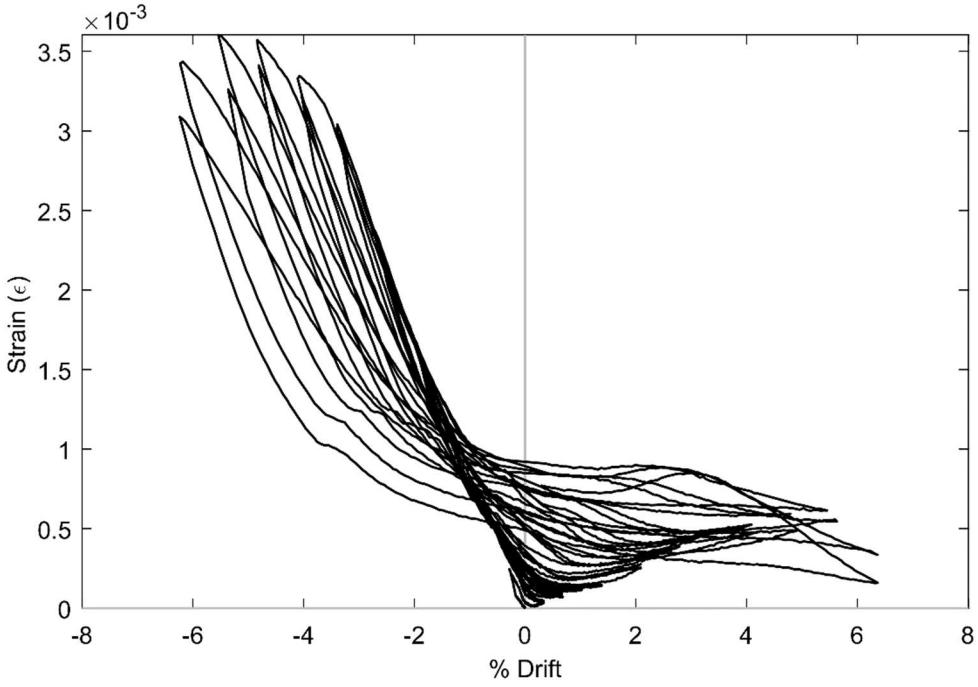

Figure 66. SG STL6 (PTB_9_2_0_6)

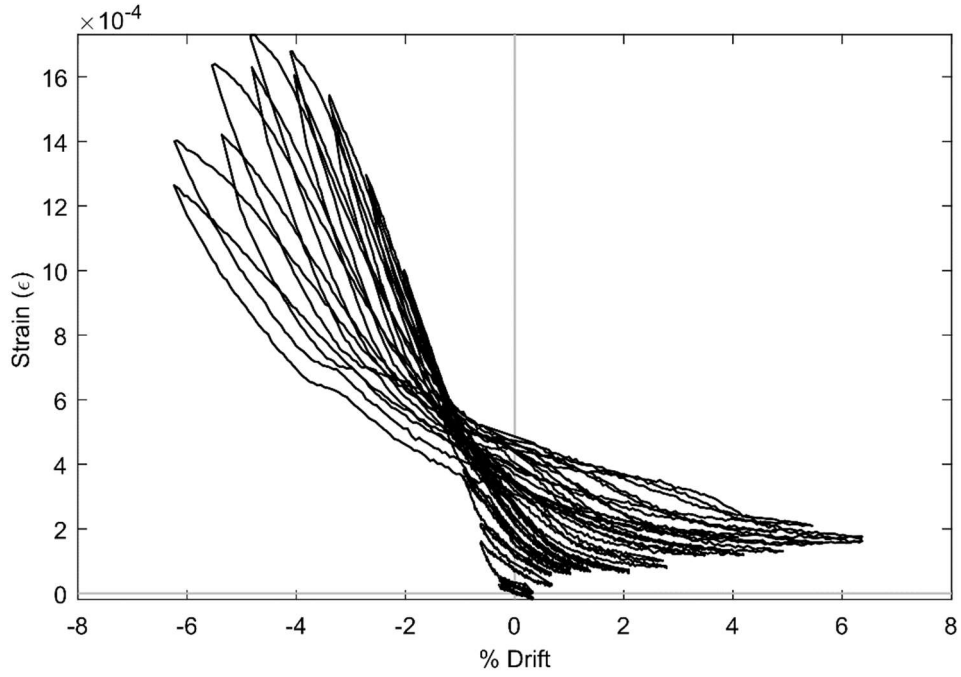

Figure 67. SG STN6 (PTB_9_2_0_6)

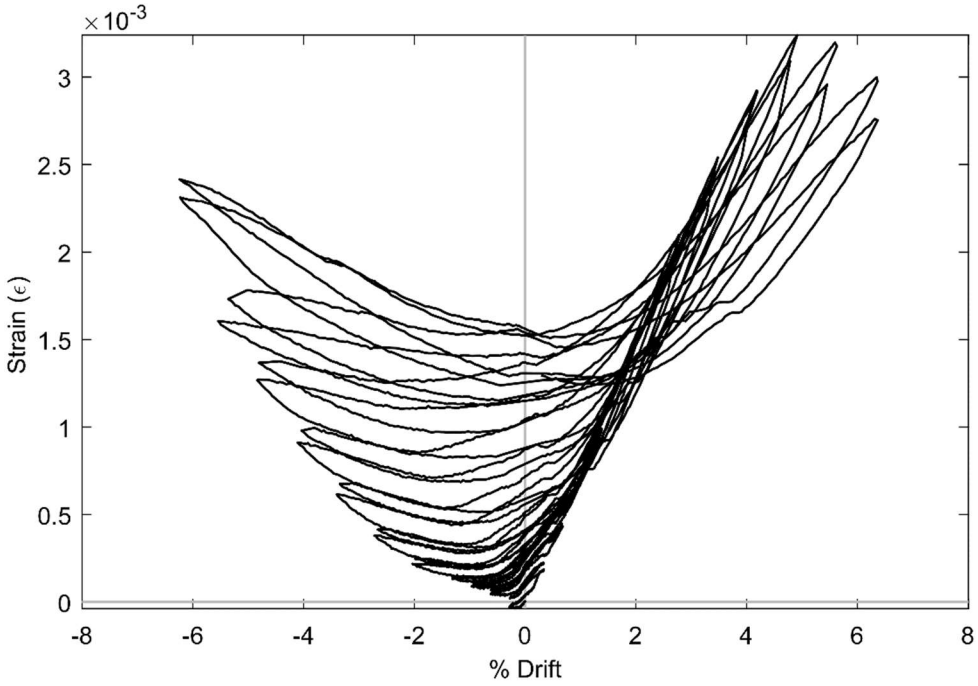

Figure 68. SG STG7 (PTB_9_2_0_6)

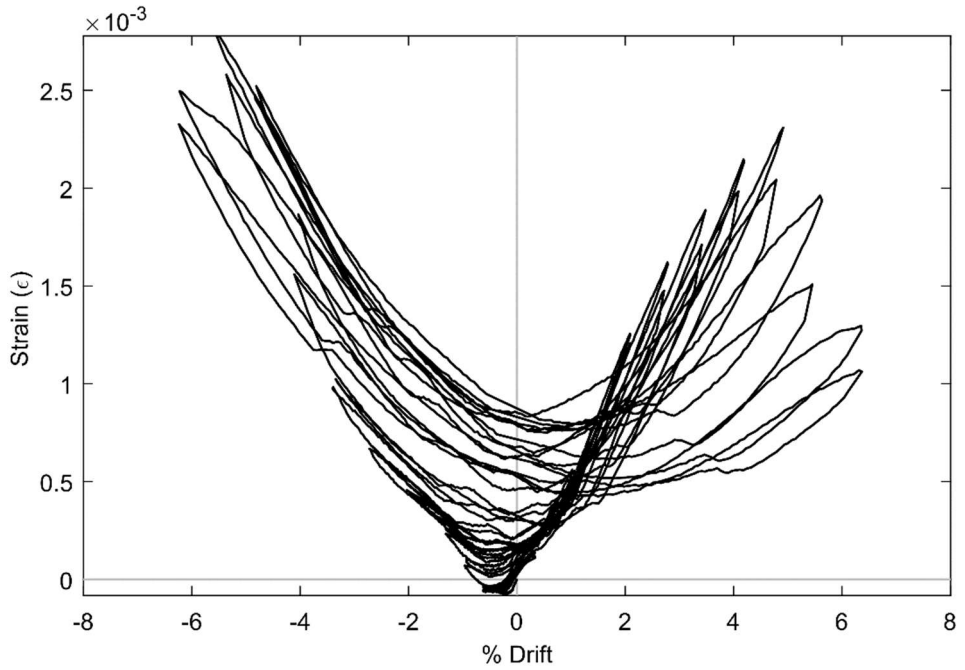

Figure 69. SG STI7 (PTB_9_2_0_6)

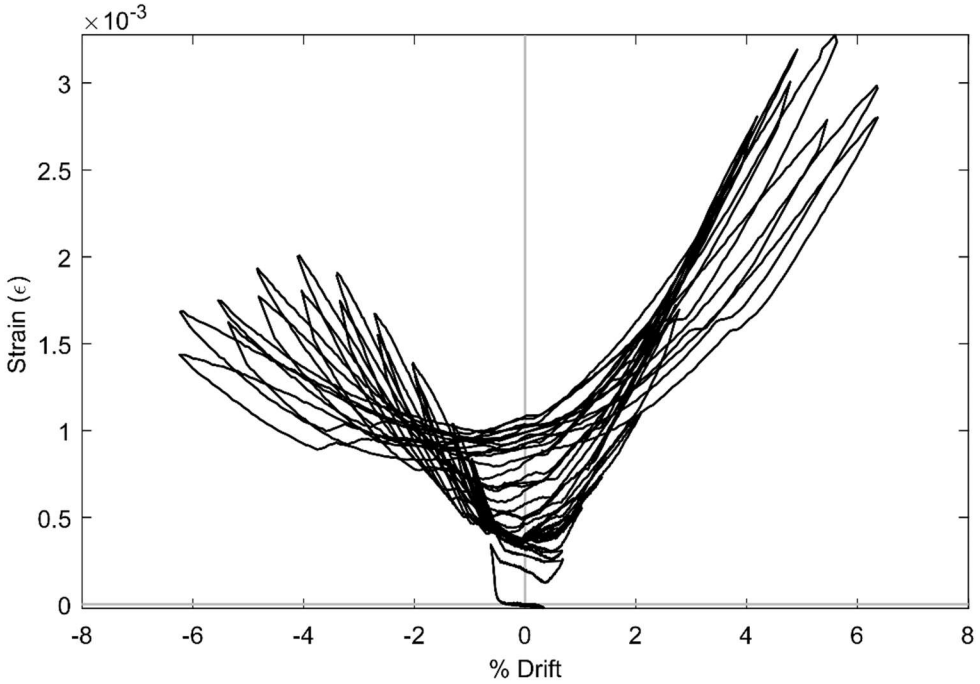

Figure 70. SG STJ7 (PTB_9_2_0_6)

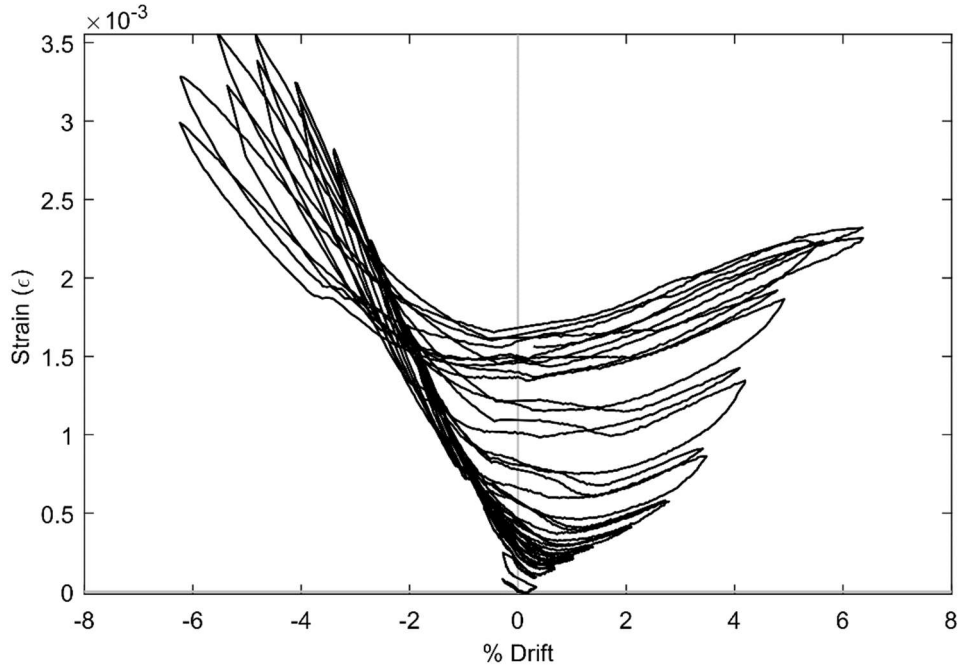

Figure 71. SG STL7 (PTB_9_2_0_6)

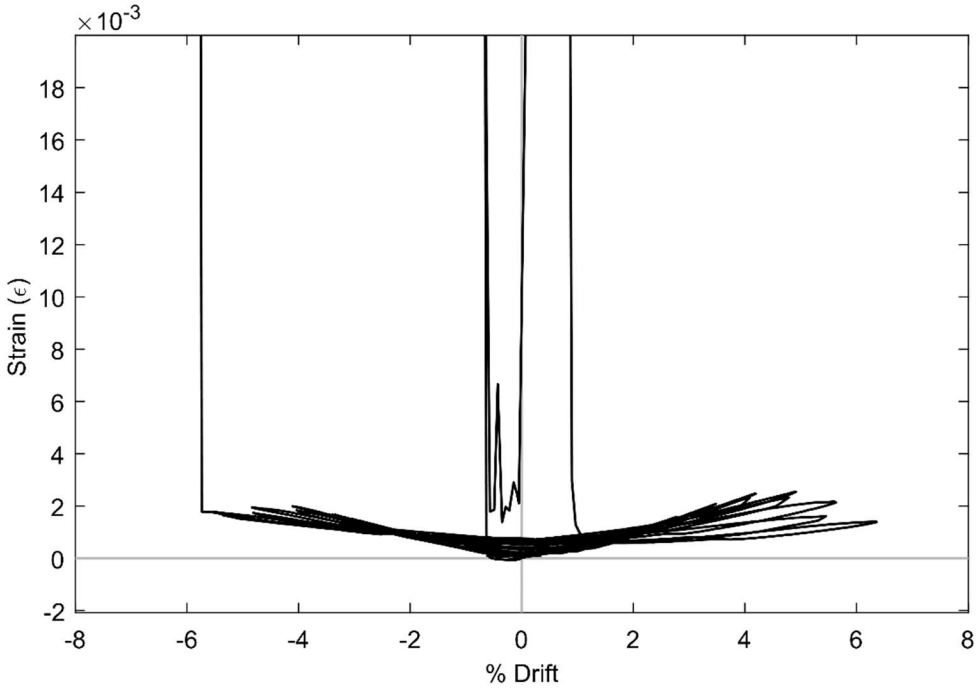

Figure 72. SG STI8 (PTB_9_2_0_6)

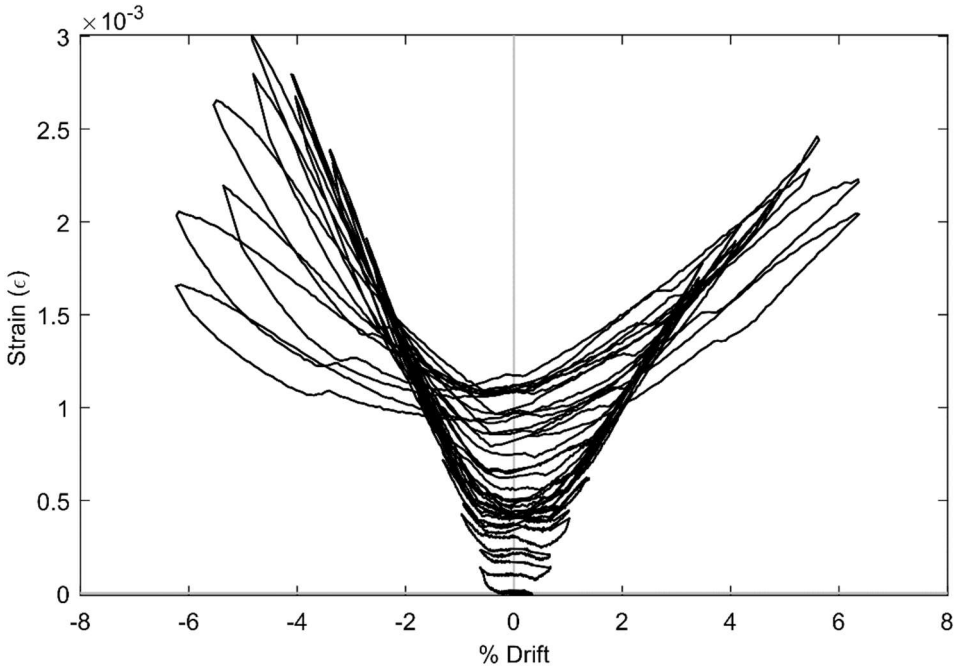

Figure 73. SG STJ8 (PTB_9_2_0_6)

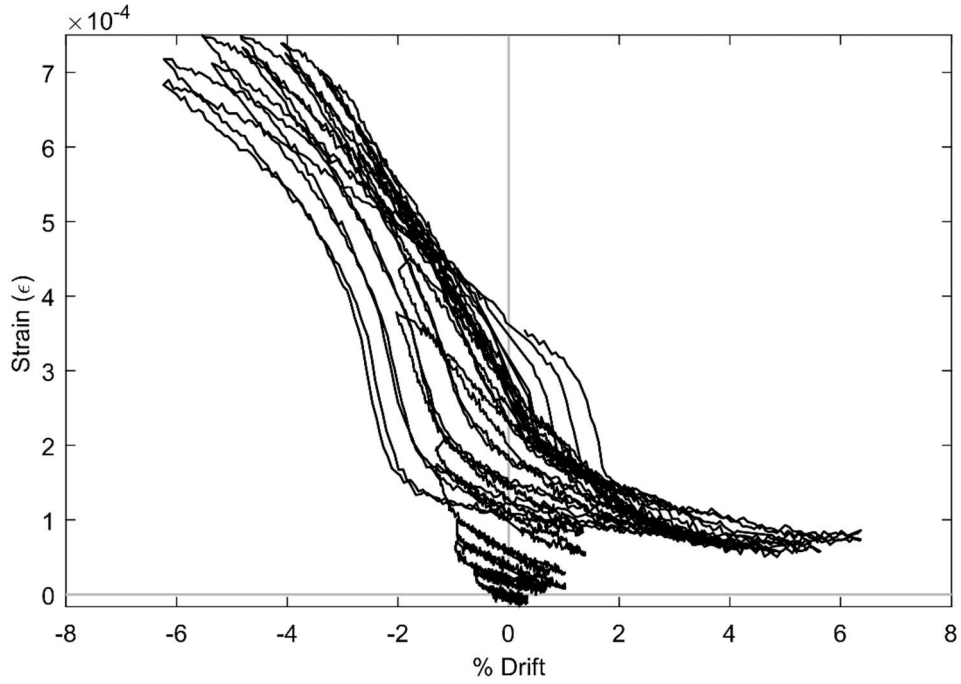

Figure 74. SG SBC5 (PTB_9_2_0_6)

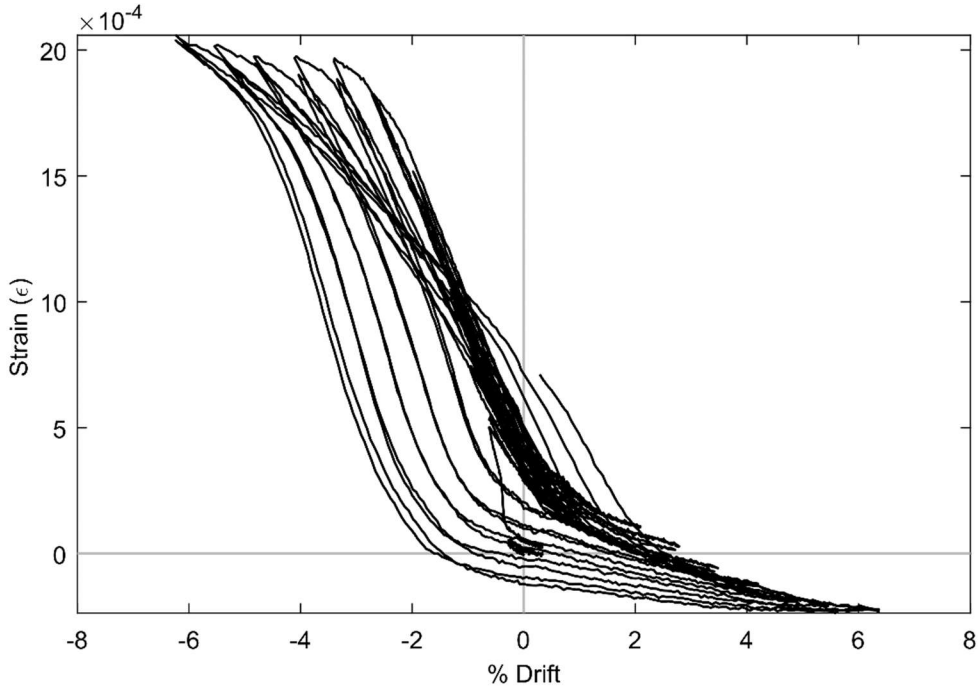

Figure 75. SG SBE5 (PTB_9_2_0_6)

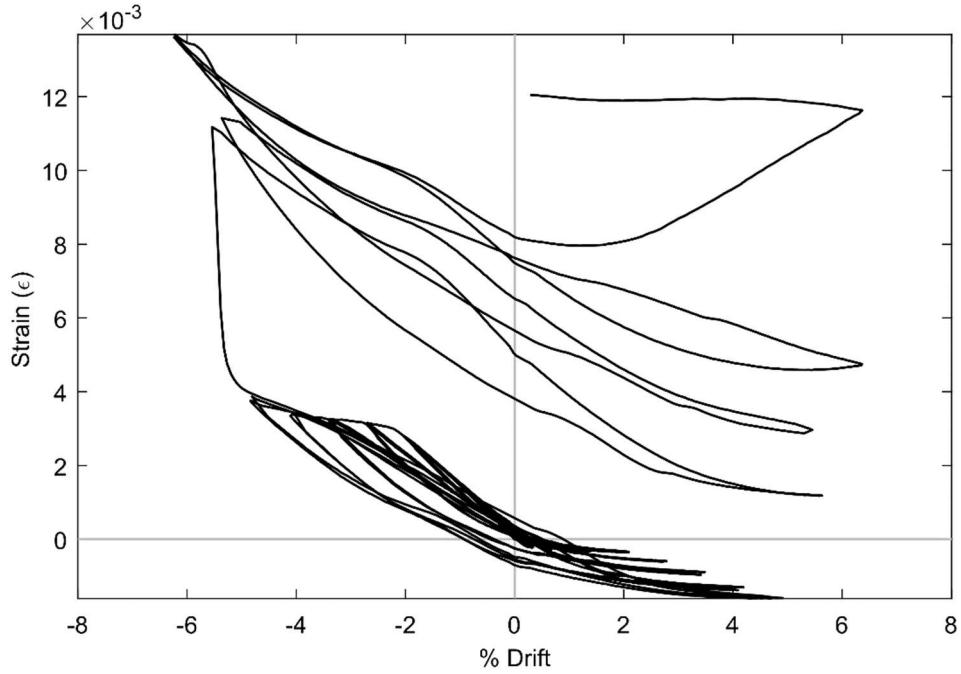

Figure 76. SG SBG5 (PTB_9_2_0_6)

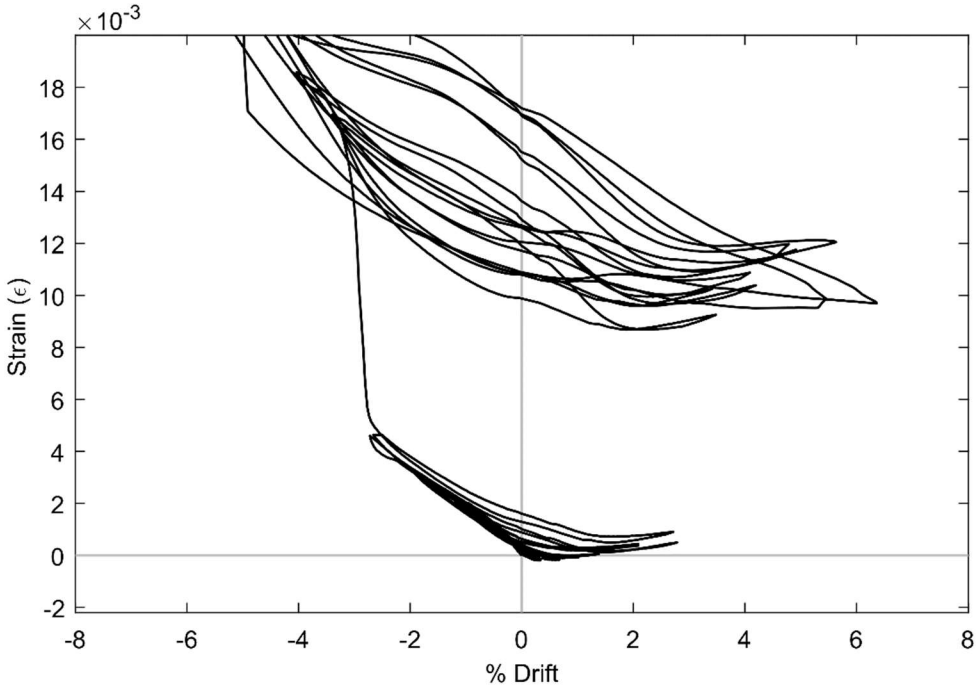

Figure 77. SG SBH5 (PTB_9_2_0_6)

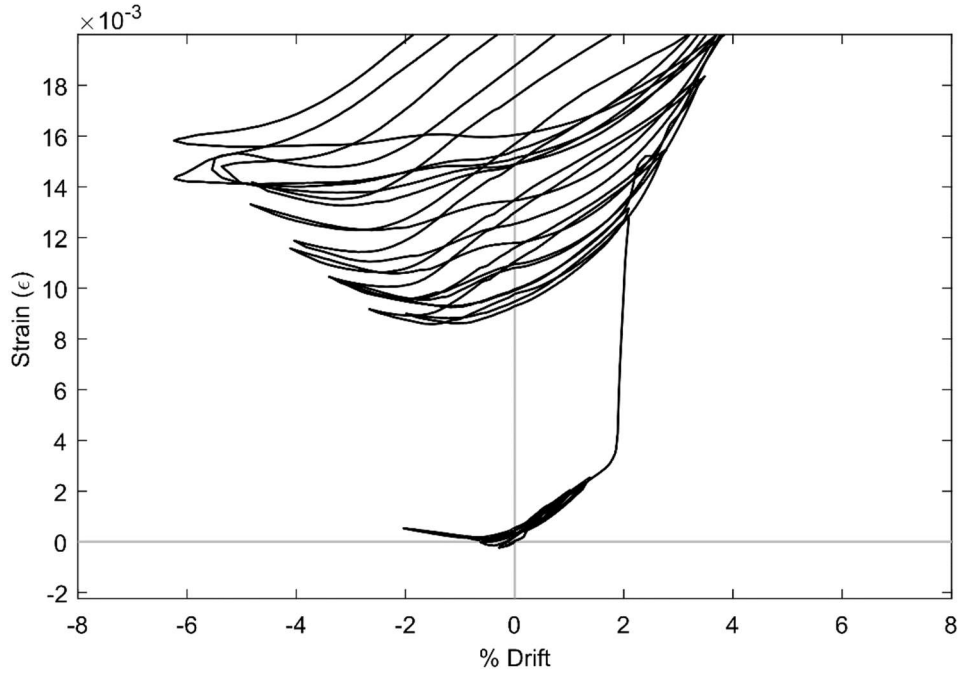

Figure 78. SG SBK5 (PTB_9_2_0_6)

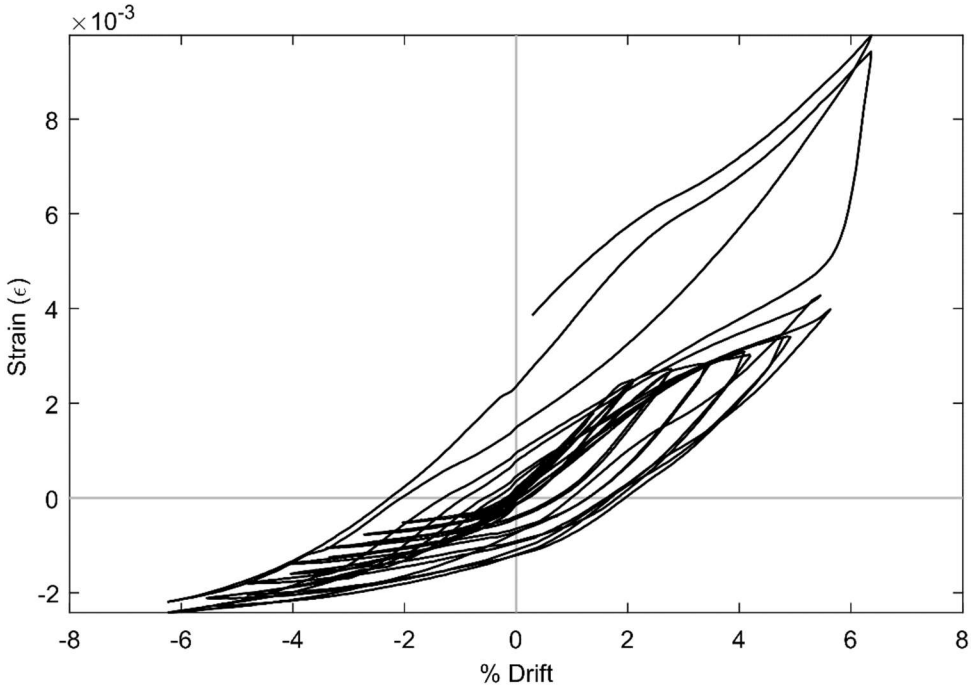

Figure 79. SG SBL5 (PTB_9_2_0_6)

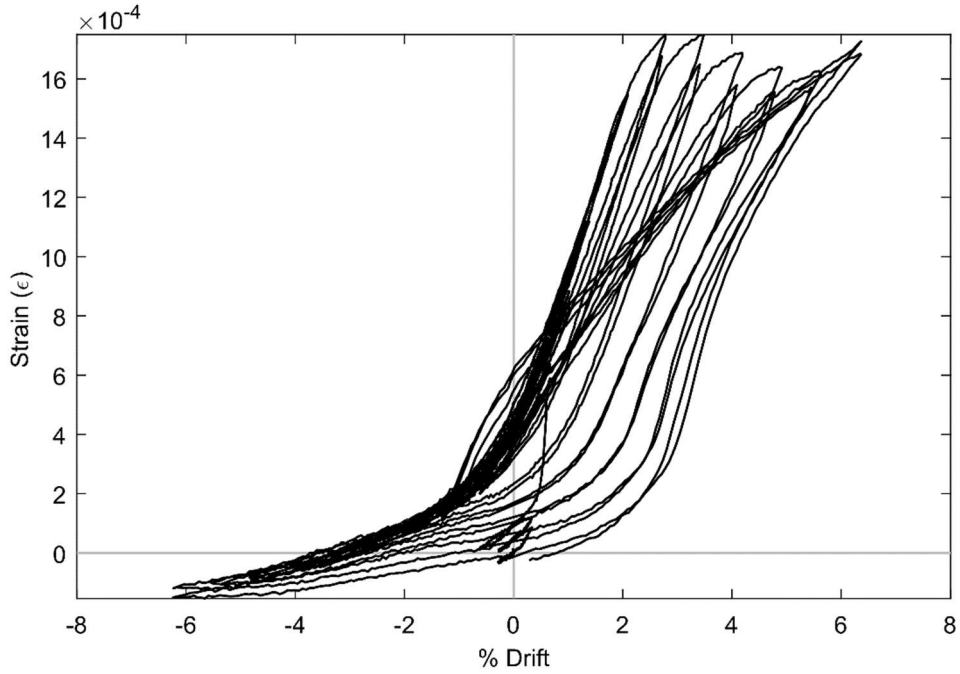

Figure 80. SG SBN5 (PTB_9_2_0_6)

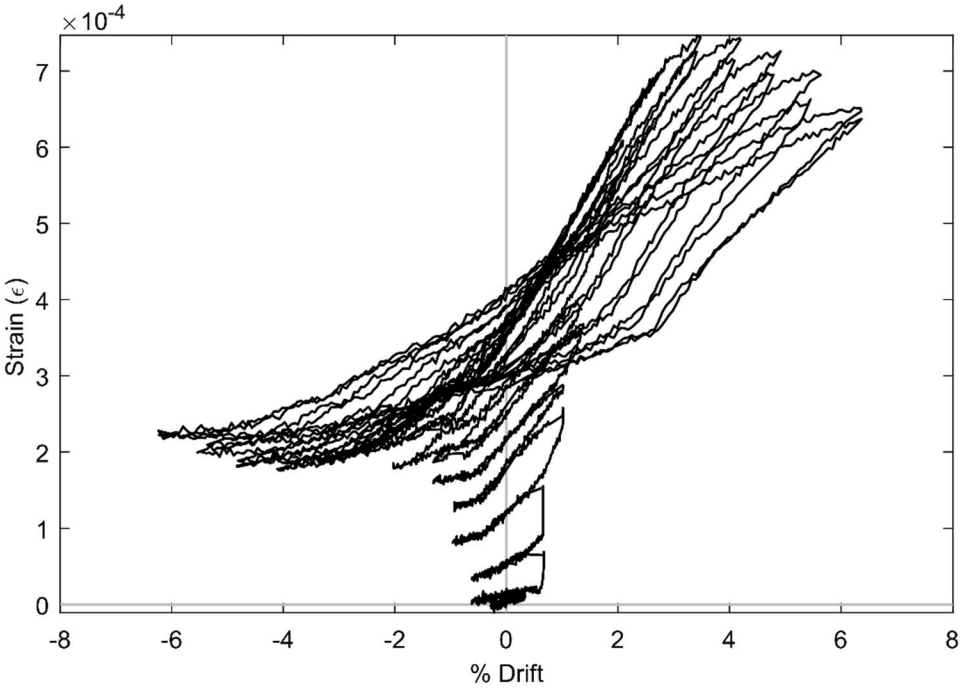

Figure 81. SG SBP5 (PTB_9_2_0_6)

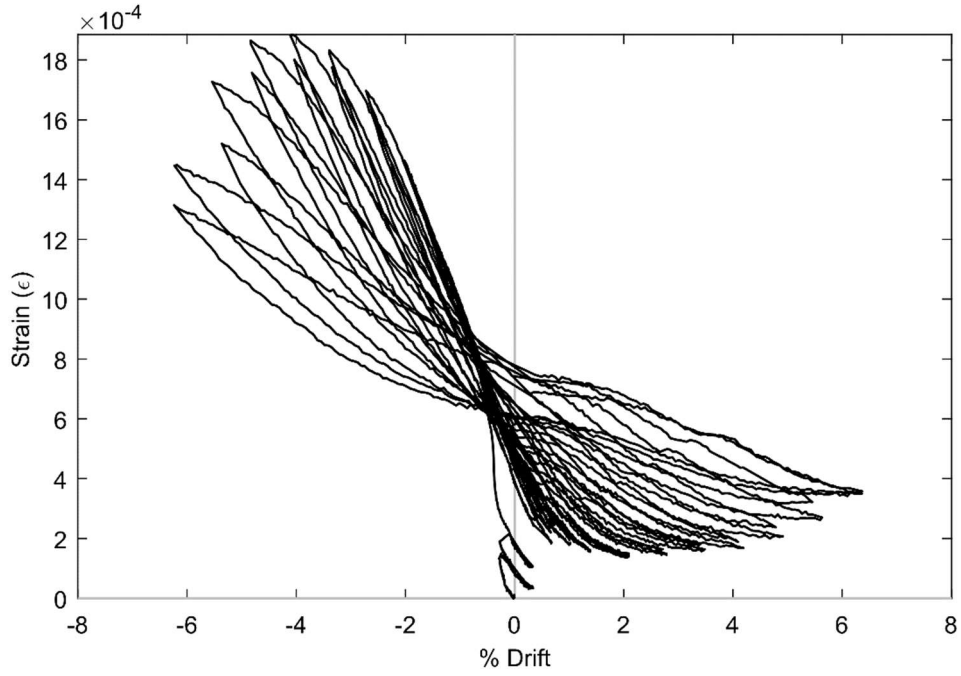

Figure 82. SG SBE6 (PTB_9_2_0_6)

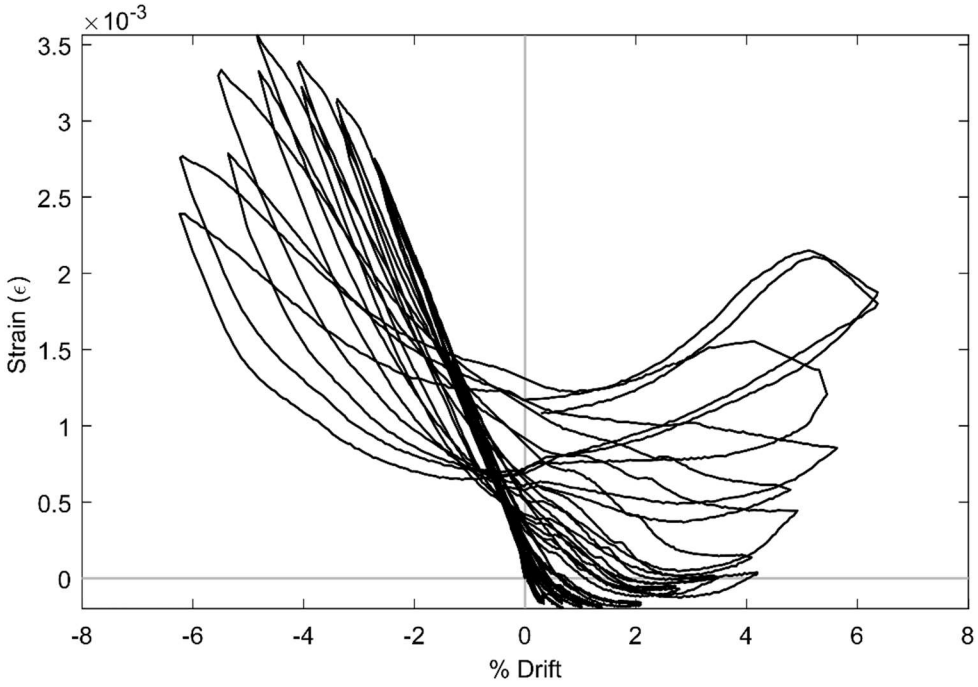

Figure 83. SG SBG6 (PTB_9_2_0_6)

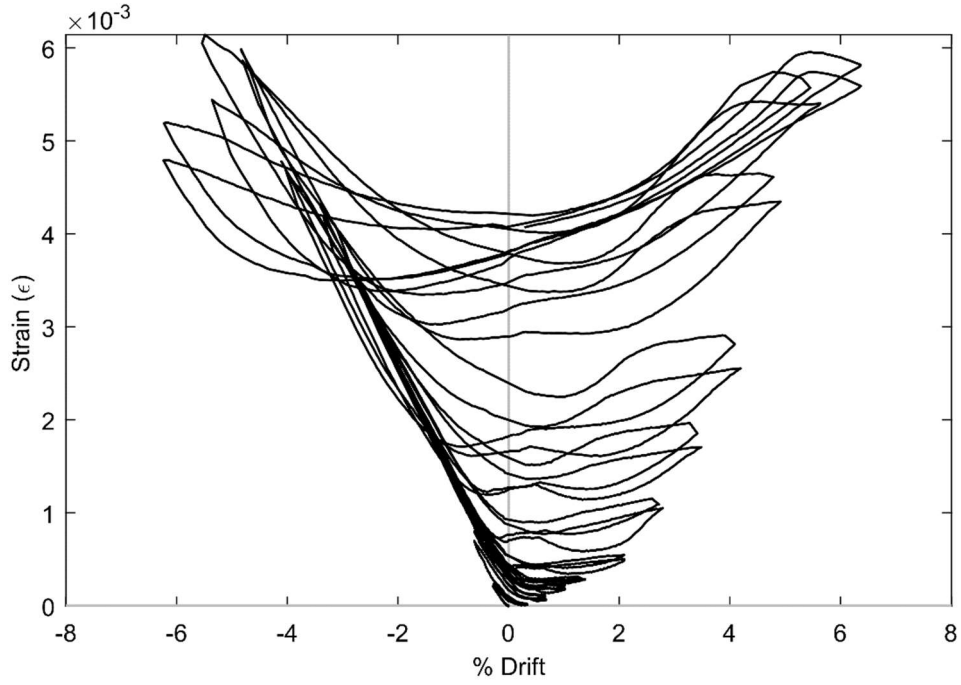

Figure 84. SG SBI6 (PTB_9_2_0_6)

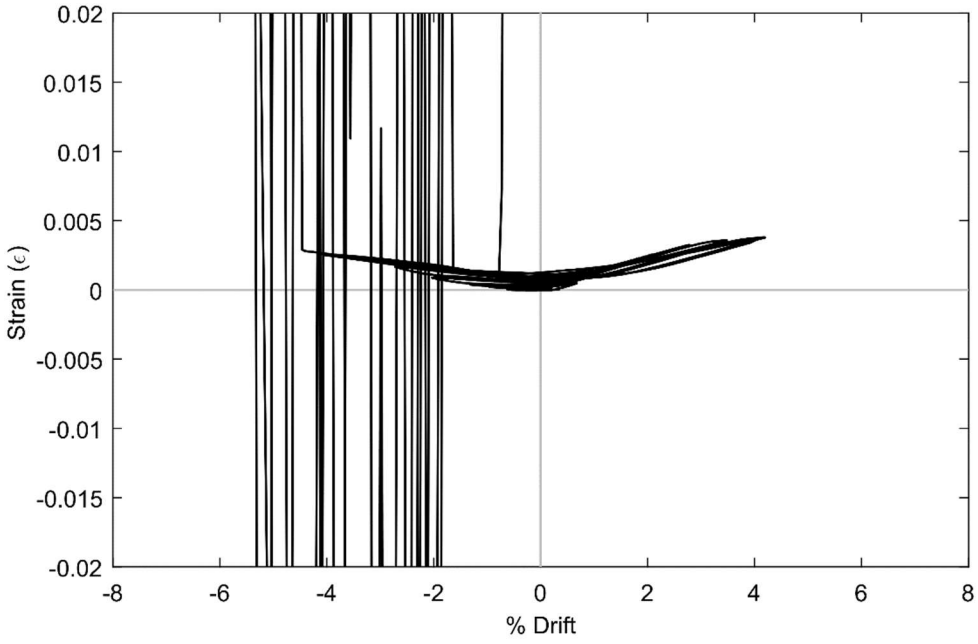

Figure 85. SG SBJ6 (PTB_9_2_0_6)

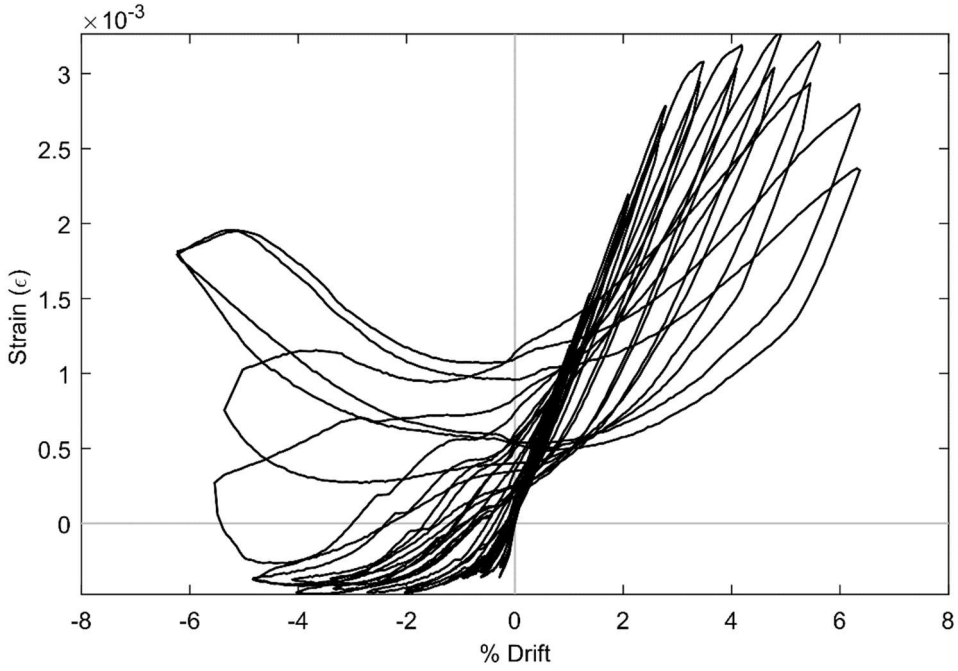

Figure 86. SG SBL6 (PTB_9_2_0_6)

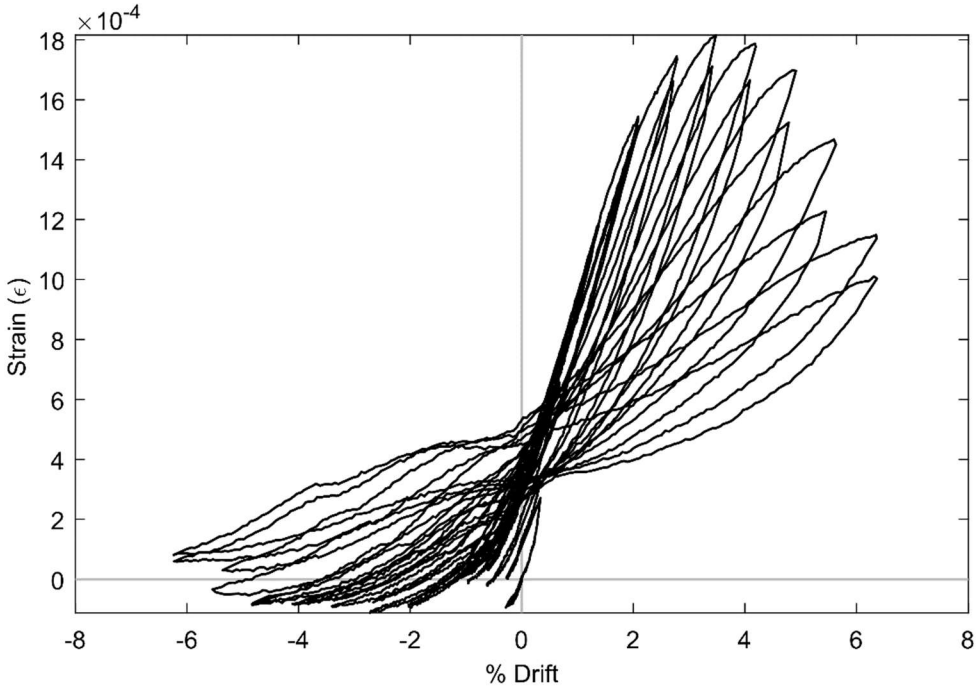

Figure 87. SG SBN6 (PTB_9_2_0_6)

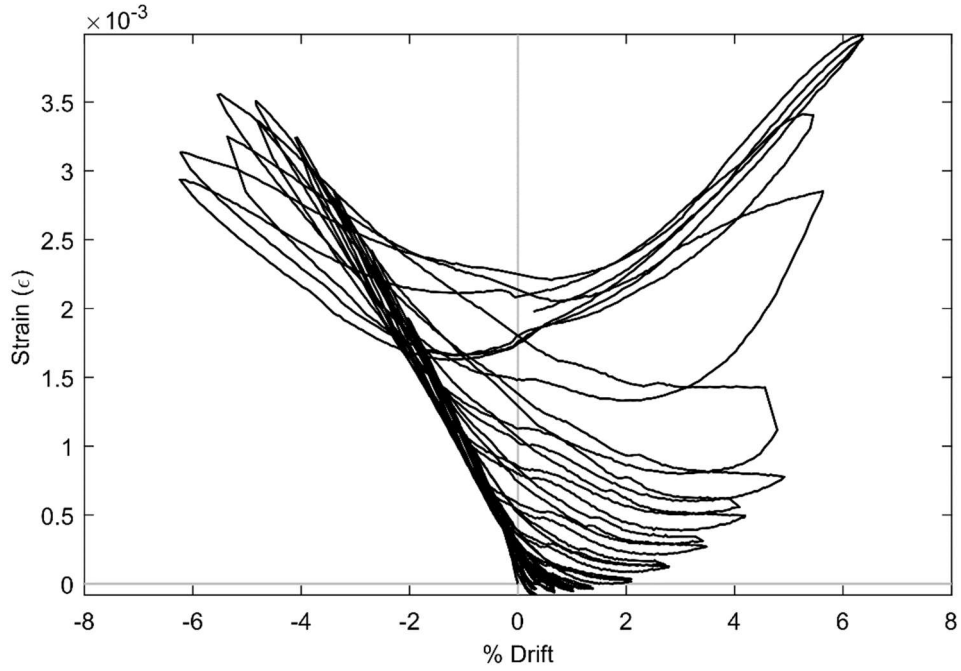

Figure 88. SG SBG7 (PTB_9_2_0_6)

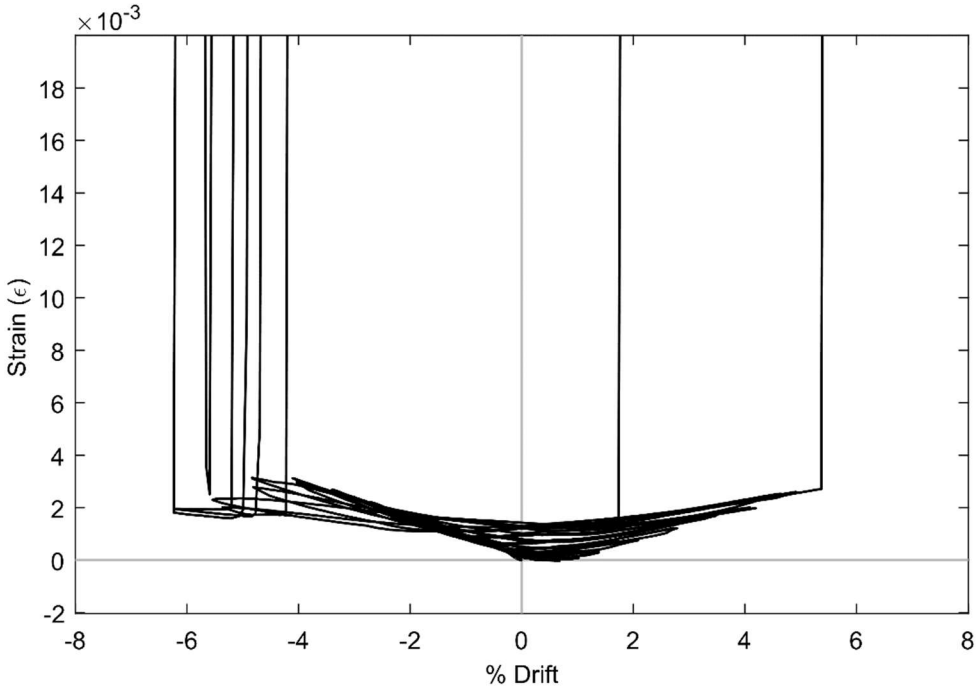

Figure 89. SG SBI7 (PTB_9_2_0_6)

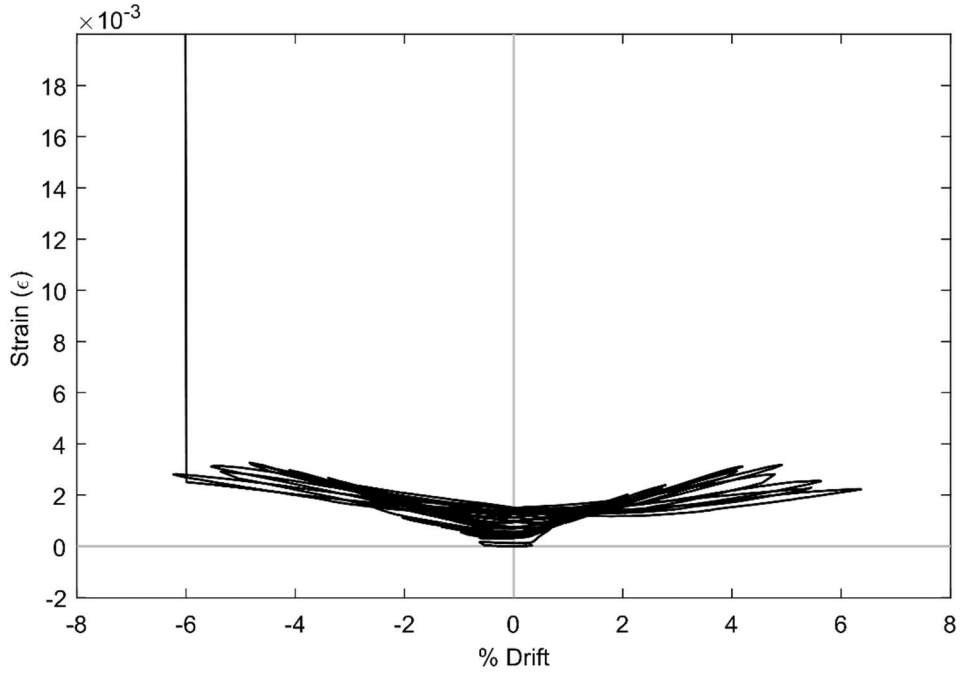

Figure 90. SG SBJ7 (PTB_9_2_0_6)

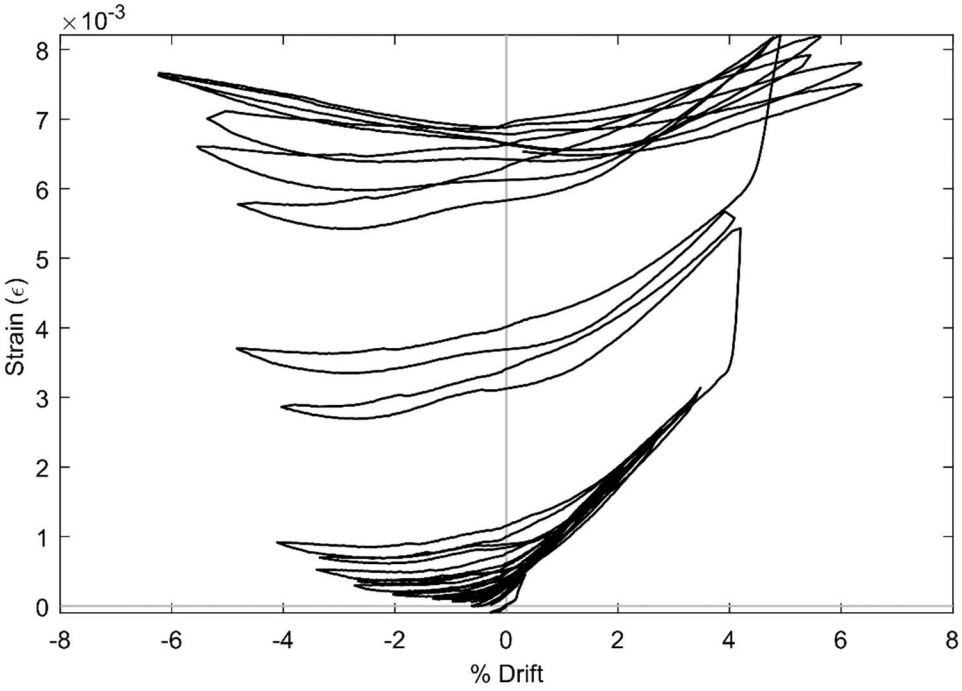

Figure 91. SG SBL7 (PTB_9_2_0_6)

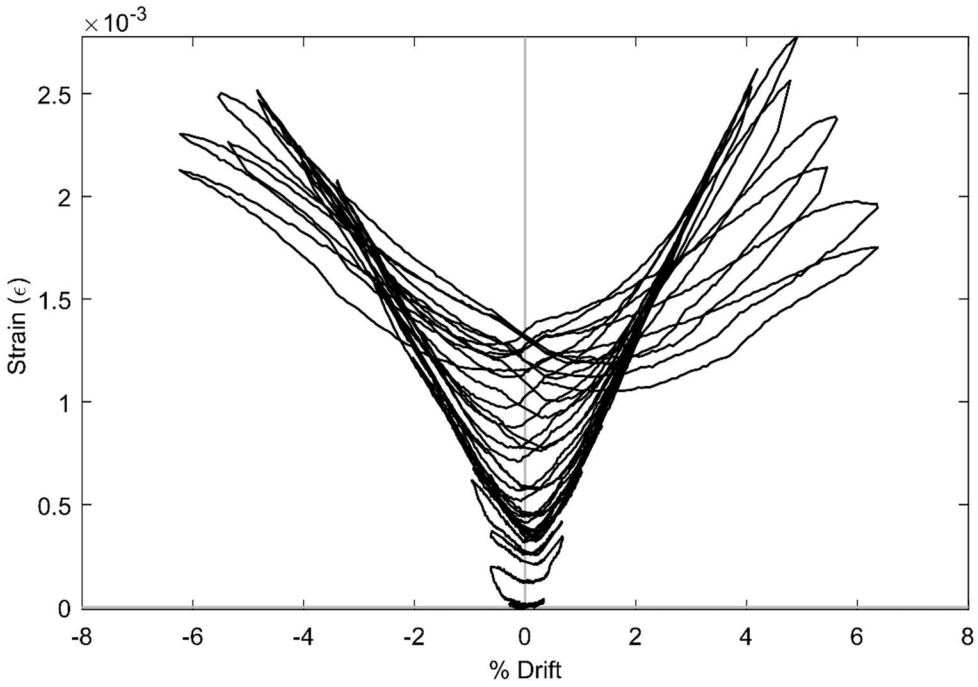

Figure 92. SG SBJ8 (PTB_9_2_0_6)

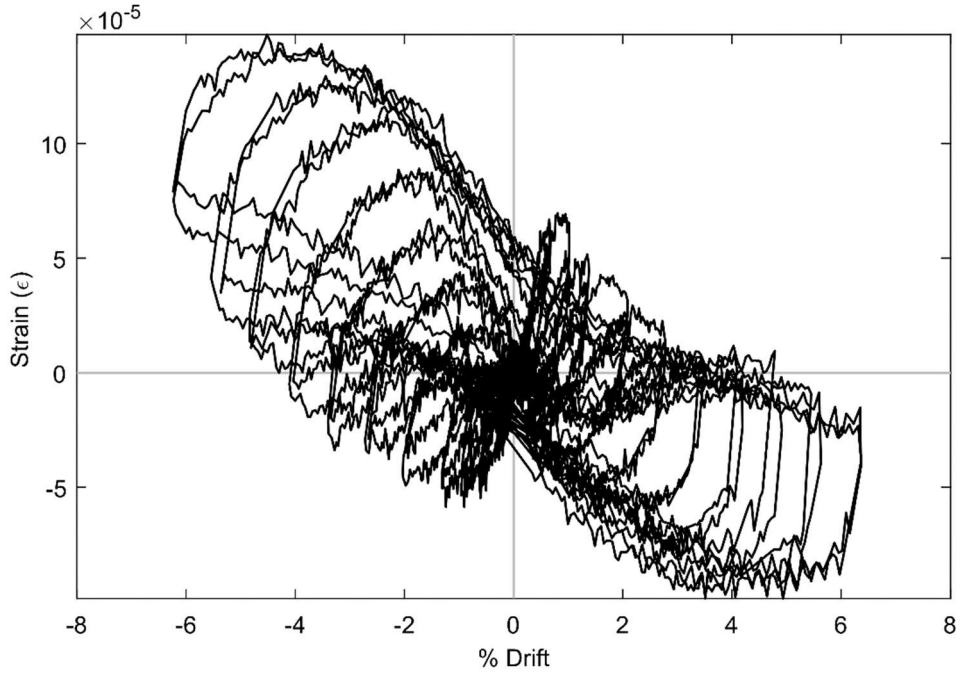

Figure 93. SG CC1 (PTB_9_2_0_6)

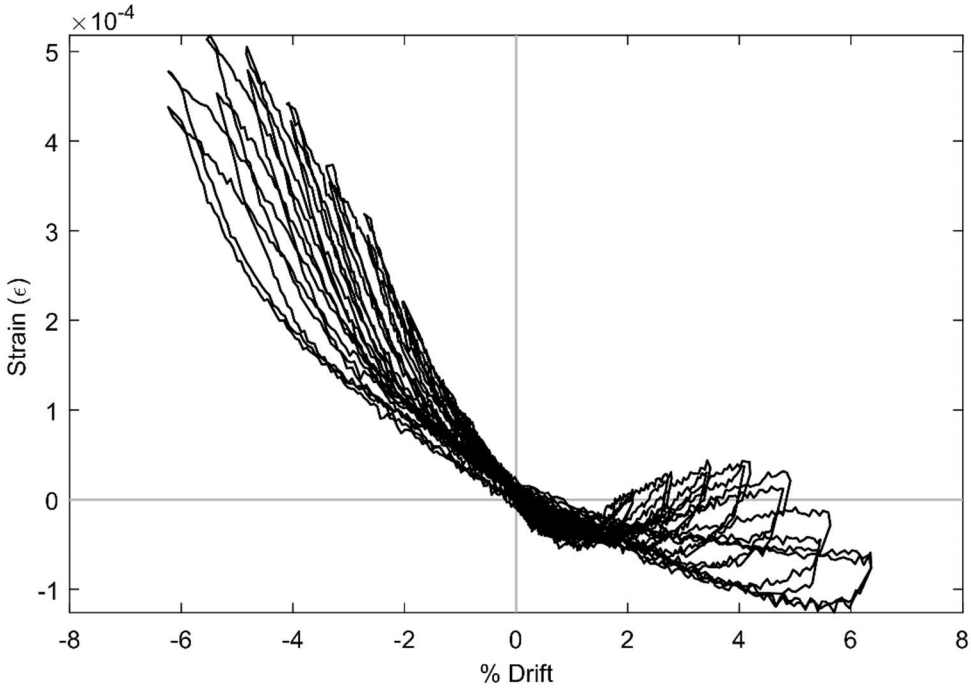

Figure 94. SG CC2 (PTB_9_2_0_6)

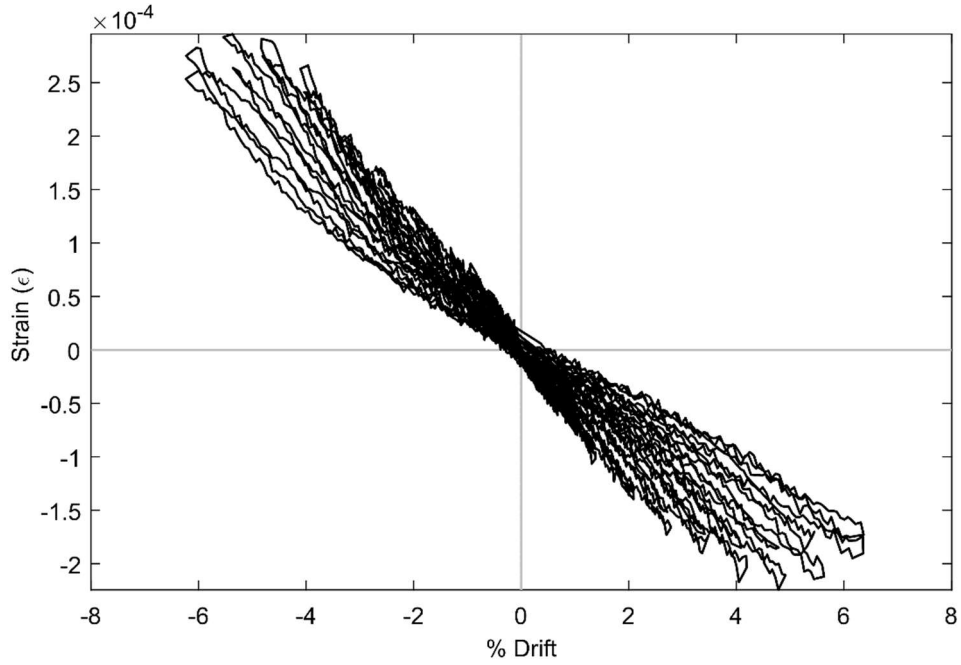

Figure 95. SG CC3 (PTB_9_2_0_6)

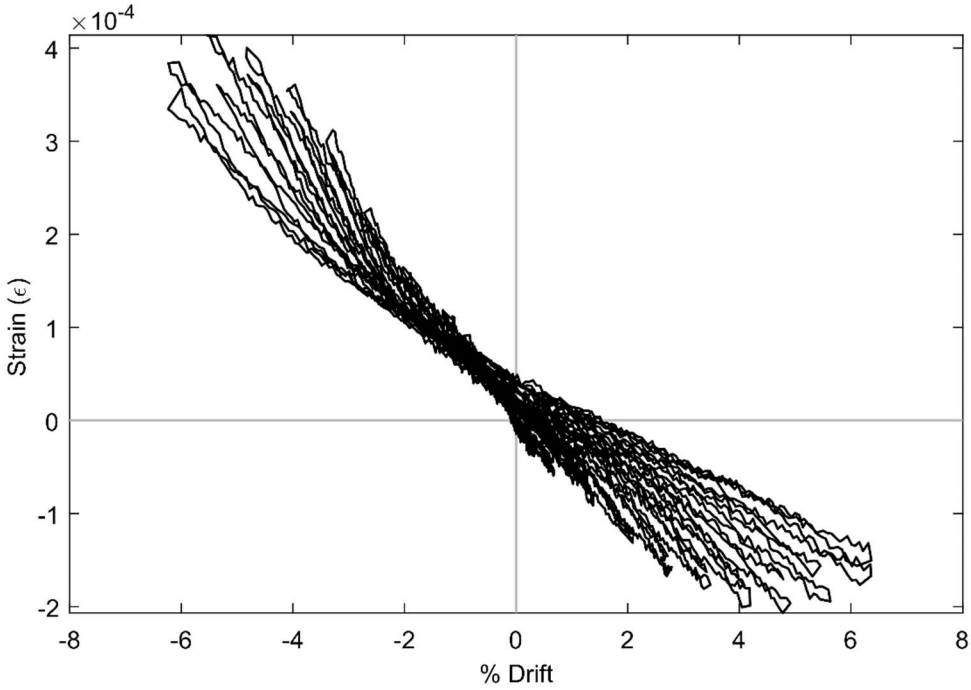

Figure 96. SG CC4 (PTB_9_2_0_6)

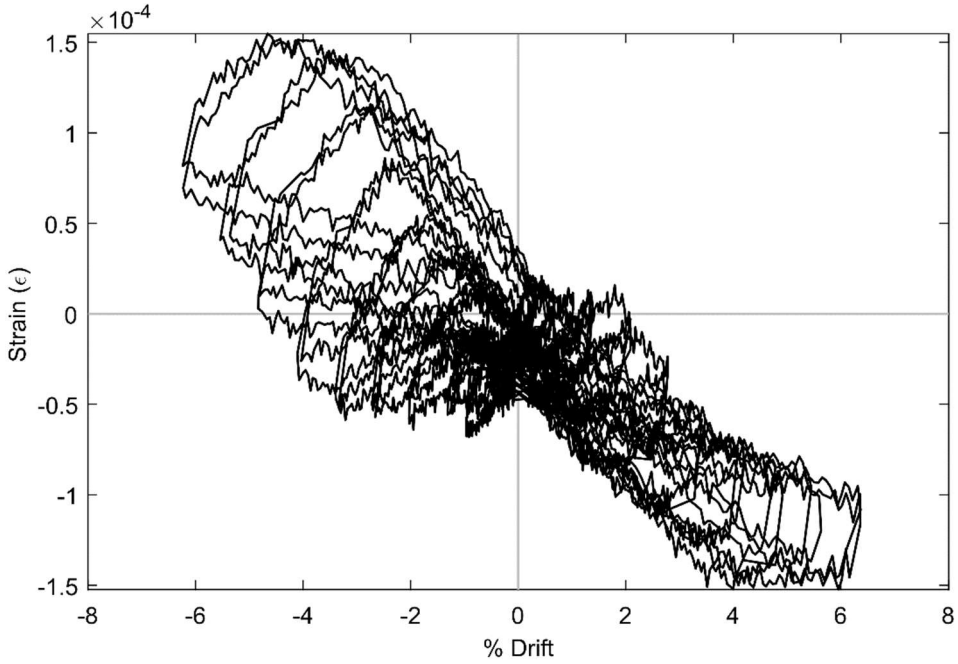

Figure 97. SG CD1 (PTB_9_2_0_6)

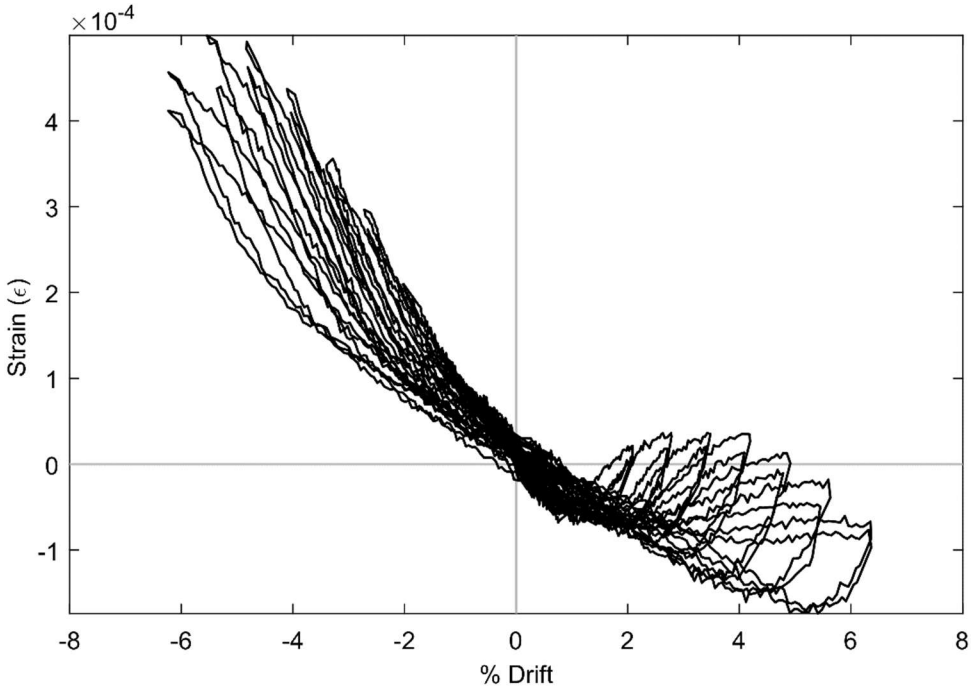

Figure 98. SG CD2 (PTB_9_2_0_6)

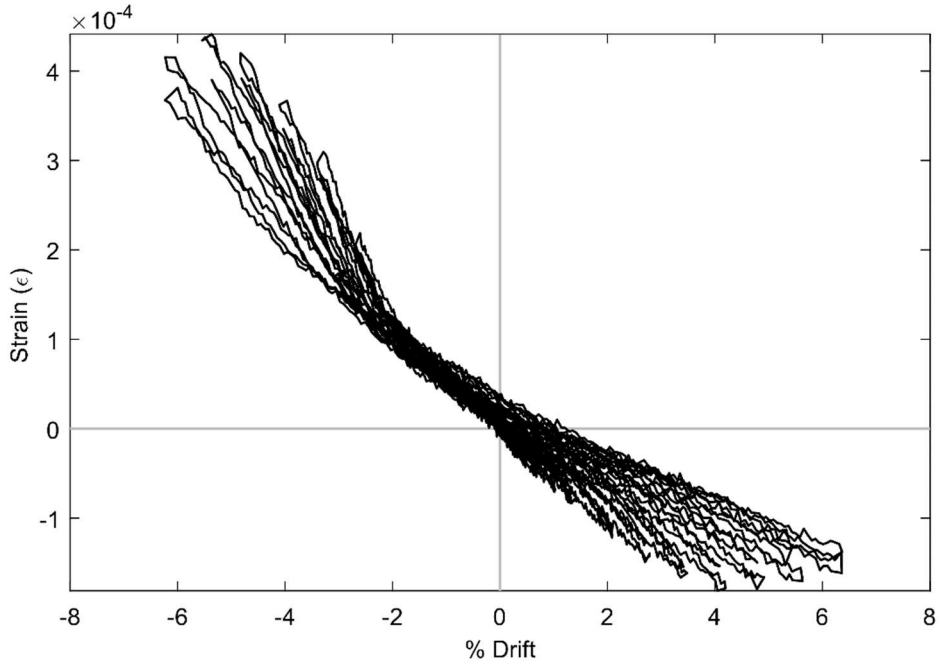

Figure 99. SG CD3 (PTB_9_2_0_6)

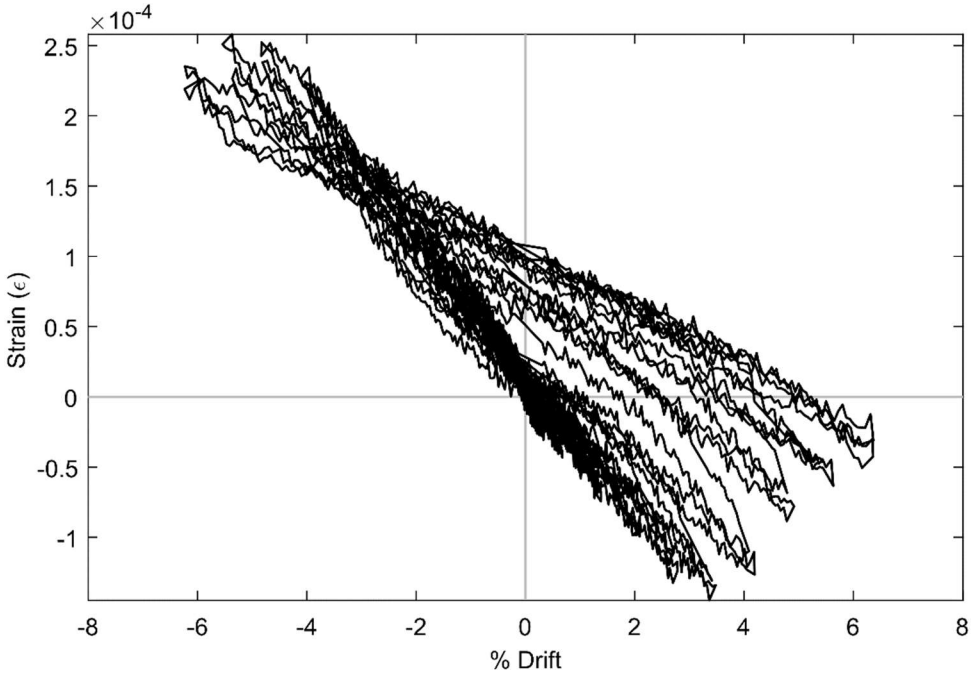

Figure 100. SG CD4 (PTB_9_2_0_6)

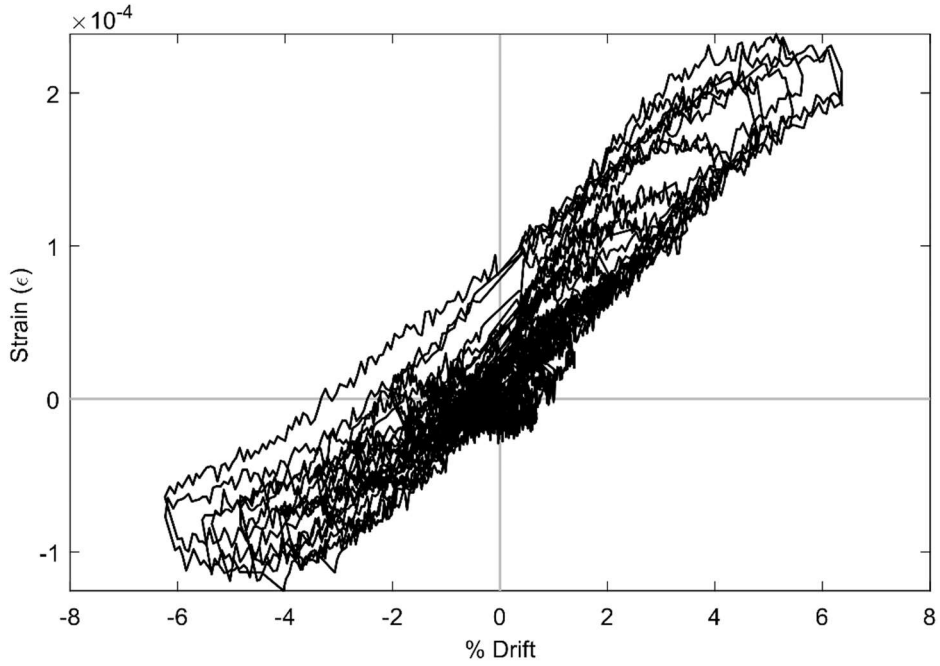

Figure 101. SG CH1 (PTB_9_2_0_6)

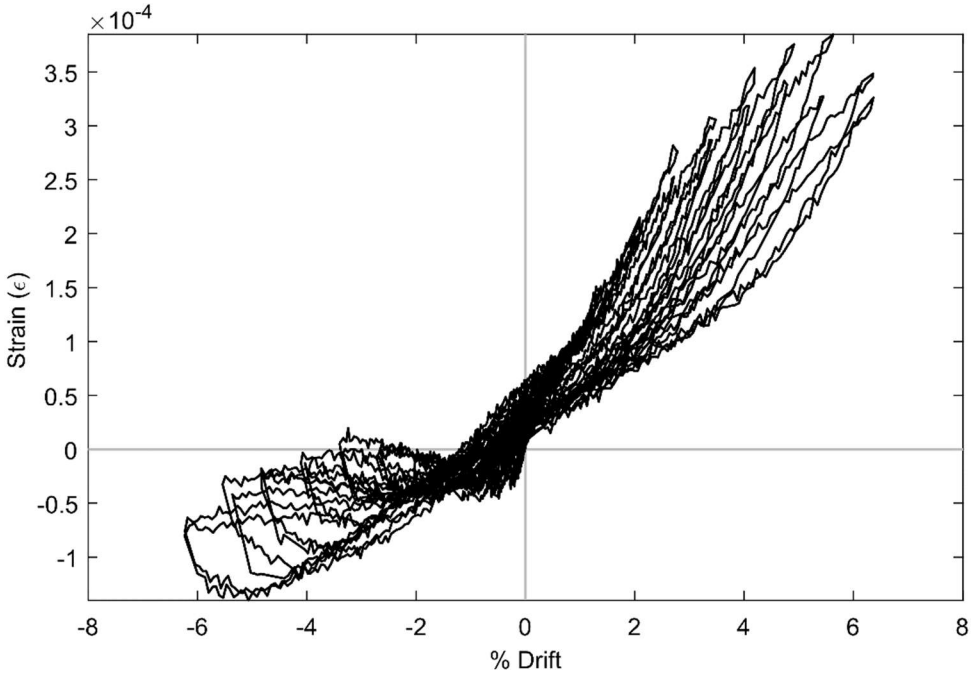

Figure 102. SG CH2 (PTB_9_2_0_6)

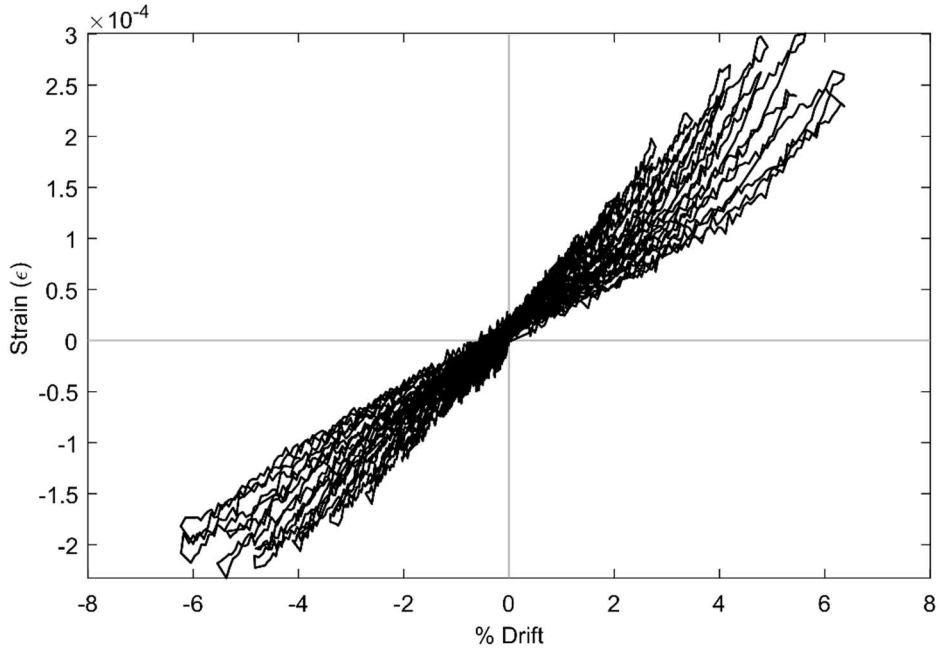

Figure 103. SG CH3 (PTB_9_2_0_6)

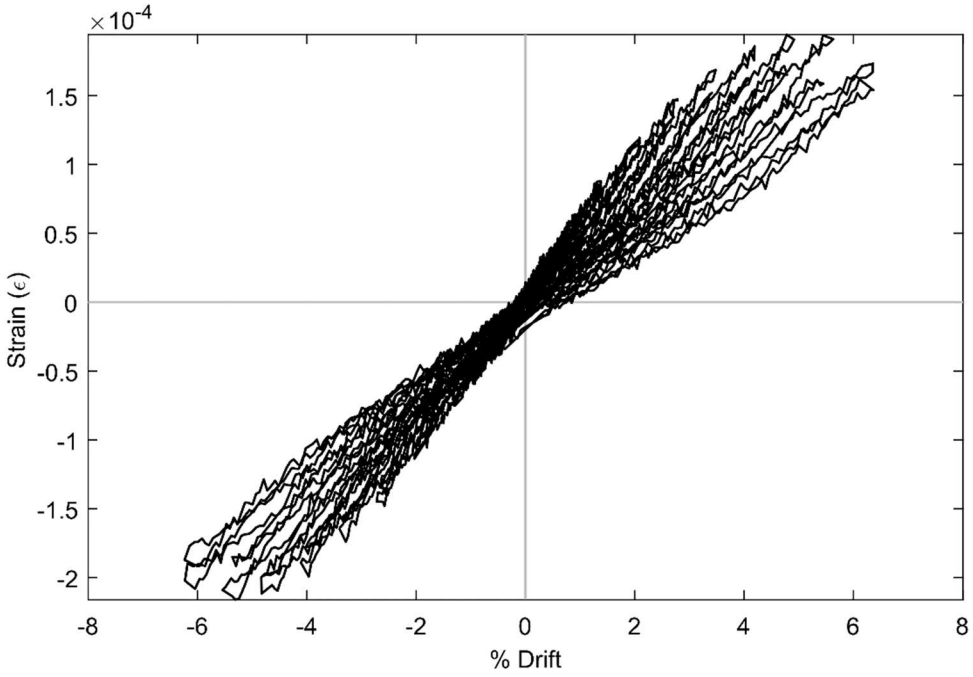

Figure 104. SG CH4 (PTB_9_2_0_6)

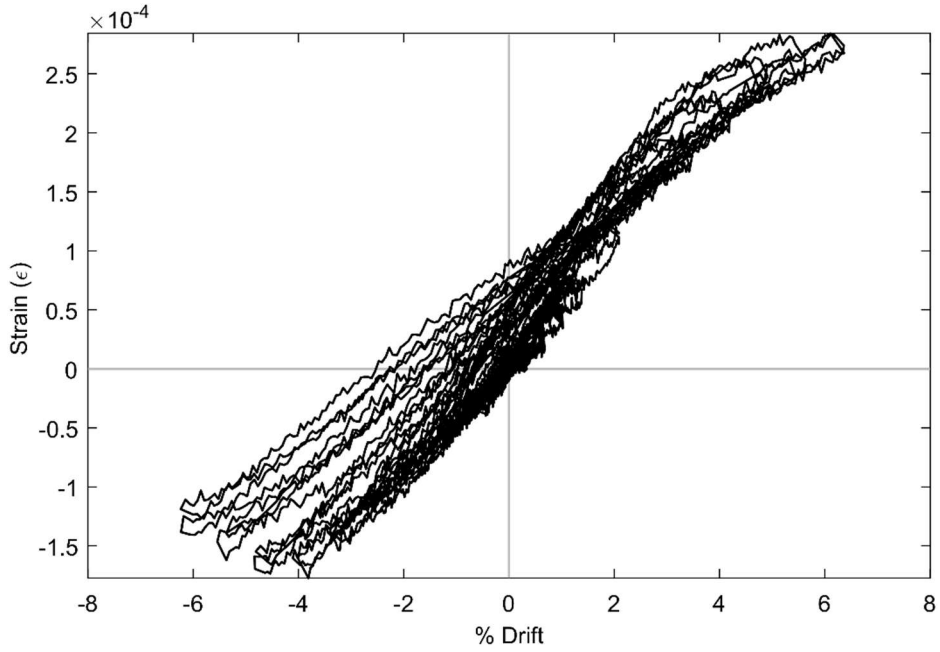

Figure 105. SG CI1 (PTB_9_2_0_6)

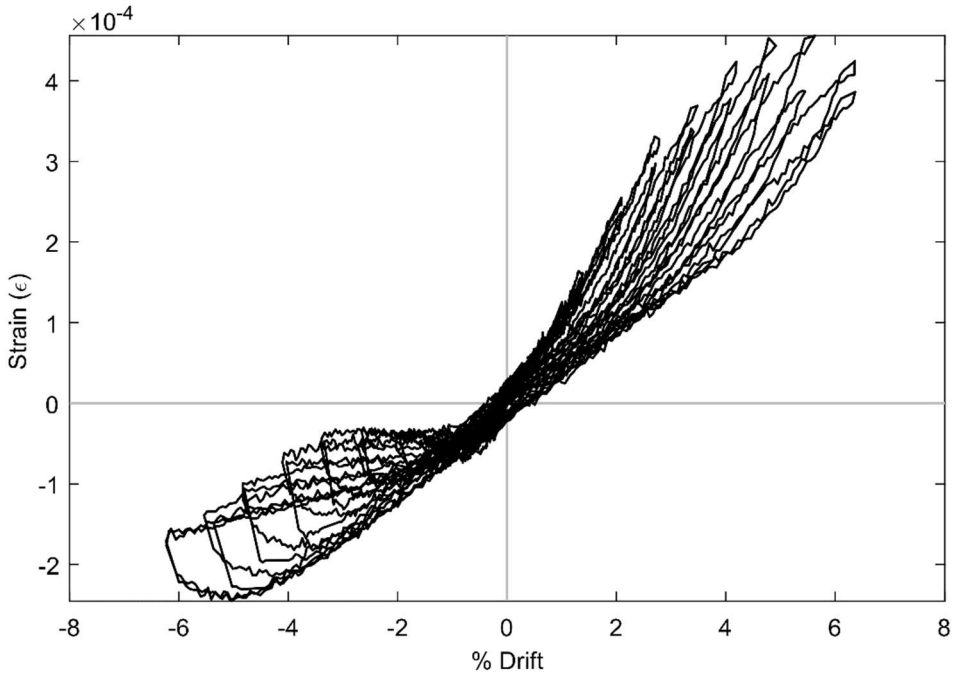

Figure 106. SG CI2 (PTB_9_2_0_6)

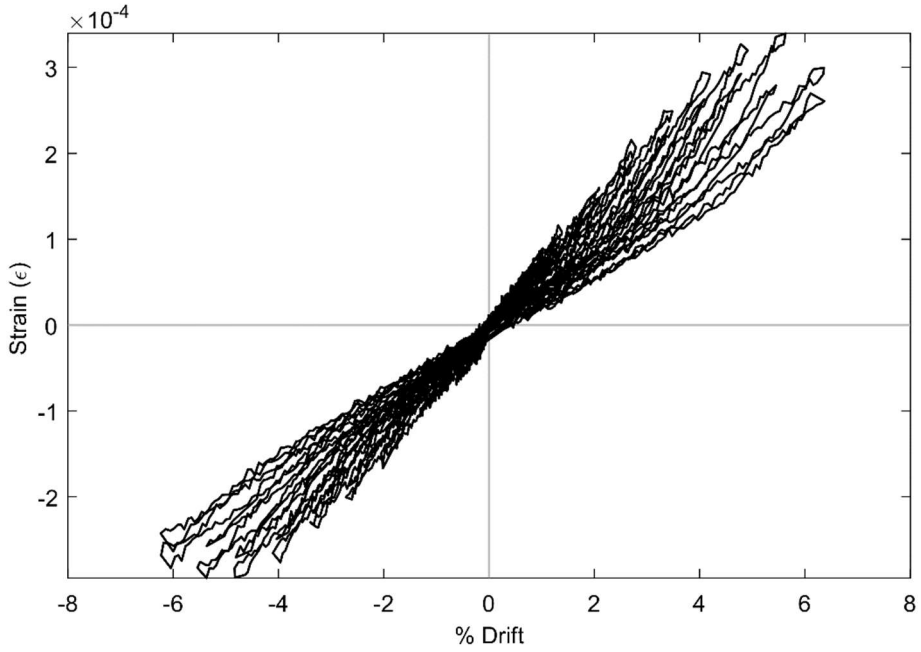

Figure 107. SG CI3 (PTB_9_2_0_6)

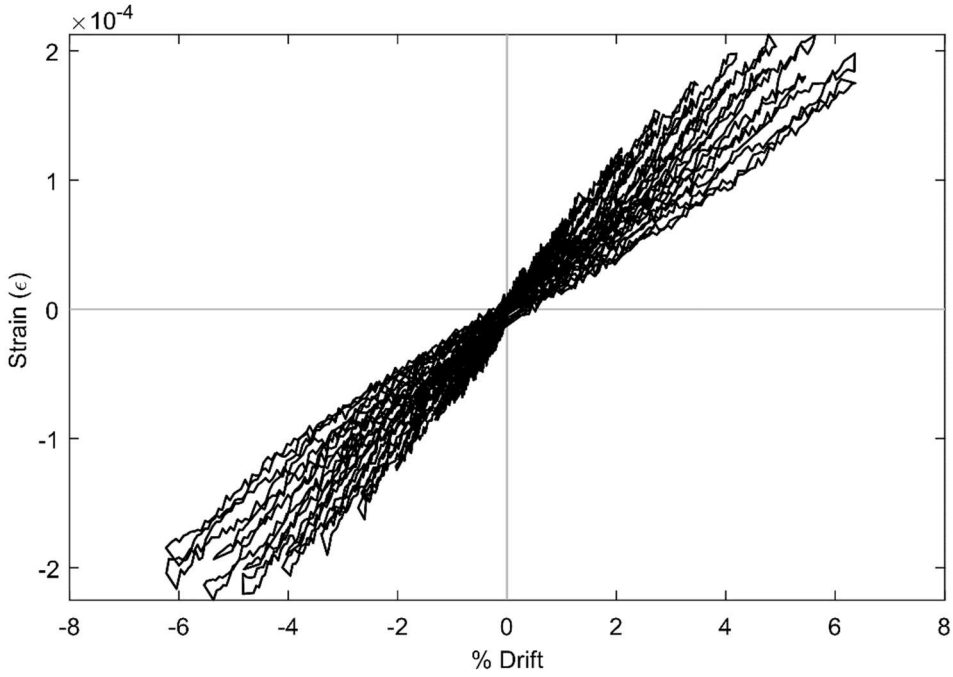

Figure 108. SG CI4 (PTB_9_2_0_6)